Early Seeds and Cosmic Skies:
Quantum Origins of the Universe and Insights from Large-Scale Structure

Yaniv Donath

Department of Applied Mathematics and Theoretical Physics
University of Cambridge

This dissertation is submitted for the degree of

Doctor of Philosophy

Homerton College

April 2025

Let's cook up a universe, shall we?

Declaration of Originality

This thesis is the result of my own work and includes nothing which is the outcome of work done in collaboration except as declared in the preface and specified in the text. It is not substantially the same as any work that has already been submitted, or is being concurrently submitted, for any degree, diploma or other qualification at the University of Cambridge or any other University or similar institution except as declared in the preface and specified in the text. It does not exceed the prescribed word limit for the relevant Degree Committee.

Chapters 1-4 have been entirely written by me. Although they sometimes present topics in a new way, they do not contain novel results.

Chapter 5 is based on the publication [1]: YD and E. Pajer, "The in-out formalism for in-in correlators," *JHEP* **07** (2024) 064. This work was carried out under the supervision of Enrico Pajer. Almost all results and writing have been done in collaboration. The non-perturbative proof was performed by Enrico Pajer, and the perturbative ones by myself. The pole bagging was discovered in a flat space by Enrico Pajer and generalised to other spacetimes by me. I mostly wrote recursion relations and cutting rules under the supervision of Enrico Pajer, who also developed the scattering preview.

Chapter 6 is based on the publication [2]: G. D'Amico, YD, M. Lewandowski, L. Senatore, and P. Zhang, "The one-loop bispectrum of galaxies in redshift space from the Effective Field Theory of Large-Scale Structure," *JCAP* **07** (2024) 041. This paper was primarily written by Matthew Lewandowski and me under the supervision of Leonardo Senatore. My focus was slightly more on developing the bias expansions and renormalisation for biased tracers in redshift space. This inevitably led to the more careful renormalisation of dark matter, which was done in collaboration with Matthew Lewandowski. The full renormalisation in real and redshift space and the UV checking have been done in collaboration. The writing of the paper has been split between Matthew Lewandowski and myself, where I focused more on biased tracers. Large sections have also been written by Leonardo Senatore, and the whole work was in collaboration with him. Pierre Zhang and Guido D'Amico were primarily responsible for writing the Python implementation.

Chapter 7 is based on the publication [3]: G. D'Amico, YD, M. Lewandowski, L. Senatore, and P. Zhang, "The BOSS bispectrum analysis at one loop from the Effective Field Theory of Large-Scale Structure," *JCAP* **05** (2024) 059. My involvement in this paper was smaller than in the previous ones. The data analysis was largely performed by Guido D'Amico, Pierre Zhang and Leonardo Senatore. My largest contribution to this paper was the Mathematica implementations of the Bispectrum loop for biased tracers in redshift space, eventually leading to the Python implementation. I was involved with the binning formulas in the appendix and the formalism for the multipoles. Matthew Lewandowski and I wrote up the theory model.

Chapter 8 is based on the publication [4]: D. Braganca, YD, L. Senatore, and H. Zheng, "Peeking into the next decade in Large-Scale Structure Cosmology with its Effective Field Theory," arXiv:2307.04992. I developed this paper under the supervision of Leonardo Senatore and I implemented the formulas and approximations for the Fisher forecast. Independent codes and checks of all results were done by Henry Zheng, and further inputs were given by Diogo Braganca. These two authors also implemented the integration technique for the loops. The perturbativity prior was proposed by Leonardo Senatore and was developed by me together with Henry Zheng. The paper was written partly by Leonardo Senatore and largely by me.

Chapter 9 is based on the publication [5]: YD, M. Lewandowski, and L. Senatore, "Direct signatures of the formation time of galaxies," *Phys. Rev. D* **109** (2024) 123510. This paper was done in close collaboration with Matthew Lewandowski under the supervision of Leonardo Senatore. The initial effect of the non-locality in time at fifth order was derived by myself and later confirmed and systematised with Matthew Lewandowski. I found the recursion relations, and the proof was done in collaboration with Matthew Lewandowski. The paper was written in collaboration with Matthew Lewandowski and Leonardo Senatore.

Chapter 10 is based on the publication [6]: G. D'Amico,YD, L. Senatore, and P. Zhang, "Limits on clustering and smooth quintessence from the EFTofLSS," *JCAP* **03** (2024) 032. In this paper, I developed and wrote the theory of biased tracers in redshift space in the presence of quintessence under the supervision of Leonardo Senatore. Guido D'Amico and Pierre Zhang performed the data analysis, which was also written up by those authors.

Summary

Dark matter, dark energy and inflation form the backbone of the current cosmological model. Collectively, they paint a picture of a universe's structure sourced by quantum fluctuations and then billions of years of gravitational clustering in an expanding universe. These concepts are illustrated in Part I, which serves as an introduction. This thesis then breaks new ground on all three topics: we simplify inflationary calculations, showcase the power of current and future large-scale structure analyses, and advance our understanding of galaxy formation and the nature of dark energy.

In Part II, we establish a technique to better understand cosmological correlators, the primary observable in the inflationary universe. Traditionally, cosmological correlators are computed with the standard but complicated Schwinger-Keldysh in-in formalism. Here, we show that for non-dissipative systems, we can calculate correlators using the more widely used in-out formalism. In de Sitter space, we achieve this by extending the expanding Poincaré patch with a contracting one. This leads to simplified calculations with fewer Feynman diagrams and only one propagator.

Part III jumps forward a couple of billion years, and we study the clustering of dark matter and galaxies in the mildly nonlinear regime using its Effective Field Theory. Specifically, we develop the one-loop bispectrum of galaxies in redshift space, addressing key subtleties about its renormalisation. We then analyse BOSS data and demonstrate that the inclusion of the bispectrum significantly reduces error bars in key cosmological parameters compared to using only the power spectrum, showcasing the importance of including the one-loop bispectrum in future data analyses. Finally, we forecast the predictive power of two next-generation galaxy surveys, DESI and MegaMapper, again using the loop power spectrum and bispectrum. Our analysis focuses on new physics, such as neutrino masses, and, more ambitiously, on primordial Non-Gaussianity - a key probe of the nature of inflation.

In Part IV, we discuss two topics in the late universe. We develop a method to obtain direct signals of the formation time of galaxies and show that the large-scale distribution of galaxies is sensitive to their formation time. This is due to additional parameters appearing in the bias expansion when assuming galaxies form over a prolonged period of time. Lastly, we turn to dark energy, where we model the influence of clustering quintessence on the distribution of galaxies. Again, we analyse BOSS data, this time with particular emphasis on the dark energy equation of state parameter.

Acknowledgements

If you want to become a great chef, you have to work with great chefs.
And that's exactly what I did.

- Gordon Ramsay

First and foremost, I would like to thank my supervisors, Paul Shellard and James Fergusson, for their support during my PhD and for their trust in the many paths I followed in my work.

I am immensely lucky to have crossed paths with Leonardo Senatore early in my career, who has since become my main collaborator on half a dozen projects. Your profound understanding of physics - and fields beyond - is truly enriching. Your energetic approach to physics, coupled with your deep conviction in the necessity of doing proper, robust, and effective physics (pun intended), has profoundly shaped my approach to science.

I am greatly indebted to Enrico Pajer, both as a collaborator and as a steadfast support at DAMTP. From our earliest discussions on in and out states, I truly enjoyed the free exploration of ideas in hour-long sessions that were simply fun. Your patience, kindness and strive for intuition and clarity have transformed my understanding of physics, truly pushing me forward.

To my excellent collaborators along the way, Matt, Guido, Pierre, Henry, and Diogo, thank you for your incredible contributions. These projects would not have been possible without our outstanding teamwork and the complementary skills you bring.

I am incredibly grateful to DAMTP for providing the academic ground we build on daily. Starting by giving me an office next to the former office of the great Stephen Hawking, to the many outstanding seminars, speakers and people. To my fantastic office mates, Johnnie, Harry, Irene and my other fellow PhD students, David, Alexander, Yoann, Ericka, Petar, Bowei, Lasse, Andrea, Santi, Ciaran, and Gordon, it was a pleasure being surrounded by you both at DAMTP and especially on conferences near and far.

To the many lifelong friends I've made along the way - you are the real magic of Cambridge. This acknowledgements section would be too long if I listed you all, so I

have to coarse-grain. To everyone in those infamous group chats: The "Griff?" that usually ended in wine and cheese and not the Griff [1], succeeded by the "Homies" chat and then the "Market Much" eventually turning into "Survivors", as all the masters students left. To my cultural lifeline in the "Friday Night Dinner" chat and finally to my foodie friends in "In the mood for food" ensuring I eat well - even in England.

To my incredible family for their steadfast, unwavering support. In particular, I thank my mom for providing me with the foundation and courage to pursue my dreams. To my dad for guidance in the academic world, philosophical depth, and many culinary adventures. To my brothers for always pushing me, welcoming me around the world, and sometimes letting me win in tennis.

I'm incredibly grateful to have had the opportunity to work on this thesis from over 22 countries; this is genuinely the marvel of a dry lab PhD. I want to thank the hospitality of each one of them: Australia, Cambodia, Costa Rica, Czech Republic, Dominican Republic, England, France, Germany, Guadeloupe, Israel, Italy, Japan, Jordan, Panama, Portugal, Scotland, South Korea, Spain, Switzerland, Thailand, United States, Vietnam.

Lastly, I want to thank me. Nivu, we've come a long way.

[1] The "Griff', short for "The Griffin Bar", refers to the Homerton College bar.

Contents

1

Introduction

The history of the universe spans incomprehensibly vast scales of time and space. According to our current cosmological models, we can describe the universe from approximately 10^{-35} seconds after the beginning of time. During this infinitesimally early stage, we believe that one or more quantum fields drove a phase of dramatically rapid, accelerated expansion, commonly referred to as inflation. Eventually, these fields decayed, transferring their energy to the Standard Model particles known to us, such as electrons, photons, quarks, and neutrinos. This period left behind a crucial signature: tiny quantum fluctuations from inflation seeded slightly denser (hotter) and less dense (cooler) regions of the primordial universe.

After about 370,000 years, as the universe expanded and cooled sufficiently, protons and electrons combined to form neutral atoms. Light, no longer bound by the primordial plasma, was then able to detach and travel freely to reach us today, forming the Cosmic Microwave Background (CMB) - a snapshot of the very early universe. Though this afterglow from the Big Bang is extremely uniform, the tiny ripples visible to us make the CMB the most precise cosmological probe to date.

Over the next hundreds of millions of years, the universe entered a phase of gravitationally induced magnification of these fluctuations. Matter streamed toward the denser regions, leaving the slightly underdense areas even emptier. This period exemplifies the immense hierarchy of scales in physics: It took hundreds of millions of years of gravitational collapse to eventually light up the first stars. About one billion years later, the first galaxies formed, and fast forward to today - 13.8 billion years after the universe's inception - the gravitational pull resulted in billions of galaxies in colossal clusters.

The visible narrative is, however, only a small part of the story. Two integral components of the cosmological model dominate the universe. Dark matter, unlike ordinary matter, is not visible to us other than through its gravitational effects. We

can 'see' it through its gravitational lensing effects [1], it is essential to explain the measurements of the CMB, and in the large-scale structure, dark matter is necessary to form the gravitational wells to form galaxies. Meanwhile, dark energy, which constitutes the majority of the universe's energy, is driving the accelerated expansion of space itself, likely driven by a cosmological constant - a constant vacuum energy with ever-increasing influence as space expands.

Cosmology has now evolved into a precision science, coalesced into a robust framework known as the ΛCDM - Λ is the symbol for the cosmological constant, and CDM stands for Cold Dark Matter. The solidity of this base model positions cosmology at the forefront of efforts to measure physics beyond our current models. In the mission to extract as much information as possible from the cosmos, the work presented in this thesis can be roughly categorised into three interwoven efforts of cosmology.

Our clearest insights into the universe's composition and evolution - including early hints at the initial quantum fluctuations - thus far come from studying the distribution of the fluctuations in the CMB. However, the CMB ultimately only provides a two-dimensional snapshot of the early epoch of the universe. Recognising that the early fluctuations gave rise to the structures we see today - galaxies and a web of dark matter - Large-Scale structure (LSS) cosmology can extract three-dimensional data from billions of years of cosmic evolution. While this offers greater sensitivity to the evolution of the universe, the three-dimensional nature of LSS data also surpasses the information content in the CMB. The challenge lies in untangling billions of years of gravitational clustering - an issue less dominant in the CMB. A major theoretical breakthrough in the modelling of gravitational clustering of dark matter and galaxies is the Effective Field Theory of Large-Scale Structure (EFTofLSS). It disentangles the large scales of interest from the complicated small-scale physics while still capturing how the small-scale physics affects the larger scales. The EFTofLSS has already been able to extract cosmological information from galaxy surveys [7], and there is a large ongoing effort to refine its predictions for current and future data sets.

Although ΛCDM explains almost all current observations exceedingly well, it must be incomplete. It does not integrate with the broader model of high-energy physics. For example, we have very little knowledge of the particle nature of dark

[1] Light follows the shortest path in space, which is curved by the presence of dark matter, effectively bending the light like a lens.

matter [2], the quantum field theory (QFT) in curved spacetime that underpins inflation remains poorly understood, and the nature of dark energy remains an open question - both theoretically and in light of tensions between early and late time measurements. This avenue of cosmology pursues more complete models of the universe, exploring extensions to the standard cosmological model.

Perhaps the most exciting prospect in cosmology is its potential to access energy scales that are far beyond the energy scales we can test on Earth. Inflation is estimated to have occurred at an energy scale about 10^{12} times higher than the highest energies probed by current colliders, making the early universe the ultimate observational probe of high-energy physics - possibly even for quantum gravity. This idea, called the cosmological collider program [8], explores the possibility that high energy particles in the early universe may have interacted with the inflaton, leaving an imprint on the distribution of matter. We need to have an extraordinary understanding of the inflationary universe to achieve the precision needed to detect these faint signals - much like our extraordinary understanding of structure formation and the composition of the universe will likely soon allow us to measure the mass of neutrinos. If we reach a similar level of understanding of the inflationary universe, we can probe for the highest of energies in physics.

[2]The mass of the dark matter particle is among the least constrained numbers in all of physics.

Overview of this Thesis

This thesis consists of four parts. The first part serves as an introduction, and the remaining parts are ordered according to the evolution of the universe.

Part I introduces all the cosmological parameters that we discuss in this thesis. In the process of introducing all of those parameters, we simultaneously also cover the key concepts upon which the later chapters build. In Ch. 2, we introduce the Hubble parameter H_0, the key fractional densities $\{\Omega_m, \Omega_k, \omega_{cdm}, \omega_b\}$, the dark energy equation of state parameter of w, and the sum of neutrino masses $\sum_i m_{\nu_i}$ in the context of the background constituents and evolution of the universe. We then turn to the perturbed universe in Ch. 3, where we introduce dark matter clustering parameters, σ_8 and S_8. This chapter also provides an overview of relativistic and non-relativistic perturbation theory, including the conceptual introduction to the EFTofLSS. Finally, Ch. 4 focuses on inflation, where we derive the inflationary power spectrum, introducing the amplitude parameter A_s and the spectral index n_s. We complete the set of parameters by presenting the non-Gaussianity parameters $\{f_{NL}^{\text{loc.}}, f_{\text{NL}}^{\text{eq.}}, f_{\text{NL}}^{\text{orth.}}\}$, derived explicitly with in-in calculations from the Effective Field Theory (EFT) of Inflaton. This discussion also introduces the in-in formalism, which lays the basis for the next part of this thesis.

Part II aims to better understand cosmological correlators and inflation. Here, we show that instead of relying solely on the in-in formalism introduced in Ch. 4, cosmological correlators can also be computed using the more familiar in-out formalism. This approach allows us to calculate with standard in-out Feynman rules, and we can leverage established techniques from the in-out framework to be directly applied to cosmological correlators. We illustrate this with a number of examples, such as obtaining correlators as a sum over residues of Feynman propagators, deriving recursion relations for flat space correlators, and developing new cutting rules. Finally, with the in-out formalism for cosmological correlators, we can define an S-matrix that satisfies the standard optical theorem.

Part III is composed of three chapters based on a series of papers in large-scale structure cosmology, bridging the early and late universe. In Ch. 6, we extend the introductory EFTofLSS material from Ch. 3 and present the full development of the power spectrum and bispectrum of galaxies in redshift space at one loop. This is a very technical chapter showcasing the full renormalisation of these observables. We then show two applications of this theory. First, in Ch. 7, we analyse BOSS data [9] using the EFTofLSS power spectrum and bispectrum prediction, highlighting the

importance of the bispectrum loop. Finally, in Ch. 8, we analyse the constraining power of future galaxy surveys. In particular, we focus on the detectability of neutrino masses and primordial non-Gaussianity. The parameters analysed and forecasted in the latter two chapters have all been introduced in Part I.

Part IV explores two key aspects of late-universe cosmology. In Ch. 9, we investigate how the timescales of galaxy formation imprint themselves on the large-scale distribution of galaxies - an effect captured by three parameters in the EFTofLSS. In this process, we find great simplifications for bias expansions in the form of recursion relations, which we also prove in this chapter. This work extends the discussion of the non-locality in time from Ch. 3. Finally, we analyse dark energy models motivated by the EFT of dark energy, specifically clustering and smooth quintessence. Here, we develop the theory of biased tracers in the presence of quintessence in the EFTofLSS up to the one-loop power spectrum. This entails doing perturbation theory with exact time dependence, leading to several subtleties in Ch. 10. Using BOSS data, we finally analyse the equation of state parameter of dark energy in great detail.

Part I

How we Parametrise and Model the Universe

2

The Smooth Universe

2.1 Introduction

It is ambitious in and of itself to try to describe the universe as a whole. In this ambitious quest, it is likely the best idea to start as simple as we can. This is what we start with in this section. We introduce the defining symmetries of the universe on large scales and discuss the contents of this smooth universe. We can then, through the general theory of relativity, derive the universe's evolution at large. Luckily, our universe is, in fact, quite smooth, and therefore, some parameters that determine the evolution of the universe can already be introduced in this chapter. In particular, relevant for Chs. 7 and 8 we here introduce the Hubble parameter H_0 and the dimensionless Hubble parameter h, key fractional densities $\{\Omega_m, \Omega_k, \omega_{cdm}, \omega_b\}$ as well as the dark energy equation of state parameter w relevant for Ch. 10 and neutrino masses $\sum_i m_{\nu_i}$ for Ch. 8.

2.2 The Background Geometry

As stated in the introduction, cosmology is concerned with describing the universe as a system. One of the first things we can ask about a system is what its geometry is. Is the universe flat? Is it evolving? What do we even know about the universe? The answer to this is in part based on evidence and partly based on philosophy. The first important observation is that on very large scales, the universe looks the same in every direction we look. We call this principle isotropy, which is observationally confirmed to extreme precision [10]. Then, we invoke a philosophical argument, assuming that Earth, or even the Milky Way, does not have a special place in the universe. That is, if one were to observe the universe from a completely different point, the universe would also seem isotropic. We call this principle of the universe looking the same from every place homogeneity, and of course, it is hard to test since, on cosmological scales, we cannot really move. Nevertheless, it is difficult

to picture a universe that is not homogeneous. Together, homogeneity and isotropy form the cosmological principle, and to first approximation, almost all cosmology is described this way.

One can show that only three three-dimensional spaces satisfy homogeneity and isotropy: flat space, a sphere and hyperbolic space. The principles invoked so far do not say anything about the evolution of the universe. Historically, there were many attempts to model the universe as a steady, time-invariant object [11]. There was, however, overwhelming evidence against it, as well as difficulties modelling it even mathematically [12, 13]. In the most fundamental geometric construction of the universe, we, therefore, are inclined to stay neutral about the time evolution of the universe.

To summarise, we assume the universe is homogeneous and observe the universe to be isotropic. Furthermore, we are agnostic about its time evolution. This leads us to the Friedmann-Robertson-Walker (FRW) metric, which describes the spacetime of a universe satisfying the above principles [1]

$$ds^2 = -dt^2 + a(t)^2 \left[d\vec{x}^2 - K \frac{x_i x_j dx^i dx^j}{1 - K\vec{x}^2} \right] \quad \text{with} \quad K = \begin{cases} +1, & \text{spherical,} \\ 0, & \text{flat,} \\ -1, & \text{hyperbolic,} \end{cases} \tag{2.1}$$

where $a(t)$ is called the scale factor and is a measure of how the universe expands (or may contract). Through the scale factor, we directly introduce one of the most important scales in cosmology, called the Hubble rate $H = \frac{\dot{a}}{a}$, where the dot denotes the time derivative $\dot{} = d/dt$. The Hubble scale $1/H$ separates the scales for which the expansion is relevant from the ones it is not relevant. Today, the Hubble radius is around 14 billion light years and thus cosmic expansion only becomes significant on scales vastly exceeding those encountered in our daily lives. In contrast, we think the Hubble radius in the early universe was $\sim 10^{-35}$ smaller! Therefore, the present-day Hubble parameter H_0 tells us something about the scale of the universe and, as we will see further below, also about its age. This is the first of the parameters we introduce in this section, and we will constrain in Ch. 7 using large-scale structure (LSS). For simplicity one usually normalises $H_0 = 100\,h\,\mathrm{km\ s^{-1}Mpc^{-1}}$, so that we measure h which is a dimensionless number or order one. The subindex 0 here and everywhere throughout this thesis indicates the present time value of the parameter.

[1] Throughout this thesis, we use natural units, i.e. $c = \hbar = 1$

We have set up the background geometry of a universe with a homogeneous and isotropic background. Right now, this universe is empty, which is obviously not true since, for example, this thesis could not exist otherwise. Hence, in the next section, we look at how we can populate the universe with ingredients like matter and radiation and how, in turn, the scale factor behaves because of the matter content.

2.3 The Background Constituents

As we mentioned in the introduction, on large scales, the universe appears isotropic, and our metric in Eq. (2.1) is currently set out to do exactly that. Therefore, the background matter fields will also be homogeneous and isotropic. From symmetry alone, homogeneity and isotropy completely restrict the background fields to have an energy-momentum tensor of the form

$$\bar{T}_{\mu\nu} = (\bar{\rho} + \bar{p})\bar{U}_\mu \bar{U}_\nu + \bar{p}\bar{g}_{\mu\nu}, \tag{2.2}$$

where $\bar{U}_\mu$ is the fluid's velocity relative to a comoving observer [2]. The functions $\bar{\rho}(t)$ and $\bar{p}(t)$ are the definitions of the coarse-grained [3] density and pressure of the fluid. Energy conservation on the level of the energy-momentum tensor means its divergence vanishes. For the 0 component, this implies

$$0 = \nabla_\mu \bar{T}^{0\mu} = \dot{\bar{\rho}} + 3H(\bar{p} + \bar{\rho}). \tag{2.3}$$

On large scales, the relation between the pressure and the density can be captured by a simple equation of state parameter $w = \bar{p}/\bar{\rho}$. As we discuss below, the equation of state parameter can be calculated for each of the different constituents of the universe. While w is known for most of the fields (like dark matter or radiation), different dark energy models predict different equation of state parameters. We derive and analyse this from first principles in detail in Ch. 10.

This simple form of Eq. (2.3) allows us to solve it exactly. In almost all scenarios, w can be taken as a constant [4] as we assume the physical laws governing the

[2] Comoving, means an observer moving with the expansion of the universe, but otherwise having constant spatial coordinates.

[3] Coarse grained, i.e. averaged over large scales because for now, we do not care what the microphysics of these fluids are. We care about their macroscopic description, purely relying on their symmetry properties on large scales.

[4] In [14], a weakly time-dependent equation of state was introduced to probe some dark energy

background fields do not change over the history of the universe. Then we have

$$\bar{\rho} = \bar{\rho}_0 \left(\frac{a}{a_0} \right)^{-3(1+w)}, \tag{2.4}$$

where $\bar{\rho}_0$ and a_0 are the density's and scale factor's present-day values. The exact value of w depends on which species of matter we want to consider. We briefly discuss the most important ones here.

For matter, pressure is caused by particle motion, and the energy density is the rest mass energy. For non-relativistic matter particles, the rest mass energy is much greater than the pressure, and therefore, we take $w_m = 0$. Within the total matter density $\bar{\rho}_m$, we can distinguish between baryonic matter $\bar{\rho}_b$ (like galaxies), $\bar{\rho}_{cdm}$ dark matter, and as we discuss below - neutrinos. We make special mention of these three components since we will be encountering them throughout this thesis.

By contrast, for massless particles like photons, radiation pressure becomes comparable to the energy density. The electromagnetic energy-momentum tensor is traceless $\bar{T}^{\mu}_{\mu} = 0$ [5], and therefore $-\bar{\rho} + 3\bar{p} = 0$. Hence, for radiation we have $w_\gamma = 1/3$.

Neutrinos need more careful modelling and are in between matter and radiation. In the early universe, when they were relativistic, we count them towards the radiation with equation of state parameter $w_\nu = 1/3$. From neutrino oscillations, we, however, know that the sum of neutrino masses must satisfy $\sum_i m_{\nu_i} > 0.06\text{eV}$ [15]. This means that with the decrease in temperature over the course of the evolution of the universe, we expect neutrinos to have become non-relativistic and behave like matter with $w_\nu = 0$. This transition from relativistic to non-relativistic leaves an imprint on the large-scale structure of the universe. In addition, the energy density of neutrinos at late times is proportional to their masses, i.e. $\bar{\rho} \propto \sum_i m_{\nu_i}$. While there is a lot of ongoing research [16, 17] on how exactly to model neutrinos for cosmological structure formation, these two signatures already let us constrain neutrino masses, and we will come back to this in Ch. 8.

For cosmology, perhaps the most interesting and uncertain equation of state parameter is the dark energy one. A prime candidate for dark energy is the cosmological constant, describing a constant vacuum energy parametrised by the constant

aspects capturing a large number of models beyond ΛCDM. There we take $w(a) = w_0 + (a_0 - a)w_a$, and can also be solved exactly to be $\bar{\rho} = \bar{\rho}_0 \left(\frac{a}{a_0} \right)^{-3(1+w_0+a_0 w_a)} e^{-3w_a(a_0-a)}$.

[5] One can find that the energy-momentum tensor for radiation must be traceless either through direct calculation, or purely by the conformal symmetry of Maxwell's equations.

Λ, describing the accelerated expansion of the universe exceedingly well. One typically adds the term $\Lambda g^{\mu\nu}$ to the Einstein Field equations, which we will encounter in the next section, describing the expansion as a purely geometrical property sourced by the vacuum energy of space. To discuss its properties in terms of the coarse-grained pressure and density, however, it is insightful to write it as an induced energy-momentum tensor

$$T^{\mu\nu} = -\rho_\Lambda g^{\mu\nu}, \tag{2.5}$$

where $\rho_\Lambda = \frac{\Lambda}{8\pi G}$ and from Eq. (2.2) we can immediately read off $\bar{p}_\Lambda = -\bar{\rho}_\Lambda$ and therefore $w_\Lambda = -1$. It is not clear, however, if the accelerated expansion is indeed caused by the cosmological constant. From a theoretical point of view, the size of the cosmological constant, as measured in cosmology, seems to be in stark disagreement with the vacuum energy predicted by quantum field theory [6]. Alternatives to the cosmological constant are an active area of research, in particular with regards to the Hubble tension [20, 21] and through recent measurements from DESI [22, 23]. In Ch. 10, we will in detail discuss one such proposal inspired by the Effective Field Theory of dark energy. We will, in particular, discuss the implications on the distribution of galaxies if there is a dark energy component with an equation of state parameter $w \neq -1$ and then also constrain this parameter with the data available. We typically reserve w, without any subscript for the general equation of state parameter for dark energy; as noted above, this is $w \to w_\Lambda = -1$ for a cosmological constant.

Finally, we note that, of course, all these constituents are present in the universe simultaneously, and we have to consider them all together for an accurate picture of the evolution of the universe. Therefore, for the large-scale behaviour of the universe, we typically consider an energy-momentum tensor with more than one field present. The full energy-momentum tensor is thus the sum of the individual ones so that $T_{\mu\nu} = \sum_i T_i^{\mu\nu}$ and therefore $\bar{\rho} = \sum_i \bar{\rho}_i$ and $\bar{p} = \sum_i \bar{p}_i$.

2.4 The Background Equations of Motion

In the last two sections, we have described the geometry of our homogeneous and isotropic spacetime and then analysed the general structure of the components of such a universe. The way these two parts interact is through the dynamics governed

[6] This is known as the cosmological constant problem, pointed out over fifty years ago [18, 19].

by the Einstein Field equations

$$R^{\mu\nu} - \frac{1}{2}Rg^{\mu\nu} = 8\pi G\, T^{\mu\nu}. \tag{2.6}$$

Note that by homogeneity and isotropy, the entire dynamics of the spacetime is parametrised through the scale factor. For a general energy-momentum tensor of the form Eq. (2.2) and the FRW-metric Eq. (2.1), we can then obtain the dynamics of the spacetime with the equations of motion for a, called Friedmann-equations:

$$\left(\frac{\dot{a}}{a}\right)^2 = \frac{8\pi G}{3}\bar{\rho} - \frac{k}{a^2}, \quad \text{and} \quad \frac{\ddot{a}}{a} = -\frac{4\pi G}{3}(\bar{\rho} + 3\bar{p}). \tag{2.7}$$

These equations govern the evolution of the scale factor a as a function of the constituents of the universe described by their pressure and density. As mentioned at the end of the last sections, the pressure and densities can be the sum of several types of fields.

A particularly useful way to write the first Friedmann equation is in the form of an energy budget. For this purpose for each species i, we introduce the fractional energy densities $\Omega_i = \frac{8\pi G}{3H^2}\bar{\rho}_i$. Combining this with Eq. (2.4) we have

$$\Omega_i = \Omega_{i,0}\frac{H_0^2}{H^2}\left(\frac{a}{a_0}\right)^{-3(1+w)}. \tag{2.8}$$

To bring the curvature into a similar form, we can define $\Omega_k = -\frac{K}{a^2H^2}$ so that we can relate it to the present day value with

$$\Omega_k = \Omega_{k,0}\frac{H_0^2}{H^2}\left(\frac{a}{a_0}\right)^{-2}. \tag{2.9}$$

The curvature parameter is currently constrained to be extremely close to zero. This was one of the original motivators to develop the theory of inflation, known as the flatness problem. This problem states that a small deviation from zero of the curvature parameter today means an enormously small deviation from zero in the early universe, which seems highly tuned. Inflation, which we will discuss in more detail in Ch. 4, gives a mechanism for this and naturally predicts a very small value for curvature. How small it is and what sign the curvature exactly has, however, can distinguish between inflationary models. We will discuss the measurability of Ω_k with galaxy surveys in Ch. 8.

With these definitions, we can now rewrite the Friedmann equation as a simple

energy budget equation

$$\sum_i \Omega_i = 1. \tag{2.10}$$

The power of the above equation is that we can go through the known sources like radiation, matter, dark energy and neutrinos and see if their fractional energy densities add up to one. Any deviation from one would imply that we are missing some new form of matter. In Chs. 7, 8 and 10, we will encounter measurement of several fractional densities as introduced here. Sometimes, we also define $\omega_i = \Omega_i h^2$ to reduce the parameter degeneracy, which is what is measured in the CMB analyses [24]. We note that in almost all contexts in these chapters unless marked specifically otherwise, we mean the present-day values of the parameters. Explicitly, we will discuss ω_b and ω_{cdm}, which are the baryon and cold dark matter densities in these chapters. We will measure and forecast constraints on Ω_m, the total fractional matter density, implicitly Ω_d the dark energy fractional density since in the late universe $\Omega_d + \Omega_m \simeq 1$ and forecast the curvature parameter Ω_k.

These parameters are insightful in and of themselves in that they tell us what the universe consists of at different times. This is imperative, for example, to understand how the universe will evolve. Therefore, the parameters we have introduced so far already give us deep information about the universe. One classic example that we can calculate from the parameters introduced so far is the age of the universe. As has been verified very well by CMB and LSS measurements, the universe is flat $\Omega_k \simeq 0$, and most of the energy is split between a cosmological constant Ω_Λ, matter Ω_m and a little bit of radiation Ω_r. So we can write the Friedmann equation as

$$\frac{H^2}{H_0^2} = \Omega_{\Lambda,0} + \Omega_{m,0}\left(\frac{a}{a_0}\right)^{-3} + \Omega_{r,0}\left(\frac{a}{a_0}\right)^{-4}. \tag{2.11}$$

In this quite accurate model, we now calculate the age of the universe. So starting

the clock at $t = 0$, and denoting the age of the universe as t_0, we have:

$$\begin{aligned} t_0 &= \int_0^{t_0} dt \\ &= \int_0^{a_0} \frac{1}{aH(a)} da \\ &= \frac{1}{H_0} \int_0^1 \frac{1}{a\sqrt{\Omega_{\Lambda,0} + \Omega_{m,0} a^{-3} + \Omega_{r,0} a^{-4}}} da \\ &\simeq 13.8 * 10^9 \text{ years}, \end{aligned} \tag{2.12}$$

where from the first to the second line, we used $dt = \frac{da}{aH}$ and from the second to the third line, we used the rescaling symmetry of the FRW-metric. The values for H_0, $\Omega_{m,0}$, $\Omega_{\Lambda,0}$ and $\Omega_{r,0}$ are derived from observations [24].

2.5 The Einstein de Sitter Universe

Sometimes, it is useful to study a toy model of the universe in detail since it is analytically exactly solvable. These kind of model universes can give rise to properties that generalise to the real universe, or at least provide motivated approximations. One particularly useful model we take inspiration from in Chs. 6 and 9 is the Einstein de Sitter (EdS) universe [7]. We will see that since some formulas become much simpler in this universe, they lead to informed approximations. In this model, we assume a flat universe and that the only component is matter, i.e. $\Omega_m = 1$. With the Friedmann equations, we can then solve for the scale factor and Hubble constant exactly. By finding

$$\frac{H^2}{H_0^2} = \left(\frac{a}{a_0}\right)^{-3}, \tag{2.13}$$

this becomes solvable quite easily, and we can express the scale factor and the Hubble rate as a function of time: [8]

$$a(t) = a_0 \left(\frac{3}{2} H_0 t\right)^{2/3}, \quad \text{and} \quad H(t) = \frac{2}{3t}. \tag{2.14}$$

[7] We note, in neither of these sections will we be working in an EdS universe, but we draw inspiration from its analytic structure for approximations. In Ch. 10 in contrast, we explicitly do not work with this approximation.

[8] We here chose the expanding solution.

This model is instrumental since it inspires a lot of simplifications that, to good approximation, can be used in almost all large-scale structure perturbation theory. For a complete discussion on perturbation theory in an EdS universe, see App. B.1.1.

Finally, we note that it is possible to solve for the scale factor and the Hubble rate as in Eq. (2.14) for other ingredients and several fluids. However, beyond the presence of two different species, it becomes increasingly complex, to the point where, in practice, it is done numerically to capture the whole physics.

2.6 De Sitter Space

Another spacetime of fundamental importance, especially in the later chapter about inflation Ch. 4, is de Sitter space. We will see there that we eventually will need to formulate quantum fluctuations on a (quasi) de Sitter space background. Then, in Ch. 5, we will delve further into the geometry of de Sitter space to introduce new techniques for QFT in curved space and give an explicit construction of how this works in de Sitter space. We here want to give a simple definition of de Sitter space and highlight some of its features.

There are many ways to introduce de Sitter space [9], we will here view it as a subclass of an FRW universe [10]. The defining property is that the Hubble parameter H is a positive constant, and we take $k = 0$. That is, we have

$$H = \text{const.}, \quad \text{and} \quad a(t) = a_0 e^{Ht}. \tag{2.15}$$

Very typically, in this context, we consider the metric in conformal time, that is, $\eta = -H^{-1}e^{-Ht}$, with $\eta \in (-\infty, 0)$. The metric in these new coordinates then has the nice property that it looks like rescaled Minkowski space, that is

$$ds^2 = \frac{1}{(H\eta)^2}(-d\eta^2 + d\vec{x}^2) \ , \tag{2.16}$$

which we will be using when talking about inflation. Note that one of the symmetries of de Sitter is dilation symmetry; that is, the metric is invariant under $\eta \to \lambda\eta, \quad \vec{x} \to \lambda\vec{x}$, for a positive real λ. This is why dynamics in de Sitter space end up being the same on all scales, i.e. scale invariant.

[9] For example, as one of the maximally symmetric spacetimes along with Minkowski and Anti-de Sitter spacetimes, or as an embedded hyperboloid in higher dimensional Minkowski space.

[10] Technically, this metric only covers the expanding Poincaré patch and not the entire de Sitter geometry. For the introduction here, we, however, leave it at that.

Finally, note that $a(t) = a_0 e^{Ht}$ implies that $\frac{\ddot{a}}{a} = H^2$ and the two Friedmann equations Eq. (2.7) have the same left-hand side. If we combine them, we get the condition $\bar{\rho} = -\bar{p}$, which is the same as for dark energy. In fact, we could have introduced de Sitter space, similarly to the EdS universe in the previous section, simply by demanding $\Omega_\Lambda = 1$, which we can see from Eq. (2.11), to give a constant Hubble parameter. Indeed, the symmetries for dark energy and the ones we will encounter for inflation are very similar, even though inflation is a theory of the very early universe and dark energy dominates only in the late universe.

3

The Perturbed Universe and the Effective Field Theory of Large-Scale Structure

3.1 Introduction

In the last chapter, we saw that on the largest scale possible, the entire universe, symmetries like homogeneity and isotropy allow us to describe the universe in relatively simple terms. As is often the case in physics, nature becomes more complicated when we go to smaller scales. In cosmology, small scales encompass galactic physics, baryonic physics, and active galactic nuclei. Splitting the physics of interest on large scales from the small-scale physics that we cannot describe with our current understanding, which is analogous to the situation in particle physics. There, we assume a fundamental theory of quantum gravity should, in the low-energy limit, give rise to the standard model of particle physics. In cosmology, we have no hope of describing the entire universe down to every galaxy, or even every electron, in detail. Instead, we again focus on the lower energies, i.e. on the larger scales. We will see that through Effective Field Theory, we can still perturbatively capture the effects that small-scale physics exerts on the large scales.

To make progress, from our background description in the previous chapter, we have to alleviate some of the assumptions. If the universe were entirely homogeneous, no galaxies could exist - we call objects that break homogeneity inhomogeneities. These inhomogeneities are initially small fluctuations; thus, we can treat them as perturbations to the background that we discussed in the last section. Even after they become sizeable, we can still formulate a perturbation theory for the relevant scales, as we will see in Sec. 3.3.

We will start with relativistic perturbation theory, which has at least three applications relevant to us. The first application is in the early universe, during re-

combination [1]. Before recombination, the universe was hot, relativistic, and the different components of the universe, i.e. neutrinos, photons, matter, etc., were interacting with each other. A prime example of this interaction between baryons and photons are baryon acoustic oscillations (BAO), which are sound waves that arise in the early universe from the interplay between photon pressure and matter overdensities. We encounter these oscillations even in large-scale structure after billions of years of gravitational clustering. While relativistic and complicated, perturbations at that time were very small, and therefore, linearised relativistic perturbation can be applied.

The task for large-scale structure cosmology can be framed to model the gravitational interaction of those initial perturbations over the evolution of the universe. Hence, a very well-modelled early universe with all its different parts is the starting point for large-scale structure cosmology. The second relevant application of relativistic perturbation theory for us is large-scale structure, where we will, in fact, see how we can reduce it to the Newtonian perturbation theory. In essence, this is because after the decoupling from the cosmic fluid, matter behaves non-relativistically on the scales we are interested in. So, we can neglect a lot of the terms from the relativistic equations.

In the context of large-scale structure, another challenge arises. Throughout the evolution of the universe, the initially small fluctuations cluster through gravity and can become large, even larger than the background density. This led to the development of the Effective Field Theory of large-scale structures, which smoothes over the small scales where we have very large overdensities and describes a consistent theory of the larger, perturbative scales, taking into account the non-linear effects through effective interactions. In Sec. 3.3, we will discuss in detail the conceptual ideas behind a consistent effective theory of gravitational clustering on large scales. We leave explicit calculations to Ch. 6, which builds up the basic calculations from the equations of motion derived here.

Finally, one can ask why inhomogeneities even exist in the first place [2]? We will answer this when discussing the very beginning of the universe in Ch. 4. The third application of the perturbation theory discussed in Sec. 3.2 is, therefore, inflation (and, in fact, dark energy). This is because some of the symmetries are the same,

[1] Recombination is the name we give to the time in the early, hot universe, when the CMB was produced when electrons and protons recombined to form neutral hydrogen, letting the now unbound photons stream freely.

[2] We note that this is not the original motivator for inflation, but it is a very natural question that is answered by inflation.

and there, as well, we consider relativistic perturbations on an FRW background. The key difference is that in Ch. 4, these perturbations are so small that we have to treat them quantum mechanically.

3.2 The Perturbed FRW Universe

Now let us go back to the geometry of the universe, and its constituents, this time assuming there are small perturbations on top of our homogeneous and isotropic background. We do this both for the geometry of space-time, which is a modification from Eq. (2.1), and also allow for more complicated behaviour of the constituents in the universe, leading to a more general approach to Eq. (2.3).

As we will see, a major subtlety in describing the perturbations is the gauge freedom, that is, the coordinate choice [3]. The right choice of coordinates to describe our theory will be key to simplifying the calculations. This will, in fact, be highly relevant to the introduction to inflation in Ch. 4 as well.

We will perturb the metric into a time-dependent and a small spatially dependent piece, that is $g_{\mu\nu}(\vec{x},t) = \bar{g}_{\mu\nu}(t) + \delta g_{\mu\nu}(\vec{x},t)$ and similarly for the energy-momentum tensor $T_{\mu\nu}(\vec{x},t) = \bar{T}_{\mu\nu}(t) + \delta T_{\mu\nu}(\vec{x},t)$, where the background parts $\bar{g}_{\mu\nu}$ and $\bar{T}_{\mu\nu}(t)$ are simply Eqs. (2.1) and (2.2). For the metric, we adopt $K = 0$ from now in Eq. (2.3), since it is now measured to almost certainty that the universe is flat [25].

A general linearly perturbed FRW-metric, in principle, has scalar vector and tensor modes. This decomposition is a particularly suitable treatment because, to linear order, the scalar, vector and tensor modes do not mix. Tensor modes, i.e. gravitational waves, are a key probe for inflation and an active area of research. However, this is not the main focus for us in this thesis. Without a continuous source, vector modes decay away very rapidly and, therefore, are not usually of key importance in standard cosmology [4]. We will, therefore, omit them in this section. Our focus will be on scalar modes, which are the prime source for large-scale structure and one of the key interests in inflation.

The most general expression, including only scalar perturbations on top of an FRW background, includes four functions. There are the “Newtonian" potentials

[3] For example, to describe the altitude, we choose sea level as the zero point. However, the freedom to specify the zero point is a key simplification we can exploit, which is called gauge freedom. There are also Gauge-invariant, physical quantities that do not depend on the Gauge, like the height of a human.

[4] For cosmic string or modified gravity theories, they might be a key observable, but this is beyond the scope of this thesis.

$\Psi(\vec{x},t)$ and $\Phi(\vec{x},t)$ and the functions $A(\vec{x},t)$, and $B(\vec{x},t)$. Then, the perturbed metric is given by

$$ds^2 = -(1+2\Psi)dt^2 + 2a(t)\partial_i A dt dx^i + a(t)^2\left[(1-2\Phi)\delta_{ij} + \partial_i\partial_j B\right]dx^i dx^j \ , \quad (3.1)$$

where we omitted to write the functional dependence of the scalar perturbations for brevity. As mentioned, a key subtlety is the choice of coordinates or the gauge. This subtlety, in principle, comes from the fact that perturbing a metric and splitting small and large scales is not a covariant procedure and introduces a gauge dependence. However, physical observables should be gauge invariant or independent of who observes them. When only considering the metric, this leads to the "Bardeen variables, " which is what we will work with in this section. There are two scalar Bardeen variables, meaning that the four functions in Eq. (3.1) describe only two physical scalar functions. In the Newtonian gauge [5] we choose coordinates, so that $A = B = 0$, and in those coordinates Φ and Ψ coincide with the Bardeen potentials. Now, given that these variables are gauge-independent, we can calculate observables in Newtonian gauge, which then will be true in any gauge. The metric, which is the same as we write in Eq. (6.10), is then given by

$$ds^2 = -(1+2\Psi(\vec{x},t))dt^2 + a(t)^2(1-2\Phi(\vec{x},t))d\vec{x}^2 \ , \quad (3.2)$$

where one can recognise that in the absence of the potentials Φ and Ψ, we simply have the unperturbed metric Eq. (2.1) for $K = 0$.

There will be additional important gauge invariant quantities when considering the matter sector as well. We will encounter this and other gauge choices in Ch. 4 when discussing inflation. Let us introduce those matter fluctuations then. Throughout this treatment, while in principle we introduce generic variables, their interpretability is quite clear. For example, it is quite intuitive to think that a comoving observer with the FRW metric, that just moves with the expansion of the universe, might have an additional velocity on top of that describing a more "individual" movement. We then treat this velocity as a small perturbation relative to the cosmic expansion. Formally, we start with describing momentum, π^i instead since it is the more fundamental quantity [6]. Momentum and velocity will play a

[5] The Newtonian Gauge is reminiscent of the weak field limit, which is how we obtain Newtonian dynamics from the full theory of general relativity.

[6] Apart from simplifying calculations, it is also the natural moment arising from the Boltzmann Hierarchy.

key role in formulating the EFTofLSS and is a big discussion point in Ch. 6 in the context of renormalisation.

Apart from the momentum, we can also promote the energy density $\rho(\vec{x},t) = \bar{\rho}(t) + \delta\rho(\vec{x},t)$ and pressure $p(\vec{x},t) = \bar{p}(t) + \delta p(\vec{x},t)$ to also allow for spatial dependence, since we consider effect beyond homogeneity and isotropy. However, we, for now, do not assume $\delta\rho$ and δp to be small. This is important eventually for large-scale structure, where the density perturbations can become sizeable. The splitting is simply to remind that $\bar{\rho}(t)$ and $\bar{p}(t)$ are the quantities we introduced for the background in Eq. (2.2). Finally, we can also consider anisotropic stress as a perturbation Π^i_j, which is a directional shear that the fluid may experience. The energy-momentum tensor we then consider is given by [7]

$$T^\mu_\nu = \begin{pmatrix} -\rho(\vec{x},t) & a(t)\pi_j(\vec{x},t) \\ -a(t)^{-1}\pi^i(\vec{x},t) & p(\vec{x},t)\delta^i_j + \Pi^i_j(\vec{x},t) \end{pmatrix}, \tag{3.3}$$

where one can take the anisotropic stress to have vanishing trace $\Pi^i_i = 0$ since we can always absorb it into other components. From here on, we can proceed exactly as in the previous chapter. We get fluid equations from the energy-momentum tensor conservation $\nabla_\mu T^\mu_\nu = 0$ and then the relationship to the geometry through the Einstein equation in Eq. (2.6). Let us start with the energy and momentum conservation equations and start with the $\nu = 0$ component. This is in complete analogy to Eq. (2.3), just that we now have a perturbed metric and energy-momentum tensor. Neglecting products of metric perturbations and momentum, we have

$$\nabla_\mu T^\mu_0 = -\dot{\rho} - \frac{1}{a}\partial_i\pi^i - 3H(\rho + p) + 3\dot{\Phi}(\rho + p) = 0, \tag{3.4}$$

which is the relativistic continuity equation, linear in metric and momentum perturbations. We will come back to this equation in detail when studying non-linearities. Let us continue with the spatial components of the energy-momentum conservation. Again, keeping terms linear in the metric perturbations and momentum perturbations, we have

$$\nabla_\mu T^\mu_i = a\dot{\pi}_i + 4aH\pi_i + \partial_i p + \partial_j\Pi^j_i + (\rho + p)\partial_i\Psi = 0. \tag{3.5}$$

Before moving on to the Einstein equations, we want to highlight that in the absence

[7] For comparison, written in this form, the unperturbed energy-momentum tensor from Eq. (2.2) reads $\bar{T}^\mu_\nu = \mathrm{diag}(-\bar{\rho}(t), \bar{p}(t), \bar{p}(t), \bar{p}(t))$

of pressure, and in the Newtonian limit Eqs. (3.4) and (3.5) already resemble the EFTofLSS equations of motion Eq. (6.12) [8]. We will discuss this in much more detail in the next section, where, in particular, we expand the discussion to account for the effect of non-linearities.

The Einstein equations tell us more about the evolution of the metric perturbations as well as their interaction with the matter components. We set up the whole system with Eqs. (3.2) and (3.3) and calculate both sides of Eq. (2.6). In the unperturbed case, this gave us the Friedmann equations Eq. (2.7). Here, we instead get four equations, which, to linear order in perturbations, are [9]

$$3H^2(1-2\Psi) - 6H\dot{\Phi} + 2a^{-2}\partial^2\Phi = 8\pi G\rho \tag{3.6}$$

$$\partial_i(H\Psi + \dot{\Phi}) = -4\pi G a \pi_i \tag{3.7}$$

$$\left(\partial_i\partial_j - \frac{1}{3}\delta_{ij}\partial^2\right)(\Phi - \Psi) = 8\pi G a^2 \Pi_{ij} \tag{3.8}$$

$$\left(\frac{\ddot{a}}{a} + \frac{1}{2}H^2\right)(1-2\Psi) - \ddot{\Phi} - H\left(3\dot{\Phi} + \dot{\Psi}\right) + \frac{1}{3a^2}\partial^2(\Phi - \Psi) = -4\pi G p. \tag{3.9}$$

One can see that in the absence of perturbations, i.e. $\Phi = \Psi = 0$, $\rho = \bar{\rho}$, and $p = \bar{p}$, Eqs. (3.6) and (3.9) give the background Friedmann equations Eq. (2.7). Furthermore, in the absence of anisotropic stress, or when isotropic stress is very small, we can take $\Phi = \Psi$, which is what we typically do in large-scale structure.

As mentioned in the introduction of this chapter, there are two (eventually three when counting inflation) very important limits of these equations to us. In the hot early universe, photons, matter and neutrinos all interacted with each other and were highly relativistic. This means the full set of equations is relevant here. However, both metric and fluid perturbations were small compared to the background, and we can fully treat them linearly. The set of equations we then have to consider are the perturbed continuity equations and the Euler equations, yet with slight modifications to capture interactions with each other, like Thomson scattering of photons and baryons. Photons and neutrinos themselves require extensive modelling with a much more detailed Boltzmann hierarchy. On top of that, we have the Einstein equations that should be read with all fluids present simultaneously, i.e. $\rho = \sum_\alpha \rho_\alpha$.

[8] For the sake of comparison, in those limits we have $p = 0$, a weakly varying gravitational field $\dot{\Phi} = 0$, to linear order $\Phi = \Psi$, and $\Pi^{ij} = \frac{\pi^i\pi^j}{\rho} + \tau^{ij}$. However, we emphasise that in this section, we derived fluctuations to linear order, and especially the inclusion of non-linear terms in Π^{ij} is purely schematic.

[9] The spacial Laplacian is simply $\partial^2 = \partial_i\partial_j\delta^{ij}$, and in general, the i and j spatial indices are raised/lowered with δ^{ij}.

This leads to a large and complicated set of equations involving all matter and radiation species. It should not be astonishing that a hot relativistic soup of particles is difficult to model. To solve these coupled Boltzmann and Einstein differential equations, we use numerical solvers like CAMB or CLASS [26, 27]. While they were initially introduced to study the CMB anisotropies, for us, these solvers provide the initial matter overdensity, which is the starting point of all the gravitational modelling we do afterwards. For Chs. 6, 7, and 10, these codes, is what gives us the linear power spectrum $P_{11}(k)$. What this object is, we will discuss in more detail in Sec. 3.4.

This brings us to the other use of these equations, which is the gravitational clustering of matter. After decoupling, matter largely evolves through gravity and non-relativistically. This is simpler in a lot of ways to the early universe since now we effectively only have to consider the matter species and only consider non-relativistic terms. However, the matter perturbations cannot be treated linearly anymore in the later universe as clustering leads to very over and under-dense regions such as galaxies or voids. On top of that, it is computationally infeasible to model all the effects of galactic physics on the large-scale distribution of matter. This is the reason the Effective Field Theory of large-scale structure is required. We aim to model the large-scale distribution of matter while perturbatively taking into account the effects the small-scale physics has. We will discuss this in detail in the next section.

3.3 The Effective Field Theory of Large-Scale Structure - Conceptual Aspects

In Ch. 2, we discussed the background evolution of the universe, assuming complete isotropy and homogeneity. There, one can think of the universe as averaged entirely over all space. Then, in Sec. 3.2, we put small linear perturbations on top of this smooth background, with, in principle, infinite detail regarding the size of these fluctuations at any point in space. In the late universe, this level of detail becomes unfeasible since perturbations become enormously complicated. Just imagine a function $\rho(\vec{x}, t)$ containing the information of every galaxy, star or electron in the universe! What we do instead is an approach in between: we smooth over the very small scales, blurring out the very small-scale physics. This means we have some sensitivity to the small scales, while still focusing on physics that we can model relatively well with perturbation theory.

This framework is called the Effective Field Theory of Large-Scale Structure, which is the theory of the large-scale dynamics of dark matter. It consistently incorporates the effects of small-scale physics in a perturbative expansion, allowing us to model the matter overdensity all the way into the mildly non-linear regime.

3.3.1 The Newtonian Equations of Motion

We first do a lot of simplifications before we delve into the subtleties of non-linear dynamics. We will see that eventually, the dynamics we encounter will simplify substantially. This is primarily because we consider the matter to be non-relativistic, and most importantly, the clustering of dark matter is a causal process hence we consider sub-horizon scales. More intuitively, we do not consider the whole universe to affect the clustering of matter, but only the matter that is in causal contact with each other. This means that we are interested in the length scale $\lambda \ll H^{-1}$. In practice, this means that the derivative term in Eq. (3.6) dominates [10], and we simply get the Newtonian limit of the Poisson equation

$$\partial^2\Phi \;=\; 4\pi G a^2 \delta\rho. \tag{3.10}$$

At late times and for matter on sub-horizon scales, anisotropic pressure also becomes negligible, which through Eq. (3.9) implies that from here on, we can take $\Psi = \Phi$. We will see that exactly this sub-horizon limit that we took above will also give us the Euler and continuity equations in the Newtonian limit. To see this, let us be a bit more specific about the type of energy-momentum tensor we would like to consider.

From here on, we are interested in the overdensity of matter. The other constituents influence the matter perturbations in the early universe before decoupling and through the background evolution. However, after decoupling, as the name suggests, the matter perturbations can be described on their own, in particular since photon and neutrino perturbations are extremely small compared to the matter perturbations in the later universe. We can then go back to Eq. (2.2) and consider perturbations and the absence of pressure, but again with a perturbed velocity, or as we will prefer momentum. We then have

$$T^\mu_\nu = \rho U^\mu U_\nu, \tag{3.11}$$

[10] In Fourier space this implies $k \gg aH$ and hence $3a^2H(\Psi + H\dot{\Phi}) \ll k^2\Phi$.

where in contrast to Eq. (2.2), the four velocity has a general but small velocity perturbation $U_\mu = \bar{U}_\mu + \delta U_\mu$. The normalisation condition $U_\mu U^\mu = -1$ then implies that $U^\mu = (\gamma(1-\Phi), a^{-1}(1+\Phi)v^i)$, where $\gamma(v)$ is the Lorentz factor. Therefore, the energy-momentum tensor for matter that we need to consider is given by [11]

$$T^\mu_\nu = \begin{pmatrix} -\rho(1+v^2) & a\ \rho v_j \\ -a^{-1}\ \rho v^i & \rho v^i v_j \end{pmatrix}, \tag{3.12}$$

where we opted to write the entries in terms of the velocity to connect to the four-velocity we defined above. However, we will shortly go back to using the momentum $\pi^i = \rho v^i$. We note that in the previous section, we derived equations that were linear in the metric fluctuations, but we never assumed the fluid perturbations to be small. This comes in handy now, since we can simply take - symbolically - $\Pi^i_j \to v^i v_j - \frac{1}{3}\delta^i_j v^2$ [12], and $p \to \frac{1}{3}v^2$. The full continuity equation we get from the energy conservation, just as in Eq. (3.4), is then given by

$$\nabla_\mu T^\mu_0 = -\dot{\rho}(1+v^2) - 2\rho \dot{v}_i v^i - \frac{1}{a}\partial_i \pi^i - 3H\rho - Hv^2 + 3\dot{\Phi}\rho + \dot{\Phi}v^2 = 0. \tag{3.13}$$

Again, considering we are interested in non-relativistic physics deep inside the horizon, these equations will simplify to their Newtonian limits. To see this, note that the size of the velocity terms in the linear regime we have $v^2 \sim \frac{\delta\rho}{\rho}\Phi$, and so in the non-linear regime, i.e. $\delta\rho \sim \rho$, v^2 is at best of the size of a metric perturbation Φ. This immediately makes the last term second order in metric fluctuations. Furthermore, again, terms with a time derivative are similar in size to those multiplied by the Hubble parameter, for example, $\dot{\Phi} \sim H\Phi$, and so again, given we are deep inside the horizon, and the derivative term $\propto \partial_i$ dominates over the horizon terms $\propto H$. In summary, all of the terms involving v^2 or $\dot{\Phi}$ in Eq. (3.14) containing go as $H\Phi \ll \partial_i \pi^i$, which is how we get to the Newtonian limit

$$\dot{\rho} + 3H\rho + \frac{1}{a}\partial_i \pi^i = 0. \tag{3.14}$$

The same argument can be made for the Euler equation. The full relativistic equa-

[11] In order to eventually get the kinetic tensor σ_{ij} on the right-hand side of the Euler equation defined as the second moment from the Boltzmann hierarchy as in [28], one could add it in the space-space part. We neglect it here since it will simply feed into the effective stress tensor we will motivate below.

[12] It is this identification that tells us that anisotropic stress is small, i.e. the right-hand side of Eq. (3.8) is negligible and hence we can set the two metric perturbations equal to each other.

tion is given by

$$\nabla_\mu T_i^\mu = a\dot{\pi}_i + 4aH\pi_i + \partial_j(\rho v_i v^j) + \rho\partial_i\Phi + \frac{1}{3}v^2\partial_i\Phi = 0, \tag{3.15}$$

where we can again immediately see that the last term is of the size of a second-order metric perturbation and thus negligible. All other terms are of the size of linear metric perturbations. Then, the final sub-horizon Euler equation is again simply the Newtonian limit

$$\dot{\pi}_i + 4H\pi_i + a^{-1}\partial_j\left(\frac{\pi_i\pi^j}{\rho}\right) + a^{-1}\rho\partial_i\Phi = 0, \tag{3.16}$$

where we again chose to write it in terms of the momentum. We can recognise that Eqs. (3.14) and (3.16) are now exactly Eq. (6.12), however, without the effective stress tensor τ_{ij}, which we will discuss in the next section.

While the above derivation shows in detail how we obtain the Newtonian limit, when we consider perturbations on sub-horizon scales, the relativistic derivation somewhat obscures the connection to the Boltzmann equation. Confident, therefore that the Newtonian limit sufficiently describes perturbations on sub-horizon scales, we could have alternatively started our discussion by modeling dark matter as a collisionless fluid described by its phase space distribution function $f(\vec{x}, \vec{p}, t)$, as done for example in [28]. In the Newtonian limit, the equations of motion then stem from the collisionless Boltzmann equation[13]

$$\frac{\partial f}{\partial t} + \frac{p_i}{ma^2}\frac{\partial f}{\partial x^i} - m\frac{\partial\Phi}{\partial x^i}\frac{\partial f}{\partial p^i} = 0, \tag{3.17}$$

where m is the mass of the dark matter particle, which, however, eventually drops out. The various fluid quantities that we have encountered are simply the moments of the phase space distribution. The first three are the density ρ, momentum π^i and kinetic tensor σ^{ij}, and are defined by

$$\rho = \frac{m}{a^3}\int d^3p f, \quad \pi^i = \frac{1}{a^4}\int d^3p p^i f, \quad \sigma^{ij} = \frac{1}{ma^5}\int d^3p p^i p^j f - \frac{\pi^i\pi^j}{\rho}, \tag{3.18}$$

where we omit writing the dependencies for brevity. The equations of motion arise from integrating successive moments of the collisionless Boltzmann equation: the

[13] This is the Boltzmann equation one obtains in the sub-horizon limit when starting from the full relativistic collisionless Boltzmann equation $p^\mu\partial_\mu f - \Gamma^\mu_{\alpha\beta}p^\alpha p^\beta\frac{\partial f}{\partial p^\mu} = 0$.

zeroth moment yields the continuity equation, Eq. (3.14), and the first moment leads to the Euler equation, Eq. (3.16), now featuring the kinetic tensor on the right-hand side, as noted in footnote [11]. For a perfect fluid, σ^{ij} vanishes exactly; however, on small scales, this is not true for dark matter. Applying a smoothing procedure ensures that the Boltzmann hierarchy can be consistently truncated, but generates a non-zero stress tensor that contributes to the effective fluid description. This brings us to the last conceptual point of this section.

3.3.2 Smoothing and the Effective Stress Tensor

So far, we have taken the full theory of general relativity and reduced it to the scales and limits relevant for gravitational clustering. We have done this by setting an upper limit on the scales we want to consider, that is the sub-horizon limit, which are scales smaller than Hubble. As mentioned earlier, the key point of the EFTofLSS is to set a lower scale of interest as well. We enforce this by smoothing over the very small scales [14]. We will now see that it is this smoothing that leads to the effective stress tensor on the right-hand side of the Euler equation, show why it is necessary and finally, how we integrate out the small scales.

The fields we can perturbatively control are the long-wavelength fields X_l, where $X \in \{\rho, \Phi, \pi^i\}$. The X_l are the original fields but smoothed over with a window function so as to blur out the very small fluctuations. We will define this momentarily. Eventually, we are neither interested in the exact way this smoothing process works nor over what scales this smoothing happens [15], but we want to make sure to have a theory that is consistent for the regime we are interested in.

Let us imagine we want to smooth over scales of order $1/\Lambda$ with a window function $W_\Lambda(\vec{x}) = \left(\frac{\Lambda}{\sqrt{2\pi}}\right)^3 e^{-\frac{1}{2}\Lambda^2 x^2}$. We then define the short and long-wavelength fields to be the convolution with this window function

$$X_l(\vec{x}, t) := \int d^3x' W_\Lambda(\vec{x} - \vec{x}') X(\vec{x}', t), \tag{3.19}$$

and define the short wavelength field $X_s = X - X_l$. To see what this does in practice, we can look at Fig. 3.1, where we illustrate this with a fictitious example of a density perturbation. While we can see very clear spikes that are perturbatively hard to

[14] Note that by assuming the matter fields are non-relativistic, we already implicitly assumed that we are not going to formulate a theory about the smallest scales, since, for example, the velocity field at the centre of a galaxy is very non-perturbative.

[15] That is, after renormalisation, the EFT is independent of the cutoff scale.

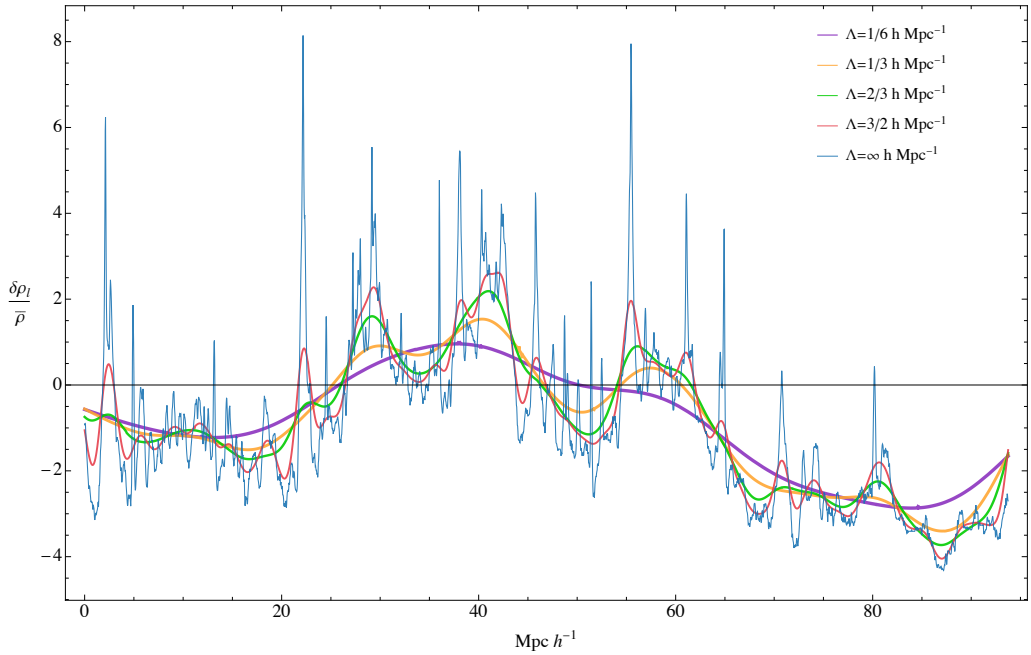

Figure 3.1: Fictitious example of raw and smoothed overdensity profiles of dark matter. The sample is taken from the Millennium Simulation [29] at $z = 0$ and created through pixel brightness of a 1D slice of 2048 pixels. The raw overdensity was smoothed with Eq. (3.19), with different smoothing scales.

control, the reality in nature is, in principle, even worse. We note that Fig. 3.1 was created by capturing the brightness of a 1D slice containing 2048 pixels. Each pixel can be viewed as an already smoothed over region, therefore the $\Lambda = \infty$ case really is, $\Lambda \simeq \frac{2048}{93.75\text{Mpc}\,h^{-1}} = 22h\,\text{Mpc}^{-1}$, which smoothes over scales just about the size of the Milky Way.

Now that we have gained some intuition about smoothing, let us see how this idea manifests in the equations of motion. This is quite straightforward for linear equations since we can simply smooth the whole equation. For the Poisson and continuity equation, Eqs. (3.10) and (3.14), this simply implies that

$$\begin{aligned} \partial^2\Phi_l &= 4\pi G a^2 \delta\rho_l \\ \dot{\rho}_l + 3H\rho_l + \frac{1}{a}\partial_i\pi_l^i &= 0. \end{aligned} \tag{3.20}$$

However, when we have products of fields, as we do in the Euler equation Eq. (3.16), the smoothing leads to more subtleties. This is because the smoothed products of fields is not equal to the product of the smoothed fields, i.e. $(XY)_l \neq X_l Y_l$. In fact, the smoothed products of fields explicitly depend on the short wavelength fields,

and we have (see for example [30])

$$(XY)_l = X_l Y_l + (X_s Y_s)_l + \frac{1}{\Lambda^2}\partial_i X_l \partial^i Y_l + O(\Lambda^{-4}), \tag{3.21}$$

where we note that the scales we are eventually interested in are much larger than $1/\Lambda$, hence $\frac{\partial}{\Lambda} \ll 1$. This is a general pattern in the EFTofLSS. We always understand the product of fields to be the smoothed version of that product. This smoothing each time then depends explicitly on the short modes and hence needs special care. We will encounter this subtlety a lot more in Ch. 6 when discussing bias and redshift space renormalisation.

Now, if we smooth the Euler equation. The last two terms of Eq. (3.16) are non-linear. Therefore, as exemplified in Eq. (3.21), there will be terms that explicitly depend on the short modes, and also, we will get higher derivative terms. Let us collect all of these terms into a quantity we for now just call τ_{ij}[16]. Then, the smoothed Euler equation reads

$$\dot{\pi}_l^i + 4H\pi_l^i + a^{-1}\bar{\rho}\,\partial^i\Phi_l = -a^{-1}\partial_j\left(\frac{a^{-2}}{4\pi G}\left(\partial_i\Phi_l\partial_j\Phi_l - \frac{1}{2}\delta_{ij}(\partial\Phi_l)^2\right) + \frac{\pi_l^i\pi_l^j}{\rho_l} + \tau_{ij}\right), \tag{3.22}$$

where we rearranged some terms so that all the linear terms are on the left and the non-linear ones on the right, and used the Poisson equation.

Now let us discuss τ_{ij} in detail. In some sense, it is the backbone of the EFTofLSS as it is the key feature that allows us to formulate a consistent and renormalisable field theory. This is because the effective stress tensor will eventually give rise to the counterterms that absorb the UV dependence of the loops.

As mentioned in Eq. (3.21), we will get for example the following terms after smoothing $\tau_{ij} \supset \frac{a^{-2}}{4\pi G}\left(\partial_i\Phi_s\partial_j\Phi_s\right)_l$. Hence, the exact structure of τ_{ij} is an incredibly complicated function and dependent on very high-energy physics, far beyond what we can describe analytically. However, our aim is to capture the effects of the high-energy physics, relevant for the long-wavelength fields - this is what we call effective interactions. To capture the effective interaction, we integrate out the short-scale physics by ensemble averaging [17]. This average, by design, only depends on the long-wavelength fields and introduces a stochastic part uncorrelated to the dark matter fields. That is, schematically $\tau_{ij} = \langle\tau_{ij}^s\rangle + \tau_{ij}^\partial + \tau_{ij}^\epsilon$, where the second

[16] This includes the smoothed kinetic tensor, σ_l^{ij}, introduced at the end of the last section.

[17] We will discuss what exactly we mean by ensemble averaging in much more detail in Sec. 3.4.

and third part are the higher derivative and stochastic terms. We will expand the ensemble-averaged part in an EFT expansion, an expansion based on every term allowed by the symmetries. To do this, we need to investigate the symmetries of the problem and the relevant dependence of this effective stress tensor, τ_{ij}, on the long-wavelength fields. In short, we need to check what and how τ_{ij} can depend on. Let us start with the first.

From here on, we will drop the sub-index $X_l \to X$ since all fields we consider in this thesis from here on are implicitly the long modes. We emphasise that all the equations in Ch. 6 and onward are meant to represent the long-wavelength fields; we omit writing the subindex every time. Now, to investigate τ_{ij}, let us rewrite the Euler equation in its final form. We have

$$\dot{\pi}_i + 4H\pi_i + a^{-1}\partial_j\left(\frac{\pi_i\pi^j}{\rho}\right) + a^{-1}\rho\partial_i\Phi = -a^{-1}\partial_j\tau^{ij}, \tag{3.23}$$

which is just Eq. (3.16) with the additional term on the right-hand side. The symmetries of τ_{ij} are therefore dictated by the left-hand side of the above equation. We notice immediately that the left-hand side is rotationally invariant, implying that the right-hand side must be as well. Less trivially, the equations of motion are invariant under the subset of diffeomorphisms that keep us in the Newtonian gauge in the non-relativistic limit. These are the Galilean shifts given by [18]

$$t \to t + a^2\xi^i(t)x_i, \quad x^i \to x^i + \xi^i(t). \tag{3.24}$$

It is useful to show how the different fields change under such shifts. We have (see for example [31])

$$\begin{aligned} &\partial_i \to \partial_i\ , \quad \partial_t \to \partial_t - \dot{\xi}^i(t)\partial_i\ , \quad \pi^i \to \pi^i + \rho\, a\dot{\xi}^i(t), \quad v^i \to v^i + a\dot{\xi}^i(t)\ , \\ &\rho \to \rho, \quad \Phi \to \Phi - a^2(\ddot{\xi}^i(t) + 2H\dot{\xi}^i(t))x^i\ , \end{aligned} \tag{3.25}$$

and it is quite simple to see that the left-hand side of Eq. (3.23) is invariant under these shifts, implying that τ^{ij} must be invariant as well. These symmetry considerations are enough to find the dependence of τ_{ij} on the long-wavelength fields. One typically chooses to take Φ and v^i for this expansion as we do, for example, in Ch. 6. Then Galilean invariance tells us that τ_{ij} can only depend on the metric perturba-

[18] These are the same shifts we impose for the velocity in Sec. 6.5.2, with the identification $\chi^i = a\dot{\xi}^i$.

tion with at least two derivatives, so it is of the form $\partial_i\partial_j\Phi$ and the velocity field would need to come with at least one derivative to be an invariant, that is $\partial_i v^j$. Additionally, note that we defined τ^{ij} to also contain the higher derivative terms mentioned in Eq. (3.21). Finally, as mentioned above, to account for the difference between a given realisation and the mean when taking the ensemble average of the short modes, we also introduce a stochastic field ϵ that is uncorrelated with the dark matter fields. Now that we know what fields the effective stress tensor depends on, we have to consider what this dependence looks like.

This question boils down to asking how the short modes affect the long modes. Clearly, the effect of the short modes on the long modes is spatially local; that is, a galaxy at the other end of the universe will not greatly affect the behaviour of a long wavelength field here. This makes the dependence local in space. In contrast, a short mode in the distant past has affected the long modes today. This is because the short modes evolve over similar time scales to the long modes; hence, the short modes influence the long modes over their whole history. Therefore, we cannot simply average over these time scales, making the expansion non-local in time. In summary, the effective stress tensor must have the following form,

$$\begin{aligned}\tau^{ij}(\vec{x},t) &= \int^t dt' H(t') F^{ij}(\partial_n\partial_m\Phi(\vec{x}_{\rm fl},t'),\partial_n v_m(\vec{x}_{\rm fl},t'),\partial_i,\epsilon,t',...) \\ &= \int^t dt' H(t') K(t,t')\partial^i\partial^j\Phi(\vec{x}_{\rm fl}(x,t,t'),t') + ...\,,\end{aligned} \tag{3.26}$$

where F^{ij} is a completely general rotationally invariant function, and in the second line, we wrote the first leading term, with K being an arbitrary kernel capturing the influence of $\partial^i\partial^j\Phi$ on the effective stress tensor over its history [19]. Finally, we note that we do not evaluate the fields at $\vec{x}$ but at their fluid position over its history, which is given by $\vec{x}_{\rm fl}$. The exact structure of $\vec{x}_{\rm fl}$ allows us to integrate over the field's history while remaining invariant under Galilean shifts. The fluid line element is recursively given by

$$\vec{x}_{\rm fl}(\vec{x},t,t') = \vec{x} + \int_t^{t'} dt'' H(t'')\vec{v}(\vec{x}_{\rm fl}(\vec{x},t,t''),t'')\ , \tag{3.27}$$

and in practice, one can perturbatively expand it in powers of v up to the required order.

[19] Local in time would mean $K(t,t') = \kappa(t)\delta_D(t-t')$, which collapses the integral, and makes the left-hand side only dependent on the values at t.

On the field level, we have now established all the relevant ideas to discuss the Effective Field Theory of large-scale structure in the context of dark matter. We have formulated a consistent theory of the long-wavelength fields, integrating out the short scales that led to an effective stress tensor. There are standard ways to perturbatively expand the overdensity and momentum and then solve the Euler and continuity equation order by order. We refrain from going into the technical details of this here since it is done in detail in Ch. 6 from the ground up, which is also why, in this section, we focused on conceptual aspects rather than computational ones. Nevertheless, in the next section, we briefly connect to what we eventually measure.

We note that the description of galaxies - often called biased tracers - in the EFTofLSS follows the same symmetry principles we laid out in detail here for τ_{ij}. Indeed, in Ch. 6 we proceed in an analogous way, and the general equation we give Eq. (6.124) is almost the same as for τ_{ij} in Eq. (3.26). The non-locality in time we have encountered here is discussed in the context of galaxies in detail in Ch. 9, where we will see that it becomes a measurable effect.

3.4 Large-scale Structure Observables

In the last sections, we went from describing the uniform background of the universe to describing linear and then non-linear perturbations. These perturbations, importantly, are functions of space and contain a wealth of information. The challenge we then face is how we summarise this wealth of information.

While there are more and more approaches as to what the best way is to extract information from galaxy surveys as for example, in [32, 33], we here focus on n-point functions, which is what will be relevant for us in the later chapters. We keep the discussion in the context of dark matter since we just introduced it in the last section, but it is the analogous concept for any density field. Let us first introduce the dark matter overdensity that is

$$\delta(\vec{x},t) = \frac{\rho(\vec{x},t)}{\bar{\rho}(t)} - 1, \tag{3.28}$$

where here and from now on, we drop the subscript m for matter. The most common observables in cosmology are then the n-point statistics of the overdensity, which are products of the overdensity field at different points.

The origin of the fluctuations in the universe is likely quantum mechanical, as we will establish in Ch. 4. So, we understand the origin of the fluctuations as the

realisation of one of the many possible quantum mechanical outcomes. The expectation values, therefore, should be understood as an ensemble average of different realisations of the universe. In practice, we have access to only one realisation of the universe, and therefore, we rely on spatial averaging. This works since sufficiently distant regions can be causally disconnected and can be viewed as independent realisations. Invoking ergodicity, spatial averaging provides a reasonable estimate of the ensemble average. Depending on how many causally disconnected regions we have access to, this leads to a better or worse estimate of the ensemble average, and therefore, there is a sample variance. Given the finite observable volume and, hence, accessibility to information in the universe, there is an upper bound on the sample size, which then defines the cosmic variance - the fundamental limit to statistical precision in cosmology.

Now, let's go back to the n-point functions. The most straightforward one-point statistic we have actually already seen is $\langle \rho(\vec{x}, t) \rangle = \bar{\rho}(t)$, making the spatial averaging explicit. Of course, Eq. (3.28) implies for the one point statistic of the overdensity $\langle \delta \rangle = 0$ [20]. The simplest non-zero correlation function is then simply the 2-point correlation function, which is the most prominent to date in cosmology. It is defined as

$$\xi(\vec{x}_1, \vec{x}_2) = \langle \delta(\vec{x}_1) \delta(\vec{x}_2) \rangle, \tag{3.29}$$

where we left the time dependence implicit. Now, let us briefly revisit homogeneity and isotropy on large scales since they greatly simplify the statistics of interest in cosmology. We have already seen for the one-point function how this ended up reducing the complexity. While we have established that perturbations explicitly break homogeneity and isotropy, their statistical properties still obey them. This, for example, means that no matter in what direction we look, we expect the probability of two galaxies (or dark matter overdensities) to have a certain distance from each other to be the same. To be precise, homogeneity and isotropy imply that the two-point function is only a function of the distance, i.e. $\xi(\vec{x}_1, \vec{x}_2) = \xi(|\vec{x}_1 - \vec{x}_2|)$, and this generalises to higher n-point functions.

It is often much simpler to analyse the n-point correlation functions in Fourier space. For example, because on linear scales, the different Fourier modes evolve independently. We therefore define $\delta(\vec{k}, t)$ as the Fourier transform of Eq. (3.28).

[20] For the EFT expansion of biased tracers, the vanishing of the mean needs to be implemented explicitly, in particular in the context of redshift space distortions, as in Ch. 6.

Then of fundamental importance is the power spectrum, which is given by

$$\langle \delta(\vec{k},t)\delta(\vec{k}',t)\rangle = (2\pi)^3\delta_D(\vec{k}+\vec{k}')P(k,t), \tag{3.30}$$

and one can show quite easily that the power spectrum is simply the Fourier transform of ξ. Of great importance is also the 3-point function, or the Fourier space version, the Bispectrum

$$\langle \delta(\vec{k}_1,t)\delta(\vec{k}_2,t)\delta(\vec{k}_2,t)\rangle = (2\pi)^3\delta_D(\vec{k}_1+\vec{k}_2+\vec{k}_3)B(k_1,k_2,k_3,t). \tag{3.31}$$

The power spectrum and bispectrum for galaxies in redshift space will be the primary focus for us in Chs. 6, 7 and 8.

Finally, in our quest to introduce all the cosmological parameters of interest for this thesis, we here introduce the ones related to the linear dark matter power spectrum. The linear power spectrum, $P_{11}(k)$, is the power spectrum we obtain from the Boltzmann codes mentioned at the end of Sec. 3.2, i.e. we get them from the full relativistic linearised equations of motions. Importantly, this is before gravitational non-linearities become sizeable. The dark matter parameters are motivated by early measurements of the dark matter power spectrum in lensing surveys and have gained more attention because of recent disagreements between their early and late time measurements. To define them, let us introduce another type of smoothing to the one we encountered in the last section, which simply averages everything in a sphere of radius R. this is called a top-hat distribution $W_R(r) = \theta_H(R-r)\frac{3}{4\pi R^3}$, where θ_H is the Heaviside function. We might then be interested in the variance of fluctuations on a certain scale. This can be expressed as

$$\sigma_R^2 = \int \frac{dk}{2\pi^2}k^2 P_{11}(k)\tilde{W}_R^2(kR), \tag{3.32}$$

where $\tilde{W}_R$ is the Fourier transform of W_R. Historically, the scale $R = 8h^{-1}$Mpc has been chosen as it roughly marks the transition between linear and non-linear regimes of structure formation. Another parameter introduced because of particular sensitivity to it in lensing is $S_8 = \sigma_8\sqrt{\Omega_m/0.3}$, where Ω_m is the matter density parameter we have introduced in Sec. 2.4. These parameters have become very familiar in cosmology and are viewed as benchmarks by some. Therefore, while we measure the full set of cosmological parameters in Ch. 7, we deduce these benchmark parameters from galaxy surveys, offerting another late-time datapoint as, for example, in [34].

4

The Inflationary Paradigm and its Parameters

4.1 Introduction

Inflation is the leading candidate for a consistent theory of the early universe and will be one of the key topics in the first two parts of this thesis. At its core, it describes a period of accelerated expansion at the very beginning of the universe. Guth initially proposed inflation [35] to solve two shortcomings of the Big Bang model. One of them is the flatness problem, which we already briefly discussed in Sec. 2.4, addressing the very small value of the curvature today and its projected even smaller value in the early universe. The other problem arises from the uniformity in the CMB, where we see regions that are not in causal contact but are in thermal equilibrium. This is called the horizon problem, which is an apparent violation of causality. Even more strikingly, these causally disconnected regions have correlated density fluctuations. Said intuitively, regions of space seem to have communicated with each other, even though the time it would have taken them to communicate is longer than the time the universe existed. The inflationary paradigm proposes that these very faraway regions were very close to each other in an earlier period, had time to communicate and then, through a quasi-exponential expansion, were brought very far apart from each other. This rapid expansion would also decrease any initial curvature present to a very small value, thus solving both problems and, in fact, many others [1].

Perhaps the most striking consequence of inflation is that it provides a mechanism for the seed of structure. This is so striking because inflation was engineered to solve the problems above but then predicted the primordial distribution of structure through quantum mechanical formulations of inflation.

[1] Inflation also gives a mechanism to dilute magnetic monopoles predicted by grand unification theories and also gives a mechanism for the low entropy in the early universe.

So far, the story we told is of a smooth universe in Ch. 2, and we put small relativistic perturbations on top in Sec. 3.2. The initially small matter perturbations then start to become sizeable through gravitational clustering, which we discussed in Sec. 3.3. However, we have not answered yet why there even are perturbations and, more strikingly, why in the very early universe, they appear to be Gaussian to very good approximation. As we will see, the short answer to this is that this very rapid expansion was driven by a scalar field that governed the amount of time that inflation takes place. Through quantum fluctuations in this scalar field, the rapid expansion of the universe ended slightly sooner or later in some regions of space. So regions started to dilute sooner or later, making them have slightly lower or higher energy density. In essence, quantum fluctuations in the early universe are likely responsible for seeding all the structures we see in the universe today.

The aim of this chapter is twofold, somewhat representative of the state of cosmology regarding inflation [2]. On the one hand, there remain many open questions regarding the theoretical framework of inflation as well as the possible models that can even exist. On the other hand, while slow roll inflation has remarkably predicted an approximately scale invariant power spectrum that has been well confirmed by now, there are further discoveries such as non-Gaussianity that would be the smoking gun confirmation for inflation. In this quest, we derive the relevant inflationary parameters that we eventually constrain with large-scale structure surveys.

We start with an introduction to quantum field theory in curved space and introduce the idea of slow-roll inflation. We then move on to more general inflationary models and will do some more explicit calculations. This does not only highlight the difference between the calculations that are classically done in inflation as opposed to the ones we introduce in Ch. 5 but will also allow us to later derive the key parameters which we will be forecasting in Ch. 8 coming from the inflationary bispectrum. In this process, we will also encounter the inflationary parameters from the power spectrum, which we will be measuring eventually in Ch. 7.

4.2 Inflation - Setting the Stage

Let us go back all the way to the unperturbed geometry discussed in Eq. (2.1) and again in flat space. As mentioned, inflation aims to describe a period of accelerated expansion. It can be seen quite quickly why this solves the flatness problem, for

[2]The potentially third pillar one can consider are string compactifications leading to de Sitter vacua, setting the stage for inflation [36]. This will not be the focus of this chapter.

example. From Eq. (2.9), if we want the left-hand side to become small, we need a period where $\frac{1}{aH}$ decreases and the same conclusion can be made to solve the horizon problem. Now $\partial_t \frac{1}{aH} < 0$, is equivalent to $\ddot{a} > 0$, which can be viewed as the defining characteristic of inflation.

There are two more deep insights we obtained from observations of the CMB. On the one hand, we observe that the small fluctuations for each component have the same overdensity profile. That is, for example for two species (for example dark matter and photons), right after inflation, we have $\frac{\delta\rho_a}{\bar{\rho}_a+\bar{p}_a} = \frac{\delta\rho_b}{\bar{\rho}_b+\bar{p}_b}$. We call this property adiabaticity. This means fluctuations can be captured by a single function of space, i.e. a scalar field that affected all other fields similarly. Phrased differently we believe the initial fluctuations were not created by several complicated processes, but one fundamental degree of freedom, that gave rise to all fluctuations.

Another implication of CMB measurements is that the perturbations seem to have the same power on almost all scales. This means that when looking at the fluctuations of the CMB, we see roughly the same distribution of fluctuations, whether one looks at a very small part of the sky or a very large part of the sky. This is shown in Fig. 4.1 showcasing the latest CMB results [25]. A constant line there would mean complete scale invariance. We note, however, that the scale invariance is approximate, with slightly more power in large fluctuations.

As mentioned in Sec. 2.6, scale invariance is a property that arises for the dynamics in de Sitter space. Therefore, the measured approximate scale invariance, combined with the required accelerated expansion, leads us to believe that the spacetime at the time of inflation was very close to de Sitter, i.e. quasi de Sitter. We saw that in Sec. 2.6 exact de Sitter space $\frac{\ddot{a}}{a} = H^2$. Instead, for quasi de Sitter space, we introduce deviations from that $\frac{\ddot{a}}{a} = H^2(1-\epsilon)$, where we can see

$$\epsilon = -\frac{\dot{H}}{H^2}, \tag{4.1}$$

and given we are interested in small deviations, we take $0 < \epsilon \ll 1$ [3]. The parameter ϵ is called the slow roll parameter, and as we will see shortly, relates to the potential of the scalar field responsible for inflation. Inflation ends when $\epsilon \to 1$; this is equivalent to saying $\ddot{a} \to 0$. In order to make sure that the accelerated expansion lasts long enough to solve the horizon and flatness problem mentioned above, ϵ cannot evolve too fast either. This leads us to introduce a second slow roll parameter $\xi_2 = \frac{\dot{\epsilon}}{H\epsilon}$ [4],

[3] The positivity of ϵ is given as long as the matter sector satisfies the null energy condition.

[4] We omit using the letter η as is typical for the second slow roll parameter since we use it as

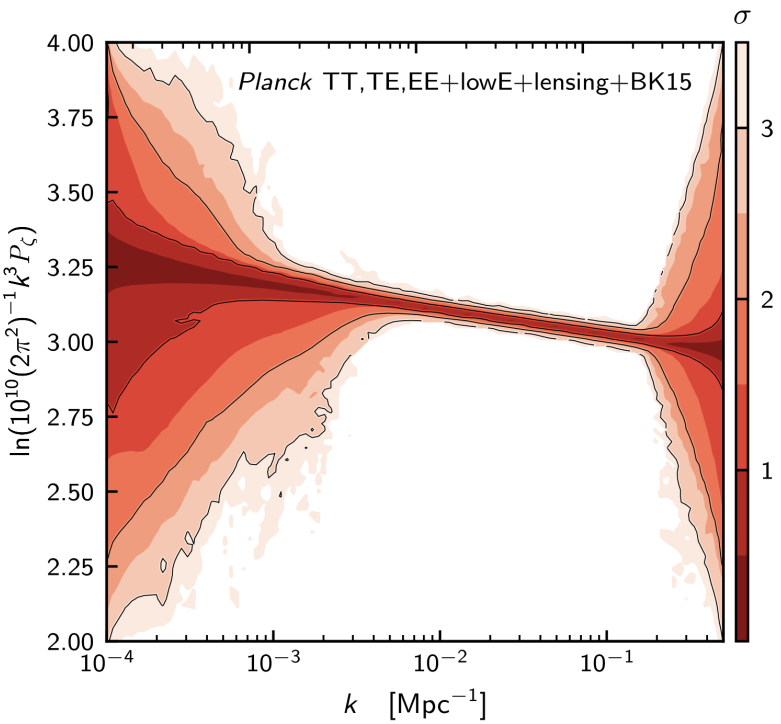

Figure 4.1: Reconstructed primordial power spectrum from the observed power spectrum of the CMB measurements, showcasing the approximate scale invariance of primordial fluctuations. The figure is taken from [25], with some variables adjusted to match the formalism used in this thesis.

which when assumed to be small, restricts ϵ to only evolve slowly.

Now let us explore the simplest and earliest models of inflationary backgrounds that can achieve the conditions mentioned above. This means we want to look at the background evolution in the presence of a scalar field in a for now general FRW background. To start, let us simply consider a scalar field with some potential

$$S = \int d^4x\sqrt{-g}\left[\frac{1}{2}(\partial_\mu\phi)^2 - V(\phi)\right], \tag{4.2}$$

and to make connections with all the formulas we developed in Ch. 2, we also write out the energy-momentum tensor given by

$$T_{\mu\nu} = \partial_\mu\phi\partial_\nu\phi - g_{\mu\nu}\left[\frac{1}{2}(\partial_\mu\phi)^2 + V(\phi)\right]. \tag{4.3}$$

Now we proceed similarly to Ch. 2 with a smooth background, and so we can, for now, neglect all spatial derivates and focus on the temporal ones only. That is, we, similarly to the previous matter variables, split the field into a time-dependent background part called $\bar{\phi}$ and a small spatially dependent perturbation, which we will discuss in the next section. From the energy-momentum tensor and our earlier definitions of density and pressure, we then get

$$\bar{\rho} = \frac{1}{2}\dot{\bar{\phi}}^2 + V(\bar{\phi}), \quad \bar{p} = \frac{1}{2}\dot{\bar{\phi}}^2 - V(\bar{\phi}). \tag{4.4}$$

We can get the equation of motion $\ddot{\bar{\phi}} + 3H\dot{\bar{\phi}} + V'(\bar{\phi}) = 0$, by plugging in the density and pressure into Eq. (2.3). Furthermore through Eq. (2.7), we can write $\epsilon = \frac{3\dot{\bar{\phi}}^2}{\frac{1}{2}\dot{\bar{\phi}}^2+2V}$. So if we want inflation to start with a very small value of ϵ and end when it becomes order one, we need to transition from most of the energy being in the potential

$$\frac{1}{2}\dot{\bar{\phi}}^2 \ll V, \tag{4.5}$$

to a point where the kinetic energy takes over. The second slow roll parameter can be written as $\xi_2 = 2\left(\frac{\ddot{\bar{\phi}}}{H\dot{\bar{\phi}}} + \epsilon\right)$. In the slow roll regime, this implies $\ddot{\bar{\phi}} \ll H\dot{\bar{\phi}}$, which through the equations of motions tells us that $H\dot{\bar{\phi}} \sim V'(\bar{\phi})$. Putting everything together and also using $H^2 \sim V$, we therefore get

$$|V'| \ll |V| \tag{4.6}$$

the conformal time variable throughout the inflation sections and in Ch. 5.

in the slow roll regime. Finally, taking the derivative of $H\dot{\bar{\phi}} \sim V'(\bar{\phi})$ and combining it with the smallness of the second derivative of $\bar{\phi}$, we obtain

$$|V''| \ll |V|, \tag{4.7}$$

in the regime where the slow roll parameters are small. So we now have three equations describing the potential in the slow roll phase, i.e., at the beginning of inflation. From Eq. (4.5), we see most of the energy is in the potential and not in the kinetic energy. Then Eqs. (4.6) and (4.7), tell us the potential changes very little in this regime, and the small slope is also not changing very much. This is why we called the parameters *slow roll* this whole time: the scalar field is slowly rolling down this very slightly varying potential. So to summarise, $\epsilon \ll 1$ makes sure we're rolling down this potential slowly, and $\xi_2 \ll 1$ make sure we do so for a prolonged period of time [5].

4.2.1 The Comoving Curvature Perturbation

In order to eventually make contact with observations, we have to address a similar subtlety as we did in Sec. 3.2, with the key difference that the perturbations we consider are so small that we have to quantise them. In Sec. 3.2, we encountered the gauge invariant Bardeen potentials, which are combinations of metric perturbations that do not change under changes of coordinates. We said there that there are more gauge invariant quantities when considering the matter sector as well, which will be the key for us when discussing inflation. We will focus again just on scalar perturbations, which allows us to compute all the parameters we will measure and forecast in Chs. 7 and 8 and is also the primary focus in Ch. 5.

Now with the exact same perturbation variables as defined in Sec. 3.2, and with $q = \frac{\partial_i}{\partial^2}\pi^i$ we can recognise that the combination

$$\zeta = \Phi - \frac{H}{\bar{\rho} + \bar{p}} q, \tag{4.8}$$

is gauge invariant and is called the comoving curvature perturbation. The correlations of ζ are the key observables of inflation [6], an example of which we have already

[5] We note that Eqs. (4.6) and (4.7) are a consequence of the smallness of the slow roll parameters, but only in that regime. That is, the smallness of the parameters implies the potential, but the potential is not the starting point of our discussion.

[6] There are, of course, other observables from the tensor or even vector sector, but we here focus on scalars.

seen in Fig. 4.1. The reason ζ is such a powerful variable for inflation is that for single field and adiabatic models $\dot{\zeta} = 0$ on super-horizon scales (so scales larger than the horizon at the time), and hence does not evolve [37, 38, 39]. This means that once the mode exits the horizon, they are frozen in time and, in particular, unaffected by how inflation ended. This is important because we currently have very little knowledge about how the energy in inflation was passed on to the standard model particles [7]. In turn, this also means that when computing observables in inflation, we want to predict them at the time of horizon crossing and match that to observations after horizon re-entry.

In the following sections, we will see how we can capture the quantum mechanical effects of the perturbed scalar field. We will first do quantum field theory on a curved spacetime to exemplify how we are quantising those systems and what calculations they entail, especially including interactions. Then, in Sec. 4.4, we will do explicit calculations in the Effective Field Theory of inflation. Note that, in the end, to make contact with observation, we will want to relate the model to ζ that we defined in Eq. (4.8), which we will do as well in Sec. 4.4.

4.3 Quantum Field Theory in FRW Universes and the In-In Formalism

In this section, we want to exemplify how we eventually treat fluctuations to the scalar field we discussed so far in a quantum mechanical way. In particular, we here assume that the metric is not perturbed. We will address this subtlety in the next section, where we will see that the theory that eventually describes the inflationary fluctuations operates exactly in the way we describe here, just with very particular interactions present. Furthermore, the formalism for the calculations we perform here is exactly what we challenge in Ch. 5. In order for the notation to be the same as there and to better discuss the symmetries, we will sometimes switch to conformal time $dt = a(\eta)d\eta$ and use the conformal Hubble parameter $\mathcal{H} = \partial_\eta a/a$.

Let us start by writing the scalar field as the background and fluctuation part $\phi_{\text{full}} = \bar{\phi}(\eta) + \phi(x, \eta)$. While we discussed the background in detail in Sec. 4.2, we, from here on, will always denote the fluctuation by ϕ, which we will now outline how we quantise it in curved space. Let us first consider the theory without interactions

[7] We note, however, that the modes eventually reenter the horizon and, after reentry, directly affect gravitational clustering.

with a general mass. We call this the free theory. On a general FRW background, the action then reads

$$S = \frac{1}{2}\int d^3x d\eta a(\eta)^4 \left[(\partial_\mu\phi)^2 + m^2\phi^2\right], \tag{4.9}$$

and the equations of motion can be read of as

$$\frac{1}{a^2}(\partial_\eta^2 + 2\mathcal{H}\partial_\eta - \partial_i^2 + a^2m^2)\phi(x,\eta) = 0. \tag{4.10}$$

To quantise the field and to solve the equations, we write the field out in its Fourier modes

$$\phi(x,\eta) = \int \frac{d^3k}{(2\pi)^3} e^{i\vec{k}\cdot\vec{x}} \left(f_k(\eta)a_{\vec{k}} + f_k^*(\eta)a^\dagger_{-\vec{k}}\right), \tag{4.11}$$

where a_k and $a_k^\dagger$ are the typical creation and annihilation operators [8], and it is often useful to call the term in the bracket in Eq. (4.11) $\phi(k,\eta)$, which is just the Fourier transformed field. The mode functions f_k are the classical solutions to the equations of motion in Fourier space, that is

$$\frac{1}{a^2}(\partial_\eta^2 + 2\mathcal{H}\partial_\eta + k^2 + a^2m^2)f_k(\eta) = 0. \tag{4.12}$$

Unfortunately we cannot solve the above equation in full generality. However, there are several useful examples that we will also use in Ch. 5 to showcase the results there. The normalisations of the mode functions, i.e. the boundary conditions, are given by the canonical commutation relations and annihilation of the flat space vacuum state in the infinite past [9]. Then some commonly used constellations are

$$f_k(\eta) = -i\frac{\sqrt{\pi}H}{2}e^{i\frac{\pi}{4}(1+2\nu)}(-\eta)^{3/2}H_\nu^{(1)}(-k\eta) \quad \text{(massive, dS)}, \tag{4.13}$$

$$f_k(\eta) = i\eta\frac{H}{\sqrt{2k}}e^{-ik\eta} \quad \text{(conformally coupled, dS)}, \tag{4.14}$$

$$f_k(\eta) = \frac{H}{\sqrt{2k^3}}(1+ik\eta)e^{-ik\eta} \quad \text{(massless, dS)}, \tag{4.15}$$

$$f_E(t) = \frac{e^{-iEt}}{\sqrt{2E}}. \quad \text{(Minkowski, } E = \sqrt{k^2+m^2}\text{)}, \tag{4.16}$$

[8] Typical in the sense that $[a_{\vec{k}}, a_{\vec{k}'}] = 0$, $[a_{\vec{k}}, a^\dagger_{\vec{k}'}] = \delta(\vec{k}-\vec{k}')$ and $a_{\vec{k}}|0\rangle$ defines the ground state of the Fock space.

[9] In de Sitter space, this defines the Bunch Davies vacuum.

where $\nu \equiv \sqrt{\frac{9}{4} - \frac{m^2}{H^2}}$, $H^{(1)}$ is a Hankel function and conformally coupled, means $\nu = 1/2$. These are the same examples we use in Eqs. (5.4) - (5.7). Conformally coupled are particularly interesting to study (for example [8, 40]) since they are closely related to the Minkowski ones, where we know quantum field theory very well. We will see in the next section that for the standard model of single field inflation, we will mostly be interested in a slightly modified version of the massless mode function in de Sitter space. The slight modification takes into account that we are not exactly in de Sitter space, but quasi de Sitter space captured by the slow roll parameters, and also introduces a general speed of sounds parameter.

Eventually, we are interested in correlation functions of these fields, at the time of reheating, which is when inflation ends, i.e. we are no longer in the accelerated expansion phase. We, therefore, take the limit $\eta \to 0$ when computing correlators. For example, the power spectrum is defined as

$$\lim_{\eta\to 0}\langle 0|\phi(k,\eta)\phi(k',\eta)|0\rangle = (2\pi)^3\delta_D(\vec{k}+\vec{k}')P_\phi(k), \tag{4.17}$$

and for a massless scalar field in de Sitter space, we have

$$P_\phi(k) = \lim_{\eta\to 0}|f_k|^2 = \frac{H^2}{2k^3}. \tag{4.18}$$

While slightly hard to spot, this power spectrum is scale invariant [10]. This is reminiscent of the approximate scale invariance in Fig. 4.1, and if we were to add Eq. (4.18) to Fig. 4.1, we would simply see a constant line. We will discuss how scale invariance is very slightly broken in the next section. The inflationary power spectrum will also give rise to two parameters that are still of great interest in observation, one of them measuring the deviation from exact scale invariance.

Note the similarity in the definition of Eq. (4.17) to Eq. (3.30), where we defined the power spectrum for classical late-time matter perturbations. Here, however, we are taking vacuum expectation values of a quantum mechanical system. As we noted there, however, the probabilistic nature of these late-time perturbations does, in fact, have its origin in the quantum mechanical perturbations we describe here.

Next, let us look at the interacting theory. That is, we allow the action in Eq. (4.9) to have terms that go as ϕ^3 or more. What exact interactions are present is a very complicated question, which, for single field inflation, we will answer in

[10] The condition for an n-point function in Fourier space to be scale invariant is for it to scale as $k^{-3(n-1)}$.

the next section. The exact interactions determine the shape of the potential we described in Sec. 4.2. Hence, the parameters we will derive in the next section that constrain the single-field interactions are fundamental to the understanding of inflation.

The primary objects we eventually hope to measure in cosmology are the late-time n-point spectra,

$$B_n(\vec{k}_1, ..\vec{k}_n) = \delta_D \left(\sum_{a=1}^{n} \vec{k} \right) \langle \prod_{a=1}^{n} \mathcal{O}(\vec{k}_a) \rangle, \tag{4.19}$$

where we defined inflationary n-point correlation functions

$$\langle \prod_{a} \mathcal{O}(\vec{k}_a) \rangle := \lim_{\eta \to 0} \langle \Omega | \prod_{a} \mathcal{O}(\vec{k}_a, \eta) | \Omega \rangle. \tag{4.20}$$

For simplicity, we restricted the discussion to equal time correlators, and $\mathcal{O}$ might be any operator of interest, such as ϕ or ζ. Let us briefly comment on our quantum mechanical picture that is best suited for this calculation [11]. In standard quantum mechanics, we typically work in the Schrödinger picture, where the states capture the time dependence of the system, and the operators stay fixed. In contrast, in the equivalent Heisenberg picture, the time dependence is carried by the operators, and the states are fixed. In perturbation theory, we will work in the commonly used interaction picture, which is a middle way between the two. By introducing interactions, we inherently changed the time evolution operator of the theory, i.e. the Hamiltonian. We split it into the free part, which we discussed above, and the interaction part that is new here. So we have $H = H_0 + H_{\rm int}$. The operators then evolve with the free Hamiltonian, while the states evolve with the interaction Hamiltonian, assuming we can do so perturbatively.

Now note that we introduced the vacuum of the interacting theory $|\Omega\rangle$ in Eq. (4.20). This vacuum is likely not the same as the one of the free theory. This is for the simple reason that in the free theory, the lowest energy eigenstate is the absence of particles. In an interacting theory, we do not per se know the lowest energy state. The key to even being able to compute any correlators in the presence of interactions is to find a way to relate the interacting vacuum to the free one. Indeed, it is this correspondence to the free vacuum that is new in Ch. 5, where we relate the interacting vacuum to a different free vacuum than is commonly done.

[11] We note that the result does not depend on what framework we work in; for us, this is simply a simplification in the calculation.

Commonly in cosmology, one relates all the interacting vacuums to the free vacuum in the infinite past, which is where we have a Minkowski-like free vacuum. This is then what we call the Schwinger-Keldysh [41, 42] in-in formalism, as was revived by Maldacena in [43]. We will see in Ch. 5 that the correlator, as defined in Eq. (4.20), is agnostic about this choice of computation technique. For now, we stay with the in-in formalism and show how we compute correlators in the standard way.

Throughout this section, we will assume unitary time evolution and neglect any form of dissipation. This is also a crucial assumption for Ch. 5. The time evolution operators satisfy $\partial_{\eta_2} U(\eta_2, \eta_1) = -iH_{\rm int}(\eta_2)U(\eta_2, \eta_1)$ and through unitarity $U(\eta_2, \eta_1) = U^\dagger(\eta_1, \eta_2) = U^{-1}(\eta_1, \eta_2)$. We can formally solve the time evolution operator by the Dyson formula

$$U(\eta_2, \eta_1) = T\exp\left(-i\int_{\eta_1}^{\eta_2} d\eta' H_{\rm int}(\eta')\right), \tag{4.21}$$

where T is the time ordering operator. We mentioned earlier that the primary purpose of the time evolution operator in this discussion is to relate the interacting vacuum to the free vacuum in the infinite past. In this process of 'switching off (on)' the interactions, a key concept is the adiabaticity, [12] meaning we want to turn them off slowly and smoothly. To make sure of this when projecting the vacuum, we introduce a factor $H_{\rm int} \to e^{-\epsilon|\eta|}H_{\rm int}$, always with implicitly taking $\epsilon \to 0$ [44]. In practice, to achieve this, when integrating from the infinite past, we rotate the time integral slightly so that we get an imaginary part, i.e. we integrate from $-\infty(1-i\epsilon)$. This is computationally simpler than writing $e^{-\epsilon|\eta|}H_{\rm int}$ every time and in almost all cases is equivalent. We are now in the position to relate the interacting vacuum to the free one, fully writing out Eq. (4.20) in the in-in formalism. We have

$$\begin{aligned}\langle\Omega|\prod_a \mathcal{O}(k_a,\eta)|\Omega\rangle &= \langle 0|U(-\infty,\eta)\prod_a \mathcal{O}(k_a,\eta)U(\eta,-\infty)|0\rangle \\ &= \langle 0|\left[\bar{T}e^{\left(i\int_{-\infty(1+i\epsilon)}^{\eta} d\eta' H_{\rm int}(\eta')\right)}\right]\prod_a \mathcal{O}(k_a,\eta)\left[Te^{\left(-i\int_{-\infty(1-i\epsilon)}^{\eta} d\eta' H_{\rm int}(\eta')\right)}\right]|0\rangle,\end{aligned} \tag{4.22}$$

where in the first line we can follow the intuition (from left to right) that we start with an asymptotically free vacuum, we evolve it forward to time η we insert the operator of interest, and sandwich it with another free theory vacuum that has been evolved to time η. What in-in (and other) contours look like in the η plane is shown

[12] The adiabaticity here is not to confuse with the fact that inflation primarily produced adiabatic perturbations.

in Fig. 5.3. The important notion here is that we projected both states on the infinite past vacuum, and interactions were turned off (on) adiabatically.

Apart from the power spectrum, which we have already showcased in Eq. (4.18), some of the currently more ambitious observables of inflation relate to three-point function, which we will explicitly calculate in the next section to leading order. For that, it is useful to explicitly expand Eq. (4.22) to first order. For a three-point function of a field ϕ to leading order, i.e. the Bispectrum, we have

$$\begin{aligned}
&\langle\Omega|\prod_{a=1}^{3}\phi(k_a,\eta)|\Omega\rangle = \qquad (4.23)\\
&= \langle 0|\left[1+i\int_{-\infty(1+i\epsilon)}^{\eta}d\eta' H_{\rm int}(\eta')\right]\prod_{a=1}^{3}\phi(k_a,\eta)\left[1-i\int_{-\infty(1-i\epsilon)}^{\eta}d\eta' H_{\rm int}(\eta')\right]|0\rangle\\
&= 2{\rm Im}\left(\int_{-\infty(1-i\epsilon)}^{\eta}d\eta'\langle 0|\prod_{a=1}^{3}\phi(k_a,\eta)H_{\rm int}(\eta')|0\rangle\right).
\end{aligned}$$

There are extensive Feynman rules to compute these diagrams very efficiently. We will refer to Sec. 5.3.2 for a full discussion. The three-point function above, at leading order, can be computed directly, which we show in the next section.

To conclude, we have established how we can compute 2-point correlators of the free theory in Eq. (4.18), as well as the leading order interaction of a three-point function in Eq. (4.23). We have not yet specified $H_{\rm int}$, or even ϕ, i.e. the theory we want to compare to observables. In the next section, we will showcase the interactions we want to consider and parametrise the results to make contact with observations.

4.4 Bispectrum Shapes and the EFT of Inflation

The exact interactions during inflation are not known, and numerous models were proposed over the years as possible candidates, including the simple slow roll model we discussed in Sec. 4.2, k-inflation [45], Dirac-Born-Infeld (DBI) inflation [46], and many others. The paradigm that emerged as the primary theory to make contact with observations is the Effective Field Theory of inflation [47]. As the name suggests, this is the theory that captures the relevant degrees of freedom from inflation at the inflationary energy scale without relying on knowing the full UV physics at the time. While primarily all perturbations are considered, including

metric perturbations, it eventually turns out that we can capture the physics of single field inflation by very particular interaction on a quasi-de Sitter background.

So let us comment on the Effective Field Theory of inflation since it is a key motivator for some of the parameters we try to measure nowadays using galaxy surveys [13]. The idea here is to build up an effective theory from the ground up, relying on symmetries only. The key to this is the fundamental property that inflation is a period of quasi-exponential expansion that had to end. This spontaneously breaks time-translations, which is the key to formulating the effective theory. Intuitively, given that the inflaton chooses a preferred slicing of space, we view it as a clock, measuring the time until inflation ends. To see how the symmetries play out here, note that we have explicitly split the field into the background and fluctuation $\phi_{\text{full}} = \bar{\phi}(\eta) + \phi(x, \eta)$. While ϕ_{full} is a scalar under spatial and temporal diffeomorphisms, the perturbation $\phi(x, \eta)$ is not. Explicitly, we have,

$$t \to t + \xi^0(t, \vec{x}), \quad \phi \to \phi + \dot{\bar{\phi}}\xi^0(\vec{x}). \tag{4.24}$$

To formulate the Effective Field Theory of inflation, we are now going to gauge away this fluctuation; that is, we choose a coordinate system where $\phi = 0$, which is exactly possible because ϕ is not gauge invariant as we see above. This means that all the fluctuations are in the metric. This might seem unintuitive, but it is simply a choice of coordinates that makes it simpler to formulate the Effective Field Theory. Eventually, we will reformulate the theory in terms of a scalar field. Note that we fixed the time diffeomorphisms, that is, ξ^0, and we only have spatial diffeomorphisms as a symmetry. In the intuitive picture, where we are describing a clock, this means we have fixed the space to be characterised by where the clock is set to zero.

The task is now to formulate all the possible terms of the metric that are invariant under spatial diffs. Of course, the regular general relativity terms are, as they are invariant under all diffs. The way to construct these building blocks is typically done in the ADM formalism [50], which splits writes the space in terms of hypersurfaces of constant time, keeping the spatial diffs manifest on each hypersurface Σ_t. There are eventually two fundamental building blocks for the EFT that are invariant under spatial diffs [51, 47]. Simply the 00 component of the metric g^{00}, and the extrinsic curvature $K_{\mu\nu}$ of the constant time hypersurfaces. We write the Lagrangian in those variables, with respect to the unperturbed FRW ones, that is $\delta g^{00} = 1 + g^{00}$ and

[13] As we will see, the Effective Field Theory of inflation is very similar to the Effective Field Theory of dark energy [48, 49], and is therefore somewhat relevant to Ch. 10.

$\delta K_{\mu\nu} = K_{\mu\nu} - a^2 H h_{\mu\nu}$, and $h_{\mu\nu}$ is the induced metric on the hyper slices. Note that the situation is extremely similar as in Sec. 3.3.2, where we first established the symmetries we need to be invariant under and then expanded in all the independent fields that satisfy the symmetries. Furthermore, as is typical in any EFT, we do not know the coupling strength of these effective interactions, and we introduce coefficients in front of all operators that can, in general, be time dependent [14]. The most general spatially invariant Lagrangian in terms of metric perturbations then reads

$$\begin{aligned} S &= \int d^4x \sqrt{-g}\Big[\frac{1}{2}M_{\rm Pl}^2 R - c(t)g^{00} - \Lambda(t) + \frac{1}{2!}M_2(t)^4(\delta g^{00})^2 + \frac{1}{3!}M_3(t)^4(\delta g^{00})^3 + \\ &\quad -\frac{\bar{M}_1(t)^3}{2}\delta g^{00}\delta K^{\mu}{}_{\mu} - \frac{\bar{M}_2(t)^2}{2}\delta K^{\mu}{}_{\mu}{}^2 - \frac{\bar{M}_3(t)^2}{2}\delta K^{\mu}{}_{\nu}\delta K^{\nu}{}_{\mu} + ...\Big]\,, \end{aligned} \tag{4.25}$$

where we opted for the same notation as in [47], but in fact, this is the same effective Lagrangian that we will discuss in the context of dark energy in Ch. 10, in particular Eq. (10.1), and as we can see there, the background quantities can be related to the unperturbed terms [15], in particular, $c(t) = -2\dot{H}M_{\rm Pl}^2$, where $M_{\rm Pl}^2 = 1/(8\pi G)$ is the Planck mass.

So, we have formulated the most general Lagrangian in terms of metric perturbations invariant under spatial diffs. Now, the task remains to formulate this in terms of the fluctuating scalar degree of freedom that we earlier introduced as being the clock. We introduce the fluctuations in this clock by shifting $t \to t + \pi(\vec{x}, t)$, which restores the time diffeomorphism invariance. Under this shift, the metric 00 perturbation, for instance, changes as

$$\delta g^{00} \to 1 + (1+\dot{\pi})^2 g^{00} + 2g^{0i}\partial_i\pi + g^{ij}\partial_i\pi\partial_j\pi. \tag{4.26}$$

Finally, a couple of technical considerations show that to the order we work we don't have to consider the extrinsic curvature, and mixing with gravity is a higher order effect. Collecting all the terms from Eqs. (4.25) and (4.26), we finally get the action for the Goldstone boson π up to third order

$$S_\pi = -\int d^4x \sqrt{-g}\frac{M_{\rm Pl}^2\dot{H}}{c_s^2}\left[\dot{\pi}^2 - c_s^2\frac{(\partial_i\pi)^2}{a^2} + \left(c_s^2 - 1\right)\dot{\pi}\frac{(\partial_i\pi)^2}{a^2} + \lambda_1\dot{\pi}^3\right], \tag{4.27}$$

[14] In Sec. 3.3.2 we even had non-local in time couplings, so there we had time-kernels.

[15] We have seen similarities between dark energy and inflation already when we discussed de Sitter space in Sec. 2.6, where we had a negative equation of state parameter w.

where we defined the speed of sound $c_s^{-2} = 1 - \frac{2M_2^4}{M_{\rm Pl}^2\dot{H}}$, the coupling constant $\lambda_1 = \frac{4}{3}\frac{c_s^2 M_3^4}{M_{\rm Pl}^2\dot{H}} - (c_s^2 - 1)$ and in the process did some normalisations. This is the Lagrangian we will work with to compute the power spectrum and bispectrum according to the methods in the previous section. Let us start with the mode functions. We have a massless scalar in de Sitter, with slightly more complicated normalisation, and the sole real difference is that every factor of k is accompanied by a speed of sound term. We therefore have

$$f_k(\eta) \;=\; \frac{i}{2\sqrt{M_{\rm Pl}^2 c_s \epsilon k^3}}(1 + ic_s k\eta)e^{-ic_s k\eta}, \tag{4.28}$$

which from here on allows us to use all the formulas derived in the previous section. The final piece now is that we have to relate the field π we introduced here to the comoving curvature perturbation Eq. (4.8) that we eventually measure. The two can be related by simply considering the gauges they are defined in as is done in [52, 43] to find $\zeta = -H\pi$ [16]. So, we can start with the power spectrum; we have

$$P_\zeta(k) = H^2 P_\pi(k) = H^2 \lim_{\eta\to 0} |f_k|^2 = \frac{H^2}{4c_s M_{\rm Pl}^2 \epsilon k^3}. \tag{4.29}$$

As mentioned in the last section, the correlations we observe today after reentry into the horizon have been frozen from the time they exited the horizon at $k = aH$. Since H is slowly evolving as given by Eq. (4.1), this means that the different modes exit the horizon slightly earlier than others, which is exactly what causes the slight scale dependence in Fig. 4.1. Note that this is a direct consequence of the 'quasi' de Sitter expansion, and therefore, this scale invariance should depend on the slow roll parameters. To measure this deviation from scale invariance, we introduce a parameter n_s called the spectral index, defined by [17]

$$n_s - 1 = \frac{d\log k^3 P_\zeta(k)}{d\log k} \simeq \frac{1}{H}\frac{d}{dt}\log\left(\frac{H^2}{c_s\epsilon}\right) = -2\epsilon - \xi_2 - s, \tag{4.30}$$

where similarly to [52] we have introduced $s = \frac{\dot{c}_s}{Hc_s}$, which is also expected to be small. So we see that the deviation from scale invariance $n_s - 1$ is directly related to the slow roll parameters, which are responsible for the small deviation from scale

[16] In essence we relate the ζ gauge, with spatial metric $h_{ij} = a(t)^2 e^{2\zeta} d\vec{x}^2$, and $\pi = 0$, to the gauge here where $h_{ij} = a(t)^2 d\vec{x}^2$ and $\pi \neq 0$, by a time shift.

[17] We note again that scale invariance in Fourier space would mean the power spectrum would go as k^{-3}. Hence we define a measure of the deviation from $k^3 P_\zeta(k)$.

invariance. With this parameter in hand, we typically parameterise the primordial power spectrum as

$$P_\zeta(k) = \frac{2\pi^2}{k^3} A_s \left(\frac{k}{k_0}\right)^{n_s - 1}, \tag{4.31}$$

where k_0 is a chosen pivot scale, and we introduced the amplitude $A_s = \frac{H^2}{8\pi^2 c_s M_{\rm Pl}^2 \epsilon}$. Current measurements the parameters A_s and n_s and constraints from the CMB are quite conclusive with $A_s = (2.098 \pm 0.023)10^{-9}$ and $n_s = 0.965 \pm 0.004$ [25], where a pivot scale of $k_0 = 0.05\text{Mpc}^{-1}$. These results can almost be read off from Fig. 4.1; we simply have to look at the value of the function at the pivot scale to find roughly $\ln(10^{10} A_s) \simeq 3.04$ and the slope gives us $n_s - 1$. We will encounter these parameters again in Chs. 7 and 8, where we will constrain and forecast constraints using galaxy surveys.

If no interactions were present, the free theory predicts a Gaussian distribution of fluctuations. Now, let us turn to the more ambitious parameters from inflation, measuring deviations from complete Gaussianity. To leading order, these are the three-point functions induced by the $\mathcal{O}(\pi^3)$ terms. We can see from Eq. (4.27) that unless the speed of sound is exactly one, the effective theory predicts there must be non-Gaussianity present. Note that to leading order in interactions, the interaction Hamiltonian simply splits into two parts $H_{\rm int} = H_{\rm int}^{\dot\pi(\partial_i\pi)^2} + H_{\rm int}^{(\dot\pi)^3}$ and we distinct contributions for each of the two interactions in Eq. (4.27). The two bispectra we get are then given by [18]

$$\begin{aligned} B_\zeta^{(\dot\pi)^3} &= \frac{3H^4\lambda_1}{8c_s^2 M_{\rm Pl}^4 \epsilon^2} \frac{1}{e_3 k_T^3} \\ B_\zeta^{\dot\pi(\partial_i\pi)^2} &= \frac{H^4}{64 c_s^2 M_{\rm Pl}^4 \epsilon^2} \left(1 - \frac{1}{c_s^2}\right) \frac{6e_2 k_T^4 - 22 e_3 k_T^3 + 8 e_2^2 k_T^2 + 8 e_2 e_3 k_T - 24 e_3^2 - 2k_T^6}{e_3^3 k_T^3}, \end{aligned} \tag{4.32}$$

where $k_T = k_1 + k_2 + k_3$ is the total energy, and $e_2 = k_1k_2 + k_2k_3 + k_1k_3$ and $e_3 = k_1k_2k_3$ are the two other elementary symmetric polynomials. Similar to the power spectrum in Eq. (4.31), we want to parametrise the theory in terms of its scale-invariant parts and introduce coefficients that capture the new physics. For

[18] The same discussion about the approximate scale invariance and n_s can be done for the bispectrum. That is, we are still interested in the modes when they exit the horizon. However, this is a subleading effect here.

the bispectrum, we define the template

$$B_\zeta = \frac{9}{10}\frac{H^4}{4M_{\rm Pl}^4\epsilon^2 c_s^2}\sum_i f_{NL,i}\frac{\mathcal{S}_i(k_1,k_2,k_3)}{(k_1k_2k_3)^2}, \tag{4.33}$$

where the numerical prefactor is there for historical reasons and the shape function has normalisation $\mathcal{S}(k,k,k)=1$. We made explicit that the total bispectrum can be a function of many different shape functions, for example, the two we calculated in Eq. (4.32). There are many other shapes one could consider, and the choice of basis for the $\mathcal{S}_i$ is a field in of itself [53].

Now, from the definition of the shape functions and $f_{\rm NL}$ in Eq. (4.33) and the definitions of the parameters below Eq. (4.27), we get the two non-Gaussianity parameters as predicted by the EFT of inflation

$$f_{\rm NL}^{(\dot\pi)^3} = \frac{5}{81}\lambda_1, \quad \text{and} \quad f_{\rm NL}^{\dot\pi(\partial_i\pi)^2} = \frac{85}{324}\left(1-\frac{1}{c_s^2}\right), \tag{4.34}$$

and the shape functions can be read off from Eq. (4.32) immediately. In Eq. (4.33), it is left implicit what basis of shape functions we use to describe the full bispectrum. The canonical choice of using the bispectra that are coming directly from the theoretical motivation in Eq. (4.32) turns out to not be optimal for the data analysis. For practical use, optimal templates have been developed to generate shape functions that are as independent as possible [19]. This led to the introduction of the equilateral and orthogonal templates

$$\begin{aligned}\mathcal{S}_{\rm eq.}(k_1,k_2,k_3) &= \frac{4e_2k_T-8e_3-k_T^3}{e_3},\\ \mathcal{S}_{\rm orth.}(k_1,k_2,k_3) &= \frac{12e_2k_T-26e_3-3k_T^3}{e_3},\end{aligned} \tag{4.35}$$

and the parameters can be related to the one directly coming from the EFT of inflation by a simple linear combination [20]

$$\begin{pmatrix} f_{\rm NL}^{\rm equil.}\\ f_{\rm NL}^{\rm orth.}\end{pmatrix} = \begin{pmatrix} 1.040 & 1.210\\ 0.1079 & -0.06572\end{pmatrix}\begin{pmatrix} f_{\rm NL}^{\dot\pi(\partial_i\pi)^2}\\ f_{\rm NL}^{(\dot\pi)^3}\end{pmatrix}. \tag{4.36}$$

[19] The independence can be made quantitative through a scalar product, as developed in [54].

[20] This change of basis is not exact, as the bases are finite and do not span the exact same space. However, this deviation is currently a much smaller effect than the size of the error in the experiments.

Finally, there is one more type of non-Gaussianity that we are typically interested in. In contrast to the previous parameters that are direct predictions from the EFT of Inflation, the historically first template that was introduced in the context of inflation was done from phenomenological considerations. This first template for non-Gaussianity was introduced in [55], called the local type template. This is motivated by the simplest modification to the field itself, assuming the full curvature perturbation is a local function of the free (i.e. Gaussian) field ζ_G. Then, the modification we consider is given by

$$\zeta = \zeta_G + \frac{3}{5} f_{NL}^{\text{loc.}} \left(\zeta_G^2 - \langle \zeta_G^2 \rangle \right) , \tag{4.37}$$

where we made sure we still have a mean zero field by subtracting the mean and the prefactor of $\frac{3}{5}$ is again for historical reasons. From this modification, we, by design, get a bispectrum as well that reads

$$B_\zeta^{\text{loc.}} = \frac{6}{5} f_{NL}^{\text{loc.}} P_\zeta(k_1) P_\zeta(k_2) + 2\text{perms.} , \tag{4.38}$$

and so we get the shape function

$$\mathcal{S}_{\text{loc.}}(k_1, k_2, k_3) \;\; = \;\; \frac{1}{3} \frac{k_3^2}{k_1 k_2} + 2\text{perms.} . \tag{4.39}$$

This type of non-Gaussianity is not predicted by the Effective Field Theory and detection would hence rule out single-field inflation. Indeed, even before the formulation of the EFT of inflation, it was shown to have to be very small in any single field inflationary model [43]. It was later shown that, while zero in single field models, it can be generated in multifield models of inflation [56]. Therefore, this parameter is a direct test of whether multiple fields were present in the inflationary period.

These are the final three non-Gaussianity parameters that we will eventually be interested in in this thesis when making contact with observations. We note that there are now many more templates trying to capture very different effects during inflation (for example [57, 58, 59]). However, even constraints on the three standard non-Gaussianity parameters are quite weak at the moment [60], with $f_{NL}^{\text{loc.}} = -0.9 \pm 5$, $f_{\text{NL}}^{\text{eq.}} = -26 \pm 47$, $f_{\text{NL}}^{\text{orth.}} = -38 \pm 24$. Therefore, we focus on these major inflationary parameters in Ch. 8, where we will see how galaxy surveys might improve on those constraints and potentially even lead to a detection.

To conclude, we have introduced five inflationary parameters, two from the power spectrum Eq. (4.31), and three different types of non-Gaussianity from the bispectrum Eq. (4.33). The local type $f_{NL}^{\text{loc.}}$ is a measure of finding out whether there was more than one field present in inflation. The other two types, $f_{\text{NL}}^{\text{eq.}}$ and $f_{\text{NL}}^{\text{orth.}}$ give direct insight into the interactions present in inflation as motivated by the Effective Field Theory of inflation.

Part II

The Very Early Universe

The Ins and Outs of Inflation

5

The In-Out Formalism for In-In Correlators

5.1 Summary

Cosmological correlators, the natural observables of the primordial universe, have been extensively studied in the past two decades using the in-in formalism pioneered by Schwinger and Keldysh for the study of dissipative open systems. Ironically, most applications in cosmology have focused on non-dissipative closed systems. We show that, for non-dissipative systems, correlators can be equivalently computed using the in-out formalism with the familiar Feynman rules. In particular, the myriad of in-in propagators is reduced to a single (Feynman) time-ordered propagator and no sum over the labelling of vertices is required. In de Sitter spacetime, this requires extending the expanding Poincaré patch with a contracting patch, which prepares the bra from the future. Our results are valid for fields of any mass and spin but assuming the absence of infrared divergences.

We present three applications of the in-out formalism: a representation of correlators in terms of a sum over residues of Feynman propagators in the energy-momentum domain; an algebraic recursion relation that computes Minkowski correlators in terms of lower order ones; and the derivation of cutting rules from Veltman's largest time equation, which we explicitly develop and exemplify for two-vertex diagrams to all loop orders.

The in-out formalism leads to a natural definition of a de Sitter scattering matrix, which we discuss in simple examples. Remarkably, we show that our scattering matrix satisfies the standard optical theorem and the positivity that follows from it in the forward limit.

5.2 Introduction

Conquering of the atomic scale required not only cutting-edge mathematical structures but also a major overhaul of our ideas of the natural world. The demise of determinism implied by the uncertainty principle and a new picture of physical reality were not, and still are not, easy to swallow. Nevertheless, repeated confrontation with data and mathematical consistency has left us no choice but to abandon classical realism and embrace the confounding beauty of the quantum world. Many of us suspect, hope and fear that the conquering of the Planck scale will similarly require abandoning cherished principles of physics such as locality and the fundamental nature of space and time. To be successful we will no doubt need new advanced mathematics and, at the same time, a tight web of experiments and observation that yet again leave us no choice but to abandon our old prejudices. Currently, our best hope for a confrontation with nature about the character of gravity and spacetime comes from the study of the primordial universe and the treasure trove of information that is stored in cosmological correlators. Meaningful observational data might not be collected next year, the next decade, or even during our life span. Nevertheless, such data will one day be collected and will constitute a milestone of human civilization. In this work, we put forward a small piece of technology that we hope will help us better compute and understand cosmological correlators in quantum field theory.

A correlator is the quantum expectation value of the product of a set of operators in a given state. When we apply quantum field theory in curved spacetime to the study of the primordial universe, we are interested in local quantum fields that we can later measure in cosmological data sets. Moreover, we focus on the unique de Sitter invariant quantum state that reduces to the Minkowski vacuum on short distances, namely the Bunch-Davies state [61] (a.k.a. Hartle-Hawking or Euclidean state [62]). In the past twenty years, these correlators have been studied using the so-called *in-in formalism*, following suggestions in [43, 63] (see [64] for a review). This formalism had been developed much earlier in the pioneering work of Schwiger [41], Keldysh [42] and Feynman and Vernon [65] for the study of out-of-equilibrium open quantum systems (see e.g. [66, 67] for modern textbooks). The main raison d'être of this formalism is to account for the exchange of energy and information between an open system and its environment, which leads to dissipation, fluctuations and non-unitary evolution. Ironically, the vast majority of applications of the

in-in formalism to cosmology have been restricted to closed quantum systems undergoing unitary, non-dissipative time evolution. Here we point out that, for these non-dissipative systems, we actually have the alternative and equivalent option of using the *in-out formalism*, which is more familiar to many from the study of scattering amplitudes.

Indeed, correlators in the Heisenberg picture have no allegiance to in-in or in-out: they are just correlators of operators on a given state, which is often taken to be the "vacuum" $|\Omega\rangle$ of the interacting theory. The catch is that often we don't know non-perturbatively what $|\Omega\rangle$ is. Instead, we approximate it via an iteratively perturbative expansion. This is most apparent in the so-called interaction picture, where the easy evolution described by the quadratic Hamiltonian is accounted for by working with free fields and the difficult non-linear interactions appear in the preparation of the bra and ket of a correlator. It is here that we face a choice. We can prepare the bra and the ket by adiabatically turning on interactions in the infinite past and evolving forward or in the infinite future and evolving backwards. A natural choice may be to mimic the physical problem under investigation. For example in a scattering experiment we like to think of particles coming from the infinite past and wandering off to the infinite future and the in-out formalism fits this intuition. But we don't have to make this choice. We can perfectly well use the Lehmann–Symanzik–Zimmermann (LSZ) formula on the in-in correlators instead. A major advantage of the in-out formalism is that it minimizes bookkeeping: all operators are in the same time ordering, whether they are fields or interactions in the Hamiltonian. As a consequence, each Feynman diagram corresponds to a single product of propagators and vertices and most importantly all propagators are time-ordered Feynman propagators.

When working with a given physical system, there may be limits in which it is consistent to adiabatically turn on and off interactions and limits in which this is not possible. For example, for correlators in de Sitter spacetime in the expanding Poincaré patch, as relevant for cosmology, we have the spacelike future conformal boundary and the null past cosmological horizon (which can be reached in finite proper time but always with an infinite proper volume [68]). The condition of starting with the Bunch-Davies state tells that we can prepare both the bra and the ket by evolving from the Fock vacuum on the past cosmological horizon and this is why this has been the prominent choice in the literature so far. Conversely, it seems more

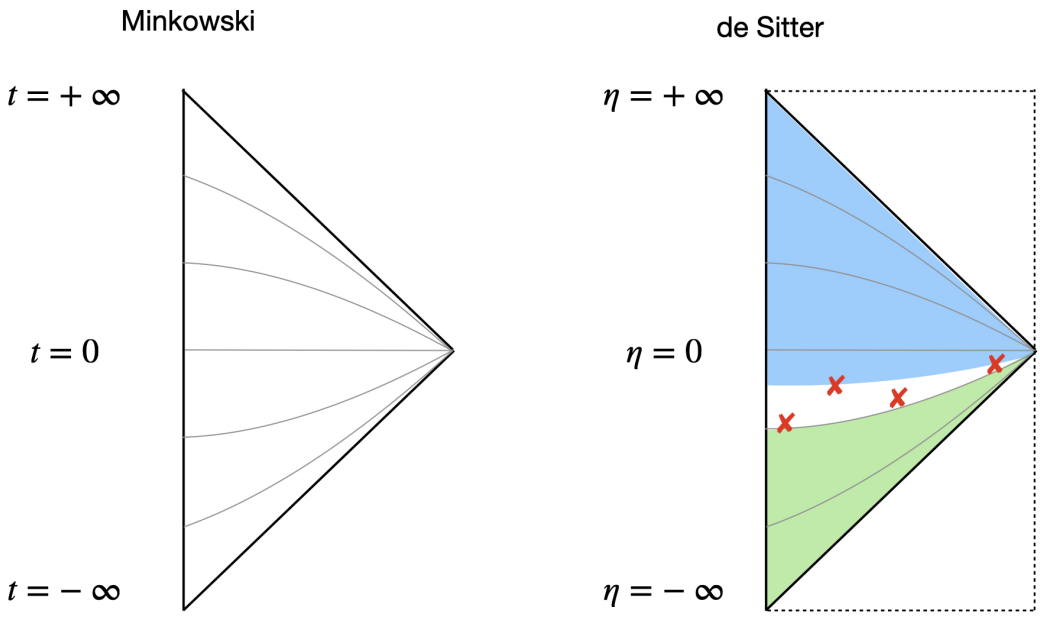

Figure 5.1: The Penrose diagrams of Minkowski (left) and de Sitter spacetime (right). The de Sitter diagram has been extended with an additional copy of the contracting Poincaré patch that allows one to prepare the bra (blue-shaded region) using the in-out formalism. The green shaded region is the preparation of the ket and the red crosses represent insertions of local operators.

complicated to turn off interactions towards the future conformal boundary because of the phenomenon of particle production and the decay instability of particles of any mass. It turns out that these are not insurmountable obstacles and concrete constructions have been devised to obtain a well-defined set of amplitudes [68, 69]. Here instead we explore a different possibility: we prepare the ket from the past null cosmological horizon as usual, but instead *we prepare the bra from the future null conformal horizon of an auxiliary contracting Poincaré patch*, as shown in the right panel of Fig. 5.1. The similarity to Minkowski spacetime is evident. With this extended spacetime in mind, we set up the in-out formalism and we prove it's equivalent to the traditional in-in formalism, in the context of QFT in curved spacetime.

Our main motivation to develop an in-out formalism was to find a non-perturbative optical theorem that can be used in cosmology to constrain low-energy theories that admit a standard UV completion. At the perturbative level, some consequences of unitary time evolution in FLRW spacetime have been understood in the form of the cosmological optical theorem [70, 71, 72, 73, 74, 75, 76]. This has been useful to bootstrap [77] perturbative correlators [78, 79, 80, 81, 82], but it is insufficient to derive general positivity bounds, where one constrains an unknown and not-necessarily perturbative UV-completion. Beautiful progress on the non-perturbative side has been obtained in [83, 84] using the Kähllen-Lehman representation (see also [85, 86, 87]) and related ideas that leverage group theory and harmonic analysis. In this work, a non-perturbative constraint from unitarity can be obtained because the textbook derivation of the optical theorem in Minkowski also applies to our de Sitter scattering matrix (see Sec. 5.7), which is naturally defined in our in-out formalism. We only preview some results about this topic, which will be discussed in a separate publication.

Shopping Advice So you have to compute a few correlators explicitly, but don't know what formalism to choose? Here are some handy top tips to consider before you start scribbling away on your tablet:

- In-in formalism.

  Pros: It can handle dissipation, fluctuations and non-unitary evolution. Indeed this was the main reason why this formalism was developed (see e.g. [67] and [88]). Even if the evolution of a "closed" system such as the universe is expected to be unitary (but see [89, 90] for a different point of view), if

we only observe part of the systems we are working with an *open system* and at the quantum level we need to use words such as density operator, Liouvillian, pure-to-mix state evolution and Markovian approximation.

Cons: The large number of propagators (four bulk-bulk and two bulk boundary) and the exponential proliferation of labellings of diagrams (2^{V-1} for a diagram with V vertices) are a considerable nuisance. Moreover, we miss out on a lot of the intuition coming from the extensive study of scattering amplitudes.

- In-out formalism.

Pros: There is a single propagator! And it's everyone's favourite: the time-ordered Feynman propagator. The 2^{V-1} contributions of the in-in calculation are nicely repackaged into a "single" (nested) integral expression [1].

Cons: It cannot handle dissipation. For scattering experiments, this is not a problem because of the excruciating care that experimentalists put into shielding particle collisions from the rest of the world. Conversely, in less artificial systems such as many condensed matter systems and cosmology, this limitation prevents us from accessing many beautiful phenomena.

Summary of the Results For the convenience of the reader we summarize here our main results:

- We developed an in-out formalism to compute unequal time correlators in Minkowski, de Sitter and more general cosmological spacetimes. The formalism crucially assumes the absence of late-time IR divergences, which in practice means that the divergence of the flat-slicing volume at future infinity, $\eta \to 0$, has to be offset by the decay of fields and their derivatives (see discussion around Eq. (5.27)). The formalism applies to fields of any mass and spin. The Feynman rules, outlined around Eq. (5.43), are the same as for the standard in-out Minkowski correlators (also the same as for amplitudes except one does not amputate external legs). In particular, all lines, both internal and external, correspond to a time-order Feynman propagator. As compared to the in-in formalism, this removes the need to sum over all the possible ways

[1] To be fair we should point out that in the time domain, the Feynman propagator has two time orderings. However in the frequency/energy domain in Minkowski both are captured by a single term, courtesy of the Feynman $i\epsilon$ prescription, $1/(p^2 + i\epsilon)$.

to label each vertex as “left" and “right". We presented a formal argument for the equivalence of in-in and in-out formalism and some explicit checks in perturbation theory. The equivalence is depicted in Fig. 5.2.

- We used the in-out formalism to provide two new procedures to compute correlators, and for concreteness we focus on equal time products of scalars. These results are obtained with similar manipulations as in a parallel study of the wavefunction [91]. The first procedure, which we dub “pole bagging", leverages the simplicity of the Feynman propagator in the energy-momentum domain in Minkowski to write a (loop integrand of a) correlator as a sum of residues of products of propagators. This can also be extended to massless and conformally coupled scalars in de Sitter. The second procedure consists of an algebraic recursion relation that iteratively removes internal lines of a diagram reducing it to linear combinations of simpler diagrams. The main novelty of our results is that we work directly at the level of the observable correlators, rather than the somewhat more primitive wavefunction.

- Time-ordered and anti-time-ordered products of operators are related by an operator identity [2], Eq. (5.108), which is sometimes equivalently stated as the “largest time equation" [94] and leads to the amplitude cutting rules. We use this identity to derive an infinite number of cutting rules for correlators in Minkowski and cosmological spacetimes including de Sitter, where we restrict to massless and conformally coupled scalars. The number of correlator cutting rules grows quickly with the complexity of the diagram and we provide a systematic study of one- and two-vertex diagrams (see Sec. 5.6 and the summary Eq. (5.139)) to all loop orders and discuss three-vertex diagrams in App. A.2.

- The in-out formalism suggests a straightforward definition of a de Sitter S-matrix describing scattering from the past to the future null horizon (see also [69] for the discussion of a similar but not identical object). We show some simple examples for a number of conformally coupled scalars. A main advantage of our definition is that amplitudes satisfy the standard optical theorem. Moreover, the symmetry between the initial and final states ensures that the imaginary part of the forward scattering amplitudes, which in Minkowski becomes a discontinuity under appropriate analyticity assumptions, is positive

[2] This was used in a related context in [92, 93], where it was called “CFT optical theorem".

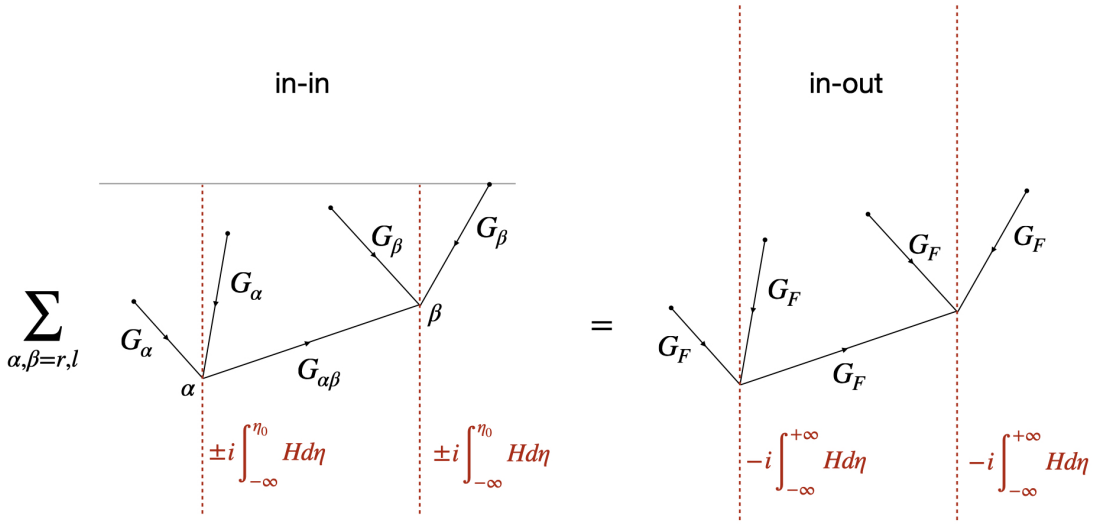

Figure 5.2: An example of the equivalence of the in-in and in-out formalism. Left: the in-in formalism requires summing over all possibilities to label vertices as "l" (left) or "r" (right); the bulk-boundary propagators G_r and G_l and bulk-bulk propagators G_{ll}, G_{lr}, G_{rl} and G_r are then chosen accordingly. Right: the in-out formalism is a single expression where all propagators are Feynman propagators.

because of unitarity (see Sec. 5.7). A dedicated analysis will appear in a separate publication.

Relation to Previous Work Some aspects of our discussion are closely related to previous work (see e.g. [95] for a review of in-in, in-out and Euclidean formalism in the finite temperature context). In particular, in a series of nice papers initiated with [96, 68], Marolf and Morrison studied perturbation theory in de Sitter. Particularly relevant for us is their construction of an S-matrix for *global* de Sitter spacetime by glueing together a contracting and an expanding Poincaré patch *along the common cosmological horizon*. An interesting aspect of their setup is that the cosmological horizon of the Poincaré patch can be reached from anywhere in global dS in a *finite* proper time. Hence it is natural to extend the path integral contour right through this surface. Here we take a similar but complementary route by glueing two Poincaré patches along their future/past conformal boundaries (see Fig. 5.1). This has the advantage that our path integral contour runs straight, just like in Minkowski. In particular, our path integral does not bend on itself creating

so-called “timefolds" and hence we avoid the associated proliferation of propagators and labelling of interaction vertices. Conversely, since it takes an infinite amount of proper time to reach the future conformal boundary, in our construction perturbations can move from one Poincaré patch to the other only in a conformal sense, i.e. only after jettisoning a divergent conformal factor. While we concede that this makes the physical interpretation less intuitive, we don't think this is a problem because all operators are inserted in a single patch and the second patch is just invoked as an equivalent preparation of the bra of the correlator. Moreover, we postpone to future work a discussion of how to apply an LSZ-like reduction to correlators in our in-out formalism to derive an S-matrix.

The “extended" spacetime in Fig. 5.1 is reminiscent of the suggestion of so-called “conformal cyclic cosmology" [97]. Here however the (upper) contracting Poincaré patch is just auxiliary and all operators are inserted in the (lower) expanding patch. In passing we do notice that correlators of a Lorentzian conformal field theory naturally live on an infinite cylinder, rather than on a single copy of the conformal Minkowski diagram [98]. This ensures that finite special conformal transformations don't violate causality (see e.g. [99]). Since de Sitter is conformally flat it is equally natural to consider an infinite conformal extension, of which we are only making partial use here.

The in-out formalism suggests a natural definition of a dS scattering matrix, with asymptotic states in the past and future null infinities of Fig. 5.1. This S-matrix turns out to be quite similar to the “Bunch-Davies S-matrix" recently discussed in [69]. We comment on this in Sec. 5.7.

We are not the first to propose a rotation of the in-in contour that leads to a simplification of the calculation. One proposal, going back to [43] and then fully developed in [100] and [84], is to straighten out the closed-time contour by rotating the time-ordered and anti-time-ordered branches by 90 degrees counterclockwise and clockwise respectively, so that the contour coincides with the purely imaginary axis of the complex η plane (see Fig. 5.3). The result is then precisely related to a perturbative calculation in Euclidean AdS, where the imaginary part of η is interpreted as the radial coordinate. A second and related proposal was put forward in [101] and used again in [102]. It consists of the same contour rotation where one recognizes that the time and anti-time ordering of the in-in contour combine into a single anti-time ordered Euclidean Green's function. Our proposal in this work shares with previous proposals the idea of straightening the in-in contour so that

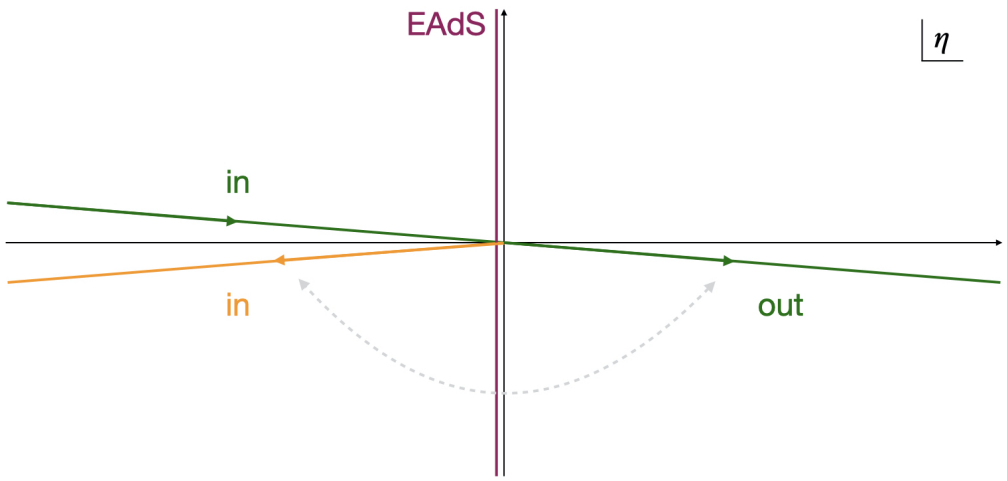

Figure 5.3: The figure shows various equivalent contours that have been proposed for the calculation of cosmological correlators. In the traditional Schwinger-Keldysh formalism, the path integral runs forwards over the “in" green line and then backwards over the "in" orange line. Rotating both contours to the imaginary axis connects to the Euclidean AdS calculation. The "in-out" contour discussed in this chapter (the green line) rotates the backwards "in" contour to the forwards "out" contour.

the multiple propagators reduce to a single one. In contrast to previous proposals our rotation of the anti-time ordered in-in contour goes all the way to the positive real axis, so that the calculation remains firmly within the realm of Lorentzian time. All these proposals are summarised and compared in Fig. 5.3. Finally, we should mention that the relation between in-in and in-out formalisms in Minkowski has also been investigated recently in [103, 104], where it was shown, among other things, that imposing initial conditions in the infinite past is a necessary requirement.

The rest of this chapter is organized as follows. In Sec. 5.3 we define the in-out formalism and prove that it gives the same result for time-ordered unequal time correlators as the in-in formalism. To this end, we review a formal non-perturbative argument in Minkowski and adapt it to de Sitter and then provide explicit checks of the equivalence to various orders in perturbation theory at tree level. In Sec. 5.4 we consider two applications of the in-out formalism to correlators. The first, in Secs. 5.4.1 and 5.4.2 is a representation of correlators as a sum of residues of the product of Feynman propagators in the energy-momentum domain. The second, in Sec. 5.5.2, is a set of purely algebraic set of recursion relations for equal-time Minkowski correlators, which computes all tree-level diagrams and a large class of

"melonic" loop diagrams. Next, in Sec. 5.6, we use Veltman's largest time equation to derive an infinite set of propagator identities, which can in turn be expressed in terms of correlator identities. We present explicit formulae for all two-vertex diagrams to any number of loops and external legs. In Sec. 5.7 we give a preview of how the in-out formalism leads to a natural definition of a de Sitter scattering matrix, which moreover obeys the standard optical theorem. We present some simple examples and consistency checks. Finally, we conclude in Sec. 5.8.

Notation and Conventions We use a prime to remove the ubiquitous momentum-conserving Dirac delta,

$$\langle \prod_a^n \phi(\eta, \mathbf{k}_a) \rangle \equiv (2\pi)^3 \delta \left(\sum_a^n \mathbf{k}_a \right) \langle \prod_a^n \phi(\eta, \mathbf{k}_a) \rangle' \,. \tag{5.1}$$

We denote time-ordered correlators by

$$\langle T \prod_a^n \phi(\eta, \mathbf{k}_a) \rangle' \equiv B_n(\{\eta_a, \mathbf{k}_a\}) \,, \tag{5.2}$$

where $\{\eta_a, \mathbf{k}_a\}$ collectively refers to the spacetime positions of the operators. We define the following two-point functions or propagators as

$$\begin{aligned} G^+(\eta_1, \eta_2, p) &\equiv \langle 0| \, \phi(\eta_1, \mathbf{p}) \phi(\eta_2, \mathbf{p}') \, |0\rangle' = f_p(\eta_1) f_p^*(\eta_2) \,, \\ G_F(\eta_1, \eta_2, p) &\equiv \langle 0| \, T\phi(\eta_1, \mathbf{p}) \phi(\eta_2, \mathbf{p}') \, |0\rangle' \\ &\quad = f_p(\eta_1) f_p^*(\eta_2) \theta(\eta_1 - \eta_2) + f_p^*(\eta_1) f_p(\eta_2) \theta(\eta_2 - \eta_1) \,, \end{aligned} \tag{5.3}$$

where the mode functions in de Sitter and Minkowski are [3]

$$f_k(\eta) = -i \frac{\sqrt{\pi} H}{2} e^{i\frac{\pi}{4}(1+2\nu)} (-\eta)^{3/2} H_\nu^{(1)}(-k\eta) \,, \quad \nu \equiv \sqrt{\frac{9}{4} - \frac{m^2}{H^2}} \,, \tag{5.4}$$

$$f_k(\eta) = i\eta \frac{H}{\sqrt{2k}} e^{-ik\eta} \,. \quad \text{(conformally coupled)} \,, \tag{5.5}$$

$$f_k(\eta) = \frac{H}{\sqrt{2k^3}} (1 + ik\eta) e^{-ik\eta} \quad \text{(massless, dS)} \,, \tag{5.6}$$

$$f_E(t) = \frac{e^{-iEt}}{\sqrt{2E}} \,. \tag{5.7}$$

[3] Here we restrict our discussion to positive masses, but see [105] for an extensive discussion of tachyonic fields and their phenomenology.

Many of the integrals we encounter lead to distributions rather than functions and should be understood as acting on appropriate test functions. As commonly done in the physics literature, we will often represent these distributions as the limit of functions using a small parameter that is taken to zero at the end of the calculation as for example in the Sokhotski–Plemelj theorem or the Feynman propagator. More in detail, we specify that a certain integral to $t, \eta = \pm\infty$ should be computed assuming a positive or negative imaginary part to guarantee convergence even in the absence of a test function. To convey this in a compact way we use the shorthand notation

$$\pm\infty_+ \equiv \pm\infty(1 + i\epsilon)\,, \qquad\qquad \pm\infty_- \equiv \pm\infty(1 - i\epsilon)\,, \tag{5.8}$$

where $\epsilon > 0$ is a real and positive parameter that should be taken to zero at the end of the derivation.

5.3 In-In Equals In-Out

The main motivation behind the construction of the in-in formalism by Keldysh [42], foreshadowed by the work of Schwinger [41], was to describe the non-unitary and dissipative evolution of an open system in contact with an environment. However, it can also be used to study the unitary evolution of isolated systems and indeed almost all applications of the in-in formalism in early universe cosmology have considered a situation of this type. As we discussed, for the unitary evolution of an isolated system, there is an equivalent in-out description that computes correlators. In the following we review a general non-perturbative argument for the equality between in-in and in-out, we specify the conditions under which this holds and finally, we present some explicit checks.

First of all, let's clarify some nomenclature. In the *interaction picture*, where states evolve according to the interaction Hamiltonian and operators according to the free Hamiltonian, we say that a certain matrix element is an *in-out correlator* if it contains a single time [4] ordering. This corresponds to a single time evolution operator, possibly with some insertion of local operators. Conversely, *in-in correlators* contain two separate time orderings, one going forward in time, which evolves

[4]Here we focus on time-ordering as opposed to path ordering to set up our nomenclature. When re-writing these correlators as path integrals one can sometimes combine different time orderings into a single path ordering, as famously done with the closed time contour of the in-in path integral.

the ket, and one going backwards in time, which evolves the bra. With this nomenclature in place, we move on to define our main objects of study.

We define an *in-out correlator* of the product $\mathcal{O}(\{t, \mathbf{x}\})$ of local operators at positions $\{t_a, \mathbf{x}_a\}$ for $a = 1, \ldots, n$, as the following expectation value in the interaction picture

$$B_{\text{in-out}} \equiv \frac{\langle 0| \, T \left[\mathcal{O}(\{t, \mathbf{x}\}) e^{-i \int_{-\infty(1-i\epsilon)}^{+\infty(1-i\epsilon)} H_{\text{int}} dt} \right] |0\rangle'}{\langle 0| \, T \left[e^{-i \int_{-\infty(1-i\epsilon)}^{+\infty(1-i\epsilon)} H_{\text{int}} dt} \right] |0\rangle'} \,, \tag{5.9}$$

where a prime removes the Dirac delta of momentum conservation. Here H_{int} is the interaction Hamiltonian that generates time evolution of states, T denotes time ordering (early to the right, late to the left) and $|0\rangle$ is the Fock vacuum, a.k.a. the "vacuum" of the free theory. Notice that the factor in the denominator does not depend on where the fields are inserted: it is the familiar sum over so-called *vacuum bubbles*. Heuristically one can simply justify it by demanding that $B_{\text{in-out}}$ becomes unity when we don't insert any operators. In diagrammatic language, the denominator in $B_{\text{in-out}}$ simply tells us that we should disregard all diagrams that contain a subdiagram that is not connected to any inserted operator, i.e. a vacuum bubble. More precisely this factor arises when we re-write the vacuum of the interacting theory $|\Omega\rangle$ as that of the free theory $|0\rangle$ with interactions turned on adiabatically. The adiabatic turning on and off of interactions in the asymptotic past and future is implemented by the $i\epsilon$ rotations of the boundary of integration in Eq. (5.9). The correct sign of this imaginary part, namely $\pm\infty(1 - i\epsilon)$ can be simply determined by demanding convergence of the integral in perturbation theory.

Typically we will consider operators of the form

$$\mathcal{O}(\{t, \mathbf{x}\}) = \prod_{a}^{n} \phi(t_a, \mathbf{x}_a) \,. \tag{5.10}$$

Notice that $B_{\text{in-out}}$ is a very familiar object in QFT: it is precisely the object appearing on the right-hand side of the Lehmann–Symanzik–Zimmermann (LSZ) reduction formula, which gets amputated and delivers scattering amplitudes in Minkowski. Since all the operators in Eq. (5.9) appear inside the same time ordering, $B_{\text{in-out}}$ is computed in perturbation theory from the product of time-ordered two-point func-

tions, a.k.a. Feynman propagators, stitched together by non-linear interactions. While we will say more about this later, for the moment the reader should have in mind that the time foliation of spacetime has been chosen such that $t = \pm\infty$ represents a null "initial" surface and a null "final" surface, as it is familiar from Minkowski.

Next, let's define *in-in correlators* of the product $\mathcal{O}(\{t, \mathbf{x}\})$ of local operators at positions $\{t_a, \mathbf{x}_a\}$ as the following expectation value in the interaction picture

$$B_{\text{in-in}} \equiv \langle 0|\, \bar{T}\left[e^{+i\int_{-\infty(1+i\epsilon)}^{t_0} H_{\text{int}} dt}\right] T\left[\mathcal{O}(\{t, \mathbf{x}\}) e^{-i\int_{-\infty(1-i\epsilon)}^{t_0} H_{\text{int}} dt}\right] |0\rangle' \,. \tag{5.11}$$

Here $\bar{T}$ indicates anti-time ordering (early to the left, late to the right) and t_0 is an arbitrary time that is *later* than any of the t_a appearing in the inserted fields, $t_0 > t_a$. Notice the absence of the vacuum bubble factor appearing in $B_{\text{in-out}}$. Heuristically this is easily understood noticing that if we insert the identity operator, namely $\mathcal{O} = 1$, then $B_{\text{in-in}}$ is already equal to 1, just like $B_{\text{in-out}}$. The imaginary part in the boundary of integration, namely $-\infty(1-i\epsilon)$ in the time-ordered part and $-\infty(1+i\epsilon)$ in the anti-time-ordered part, ensure convergence and implement mathematically the adiabatically switching on of interactions in the infinite past.

Note that our definition of $B_{\text{in-in}}$ is slightly more general than what is usually considered in the cosmological literature because we allow for unequal time operators. An even more general possibility would be to insert some operators in the time ordering, some in the anti-time-ordering and some in between [5]. In this case, we don't expect it to be possible to find a simple relation to the "straight" in-out formalism. However these situations are examples of out-of-time-order contours or "time-folds" and have also been studied extensively (see e.g. [106, 107]).

As long as $t_0 > \bar{t}$ with $\bar{t} = \max_a(t_a)$, $B_{\text{in-in}}$ does not depend on t_0 because the time evolution after the latest t_a cancels out,

$$B_{\text{in-in}} = \langle \bar{T}\left[e^{+i\int_{-\infty}^{\bar{t}} H_{\text{int}}\, dt}\right] U^{-1}(t_0, \bar{t}) U(t_0, \bar{t}) T\left[\mathcal{O}(\{t, \mathbf{x}\}) e^{-i\int_{-\infty}^{\bar{t}} H_{\text{int}}\, dt}\right]\rangle' \tag{5.12}$$

$$= \langle \bar{T}\left[e^{+i\int_{-\infty}^{\bar{t}} H_{\text{int}}\, dt}\right] T\left[\mathcal{O}(\{t, \mathbf{x}\}) e^{-i\int_{-\infty}^{\bar{t}} H_{\text{int}}\, dt}\right]\rangle' \,, \tag{5.13}$$

where we used the following notation for the time evolution operator U in the in-

[5] The case where all operators are in the anti-time-ordering is trivially related to the case we consider in this chapter

teraction picture

$$\bar{T}\exp\left[+i\int_{t_1}^{t_2} H_{\rm int}dt\right] = U^\dagger(t_2,t_1) = U^{-1}(t_2,t_1) \quad \text{for } t_2 > t_1\,. \tag{5.14}$$

Notice that our definition of $B_{\text{in-in}}$ is slightly more general than what is usually encountered in the cosmology literature. Usually one considers the product of operators at the same time. In that case, it does not matter if the operators are inside the time ordering, the anti-time-ordering or just in between,

$$\begin{aligned}\langle\bar{T}\left[e^{+i\int_{-\infty}^{\bar{t}} H_{\rm int}\,dt}\right] T\left[\mathcal{O}(\bar{t})e^{-i\int_{-\infty}^{\bar{t}} H_{\rm int}\,dt}\right]\rangle &= \langle\bar{T}\left[e^{+i\int_{-\infty}^{\bar{t}} H_{\rm int}\,dt}\right]\mathcal{O}(\bar{t})T\left[e^{-i\int_{-\infty}^{\bar{t}} H_{\rm int}\,dt}\right]\rangle \\ &= \langle\bar{T}\left[e^{+i\int_{-\infty}^{\bar{t}} H_{\rm int}\,dt}\mathcal{O}(\bar{t})\right]T\left[e^{-i\int_{-\infty}^{\bar{t}} H_{\rm int}\,dt}\right]\rangle\,.\end{aligned} \tag{5.15}$$

Also, we usually don't write the time ordering of operators when computing in-in correlators because we compute them at the same time. When we extend to unequal time of course we can choose whether to time order or not. The object that nicely relates to $B_{\text{in-out}}$ is the time-ordered in-in correlator.

5.3.1 A Formal Proof

Here is a formal proof that $B_{\text{in-out}} = B_{\text{in-in}}$ following the intro of [67]. First we notice that if we start with the Fock vacuum $|0\rangle$, which is annihilated by the lowering ladder operators of all fields for all momenta, and turn on and off interactions adiabatically, we expect to go back to $|0\rangle$ up to a multiplicative factor corresponding to the sum over vacuum bubbles [6]

$$U(+\infty,-\infty)\,|0\rangle = |0\rangle\,\langle 0|\,U(+\infty,-\infty)\,|0\rangle\,, \tag{5.16}$$

where we are assuming the normalization $\langle 0|0\rangle = 1$. This expectation can be justified in a few ways. Here we simply remark that the standard $i\epsilon$ rotation of the time integral contour induces a suppression $e^{-2\epsilon T(E_n - E_0)}$ for time evolution $U(T,-T)$ on excited energy eigenstates with eigenvalues E_n, compared to the lowest energy state. In the limit $T \to +\infty$ all excited states are projected out and only the Fock vacuum survives. To see this more explicitly, we compute in perturbation theory

[6] Here we are in the interaction picture and U is the associated time-evolution operator, which depends on the interaction Hamiltonian H evaluated on free fields (i.e. fields evolved with the free Hamiltonian H_0).

the projection of the left-hand side of Eq. (5.16) onto an n-particle state $|n\rangle$, with total energy k_T. To lowest order in the coupling constants, the result [7] of the time integral is proportional to derivatives of a Dirac delta of energy conservation

$$\langle n|\, U(+\infty,-\infty)\,|0\rangle \propto \partial^n_{k_T}\delta(k_T)\,. \tag{5.17}$$

This distribution does not have support on physical states and hence $U(+\infty,-\infty)\,|0\rangle$ does not have support on any excited state [8].

Since unitary evolution preserves the norm, the multiplicative factor on the right-hand side of Eq. (5.16) is a pure phase

$$\langle 0|\, U(+\infty,-\infty)\,|0\rangle\, \langle 0|\, U(+\infty,-\infty)\,|0\rangle^* = 1\,. \tag{5.18}$$

This is precisely the vacuum bubble factor, by which we divided out in the definition of in-out correlators $B_{\text{in-out}}$, Eq. (5.9). Taking the dagger of Eq. (5.16) (more precisely using the Riesz representation theorem) gives us

$$\langle 0|\, U^\dagger(+\infty,-\infty) = \langle 0|\, \langle 0|\, U(+\infty,-\infty)\,|0\rangle^*\,. \tag{5.19}$$

The imaginary rotation of the contour at infinity is quite important in the derivation. To keep our expression compact we introduce the useful shorthand notation

$$\pm\infty_+ \equiv \pm\infty(1+i\epsilon)\,, \qquad\qquad \pm\infty_- \equiv \pm\infty(1-i\epsilon)\,, \tag{5.20}$$

[7] The exact result is given in Eq. (5.145) where we also discuss that this matrix element can be interpreted as a 0 to n scattering in de Sitter.

[8] This argument might be subtle due to IR divergences in the initial and final state, $|\eta| \to \infty$ (not at $\eta \to 0$), where the analogue of soft and collinear divergences might arise. We hope to come back to this issue in the future.

Then the derivation proceeds as follows

$$B_{\text{in-out}} = \frac{\langle T\left[\prod_a^n \phi(t_a) e^{-i\int_{-\infty_-}^{+\infty_-} H_{\text{int}}dt}\right]\rangle'}{\langle T\left[e^{-i\int_{-\infty_-}^{+\infty_-} H_{\text{int}}dt}\right]\rangle'} \tag{5.21}$$

$$= \langle U^\dagger(+\infty_+, -\infty_+) T\left[\prod_a^n \phi(t_a) e^{-i\int_{-\infty_-}^{+\infty_-} H_{\text{int}}dt}\right]\rangle' \tag{5.22}$$

$$= \langle \bar{T}\left[e^{+i\int_{-\infty_+}^{+\infty_+} H_{\text{int}}dt}\right] T\left[e^{-i\int_{t_0}^{+\infty_-} H_{\text{int}}dt}\right] T\left[\prod_a^n \phi(t_a) e^{-i\int_{-\infty_-}^{t_0} H_{\text{int}}dt}\right]\rangle' \tag{5.23}$$

$$= \langle \bar{T}\left[e^{+i\int_{-\infty_+}^{t_0} H_{\text{int}}dt}\right] U^\dagger(+\infty, t_0) U(+\infty, t_0) T\left[\prod_a^n \phi(t_a) e^{-i\int_{-\infty_-}^{t_0} H_{\text{int}}dt}\right]\rangle' \tag{5.24}$$

$$= B_{\text{in-in}}\,, \tag{5.25}$$

where in the second line we used Eq. (5.19) and in the third line the fact that $t_0 > t_a$.

This equality can be stated with more evocative language. The only difference between the in-in and in-out formalism is how the bra is prepared. In both cases, we would like to prepare it by acting on the Fock vacuum with an evolution operator, which we can readily expand in perturbation theory for practical calculations. The in-in formalism prepares this bra by slowly turning on interactions from past (null) infinity. The in-out formalism instead slowly turns on interactions from future (null) infinity and evolves “backwards" in time.

An Extended de Sitter Spacetime The equality of in-in and in-out correlators is not surprising in Minkowski and is already well-known (see e.g. [67]). Here we claim that the same result also applies to de Sitter spacetime. In particular, we propose to extend the expanding Poincaré patch of dS by glueing on top of it a copy of the contracting Poincaré patch, as in Fig. 5.1. This means that the standard conformal time now can run over all real values, $-\infty < \eta < \infty$, with positive values representing the expanding patch, namely $a = e^{+Ht}$ in cosmological time, and negative values representing the contracting patch, $a = e^{-Ht}$. The two patches are glued together at $\eta = 0$, which represents the future and past conformal boundary of the two Poincaré patches. To be absolutely explicit, we can hence define in-out

correlators in de Sitter by

$$B_{\text{in-out}} \equiv \frac{\langle 0|\, T\left[\mathcal{O}(\{\eta,\mathbf{x}\})e^{-i\int_{-\infty(1-i\epsilon)}^{+\infty(1-i\epsilon)} H_{\text{int}}(\eta)d\eta}\right]|0\rangle'}{\langle 0|\, T\left[e^{-i\int_{-\infty(1-i\epsilon)}^{+\infty(1-i\epsilon)} H_{\text{int}}(\eta)d\eta}\right]|0\rangle'}\,. \tag{5.26}$$

This glueing at $\eta = 0$ is consistent as long as no divergences take place at $\eta = 0$. In turn, this means that the divergent volume factor $\sqrt{-g} = (H\eta)^{-4}$ coming from the measure of time integration must be more than offset by powers of η coming from the inverse metric contracting space and time derivatives and by the decay of massive fields towards $\eta \to 0$. To be more specific, let the conformal dimension Δ of a scalar field of mass m be [9]

$$\Delta \equiv \frac{3}{2} - \sqrt{\frac{3}{2} - m^2H^2}\,. \tag{5.27}$$

For an interaction involving n fields of dimensions Δ_a with $a = 1,\ldots,n$ and a number n_{∂_i} of spacial derivatives the condition for tree-level IR finiteness is

$$\sum_a^n \Delta_a + n_{\partial_i} > 3\,. \tag{5.28}$$

For massless fields, we have $\Delta = 0$ and then the condition becomes

$$2n_{\partial_\eta} + n_{\partial_i} > 3\,. \tag{5.29}$$

where n_{∂_η} is the number of time derivatives.

In the rest of the chapter, we will assume that *there are no IR divergences at* $\eta \to 0$. It is possible that our result can be extended also to the case of IR divergent interactions (recently discussed in [109]). This would require introducing an IR regulator that respects the relation in Eq. (5.16). Our preliminary investigation suggests that such a regulator exists but we postpone a thorough discussion to future work.

5.3.2 In-In and In-Out Feynman Rules

The Feynman rules are familiar both for the in-in and in-out formalism. Here we briefly review them for completeness. In both cases, we consider diagrams with

[9] For an extension to d spacial dimensions set $3 \to d$. For the scaling of spinning fields see e.g. [108].

V vertices, I internal lines, each connecting two vertices, and n external lines for an n-point correlator (time runs vertically with the past below the future). For concreteness, we use η for time, but the same expressions apply to Minkowski changing η to t.

In-In Feynman Rules Our definition of the un-equal time in-in correlators in Eq. (5.11) generalised what is typically used in cosmology, where fields are inserted at the same time. Hence the Feynman rules below are also slightly different in the case of un-equal time correlators but "backward compatible" with the equal-time case. Then, for in-in correlators:

- A vertex can be either a "right" vertex, labelled by "r" or a left vertex, labelled by "l". Hence one needs to sum over 2^V possible labellings.
- External lines are associated to a momentum $\mathbf{k}_a$ with $a = 1, \ldots, n$. Each vertex comes with a momentum-conserving Dirac delta. The $L = I - V + 1$ internal "loop" momenta are not fixed by these Dirac deltas and must be integrated over.
- Internal lines are called bulk-to-bulk propagators and come in four types

$$\bullet - \bullet = G_{rr}(\eta_1, \eta_2, p) = \langle 0| \, T\phi(\eta_1, \mathbf{p})\phi(\eta_2, \mathbf{p}') \, |0\rangle' = G_F(\eta_1, \eta_2, \mathbf{p}) \tag{5.30}$$

$$= f_p(\eta_1) f_p^*(\eta_2)\theta(\eta_1 - \eta_2) + f_p^*(\eta_1) f_p(\eta_2)\theta(\eta_2 - \eta_1) \tag{5.31}$$

$$\circ - \bullet = G_{lr}(\eta_1, \eta_2, p) = \langle 0| \, \phi(\eta_1, \mathbf{p})\phi(\eta_2, \mathbf{p}') \, |0\rangle' = f_p(\eta_1) f_p^*(\eta_2) \tag{5.32}$$

$$\bullet - \circ = G_{rl}(\eta_1, \eta_2, p) = \langle 0| \, \phi(\eta_2, \mathbf{p}')\phi(\eta_1, \mathbf{p}) \, |0\rangle' = G_{lr}^*(\eta_1, \eta_2, p) \tag{5.33}$$

$$\circ - \circ = G_{ll}(\eta_1, \eta_2, p) = \langle 0| \, \bar{T}\phi(\eta_1, \mathbf{p})\phi(\eta_2, \mathbf{p}') \, |0\rangle' = G_{rr}^*(\eta_1, \eta_2, p) \tag{5.34}$$

$$= f_p^*(\eta_1) f_p(\eta_2)\theta(\eta_1 - \eta_2) + f_p(\eta_1) f_p^*(\eta_2)\theta(\eta_2 - \eta_1) \,, \tag{5.35}$$

  where $f_p(\eta)$ are the mode functions, namely the solutions of the linearized classical equations of motion with momentum $\mathbf{p}$. For later use, we denote the non-time-ordered two-point function as

$$G^+(\eta_1, \eta_2, p) \equiv \langle 0| \, \phi(\eta_1, \mathbf{p})\phi(\eta_2, \mathbf{p}') \, |0\rangle' = f_p(\eta_1) f_p^*(\eta_2) \,, \tag{5.36}$$

  which is not symmetric under the exchange of the time variables. Notice that

$$G_{lr} = G^+ = G_{rl}^* \,. \tag{5.37}$$

For spinning fields, it is convenient to strip off all polarization tensors from the propagators and move them to the vertices, where they are contracted with each other and with derivatives. Here G_{rr} is the Feynman propagator, and G_{ll} is its complex conjugate.

- External lines connected to external fields at times η_a with $a = 1, \ldots, n$ are called bulk-to-boundary propagators and come in two types [10]

$$\bullet\!- = G_r(\eta, \eta_a, p) = G_F(\eta, \eta_a, p)\,, \tag{5.38}$$

$$\circ\!- = G_l(\eta, \eta_a, p) = G^+(\eta, \eta_a, p)\,. \tag{5.39}$$

  Notice that G_r is symmetric in its time arguments while G_l is not. This is where our definition of in-in correlators generalizes the traditional one for equal-time correlators where G_r is not time-ordered because one assumes that $\eta < \eta_a$.

- The time η of a vertex must be integrated over $d\eta$ with a measure $\sqrt{-g} = (\eta H)^{-4}$ and boundaries

$$\text{right vertex:} \quad -\infty(1 - i\epsilon) < \eta \leq 0\,, \tag{5.40}$$

$$\text{left vertex:} \quad -\infty(1 + i\epsilon) < \eta \leq 0\,. \tag{5.41}$$

  where we are assuming IR finiteness. As can be seen from Eq. (5.11), right vertices come with a $-i$ times the appropriate interaction, while for left vertices we have a $+i$.

- A discussion of the combinatorial factors can be found in [110].

It turns out that half of the above diagrams are related to the other half simply by complex conjugation,

$$D[\sigma] = D[\bar{\sigma}]^*(-)^{n_i}\,, \tag{5.42}$$

where n_i is the total number of spatial derivatives. Here D represents a diagram, σ represents the collection $\{r, l\}$ labels of its vertices and $\bar{\sigma}$ refers to the opposite labelling, $r \leftrightarrow l$.

[10] Actually the bulk-boundary propagator G_r coincides with the time-ordered bulk-bulk propagator G_{rr} and the other bulk-boundary propagator G_l coincides with non-time ordered bulk-bulk propagator G_{lr}.

In-Out Feynman Rules We now move on to the discussion of in-out rules. These are exactly the well-known Feynman rules we all learn in introductory courses on QFT. Because of this we will be very concise and focus only on what's different with respect to the in-in rules:

- All interaction vertices and external fields are inside the same time ordering, they are on the same footing. Hence, there is no need to label them in different ways or to distinguish between bulk and boundary, as we did in the in-in formalism. All vertices receive a factor of $-i$ as appropriate for expanding the time evolution operator $e^{-i\int H_{\rm int}}$.

- Internal lines connecting two interaction vertices and external lines connecting a vertex to an external field correspond to one and the same propagator, the time-ordered Feynman propagator:

$$\bullet - \bullet = G_F(\eta_1, \eta_2, p) = \langle 0|\, T\phi(\eta_1, \mathbf{p})\phi(\eta_2, \mathbf{p}')\, |0\rangle' \tag{5.43}$$

$$= f_p(\eta_1) f_p^*(\eta_2)\theta(\eta_1 - \eta_2) + f_p^*(\eta_1) f_p(\eta_2)\theta(\eta_2 - \eta_1)\,. \tag{5.44}$$

- The time η of a vertex must be integrated over the whole real line, with a measure $\sqrt{-g} = (\eta H)^{-4}$ and boundaries

$$-\infty(1 - i\epsilon) < \eta < +\infty(1 - i\epsilon)\,, \tag{5.45}$$

  where we are again assuming IR finiteness. This contour ensures the convergence of all time integrals for (interaction picture) correlators in the Fock vacuum where fields are inserted at arbitrary but finite and negative times.

Two comments are in order. First, let us stress that these in-out diagrams should not be amputated, as we do when computing amplitudes. They include all the propagators relevant for connecting to external fields. Second, as it is well known, one should only include diagrams where each propagator is eventually connected to an external field. This excludes all the vacuum bubble contributions which are exactly cancelled by the denomination in $B_{\text{in-out}}$.

5.3.3 Explicit Checks

Here we will present some very simple calculations to see how the equality between in-in and in-out pans out in practice. Since the calculations are very similar

between Minkowski and de Sitter, with the simple identification of t with η, we will discuss both spacetimes jointly in each example.

Tree-Level Contact Diagrams Now consider a simple theory of a scalar with a cubic interaction [11]

$$H_{\rm int}(\eta) = \int_{\mathbf{x}} \frac{\lambda}{(n!)} F(\eta\partial_i, \eta\partial_\eta)\phi^n(\eta) \tag{5.46}$$

where F represents a generic set of space and time derivatives that can act on any of the fields. Moreover, ϕ can be any set of fields of any mass and spin, but to simplify the presentation we focus on a single massive scalar. We will now compute the n-point function to $\mathcal{O}(\lambda)$ with fields inserted at time $\eta_a \leq 0$ for $a = 1, \ldots, n$. For the in-in formalism, we find (setting for simplicity $H = 1$)

$$\begin{aligned} B_{\text{in-in}} &= B^r_{\text{in-in}} + B^l_{\text{in-in}} \\ &= -i\lambda \int_{-\infty(1-i\epsilon)}^{0} \frac{d\eta}{\eta^4} F \prod_a^n G_F(\eta, \eta_a; k_a) + i\lambda \int_{-\infty(1+i\epsilon)}^{0} \frac{d\eta}{\eta^4} F \prod_a^n G^+(\eta, \eta_a; k_a)^* \,, \end{aligned} \tag{5.47}$$

As long as there are more than four factors of η coming from F and the propagators this is convergent at $\eta = 0$. This is for example the case of any local interaction with more than three conformally coupled scalars or an interaction of massless scalars with $2n_{\partial_\eta} + n_{\partial_i} \geq 4$. Using the in-out formalism we find

$$B_{\text{in-out}} = -i\lambda \int_{-\infty(1-i\epsilon)}^{+\infty(1-i\epsilon)} \frac{d\eta}{\eta^4} F \prod_a^n G_F(\eta, \eta_a; k_a) \,. \tag{5.48}$$

To check that this is equivalent to the in-in expression we compute the difference. The part of the in-out time integral form $-\infty$ to 0 exactly cancels out the “right"

[11] This notation is meant to account for both time and space derivatives. A more explicit notation would specify on which field the time derivative acts, as e.g. in [73]. Since at the end, the proof proceeds unchanged with or without time derivatives, we prefer to adopt a sloppier but more streamlined notation.

contribution of $B_{\text{in-in}}$ and we are left with

$$B_{\text{in-out}} - B_{\text{in-in}} = \tag{5.49}$$
$$= -i\lambda \int_0^{+\infty_-} \frac{d\eta}{\eta^4} F \left[\prod_a^n f_a(\eta) f_a^*(\eta_a)\right] - i\lambda \int_{-\infty_+}^0 \frac{d\eta}{\eta^4} F \left[\prod_a^n f_a(\eta) f_a^*(\eta_a)\right]$$
$$= -i\lambda \prod_a^n f_a^*(\eta_a) \int_{-\infty(1+i\epsilon)}^{+\infty(1-i\epsilon)} \frac{d\eta}{\eta^4} F f_a(\eta)\,, \tag{5.50}$$

where the label a on the mode function refers to the different momenta $\mathbf{k}_a$, but may also indicate different fields with different masses. As a warm-up, let's see what happens for conformally coupled or massless fields, in which case the mode functions are just an exponential multiplied by a polynomial in $k\eta$ (see Eq. (5.5)). We find

$$B_{\text{in-out}} - B_{\text{in-in}} \propto \sum_p \int_{-\infty(1+i\epsilon)}^{+\infty(1-i\epsilon)} d\eta\, \eta^p e^{-ik_T\eta}\,, \tag{5.51}$$

where the polynomial in η makes explicit the factors present in the vertex F and in the mode functions that make the $\eta \to 0$ limit convergent. The key to computing this integral is to notice the "mixed" $i\epsilon$ deformations at the two different boundaries of the integral. One comes from the in-in and one from the in-out. They are such that the integral is exponentially converging in both limits, as it should be. These boundaries invite us to close the contour in the lower-half complex plane, where we can drop the circle at infinity [12]. Since the integrand is analytic in η in the lower-half complex plane, the integral vanishes and $B_{\text{in-in}}$ coincides with $B_{\text{in-out}}$.

More generally, we observe that the equivalence of in-in and in-out for contact diagrams relies on two properties: the mode functions and interaction vertices are analytic in the lower-half complex plane, and their product vanishes for $\text{Im}\,\eta < 0$ and $|\eta| \to \infty$. For fields of mass m the mode functions are Hankel functions of $-k\eta$ times appropriate factors of η,

$$f_k(\eta) = -i\frac{\sqrt{\pi}H}{2} e^{i\frac{\pi}{4}(1+2\nu)} (-\eta)^{3/2} H_\nu^{(1)}(-k\eta)\,, \quad \nu \equiv \sqrt{\frac{9}{4} - \frac{m^2}{H^2}}\,. \tag{5.52}$$

We can choose $f(\eta)$ to have a single branch cut running along the negative real axis and to be analytic everywhere else. Moreover, $f_k(\eta)$ vanishes for $\text{Im}\,\eta < 0$

[12] Here we are assuming $k_T \neq 0$. To be more precise we should add a Dirac delta $\delta(k_T)$. These distributional terms were discussed in [111] and in greater detail in [112].

and $|\eta| \to \infty$. This can be seen by expanding it in this limit or from the integral representation

$$H_\nu^{(1)}(z) = \frac{e^{-i\pi\nu/2}}{i\pi} \int_{-\infty}^{+\infty} e^{iz\cosh t - \nu t} dt\,, \quad \text{for} \quad \pi < \text{Arg}z < 0\,. \tag{5.53}$$

These two properties combined tell us that we can close the integral in Eq. (5.50) in the lower-half complex plane where it is analytic and hence the equivalence between in-in and in-out is established. Finally, we note that the above calculation can be easily adapted to Minkowski: switch η to t and drop the time-dependent factors in the measure of integration η^{-4} and in the interactions. The conclusion is hence unchanged.

Tree-Level Exchange Diagram For in-in diagrams, we generally need to consider 2^V (2^{V-1} if we use that half of the diagrams are conjugate) diagrams. We here give the explicit matching of diagrams from the in-in to the in-out formalism, for the two-to-two exchange diagram. The correspondence is then readily generalised to more complicated diagrams. We consider two interactions of the form

$$H_{\text{int}} = \int_{\mathbf{x}} \frac{\lambda_1}{(n+1)!} F_1(\eta\partial_i, \eta\partial_\eta)\phi^{n+1} + \int_{\mathbf{x}} \frac{\lambda_2}{(m+1)!} F_2(\eta\partial_i, \eta\partial_\eta)\phi^{m+1}, \tag{5.54}$$

where F_1 and F_2 again capture derivatives. Furthermore, we here focus on a particular channel with $k_1, ..., k_n$ attaching to the λ_1 vertex and $k_{m+1}, ..., k_{n+m}$ attaching the λ_2 vertex. The in-out correlator is then given by

$$\begin{aligned} &B_{\text{in-out}} = \\ &= -\lambda_1\lambda_2 \int_{-\infty_-}^{\infty_-} \int_{-\infty_-}^{\infty_-} \frac{d\eta}{\eta^4}\frac{d\eta'}{\eta'^4} F_1 F_2 \left[G_F(\eta, \eta'; s) \prod_{a=1}^{n} G_F(\eta, \eta_a; k_a) \prod_{b=n+1}^{n+m} G_F(\eta', \eta_b; k_b) \right], \end{aligned} \tag{5.55}$$

where s is the energy of the internal leg. As we know, the in-in correlator comes in four parts:

$$B_{\text{in-in}} = B_{\text{in-in}}^{rr} + B_{\text{in-in}}^{rl} + B_{\text{in-in}}^{lr} + B_{\text{in-in}}^{ll}\,, \tag{5.56}$$

each given by

$$
\begin{aligned}
&B^{rr}_{\text{in-in}} = \qquad (5.57)\\
&= -\lambda_1\lambda_2 \int_{-\infty_-}^{0}\int_{-\infty_-}^{0} \frac{d\eta}{\eta^4}\frac{d\eta'}{\eta'^4} F_1F_2 \left[G_F(\eta,\eta';s)\prod_{a=1}^{n} G_F(\eta,\eta_a;k_a)\prod_{b=n+1}^{n+m} G_F(\eta',\eta_b;k_b)\right],\\
&B^{ll}_{\text{in-in}} =\\
&= -\lambda_1\lambda_2 \int_{-\infty_+}^{0}\int_{-\infty_+}^{0} \frac{d\eta}{\eta^4}\frac{d\eta'}{\eta'^4} F_1F_2 \left[G^*_F(\eta,\eta';s)\prod_{a=1}^{n} G_l(\eta,\eta_a;k_a)\prod_{b=n+1}^{n+m} G_l(\eta',\eta_b;k_b)\right],\\
&B^{lr}_{\text{in-in}} =\\
&= \lambda_1\lambda_2 \int_{-\infty_+}^{0}\int_{-\infty_-}^{0} \frac{d\eta}{\eta^4}\frac{d\eta'}{\eta'^4} F_1F_2 \left[G_l(\eta,\eta';s)\prod_{a=1}^{n} G_l(\eta,\eta_a;k_a)\prod_{b=n+1}^{n+m} G_F(\eta',\eta_b;k_b)\right],\\
&B^{rl}_{\text{in-in}} =\\
&= \lambda_1\lambda_2 \int_{-\infty_-}^{0}\int_{-\infty_+}^{0} \frac{d\eta}{\eta^4}\frac{d\eta'}{\eta'^4} F_1F_2 \left[G^*_l(\eta,\eta';s)\prod_{a=1}^{n} G_F(\eta,\eta_a;k_a)\prod_{b=n+1}^{n+m} G_l(\eta',\eta_b;k_b)\right],
\end{aligned}
$$

where we have used that $G_r = G_{rr} = G_F$, and $G_{lr} = G_l = G^+$, as well as the fact that a lot of the propagators are conjugates of each other. The trick to match the two diagrams is now to split the in-out integrals in a similar way

$$B_{\text{in-out}} = B^{rr}_{\text{in-out}} + B^{rl}_{\text{in-out}} + B^{lr}_{\text{in-out}} + B^{ll}_{\text{in-out}}, \qquad (5.58)$$

where

$$
\begin{aligned}
&B^{rr}_{\text{in-out}} := \\
&-\lambda_1\lambda_2 \int_{-\infty_-}^{0} \frac{d\eta}{\eta^4} \int_{-\infty_-}^{0} \frac{d\eta'}{\eta'^4} F_1 F_2 \left[G_F(\eta,\eta';s) \prod_{a=1}^{n} G_F(\eta,\eta_a;k_a) \prod_{b=n+1}^{n+m} G_F(\eta',\eta_b;k_b) \right], \\
&B^{ll}_{\text{in-out}} := \\
&-\lambda_1\lambda_2 \int_{0}^{\infty_-} \frac{d\eta}{\eta^4} \int_{0}^{\infty_-} \frac{d\eta'}{\eta'^4} F_1 F_2 \left[G_F(\eta,\eta';s) \prod_{a=1}^{n} G_F(\eta,\eta_a;k_a) \prod_{b=n+1}^{n+m} G_F(\eta',\eta_b;k_b) \right], \\
&B^{lr}_{\text{in-out}} := \\
&-\lambda_1\lambda_2 \int_{0}^{\infty_-} \frac{d\eta}{\eta^4} \int_{-\infty_-}^{0} \frac{d\eta'}{\eta'^4} F_1 F_2 \left[G_F(\eta,\eta';s) \prod_{a=1}^{n} G_F(\eta,\eta_a;k_a) \prod_{b=n+1}^{n+m} G_F(\eta',\eta_b;k_b) \right], \\
&B^{rl}_{\text{in-out}} := \\
&-\lambda_1\lambda_2 \int_{-\infty_-}^{0} \frac{d\eta}{\eta^4} \int_{0}^{\infty_-} \frac{d\eta'}{\eta'^4} F_1 F_2 \left[G_F(\eta,\eta';s) \prod_{a=1}^{n} G_F(\eta,\eta_a;k_a) \prod_{b=n+1}^{n+m} G_F(\eta',\eta_b;k_b) \right].
\end{aligned}
\tag{5.59}
$$

We can now show that each of these four terms exactly cancel each other. Trivially we can see that $B^{rr}_{\text{in-out}} = B^{rr}_{\text{in-in}}$. Then for the mixed rl case, we have

$$
\begin{aligned}
&B^{rl}_{\text{in-in}} - B^{rl}_{\text{in-out}} = \\
&= \lambda_1\lambda_2 \int_{-\infty_-}^{0} \frac{d\eta}{\eta^4} \int_{-\infty_+}^{\infty_-} \frac{d\eta'}{\eta'^4} F_1 F_2 \left[G_l(\eta',\eta;s) \prod_{a=1}^{n} G_F(\eta,\eta_a;k_a) \prod_{b=n+1}^{n+m} G_l(\eta',\eta_b;k_b) \right] \\
&\propto \int_{-\infty_-}^{0} \frac{d\eta}{\eta^4} F_1 \left[\prod_{a=1}^{n} G_F(\eta,\eta_a;k_a) f_s^*(\eta) \right] \int_{-\infty_+}^{\infty_-} \frac{d\eta'}{\eta'^4} F_2 \left[f_s(\eta') \prod_{b=n+1}^{n+m} f_{k_b}(\eta') \right],
\end{aligned}
\tag{5.60}
$$

which vanishes by the same argument given for contact diagrams, since the last integral is exactly the one found in Eq. (5.50). Note that, from their definition in the in-out case, some of the Feynman propagators collapsed to unordered propagators since in the rl case $\eta_b < 0$ for all b, and in the in-out definition, $\eta < \eta'$ by the integral structure. The lr case follows a similar story. The ll case is the one that requires the most work. First let's rewrite the in-out case, using that $\eta_a < 0$ and $\eta_b < 0$. Moreover, we expand the Feynman propagator into two parts and write everything

in terms of mode functions

$$
\begin{aligned}
&B^{ll}_{\text{in-out}} = \\
&= -\lambda_1\lambda_2 \prod_{a=1}^{n+m} f^*_{k_a}(\eta_a) \int_0^{\infty_-} \frac{d\eta}{\eta^4} F_1 \left[f_s(\eta) \prod_{a=1}^{n} f_{k_a}(\eta) \right] \int_0^{\eta} \frac{d\eta'}{\eta'^4} F_2 \left[f^*_s(\eta') \prod_{b=n+1}^{n+m} f_{k_b}(\eta') \right] \\
&-\lambda_1\lambda_2 \prod_{a=1}^{n+m} f^*_{k_a}(\eta_a) \int_0^{\infty_-} \frac{d\eta'}{\eta'^4} F_2 \left[f_s(\eta') \prod_{b=n+1}^{n+m} f_{k_b}(\eta') \right] \int_0^{\eta'} \frac{d\eta}{\eta^4} F_1 \left[f^*_s(\eta) \prod_{a=1}^{n} f_{k_a}(\eta) \right] ,
\end{aligned}
\tag{5.61}
$$

where we assume that the differential operators in F_1 and F_2 only act on the mode functions, not the Heaviside functions in the Feynman propagator. When they act on the Heaviside functions we go back to the contact diagram we discussed in the previous example. For the equivalent expressions of the in-in correlator, we get

$$
\begin{aligned}
&B^{ll}_{\text{in-in}} = \\
&= \lambda_1\lambda_2 \prod_{a=1}^{n+m} f^*_{k_a}(\eta_a) \int_{-\infty_+}^{0} \frac{d\eta}{\eta^4} F_1 \left[f_s(\eta) \prod_{a=1}^{n} f_{k_a}(\eta) \right] \int_0^{\eta} \frac{d\eta'}{\eta'^4} F_2 \left[f^*_s(\eta') \prod_{b=n+1}^{n+m} f_{k_b}(\eta') \right] \\
&+\lambda_1\lambda_2 \prod_{a=1}^{n+m} f^*_{k_a}(\eta_a) \int_{-\infty_+}^{0} \frac{d\eta'}{\eta'^4} F_2 \left[f_s(\eta') \prod_{b=n+1}^{n+m} f_{k_b}(\eta') \right] \int_0^{\eta'} \frac{d\eta}{\eta^4} F_1 \left[f^*_s(\eta) \prod_{a=1}^{n} f_{k_a}(\eta) \right] ,
\end{aligned}
\tag{5.62}
$$

and therefore

$$
\begin{aligned}
B^{ll}_{\text{in-in}} - B^{ll}_{\text{in-out}} \;\propto\; & \int_{-\infty_+}^{\infty_-} \frac{d\eta}{\eta^4} F_1 \left[f_s(\eta) \prod_{a=1}^{n} f_{k_a}(\eta) \right] \int_0^{\eta} \frac{d\eta'}{\eta'^4} F_2 \left[f^*_s(\eta') \prod_{b=n+1}^{n+m} f_{k_b}(\eta') \right] \\
& + \int_{-\infty_+}^{\infty_-} \frac{d\eta'}{\eta'^4} F_2 \left[f_s(\eta') \prod_{b=n+1}^{n+m} f_{k_b}(\eta') \right] \int_0^{\eta'} \frac{d\eta}{\eta^4} F_1 \left[f^*_s(\eta) \prod_{a=1}^{n} f_{k_a}(\eta) \right] .
\end{aligned}
$$

The general proof that this expression vanishes for fields of arbitrary mass is a bit lengthy and therefore we postpone it to App. A.1. Here instead we focus on massless and conformally couples fields, for which the calculation is straightforward. Let's focus on the first line of the above expression since the story is analogous for the second line. The $d\eta'$ integrand takes the form

$$
\int_0^{\eta} \frac{d\eta'}{\eta'^4} F_2 \left[f^*_s(\eta') \prod_{b=n+1}^{n+m} f_{k_b}(\eta') \right] = \int_0^{\eta} d\eta' \, \text{Poly}(k, s, \eta') e^{-i(k_R - s)\eta'} , \tag{5.63}
$$

where $k_R = \sum_{i=n+1}^{n+m} k_i$ and the polynomial depends on the details of the interaction and on whether we have massless or conformally coupled scalars. Then the integral

in $d\eta'$ can be easily performed and leads to some other polynomial in k_a, s and η times $e^{-i(k_R-s)\eta}$. The final $d\eta$ integral can then be easily seen to vanish because the integrand is analytic and vanishes on the arc at infinity in the lower-half complex plane,

$$B^{ll}_{\text{in-in}} - B^{ll}_{\text{in-out}} \propto \int_{-\infty_+}^{\infty_-} \frac{d\eta}{\eta^4} F_1 \left[f_s(\eta) \prod_{a=1}^{n} f_{k_a}(\eta) \right] \text{Poly}(k_a, s, \eta) e^{-i(k_R-s)\eta} \tag{5.64}$$

$$= \int_{-\infty_+}^{\infty_-} \text{Poly}'(k_a, s, \eta) e^{-i(k_R-s+s+k_L)\eta} = 0\,, \tag{5.65}$$

where Poly' is some other polynomial and $k_L = \sum_{a=1}^{m} k_a$. Just like for the contact case, the two key steps of the proof are (i) that the integrand of the $d\eta$ integral from $+\infty(1-i\epsilon)$ to $-\infty(1+i\epsilon)$ is analytic in the lower-half complex plane and (ii) that it vanishes on the arc at infinity $\eta \sim \infty e^{i\theta}$ with $-\pi < \theta < 0$. This is exactly what we show for general masses in App. A.1.

5.4 Pole Bagging: In-In Correlators from Feynman Propagators

In this section, we show a first application of the in-out formalism to the calculation of correlators that leverages the simplicity of the Feynman propagator in energy-momentum space and is dubbed “pole bagging" because it boils down to summing over poles. We discuss explicitly the case of Minkowski and comment on how the analysis can be extended to massless and conformally coupled scalars in de Sitter.

5.4.1 Flat Space

We have argued that in-in correlators equal in-out correlators. In Minkowski, in-out correlators take a very simple form in energy-momentum space, with both time orderings combined in a single term by Feynman's $i\epsilon$ prescription. Indeed, tree-level Feynman diagrams in the energy-momentum domain can be computed by purely algebraic manipulations, no integral needed. Here we want to show how to use this simplicity to compute correlators in the time domain. The only work we need to do is to transform energies of the external fields back into time. This is easily done using the residue theorem because the integrands are simple rational functions

and the $i\epsilon$ prescription instructs us to pick up only half of the poles (those in the upper-half complex plane in our conventions). The result is a very different way to compute tree-level correlators or integrands for loop correlators simply by evaluating the products of Feynman diagrams on the relevant poles. Our manipulations below are analogous to similar manipulations presented in [91]. The main difference is that (i) we work directly with correlators instead of wavefunction coefficients, and (ii) the Feynman propagators we encounter are simpler than the wavefunction propagators in that they don't have the extra boundary term, which often leads to a considerable algebraic simplification.

Contact Diagrams Consider the equal-time three-point function of a scalar in the time-momentum domain. Using the in-out formalism, this is simply the Fourier transform from frequency to time of the product of Feynman propagators

$$B_{n,\text{in-out}} = (2\pi)^4\delta^{(4)}(\sum_a p_a^\mu) \times (-iF) \times \prod_b^n \frac{i}{p_b^2 + i\epsilon} \quad (\text{contact})\,, \tag{5.66}$$

where F is some vertex accounting for derivatives. To see how the calculation progresses, let's focus on the simplest case of a cubic polynomial interaction $\lambda\phi^3/(3!)$ so that $F = \lambda$ and $n = 3$. The Fourier transform to *equal-time* correlators then gives

$$B_3^{\text{flat}} = \int_{-\infty}^{\infty} \frac{d\omega_1 d\omega_2 d\omega_3}{(2\pi)^3}(2\pi)\delta\left(\sum_a^3 \omega_a\right) e^{it\sum_a \omega_a}\lambda \prod_b^3 \frac{1}{p_b^2 + i\epsilon} \tag{5.67}$$

$$= \int_{-\infty}^{\infty} \frac{d\omega_1 d\omega_2}{(2\pi)^2} \frac{\lambda}{(\omega_1^2 - \Omega_1^2 + i\epsilon)(\omega_2^2 - \Omega_2^2 + i\epsilon)((\omega_1+\omega_2)^2 - \Omega_3^2 + i\epsilon)}\,, \tag{5.68}$$

where the prime on the correlator means that we have dropped $(2\pi)^3\delta^{(3)}\left(\sum \mathbf{k}_a\right)$ and

$$\Omega_a^2 \equiv |\mathbf{k}_a|^2 + M_a^2\,. \tag{5.69}$$

The integrals can be computed using the residue theorem (we close the contour in the upper-half plane). The first integral has poles at $\omega_1 = -\Omega_1$ and $\omega_1 = -\omega_2 - \Omega_3$. This gives

$$-i\lambda \int \frac{d\omega_2}{2\pi} \frac{\Omega_{13}}{2\Omega_1\Omega_3(\omega_2 - \Omega_2)(\omega_2 + \Omega_2)(\omega_2 + \Omega_{13})(\omega_2 - \Omega_{13})}\,, \tag{5.70}$$

where

$$\Omega_{ij} = \Omega_i + \Omega_j \,, \tag{5.71}$$

and we left the $i\epsilon$'s implicit. Notice that there is a cancellation between the two residues which removes two of the zeros in the denominator ($\omega_2 = \pm(\Omega_1 - \Omega_3)$), leaving only the zeros at $\omega_2 = \pm\Omega_2$ and $\omega_2 = \pm(\Omega_1 + \Omega_3)$. The $i\epsilon$ prescription [13] instructs us to pick up only the two poles on the negative real axis, $-\Omega_2$ and $-\Omega_{13}$, which gives

$$B_3^{\rm flat} = -\frac{\lambda}{4\Omega_1\Omega_2\Omega_3(\Omega_1+\Omega_2+\Omega_3)} \,. \tag{5.72}$$

This is indeed the expected results from the bulk time integral with the simple E_T pole and the correct normalization factor for each $1/\Omega_a$. The same calculation actually works for all contact correlators in just the same way. To see this one can make repeated use of the master formula

$$\int_{-\infty}^{\infty} \frac{d\omega_i}{2\pi} \frac{1}{(\omega_i^2-\Omega_i^2)((\omega_i+\omega_X)^2-\Omega_j^2)} = -i\frac{\Omega_{ij}}{2\Omega_i\Omega_j(\omega_X^2-\Omega_{ij}^2)} \,. \tag{5.73}$$

This can be understood either as a brute force sum over two residues or as first separating the integrand into four partial fractions, corresponding to the four poles and then picking up the two partial fractions with poles on the negative real axis. At each iteration, one finds an additional factor of the pole Ω and the numerator is cancelled and substituted by itself plus the new pole. In the last integral one has $\omega_X = 0$ and the numerator cancels the denominator leaving a simple Ω_T pole.

Exchange Diagram Here we see explicitly how the same derivation also goes through for the tree-level exchange diagram. The idea is just the same, namely sum over the residues along the negative real axis for each of the integrals in $d\omega_a$. The only difference is that there are three residues for two of the integrals because of the extra factor of the exchange propagator. We focus on a single cubic polynomial

[13] A way to keep clarity in this calculation is to remove the $i\epsilon$s in the integrand and introduce a small counterclockwise rotation of the integration contours so that in practice one picks up only the residues from poles on the negative real axis.

interaction and on the kinematics of the s-channel. More in detail

$$B_4^{ex.} = \int \frac{d^4\omega_a}{(2\pi)^4} \frac{e^{it\sum_a \omega_a}\delta\left(\sum_a \omega_a\right)}{(\omega_s^2 - \Omega_s^2 + i\epsilon)} \times (-i)^2 \times \prod_a^4 \frac{i}{(\omega_a^2 - \Omega_a^2 + i\epsilon)} \tag{5.74}$$

$$= \int_{\omega_{1,2}} \frac{\Omega_{34}}{2\Omega_3\Omega_4\left(\omega_1^2 - \Omega_1^2\right)\left(\omega_2^2 - \Omega_2^2\right)\left((\omega_1+\omega_2)^2 - \Omega_{34}^2\right)\left((\omega_1+\omega_2)^2 - \Omega_s^2\right)} \tag{5.75}$$

$$= \int_{\omega_2} \frac{\omega_2^2\Omega_1 - \Omega_{134}\left(\Omega_s + \Omega_1\right)\left(\Omega_s + \Omega_{134}\right)}{4\Omega_1\Omega_3\Omega_4\Omega_s\left(\Omega_s + \Omega_{34}\right)\left(\omega_2^2 - \Omega_2^2\right)\left(\omega_2^2 - \Omega_{134}^2\right)\left(\omega_2^2 - (\Omega_s + \Omega_1)^2\right)} \tag{5.76}$$

$$= -\frac{\Omega_s + \Omega_T}{8\Omega_1\Omega_2\Omega_3\Omega_4\Omega_T\Omega_s\left(\Omega_s + \Omega_{12}\right)\left(\Omega_s + \Omega_{34}\right)}\,, \tag{5.77}$$

where

$$\Omega_s^2 = |\mathbf{k}_1 + \mathbf{k}_2|^2 + M^2\,, \qquad\qquad \omega_s = \omega_1 + \omega_2\,. \tag{5.78}$$

The result exactly agrees with the time-integral calculation and displays the characteristic E_L, E_R and $E_T = \sum \Omega_a$ poles, which are present in the quartic wavefunction coefficient, as well as the E_s pole which appears only in the correlator.

The same procedure works for arbitrary tree-level diagrams and for the integrands of loop diagrams. However, the bookkeeping becomes a hindrance for more complicated diagrams. One should develop a more streamlined graphical notation. In Sec. 5.6 we will see that this can be achieved from a different point of view and so we refrain from developing this further here.

In passing, we would like to notice that Eq. (5.74) is a springboard for the discussion of the nature of Effective Field Theory for equal-time "bulk" correlators. This is quite different from the usual expectation of effective field theories for amplitudes. For example, for amplitudes, we expect that a heavy field with mass M can be removed at tree-level by collapsing its propagators and inserting an infinite sum over higher derivative operators, which are organised in powers of $\Box/M^2$. Conversely, by expanding Eq. (5.74) in large M one finds terms that are odd in $1/M$ and are hence not captured by this expansion (as also noticed in [111]). This is where dissipation rears its head and we come to appreciate the real power of the in-in formalism. We will discuss this elsewhere.

5.4.2 Massless and Conformally Coupled Scalars in de Sitter

For massless and conformally coupled scalars we can generalise the pole bagging procedure from flat space to de Sitter. The key ingredient is that, when ν a half-integer, we can re-write the Feynman propagator as

$$G_F^{dS}(\eta,\eta',k) = \left(\frac{1}{2\pi i}\right)\int_{-\infty}^{\infty} d\omega \frac{2\omega f_\omega(\eta) f_\omega^*(\eta')}{\omega^2-k^2+i\epsilon}. \tag{5.79}$$

This only works for half-integer values of ν because the residue at $\omega = 0$ is only zero for these masses. Nevertheless, it allows us to compute cosmological correlators through an interesting integral. For simplicity, we here focus on conformally coupled fields, but the procedure is exactly the same for massless scalars. We have

$$G_F^{cc}(\eta,\eta',k) = \left(\frac{1}{2\pi i}\right)\int_{-\infty}^{\infty} d\omega \frac{H^2\eta\eta' e^{-i\omega(\eta-\eta')}}{\omega^2-k^2+i\epsilon}. \tag{5.80}$$

The simplest example is the contact four-point function with a ϕ^4 interaction. Since this interaction is conformally invariant at this order, the calculation is identical to the Minkowski calculation (technically the η in the four mode functions cancels the $\eta-4$ in the volume measure). A slightly more interesting computation shows the general strategy of how we can perform a pole bagging calculation in de Sitter and rephrase it as derivatives of the flat-space result. Consider now the five-point contact diagram with a $\phi^5/(5!)$ interaction. This interaction is not conformal invariant and so now the peculiarities of de Sitter will show up. Using the shorthand notation $\omega_T = \sum_{i=1}^5 \omega_i$ we write

$$\begin{aligned}
B_5^{cc} &= -iH^6\left(\frac{\eta_0}{2\pi i}\right)^5\int_{-\infty}^{\infty}\left(\prod_{i=1}^5\frac{d\omega_i}{\omega_i^2-k^2+i\epsilon}\right)e^{i\omega_T\eta_0}\int_{-\infty}^{\infty}d\eta\eta e^{-i\omega_T\eta} \qquad (5.81)\\
&= 2\pi H^6\left(\frac{\eta_0}{2\pi i}\right)^5\int_{-\infty}^{\infty}\left(\prod_{i=1}^5\frac{d\omega_i}{\omega_i^2-k_i^2+i\epsilon}\right)e^{i\omega_T\eta_0}\delta'(\omega_T)\\
&= -2\pi i H^6\left(\frac{\eta_0}{2\pi i}\right)^5\int_{-\infty}^{\infty}\frac{d\omega_1 d\omega_2 d\omega_3 d\omega_4(\eta_0((\omega_T-\omega_5)^2-k_5^2))-2i(\omega_T-\omega_5))}{\left(\prod_{i=1}^4(\omega_i^2-k_i^2+i\epsilon)\right)\left((\omega_T-\omega_5)^2-k_5^2+i\epsilon\right)^2}\\
&= \frac{(H\eta_0)^6}{(k_1+k_2+k_3+k_4+k_5)(16k_1k_2k_3k_4k_5)}
\end{aligned}$$

.

Therefore the general strategy is to transfer the derivatives acting on the Dirac

delta to the rest of the integral, which effectively is the flat space analogue of the integrals above. The only thing one has to keep track of is the number of these derivatives. The integrals pick up the poles in the upper half plane and can be computed in an algorithmic manner. So algorithmic in fact, that we can quite easily derive the general formula for the conformally coupled contact diagrams for any n.

Conformally Coupled n-Point Correlators With pole bagging, it is quite simple in fact to do any n-point correlator with a $\phi^n/(n!)$ interaction. We solve the integral

$$\begin{aligned} B_n^{cc} &= -iH^{2n-4}\left(\frac{\eta_0}{2\pi i}\right)^n \int_{-\infty}^{\infty}\left(\prod_{i=1}^{n}\frac{d\omega_i}{\omega_i^2-k_i^2+i\epsilon}\right)e^{i\omega_T\eta_0}\int_{-\infty}^{\infty}d\eta\eta^{n-4}e^{-i\omega_T\eta} \\ &= -2\pi i(i)^{n-3}H^{2n-4}\left(\frac{\eta_0}{2\pi i}\right)^n \int_{-\infty}^{\infty}\left(\prod_{i=1}^{n}\frac{d\omega_i}{\omega_i^2-k_i^2+i\epsilon}\right)e^{i\omega_T\eta_0}\delta^{(n-4)}(\omega_T) \\ &= -(-i\eta_0)^nH^{2n-4}\left(\frac{1}{2\pi i}\right)^{n-1}\int_{-\infty}^{\infty}\partial_{\omega_n}^{n-4}\left(\left(\prod_{i=1}^{n}\frac{d\omega_i}{\omega_i^2-k_i^2+i\epsilon}\right)e^{i\omega_T\eta_0}\right)\delta(\omega_T). \end{aligned} \tag{5.82}$$

The derivatives can be fully done using Leibniz rule and then transferred to derivatives in k_n. We have

$$\begin{aligned} &\partial_{\omega_n}^k\left(\left(\frac{1}{\omega_n^2-k_n^2+i\epsilon}\right)e^{i\omega_T\eta_0}\right) = \\ &\quad=\sum_{l=0}^{k}\binom{k}{l}(i\eta_0)^{k-l}e^{i\omega_T\eta_0}\partial_{\omega_n}^{k-l}\left(\frac{1}{\omega_n^2-k_n^2+i\epsilon}\right) \\ &\quad=-\sum_{l=0}^{k}\binom{k}{l}(i\eta_0)^{k-l}e^{i\omega_T\eta_0}\frac{1}{2k_n}\partial_{k_n}^{l}\left(\frac{(-1)^l}{(\omega_n+k_n-i\epsilon)}-\frac{1}{(\omega_n-k_n+i\epsilon)}\right). \end{aligned} \tag{5.83}$$

Having done all the derivatives, this is just a flat space correlator, however with the subtlety that we have some non-square terms in the denominator, such as $\omega_n \pm (k_n - i\epsilon)$. However, we can solve this by seeing that

$$\pm k_n B_n^{\text{flat}} = \left(\frac{1}{2\pi i}\right)^{n-1}\int_{-\infty}^{\infty}\frac{d\omega_n}{\omega_n\pm(k_n-i\epsilon))}\left(\prod_{i=1}^{n-1}\frac{d\omega_i}{\omega_i^2-k_i^2+i\epsilon}\right)e^{i\omega_T\eta_0}\delta(\omega_T). \tag{5.84}$$

Then putting this back into Eq. (5.82), we get

$$B_n^{cc} = (\eta_0 H)^{2n-4} \sum_{l=0}^{n-4} \binom{n-4}{l} (i\eta_0)^{-l} \left((-1)^l + 1\right) \frac{1}{2k_n} \partial_{k_n}^l (k_n B_n^{\text{flat}}). \quad (5.85)$$

While it is nice to know, that we can always write conformally coupled scalars as derivatives of flat space ones, since we even know what the flat space answer is, we can fully write the conformally coupled solution. Shifting the index in the sum, and doing some simplification, we have

$$B_n^{cc} = H^{2n-4}(-i\eta_0)^n k_T^{4-n} \frac{(n-4)!}{\prod_{i=1}^n 2k_i} \frac{1}{k_T} \sum_{l=0}^{n-4} \frac{(i\eta_0 k_T)^l}{l!} \left((-1)^{n-l} + 1\right). \quad (5.86)$$

Interestingly, in the $n \to \infty$ limit, this is giving us an exponential. Therefore the final answer can be written as a Taylor expansion to a certain order in η_0 given by

$$B_n^{cc} = \frac{(n-4)! H^{n-4}(-H\eta_0)^n}{\left(\prod_{i=1}^n 2k_i\right) k_T^{n-3}} 2\text{Re}\left[i^n e^{i\eta_0 k_T} \Big|_{n-4} \right]. \quad (5.87)$$

Then shifting $n \to n+4$ gives us the compact formula

$$B_{n+4}^{cc} = \frac{n! H^n (-H\eta_0)^{n+4}}{\left(\prod_{i=1}^{n+4} 2k_i\right) k_T^{n+1}} 2\text{Re}\left[i^n e^{i\eta_0 k_T} \Big|_{n} \right] \quad (5.88)$$

where the bar indicates the Taylor series in η_0 up to that order.

In summary, we wrote this diagram in terms of the derivatives of its flat space analogue and furthermore got a simple closed-form expression for contact diagrams of conformally coupled scalars in de Sitter.

This technique can be further developed, for example for exchange diagrams. In particular, one can show that we can always write diagrams for conformally coupled scalars as sums of derivatives of the flat space one, as in Eq. (5.86), but we will not do this in this work. Other examples can be obtained using integration by parts, perhaps along the lines of [113].

5.5 Correlator Recursion Relations

We here leverage that with the in-out formalism, there is no longer a distinction between bulk-to-bulk and bulk-to-boundary propagators. This allows us to find an algebraic recursion relation valid at all loop orders that computes correlat-

ors in Minkowski, somewhat analogous to the recursion relation for wavefunction coefficients derived in [91].

5.5.1 From Correlators to Chains in Flat Space

In Minkowski, bulk-to-boundary propagators $K_E(t)$ for the calculation of the wave function have the nice property that

$$K_{E_1}(t)K_{E_2}(t) = K_{E_1+E_2}(t). \tag{5.89}$$

This allows us to describe a diagram with any number of external legs, by simply considering the total energy flowing into a vertex [91]. Therefore, it is natural to summarize a large family of Feynman-Witten diagrams by so-called "chains", namely diagrams that have exactly one external leg per vertex. Since all vertices have a single external leg, one often omits to draw them and simply adds an "external" energy x to each vertex.

For correlators, the situation can in fact be simplified in a similar way. Given the in-out formalism described in Sec. 5.3, the analogue to a bulk-to-boundary correlator is a Feynman propagator. In flat space, Feynman propagators in the time-momentum domain obey

$$G_F(t,t',E_1)G_F(t,t',E_2) = \frac{E_1+E_2}{2E_1E_2}G_F(t,t',E_1+E_2). \tag{5.90}$$

Notice that it is crucial that the propagators have the same time variables, which ensures that there are only two possible time orderings, which match on the left- and the right-hand side. More generally, the product of n Feynman propagators obeys

$$G_F(t,t',E_1)...G_F(t,t',E_n) = \frac{2E_T}{\prod_{i=1}^{n}2E_i}G_F(t,t',E_T). \tag{5.91}$$

We stress that the Feynman rules for the "correlator-chains" we discuss here are different to the "wavefunction-chains" discussed in [91].

The above discussion leads us to the following set of Feynman-rules for what we call a chain in the context of correlators:

- Every vertex with energy x_i and time t_i leads to a Feynman-propagator

$G_F(t_i, t_0, x_1)$. This corresponds to the omnipresent single external line that we omit to draw.

- Every internal line connecting a vertex $\{x_i, t_i\}$ to $\{x_j, t_j\}$ leads to a factor $G_F(t_i, t_j, y_{ij})$, with y_{ij} being the exchanged momenta (which could be loops).

Therefore, if we label the energies at vertices of the chain with $\{x_1, ..., x_m\}$ and the external legs of the correlator carry energies $\{E_1, ..., E_n\}$ (note $n \geq m$) we can write.

$$\text{correlator} = \frac{\prod_{i=1}^{m} 2x_i}{\prod_{i=1}^{n} 2E_i} \times \text{chain} \tag{5.92}$$

For example, with $x_1 = E_1 + E_2$, $x_2 = E_3$ and $x_3 = E_4 + E_5$, we have

$\prod_{i=1}^{5} 2E_i$ 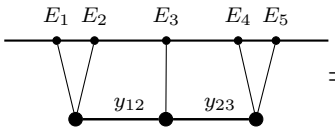

$= \prod_{i=1}^{3} 2x_i$ 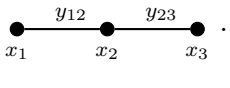

. (5.93)

With the rules above, we can comfortably consider chains exclusively and eventually relate them easily back to correlators. Let us make two simple examples. The contact diagram would simply be

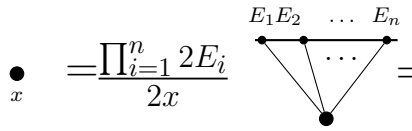

$= -\frac{1}{x^2}$. (5.94)

And for a single exchange, we have the identification

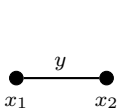

$= \frac{\prod_{i=1}^{n} 2E_i}{4x_1x_2}$ 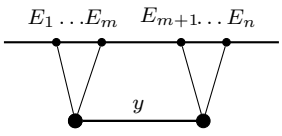

$= \frac{x_1+x_2+y}{2x_1x_2y(x_1+x_2)(x_1+y)(x_2+y)}$. (5.95)

With these definitions, we can move on to derive recursion relations following [91].

5.5.2 Recursion Relations

In [91], two sets of recursion relations for wavefunction coefficients were derived. We did not find a counterpart of the “primary" recursion relations obtained by

inserting the time-translation operator and integrating by part. We will comment on this at the end of the section. Instead here we focus on the "secondary" recursion relations derived by integrating one site of a tree-level chain. In that context, the generalization to loop diagrams was found to be possible but cumbersome because of the proliferation of diagrams induced by the boundary term in the wavefunction calculation [14]. Here we follow the same logic for the correlators computed in the in-out formalism and find a remarkable simplification. Since now all the propagators are Feynman propagators, without any boundary terms, we are able to derive recursion relations both for tree-level diagrams and for a class of "melonic" loop diagrams.

Tree-Level Relations For the tree-level case, we similarly start with a single tree-level edge, and an arbitrary remainig tree-level chain. That is

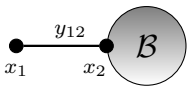

$$\equiv \int_{-\infty}^{\infty} \prod_{v\in\mathcal{B}\setminus\{2\}} i\,dt_v\, G_F(t_v,t_0,x_t)\times \tag{5.96}$$
$$\times \int_{-\infty}^{\infty} i\,dt_2 G_F(t_2,t_0,x_2)\prod_{e\in\mathcal{B}} G_F(t_{v_e},t_{v'_e},y_{v_e}) I_1(y_{12},t_2),$$

where

$$I_1(y_{12},t_2) \equiv \int_{-\infty}^{\infty} i\,dt_1\, G_F(t_1,t_0,x_1)G_F(t_1,t_2,y_{12}). \tag{5.97}$$

We can fully perform this integral

$$\begin{aligned} I_1(y_{12},t_2) &= \\ &= \left(\frac{1}{2\pi i}\right)^2 \int_{-\infty}^{+\infty} d\omega_1 \int_{-\infty}^{+\infty} d\omega_2 \int_{-\infty}^{\infty} i\,dt_1\ \frac{e^{i\omega_1(t_0-t_1)}}{\omega_1^2-x_1^2+i\varepsilon}\frac{e^{i\omega_2(t_1-t_2)}}{\omega_2^2-y_{12}^2+i\varepsilon} \\ &= 2\pi i\ \left(\frac{1}{2\pi i}\right)^2 \int_{-\infty}^{+\infty} d\omega_1 \int_{-\infty}^{+\infty} d\omega_2 \delta(\omega_1-\omega_2)\ \frac{e^{i\omega_1 t_0}}{\omega_1^2-x_1^2+i\varepsilon}\frac{e^{-i\omega_2 t_2}}{\omega_2^2-y_{12}^2+i\varepsilon} \\ &= \left(\frac{1}{2\pi i}\right) \int_{-\infty}^{+\infty} d\omega\ \frac{e^{i\omega(t_0-t_2)}}{\omega^2-x_1^2+i\varepsilon}\frac{1}{\omega^2-y_{12}^2+i\varepsilon} \\ &= \left(\frac{1}{2\pi i}\right) \int_{-\infty}^{+\infty} d\omega\ \frac{1}{x_1^2-y_{12}^2}\left[\frac{e^{i\omega(t_0-t_2)}}{\omega^2-x_1^2+i\varepsilon}-\frac{e^{i\omega(t_0-t_2)}}{\omega^2-y_{12}^2+i\varepsilon}\right] \\ &= \frac{1}{x_1^2-y_{12}^2}\left[G_F(t_0,t_2,x_1)-G_F(t_0,t_2,y_{12})\right]. \end{aligned} \tag{5.98}$$

[14] Here we refer to the fact that, since the wave function answers a boundary value question rather than computing an average like a correlator, its propagator contains both the time-order Feynman propagator and a homogeneous solution to the equations of motion that enforces the vanishing of the propagator at the time surface where the wavefunction is evaluated.

Finally, these Feynman propagators can be viewed as an additional external leg connecting to the x_2 vertex. Therefore, absorbing the propagators with the appropriate rules in Eq. (5.90), we can write the recursion relation

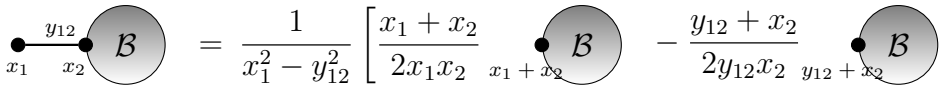

(5.99)

As an example consider the two chain and one chain in Eqs. (5.93) and (5.94), we have

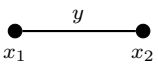

$$= \frac{1}{x_1^2 - y^2}\left[\frac{x_1+x_2}{2x_1x_2}\left(-\frac{1}{(x_1+x_2)^2}\right) - \frac{y+x_2}{2yx_2}\left(-\frac{1}{(y+x_2)^2}\right)\right]. \tag{5.100}$$

The way this recursion relation can be used repeatedly was shown in [91], and it can also iteratively be used for instance to relate the double exchange to a number of contact diagrams, which works similarly here. The interesting thing in the case here, however, is that we can generalise this to loops.

Recursion Relations for Melonic Loop Integrands The derivation for the recursion relation at loop level does in principle require not many more steps. We simply need to utilise Eq. (5.91). The recursion relations we write here are purely for the integrand, and all results in this section should be interpreted to be integrated over internal momenta. Furthermore, we focus on any number of loops, but we keep the number of vertices fixed, that is, we for instance do not consider box diagrams. The methods we present here do however generalize to these kinds of diagrams. In conclusion, we focus on diagrams of the type

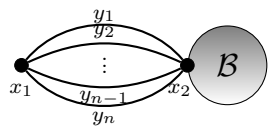

$$\equiv \int_{-\infty}^{\infty} \prod_{v\in\mathcal{B}\setminus\{2\}} i\,dt_v\, G_F(t_v, t_0, x_t) \times \tag{5.101}$$

$$\times \int_{-\infty}^{\infty} i\,dt_2 G_F(t_2, t_0, x_2) \prod_{e\in\mathcal{B}} G_F(t_{v_e}, t_{v'_e}, y_{v_e}) I_n(\{y_i\}, t_2),$$

where now we have

$$I_n(\{y_i\}, t_2) \equiv \int_{-\infty}^{\infty} i\,dt_1\, G_F(t_1, t_0, x_1) \prod_{i=1}^{n} G_F(t_1, t_2, y_i) = \frac{2y_T}{\prod_{i=1}^{n} 2y_i} I_1(y_T, t_2), \tag{5.102}$$

where in the last step we related I_n to I_1 using Eq. (5.91). On the level of the diagrams we, therefore, have

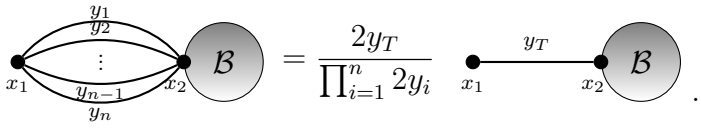

(5.103)

Of course, as in the previous section we can also fully find I_n to get a generalisation of Eq. (5.99) by writing

$$I_n(\{y_i\}, t_2) = \frac{2y_T}{\prod_{i=1}^n 2y_i} \frac{1}{x_1^2 - y_T^2} \left[G_F(t_0, t_2, x_1) - G_F(t_0, t_2, y_T) \right], \quad (5.104)$$

which written as diagrams, means

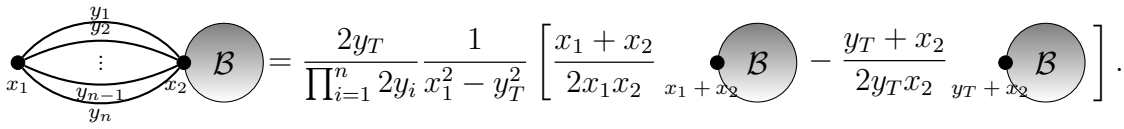

(5.105)

For a simple application, consider a 1-loop exchange diagram. Then we have

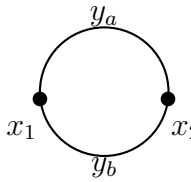

$$= \frac{y_a + y_b}{2y_a y_b} \frac{1}{x_1^2 - (y_a + y_b)^2} \left[\frac{x_1 + x_2}{2x_1 x_2} \left(-\frac{1}{(x_1 + x_2)^2} \right) - \right.$$
$$\left. - \frac{y_a + y_b + x_2}{2(y_a + y_b)x_2} \left(-\frac{1}{(y_a + y_b + x_2)^2} \right) \right]$$
$$= \frac{x_1 + x_2 + y_a + y_b}{4x_1 x_2 y_a y_b (x_1 + x_2)(x_1 + y_a + y_b)(x_2 + y_a + y_b)},$$

(5.106)

and the result for the n-loop exchange can be derived very similarly.

We would like to conclude with a final comment. In [91] the main recursion relation was derived by using the fact that a time-translation of the Minkowski wavefunction is simple in terms of the external energies. Upon integration by parts and by virtue of the properties of the wavefunction propagator, a diagram can written as an appropriate sum of single cuts. Unfortunately, we were not able to export this type of recursion relation to the correlators. There are two reasons for

this. First, for wave function coefficients the time translation operator acts non-trivially on bulk-bulk propagators, since the boundary term is not time translation invariant, even in Minkowski. In our case, we simply have Feynman propagators and get zero. The second reason is that after integrating by parts, in the case of wave function coefficients, the derivative of the bulk-boundary propagators is proportional to the bulk-boundary propagator. However, the derivative of the Bulk-boundary Feynman propagator simply gives us a derivative interaction, that we cannot be related to the original expression. For the exchange, for example, the results we get are

$$\int dtdt' \Big[G_F^{\phi\dot{\phi}}(t_0,t,x_1) G_F(t,t',y_{12}) G_F(t_0,t',x_2) + \\ + G_F(t_0,t,x_1) G_F(t,t',y_{12}) G_F^{\phi\dot{\phi}}(t,t',x_2) \Big] = 0, \tag{5.107}$$

of which we could not make practical use.

5.6 Cutkosky Cutting Rules for Correlators

Let us now move on to a different application of the in-out formalism: cutting rules for correlators. Given that the in-out formalism features only one type of propagator, one might expect that a version of Cutkosky's cutting rules might apply [114]. In this section, we confirm this expectation and derive explicit results for all diagrams with one or two interaction vertices, to all loops. As long as we consider IR-finite interactions, our results apply to Minkowski as well as to de Sitter space-time.

The "primum mobile" of Cutkosky's cutting rules is Veltman's largest time equation [94], which in turn can be traced back to the following operator identity:

$$\sum_{r=0}^{n} (-1)^r \sum_{\sigma \in \Pi(r,n-r)} \bar{T} \left[\mathcal{O}_{\sigma(1)}(t_{\sigma(1)}) ... \mathcal{O}_{\sigma(r)}(t_{\sigma(r)}) \right] T \left[(\mathcal{O}_{\sigma(r+1)}(t_{\sigma(r+1)}) ... \mathcal{O}_{\sigma(n)}(t_{\sigma(n)}) \right] = 0 \,. \tag{5.108}$$

Here $\Pi(r, n-r)$ is the set of partitions of $\{1, .., n\}$ into two subsets of lengths r and $n-r$, so the sum involves 2^n terms. The fields $\mathcal{O}_i$ are arbitrary products of operators at the same time. We will mostly focus on cases where these operators

are monomials in the fields of the theory and their derivatives. The identity above can be proven by induction. To lowest non-trivial order, $n = 2$, Eq. (5.108) simply restates the well-known fact that the two non-time-ordered propagators and the two time-ordered and anti-time ordered propagators are related by [15]

$$G_F(t,t') + G_F^*(t,t') - G^+(t,t') - G^+(t,t')^* = 0\,. \tag{5.109}$$

In this simple case, the connection to the largest time equation becomes apparent: whatever t and t' may be, one of the two must be larger [16], say $t > t'$. Then the Feynman propagator G_F reduces to G^+ and the anti-time-ordered propagator G_F^* reduces to $(G^+)^*$, hence proving the validity of Eq. (5.109).

When one furthermore assumes that all the operators in Eq. (5.108) are Hermitian the equation becomes a real equation, even though this is not apparent in that form. Indeed, we can combine terms pairwise to re-write it as

$$\begin{aligned}\sum_{r=0}^{n/2-1} \sum_{\sigma\in\Pi(r,n-r)} (-1)^r 2\,\mathrm{Re}\langle \bar{T}\left[\prod_{a=1}^{r}\mathcal{O}_{\sigma(a)}\right] T\left[\prod_{b=r+1}^{n}\mathcal{O}_{\sigma(b)}\right]\rangle \\ + \sum_{\sigma\in\Pi(n/2,n/2)} (-1)^{n/2}\,\mathrm{Re}\langle \bar{T}\left[\prod_{a=1}^{n/2}\mathcal{O}_{\sigma(a)}\right] T\left[\prod_{b=n/2+1}^{n}\mathcal{O}_{\sigma(b)}\right]\rangle = 0\,,\end{aligned} \tag{5.110}$$

for n even and as

$$\sum_{r=0}^{(n-1)/2} \sum_{\sigma\in\Pi(r,n-r)} (-1)^r\,\mathrm{Im}\langle \bar{T}\left[\prod_{a=1}^{r}\mathcal{O}_{\sigma(a)}\right] T\left[\prod_{b=r+1}^{n}\mathcal{O}_{\sigma(b)}\right]\rangle = 0\,, \tag{5.111}$$

for n odd, where we left the time arguments implicit.

We now follow a similar route to Veltman's derivation of cutting rules [94]. We note, however, that the set of rules we establish here are slightly different form their amplitude counterparts because we are not amputating the diagrams, and so we still have to deal with the time ordering acting on the operator insertions. This is not an issue for amplitudes because the LSZ formula effectively pushes all the field insertions to future or past infinity for outgoing and incoming particles, respectively.

[15] Since Eq. (5.108) is an operator identity, this propagator identity is valid in any state of the theory.

[16] The case $t = t'$ is trivial because all propagators are equal in that case and the identity is trivially satisfied.

Before getting into the details, let's summarize our general two-step strategy:

1. **From the largest time equation to propagator identities:** We use the largest time equation on the operators appearing inside a correlator to a given order in perturbation theory. This includes the operators appearing explicitly in a correlator and any number of powers of the interaction Hamiltonian. The outcome is a set of identities relating different products of time-ordered and non-time-ordered propagators. We employ a nifty diagrammatic notation to write these identities in terms of cut diagrams.

2. **From propagator identities to cutting rules for correlators:** Using properties of the propagators, we re-write the above propagator identities as relations among correlators for which some of the energies have been analytically continued to negative real values.

We will derive explicitly cutting rules for diagrams with at most two interaction vertices, with any number of external legs and any number of loops. For three or more vertices, we can still write propagator identities, but to transform them into cutting rules for correlators one would need to appropriately generalise our derivation. Let us now proceed to the derivation of propagator identities.

5.6.1 Propagator Identities

Here we use the largest time equation to find propagator identities. The starting point is to expand the time-evolution operator in an in-out correlator to some order in perturbation theory. Then we want to think of the various powers of ϕ and $H_{\rm int}$ as the different operators appearing in Eq. (5.108). This gives us a set of identities. To see how this works, let's start with 1-vertex diagrams and work our way up to two vertices. The case of three vertices is discussed in App. A.2.

1-Vertex Diagrams A one vertex diagram has a single power of $H_{\rm int}$ and n copies of the field ϕ. As a simple example, consider the choice

$$\mathcal{O}_1 = \phi(\mathbf{x}_1, t_0)^m\,, \qquad \mathcal{O}_2 = \phi(\mathbf{x}_2, t_0)^{n-m}\,, \qquad \mathcal{O}_3 = H_{\rm int}(t)\,, \tag{5.112}$$

where t_0 is an arbitrary time in Minkowski or in de Sitter. Since we restrict our derivation to equal-time correlators we will omit this time dependence in the following. Inserting the above choice of operators into Eq. (5.111) and sandwiching between

two ground states we get (in position space)

$$\mathrm{Im}\left\{\langle T[\phi^n H_{\rm int}]\rangle - \langle \phi^m T[\phi^{n-m} H_{\rm int}]\rangle - \langle \phi^{n-m} T[\phi^m H_{\rm int}]\rangle\right\} \simeq 0, \tag{5.113}$$

where we omitted to write the time-ordering or anti-time-ordering when a single time is present. Here we wrote $\simeq 0$ to indicate that this identity is only valid after time integration because we dropped the term $H_{\rm int}T[\phi^n]$. This is allowed because every term where a Hamiltonian interaction is not in the same time ordering as a field, it integrates to zero. Indeed, if the interaction has no relative time ordering to the boundary, we obtain an integral over the mode functions from minus infinity to infinity. As discussed previously, the integral over the mode functions in the in-out formalism is regularized in such a way that it goes to zero in the infinite past and future, so that the full integral evaluates to zero. We have hence omitted those terms in this expression and we used the symbol $\simeq 0$ as a reminder of this simplification.

To find the equivalent of Eq. (5.113) in momentum space we have to deal with the fact that $\phi(\mathbf{k})$ is not Hermitian because $\phi(\mathbf{k})^* = \phi(-\mathbf{k})$ by the reality of $\phi(\mathbf{x})$. To remove the extra minus sign we have to separate the discussion between interactions that are even (+) or odd (-) under spatial parity (point inversion). For example, we have

$$\langle T[\phi(\mathbf{k})^n H_{\rm int}(t)]\rangle_{\rm PE} = +\langle \bar{T}[\phi(\mathbf{k})^n H_{\rm int}(t)]\rangle^*_{\rm PE}\,, \tag{5.114}$$

$$\langle T[\phi(\mathbf{k})^n H_{\rm int}(t)]\rangle_{\rm PO} = -\langle \bar{T}[\phi(\mathbf{k})^n H_{\rm int}(t)]\rangle^*_{\rm PO}\,, \tag{5.115}$$

where the labels parity even (PE) and parity odd (PO) mean

$$\langle F(\mathbf{k})\rangle_{\rm PE} \equiv \frac{1}{2}\left[\langle F(\mathbf{k})\rangle + \langle F(-\mathbf{k})\rangle\right]\,, \quad \langle F(\mathbf{k})\rangle_{\rm PO} \equiv \frac{1}{2}\left[\langle F(\mathbf{k})\rangle - \langle F(-\mathbf{k})\rangle\right]\,. \tag{5.116}$$

Hence in momentum space, the parity-even component satisfies the same equation as in Eq. (5.113), while for the parity-odd component, the imaginary part is substituted by the real part.

We notice that the cutting rule is really a statement about the imaginary (parity even) or real (parity odd) part of Eq. (5.113). As we will see, these are exactly the parts of the diagrams we are interested in, so this will lead to useful relations between diagrams. But first, let's give another example.

2-Vertex Diagrams The procedure for two-vertex diagrams is very similar. We simply take a different group of operators in an in-out correlator and use the largest

time equation. Here we will focus on a particular channel, but all other channels can be discussed in the same way. For example, after expanding the evolution operator to second order, let's insert the following identifications in the largest time equation,

$$\mathcal{O}_1 = \phi(t_0)^m\,, \qquad \mathcal{O}_2 = \phi(t_0)^{n-m}\,, \qquad \mathcal{O}_3 = H^{(1)}_{\rm int}(t)\,, \qquad \mathcal{O}_4 = H^{(2)}_{\rm int}(t')\,. \tag{5.117}$$

We get in real space

$$\begin{aligned} 0 \;\simeq\; & \mathrm{Re}\Big\{\langle T[\phi^n H^{(1)}_{\rm int} H^{(2)}_{\rm int}]\rangle - \langle \phi^m T[\phi^{n-m} H^{(1)}_{\rm int} H^{(2)}_{\rm int}]\rangle - \langle \phi^{n-m} T[\phi^m H^{(1)}_{\rm int} H^{(2)}_{\rm int}]\rangle \\ & + \langle \bar{T}[\phi^m H^{(1)}_{\rm int}] T[\phi^{n-m} H^{(2)}_{\rm int}]\rangle + \langle \bar{T}[\phi^m H^{(2)}_{\rm int}] T[\phi^{n-m} H^{(1)}_{\rm int}]\rangle \Big\}\,, \end{aligned} \tag{5.118}$$

where $\simeq 0$ again indicates that the identity is valid after integrating over the time of the interactions because we omitted a number of terms that integrate to zero. This is again due to the fact that the Hamiltonian interactions do not have a time ordering with respect to the insertions of the operators. In momentum space, the above expression is unchanged for the parity-even part, while for the parity-odd part, one needs to change Re $\to$ Im. The above procedure is straightforward but leads to lengthy expressions. Here we show how to streamline it using the diagrammatic notation of "cut diagrams".

A Diagrammatic Representation: Cut Diagrams We would like to represent expressions such as Eqs. (5.113) and (5.118) in terms of diagrams. To this end, consider a Feynman diagram and imagine separating it into two subsets of vertices [17] by a "cut". The meaning of a cut is that (i) all operators on one side of the cut are time-ordered with respect to each other, (ii) those on the other side are anti-time ordered with respect to each other and (iii) operators on different sides of the cut have no relative time ordering. As an intermediate step, let's introduce Feynman rules for shaded cuts, where the shading refers to the side that is anti-time-ordered, while the un-shaded side is time-ordered:

$$\text{Shaded} \sim \text{anti-time ordered}\,, \qquad \text{Un-shaded} \sim \text{time ordered}\,. \tag{5.119}$$

The Feynman rules for a shaded cut diagram are as follows [94]:

1. A vertex at t on the shaded side of the cut connected to a vertex at t' on the

[17] This is different from deciding to cut or not cut *each* line. For example, for a one-loop two-vertex diagram we cannot cut only one of the two loop propagators because cutting only one does not create two separated subsets of vertices.

un-shaded side of the cut leads to a factor $G^+(t,t') = f(t)f^*(t')$.

2. Two vertices t and t' on the un-shaded side of the cut that are connected to each other lead to a time-ordered propagator $G_F(t,t')$.

3. Two vertices t and t' on the shaded side of the cut that are connected to each other lead to an anti-time ordered propagator $G_F^*(t,t')$.

4. A vertex on the un-shaded (shaded) side gets a $-i$ $(+i)$ factor times the appropriate coupling constant. This choice corresponds to the process of expanding the forward time evolution operator Te^{-iH} on the un-shaded side, and reverse time evolution operator $\bar{T}e^{+iH}$ on the shaded side.

Vertex factors and integration over the vertices are as usual. The only difference from the standard Feynman rules are the propagators. The rules for a right-shaded cut, are the same just under the exchange of the word 'left' and 'right'. Finally, an unshaded cut is the average of the two shadings, that is:

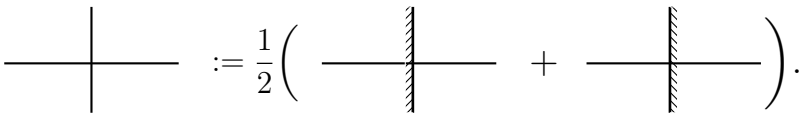

(5.120)

Comments Three comments are in order. The first is that cut diagrams have a meaning that is independent of the largest time equation. For example, we can consider the s-channel exchange for the four-point function in Minkowski with two insertions of a $\phi^3/(3!)$ interaction and directly write

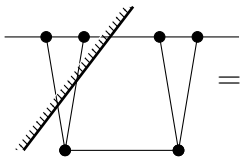

$$= -\int_{-\infty}^{\infty}\int_{-\infty}^{\infty} dtdt' \left(\prod_{i=1}^{2} G^+(t_0,t,E_i)\right) G_F(t,t',s) \left(\prod_{i=3}^{4} G_F(t_0,t',E_i)\right), \tag{5.121}$$

where s is the energy of the internal line. This emphasises that a cut diagram is just a diagrammatic representation of the integral of the product of propagators.

Second, we want to discuss how to diagrammatically identify those terms in the largest time equation that vanish upon integration over time, namely cases where a Hamiltonian interaction does not appear in the same time ordering as an external operator. This observation leads to the diagrammatic rule that *a diagram integrates*

to zero if it contains an interaction vertex that is separated by the cut from all (fixed) operator insertions. As an example of this rule, consider a contact diagram in flat space with a single power of the interaction Hamiltonian, which we take to be a simple $\phi^3/(3!)$ interaction. This results in a correlator of the form

$$\left\langle T\left(\prod_a^n \phi_{E_a}(t_0) H_{\rm int}(t)\right)\right\rangle . \tag{5.122}$$

Applying the largest time Eq. (5.108) to this diagram (viewing $\phi(t_0)^n$ as a single operator and $H_{\rm int}(t)$ as a second operator), we obtain a sum over terms, one of which takes the form

$$\int_{-\infty}^{\infty} dt \left\langle H_{\rm int}(t) T\left(\phi_{E_1}(t_0)\phi_{E_2}(t_0)\phi_{E_3}(t_0)\right)\right\rangle \sim \int_{-\infty}^{\infty} dt \left\langle \phi(t)^3 T\left(\phi_{E_1}(t_0)\phi_{E_2}(t_0)\phi_{E_3}(t_0)\right)\right\rangle \tag{5.123}$$

This integrates to zero because the mode functions do

$$\propto \int_{-\infty}^{\infty} dt \prod_{i=1}^{3} G^+(t, t_0, E_i) = 0 . \tag{5.124}$$

Graphically this corresponds to

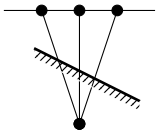

$= 0.$ (5.125)

Therefore, the actual number of cut diagrams that we have to consider when rephrasing the largest time equation as a propagator identity is less, and often much less, than the number of parting into two sets appearing in Eq. (5.108).

The third and final comment is that the results derived in this section are valid for fields of any mass in de Sitter or Minkowski. It is only in the next section that we will restrict to massless and conformally coupled fields in de Sitter.

$V = 1$ **Cut Diagrams** Let's see now how the one- and two-vertex examples we considered before look like in terms of cut diagrams. For contact operators

Eq. (5.113) becomes

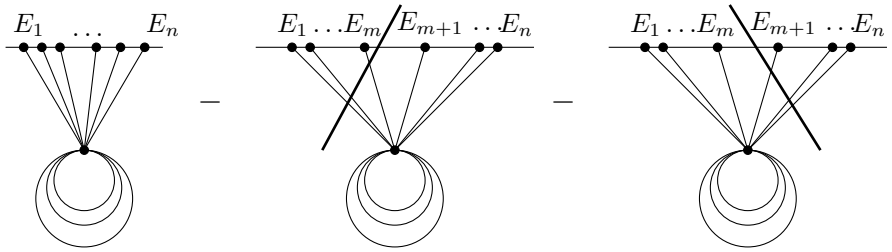

$$= 0. \qquad (5.126)$$

where a diagram without a cut should be understood as having a cut all the way to the right or, equivalently, to the left. Notice that this relation is valid for the loop integrand to all loop orders (but only for a single vertex). In other words, we can contract any number of pairs of fields in H_{int}, since they are still associated to the same time in the largest time equation.

$V = 2$ **Cut Diagrams** For the exchange diagram we would find that the cut diagram representation of Eq. (5.118) contains five terms. However, if we specify a specific channel, namely a way to pairwise contract fields and the interaction Hamiltonians, the last term in Eq. (5.118) vanishes because an interaction Hamiltonian is contracted only with fields outside of its time ordering. Dropping this vanishing term we find the diagrammatic representation

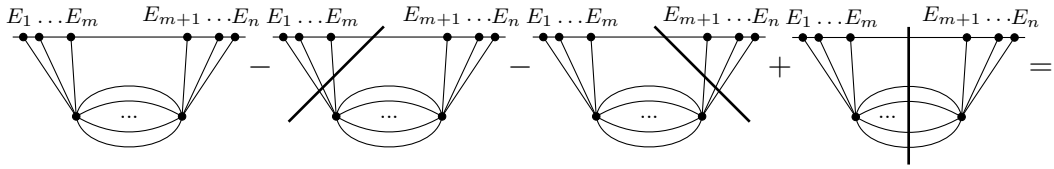

$$= 0. \qquad (5.127)$$

We will see in the next section how these identities can be transformed into cutting rules for correlators.

$V > 2$ **Cut Diagrams** Here we briefly discuss the general properties of diagrams with more than two vertices. While it would be interesting to perform a serious combinatorial analysis of the problem, here we limit ourselves to some simple remarks. First of all, we notice that the number of terms appearing in the largest time equation grows fast and it's desirable to consider only the new constraints that arise at higher order. Moreover, the really useful power of these relations arises when a complicated diagram is reduced to the sum over products of simpler ones.

To focus on this case, it is convenient to only discuss cases where all the external fields connected to a single vertex are treated as a single operator in the largest time equation. Then we have to deal with diagrams where each interaction vertex is attached to exactly one external line. Very generally we then have V bulk vertices and V external vertices. Given that a cut separates these $2V$ vertices into two groups, we know the largest time equation generates 2^{2V} terms. These are then related pairwise by complex conjugation as in Eqs. (5.110) and (5.111) leading to 2^{2V-1} terms. Of these terms, many vanish because of the general rule stated above Eq. (5.122). We were only able to find an upper bound on the number of vanishing diagrams by counting all cuts in which interaction vertices are not in the same time order as an external operator. These can be counted by summing the binomials $\binom{V}{k}$ over $1 \leq k \leq V$, which gives $2^V - 1$. This leads to the upper bound on the number N of non-vanishing terms in the largest time equation (with one external leg per vertex)

$$N \leq 2^{2V-1} - 2^V + 1\,. \tag{5.128}$$

For example, for $V = 1$ we find $N \leq 1$. In this case, the bound is saturated and we have a single term and we find the constraint


$= 0.$ (5.129)

For $V = 2$ we find $N \leq 5$. The actual number of non-vanishing terms is $N = 4$. The one diagram that does vanish but is not accounted for in our bound is

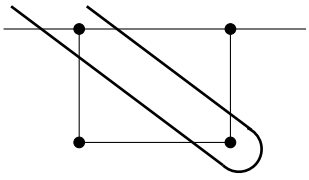
$= 0\,.$ (5.130)

This is the fifth term in Eq. (5.118) [18], and the external legs connected to each vertex have been represented graphically as a single line. It will be interesting to pursue this further in the future.

[18] Depending on the channel it can be the fourth or fifth.

5.6.2 Cutting Rules for Correlators

Finally, we would like to relate the propagator identities represented by cut diagrams to correlators with shifted kinematics. For technical reasons, we will restrict our discussion to fields of any mass in Minkowski but only massless and conformally coupled fields in de Sitter, but we include all derivative interactions. To do this, we first assume Hermitian analyticity, i.e. for all propagators, we assume

$$G(\eta,\eta',k) = -G(\eta,\eta',-k)^*\,, \qquad G(t,t',E) = -G(t,t',-E)^*\,. \tag{5.131}$$

In the following, we will therefore restrict ourselves to these three cases, but include all derivative interactions, as they preserve hermitian analyticity. This is true for all the fields we consider in this section. Furthermore, we write all expressions at the leading order of η_0 of the uncut correlator [19]. As we show in App. A.3 this then allows us to relate the three types of cuts we consider in this section, to be related to the contact correlator, B_n^c, and exchange correlator B_n^{ex} in the following way. For contact diagrams, we find

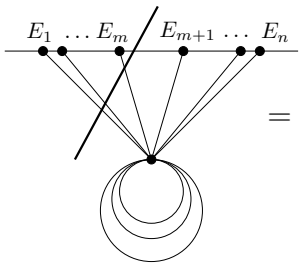

$$= \frac{1}{2}\left[B_n^c(\{E_i\}_{i=1}^n) + (-1)^m B_n^c(\{-E_i\}_{i=1}^m, \{E_i\}_{i=m+1}^n))\right]. \tag{5.132}$$

For exchanges, we consider cuts that run along internal lines, or cuts of external lines that all connect to the same vertex, as in Eq. (5.127). We then have

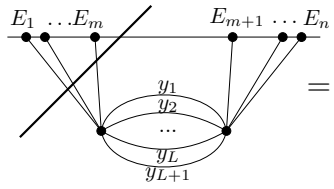

$$= \frac{1}{2}\left[B_n^{ex}(\{E_i\}) + (-1)^m B_n^{ex}(\{-E_i\}_{i=1}^m, \{E_i\}_{i=m+1}^n))\right], \tag{5.133}$$

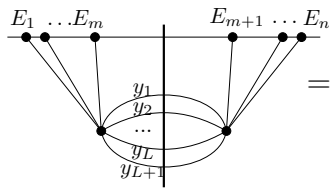

$$= -\frac{B^{\rm c,cut}_{m,L+1}(\{E_i\}_{i=1}^m, \{y_i\}_{i=1}^{L+1}) B^{\rm c,cut}_{n-m,L+1}(\{E_i\}_{i=m+1}^n, \{y_i\}_{i=1}^{L+1})}{\prod_{i=1}^{L+1} P(y_i)}, \tag{5.134}$$

[19] This is necessary, because cut diagrams, will in some cases have subleading terms in η_0, that however cancel between terms.

where $P(y)$, is the power spectrum of ϕ and we defined

$$B^{\mathrm{c,cut}}_{n,L}(\{E_i\}_{i=1}^n, \{y_i\}_{i=1}^L) = \tag{5.134}$$
$$= \frac{1}{2}\left[B^{\mathrm{c}}_{n+L}(\{E_i\}_{i=1}^n, \{y_i\}_{i=1}^L) + (-1)^L B^{\mathrm{c}}_{n+L}(\{E_i\}_{i=1}^n, \{-y_i\}_{i=1}^L))\right].$$

1-Vertex Cutting Rules We can in principle get a multitude of cutting rules from Eq. (5.108), depending on how we identify operators with powers of ϕ and H_{int}. We here show one example for contact diagrams. We use the relation Eq. (5.132) between cut diagrams and analytically continued propagators inside the propagator identity Eq. (5.126). The result can be manipulated as follows:

$$B^c_n(\{E_i\}_{i=1}^n) - \frac{1}{2}\left[B^c_n(\{E_i\}_{i=1}^n) + (-1)^m B^c_n(\{-E_i\}_{i=1}^m, \{E_i\}_{i=m+1}^n))\right] \tag{5.135}$$
$$-\frac{1}{2}\left[B^c_n(\{E_i\}_{i=1}^n) + (-1)^{n-m} B^c_n(\{E_i\}_{i=1}^m, \{-E_i\}_{i=m+1}^n))\right] = 0$$

We can then see that $B^c_n(\{E_i\}_{i=1}^n)$ cancels, and finally the we can invert the first m energies, to obtain

$$B^c_n(\{E_i\}_{i=1}^n) + (-1)^n B^c_n(\{-E_i\}_{i=1}^n) = 0. \tag{5.136}$$

2-Vertex Cutting Rules For two insertions of an interaction Hamiltonian, the number of relations one can obtain from Eq. (5.108) is in principle even larger. The rules we formulate here for the exchange focus on a particular channel, but the full rule then simply applies to all permutations.

If we insert $\mathcal{O}_1 = \phi(t_0)^m$, $\mathcal{O}_2 = \phi(t_0)^{n-m}$, $\mathcal{O}_3 = H^{(1)}_{\mathrm{int}}(t)$, and $\mathcal{O}_4 = H^{(2)}_{\mathrm{int}}(t')$ into Eq. (5.108), and denote the s channel where the $\mathcal{O}_1$ are connected to the $H^{(1)}_{\mathrm{int}}$ and the remaining legs to $H^{(2)}_{\mathrm{int}}$, we obtain the rule for exchange diagrams at $L+1$-loops given in Eq. (5.127). Before inserting the relations found in Eq. (5.133) into Eq. (5.127), note that using Eq. (5.136), one can see that

$$B^{\mathrm{c,cut}}_{n,L}(-\{E_i\}_{i=1}^n, \{y_i\}_{i=1}^L) = (-1)^{n+1} B^{\mathrm{c,cut}}_{n,L}(\{E_i\}_{i=1}^n, \{y_i\}_{i=1}^L) \tag{5.137}$$

Now, again with Eq. (5.133), we can directly and generally relate to correlators with flipped energies. We denote the internal energies' dependence on the internal momenta, by $y_i = y_i(\vec{p_i})$. Then, the first three terms of Eq. (5.127) combine, similarly

to Eq. (5.135), to give

$$\frac{(-1)^{m+1}}{2}\left[B_n^{ex}(\{-E_i\}_{i=1}^m,\{E_i\}_{i=m+1}^n)+(-1)^n B_n^{ex}(\{E_i\}_{i=1}^m,\{-E_i\}_{i=m+1}^n)\right]= \\ =\int_{\vec{p}_1\ldots\vec{p}_{L+1}}\frac{B^{\rm c,cut}_{m,L+1}(\{E_i\}_{i=1}^m,\{y_i\}_{i=1}^{L+1})B^{\rm c,cut}_{n-m,L+1}(\{E_i\}_{i=m+1}^n,\{y_i\}_{i=1}^{L+1})}{\prod_{i=1}^{L+1}P(y_i)}, \tag{5.138}$$

then flipping $\{E_i\}_{i=1}^m \to \{-E_i\}_{i=1}^m$ on both sides, and using Eq. (5.137) for the cut diagrams, we finally find

$$B_n^{\rm ex,s}(\{E_i\}_{i=1}^n)+(-1)^n B_n^{\rm ex,s}(\{-E_i\}_{i=1}^n)= \\ =2\int_{\vec{p}_1\ldots\vec{p}_{L+1}}\frac{B^{\rm c,cut}_{m,L+1}(\{E_i\}_{i=1}^m,\{y_i\}_{i=1}^{L+1})B^{\rm c,cut}_{n-m,L+1}(\{E_i\}_{i=m+1}^n,\{y_i\}_{i=1}^{L+1})}{\prod_{i=1}^{L+1}P(y_i)}. \tag{5.139}$$

For $L=0$ this simply reduces to a tree-level identity and the integrals can be ignored. This is a generalisation of the relation found in [70], which we recover for $L=0, n=4$, and $m=2$.

We end this section with a number of comments. The cutting rules we obtained for the 1-vertex and 2-vertex diagrams here, by no means represent the full information one can obtain from Eq. (5.108). For instance in App. A.2, we derive the propagator identities for the 3-vertex case. Additionally, one could consider more general choices of operators in the largest time equation. However, the results we have presented in this work are not yet sufficient to relate these diagrams to correlators with shifted kinematics.

5.7 Scattering in de Sitter: a Preview

In this section, we present a brief discussion of scattering in de Sitter, which follows naturally from the in-out formalism we have introduced. The S-matrix we define is similar to an S-matrix that has recently been independently introduced by Melville and Pimentel in [69]. We comment on the few differences and many similarities below.

Fig. 5.1 suggests a natural way to define scattering in the (double) Poincaré patch of de Sitter: consider a state of n free particles at the past null horizon, let them evolve in an interacting theory and project the resulting state on the tensor

product of free particles at future null infinity. In the Schrodinger picture this looks very familiar:

$$S_{n,n'} = \langle n', +\infty | n, -\infty \rangle \ . \tag{5.140}$$

Following Wigner, a "free particle" should correspond to an irreducible representation of the dS isometry group and is hence characterized by two quadratic Casimir operators, the conformal dimension Δ (related to the mass by Eq. (5.27)) and spin s (we use the notation of [83, 115, 116]), plus a set of eigenvalues for some conveniently chosen maximal abelian ideal (Cartan subalgebra). We choose to diagonalize the three (commuting) generators of spatial translations P_i and denote single-particle states by $|\Delta, \mathbf{k}, s, \sigma\rangle$, with σ the spin along some direction. These states are created by acting on the Bunch-Davies vacuum with creation operators, which in turn can be repackaged in the standard way into fields. We adopt a relativistic normalisation of the states. The in and out states of the S-matrix are then just tensor products of free particles,

$$|n\rangle = \bigotimes_a^n |\Delta_a, \mathbf{k}_a, s_a, \sigma_a\rangle \ . \tag{5.141}$$

To compute the S-matrix we work in perturbation theory in the interaction picture with a time evolution operator given by

$$S_{n,n'} = \langle n' | \, U(+\infty, -\infty) \, | n \rangle = \langle n' | \, T e^{-i \int_{-\infty}^{+\infty} H_{\rm int}(\eta) d\eta} \, | n \rangle \ , \tag{5.142}$$

where again $H_{\rm int}$ is the interaction Hamiltonian written in terms of the interaction picture fields (free fields in the Heisenberg picture). This is the same in-out time-evolution operator [20] we defined in Eq. (5.26) and hence we are naturally thinking of the "extended" de Sitter spacetime in Fig. 5.1. In the absence of IR divergences, this is a well-defined operator, as we discussed previously. The Feynman rules are pretty much the same as in Minkowski, except that we will use them in the time-momentum domain, as opposed to time-position or energy-momentum domains that are more familiar in Minkowski. The detailed prescription can be extracted from Eq. (5.142),

[20] There is subtlety here. If we use the same $i\epsilon$ prescription as for computing in-out correlators, namely Eq. (5.45), we find a divergence because some incoming or outgoing particles have been inserted before or after all Hamiltonian interactions. In other words, since we are not projecting onto the vacuum of the free theory we should not use the $i\epsilon$ rotation of the contour. Rather, we should adiabatically turn on interactions à la Gell-Mann and Low, namely with the shift $H_{\rm int} \to e^{-\epsilon|\eta|} H_{\rm int}$ [44].

but it is easier to notice that the S-matrix is related to the in-out correlators simply by replacing each off-shell external leg by an on-shell mode function evolving an incoming (outgoing) particle all the way to past (future) null infinity, as dictated by the LSZ projection. In our setup, this procedure works very similarly to Minkowski with the difference that one needs to use the dS mode function appropriate to the fields corresponding to the particle under consideration. This was nicely discussed in [69] (see also [111] for a similar projection of in-out correlators to the wavefunction).

We define amplitudes A by

$$\langle f|\, U(+\infty,-\infty)-1\,|i\rangle = i(2\pi)^4\delta^{(3)}(\mathbf{k}_{\rm in}-\mathbf{k}_{\rm out})A_{if}\,, \tag{5.143}$$

for $|i\rangle$ and $|f\rangle$ some initial and final states respectively. Similarly to Minkowski, A is proportional to the matrix element of $T=-i(S-1)$ but a crucial difference is that we strip off only the momentum-conserving Dirac delta and not the energy-conserving Dirac delta. The reason will be clear momentarily.

We are now in the position to compute the simplest scattering process of n to n' particles of mass $m^2=2H^2$, corresponding to a conformally coupled scalar, with the simple negative-frequency mode function [21]

$$f_k(\eta)=\eta\frac{He^{-ik\eta}}{\sqrt{2k}}\,. \tag{5.144}$$

We choose a simple polynomial interaction $H_{\rm int}=\lambda\phi^{n+n'}/(n+n')!$ and restrict to $n+n'\geq 4$ to ensure the absence of IR divergences. The relativistic normalization of the states gives us

$$|\Delta,\mathbf{k}\rangle=\sqrt{2|\mathbf{k}|}a^\dagger_{\mathbf{k}}\,|0\rangle\ . \tag{5.145}$$

Then to linear order in λ the result is

$$A_{nn'}=-\lambda\,(-iH\partial_{E_T})^{n+n'-4}\delta(E_T)\,, \tag{5.146}$$

where E_T is the total energy accounting for the opposite sign of incoming and

[21] Note that we here drop the factor of i for conformally coupled scalars from Eq. (5.4), for simplicity. This simply corresponds to a different choice of normalisation.

outgoing particles

$$E_T = -\sum_a^n |\mathbf{k}_a| + \sum_b^{n'} |\mathbf{k}_b| \,, \tag{5.147}$$

and we found the $(n + n' - 4)$-th derivative of the Dirac delta. Notice that, at least in perturbation theory, the S-matrix enjoys crossing symmetry and so could simply choose all particles to be outgoing (this was also noticed in [69]), so that E_T is the usual positive sum of norms.

As a less trivial example, consider the exchange diagram mediating the elastic scattering of $3 + r$ particles mediated by the interaction $\lambda\phi^{4+r}/(4 + r)!$. This is IR finite as long as $r \geq 0$, hence the unusual definition of r. A direct calculation gives

$$A_{3+r,3+r} = \frac{\lambda^2 H^{2r}}{2} \sum_{l=0}^{r} b_l \frac{(k_{\rm in} - E_{\rm in})^{1+r-l} + (k_{\rm in} + E_{\rm in})^{1+r-l}}{2k_{\rm in}(-E_{\rm in}^2 + k_{\rm in}^2)^{1+r-l}} \partial^{r+l} \delta(E_{\rm in} - E_{\rm out}) \,, \tag{5.148}$$

where

$$E_{\rm in} = \sum_{a=1}^{3+r} |\mathbf{k}_a| \,, \qquad E_{\rm out} \equiv \sum_{a=4+r}^{6+2r} |\mathbf{k}_a| \,, \tag{5.149}$$

$$\mathbf{k}_{\rm in} = \sum_{a=1}^{3+r} \mathbf{k}_a \qquad \mathbf{k}_{\rm out} \equiv \sum_{a=4+r}^{6+2r} \mathbf{k}_a \qquad b_l \equiv \frac{r!}{l!}(-1)^l \,. \tag{5.150}$$

A useful check is that we should recover the tree-level single-exchange Minkowski amplitude for $r = 0$, in which case the ϕ^4 interaction is classically conformal. In this case, the sum disappears, the numerator cancels the factor $2k_{\rm in}$ at the denominator and we are left with the familiar $1/S$ with S the Mandelstam variable $S = -E_{\rm in}^2 + \mathbf{k}_{\rm in}^2$. The absence of a mass is what we would expect since a conformally coupled scalar is massless in Minkowski, where the Riemann tensor vanishes.

Unitarity and Positivity The amplitudes defined in Eq. (5.143) satisfy the textbook generalised optical theorem

$$A_{if} - A_{fi}^* = i \sum_X \int d\Pi_X \, (2\pi)^4 \delta^{(3)}(\mathbf{k}_{\rm in} - \mathbf{k}_X) A_{iX} A_{fX}^* \,, \tag{5.151}$$

where the sum is over all possible states and the only difference from Minkowski is that we have not removed any energy-conserving Dirac deltas, and so none needs to be added explicitly on the right-hand side. A powerful consequence of this theorem is that the right-hand side is manifestly positive for forward scattering and this constrains the imaginary part of A_{ii} non-perturbatively.

Let's check explicitly the optical theorem for the tree-level elastic scattering of four conformally coupled scalars in de Sitter with a polynomial interaction $\lambda\phi^5/(5!)$. We can copy the result from Eq. (5.146) and the right-hand side is simply computed as

$$\text{RHS} = i\int \frac{dk_X^3}{(2\pi)^3}\frac{1}{2E_X}(2\pi)^4\delta^{(3)}(\mathbf{k}_{\text{in}}-\mathbf{k}_X)|A_{4,1}|^2 \tag{5.152}$$

$$= 2\pi i\lambda^2 H^2\delta'(E_{\text{out}}-E_{\text{in}})\frac{\delta'(E_{\text{in}}-k_{\text{in}})}{2E_{\text{in}}}\,. \tag{5.153}$$

The left-hand side can be computed from Eq. (5.148) setting $r = 1$. Two terms appear in the sum over l:

$$\text{LHS} = \frac{\lambda^2H^2}{2}2i\,\text{Im}\left[-\frac{1}{(-E_{\text{in}}^2+k_{\text{in}}^2)}\delta''(E_{\text{in}}-E_{\text{out}}) + \frac{k_{\text{in}}^2+E_{\text{in}}^2}{k_{\text{in}}(E_{\text{in}}^2-k_{\text{in}}^2)^2}\delta'(E_{\text{in}}-E_{\text{out}})\right] \tag{5.154}$$

In the first term, corresponding to $l = 1$, the Dirac delta needs to be integrated by parts. Hence the two terms can be combined and the numerator cancels the negative energy poles at $E_{\text{in}} = -k_{\text{in}}$ in the denominator, leaving only the positive-energy pole, at $E_{\text{in}} = k_{\text{in}}$, as expected for a physical and on-shell exchanged particle,

$$\text{LHS} = i\frac{\lambda^2H^2}{k_{\text{in}}}\delta'(E_{\text{in}}-E_{\text{out}})\,\text{Im}\,\frac{1}{(E_{\text{in}}-k_{\text{in}}+i\epsilon)^2}\,. \tag{5.155}$$

One can now re-write $\text{Im}(E_{\text{in}}-k_{\text{in}}+i\epsilon)^{-2} = \partial_{k_{\text{in}}}\,\text{Im}(E_{\text{in}}-k_{\text{in}}+i\epsilon)^{-1}$. Then, using the Sokhotski–Plemelj theorem, $\text{Im}(x+i\epsilon)^{-1} = -\pi\delta(x)$, we have $\partial_{k_{\text{in}}}\,\text{Im}(E_{\text{in}}-k_{\text{in}}+i\epsilon)^{-1} = -\pi\delta'(E_{\text{in}}-k_{\text{in}})$ to obtain precisely the same expression as the right-hand side in Eq. (5.153).

5.8 Conclusions and Outlook

In this work, we have developed an in-out formalism that computes cosmological correlators. Our formalism is equivalent to the well-known in-in formalism for

unitary, non-dissipative evolution and in the absence of IR divergences. The in-out formalism offers a welcome simplification of the Feynman rules and involves only the Feynman propagator. We have discussed a few applications of this formalism, such as the derivation of recursion relations for Minkowski correlators and cutting rules for de Sitter and Minkowski correlators.

Our results open many avenues for new exciting research:

- Already from Fig. 5.1 it is natural to define a scattering S-matrix in de Sitter by complete analogy with Minkowski. This S-matrix can be readily computed from the Feynman rules we have given for in-out correlators (with the usual amputation of external lines, which become on-shell mode functions). This S-matrix is very close to that recently introduced in [69], modulo some minor technical differences. The in-out S-matrix is interesting because it connects unitarity to positivity via the optical theorem, just like in Minkowski.

- Our formalism might be useful to make progress on understanding the renormalization of ultra-violet divergences in cosmological correlators (see [117] for progress in this direction). Some of the outstanding issues include the apparent inequivalence of regularization procedures [63, 118], the characterization of counterterms and a systematic formulation of effective field theories in an expanding spacetime.

- The in-out formalism might simplify calculations and lead to new constraints in the cosmological bootstrap [77], both for the de Sitter [40] and the boostless case [119].

- Our results might provide the key insight to understand the relation between the analytic structure of correlators and wavefunction coefficients. A study of the latter commenced in [91] and was systematized and generalised recently in [111], where an identification and classification of singularities in Minkowski spacetime were presented. Later, in [120], it was proven that the branch cuts in the total energy appearing in the wavefunction always cancel in correlators (this fact had previously been noticed in a particular case in [121]). In [122], it was shown that wavefunction singularities can be classified in "amplitude-like" singularities, which appear also in S-matrix elements, and "wavefunction-type" singularities that don't. There it was conjectured that only the amplitude-like singularities survive in correlators, while wavefunction-type singularities cancel

out. The equivalence between in-in and in-out formalism seems to provide a rational for this phenomenon.

- We have provided a formal argument for the equivalence of the in-in and in-out formalism, but we have presented explicit checks only at tree level. It would be important to make an explicit check at loop order. Moreover, our cutting rules for correlators might be useful to understand the peculiar behaviour of loop contributions to parity-odd correlators, recently computed in [121]. The surprising simplicity of the parity-odd loop correlators might be clarified by relating them to tree-level diagrams and leveraging the nice results derived in [123].

- As it is clear from our results, the number and complexity of the possible relation among correlators, such as the cutting rules, grow quickly for larger diagrams. It would be very interesting to see if a more abstract and probably geometric organising principle emerges, in analogy to the role that polytopes play in understanding wavefunction coefficients [91, 124, 125, 125, 112]. Perhaps the techniques developed in [126, 127] can help systematize our derivation of cutting rules.

Our main result, namely the derivation of an in-out formalism for cosmological correlators, is a technical one. However, it is not rarely the case that a different technical formulation of a problem leads to a new conceptual understanding or new unexplored connections. Posterity will judge.

Part III

Bridging the Early and Later Universe

Theory, Constraints and Forecasts with the EFTofLSS Bispectrum and Galaxy Surveys

6

Theory: The One-Loop Bispectrum of Galaxies in Redshift Space from the EFTofLSS

6.1 Summary

We derive the Effective Field Theory of Large-Scale Structure kernels and counterterms for the one-loop bispectrum of dark matter and of biased tracers in real and redshift space. This requires the expansion of biased tracers up to fourth order in fluctuations. In the process, we encounter several subtleties related to renormalization. One is the fact that, in renormalizing the momentum, a local counterterm contributes non-locally. A second subtlety is related to the renormalization of local products of the velocity fields, which need to be expressed in terms of the renormalized velocity in order to preserve Galilean symmetry. We check that the counterterms we identify are necessary and sufficient to renormalize the one-loop bispectrum at leading and subleading order in the derivative expansion. The kernels that we present here will be used for the analyses of the one-loop bispectrum in Chs. 7 and 8.

6.2 Introduction and Conclusion

The Effective Field Theory of Cosmological Large-Scale Structure (EFTofLSS) [30, 28] describes the long distance dynamics of matter and galaxies in the universe. It is quite a complex endeavor. The dark matter [30, 28] and baryons [128, 31] are described through their density and momenta, and satisfy some equations of motion that resemble those of fluids. Galaxies are described as composite operators in terms of the dark-matter long-wavelength fields (see e.g. [129, 130, 131, 132, 133, 134, 135], and also [136]). The effect on short fluctuations of long wavelength modes that represent displacements needs to be resummed [137, 138, 139, 140, 141]. Predictions for observables, such as correlation functions of galaxies in redshift space, typically involve all of these ingredients. It took quite a large and long endeavor to develop all of this formalism.

Starting from [7, 142, 143], the EFTofLSS has been successfully applied to large-scale structure data, specifically to BOSS data [9], where the analysis of the full shape of the power spectrum has led to the measurement of all the ΛCDM parameters using just a prior from Big Bang Nucleosynthesis. Since then, many applications to data have followed.

In Ch. 7 we will perform the analysis of the BOSS data using the one-loop prediction of the bispectrum of galaxies in redshift space. Doing such an analysis requires the development of the kernels for biased tracers in redshift space up to fourth order, and the real and redshift space counterterms up to second order in the fluctuations and at subleading order in the derivatives (*i.e.* at order $k^2/{k_{\rm NL}}^2$ with k being the typical wavenumber of interest, and $k_{\rm NL}$ the wavenumber associated to the non-linear scale).

While naively it might appear that there is only a computational challenge facing us, *i.e.* the need to write all possible operators for biased tracers in redshift space up to fourth order, in reality there are also two conceptual subtleties we will need to face, and that we now explain. The first such subtlety stems from the non-local Green's function associated to the momentum operator, while the second is associated to the renormalization of composite operators involving the velocity.

The Local Counterterm that Contributes Non-Locally: Let us start from the first subtlety, focussing initially on the case of dark matter. So far, the counterterms in the EFTofLSS have been explored at high order only for dark matter in real space. This fact has prevented the emergence of a subtlety that, on hindsight,

is rather straightforward. The equations in the Newtonian limit contain the Poisson equation, whose solution is famously not local in space. This is mapped for example in the non-locality of the perturbative kernels. In fact, even though the absence of a tree-level speed of sounds makes the kernels just space dependent (rather than spacetime dependent), the dependence on the spatial wavenumber is not analytic, so that, once written in real space, they are non-local. For example, the solution of the locally-observable tidal tensor of the gravitational field, Φ, due to a density perturbation, δ, is, schematically,

$$\partial_i\partial_j\Phi(\vec{x},t) \sim H^2\frac{\partial_i\partial_j}{\partial^2}\delta(\vec{x},t) \sim H^2\int d^3x' \frac{1}{|\vec{x}-\vec{x}'|}\frac{\partial}{\partial x'^i}\frac{\partial}{\partial x'^j}\delta(\vec{x}',t)\ , \tag{6.1}$$

with H being the Hubble constant. This is non-local unless $i = j$ and we sum over i.

As we discuss in more detail later, counterterms are local, *i.e.* the response of the stress tensor to the long-wavelength fields is local. But the way the counterterms contribute to the fields is through a convolution with the Green's functions of the fields themselves, which, as we mentioned, are not local. This subtlety does not show up for linear counterterms, though. At that order, for the dark matter overdensity, only the divergence of the momentum matters, which in turn is affected, at linear level, by Φ only through $\partial^2\Phi \sim \delta$. So, the linear equation and the resulting Green's function are accidentally local. In this way, once one uses the counterterms at linear order (*i.e.* not multiplied by other fields), one obtains a local contribution.

But this local result is an artefact of the density field and of low order in the perturbative series, which limits the available tensorial structures. Already once one looks at the momentum, π^i, one finds that the traceless part of $\partial_i\pi^j$, which is observable, is affected at linear order by the traceless part of $\partial_i\partial_j\Phi$, which, as argued above, is non-local. So the associated Green's function will be non-local. Therefore, unless accidental cancellations happen, one should expect the local counterterms to contribute non locally. This is the situation we will encounter in this chapter, as the momentum is important for redshift space distortions where, additionally, the anisotropy induced by the line of sight provides a richer tensorial structure where accidental cancellations are more rare.

Explicitly, we find that for the momentum, π^i, we need a counterterm that

contributes in a way schematically given by

$$\pi^i \supset \frac{1}{H}\frac{\partial_i\partial_j\partial_k}{\partial^2}\tau^{jk}_{(2)} \ , \tag{6.2}$$

where τ^{jk} is the stress tensor, and the subscript $_{(n)}$ or superscript $^{(n)}$ indicates n-th order in perturbations. Now, among the second-order response terms for the stress tensor, we have terms such as

$$\tau^{ij}_{(2)} \supset \quad \frac{\bar{\rho}}{{k_{\rm NL}}^2 H^2}\partial_i\partial_k\Phi\partial_k\partial_j\Phi \ , \tag{6.3}$$

with $\bar{\rho}$ being the background density. This is indeed local. This term affects non-locally the gradient of the momentum as

$$\partial_j\pi^i \supset \frac{\bar{\rho}}{{k_{\rm NL}}^2 H^2}\frac{\partial_j\partial_i\partial_k\partial_m}{H\partial^2}\left(\partial_k\partial_l\Phi\partial_l\partial_m\Phi\right) \ . \tag{6.4}$$

In turn, in redshift space, the dark matter overdensity, δ_r, at second order is affected as

$$\delta_r(\vec{x}) \supset \frac{1}{H\bar{\rho}}\hat{z}^i\hat{z}^j\partial_i\pi^j(\vec{x}) \sim \hat{z}^i\hat{z}^j\frac{\partial_i\partial_j\partial_k\partial_m}{{k_{\rm NL}}^2\partial^2}\left(\frac{\partial_k\partial_l}{H^2}\Phi(\vec{x})\frac{\partial_l\partial_m}{H^2}\Phi(\vec{x})\right) \ . \tag{6.5}$$

The $1/\partial^2$ does not simplify in the final expression: this is a counterterm that contributes non-locally to the observable δ in redshift space. There are several such terms in the perturbative expansion, and similar terms appear also when considering the stochastic counterterms. As discussed in more detail later, these terms are linked to the generation of vorticity in the cosmological fluid. As a validation of the above, we explicitly find that these terms are needed to renormalize the redshift-space matter overdensity bispectrum at one-loop order. [1]

When passing to biased tracers, a further subtlety arises. In the EFTofLSS, the biased-tracer density in redshift space, which is constructed as combinations of the biased-tracer density and momentum, is written as a spatially *local* linear combination of composite operators of the matter field [129]. We do not have the equations of motion and the associated Green's function for them. This was the way that we identified the non-locally-contributing counterterm in dark matter: by simply solving the equations of motion in the presence of a local stress tensor. But because

[1] At this point, one might wonder why counterterms are local to start with. The terms that we have identified have the property that the region that can non-locally affect a mode is at most of order of the wavelength of the mode itself. For counterterms, for example in τ^{ij}, we are integrating out short modes, and so this can affect at most regions within $1/k_{\rm NL}$, which is equivalent to a normal local response.

of the local relation to dark matter, it is expected that the non-locally-contributing counterterms should be completely determined by the one of dark matter. This is so even for the momentum of biased tracers, which, for dark matter, was the operator being affected by the non-locally-contributing counterterm. Indeed, by the equivalence principle, biased tracers should have the same velocity as the underlying dark matter field at leading order in derivatives. In fact, there is a symmetry argument based on this idea connecting the two: the non-locally-contributing counterterm for biased tracers has the same functional form and coefficient as for dark matter. We confirm and discuss this argument in detail later, and we check again that this result is sufficient for renormalizing the one-loop bispectrum of tracers in redshift space.

Renormalization of Local Products of the Velocity Field: Let us now pass to the second main subtlety that we encounter in this chapter. In redshift space, there appear several contact operators involving the long-wavelength velocity. Contact operators are operators made of products of long-wavelength fields at the same location. Performing a product of long-wavelength fields at the same location is a process sensitive to arbitrary short-distance fluctuations, and so needs to be renormalized [137, 144]. For operators involving the velocity v^i, care must be taken in preserving the non-trivial transformations under the Galilean group (which is nothing but the non-relativistic limit of the group of diffeomorphisms), and this is complicated by the fact that the velocity is itself a contact operator and so needs to be renormalized [145, 146]. In order to have the correct transformation properties under the Galilean transformation $v^i \to v^i + \chi^i$, we wish to have, for example,

$$\begin{aligned} &[v^i]_R \to [v^i]_R + \chi^i \ , \\ &[v^i v^j]_R \to [v^i v^j]_R + [v^i]_R \chi^j + [v^j]_R \chi^i + \chi^i \chi^j \ , \end{aligned} \tag{6.6}$$

where $[v^i]_R$ and $[v^i v^j]_R$ are respectively the renormalized velocity and the renormalized velocity-squared. While satisfying this constraint is quite straightforward for the velocity, we see that the velocity-squared needs to have a transformation involving the renormalized velocity itself. One way to write renormalized quantities satisfying the above in terms of the non-renormalized fields is therefore to write the renormalized velocity-squared in terms of the renormalized velocity and additional

counterterms,

$$\begin{aligned}[v^i]_R &= v^i + \mathcal{O}_v^i \ , \\ [v^i v^j]_R &= [v^i]_R [v^j]_R + \mathcal{O}_{v^2}^{ij} \ ,\end{aligned} \tag{6.7}$$

where all of the $\mathcal{O}$ terms are Galilean scalars. In our calculation of the one-loop bispectrum, we will have to implement this procedure for products up to four powers of the velocity or four powers of the velocity and one power of the overdensity.

On top of addressing these two conceptual challenges, the rest of the chapter is devoted to developing the full calculation of the kernels of the one-loop bispectrum in redshift space both for dark matter and for tracers, including the relevant counterterms, and finally to checking that indeed all the ultraviolet (UV) dependence of the loop diagrams can be cancelled by a suitable choice of the resulting Effective Field Theory (EFT) parameters. Indeed, we find that both including the non-locally-contributing counterterms and implementing the correct redshift space renormalization procedure are crucial for matching the UV limits of the loops. We will perform first the study for dark matter, and then repeat it for biased tracers. As mentioned, the resulting kernels will be instrumental in performing the one-loop analyses of the bispectrum of galaxies in large-scale structure in Chs. 7 and 8.

One final observation that is worthwhile to make is the following. The generic expression of biased tracers is non-local in time [129]. If δ_h is the tracer overdensity, we have

$$\delta_h(\vec{x}, t) = \int^t dt' \sum_i \mathrm{Ker}_i(t, t') \ \mathcal{O}_i(\vec{x}_{\rm fl}(\vec{x}, t, t'), t') \tag{6.8}$$

where $\mathcal{O}_i(\vec{x}, t')$ are all the scalar operators that can be built from the long-wavelength fields, $\vec{x}_{\rm fl}(\vec{x}, t, t')$ represents the position at time t' of the fluid element that at time t is at location $\vec{x}$, and $\mathrm{Ker}_i(t, t')$ are generic kernels, assumed to have a time scale of order Hubble. Up to fourth order in the operators, we checked that this expression is accidentally degenerate with an analogous expression where one assumes that $\mathrm{Ker}_i(t, t') \propto \delta_D(t - t')$, *i.e.* as if the biases where local in time.

6.3 Dark-matter Equations and Notation

Here we collect the relevant background equations and notation for the cold dark-matter field. We assume a background ΛCDM expansion, with metric $ds^2 =$

$-dt^2 + a(t)^2 d\vec{x}^2$, where $a(t)$ is the scale factor, which will often be used as the time variable. The dark-matter field is described in terms of the mass density $\rho(\vec{x}, a)$ and the velocity field $v^i(\vec{x}, a)$. The background expansion is driven by a non-relativistic, time-dependent, background mass density $\bar{\rho}(a)$ [2] which is given by

$$\bar{\rho}(a) = \bar{\rho}_0 \left(\frac{a}{a_0}\right)^{-3} , \tag{6.9}$$

where subscripts $_0$ refer to current-day values, and the Hubble rate is $H = \dot{a}/a$ (we use the dot to denote time derivatives, *i.e.* $\dot{g} = \partial g/\partial t$ for generic functions g).

We describe scalar perturbations in the metric with the metric potentials Φ and Ψ, [3] by writing

$$ds^2 = -(1 + 2\Psi)dt^2 + a(t)^2(1 - 2\Phi)d\vec{x}^2 . \tag{6.10}$$

In terms of the momentum density π^i, defined by

$$\pi^i(\vec{x}, a) \equiv \rho(\vec{x}, a) v^i(\vec{x}, a) , \tag{6.11}$$

the equations of motion for dark matter are (see e.g. [30, 28, 147])

$$\begin{aligned} &\dot{\rho} + 3H\rho + a^{-1}\partial_i \pi^i = 0 , \\ &\dot{\pi}^i + 4H\pi^i + a^{-1}\partial_j \left(\frac{\pi^i \pi^j}{\rho}\right) + a^{-1}\rho\, \partial_i \Phi = -a^{-1}\partial_j \tau^{ij} , \end{aligned} \tag{6.12}$$

along with the Poisson equation

$$a^{-2}\partial^2 \Phi = \frac{3}{2}\Omega_{\rm m} H^2 \delta , \tag{6.13}$$

which is in terms of the overdensity δ, given by

$$\delta(\vec{x}, a) \equiv (\rho(\vec{x}, a) - \bar{\rho}(a))/\bar{\rho}(a) , \tag{6.14}$$

and the time-dependent matter fraction $\Omega_{\rm m}(a)$. [4] The quantity τ^{ij} appearing in Eq. (6.12) is the EFTofLSS stress tensor [28], which we will describe in much more

[2] For clarity we will call the matter overdensity ρ_m in Ch. 10. Here however we always mean the matter density and overdensity hence we drop it.

[3] Anisotropic stress is small and can be neglected for our purposes, in which case the Einstein equations imply $\Phi = \Psi$, which we assume throughout this work.

[4] This is defined by $\Omega_{\rm m}(a) \equiv \bar{\rho}(a)/(3M_{\rm Pl}^2 H(a)^2)$, where $M_{\rm Pl}$ is the Planck mass, related to Newton's constant G_N by $M_{\rm Pl}^2 = 1/(8\pi G_N)$. In ΛCDM, the Hubble rate can be parameterized by $H(a)^2/H_0^2 = \Omega_{\rm m,0}(a/a_0)^{-3} + (1 - \Omega_{\rm m,0})$.

detail later. Using the Poisson equation Eq. (6.13), we can write

$$\bar{\rho}\,\delta\,\partial_i\Phi = 2M_{\rm Pl}^2 a^{-2}\partial_j\left(\partial_i\Phi\partial_j\Phi - \frac{1}{2}\delta_{ij}(\partial\Phi)^2\right)\,, \tag{6.15}$$

and consequently the equations of motion Eq. (6.12) become

$$\begin{aligned}
&\bar{\rho}\,\dot{\delta} + a^{-1}\partial_i\pi^i = 0\,, \\
&\dot{\pi}^i + 4H\pi^i + a^{-1}\bar{\rho}\,\partial_i\Phi = -a^{-1}\partial_j\left(2M_{\rm Pl}^2 a^{-2}\left(\partial_i\Phi\partial_j\Phi - \frac{1}{2}\delta_{ij}(\partial\Phi)^2\right) + \frac{\pi^i\pi^j}{\rho} + \tau^{ij}\right).
\end{aligned} \tag{6.16}$$

Next, we can decompose the momentum density into a scalar and a vector part

$$\pi_S \equiv \partial_i\pi^i\,, \quad \text{and} \quad \pi_V^i \equiv \epsilon^{ijk}\partial_j\pi^k\,, \tag{6.17}$$

which gives

$$\pi^i = \frac{\partial_i}{\partial^2}\pi_S - \epsilon^{ijk}\frac{\partial_j}{\partial^2}\pi_V^k\,, \tag{6.18}$$

where ϵ^{ijk} is the three-dimensional totally antisymmetric Levi-Civita symbol (with $\epsilon^{123} = 1$). With this decomposition, we can write the equations of motion in terms of the scalar and vector parts

$$\begin{aligned}
&\bar{\rho}\,\dot{\delta} + a^{-1}\pi_S = 0\,, \\
&\dot{\pi}_S + 4H\pi_S + \frac{3}{2}a\bar{\rho}\,\Omega_{\rm m}H^2\delta = \\
&\qquad\qquad = -a^{-1}\partial_i\partial_j\left(2M_{\rm Pl}^2 a^{-2}\left(\partial_i\Phi\partial_j\Phi - \frac{1}{2}\delta_{ij}(\partial\Phi)^2\right) + \frac{\pi^i\pi^j}{\rho} + \tau^{ij}\right)\,, \\
&\dot{\pi}_V^i + 4H\pi_V^i = -a^{-1}\epsilon^{ijk}\partial_j\partial_l\left(2M_{\rm Pl}^2 a^{-2}\partial_k\Phi\partial_l\Phi + \frac{\pi^k\pi^l}{\rho} + \tau^{kl}\right)\,.
\end{aligned} \tag{6.19}$$

We see that the scalar part π_S is determined entirely by δ, and the vector part π_V^i is only sourced non-linearly. For reference, the full differential equation for δ is

$$\begin{aligned}
a^2\delta'' + \left(2 + \frac{a\mathcal{H}'}{\mathcal{H}}\right)a\delta' - \frac{3}{2}\Omega_{\rm m}\delta = \\
= \frac{\partial_i\partial_j}{\mathcal{H}^2\bar{\rho}}\left(2M_{\rm Pl}^2 a^{-2}\left(\partial_i\Phi\partial_j\Phi - \frac{1}{2}\delta_{ij}(\partial\Phi)^2\right) + \frac{\pi^i\pi^j}{\rho} + \tau^{ij}\right)\,,
\end{aligned} \tag{6.20}$$

where $\mathcal{H} = aH$, and the prime denotes a derivative with respect to the scale factor, *i.e.* $g' = \partial g/\partial a$ for generic functions g. For dark matter in real space, all renormalization and counterterms enter through the stress tensor τ^{ij}, which is a Galilean

scalar, a tensor under spatial rotations, and a local-in-space and non-local-in-time function of second derivatives of the metric and gradients of the velocity (because of the equivalence principle), in the equations of motion above. We will return to the stress tensor in much more detail below. We also note that while the equation of motion for π^i is non-local (because of the appearance of $\partial_i\Phi$ on the left-hand side of Eq. (6.16)), the equations of motion for π_S and π_V^i Eq. (6.19) are local.

In this work, we use the following notation

$$\int_{\vec{k}_1,\ldots,\vec{k}_n} \equiv \int \frac{d^3k_1}{(2\pi)^3}\cdots\frac{d^3k_n}{(2\pi)^3} \ , \quad \int^{\vec{k}}_{\vec{k}_1,\ldots,\vec{k}_n} \equiv \int_{\vec{k}_1,\ldots,\vec{k}_n} (2\pi)^3\delta_D(\vec{k}-\sum_{i=1}^{n}\vec{k}_i) \ , \tag{6.21}$$

where δ_D is the Dirac delta function, and our Fourier conventions are

$$f(\vec{x},t) = \int_{\vec{k}} f(\vec{k},t)\, e^{i\vec{k}\cdot\vec{x}} \ . \tag{6.22}$$

For a three-dimensional vector $\vec{k}$, we write $k \equiv |\vec{k}|$ for the magnitude, and $\hat{k} \equiv \vec{k}/k$ for the unit vector parallel to $\vec{k}$. We use Latin letters like i, j, k, l to denote spatial indices, in general we do not distinguish between upper and lower spatial indices, and repeated indices imply summation. We also use the prime on correlation functions, $\langle\cdot\rangle'$ to denote the correlation function with the factor of $(2\pi)^3$ and Dirac delta function of translation invariance stripped off.

6.3.1 Perturbative Solutions and Observables in SPT

In this work, we use the so-called Einstein-de Sitter (EdS) approximation to solve the above equations which allows us to separate the time dependence from the spatial (momentum) dependence and is known to be accurate to percent level [148, 135, 149] (we give details about the EdS Green's function in App. B.1.1). Let us start with the standard perturbation theory (SPT) contribution, which is the solution ignoring EFTofLSS counterterms, *i.e.* with $\tau^{ij} = 0$. First, the solution to the linear equation for δ is called the growth factor $D(a)$, which solves

$$a^2D'' + \left(2 + \frac{a\mathcal{H}'}{\mathcal{H}}\right) aD' - \frac{3}{2}\Omega_{\rm m}D = 0 \ . \tag{6.23}$$

For the perturbations, we write

$$\delta(\vec{k},a) = \sum_n \delta^{(n)}(\vec{k},a) \ , \quad \text{and} \quad v^i(\vec{k},a) = \sum_n v^i_{(n)}(\vec{k},a) \tag{6.24}$$

where, assuming that the velocity field is irrotational, [5]

$$\begin{aligned} \delta^{(n)}(\vec{k},a) &= D(a)^n \int^{\vec{k}}_{\vec{k}_1,\ldots,\vec{k}_n} F_n(\vec{k}_1,\ldots,\vec{k}_n)\tilde{\delta}^{(1)}_{\vec{k}_1}\cdots\tilde{\delta}^{(1)}_{\vec{k}_n} \ , \\ v^i_{(n)}(\vec{k},a) &= i\frac{k^i}{k^2}\mathcal{H}(a)f(a)D(a)^n \int^{\vec{k}}_{\vec{k}_1,\ldots,\vec{k}_2} G_n(\vec{k}_1,\ldots,\vec{k}_n)\tilde{\delta}^{(1)}_{\vec{k}_1}\cdots\tilde{\delta}^{(1)}_{\vec{k}_n} \ , \end{aligned} \tag{6.25}$$

$\tilde{\delta}^{(1)}_{\vec{k}}$ is the time-independent initial field, [6] F_n and G_n are the standard symmetric kernels for dark matter (see [150, 151], for example), and the growth rate f is defined by

$$f(a) \equiv \frac{aD'(a)}{D(a)} \ . \tag{6.26}$$

In general, we use the tilde to denote time-independent fields, in particular

$$\tilde{\delta}^{(n)} \equiv \frac{\delta^{(n)}(a)}{D(a)^n} \ , \tag{6.27}$$

and we will often drop spatial or momentum arguments when the understanding is clear. The above expressions for δ and v^i solve the equations of motion under the approximation

$$\Omega_{\rm m}(a) \approx \left(\frac{aD'(a)}{D(a)}\right)^2 \ , \tag{6.28}$$

which is approximately true in our universe [148, 135, 149]. For the one-loop bispectrum, we need to consider up to $n = 4$. The SPT expression for π^i can be derived from δ and v^i using Eq. (6.11).

In this work, we are eventually interested in computing the one-loop power spectrum and the one-loop bispectrum of galaxies in redshift space, but we start in this section with dark matter in real space. In Fourier space, the power spectrum P and

[5] In the absence of counterterms, it can be shown that an initially irrotational velocity remains so. In our universe, the initial vorticity is negligible. EFT counterterms induce a vorticity, though, matching what is observed in simulations [147], and we discuss this in more detail in Sec. 6.4.3.

[6] We normalize $D(a_{\rm in}) = 1$ for some initial time $a_{\rm in}$ in matter domination where initial conditions are given, so that P_{11} is the linear power spectrum at $a_{\rm in}$.

bispectrum B are defined by

$$\begin{aligned}\langle\delta(\vec{k},a)\delta(\vec{k}',a)\rangle &= (2\pi)^3\delta_D(\vec{k}+\vec{k}')P(k,a)\ ,\\ \langle\delta(\vec{k}_1,a)\delta(\vec{k}_2,a)\delta(\vec{k}_3,a)\rangle &= (2\pi)^3\delta_D(\vec{k}_1+\vec{k}_2+\vec{k}_3)B(k_1,k_2,k_3,a)\ .\end{aligned} \tag{6.29}$$

The total one-loop power spectrum is

$$P_{\text{1-loop tot.}}(k,a) = D(a)^2P_{11}(k) + D(a)^4(P_{22}(k)+P_{13}(k))\ , \tag{6.30}$$

where $\langle\tilde{\delta}^{(1)}_{\vec{k}}\tilde{\delta}^{(1)}_{\vec{k}'}\rangle = (2\pi)^3\delta_D(\vec{k}+\vec{k}')P_{11}(k)$ defines the linear power spectrum P_{11} at the initial time a_{in}, and the one-loop terms are

$$\begin{aligned}P_{22}(k) &= 2\int_{\vec{q}} F_2(\vec{q},\vec{k}-\vec{q})^2P_{11}(q)P_{11}(|\vec{k}-\vec{q}|)\ ,\\ P_{13}(k) &= 6P_{11}(k)\int_{\vec{q}} F_3(\vec{q},-\vec{q},\vec{k})P_{11}(q)\ .\end{aligned} \tag{6.31}$$

The total one-loop bispectrum is

$$B_{\text{1-loop tot.}} = D(a)^4B_{211} + D(a)^6\left(B_{222}+B^{(I)}_{321}+B^{(II)}_{321}+B_{411}\right)\ , \tag{6.32}$$

where the tree-level bispectrum is

$$B_{211}(k_1,k_2,k_3) = 2F_2(\vec{k}_1,\vec{k}_2)P_{11}(k_1)P_{11}(k_2) + \text{ 2 perms.}\ , \tag{6.33}$$

and the one-loop contributions are

$$\begin{aligned}B_{222}(k_1,k_2,k_3) &= 8\int_{\vec{q}} P_{11}(q)P_{11}(|\vec{k}_2-\vec{q}|)P_{11}(|\vec{k}_1+\vec{q}|)\\ &\qquad\times F_2(-\vec{q},\vec{k}_1+\vec{q})F_2(\vec{k}_1+\vec{q},\vec{k}_2-\vec{q})F_2(\vec{k}_2-\vec{q},\vec{q})\ ,\\ B^{(I)}_{321}(k_1,k_2,k_3) &= 6P_{11}(k_1)\int_{\vec{q}} P_{11}(q)P_{11}(|\vec{k}_2-\vec{q}|)\\ &\qquad\times F_3(-\vec{q},-\vec{k}_2+\vec{q},-\vec{k}_1)F_2(\vec{q},\vec{k}_2-\vec{q}) + \text{ 5 perms.}\ ,\\ B^{(II)}_{321}(k_1,k_2,k_3) &= 6P_{11}(k_1)P_{11}(k_2)F_2(\vec{k}_1,\vec{k}_2)\int_{\vec{q}} P_{11}(q)F_3(\vec{k}_1,\vec{q},-\vec{q}) + \text{ 5 perms.}\ ,\\ B_{411}(k_1,k_2,k_3) &= 12P_{11}(k_1)P_{11}(k_2)\int_{\vec{q}} P_{11}(q)F_4(\vec{q},-\vec{q},-\vec{k}_1,-\vec{k}_2) + \text{ 2 perms.}\ .\end{aligned} \tag{6.34}$$

6.3.2 Dark-matter Counterterm Contributions

As is well known [28], the loop contributions Eqs. (6.31) and (6.34) are UV sensitive because they depend on momenta q much larger than the non-linear scale of structure formation where the theory is out of perturbative control. The role of the EFT counterterms in τ^{ij} is to cure this UV sensitivity and allow the theory to match reality. Concretely, we write (suppressing spatial dependence for convenience)

$$\tau^{ij}(a) = \tau^{ij}_{\Lambda_{\rm UV}}(a) + \tau^{ij}_{\rm finite}(a) \ . \tag{6.35}$$

Here, the piece $\tau^{ij}_{\Lambda_{\rm UV}}(a)$ must give the same time dependence as in Eqs. (6.31) and (6.34) in order to cancel the dependence of the loop integrals on the UV cutoff $\Lambda_{\rm UV}$. The other piece, $\tau^{ij}_{\rm finite}(a)$, does not have a fixed time dependence in general, and its role is to give the correct amount of $\Lambda_{\rm UV}$-independent contribution that matches observations.

For simplicity in this chapter, we focus on the contribution $\tau^{ij}_{\Lambda_{\rm UV}}(a)$ which has a fixed time dependence. All of our main points will be evident in this case, and we will be able to do explicit calculations with explicit numerical factors. Additionally, we want to check that the general form of τ^{ij} that we write is able to capture all of the UV behavior present in the loops Eqs. (6.31) and (6.34), and this requires assuming the same time dependence as the loops. Inclusion of a general $\tau^{ij}_{\rm finite}(a)$ is straightforward, as it is based on the same k-dependent kernels.

In general, the EFTofLSS is local in space, but non-local in time [147]. To obtain the EFT expansion one expands the stress tensor as a local function of second spatial derivatives of the gravitational potential Φ and gradients of the velocity (because of the equivalence principle), along with stochastic fields, organized, as in any EFT, in an expansion in powers of the fields and spatial derivatives, integrated along the past trajectory of the fluid element [147, 129]. More specifically, we have

$$\tau^{ij}(\vec{x}, a) = \int^a \frac{da'}{a'} \sum_\alpha \kappa_\alpha(a, a') T^{ij}_\alpha(\vec{x}_{\rm fl}(\vec{x}, a, a'), a') \ , \tag{6.36}$$

where the fluid element is defined by

$$\vec{x}_{\rm fl}(\vec{x}, a, a') = \vec{x} + \int_a^{a'} \frac{da''}{(a'')^2 H(a'')} \vec{v}(\vec{x}_{\rm fl}(\vec{x}, a, a''), a'') \ , \tag{6.37}$$

the $T^{ij}_\alpha(\vec{x}, a)$ are all local-in-time Galilean scalars (and tensors under rotations on

the i and j indices), and the $\kappa_\alpha(a, a')$ are unknown EFT kernels describing the non-locality in time. The $T^{ij}_\alpha(\vec{x}, a)$ are then organized in a local spatial-derivative expansion of the long-wavelength fields ($\partial_i\partial_j\Phi(\vec{x}, a)$, $\partial_i v^j(\vec{x}, a)$, etc.) and of stochastic fields $\epsilon^{ij}(\vec{x}, a)$. Since we do perturbation theory in this work, we can write each scalar as a sum over perturbative orders

$$T^{ij}_\alpha(\vec{x}, a) = \sum_n T^{ij}_{\alpha,(n)}(\vec{x}, a) \ , \tag{6.38}$$

and because the linear solutions are scale independent, we have a simple scaling time dependence for the n-th order perturbative pieces

$$T^{ij}_{\alpha,(n)}(\vec{x}, a') = \left(\frac{D(a')}{D(a)}\right)^{p_{\alpha,n}} T^{ij}_{\alpha,(n)}(\vec{x}, a) \ , \tag{6.39}$$

for some power $p_{\alpha,n}$. This means that Eq. (6.36) becomes

$$\begin{aligned}\tau^{ij}(\vec{x}, a) = &\sum_\alpha \sum_n K^{p_{\alpha,n}}_\alpha(a) T^{ij}_{\alpha,(n)}(\vec{x}, a) \\ &+ \sum_\alpha \sum_{n,m} \frac{1}{m} \left(K^{p_{\alpha,n-m}}_\alpha(a) - K^{m+p_{\alpha,n-m}}_\alpha(a)\right) \frac{\partial_k\theta_{(m)}(\vec{x}, a)}{\partial^2} \partial_k T^{ij}_{\alpha,(n-m)}(\vec{x}, a) + \dots \ ,\end{aligned} \tag{6.40}$$

where we have defined

$$K^p_\alpha(a) \equiv \int^a \frac{da'}{a'}\, \kappa_\alpha(a, a') \left(\frac{D(a')}{D(a)}\right)^p \ , \tag{6.41}$$

used the definition of the velocity field in Eq. (6.25) along with $\theta = -\partial_i v^i/(faH)$, and the $\dots$ in Eq. (6.40) are terms coming from Taylor expanding $T^{ij}_\alpha(\vec{x}_{\rm fl}(\vec{x}, a, a'), a')$ around $\vec{x}$ in Eq. (6.36), *i.e.* higher powers of $\vec{v}$, all of which should be included up to the desired order. The point is that the integral over da' coming from expanding $\vec{x}_{\rm fl}$ can be formally done as in Eq. (6.41) and leaves distinct functions of a, $K^p_\alpha(a)$. The same happens with the higher order terms in the Taylor expansion of $\vec{x}_{\rm fl}(\vec{x}, a, a')$, since $\vec{v}_{(n)}$ also has a simple scaling time dependence, see Eq. (6.25). This means that, in perturbation theory, the expansion of the stress tensor can be manipulated so that the time integrals disappear, in the way indicated by Eq. (6.40). In this chapter, we only need counterterms from the stress tensor up to second order, so Eq. (6.40) is sufficient for our purposes. This is the same approach taken for the

bias expansion in Sec. 6.6.2. [7]

Given this, we write the contribution to δ from τ^{ij} relevant to the one-loop bispectrum, which we call δ_τ, generally as

$$\delta_\tau(\vec{k},a) = \delta^{(1)}_{ct}(\vec{k},a) + \delta^{(2)}_{ct}(\vec{k},a) + \delta^{(1)}_{\epsilon}(\vec{k},a) + \delta^{(2)}_{\epsilon}(\vec{k},a) \ , \tag{6.42}$$

where the subscript ct denotes the response counterterms, and ϵ denotes the stochastic (and semi-stochastic) counterterms. Assuming the time dependence needed to cancel UV loop contributions, we have

$$\begin{aligned} &\delta^{(1)}_{ct}(\vec{k},a) = D(a)^3\tilde{\delta}^{(1)}_{ct}(\vec{k}) \ , \quad \delta^{(2)}_{ct}(\vec{k},a) = D(a)^4\tilde{\delta}^{(2)}_{ct}(\vec{k}) \ , \\ &\delta^{(1)}_{\epsilon}(\vec{k},a) = D(a)^2\tilde{\delta}^{(1)}_{\epsilon}(\vec{k}) \ , \quad \text{and} \quad \delta^{(2)}_{\epsilon}(\vec{k},a) = D(a)^3\tilde{\delta}^{(2)}_{\epsilon}(\vec{k}) \ , \end{aligned} \tag{6.43}$$

where we use the tilde to denote the appropriate time-independent factor. Similarly, we have the solution for π^i which we write as

$$\pi^i_\tau(\vec{k},a) = \pi^i_{ct,(1)}(\vec{k},a) + \pi^i_{ct,(2)}(\vec{k},a) + \pi^i_{\epsilon,(1)}(\vec{k},a) + \pi^i_{\epsilon,(2)}(\vec{k},a) \ , \tag{6.44}$$

with

$$\begin{aligned} &\pi^i_{ct,(1)}(\vec{k},a) = -aH\bar{\rho}fD(a)^3\tilde{\pi}^i_{ct,(1)}(\vec{k}) \ , \quad \pi^i_{ct,(2)}(\vec{k},a) = -aH\bar{\rho}fD(a)^4\tilde{\pi}^i_{ct,(2)}(\vec{k}) \ , \\ &\pi^i_{\epsilon,(1)}(\vec{k},a) = -aH\bar{\rho}fD(a)^2\tilde{\pi}^i_{\epsilon,(1)}(\vec{k}) \ , \quad \text{and} \quad \pi^i_{\epsilon,(2)}(\vec{k},a) = -aH\bar{\rho}fD(a)^3\tilde{\pi}^i_{\epsilon,(2)}(\vec{k}) \ . \end{aligned} \tag{6.45}$$

To remove clutter, we will sometimes use the notation A_* to mean both A_{ct} and A_ϵ. We note that in SPT, the time dependence of π^i, π_S, and π^i_V are all the same for each field above linear perturbations. [8] However, as can be seen in Eq. (6.19), if $\partial^i\partial^j\tau^{ij}$ and $\epsilon^{ijk}\partial_j\partial_l\tau^{kl}$ have different time dependence, then π_S and π^i_V will as well. For simplicity, in this work, we assume that the counterterms have the same time dependence as needed to cancel UV divergences in the SPT loops, in which case π_S and π^i_V have the same time dependence as in Eq. (6.45) for π^i.

[7] Note that for the growing mode solutions that we consider in this work, we have $K_\alpha^{p_{\alpha,2}}(a) = K_\alpha^{1+p_{\alpha,1}}(a)$, which shows that Eq. (6.40) is of the correct form for Galilean scalars discussed in Sec. 6.5.3.

[8] At linear level, we have $\pi^i_{V,(1)} = \bar{\rho}\epsilon^{ijk}\partial_j v^k_{(1)} = 0$ because velocity vorticity is zero. Then, at higher orders, π^i_V becomes non-zero because of the growing mode in δ in the definition of π^i. So, above linear perturbations, π_S, π^i_V, and π^i all have the same time dependence, which one can deduce from the definition of π^i in terms of δ and v^i.

6.4 Dark-Matter Renormalization in Real Space

6.4.1 Counterterm Solutions up to Second Order

We now present the solutions for δ and π^i that are sourced by the stress tensor τ^{ij} in Eq. (6.19) up to second order, leaving the derivation to App. B.1. We start by writing

$$\tau^{ij} = \frac{\Omega_{\rm m}\mathcal{H}^2\bar{\rho}}{{k_{\rm NL}}^2}\left(D^3\tilde{\tau}^{ij}_{ct,(1)} + D^4\tilde{\tau}^{ij}_{ct,(2)} + D^2\tilde{\tau}^{ij}_{\epsilon,(1)} + D^3\tilde{\tau}^{ij}_{\epsilon,(2)}\right) \ , \tag{6.46}$$

where the quantities with subscript ct source the pure response solutions of δ and π^i, the quantities with subscript ϵ source the stochastic and semi-stochastic solutions of δ and π^i, and the number in parentheses indicates the order in fields. Again, quantities with tildes are time independent, and the time dependence given above is chosen to lead to Eq. (6.43) (the factor of $\Omega_{\rm m}(a)$ can be seen from App. B.1.1). As described in more detail in App. B.1, the second-order solutions here come from two sources. The first is directly from the second-order stress tensors in Eq. (6.46), and the second is from plugging the first-order counterterm solutions back into the equations of motion Eq. (6.19).

Then, the first-order response solutions are

$$\tilde{\delta}^{(1)}_{ct} = \frac{1}{9{k_{\rm NL}}^2}\partial_i\partial_j\tilde{\tau}^{ij}_{ct,(1)} \ , \quad \text{and} \quad \tilde{\pi}^i_{ct,(1)} = \frac{1}{3{k_{\rm NL}}^2}\frac{\partial_i\partial_j\partial_k}{\partial^2}\tilde{\tau}^{jk}_{ct,(1)} \ , \tag{6.47}$$

and the second-order response solutions are

$$\tilde{\delta}^{(2)}_{ct} = \frac{2\,\partial_i\partial_j}{33{k_{\rm NL}}^2}\left[\tilde{\tau}^{ij}_{ct,(2)} + \frac{\partial_i\tilde{\delta}^{(1)}}{\partial^2}\partial_k\tilde{\tau}^{jk}_{ct,(1)} - \frac{1}{6}\delta_{ij}\frac{\partial_k\tilde{\delta}^{(1)}}{\partial^2}\partial_l\tilde{\tau}^{kl}_{ct,(1)}\right] \ , \tag{6.48}$$

and

$$\begin{aligned}\tilde{\pi}^i_{ct,(2)} = \frac{2}{9{k_{\rm NL}}^2}\Bigg[&\partial_j\tilde{\tau}^{ij}_{ct,(2)} + \frac{1}{11}\frac{\partial_i\partial_j\partial_k}{\partial^2}\left(\tilde{\tau}^{jk}_{ct,(2)} + \frac{\partial_j\tilde{\delta}^{(1)}}{\partial^2}\partial_l\tilde{\tau}^{kl}_{ct,(1)}\right) \\ &- \frac{2}{11}\partial_i\left(\frac{\partial_j\tilde{\delta}^{(1)}}{\partial^2}\partial_k\tilde{\tau}^{jk}_{ct,(1)}\right) + \frac{1}{2}\partial_l\left(\frac{\partial_i\tilde{\delta}^{(1)}}{\partial^2}\partial_m\tilde{\tau}^{lm}_{ct,(1)} + \frac{\partial_l\tilde{\delta}^{(1)}}{\partial^2}\partial_j\tilde{\tau}^{ij}_{ct,(1)}\right)\Bigg] \ .\end{aligned} \tag{6.49}$$

To find the above, we used Eq. (6.19), solved for π_S and π^i_V separately (which are given in App. B.1), and then combined them to form π^i using Eq. (6.18). Above, as we will justify in the next section, we have assumed that $\partial_i\partial_j\partial_k\tilde{\tau}^{jk}_{ct,(1)} = \partial^2\partial_j\tilde{\tau}^{ij}_{ct,(1)}$.

Similarly, for the first-order stochastic solutions, we have

$$\begin{aligned}\tilde{\delta}^{(1)}_{\epsilon} &= \frac{2}{7{k_{\rm NL}}^2}\partial_i\partial_j\tilde{\tau}^{ij}_{\epsilon,(1)}\ , \quad \text{and} \\ \tilde{\pi}^{i}_{\epsilon,(1)} &= \frac{1}{{k_{\rm NL}}^2}\left[\frac{4}{7}\frac{\partial_i\partial_j\partial_k}{\partial^2}\tilde{\tau}^{jk}_{\epsilon,(1)} - \frac{2}{5}\left(\frac{\partial_i\partial_j\partial_k}{\partial^2}\tilde{\tau}^{jk}_{\epsilon,(1)} - \partial_j\tilde{\tau}^{ij}_{\epsilon,(1)}\right)\right]\ ,\end{aligned} \tag{6.50}$$

and for the second-order stochastic solutions, we have

$$\begin{aligned}\tilde{\delta}^{(2)}_{\epsilon} = \frac{\partial_i\partial_j}{9{k_{\rm NL}}^2}\Bigg[&\tilde{\tau}^{ij}_{\epsilon,(2)} + 2\frac{\partial_i\tilde{\delta}^{(1)}}{\partial^2}\frac{\partial_j\partial_k\partial_l}{\partial^2}\tilde{\tau}^{kl}_{\epsilon,(1)} - \frac{3}{7}\delta_{ij}\left(\frac{\partial_k\tilde{\delta}^{(1)}}{\partial^2}\frac{\partial_k\partial_l\partial_m}{\partial^2}\tilde{\tau}^{lm}_{\epsilon,(1)}\right) \\ &- \frac{4}{5}\frac{\partial_i\tilde{\delta}^{(1)}}{\partial^2}\left(\frac{\partial_j\partial_k\partial_l}{\partial^2}\tilde{\tau}^{kl}_{\epsilon,(1)} - \partial_l\tilde{\tau}^{jl}_{\epsilon,(1)}\right)\Bigg]\ ,\end{aligned} \tag{6.51}$$

and

$$\begin{aligned}{k_{\rm NL}}^2\tilde{\pi}^{i}_{\epsilon,(2)} = &\frac{2}{7}\partial_j\tilde{\tau}^{ij}_{\epsilon,(2)} + \frac{1}{21}\frac{\partial_i\partial_j\partial_k}{\partial^2}\left(\tilde{\tau}^{jk}_{\epsilon,(2)} + 2\frac{\partial_j\tilde{\delta}^{(1)}}{\partial^2}\frac{\partial_k\partial_l\partial_m}{\partial^2}\tilde{\tau}^{lm}_{\epsilon,(1)}\right) \\ &- \frac{1}{7}\partial_i\left(\frac{\partial_j\tilde{\delta}^{(1)}}{\partial^2}\frac{\partial_j\partial_k\partial_l}{\partial^2}\tilde{\tau}^{kl}_{\epsilon,(1)}\right) \\ &+ \frac{2}{7}\partial_l\left(\frac{\partial_i\tilde{\delta}^{(1)}}{\partial^2}\frac{\partial_l\partial_m\partial_n}{\partial^2}\tilde{\tau}^{mn}_{\epsilon,(1)} + \frac{\partial_l\tilde{\delta}^{(1)}}{\partial^2}\frac{\partial_i\partial_m\partial_n}{\partial^2}\tilde{\tau}^{mn}_{\epsilon,(1)}\right) \\ &- \frac{4}{105}\frac{\partial_i\partial_j\partial_k}{\partial^2}\left(\frac{\partial_j\tilde{\delta}^{(1)}}{\partial^2}\left(\frac{\partial_k\partial_l\partial_m}{\partial^2}\tilde{\tau}^{lm}_{\epsilon,(1)} - \partial_l\tilde{\tau}^{kl}_{\epsilon,(1)}\right)\right) \\ &- \frac{4}{35}\partial_l\left(\frac{\partial_i\tilde{\delta}^{(1)}}{\partial^2}\left(\frac{\partial_l\partial_m\partial_n}{\partial^2}\tilde{\tau}^{mn}_{\epsilon,(1)} - \partial_m\tilde{\tau}^{lm}_{\epsilon,(1)}\right) + \frac{\partial_l\tilde{\delta}^{(1)}}{\partial^2}\left(\frac{\partial_i\partial_m\partial_n}{\partial^2}\tilde{\tau}^{mn}_{\epsilon,(1)} - \partial_m\tilde{\tau}^{im}_{\epsilon,(1)}\right)\right).\end{aligned} \tag{6.52}$$

In the above stochastic expressions, as we will discuss further in the next section, we have *not* assumed that $\partial_i\partial_j\partial_k\tilde{\tau}^{jk}_{\epsilon,(1)} = \partial^2\partial_j\tilde{\tau}^{ij}_{\epsilon,(1)}$.

As a final note, we point out that all of the various numerical coefficients above come from the linear equations of motion and the assumed time dependence $D(a)^n$ for the various contributions; they represent different combinations of Green's functions integrated over different kernels in the EdS approximation. We give the EdS Green's function in App. B.1.1.

6.4.2 Explicit Expression for the Stress Tensor

We can now write down the most general stress tensor local in second spatial derivatives of Φ and gradients of the velocity, following the discussion in Sec. 6.3.2, up to second order, that obeys the symmetries of the problem, which are rotation and Galilean invariance. We focus on the leading order in derivatives, which, because of mass and momentum conservation, is $\mathcal{O}(k^2 P_{11})$ for P_{13}, $\mathcal{O}(k^2 P_{11}^2)$ for B_{411} and $B_{321}^{(II)}$, $\mathcal{O}(k^4)$ for P_{22}, $\mathcal{O}(k^6)$ for B_{222}, and $\mathcal{O}(k^4 P_{11})$ for $B_{321}^{(I)}$. For the response terms, we have

$$\tilde{\tau}^{ij}_{ct,(1)} = c_1 \frac{\partial_i \partial_j \tilde{\delta}^{(1)}}{\partial^2} + c_3 \delta_{ij} \tilde{\delta}^{(1)} \ , \tag{6.53}$$

and

$$\begin{aligned} \tilde{\tau}^{ij}_{ct,(2)} =& c_1 \frac{\partial_k \partial_i \partial_j \tilde{\delta}^{(1)}}{\partial^2} \frac{\partial_k \tilde{\delta}^{(1)}}{\partial^2} + c_3 \delta_{ij} \partial_k \tilde{\delta}^{(1)} \frac{\partial_k \tilde{\delta}^{(1)}}{\partial^2} \\ &+ c_2 \frac{\partial_i \partial_j \tilde{\delta}^{(2)}}{\partial^2} - c_2 \frac{\partial_k \partial_i \partial_j \tilde{\delta}^{(1)}}{\partial^2} \frac{\partial_k \tilde{\delta}^{(1)}}{\partial^2} + c_4 \delta_{ij} \tilde{\delta}^{(2)} - c_4 \delta_{ij} \partial_k \tilde{\delta}^{(1)} \frac{\partial_k \tilde{\delta}^{(1)}}{\partial^2} \\ &+ c_5 \frac{\partial_i \partial_j \tilde{\delta}^{(1)}}{\partial^2} \tilde{\delta}^{(1)} + c_6 \frac{\partial_i \partial_k \tilde{\delta}^{(1)}}{\partial^2} \frac{\partial_k \partial_j \tilde{\delta}^{(1)}}{\partial^2} + c_7 \delta_{ij} \tilde{\delta}^{(1)} \tilde{\delta}^{(1)} \ , \end{aligned} \tag{6.54}$$

where all of the c_i are time independent. To determine the above list of operators, we follow the procedure laid out in Sec. 6.3.2 (which is the same approach as [129] for biased tracers, which we detail in Sec. 6.6.2 and App. B.3); we first write all contractions of $\partial_i \partial_j \Phi$ and $\partial_i v^j$ with the same tensor structure as τ^{ij} up to second order in fields and zeroth order in derivatives, and then we expand the fluid element and do the remaining time integrals which define the c_i. We then check for degeneracies in the resulting operators, and only use the minimal basis, which is given above.

For the stochastic terms, we have

$$\tilde{\tau}^{ij}_{\epsilon,(1)} = \epsilon_1^{ij} \ , \quad \text{and} \quad \tilde{\tau}^{ij}_{\epsilon,(2)} = \partial_k \epsilon_1^{ij} \frac{\partial_k \tilde{\delta}^{(1)}}{\partial^2} + \epsilon_3^{ijkl} \frac{\partial_k \partial_l \tilde{\delta}^{(1)}}{\partial^2} \ , \tag{6.55}$$

where, in momentum space, we define the correlation of the stochastic fields $\epsilon_n^{ij\cdots}$ as an expansion in powers of $\vec{k}$ of all of the terms allowed by rotation invariance [144], for example

$$\begin{aligned} \langle \epsilon_a^{ij}(\vec{k}) \epsilon_b^{kl}(\vec{k}') \rangle' =& \, c_{a,b}^{(1)} \delta^{ij} \delta^{kl} + c_{a,b}^{(2)} (\delta^{ik} \delta^{jl} + \delta^{il} \delta^{jk}) \\ &+ {k_{\rm NL}}^{-2} \left(c_{a,b}^{(3)} \delta^{ij} k^k k^l + c_{a,b}^{(4)} \delta^{kl} k^i k^j + c_{a,b}^{(5)} (\delta^{ik} k^j k^l + \delta^{il} k^j k^k) \right) + \dots \ . \end{aligned} \tag{6.56}$$

We also do a similar expansion for three-point functions of stochastic fields, for

example

$$\begin{aligned}\langle\epsilon_a^{ij}(\vec{k}_1)\epsilon_b^{kl}(\vec{k}_2)\epsilon_c^{mn}(\vec{k}_3)\rangle' &= c^{(1)}_{a,b,c}\delta^{ij}\delta^{kl}\delta^{mn} + \frac{1}{2}c^{(2)}_{a,b,c}\delta^{ij}\left(\delta^{ln}\delta^{km}+\delta^{lm}\delta^{kn}\right) \\ &+\frac{1}{2}c^{(3)}_{a,b,c}\delta^{mn}\left(\delta^{ik}\delta^{jl}+\delta^{il}\delta^{jk}\right) + \frac{1}{2}c^{(4)}_{a,b,c}\delta^{kl}\left(\delta^{in}\delta^{jm}+\delta^{im}\delta^{jn}\right) \\ &+\frac{1}{8}c^{(5)}_{a,b,c}\Big(\delta^{im}(\delta^{jl}\delta^{kn}+\delta^{jk}\delta^{ln})+\delta^{il}(\delta^{jn}\delta^{km}+\delta^{jm}\delta^{kn}) \\ &\qquad +\delta^{ik}(\delta^{jn}\delta^{lm}+\delta^{jm}\delta^{ln})+\delta^{in}(\delta^{jl}\delta^{km}+\delta^{jk}\delta^{lm})\Big)\,,\end{aligned} \tag{6.57}$$

where we only need the terms up to k^0 for the stochastic three-point functions for dark-matter renormalization in this chapter. [9] We note that the free coefficients appearing in two-point and three-point functions of stochastic fields can in general be independent, although they can be related under the assumption that the stochastic fields are purely Poissonian, for example. Since we expand the stochastic fields in all possible tensor structures, it is clear that Eq. (6.55) is the most general expression satisfying the equivalence principle.

Terms containing $\partial_i\tilde{\delta}^{(1)}/\partial^2$ are sometimes referred to as leading infrared (IR) terms. This is because they can lead to contributions $\mathcal{O}(k/q)$ as the momentum $\vec{q}$ of some field goes to zero. These terms are completely fixed by Galilean invariance. The correct terms are generated by expanding in the fluid line element, as in Secs. 6.3.2 and 6.6.2, and App. B.3.2, leading to the so-called flow terms [129]. We explicitly derive the expressions in Eq. (6.55) and point out a clarification of [129, 131] regarding the stochastic fields in App. B.1.5.

As expected, the counterterms above, when plugged into the relevant expressions for δ, allow us to absorb all UV divergences in the one-loop power spectrum and bispectrum, and we give explicit values for the free coefficients that absorb the UV divergences of the loops in App. B.1.6. In the rest of the chapter, we will often refer to the choice of counterterms that cancels UV parts of SPT loops as 'UV matching,' and in particular, we always choose signs so that the UV part cancels in the *sum* of the loop and the counterterms. Our results become much more

[9] The coefficients $c^{(i)}_{a,b,c}$ in the contraction Eq. (6.57) are defined with respect to the specific ordering of the fields on the left-hand side of Eq. (6.57), *i.e.* they are not necessarily symmetric in $\{a,b,c\}$. However, we can derive relations among the coefficients with different orderings of $\{a,b,c\}$ by permuting the $\{\vec{k}_i\}$. For example, since at the order that we work, the right-hand side is independent of the $\{\vec{k}_i\}$, by permuting the $\{\vec{k}_i\}$ on the left-hand side, we obtain relations like $c^{(1)}_{a,c,b} = c^{(1)}_{a,b,c}$, $c^{(3)}_{a,c,b} = c^{(4)}_{a,b,c}$, and $c^{(4)}_{b,a,c} = c^{(2)}_{a,b,c}$, so that all permutations of $\{a,b,c\}$ can be related back to the canonical ordering (a,b,c). This ensures that all of the correlations obey the relevant symmetries.

interesting when performing renormalization in redshift space, where non-locally-contributing counterterms in π^i are necessary, and we discuss this in much more detail in Secs. 6.4.3, 6.5.4, and 6.5.5.

As mentioned in Sec. 6.4.1, we assumed that $\partial_i\partial_j\partial_k\tilde{\tau}^{jk}_{ct,(1)} = \partial^2\partial_j\tilde{\tau}^{ij}_{ct,(1)}$, but $\partial_i\partial_j\partial_k\tilde{\tau}^{jk}_{\epsilon,(1)} \neq \partial^2\partial_j\tilde{\tau}^{ij}_{\epsilon,(1)}$, and now we can see why. For the first-order response stress tensor, $\tilde{\tau}^{ij}_{ct,(1)}$, the only two terms that we can write are $\delta_{ij}\tilde{\delta}^{(1)}$ and $\partial_i\partial_j\tilde{\delta}^{(1)}/\partial^2$, which both separately satisfy $\partial_i\partial_j\partial_k\tilde{\tau}^{jk}_{ct,(1)} = \partial^2\partial_j\tilde{\tau}^{ij}_{ct,(1)}$. For the stochastic terms, however, this is not the case. This is essentially because we allow all tensor structures when contracting stochastic fields. For example, if we have

$$\langle\epsilon_1^{ij}(\vec{k}_1)\epsilon_2^{kl}(\vec{k}_2)\rangle' \supset a_1\delta^{ij}\delta^{kl} + a_2(\delta^{ik}\delta^{jl} + \delta^{il}\delta^{jk}) \ , \tag{6.58}$$

then the combination in question gives

$$k_1^ik_1^jk_1^k\langle\epsilon_1^{jk}(\vec{k}_1)\epsilon_2^{ab}(\vec{k}_2)\rangle' - k_1^2k_1^j\langle\epsilon_1^{ij}(\vec{k}_1)\epsilon_2^{ab}(\vec{k}_2)\rangle' = a_2(2k_1^ik_1^ak_1^b - k_1^2\delta^{ia}k_1^b - k_1^2\delta^{ib}k_1^a) \ , \tag{6.59}$$

which is not zero. While we find that this makes no difference in real space, we find that the terms proportional to $\partial_i\partial_j\partial_k\tilde{\tau}^{jk}_{\epsilon,(1)}/\partial^2 - \partial_j\tilde{\tau}^{ij}_{\epsilon,(1)}$ in stochastic expressions Eqs. (6.50), (6.51), and (6.52) lead to contributions in the redshift space quantities $B_{321}^{r,(I),\epsilon}$ and $B_{222}^{r,\epsilon}$ (see App. B.1.7 for definitions and Sec. 6.5.5 for a discussion) that have a unique functional form and are not captured by any other terms that we have discussed, and indeed they are necessary to match the UV structures of $B_{321}^{r,(I)}$ and B_{222}^{r}.

6.4.3 Appearance of Non-Locally-Contributing Counterterms

As a main result of this work, we would like to draw particular attention to the way that the second-order stress tensors $\tilde{\tau}^{ij}_{*,(2)}$ enter the counterterm solutions. Although they enter with a unique derivative structure in $\tilde{\delta}^{(2)}_*$, *i.e.* $\partial_i\partial_j\tilde{\tau}^{ij}_{*,(2)}$, the second-order stress tensors appear in both of the structures

$$\partial_j\tilde{\tau}^{ij}_{*,(2)} \ , \quad \text{and} \quad \frac{\partial_i\partial_j\partial_k}{\partial^2}\tilde{\tau}^{jk}_{*,(2)} \ , \tag{6.60}$$

in the second-order solutions $\tilde{\pi}^i_{*,(2)}$ in Eqs. (6.49) and (6.52). The second term above is a spatially non-local contribution to π^i, although it originates from local contributions to π_S and π^i_V, as can be seen in Eq. (6.19), and we will often refer to

it as the new 'non-locally-contributing counterterm.' The non-locality comes simply from the Green's function for the π^i equation, as evident in Eq. (6.18), and we discuss this in more detail in Sec. 6.6.3 for biased tracers.

First, we point out that the appearance of these two structures relies on π_S and π_V^i having two different Green's functions. To see this, notice that the equations of motion Eq. (6.19) imply that

$$\pi_S \sim \alpha_S \partial_i \partial_j S_\tau^{ij} \ , \quad \text{and} \quad \pi_V^i \sim \alpha_V \epsilon^{ijk} \partial_j \partial_l S_\tau^{kl} \ , \tag{6.61}$$

for some constants α_S and α_V coming from the EdS Green's functions (which are simply numerical constants in the EdS approximation, see App. B.1.1), where we have defined

$$S_\tau^{ij} \equiv \left[2M_{\rm Pl}^2 a^{-2} \left(\partial_i \Phi \partial_j \Phi - \frac{1}{2} \delta_{ij} (\partial \Phi)^2 \right) + \frac{\pi^i \pi^j}{\rho} \right]_\tau + \tau^{ij} \ , \tag{6.62}$$

and used the notation $[\cdot]_\tau$ to mean that the term inside of the brackets is sourced by at least one insertion of the stress tensor τ^{ij} in perturbation theory. Using the definition of π^i in Eq. (6.18), these expressions lead to

$$\pi^i \sim \alpha_V \partial_j S_\tau^{ij} + (\alpha_S - \alpha_V) \frac{\partial_i \partial_j \partial_k}{\partial^2} S_\tau^{jk} \ , \tag{6.63}$$

so we see that the last term would vanish if $\alpha_S = \alpha_V$, *i.e.* if the Green's functions for π_S and π_V^i are the same. Second, we note that the new term is also absent if $\partial_i \partial_j \partial_k S_{\tau,(2)}^{jk} = \partial^2 \partial_j S_{\tau,(2)}^{ij}$, which is true for any terms in $S_{\tau,(2)}^{ij}$ proportional to δ_{ij}, for example. Thus, terms in Eq. (6.54) that lead to the new non-locally-contributing counterterm structure are the ones proportional to c_5 and c_6 and the flow terms proportional to c_1 and c_2. The term $\partial_i \partial_j \partial_k (\partial_l \tilde{\tau}_{ct,(1)}^{kl} \partial_j \tilde{\delta}^{(1)} / \partial^2) / \partial^2$ in Eq. (6.49) also allows c_3 to contribute to the non-local structure.

The two structures in Eq. (6.60) have distinct dependence on the momenta of the fields in $\tilde{\tau}_{*,(2)}^{ij}$, and so can give distinct momentum dependence for EFT counterterms. Notice, however, that for correlators that only involve δ, like the power spectrum and bispectrum of δ in real space in Sec. 6.3.1, this difference does not show up (as can be seen from Eq. (6.20) where τ^{ij} only contributes locally). The situation is different, though, in redshift space where the structures in Eq. (6.60) contribute in different ways so that one must include both possibilities in the counterterms to correctly describe the UV physics. Indeed, both terms are necessary to match the

UV structures of the loop integrals in redshift space, and we describe this in more detail in Secs. 6.5.4 and 6.5.5. The bottom line conclusion from renormalization of dark matter in real space is that as long as one correctly solves the equations of motion, all renormalization comes through a stress tensor that is a local-in-space function of $\partial_i\partial_j\Phi$ and $\partial_i v^j$, as expected. The bottom line conclusion that we will find in Sec. 6.5 for dark matter in redshift space is that, as long as one correctly solves the equations of motion (especially for π^i), renormalization happens through a local-in-space stress tensor and local-in-space redshift space counterterms.

We would like to point out, as a side note, that renormalization of the dark-matter one-loop bispectrum *requires* the generation of vorticity in the velocity field. Although absent in SPT, velocity vorticity ω^i is sourced from the symmetric stress tensor through [147]

$$\omega^i \sim \epsilon^{ijk}\partial_j\left(\epsilon^{kmn}v^m\omega^n - \rho^{-1}\partial_l\tau^{lk}\right) \ . \tag{6.64}$$

For simplicity, we focus on the response terms. In this case, since $\omega^i_{(1)} = 0$, ω^i starts being sourced at second order from the stress-tensor term $\rho^{-1}\partial_l\tau^{lk}$, which in turn means that the term $\epsilon^{kmn}v^m\omega^n$ starts at third order. We can thus ignore the latter term for this discussion. One can then check that the parameters in the stress tensor Eqs. (6.53) and (6.54) that source vorticity at second order are c_1, c_2, c_5, and c_6, and we have explicitly verified that it is impossible to renormalize the one-loop bispectrum (specifically B_{411}) if all of these parameters are zero.

Finally, let us briefly comment on some potentially confusing aspects of the renormalization and UV matching of $B^{(I)}_{321}$ with the stochastic terms, explicitly shown in Eqs. (B.11) and (B.12). Although we defined $B^{(I),\epsilon}_{321}$ by summing over all permutations in Eq. (B.12), we could have done the UV matching in terms of our Galilean invariant stress tensor by considering all terms with an external $P_{11}(k_1)$, *i.e.* just symmetrizing over $\vec{k}_2$ and $\vec{k}_3$ and considering

$$\bar{B}^{(I),\epsilon}_{321}(k_1,k_2,k_3) \equiv \langle\tilde{\delta}^{(1)}(\vec{k}_1)\tilde{\delta}^{(1)}_\epsilon(\vec{k}_2)\tilde{\delta}^{(2)}_\epsilon(\vec{k}_3)\rangle' + \langle\tilde{\delta}^{(1)}(\vec{k}_1)\tilde{\delta}^{(1)}_\epsilon(\vec{k}_3)\tilde{\delta}^{(2)}_\epsilon(\vec{k}_2)\rangle' \ . \tag{6.65}$$

A curious point about absorbing the UV divergences of $B^{(1)}_{321}$ with $\bar{B}^{(1),\epsilon}_{321}$ is that it is still possible to do even if the leading IR part of the counterterm solution Eq. (6.51) (*i.e.* those ensuring the correct Galilean properties) were wrong. However, this is only true because the IR part of Eq. (6.51) actually does not contribute to $\bar{B}^{(I),\epsilon}_{321}$

after symmetrization over $\vec{k}_2$ and $\vec{k}_3$. [10] However, as we will see in Sec. 6.5.5, this is no longer the case in redshift space, and the precise form of the IR terms in Eq. (6.51) is crucial to obtaining the correct renormalization and UV matching. This clarifies some statements made in [152] about this renormalization.

6.5 Dark-Matter Renormalization in Redshift Space

6.5.1 General Redshift-Space Equations

The distribution of matter is roughly homogeneous and isotropic in the comoving coordinate $\vec{x}$, but since we use redshift to assign distances, the coordinate that we actually measure for each galaxy is (see for example [153])

$$\vec{x}_r = \vec{x} + \frac{\hat{z}\cdot\vec{v}}{aH}\hat{z} \ , \tag{6.66}$$

where $\hat{z}$ is the line of sight direction. Mass conservation implies that $\rho(\vec{x}_r)d^3x_r = \rho(\vec{x})d^3x$, which gives

$$\delta_r(\vec{k},\hat{z}) = \delta(\vec{k}) + \int d^3x\, e^{-i\vec{k}\cdot\vec{x}}\left(\exp\left[-i\frac{(\hat{z}\cdot\vec{k})}{aH}(\hat{z}\cdot\vec{v}(\vec{x}))\right]-1\right)(1+\delta(\vec{x})) \ , \tag{6.67}$$

in Fourier space. Since we will compute up to the one-loop bispectrum, we expand to fourth order, which gives

$$\begin{aligned}\delta_r = \delta &- \frac{\hat{z}^i\hat{z}^j}{aH\bar{\rho}}\partial_i\pi^j + \frac{\hat{z}^i\hat{z}^j\hat{z}^k\hat{z}^l}{2(aH)^2\bar{\rho}}\partial_i\partial_j(\pi^k v^l) \\ &-\frac{\prod_{a=1}^{6}\hat{z}^{i_a}}{3!(aH)^3\bar{\rho}}\partial_{i_1}\partial_{i_2}\partial_{i_3}(\pi^{i_4}v^{i_5}v^{i_6}) + \frac{\prod_{a=1}^{8}\hat{z}^{i_a}}{4!(aH)^4\bar{\rho}}\partial_{i_1}\partial_{i_2}\partial_{i_3}\partial_{i_4}(\pi^{i_5}v^{i_6}v^{i_7}v^{i_8}) + \dots \ ,\end{aligned} \tag{6.68}$$

in position space. We now see the appearance of π^i contracted in a non-isotropy-preserving way, since isotropy is broken in redshift space by the preferred direction $\hat{z}$.

The n-th order expression for δ_r in SPT, *i.e.* with $\tau^{ij} = 0$ and redshift space EFT counterterms (related to contact operators in Eq. (6.68) that we will discuss

[10] This is for a reason very similar to why the LSS consistency relations are trivial for the tree-level bispectrum, because the leading term when $\vec{q}\to 0$ has to be zero because of permutation symmetry in $(\vec{q},\vec{k}_2,\vec{k}_3)$.

in the subsequent sections) set to zero, can be written

$$\begin{aligned}\delta_r^{(1)}(\vec{k},\hat{z},a) &= D(a)F_1^r(\vec{k};\hat{z})\tilde{\delta}_{\vec{k}}^{(1)} \ , \\ \delta_r^{(n)}(\vec{k},\hat{z},a) &= D(a)^n \int_{\vec{k}_1,\ldots,\vec{k}_n}^{\vec{k}} F_n^r(\vec{k}_1,\ldots,\vec{k}_n;\hat{z})\tilde{\delta}_{\vec{k}_1}^{(1)}\cdots\tilde{\delta}_{\vec{k}_n}^{(1)} \ ,\end{aligned} \tag{6.69}$$

for $n \geq 2$, where the redshift space kernels F_n^r up to $n = 3$ can be found in [153], for example. The observables that we are interested in are defined analogously to those in Sec. 6.3.1. In the plane-parallel approximation that is common in redshift space and that we use in this chapter, the power spectrum and bispectrum are defined by

$$\begin{aligned}\langle\prod_{i=1}^{2}\delta_r(\vec{k}_i,\hat{z},a)\rangle &= (2\pi)^3\delta_D(\vec{k}_1+\vec{k}_2)P^r(k_1,\hat{k}_1\cdot\hat{z},a) \ , \\ \langle\prod_{i=1}^{3}\delta_r(\vec{k}_i,\hat{z},a)\rangle &= (2\pi)^3\delta_D(\vec{k}_1+\vec{k}_2+\vec{k}_3)B^r(k_1,k_2,k_3,\hat{k}_1\cdot\hat{z},\hat{k}_2\cdot\hat{z},a).\end{aligned} \tag{6.70}$$

Notice that since translation invariance is preserved, the correlation functions still have the Dirac delta functions for total wavenumber conservation. However, since isotropy is broken, the spectra can depend on angles with respect to $\hat{z}$.

The total one-loop power spectrum is

$$P^r_{\text{1-loop tot.}}(k,\hat{k}\cdot\hat{z},a) = D(a)^2P^r_{11}(k,\hat{k}\cdot\hat{z}) + D(a)^4(P^r_{22}(k,\hat{k}\cdot\hat{z}) + P^r_{13}(k,\hat{k}\cdot\hat{z})) \ , \tag{6.71}$$

where

$$P^r_{11}(k,\hat{k}\cdot\hat{z}) = (1+f(\hat{k}\cdot\hat{z})^2)^2P_{11}(k) \ , \tag{6.72}$$

is the famous Kaiser result, and

$$\begin{aligned}P^r_{22}(k,\hat{k}\cdot\hat{z}) &= 2\int_{\vec{q}} F_2^r(\vec{q},\vec{k}-\vec{q};\hat{z})^2P_{11}(q)P_{11}(|\vec{k}-\vec{q}|) \ , \\ P^r_{13}(k,\hat{k}\cdot\hat{z}) &= 6P_{11}(k)F_1^r(\vec{k},\hat{z})\int_{\vec{q}} F_3^r(\vec{q},-\vec{q},\vec{k};\hat{z})P_{11}(q) \ .\end{aligned} \tag{6.73}$$

The total one-loop bispectrum is

$$B^r_{\text{1-loop tot.}} = D(a)^4B^r_{211} + D(a)^6\left(B^r_{222} + B^{r,(I)}_{321} + B^{r,(II)}_{321} + B^r_{411}\right) \ , \tag{6.74}$$

where here and below we suppress the argument $(k_1,k_2,k_3,\hat{k}_1\cdot\hat{z},\hat{k}_2\cdot\hat{z})$ of the bispectra

terms to remove clutter. The tree-level bispectrum is

$$B^r_{211} = 2F^r_1(\vec{k}_1;\hat{z})F^r_1(\vec{k}_2;\hat{z})F^r_2(\vec{k}_1,\vec{k}_2;\hat{z})P_{11}(k_1)P_{11}(k_2) + \text{ 2 perms. }, \tag{6.75}$$

and the one-loop contributions are

$$\begin{aligned}
B^r_{222} &= 8\int_{\vec{q}} P_{11}(q)P_{11}(|\vec{k}_2-\vec{q}|)P_{11}(|\vec{k}_1+\vec{q}|) \\
&\qquad \times F^r_2(-\vec{q},\vec{k}_1+\vec{q};\hat{z})F^r_2(\vec{k}_1+\vec{q},\vec{k}_2-\vec{q};\hat{z})F^r_2(\vec{k}_2-\vec{q},\vec{q};\hat{z}) \,, \\
B^{r,(I)}_{321} &= 6P_{11}(k_1)F^r_1(\vec{k}_1;\hat{z})\int_{\vec{q}} P_{11}(q)P_{11}(|\vec{k}_2-\vec{q}|) \\
&\qquad \times F^r_3(-\vec{q},-\vec{k}_2+\vec{q},-\vec{k}_1;\hat{z})F^r_2(\vec{q},\vec{k}_2-\vec{q};\hat{z}) + \text{ 5 perms. }, \\
B^{r,(II)}_{321} &= 6P_{11}(k_1)P_{11}(k_2)F^r_1(\vec{k}_1;\hat{z})F^r_2(\vec{k}_1,\vec{k}_2;\hat{z})\int_{\vec{q}} P_{11}(q)F^r_3(\vec{k}_1,\vec{q},-\vec{q};\hat{z}) + \text{ 5 perms. }, \\
B^r_{411} &= 12P_{11}(k_1)P_{11}(k_2)F^r_1(\vec{k}_1;\hat{z})F^r_1(\vec{k}_2;\hat{z}) \\
&\qquad \times \int_{\vec{q}} P_{11}(q)F^r_4(\vec{q},-\vec{q},-\vec{k}_1,-\vec{k}_2;\hat{z}) + \text{ 2 perms. }.
\end{aligned} \tag{6.76}$$

As a final point, we note that we have explicitly displayed and factored out the major source of time dependence, which is through the factors of $D(a)^n$ in Eq. (6.69), in the above equations. The kernels F^r_n in Eq. (6.69) are in fact time dependent as well, coming from factors of $f(a)$ that enter Eq. (6.68) through the factors of $\vec{v}$. While we fully take into account this time dependence, we do not explicitly write the time argument in the F^r_n kernels, to remove clutter; all kernels and observables with the redshift space marking 'r' are understood to contain this time dependence through $f(a)$. For details on how to evaluate the above integrals, see App. B.2.

6.5.2 Renormalization of Dark Matter in Redshift Space

Ultimately, we want a renormalized expression for the redshift space overdensity δ_r in Eq. (6.68). The first two terms, containing only δ and π^j, have already been renormalized in Sec. 6.4, and this is entirely determined by the local stress-tensor counterterms in τ^{ij}. The non-linear terms in Eq. (6.68), however, are contact operators (*i.e.* UV sensitive) and must be separately renormalized [137], which essentially amounts to adding new counterterms directly to Eq. (6.68). Here we present a systematic renormalization that preserves Galilean transformation properties, extending [144], and address some subtleties that appear since we are going to quadratic order in the counterterms.

As can be seen in Eq. (6.68), we ultimately want to renormalize products like $\pi^i v^j v^k \cdots$. In order to build up to that, let us start with the renormalization of velocity products, up to $[v^i v^j v^k v^l]_R$, where $[\cdot]_R$ denotes a renormalized quantity. In order to have the correct transformation properties under the Galilean transformation $v^i \to v^i + \chi^i$ (here and elsewhere χ^i is a constant vector), we wish for the renormalized quantities to transform in the same way as the bare operators, so we have

$$\begin{aligned}
&[v^i]_R \to [v^i]_R + \chi^i \ , \\
&[v^i v^j]_R \to [v^i v^j]_R + [v^i]_R \chi^j + [v^j]_R \chi^i + \chi^i \chi^j, \\
&[v^i v^j v^k]_R \to [v^i v^j v^k]_R + ([v^i v^j]_R \chi^k + 2 \text{ perms.}) + ([v^i]_R \chi^j \chi^k + 2 \text{ perms.}) + \chi^i \chi^j \chi^k, \\
&[v^i v^j v^k v^l]_R \to [v^i v^j v^k v^l]_R + ([v^i v^j v^k]_R \chi^l + 3 \text{ perms.}) + ([v^i v^j]_R \chi^k \chi^l + 5 \text{ perms.}) \\
&\qquad\qquad + ([v^i]_R \chi^j \chi^k \chi^l + 3 \text{ perms.}) + \chi^i \chi^j \chi^k \chi^l \ .
\end{aligned} \tag{6.77}$$

One way to write renormalized quantities satisfying the above in terms of the non-renormalized fields is

$$\begin{aligned}
&[v^i]_R = v^i + \mathcal{O}^i_v \ , \\
&[v^i v^j]_R = [v^i]_R [v^j]_R + \mathcal{O}^{ij}_{v^2} \ , \\
&[v^i v^j v^k]_R = ([v^i v^j]_R [v^k]_R + 2 \text{ perms.}) - 2[v^i]_R [v^j]_R [v^k]_R + \mathcal{O}^{ijk}_{v^3} \ , \\
&[v^i v^j v^k v^l]_R = ([v^i v^j v^k]_R [v^l]_R + 3 \text{ perms.}) - ([v^i v^j]_R [v^k v^l]_R + 2 \text{ perms}) + \mathcal{O}^{ijkl}_{v^4} \ ,
\end{aligned} \tag{6.78}$$

where all of the $\mathcal{O}$ terms are Galilean scalars. The last expression is not unique in the sense that other operators could have been used that are not independent from the ones shown, like $[v^i]_R [v^j]_R [v^k]_R [v^l]_R$ and $[v^i v^j]_R [v^k]_R [v^l]_R$, for example. Definitions using different bases can differ in their scalar parts $\mathcal{O}$. Note that v^i is renormalized here because it is the composite operator π^i/ρ [147].

We can similarly renormalize products involving δ. Demanding again that renormalized quantities transform in the same way as bare ones under Galilean transform-

ations means that we want

$$
\begin{aligned}
&[\delta v^i]_R \to [\delta v^i]_R + [\delta]_R \chi^i \ , \\
&[\delta v^i v^j]_R \to [\delta v^i v^j]_R + [\delta v^i]_R \chi^j + [\delta v^j]_R \chi^i + [\delta]_R \chi^i \chi^j \ , \\
&[\delta v^i v^j v^k]_R \to [\delta v^i v^j v^k]_R + ([\delta v^i v^j]_R \chi^k + 2 \text{ perms.}) + ([\delta v^i]_R \chi^j \chi^k + 2 \text{ perms.}) \\
&\qquad\qquad + [\delta]_R \chi^i \chi^j \chi^k \ , \\
&[\delta v^i v^j v^k v^l]_R \to [\delta v^i v^j v^k v^l]_R + ([\delta v^i v^j v^k]_R \chi^l + 3 \text{ perms.}) + ([\delta v^i v^j]_R \chi^k \chi^l + 5 \text{ perms.}) \\
&\qquad\qquad + ([\delta v^i]_R \chi^j \chi^k \chi^l + 3 \text{ perms.}) + [\delta]_R \chi^i \chi^j \chi^k \chi^l \ .
\end{aligned}
\tag{6.79}
$$

One way to write renormalized quantities satisfying the above in terms of the non-renormalized fields is

$$
\begin{aligned}
&[\delta]_R = \delta + \mathcal{O}_\delta \ , \\
&[\delta v^i]_R = [\delta]_R [v^i]_R + \mathcal{O}^i_{v\delta} \ , \\
&[\delta v^i v^j]_R = [\delta v^i]_R [v^j]_R + [\delta v^j]_R [v^i]_R - [\delta]_R [v^i]_R [v^j]_R + \mathcal{O}^{ij}_{v^2\delta} \ , \\
&[\delta v^i v^j v^k]_R = ([\delta v^i v^j]_R [v^k]_R + 2 \text{ perms.}) - \frac{2}{3}([\delta v^i]_R [v^j]_R [v^k]_R + 2 \text{ perms.}) \\
&\quad + \frac{1}{3}([\delta]_R [v^i v^j]_R [v^k]_R + 2 \text{ perms.}) - \frac{1}{3}([\delta v^i]_R [v^j v^k]_R + 2 \text{ perms.}) + \mathcal{O}^{ijk}_{v^3\delta} \ , \\
&[\delta v^i v^j v^k v^l]_R = ([\delta v^i v^j v^k]_R [v^l]_R + 3 \text{ perms.}) - \frac{1}{2}([\delta v^i]_R [v^j v^k v^l]_R + 3 \text{ perms.}) \\
&\quad - ([\delta v^i v^j]_R [v^k]_R [v^l]_R + 5 \text{ perms.}) + \frac{1}{2}([\delta v^i]_R [v^j v^k]_R [v^l]_R + 11 \text{ perms.}) \\
&\quad + \frac{1}{2}([\delta]_R [v^i v^j v^k]_R [v^l]_R + 3 \text{ perms.}) - ([\delta]_R [v^i v^j]_R [v^k v^l]_R + 2 \text{ perms.}) + \mathcal{O}^{ijkl}_{v^4\delta} .
\end{aligned}
\tag{6.80}
$$

The above expressions were determined by imposing the correct transformation law Eq. (6.79) and having the correct limit to Eq. (6.78) when $\delta \to 1$. The expression for $[\delta v^i v^j v^k]_R$ is not uniquely determined by these constraints, but the difference is immaterial; any other definitions for $[\delta v^i v^j v^k]_R$ differ by Galilean invariant terms, in terms of free EFT coefficients, which vanish when $\delta \to 1$.

Now, we can combine the above expressions to get the terms in Eq. (6.68) relevant for redshift space distortions. Specifically, we write

$$
[\pi^{i_1} v^{i_2} \cdots v^{i_n}]_R \equiv [\rho v^{i_1} v^{i_2} \cdots v^{i_n}]_R = \bar{\rho}([v^{i_1} v^{i_2} \cdots v^{i_n}]_R + [\delta v^{i_1} v^{i_2} \cdots v^{i_n}]_R) \tag{6.81}
$$

to define the renormalized quantities involving π^i. After doing that, we find it more convenient to expand the above expressions Eqs. (6.78) and (6.80) in terms of the

non-renormalized fields and write

$$
\begin{aligned}
[\delta]_R &= \delta + \mathcal{O}_\delta \ , \\
[\pi^i]_R &= \pi^i + v^i \mathcal{O}_\rho + \mathcal{O}^i_\pi \ , \\
[\pi^i v^j]_R &= \pi^i v^j + v^i v^j \mathcal{O}_\rho + v^i \mathcal{O}^j_\pi + v^j \mathcal{O}^i_\pi + \mathcal{O}^{ij}_{\pi v} \ , \\
[\pi^i v^j v^k]_R &= \pi^i v^j v^k + v^i v^j v^k \mathcal{O}_\rho + (v^i v^j \mathcal{O}^k_\pi + 2 \text{ perms.}) \\
&\quad + (v^i \mathcal{O}^{jk}_{\pi v} + 2 \text{ perms.}) + \mathcal{O}^{ijk}_{\pi v^2} \ , \\
[\pi^i v^j v^k v^l]_R &= \pi^i v^j v^k v^l + v^i v^j v^k v^l \mathcal{O}_\rho + (v^i v^j v^k \mathcal{O}^l_\pi + 3 \text{ perms.}) \\
&\quad + (v^i v^j \mathcal{O}^{kl}_{\pi v} + 5 \text{ perms.}) + (v^i \mathcal{O}^{jkl}_{\pi v^2} + 3 \text{ perms.}) + \mathcal{O}^{ijkl}_{\pi v^3} \ ,
\end{aligned}
\tag{6.82}
$$

One can show that all of the $\mathcal{O}_{\pi v^n}$ tensors above (which are all Galilean scalars) can be written in terms of δ, $\mathcal{O}_\delta$, the $\mathcal{O}_{v^n}$, and the $\mathcal{O}_{v^n\delta}$. Explicitly, we have

$$
\mathcal{O}_\rho = \bar{\rho}\,\mathcal{O}_\delta \ , \quad \mathcal{O}^i_\pi = \bar{\rho}\left((1+\delta+\mathcal{O}_\delta)\mathcal{O}^i_v + \mathcal{O}^i_{v\delta}\right) \ , \tag{6.83}
$$

$$
\mathcal{O}^{ij}_{\pi v} = \bar{\rho}\left[(1+\delta+\mathcal{O}_\delta)\mathcal{O}^i_v\mathcal{O}^j_v + \mathcal{O}^i_v\mathcal{O}^j_{v\delta} + \mathcal{O}^j_v\mathcal{O}^i_{v\delta} + \mathcal{O}^{ij}_{v^2} + \mathcal{O}^{ij}_{v^2\delta}\right] \ , \tag{6.84}
$$

$$
\begin{aligned}
\mathcal{O}^{ijk}_{\pi v^2} = \bar{\rho}\Big[&(1+\delta+\mathcal{O}_\delta)\mathcal{O}^i_v\mathcal{O}^j_v\mathcal{O}^k_v + \mathcal{O}^{ijk}_{v^3} + \mathcal{O}^{ijk}_{v^3\delta} \\
&+\mathcal{O}^i_v\left(\mathcal{O}^{jk}_{v^2} + \mathcal{O}^{jk}_{v^2\delta}\right) + \mathcal{O}^j_v\left(\mathcal{O}^{ki}_{v^2} + \mathcal{O}^{ki}_{v^2\delta}\right) + \mathcal{O}^k_v\left(\mathcal{O}^{ij}_{v^2} + \mathcal{O}^{ij}_{v^2\delta}\right) \\
&+\mathcal{O}^i_v\mathcal{O}^j_v\mathcal{O}^k_{v\delta} + \mathcal{O}^j_v\mathcal{O}^k_v\mathcal{O}^i_{v\delta} + \mathcal{O}^k_v\mathcal{O}^i_v\mathcal{O}^j_{v\delta} - \frac{1}{3}\mathcal{O}^{ij}_{v^2}\mathcal{O}^k_{v\delta} - \frac{1}{3}\mathcal{O}^{jk}_{v^2}\mathcal{O}^i_{v\delta} - \frac{1}{3}\mathcal{O}^{ki}_{v^2}\mathcal{O}^j_{v\delta}\Big] \ ,
\end{aligned}
\tag{6.85}
$$

and

$$
\begin{aligned}
\mathcal{O}^{ijkl}_{\pi v^3} = \bar{\rho}\Bigg[&(1+\delta+\mathcal{O}_\delta)\left(\mathcal{O}^i_v\mathcal{O}^j_v\mathcal{O}^k_v\mathcal{O}^l_v - \mathcal{O}^{ij}_{v^2}\mathcal{O}^{kl}_{v^2} - \mathcal{O}^{ik}_{v^2}\mathcal{O}^{jl}_{v^2} - \mathcal{O}^{il}_{v^2}\mathcal{O}^{jk}_{v^2}\right) \\
&+ \mathcal{O}^{ijkl}_{v^4} + \mathcal{O}^{ijkl}_{v^4\delta} - \frac{1}{2}\mathcal{O}^{ijk}_{v^3}\mathcal{O}^l_{v\delta} - \frac{1}{2}\mathcal{O}^{ijl}_{v^3}\mathcal{O}^k_{v\delta} - \frac{1}{2}\mathcal{O}^{ikl}_{v^3}\mathcal{O}^j_{v\delta} - \frac{1}{2}\mathcal{O}^{jkl}_{v^3}\mathcal{O}^i_{v\delta} \\
&+ \Bigg(\frac{\mathcal{O}^i_v}{6}\left(\mathcal{O}^{jkl}_{v^3} + \mathcal{O}^{jkl}_{v^3\delta} - \frac{1}{3}\mathcal{O}^{jk}_{v^2}\mathcal{O}^l_{v\delta} - \frac{1}{3}\mathcal{O}^{jl}_{v^2}\mathcal{O}^k_{v\delta} - \frac{1}{3}\mathcal{O}^{kl}_{v^2}\mathcal{O}^j_{v\delta}\right) \\
&+ \frac{\mathcal{O}^i_v\mathcal{O}^j_v}{4}\left(\mathcal{O}^{kl}_{v^2} + \mathcal{O}^{kl}_{v^2\delta}\right) + \frac{1}{6}\mathcal{O}^i_v\mathcal{O}^j_v\mathcal{O}^k_v\mathcal{O}^l_{v\delta} + 23 \text{ perms. of } \{i,j,k,l\}\Bigg)\Bigg] \ .
\end{aligned}
\tag{6.86}
$$

We note that the counterterms above associated with contact operators are in general local-in-space [147]. This can be seen by considering two operators $\sigma_1(\vec{x})$ and $\sigma_2(\vec{x})$. In the EFT, the ambiguity in the product $\sigma(\vec{x}) \equiv \sigma_1(\vec{x})\sigma_2(\vec{x})$ comes from the fact that $\tilde{\sigma}(\vec{x}) \equiv \sigma_1(\vec{x}+\delta\vec{x})\sigma_2(\vec{x})$ is just as good of a definition as $\sigma(\vec{x})$ as long as $|\delta\vec{x}|$ is below the EFT length cutoff. The two definitions differ by higher derivatives

of the original σ_1 and σ_2 fields. Thus, the origin of the non-locally-contributing counterterms in $[\pi^i]_R$ is not from the fact that it is a contact operator, but rather from the equations of motion Eq. (6.19) and the definition Eq. (6.18).

An important point about Eq. (6.82) is keeping track of how lower-order counterterms must enter higher-order renormalized products in order to preserve Galilean invariance. To renormalize the contact operators in Eq. (6.68), we simply replace all of them with the corresponding renormalized operators in Eq. (6.82). This leads us to the renormalized redshift space overdensity $[\delta_r]_R$ which for renormalization up to the one-loop bispectrum we can write as

$$[\delta_r]_R(\vec{k},\hat{z},a) = \delta_r(\vec{k},\hat{z},a) + \delta^{(1)}_{r,ct}(\vec{k},\hat{z},a) + \delta^{(2)}_{r,ct}(\vec{k},\hat{z},a) + \delta^{(1)}_{r,\epsilon}(\vec{k},\hat{z},a) + \delta^{(2)}_{r,\epsilon}(\vec{k},\hat{z},a) \ , \tag{6.87}$$

where the subscript ct denotes the response counterterms, and ϵ denotes the stochastic (and semi-stochastic) counterterms. Assuming the time dependence needed to cancel UV loop contributions, we have

$$\begin{aligned} &\delta^{(1)}_{r,ct}(\vec{k},\hat{z},a) = D(a)^3\tilde{\delta}^{(1)}_{r,ct}(\vec{k},\hat{z}) \ , \quad \delta^{(2)}_{r,ct}(\vec{k},\hat{z},a) = D(a)^4\tilde{\delta}^{(2)}_{r,ct}(\vec{k},\hat{z}) \ , \\ &\delta^{(1)}_{r,\epsilon}(\vec{k},\hat{z},a) = D(a)^2\tilde{\delta}^{(1)}_{r,\epsilon}(\vec{k},\hat{z}) \ , \quad \text{and} \quad \delta^{(2)}_{r,\epsilon}(\vec{k},\hat{z},a) = D(a)^3\tilde{\delta}^{(2)}_{r,\epsilon}(\vec{k},\hat{z}) \ , \end{aligned} \tag{6.88}$$

where we use the tilde to denote the appropriate time-independent factor.

Given the results of Sec. 6.4.1 for dark-matter renormalization, the linear terms in Eq. (6.68), δ and π^i, are automatically renormalized by the stress tensor τ^{ij}. As can be seen in Eq. (6.82), though, we still need the explicit expression for $\mathcal{O}_\rho$ and $\mathcal{O}^i_\pi$ in terms of τ^{ij} to use in higher product renormalizations. Explicitly, we have

$$\mathcal{O}_\rho = \bar{\rho}\,\delta_\tau \ , \tag{6.89}$$

where δ_τ is the solution sourced by τ^{ij}, Eq. (6.42). Then, given this, we can solve for

$$\mathcal{O}^i_\pi = \pi^i_\tau - v^i\mathcal{O}_\rho \ , \tag{6.90}$$

where π^i_τ is the solution sourced by τ^{ij}, Eq. (6.44). The counterterms $\mathcal{O}_{\pi v^n}$ entering the higher products are free functions of Galilean scalars and introduce new counterterms in addition to those coming from τ^{ij}. We give explicit expressions for the redshift space counterterms relevant to this work in Secs. 6.5.4 and 6.5.5.

6.5.3 IR-Limit Checks

Let us briefly pause to make some comments about the counterterm solutions that we found in Sec. 6.4.1. A useful consistency check is to confirm that the expressions have the correct IR behavior for their Galilean transformation types. In perturbation theory, a Galilean scalar Σ (like δ or τ^{ij}) satisfies

$$\Sigma^{(2)}\big|_{\rm IR} = \partial_i \Sigma^{(1)} \frac{\partial_i \delta^{(1)}}{\partial^2} \ , \tag{6.91}$$

where we use the notation $|_{\rm IR}$ to mean the leading term when the momentum of one of the fields goes to zero, which is a straightforward generalization of [154, 155, 156], for example. We can also find the IR behavior of the momentum counterterms directly from Eq. (6.90), since we have $\pi^i_\tau = \mathcal{O}^i_\pi + v^i \mathcal{O}_\rho$. Then since $\mathcal{O}_\rho$ and $\mathcal{O}^i_\pi$ are Galilean scalars, we must have

$$\pi^i_{\tau,(2)}\big|_{\rm IR} = \partial_j \mathcal{O}^i_{\pi,(1)} \frac{\partial_j \delta^{(1)}}{\partial^2} + \bar{\rho}\, v^i_{(1)} \delta^{(1)}_\tau \ , \tag{6.92}$$

where we have used Eq. (6.89).

First, we point out that the stress tensor that we wrote down in Eqs. (6.53), (6.54), and (6.55) is indeed a Galilean scalar, since

$$\tilde{\tau}^{ij}_{*,(2)}\big|_{\rm IR} = \partial_k \tilde{\tau}^{ij}_{*,(1)} \frac{\partial_k \tilde{\delta}^{(1)}}{\partial^2} \ , \tag{6.93}$$

for both the response and stochastic contributions, respectively $* = ct, \epsilon$. This is of course by construction, since we introduced the flow terms as in [129] (with the clarification in App. B.1.5 for the stochastic terms) specifically to make τ^{ij} a Galilean scalar.

Now we move on to the counterterm solutions for δ and π^i sourced by τ^{ij}. By inspection, one can indeed see that

$$\tilde{\delta}^{(2)}_*\big|_{\rm IR} = \partial_i \tilde{\delta}^{(1)}_* \frac{\partial_i \tilde{\delta}^{(1)}}{\partial^2} \ , \quad \text{and} \quad \tilde{\pi}^i_{*,(2)}\big|_{\rm IR} = \partial_j \tilde{\pi}^i_{*,(1)} \frac{\partial_j \tilde{\delta}^{(1)}}{\partial^2} + \frac{\partial_i \tilde{\delta}^{(1)}}{\partial^2} \tilde{\delta}^{(1)}_* \ , \tag{6.94}$$

which are the correct equations in terms of all of the tilde fields. These are much more nontrivial checks. In particular, going through the algebra to check these, one can see how both the second-order stress tensors and the first-order stress tensors plugged back into the equations of motion combine to give the correct answer.

One can also see this in another way. Following [156], we can start with the linear

equation of motion and introduce all of the non-linear leading IR terms directly into the equation of motion. For example, focusing on the counterterm solutions, we have the linear equation

$$\ddot{\delta}_*^{(1)} + 2H\dot{\delta}_*^{(1)} - \frac{3}{2}\Omega_{\rm m}H^2\delta_*^{(1)} = \frac{1}{a^2\bar{\rho}}\partial_i\partial_j\tau^{ij}_{*,(1)} \ . \tag{6.95}$$

Then, the equation of motion for the leading IR piece of the second-order field is

$$\begin{aligned}\left(\ddot{\delta}_*^{(2)} + 2H\dot{\delta}_*^{(2)} - \frac{3}{2}\Omega_{\rm m}H^2\delta_*^{(2)}\right)\Big|_{\rm IR} = \\ = \frac{1}{a^2\bar{\rho}}\partial_i\partial_j\tau^{ij}_{*,(2)}\big|_{\rm IR} - a^{-1}(\dot{v}^i\partial_i\delta_*^{(1)} + 2v^i\partial_i\dot{\delta}_*^{(1)} + Hv^i\partial_i\delta_*^{(1)}) \ .\end{aligned} \tag{6.96}$$

This way, one can see the contribution coming from the IR part of $\tau^{ij}_{*,(2)}$, and the part coming from plugging the linear solution $\delta_*^{(1)}$ back into the equation of motion. Indeed, one can show that the solution to Eq. (6.96) for $\delta_*^{(2)}$ is given by Eq. (6.94).

6.5.4 Redshift Space Counterterms: Response Terms

We now write down the explicit response counterterms (up to second order and number of derivatives discussed above Eq. (6.53), which is the same in real space and redshift space) needed to renormalize the product operators in Eq. (6.68). We start with $[\pi^i v^j]_R$. Since $\mathcal{O}_\rho$ and $\mathcal{O}_\pi^i$ are already known from Eqs. (6.89) and (6.90), we only need $\mathcal{O}_{\pi v}^{ij}$, which we can expand as

$$\mathcal{O}^{ij}_{\pi v,(0)} = (aHf)^2\bar{\rho}\frac{D^2}{{k_{\rm NL}}^2}\delta_{ij}c^{\pi v}_{{\rm DM},0} \ , \tag{6.97}$$

$$\mathcal{O}^{ij}_{\pi v,(1)} = (aHf)^2\bar{\rho}\frac{D^3}{{k_{\rm NL}}^2}\left(c^{\pi v}_{{\rm DM},1}\frac{\partial_i\partial_j\tilde{\delta}^{(1)}}{\partial^2} + c^{\pi v}_{{\rm DM},3}\delta_{ij}\tilde{\delta}^{(1)}\right) \ , \tag{6.98}$$

and

$$\mathcal{O}^{ij}_{\pi v,(2)} = (aHf)^2\bar{\rho}\frac{D^4}{{k_{\rm NL}}^2}\Bigg(c^{\pi v}_{\rm DM,1}\frac{\partial_k\partial_i\partial_j\tilde{\delta}^{(1)}}{\partial^2}\frac{\partial_k\tilde{\delta}^{(1)}}{\partial^2} + c^{\pi v}_{\rm DM,3}\delta_{ij}\partial_k\tilde{\delta}^{(1)}\frac{\partial_k\tilde{\delta}^{(1)}}{\partial^2} \\ + c^{\pi v}_{\rm DM,2}\frac{\partial_i\partial_j\tilde{\delta}^{(2)}}{\partial^2} - c^{\pi v}_{\rm DM,2}\frac{\partial_k\partial_i\partial_j\tilde{\delta}^{(1)}}{\partial^2}\frac{\partial_k\tilde{\delta}^{(1)}}{\partial^2} + c^{\pi v}_{\rm DM,4}\delta_{ij}\tilde{\delta}^{(2)} - c^{\pi v}_{\rm DM,4}\delta_{ij}\partial_k\tilde{\delta}^{(1)}\frac{\partial_k\tilde{\delta}^{(1)}}{\partial^2} \\ + c^{\pi v}_{\rm DM,5}\frac{\partial_i\partial_j\tilde{\delta}^{(1)}}{\partial^2}\tilde{\delta}^{(1)} + c^{\pi v}_{\rm DM,6}\frac{\partial_i\partial_k\tilde{\delta}^{(1)}}{\partial^2}\frac{\partial_k\partial_j\tilde{\delta}^{(1)}}{\partial^2} + c^{\pi v}_{\rm DM,7}\delta_{ij}\tilde{\delta}^{(1)}\tilde{\delta}^{(1)}\Bigg)\,. \tag{6.99}$$

We have arrived at this list of counterterms using the same procedure as in Sec. 6.4.2. The only difference is that we now allow a constant term, which did not contribute through the stress tensor because there are derivatives acting on it. Next we move to $[\pi^i v^j v^k]_R$. Since we are only going up to second order, and because it is not possible to make a Galilean scalar of the form $\mathcal{O}^{ijk}_{\pi v^2}$ at the order of fields and derivatives that we need, no new counterterms are needed, although the term $v^i\mathcal{O}^{jk}_{\pi v}$ still contributes. The situation is similar for $[\pi^i v^j v^k v^l]_R$. For the same reasons, only the term $v^i v^j\mathcal{O}^{kl}_{\pi v}$ contributes, and so again, no new counterterms are needed.

We can now build the response counterterm kernels $F_1^{r,ct}$ and $F_2^{r,ct}$, which are defined explicitly in App. B.1.7. We have found that the parameters c_1, c_2, c_6, and $c^{\pi v}_{\rm DM,0}$ are degenerate in these expressions, so we have set them to zero in the following. For the first-order kernel, we have

$$F_1^{r,ct}(\vec{k};\hat{z}) = -\frac{k^2}{18{k_{\rm NL}}^2}\Big(2c_3 + 3f(2c_3 + 3fc^{\pi v}_{\rm DM,3})(\hat{k}\cdot\hat{z})^2 + 9f^2c^{\pi v}_{\rm DM,1}(\hat{k}\cdot\hat{z})^4\Big), \tag{6.100}$$

while for the second-order kernel we have

$$F_2^{r,ct}(\vec{k}_1,\vec{k}_2;\hat{z}) = \sum_{i=1}^{11}\alpha_i^{\rm DM}\,e_i^{F_2}(\vec{k}_1,\vec{k}_2;\hat{z})\,, \tag{6.101}$$

with

$$\alpha_i^{\rm DM} = \{c_3, c_4, c_5, c_7, c^{\pi v}_{\rm DM,1}, c^{\pi v}_{\rm DM,2}, c^{\pi v}_{\rm DM,3}, c^{\pi v}_{\rm DM,4}, c^{\pi v}_{\rm DM,5}, c^{\pi v}_{\rm DM,6}, c^{\pi v}_{\rm DM,7}\}\,, \tag{6.102}$$

where the basis functions $e_i^{F_2}$ are defined, and the explicit UV matching to SPT loops is given, in App. B.1.7.

This brings us to one of the main results of this chapter. The UV limit of B^r_{411}

contains a term

$$B^r_{411}\big|_{\rm UV} \supset \frac{2(c_5-c_3)}{99}\frac{f(k_1^2-k_2^2)^2(k_1^2+k_2^2)(k_1\mu_1+k_2\mu_2)^2}{{k_{\rm NL}}^2k_1^2k_2^2k_3^2}P_{11}(k_1)P_{11}(k_2) + \text{ 2 perms. }, \tag{6.103}$$

where we choose to write the bispectrum using the variables $(k_1, k_2, k_3, \mu_1, \mu_2)$, the coefficients c_3 and c_5 are given in Eq. (B.37), and here and elsewhere, $\mu_i \equiv \hat{z}\cdot\hat{k}_i$. This should be compared to $P_{11}(k_1)P_{11}(k_2)/(k_1^2k_2^2)+$ 2 perms. in Eq. (B.35) for dark matter in real space. The fact that Eq. (6.103) contains an explicit factor of $1/k_3^2$ is a new development, novel to redshift space. [11] A term like this can only appear as a counterterm in the bispectrum, through $B^{r,ct}_{411}$ (expressions for the counterterm solutions and which loops they renormalize are given in App. B.1.7), because of the appearance of the differential operator $\partial_i\partial_j\partial_k/\partial^2$ acting on two fields in $\tilde{\pi}^i_{ct,(2)}$ in Eq. (6.49), and thus proves the necessity of the new non-locally-contributing counterterm. Indeed, the expression for $F_2^{r,ct}$ in Eq. (6.101) and the values of c_3 and c_5 given in Eq. (B.37) explicitly cancels the UV contribution in Eq. (6.103).

To see how this kind of term can be generated from the counterterms, let us consider some example counterterms and try to reproduce the form of Eq. (6.103). Given that there is a factor $P_{11}(k_1)P_{11}(k_2)$ upstairs, this term should come from a contraction like

$$\langle\delta^{(1)}(\vec{x}_1)\delta^{(1)}(\vec{x}_2)\delta^{(2)}_{r,ct}(\vec{x}_3)\rangle\ , \tag{6.104}$$

and, since there is a single factor of f, it must come from

$$\delta^{(2)}_{r,ct}(\vec{x}_3) \sim f\hat{z}^i\hat{z}^j\partial_i\tilde{\pi}^j_{ct,(2)}(\vec{x}_3)\ , \tag{6.105}$$

so let us consider the various contributions to $\tilde{\pi}^i_{ct,(2)}$ from Eq. (6.49). First of all, only $\partial_j\tilde{\tau}^{ij}_{ct,(2)}$ and the term with $\partial_i\partial_j\partial_k/\partial^2$ have a chance of giving a factor of $1/k_3^2$ because they contain a $1/\partial^2$ acting on two fields whose sum of momenta is $-\vec{k}_3$. However, it cannot come from $\partial_j\tilde{\tau}^{ij}_{ct,(2)}$ because in the only term that had a chance,

[11] The reader may notice that if one were to use μ_3 as one of the angle variables in Eq. (6.103), the factor $(k_1\mu_1+k_2\mu_2)^2 = k_3^2\mu_3^2$ in the numerator would cancel the factor of k_3^2 in the denominator. In this case, the novel feature of the expression would be that there is a factor of μ_3^2 upstairs without an accompanying k_3^2.

$\tau^{ij}_{ct,(2)} \sim c_2 \partial_i \partial_j \tilde{\delta}^{(2)}/\partial^2$, the $1/\partial^2$ is canceled after being hit by ∂_j. So we must have

$$\delta^{(2)}_{r,ct}(\vec{x}_3) \sim f \hat{z}^i \hat{z}^j \partial_i \frac{\partial_j \partial_k \partial_l}{\partial^2} \left(\tilde{\tau}^{kl}_{ct,(2)}(\vec{x}_3) + \frac{\partial_k \tilde{\delta}^{(1)}(\vec{x}_3)}{\partial^2} \partial_m \tilde{\tau}^{lm}_{ct,(1)}(\vec{x}_3) \right) . \tag{6.106}$$

Even still, some terms in the expression for $\tilde{\tau}^{kl}_{ct,(2)}$ in Eq. (6.54), like $\partial_k \partial_l \tilde{\delta}^{(2)}/\partial^2$ and those proportional to δ_{kl}, will not give what we want when plugged into Eq. (6.106), since again, the $1/\partial^2$ gets canceled. However, many will. Consider the term proportional to c_6 in Eq. (6.54). This gives

$$\delta^{(2)}_{r,ct}(\vec{x}_3) \sim f \hat{z}^i \hat{z}^j \partial_i \frac{\partial_j \partial_k \partial_l}{\partial^2} \left(\frac{\partial_k \partial_m \tilde{\delta}^{(1)}(\vec{x}_3)}{\partial^2} \frac{\partial_m \partial_l \tilde{\delta}^{(1)}(\vec{x}_3)}{\partial^2} \right) , \tag{6.107}$$

which in Fourier space, contains the form Eq. (6.103) that we desired. This and similar terms, like c_3 and c_5 that appear in Eq. (6.103), are the origin of the $1/k_3^2$ in Eq. (6.103), and we have pinpointed that it is due to the differential operator $\partial_i \partial_j \partial_k / \partial^2$ appearing in the solution for π^i and being contracted in an isotropy-breaking way (*i.e.* with $\hat{z}$). In terms of the basis $e_i^{F_2}$ that we use, the new non-locally-contributing counterterm enters in $e_1^{F_2}$ and $e_3^{F_2}$ in Eq. (B.51) and originates from the bias basis function $e_7^{K_2}$ in Eq. (B.101).

As a final point, although we have freedom in defining the various operators in the second-order stress tensor Eq. (6.54), notice that the new term $\partial_i \partial_j \partial_k \tilde{\tau}^{jk}_{ct,(2)}/\partial^2$ appears with a fixed coefficient relative to $\partial_j \tilde{\tau}^{ij}_{ct,(2)}$ in Eq. (6.49). This is important to preserve Galilean invariance, and in fact it is not possible to match the UV structure of the loops if the relative coefficient is made different, because Galilean invariance would be broken. Overall, we find that for the renormalizations of P^r_{13} and B^r_{411} at one loop, the expressions given above give a total of 15 free coefficients, 11 of which are independent, and all 11 of those are needed to match the UV parts of the loops.

6.5.5 Redshift Space Counterterms: Stochastic Terms

The stochastic terms are the final step in fully renormalizing the one-loop power spectrum and bispectrum of dark matter in redshift space, and we follow the same logic as the previous sections. As in Sec. 6.5.4, we start with $[\pi^i v^j]_R$. Similar to the case in Sec. 6.4.2, the only explicit counterterms that we have to add, for our

purposes, are

$$\begin{aligned}\mathcal{O}^{ij}_{\pi v,(1)} &= (aHf)^2\bar{\rho}\,\frac{D^2}{{k_{\rm NL}}^2}\epsilon^{ij}_4\ ,\\ \mathcal{O}^{ij}_{\pi v,(2)} &= (aHf)^2\bar{\rho}\,\frac{D^3}{{k_{\rm NL}}^2}\left(\partial_k\epsilon^{ij}_4\frac{\partial_k\tilde{\delta}^{(1)}}{\partial^2}+\epsilon^{ijkl}_5\frac{\partial_k\partial_l\tilde{\delta}^{(1)}}{\partial^2}\right)\ .\end{aligned} \tag{6.108}$$

The contractions of the stochastic fields should be expanded as in Eqs. (6.56) and (6.57). For dark-matter renormalization, expansion up to k^0 suffices because there are two derivatives acting on $\mathcal{O}^{ij}_{\pi v}$ in Eq. (6.68) already. Because we include all possible tensor structures in contractions of the stochastic fields, Eq. (6.108) is clearly the most general expression we can have up to second order that obeys the equivalence principle. Again, we find that the UV matching is no longer possible if the coefficients in Eq. (6.52) are modified, showing the importance of correctly including the terms from the dark-matter stress tensor. Additionally, as a followup to the discussion for real space, it is now the case in redshift space that UV matching is *not* possible if the numerical coefficients of $\delta^{(2)}_\epsilon$ in Eq. (6.51) are modified (*i.e.* Galilean invariance is broken). As mentioned in Sec. 6.4.3, the reason that changing the coefficients in $\delta^{(2)}_\epsilon$ in real space did not ruin UV matching was due to the fact that the IR terms simply did not contribute because of invariance of $B^{(I),\epsilon}_{321}(k_1,k_2,k_3)$ under permutations of $(\vec{k}_1,\vec{k}_2,\vec{k}_3)$.

Additionally, new functional forms appear in the UV limits of $B^{r,(I)}_{321}$ and B^r_{222} which can only be captured by the new terms $\partial_i\partial_j\partial_k\tilde{\tau}^{jk}_{\epsilon,(2)}/\partial^2$ (for reasons similar to those in the discussion near Eq. (6.103)) and $\partial_i\partial_j\partial_k\tilde{\tau}^{jk}_{\epsilon,(1)}/\partial^2-\partial_j\tilde{\tau}^{ij}_{\epsilon,(1)}$ (which is zero for the response terms) coming from the momentum-density renormalization. In particular, the UV limits of $B^{r,(I)}_{321}$ and B^r_{222} contain terms, for example, of the form

$$\begin{aligned}B^{r,(I)}_{321}\big|_{\rm UV}\supset\frac{\beta_1 f^3k_1\mu_1k_2^2\mu_2^2(k_1\mu_1+k_2\mu_2)^2}{k_1^2k_2^2k_3^2}\Big(&k_1\mu_1k_2^2(k_1^2-k_2^2+k_3^2)\\ &+k_2\mu_2(k_2^2-k_3^2)(k_1^2-k_2^2-k_3^2)\Big)P_{11}(k_1)+\ 2\text{ perms.}\ ,\end{aligned} \tag{6.109}$$

and

$$B^r_{222}\big|_{\rm UV}\supset\frac{\beta_2 f^5k_1^2\mu_1^2k_2^2\mu_2^2(k_1\mu_1+k_2\mu_2)^2\left((k_1\mu_1+k_2\mu_2)^2+k_3^2(\mu_1^2+\mu_2^2)\right)}{k_3^2}\ , \tag{6.110}$$

for some cutoff-dependent (but momentum independent) parameters β_1 and β_2. Again, these differ from the real-space expressions in Eqs. (B.39) and (B.40) because

they are proportional to an overall $1/k_3^2$. For $B_{321}^{r,(I)}$, the reason is exactly the same as the one given in Sec. 6.5.4 for B_{411}^{r}, specifically the differential operator $\partial_i\partial_j\partial_k/\partial^2$ in Eq. (6.52) applied to two fields whose momenta add up to $-\vec{k}_3$. For B_{222}^{r}, the explanation is slightly different, since the counterterm $B_{222}^{r,\epsilon}$ (expressions for the counterterm solutions and which loops they renormalize are given in App. B.1.7) is made from the contraction of first-order stochastic fields. In this case, the $1/k_3^2$ comes from the fact that $\partial_i\partial_j\partial_k\tilde{\tau}^{jk}_{\epsilon,(1)}/\partial^2 - \partial_j\tilde{\tau}^{ij}_{\epsilon,(1)}$ is non-zero for the stochastic terms, as explained below Eq. (6.58). In both cases, the difference comes because isotropy is broken in redshift space and indices can be contracted with the line-of-sight direction $\hat{z}$.

Because dark-matter renormalization of the stochastic terms starts at $\mathcal{O}(k^4)$, there are more independent counterterms than we will find for biased tracers later. For the sake of space, we do not write their explicit expressions in this chapter. However, the expressions, along with the values of the EFT coefficients that match the UV limits of stochastic loops, can be found in the accompanying Mathematica file of [2]. We write the general formulas, which match the notation of the Mathematica file, here for reference. For the power spectrum and bispectrum counterterms, we write

$$P_{22}^{r,\epsilon}(k,\hat{k}\cdot\hat{z}) = \frac{1}{\bar{n}_{\rm DM}}\sum_{i=1}^{5} c^{\rm St}_{{\rm DM},r,i} e^{(22)}_{{\rm DM},r,i}(k,\hat{k}\cdot\hat{z}) \ , \tag{6.111}$$

$$\bar{B}_{321}^{r,(I),\epsilon}(\vec{k}_1,\vec{k}_2,\vec{k}_3;\hat{z}) = \frac{1+f(\hat{k}_1\cdot\hat{z})^2}{\bar{n}_{\rm DM}} P_{11}(k_1)\sum_{i=1}^{19} c^{\rm St}_{{\rm DM},r,i} e^{\rm St}_{{\rm DM},r,i}(\vec{k}_1,\vec{k}_2,\vec{k}_3;\hat{z}) \ ,$$

$$B_{222}^{r,\epsilon}(\vec{k}_1,\vec{k}_2,\vec{k}_3;\hat{z}) = \frac{1}{\bar{n}_{\rm DM}^2}\sum_{i=1}^{10} c^{(222)}_{{\rm DM},r,i} e^{(222)}_{{\rm DM},r,i}(\vec{k}_1,\vec{k}_2,\vec{k}_3;\hat{z}) \ ,$$

where $\bar{B}_{321}^{r,(I),\epsilon}$ is defined analogously to Eq. (6.158) and $\bar{n}_{\rm DM} \sim {k_{\rm NL}}^3$ is the number density of regions of linear size ${k_{\rm NL}}^{-1}$ with $\delta \sim 1$. Overall, for $P_{22}^{r,\epsilon}$ and $B_{321}^{r,(I),\epsilon}$, we find 19 free parameters, all of which are needed to match the UV limits of the loops, and for $B_{222}^{r,\epsilon}$, we find 10 free parameters, all of which are needed to match the UV limit of the loop.

6.6 Biased Tracers in Redshift Space

6.6.1 General Formulas

We start with the general equations needed for the one-loop bispectrum of biased tracers in redshift space (ignoring EFT counterterms for now, which we will return to in Sec. 6.6.3), which are up to fourth order in perturbations. The overdensity of biased tracers in redshift space, $\delta_{r,h}$ is given by

$$\delta_{r,h}(\vec{k},\hat{z}) = \delta_h(\vec{k}) + \int d^3x\, e^{-i\vec{k}\cdot\vec{x}} \left(\exp\left[-i\frac{(\hat{z}\cdot\vec{k})}{aH}(\hat{z}\cdot\vec{v}(\vec{x})) \right] - 1 \right) (1+\delta_h(\vec{x})) \ , \tag{6.112}$$

where δ_h is the tracer overdensity in real space defined by $\delta_h(\vec{x}) - \langle\delta_h(\vec{x})\rangle = (\rho_h(\vec{x}) - \bar{\rho}_h)/\bar{\rho}_h$, where $\rho_h(\vec{x})$ is the tracer density, and $\bar{\rho}_h \equiv \langle\rho_h(\vec{x})\rangle$ is the background tracer density. In Sec. 6.6.2 we give our explicit bias expansion for δ_h, which will not satisfy $\langle\delta_h(\vec{x})\rangle = 0$. This means that in Eq. (6.112) we should replace $\delta_h \to \delta_h - \langle\delta_h\rangle$, which we choose to do explicitly in the renormalized $[\delta_h]_R$ in Sec. 6.6.3. Also, there is no velocity bias at leading order in derivatives, *i.e.* $\vec{v}_h = \vec{v}$ where $\vec{v}$ is the dark matter velocity. In configuration space this becomes

$$\begin{aligned} \delta_{r,h} \ &= \ \delta_h - \frac{\hat{z}^i\hat{z}^j}{aH\bar{\rho}_h}\partial_i\pi_h^j + \frac{\hat{z}^i\hat{z}^j\hat{z}^k\hat{z}^l}{2(aH)^2\bar{\rho}_h}\partial_i\partial_j(\pi_h^k v^l) \\ &\quad - \frac{\prod_{a=1}^6 \hat{z}^{i_a}}{3!(aH)^3\bar{\rho}_h}\partial_{i_1}\partial_{i_2}\partial_{i_3}(\pi_h^{i_4}v^{i_5}v^{i_6}) + \frac{\prod_{a=1}^8 \hat{z}^{i_a}}{4!(aH)^4\bar{\rho}_h}\partial_{i_1}\partial_{i_2}\partial_{i_3}\partial_{i_4}(\pi_h^{i_5}v^{i_6}v^{i_7}v^{i_8}) + \dots \ , \end{aligned} \tag{6.113}$$

where the tracer momentum density π_h^i is defined by

$$\pi_h^i \equiv \bar{\rho}_h(1+\delta_h)v^i \ . \tag{6.114}$$

As always, we expand in perturbations

$$\delta_{r,h}(\vec{k},\hat{z},a) = \delta_{r,h}^{(1)}(\vec{k},\hat{z},a) + \delta_{r,h}^{(2)}(\vec{k},\hat{z},a) + \delta_{r,h}^{(3)}(\vec{k},\hat{z},a) + \delta_{r,h}^{(4)}(\vec{k},\hat{z},a) + \dots \tag{6.115}$$

and define the redshift space kernels $K_n^{r,h}$ by

$$\begin{aligned} \delta_{r,h}^{(1)}(\vec{k},\hat{z},a) &= D(a)K_1^{r,h}(\vec{k};\hat{z})\tilde{\delta}_{\vec{k}}^{(1)} \ , \\ \delta_{r,h}^{(n)}(\vec{k},\hat{z},a) &= D(a)^n \int_{\vec{k}_1,\dots,\vec{k}_n}^{\vec{k}} K_n^{r,h}(\vec{k}_1,\dots,\vec{k}_n;\hat{z})\tilde{\delta}_{\vec{k}_1}^{(1)}\cdots\tilde{\delta}_{\vec{k}_n}^{(1)} \ , \end{aligned} \tag{6.116}$$

for $n \geq 2$. The power spectrum $P^{r,h}$ and bispectrum $B^{r,h}$ are defined by

$$\begin{aligned}\langle\prod_{i=1}^{2}\delta_{r,h}(\vec{k}_i,\hat{z},a)\rangle &= (2\pi)^3\delta_D(\vec{k}_1+\vec{k}_2)P^{r,h}(k_1,\hat{k}_1\cdot\hat{z},a)\ , \\ \langle\prod_{i=1}^{3}\delta_{r,h}(\vec{k}_i,\hat{z},a)\rangle &= (2\pi)^3\delta_D(\vec{k}_1+\vec{k}_2+\vec{k}_3)B^{r,h}(k_1,k_2,k_3,\hat{k}_1\cdot\hat{z},\hat{k}_2\cdot\hat{z},a)\ .\end{aligned} \tag{6.117}$$

We write the total one-loop power spectrum as

$$P^{r,h}_{\text{1-loop tot.}}(k,\hat{k}\cdot\hat{z},a) = D(a)^2P^{r,h}_{11}(k,\hat{k}\cdot\hat{z})+D(a)^4(P^{r,h}_{22}(k,\hat{k}\cdot\hat{z})+P^{r,h}_{13}(k,\hat{k}\cdot\hat{z}))\ , \tag{6.118}$$

where

$$P^{r,h}_{11}(k,\hat{k}\cdot\hat{z}) = K^{r,h}_1(\vec{k};\hat{z})K^{r,h}_1(-\vec{k};\hat{z})P_{11}(k)\ , \tag{6.119}$$

and

$$\begin{aligned}P^{r,h}_{22}(k,\hat{k}\cdot\hat{z}) &= 2\int_{\vec{q}}K^{r,h}_2(\vec{q},\vec{k}-\vec{q};\hat{z})^2P_{11}(q)P_{11}(|\vec{k}-\vec{q}|)\ , \\ P^{r,h}_{13}(k,\hat{k}\cdot\hat{z}) &= 6P_{11}(k)K^{r,h}_1(\vec{k},\hat{z})\int_{\vec{q}}K^{r,h}_3(\vec{q},-\vec{q},\vec{k};\hat{z})P_{11}(q)\ .\end{aligned} \tag{6.120}$$

The total one-loop bispectrum is

$$B^{r,h}_{\text{1-loop tot.}} = D(a)^4B^{r,h}_{211}+D(a)^6\left(B^{r,h}_{222}+B^{r,h,(I)}_{321}+B^{r,h,(II)}_{321}+B^{r,h}_{411}\right)\ , \tag{6.121}$$

where here and below we suppress the argument $(k_1,k_2,k_3,\hat{k}_1\cdot\hat{z},\hat{k}_2\cdot\hat{z})$ of the bispectra terms to remove clutter. The tree-level bispectrum is

$$B^{r,h}_{211} = 2K^{r,h}_1(\vec{k}_1;\hat{z})K^{r,h}_1(\vec{k}_2;\hat{z})K^{r,h}_2(\vec{k}_1,\vec{k}_2;\hat{z})P_{11}(k_1)P_{11}(k_2)+\ 2\text{ perms.}\ , \tag{6.122}$$

and the one-loop contributions are

$$
\begin{aligned}
B_{222}^{r,h} &= 8\int_{\vec{q}} P_{11}(q)P_{11}(|\vec{k}_2-\vec{q}|)P_{11}(|\vec{k}_1+\vec{q}|) \\
&\qquad \times K_2^{r,h}(-\vec{q},\vec{k}_1+\vec{q};\hat{z})K_2^{r,h}(\vec{k}_1+\vec{q},\vec{k}_2-\vec{q};\hat{z})K_2^{r,h}(\vec{k}_2-\vec{q},\vec{q};\hat{z}) \ , \\
B_{321}^{r,h,(I)} &= 6P_{11}(k_1)K_1^{r,h}(\vec{k}_1;\hat{z})\int_{\vec{q}} P_{11}(q)P_{11}(|\vec{k}_2-\vec{q}|) \\
&\qquad \times K_3^{r,h}(-\vec{q},-\vec{k}_2+\vec{q},-\vec{k}_1;\hat{z})K_2^{r,h}(\vec{q},\vec{k}_2-\vec{q};\hat{z}) + \ 5 \text{ perms.} \ , \\
B_{321}^{r,h,(II)} &= 6P_{11}(k_1)P_{11}(k_2)K_1^{r,h}(\vec{k}_1;\hat{z})K_2^{r,h}(\vec{k}_1,\vec{k}_2;\hat{z}) \\
&\qquad \times \int_{\vec{q}} P_{11}(q)K_3^{r,h}(\vec{k}_2,\vec{q},-\vec{q};\hat{z}) + \ 5 \text{ perms.} \ , \\
B_{411}^{r,h} &= 12P_{11}(k_1)P_{11}(k_2)K_1^{r,h}(\vec{k}_1;\hat{z})K_1^{r,h}(\vec{k}_2;\hat{z}) \\
&\qquad \times \int_{\vec{q}} P_{11}(q)K_4^{r,h}(\vec{q},-\vec{q},-\vec{k}_1,-\vec{k}_2;\hat{z}) + \ 2 \text{ perms.} \ .
\end{aligned}
\tag{6.123}
$$

For details on how to evaluate the above integrals, see App. B.2.

6.6.2 Bias Expansion to Fourth Order

With the general expressions for tracers in redshift space in hand, we turn next to the bias expansion, which is the missing piece from Eq. (6.113). For notational convenience, we define all of the perturbations, kernels, power spectra, and bispectra for tracers in real space using the notation in Sec. 6.6.1, but with subscripts or superscripts 'r,h' replaced by 'h.' From Eq. (6.113), we see that the tracer quantities in real space can be obtained from the respective quantities in redshift space by setting $f=0$.

As has been previously laid out in [129], by the equivalence principle the tracer overdensity δ_h can only depend on second derivatives of the gravitational potential and first derivatives of the velocity field, as well as higher derivative and stochastic terms. Additionally, since the tracer overdensity depends on these fields in a non-local-in-time way, we integrate over time along the fluid element $\vec{x}_{\text{fl}}$. In summary we can schematically write the tracer overdensity as

$$
\delta_h(\vec{x},t) = \int^t dt' H(t') f_h\left(\partial_i\partial_j\Phi(\vec{x}_{\text{fl}},t'), \partial_i v^j(\vec{x}_{\text{fl}},t'), \frac{\partial^i_{x_{\text{fl}}}}{k_M}, \epsilon(\vec{x}_{\text{fl}},t'), t'\right)\Bigg|_{\vec{x}_{\text{fl}}=\vec{x}_{\text{fl}}(\vec{x},t,t')} , \tag{6.124}
$$

where f_h is some complicated function describing tracer clustering, $\vec{x}_{\rm fl}$ is given by

$$\vec{x}_{\rm fl}(\vec{x},t,t') = \vec{x} + \int_t^{t'} \frac{dt''}{a(t'')} \vec{v}(\vec{x}_{\rm fl}(\vec{x},t,t''),t'') \ , \tag{6.125}$$

and k_M is the scale controlling the clustering of the tracer. [12]

As has been subsequently shown in [131, 132], using the approach of [136] (*i.e.* defining linear combinations of the dark-matter fields) still results in functional degeneracies, and so we will build our bias expansion straight from the contractions of the underlying fields and systematically remove degeneracies in a second step. For the remainder of this subsection we will only focus on the lowest-derivative, non-stochastic, real-space, bias terms and we include higher-derivative real-space and redshift-space EFT counterterms and stochastic terms in Secs. 6.6.3 and 6.6.4.

To make sure we include all possible operators, we consider all possible scalar contractions of $\partial_i\partial_j\Phi$ and $\partial_i v^j$. With $\mathcal{O}$ representing any scalar of Galilean transformations and rotations, such as δ, $\partial_i v^i$, $\partial_i\partial_j\Phi\partial_i\partial_j\Phi$, etc., we have the general expansion

$$\delta_h(\vec{x},t) = \sum_{\mathcal{O}} \int^t dt' H(t') c_{\mathcal{O}}(t,t') \mathcal{O}(\vec{x}_{\rm fl}(\vec{x},t,t'),t') \ , \tag{6.126}$$

and we give the full list of the operators $\mathcal{O}$ needed to go to fourth order in fields in Eq. (B.78). The $c_{\mathcal{O}}(t,t')$ are incalculable (within the EFT) time kernels describing the non-locality in time. We then Taylor expand the operators evaluated at $\vec{x}_{\rm fl}$ around $\vec{x}$. Going up to order N (for this work we are interested in $N = 4$), and assuming growing mode solutions, an operator $\mathcal{O}_m$ starting at m-th order has Taylor expansion

$$\mathcal{O}_m(\vec{x}_{\rm fl}(\vec{x},t,t'),t')\Big|_N = \sum_{\alpha=m}^{N} \left(\frac{D(t')}{D(t)}\right)^{\alpha} \left(\sum_{n=\alpha}^{N} \mathbb{C}^{(n)}_{\mathcal{O}_m,\alpha-(m-1)}(\vec{x},t)\right) \ , \tag{6.127}$$

where the notation $|_N$ means expansion up to and including N-th order in fields, the $\mathbb{C}^{(n)}_{\mathcal{O}_m,i}$ are all n-th order in fields, and the index i labels different descendants of $\mathcal{O}_m$ at order n. The Taylor expansion in the fluid element up to fourth order for general operators $\mathcal{O}$ is derived in App. B.3.2. Furthermore, given that in the above equation, the full t' dependence is isolated in powers of the growth factor, we can

[12] This is to distinguish it from $k_{\rm NL}$, which is the scale controlling dark-matter clustering. However, for simplicity in this chapter, we let $k_M = k_{\rm NL}$. The difference is easily restored if desired.

symbolically do the time integrals in Eq. (6.126), allowing us to define

$$c_{\mathcal{O}_m,\alpha-(m-1)}(t) \equiv \int^t dt' H(t') c_{\mathcal{O}_m}(t,t') \left(\frac{D(t')}{D(t)}\right)^\alpha \,, \tag{6.128}$$

and therefore the sum Eq. (6.126) becomes

$$\delta_h(\vec{x},t)\Big|_N = \sum_{\mathcal{O}_m} \sum_{\alpha=m}^{N} c_{\mathcal{O}_m,\alpha-(m-1)}(t) \left(\sum_{n=\alpha}^{N} \mathbb{C}^{(n)}_{\mathcal{O}_m,\alpha-(m-1)}(\vec{x},t)\right) \,, \tag{6.129}$$

up to order N.

Doing this for all operators allowed by the equivalence principle Eq. (B.78), we obtain Eq. (B.84). However this expansion is overcomplete, as the $\mathbb{C}^{(n)}_{\mathcal{O},i}$ are not linearly independent. A full list of degeneracies is given in Eq. (B.86). We then obtain the final bias expansion up to fourth order

$$\begin{aligned}
\delta_h(\vec{x},t) = {} & b_1 \left(\mathbb{C}^{(1)}_{\delta,1}(\vec{x},t) + \mathbb{C}^{(2)}_{\delta,1}(\vec{x},t) + \mathbb{C}^{(3)}_{\delta,1}(\vec{x},t) + \mathbb{C}^{(4)}_{\delta,1}(\vec{x},t)\right) \\
& + b_2 \left(\mathbb{C}^{(2)}_{\delta,2}(\vec{x},t) + \mathbb{C}^{(3)}_{\delta,2}(\vec{x},t) + \mathbb{C}^{(4)}_{\delta,2}(\vec{x},t)\right) + b_3 \left(\mathbb{C}^{(3)}_{\delta,3}(\vec{x},t) + \mathbb{C}^{(4)}_{\delta,3}(\vec{x},t)\right) \\
& + b_4\, \mathbb{C}^{(4)}_{\delta,4}(\vec{x},t) + b_5 \left(\mathbb{C}^{(2)}_{\delta^2,1}(\vec{x},t) + \mathbb{C}^{(3)}_{\delta^2,1}(\vec{x},t) + \mathbb{C}^{(4)}_{\delta^2,1}(\vec{x},t)\right) \\
& + b_6 \left(\mathbb{C}^{(3)}_{\delta^2,2}(\vec{x},t) + \mathbb{C}^{(4)}_{\delta^2,2}(\vec{x},t)\right) + b_7\, \mathbb{C}^{(4)}_{\delta^2,3}(\vec{x},t) + b_8 \left(\mathbb{C}^{(3)}_{r^2,2}(\vec{x},t) + \mathbb{C}^{(4)}_{r^2,2}(\vec{x},t)\right) \\
& + b_9\, \mathbb{C}^{(4)}_{r^2,3}(\vec{x},t) + b_{10} \left(\mathbb{C}^{(3)}_{\delta^3,1}(\vec{x},t) + \mathbb{C}^{(4)}_{\delta^3,1}(\vec{x},t)\right) + b_{11}\, \mathbb{C}^{(4)}_{r^3,2}(\vec{x},t) \\
& + b_{12}\, \mathbb{C}^{(4)}_{\delta^3,2}(\vec{x},t) + b_{13}\, \mathbb{C}^{(4)}_{r^2\delta,2}(\vec{x},t) + b_{14}\, \mathbb{C}^{(4)}_{\delta^4,1}(\vec{x},t) + b_{15}\, \mathbb{C}^{(4)}_{\delta r^3,1}(\vec{x},t) \,,
\end{aligned} \tag{6.130}$$

which through the procedure defined above, is the minimal set of linearly independent functions for the bias expansion up to fourth order. This parametrization is the same as the one used in the data analysis in Chs. 7 and 8. The operators up to third order are the same as in the basis of [131, 132], except that we use $\mathbb{C}^{(3)}_{r^2,2} = \mathbb{C}^{(3)}_{s^2,2} + \frac{1}{3}\mathbb{C}^{(3)}_{\delta^2,2}$, as it was easier to generalize. The new fourth order $\mathbb{C}^{(4)}_{\mathcal{O},i}$ are explicitly given in App. B.3.4, and expressions for $\mathbb{C}^{(n)}_{\mathcal{O},i}$ for $n \leq 3$ can be found in [131, 132]. In this way, our expression Eq. (6.130) extends the so-called basis of descendants to fourth order. The dark-matter kernels are obtained by setting $b_1 = b_2 = b_3 = b_4 = 1$, with all of the other bias parameters equal to zero. A bias expansion to fourth order in real space was also given in [157, 158], and has the same number of bias parameters as Eq. (6.130).

The procedure described above ensures that we include all possible operators,

including those related to non-locality in time. However, it is interesting to compare the basis of functions in Eq. (6.130) to what one would get assuming a strictly local-in-time expansion, which in Eq. (6.126) corresponds to setting $c_{\mathcal{O}}(t,t') = c_{\mathcal{O}}(t)\delta_D(t-t')/H(t)$ and not including any convective derivatives in the set of operators $\mathcal{O}$ included. As we show explicitly in App. B.3.3, up to fourth order, the two expansions are mathematically equivalent. [13]

In terms of the bias parameters in Eq. (6.130), we have the following dependencies of perturbative contributions

$$\begin{aligned} &P_{11}^{r,h}[b_1]\ ,\ P_{13}^{r,h}[b_1,b_3,b_8]\ ,\ P_{22}^{r,h}[b_1,b_2,b_5]\ ,\ B_{321}^{r,h,(I)}[b_1,b_2,b_3,b_5,b_6,b_8,b_{10}]\ ,\\ &B_{211}^{r,h}[b_1,b_2,b_5]\ ,\ B_{321}^{r,h,(II)}[b_1,b_2,b_3,b_5,b_8]\ ,\ B_{411}^{r,h}[b_1,\ldots,b_{11}]\ ,\ B_{222}^{r,h}[b_1,b_2,b_5]\ , \end{aligned} \tag{6.132}$$

where

$$P_{11}^{r,h}(k,\hat{k}\cdot\hat{z}) = (b_1 + f(\hat{k}\cdot\hat{z})^2)^2 P_{11}(k)\ , \tag{6.133}$$

is the famous Kaiser result from linear theory, for example. In general, we have the following dependancies of the kernels on the bias parameters

$$K_1^{r,h}[b_1]\ ,\ K_2^{r,h}[b_1,b_2,b_5]\ ,\ K_3^{r,h}[b_1,b_2,b_3,b_5,b_6,b_8,b_{10}],\text{ and }K_4^{r,h}[b_1,\ldots,b_{15}]\ . \tag{6.134}$$

Notice that the diagrams $P_{13}^{r,h}$, $B_{321}^{r,h,(II)}$, and $B_{411}^{r,h}$ depend on less bias parameters than the kernels in Eq. (6.134) would suggest. This happens because, in the particular momentum configuration of the kernels that enter the loops in Eqs. (6.120) and (6.123), some bias parameters can be removed with bias redefinitions. Let us explain this in detail.

To the order that we work in this chapter, we have

$$\langle\delta_h(\vec{x})\rangle \approx \langle\delta_h^{(2)}(\vec{x})\rangle = \int_{\vec{q}} K_2^h(\vec{q},-\vec{q})P_{11}(q) = \frac{-b_1+b_2+b_5}{2\pi^2}\int dq\, q^2 P_{11}(q)\ , \tag{6.135}$$

[13] We disagree with some references, including [130, 157], which have claimed that the local-in-time expansion in terms of $\partial_i\partial_j\Phi$ and $\partial_i v^j$ is not sufficient as a fourth-order basis. For example, they mention a term that they write as $\mathrm{tr}(\Pi^{[1]}\Pi^{[3]})$ which they claim cannot be written in the local-in-time basis. However, we explicitly find that, in terms of the basis of descendants that we use in this work,

$$\begin{aligned} \mathrm{tr}(\Pi^{[1]}\Pi^{[3]}) = &-\frac{21}{8}\mathbb{C}^{(4)}_{r^2,3} - \frac{17}{6}\mathbb{C}^{(4)}_{r^3,2} + \frac{1925}{16}\mathbb{C}^{(4)}_{\delta,4} \\ &+\frac{441}{64}\mathbb{C}^{(4)}_{r^2\delta,2} + \frac{51}{16}\mathbb{C}^{(4)}_{r^3\delta,1} - \frac{15015}{128}\mathbb{C}^{(4)}_{\delta^2,3} + \frac{1729}{16}\mathbb{C}^{(4)}_{\delta^3,2} - \frac{12681}{128}\mathbb{C}^{(4)}_{\delta^4,1}\ . \end{aligned} \tag{6.131}$$

Because we find the basis of descendants equivalent to the local-in-time basis, this means that $\mathrm{tr}(\Pi^{[1]}\Pi^{[3]})$ can be written in the local-in-time basis (which by definition is also local in space).

which as mentioned below in Sec. 6.6.3, we will explicitly subtract when renormalizing δ_h. We also note that since number and momentum are not conserved for tracers, the loops $P_{13}^{r,h}$, $B_{411}^{r,h}$, and $B_{321}^{r,h,(II)}$ start at k^0 (as opposed to k^2 for dark matter) as $k \to 0$. As described in [159, 136], this is best understood as the renormalization of lower-order bias parameters. We explicitly find that the redefinitions

$$b_1 \to b_1 + \frac{13b_1 + 34b_2 - 47b_3 + 42b_5 - 110b_6 - 82b_8 - 63b_{10}}{42\pi^2} \int dq\, q^2 P_{11}(q) \ , \quad (6.136)$$

$$\begin{aligned} b_2 \to b_2 - \frac{1}{1260\pi^2}\big(&- 469b_1 - 96b_2 - 1099b_3 + 1664b_4 - 1260b_6 + 3554b_7 - 2520b_8 \\ &+ 5150b_9 + 6489b_{11} + 1890b_{12} + 5691b_{13} + 2205b_{15}\big) \int dq\, q^2 P_{11}(q) \ , \end{aligned} \quad (6.137)$$

and

$$\begin{aligned} b_5 \to b_5 + \frac{1}{8820\pi^2}\big(&- 1001b_1 + 3876b_2 + 1729b_3 - 4604b_4 + 5460b_5 + 14280b_6 \\ &- 34214b_7 - 7140b_8 - 7250b_9 + 13230b_{10} + 17451b_{11} - 56070b_{12} \\ &- 1911b_{13} - 26460b_{14} + 6615b_{15}\big) \int dq\, q^2 P_{11}(q) \ , \end{aligned} \quad (6.138)$$

absorb the k^0 UV limits of these loops. After these redefinitions, b_{12}, b_{14}, and b_{15} are eliminated from our observables. Additionally, once the k^0 pieces are removed from the terms proportional to b_7 and b_{13} in particular, these two operators become degenerate, and so b_{13} can also be set to zero.

6.6.3 Renormalization of Biased Tracers in Redshift Space

In some ways, renormalization of biased tracers is more straightforward than dark matter because there are no equations of motion to solve, one simply writes all of the terms relevant for the final expressions. On top of this, we express the contact operators of redshift-space distortions in terms of the long-wavelength fields. We start directly with the renormalized operators that enter redshift space (the same

as Eq. (6.82) but with $\bar{\rho} \to \bar{\rho}_h$ and $\delta \to \delta_h$)

$$
\begin{aligned}
[\delta_h]_R &= \delta_h + \mathcal{O}_{\delta_h} \ , \\
[\pi_h^i]_R &= \rho_h v^i + v^i \mathcal{O}_{\rho_h} + \mathcal{O}^i_{\pi_h} \ , \\
[\pi_h^i v^j]_R &= \rho_h v^i v^j + v^i v^j \mathcal{O}_{\rho_h} + v^i \mathcal{O}^j_{\pi_h} + v^j \mathcal{O}^i_{\pi_h} + \mathcal{O}^{ij}_{\pi_h v} \ , \\
[\pi_h^i v^j v^k]_R &= \rho_h v^i v^j v^k + v^i v^j v^k \mathcal{O}_{\rho_h} + (v^i v^j \mathcal{O}^k_{\pi_h} + 2 \text{ perms.}) \\
&\quad + (v^i \mathcal{O}^{jk}_{\pi_h v} + 2 \text{ perms.}) + \mathcal{O}^{ijk}_{\pi_h v^2} \ , \\
[\pi_h^i v^j v^k v^l]_R &= \rho_h v^i v^j v^k v^l + v^i v^j v^k v^l \mathcal{O}_{\rho_h} + (v^i v^j v^k \mathcal{O}^l_{\pi_h} + 3 \text{ perms.}) \\
&\quad + (v^i v^j \mathcal{O}^{kl}_{\pi_h v} + 5 \text{ perms.}) + (v^i \mathcal{O}^{jkl}_{\pi_h v^2} + 3 \text{ perms.}) + \mathcal{O}^{ijkl}_{\pi_h v^3} \ ,
\end{aligned}
\tag{6.139}
$$

where again, all of the $\mathcal{O}$ terms are Galilean scalars, and we specifically have $\mathcal{O}_{\rho_h} \equiv \bar{\rho}_h \mathcal{O}_{\delta_h}$, which is the higher-derivative halo bias or counterterms. Although π_h^i may seem to not be a composite operator, in terms of v^i, it is given by the composite expression Eq. (6.114), and so must also be renormalized. Note that we choose to include the non-zero mean of δ_h in the renormalized $[\delta_h]_R$, so that $\mathcal{O}_{\delta_h} \supset -\langle \delta_h \rangle$. The non-trivial step now is to understand how non-locally-contributing terms containing the differential operator $\partial_i \partial_j \partial_k / \partial^2$ in the renormalization of π^i enter the renormalization for biased tracers. In the dark-matter case, the form is dictated entirely by having a local stress tensor τ^{ij} and solving the equations of motion. However, biased tracers do not have an explicit equation of motion from which to derive the form of all of the counterterms.

To proceed, we write the renormalization of the tracer momentum density in terms of the dark-matter momentum density, which we know from Sec. 6.4 and contains the new non-locally-contributing counterterm. The term $\mathcal{O}^i_{\pi_h}$ in Eq. (6.139) gives the counterterms that we explicitly add to the renormalized tracer density $[\pi_h^i]_R$, so we would like to write that in terms of dark-matter quantities. By the equivalence principle, we know that [129, 130, 133]

$$
[v_h^i - v^i]_R = \mathcal{O}^i_{\Delta v} \ , \tag{6.140}
$$

where $\mathcal{O}^i_{\Delta v}$ is a higher-derivative Galilean scalar built of spatially-local products of $\partial_i \partial_j \Phi$ and $\partial_i v^j$, that vanishes when the wavenumber of $[v_h^i - v^i]_R$ goes to zero. Now, we recall that the renormalized velocity is given by [147]

$$
[v^i]_R = \frac{[\pi^i]_R}{[\rho]_R} + \mathcal{O}^i_{v,HD} \ , \tag{6.141}
$$

where $\mathcal{O}^i_{v,HD}$ are the standard higher-derivative Galilean scalar counterterms used when defining the renormalized velocity of dark matter, which arise because v^i is a contact operator in terms of π^i and ρ (for the same reason as described in Sec. 6.5.2). Using an analogous expression to Eq. (6.141) for $[v^i_h]_R$, and plugging $[v^i]_R$ and $[v^i_h]_R$ into Eq. (6.140) gives

$$[\pi^i_h]_R = \frac{[\rho_h]_R}{[\rho]_R}[\pi^i]_R + [\rho_h]_R \left(\mathcal{O}^i_{\Delta v} - \mathcal{O}^i_{v_h,HD} + \mathcal{O}^i_{v,HD}\right) \ , \tag{6.142}$$

which using Eqs. (6.82) and (6.139) to plug in the expressions for $[\pi^i]_R$ and $[\pi^i_h]_R$ implies

$$(\rho_h + \mathcal{O}_{\rho_h})v^i + \mathcal{O}^i_{\pi_h} = \frac{[\rho_h]_R}{[\rho]_R}\left((\rho + \mathcal{O}_\rho)v^i + \mathcal{O}^i_\pi\right) + [\rho_h]_R \left(\mathcal{O}^i_{\Delta v} - \mathcal{O}^i_{v_h,HD} + \mathcal{O}^i_{v,HD}\right) \ . \tag{6.143}$$

Finally, using $\rho + \mathcal{O}_\rho = [\rho]_R$ and $\rho_h + \mathcal{O}_{\rho_h} = [\rho_h]_R$, we have

$$\mathcal{O}^i_{\pi_h} = \bar{\rho}_h(1 + \delta_h + \mathcal{O}_{\delta_h})\left(\frac{\mathcal{O}^i_\pi}{\bar{\rho}(1 + \delta + \mathcal{O}_\delta)} + \mathcal{O}^i_{\Delta v} - \mathcal{O}^i_{v_h,HD} + \mathcal{O}^i_{v,HD}\right) \ . \tag{6.144}$$

On the right-hand side of the above expression, $\mathcal{O}^i_\pi$ is already the solution for the dark-matter momentum in terms of the local stress tensor (see Eqs. (6.90) and (6.49)), and so contains the non-locally-contributing Green's function. The other terms $\mathcal{O}^i_{\Delta v}$, $\mathcal{O}^i_{v_h,HD}$, and $\mathcal{O}^i_{v,HD}$, are local functions of the dark-matter fields, so $\mathcal{O}^i_\pi$ is the only term with non-locally-contributing terms already at field level. Thus, we have

$$\frac{\mathcal{O}^i_{\pi_h}\big|_{\rm NLC}}{\bar{\rho}_h} = \frac{1 + \delta_h + \mathcal{O}_{\delta_h}}{1 + \delta + \mathcal{O}_\delta}\frac{\mathcal{O}^i_\pi\big|_{\rm NLC}}{\bar{\rho}} \ , \tag{6.145}$$

where $\mathcal{O}|_{\rm NLC}$ stands for the non-locally-contributing terms in $\mathcal{O}$. Thus, we see that, because of the equivalence principle and locality of the renormalization of contact operators, the non-locally-contributing counterterms in $[\pi^i_h]_R$ are determined by those in $[\pi^i]_R$ (and the ratio of renormalized densities $[\delta]_R$ and $[\delta_h]_R$).

We now specialize to the order relevant to this chapter. The non-locally-contributing counterterms start at second order in fields in $\mathcal{O}^i_\pi$, so we have

$$\frac{\mathcal{O}^i_{\pi_h,(2)}\big|_{\rm NLC}}{\bar{\rho}_h} = \frac{\mathcal{O}^i_{\pi,(2)}\big|_{\rm NLC}}{\bar{\rho}} + \dots \ , \tag{6.146}$$

where the ... above stand for higher order terms (note that we have also left off

the constant contribution $\langle\delta_h\rangle$ from $\mathcal{O}_{\delta_h}$ since $\langle\delta_h\rangle$ counts as two powers of $\delta^{(1)}$, as can be seen from Eq. (6.135)). Then, since it is actually the ratios $\mathcal{O}^i_\pi/\bar{\rho}$ for dark matter and $\mathcal{O}^i_{\pi_h}/\bar{\rho}_h$ for tracers that enters the renormalization of the redshift-space overdensity (as can be seen from Eqs. (6.68) and (6.113)), this means that the relevant EFT coefficients for dark matter and tracers are actually equal at this order. This fact has some intriguing consequences. First, measurement of this quantity in galaxy clustering data is a direct measurement of the underlying dark-matter properties. In fact, one can also imagine using dark-matter simulations directly to set expectations for the size of this parameter, since it is unaffected by the bias. Any mismatch between the measured value and the value expected from dark matter would point to a violation of the equivalence principle or locality. Second, since this EFT coefficient is the same for all tracers, the common value should enter any analysis of multiple tracers or sky patches at the same redshift, thus reducing the number of overall parameters of the theory. Finally, the same parameter will enter any lensing analysis (which only depends on the overall mass distribution, dominated by dark matter), thus again reducing the number of parameters of the theory and providing interesting physical consistency checks. We leave exploration of these exciting topics to future work.

6.6.4 Biased Tracers in Redshift Space Counterterms

We can now write down the most general local-in-space counterterms in a derivative expansion of $\partial_i\partial_j\Phi$ and $\partial_i v^j$, up to second order, that obey the symmetries of the problem, which are rotation and Galilean invariance. We focus on the first few orders in derivatives, which, because number and momentum of galaxies is not conserved, is $\mathcal{O}(k^2P_{11})$ for P_{13}, $\mathcal{O}(k^2P_{11}^2)$ for $B^{r,h}_{411}$ and $B^{r,h,(II)}_{321}$, $\mathcal{O}(k^0)$ and $\mathcal{O}(k^2)$ for $P^{r,h}_{22}$, $\mathcal{O}(k^0)$ and $\mathcal{O}(k^2)$ for $B^{r,h}_{222}$, and $\mathcal{O}(k^0P_{11})$ and $\mathcal{O}(k^2P_{11})$ for $B^{r,h,(I)}_{321}$. The $\mathcal{O}(k^0P_{11})$ in $P^{r,h}_{13}$ and $\mathcal{O}(k^0P_{11}^2)$ in $B^{r,h}_{411}$ and $B^{r,h,(II)}_{321}$ are taken care of by shifts in the bias parameters in Sec. 6.6.2.

For the response terms, we include the counterterms

$$\frac{{k_{\rm NL}}^2\mathcal{O}_{\rho_h}}{\bar{\rho}_h} = D^3c_1^h\partial^2\tilde{\delta}^{(1)} + D^4\Bigg(c_1^h\partial_i\partial^2\tilde{\delta}^{(1)}\frac{\partial_i\tilde{\delta}^{(1)}}{\partial^2} + c_2^h\partial^2\tilde{\delta}^{(2)} - c_2^h\partial_i\partial^2\tilde{\delta}^{(1)}\frac{\partial_i\tilde{\delta}^{(1)}}{\partial^2} + c_3^h\partial^2(\tilde{\delta}^{(1)}\tilde{\delta}^{(1)}) + c_4^h\partial^2\left(\frac{\partial_i\partial_j\tilde{\delta}^{(1)}}{\partial^2}\frac{\partial_i\partial_j\tilde{\delta}^{(1)}}{\partial^2}\right) + c_5^h\partial_i\tilde{\delta}^{(1)}\partial_i\tilde{\delta}^{(1)}\Bigg)\,, \tag{6.147}$$

$$\frac{{k_{\rm NL}}^2\mathcal{O}^i_{\pi_h}}{\bar\rho_h aHf} = D^3 c_1^\pi \partial_i\tilde\delta^{(1)} + D^4\Bigg(c_1^\pi\partial_j\partial_i\tilde\delta^{(1)}\frac{\partial_j\tilde\delta^{(1)}}{\partial^2} + c_2^\pi\partial_i\tilde\delta^{(2)} - c_2^\pi\partial_j\partial_i\tilde\delta^{(1)}\frac{\partial_j\tilde\delta^{(1)}}{\partial^2} \quad (6.148)$$
$$+ c_3^\pi\partial_i(\tilde\delta^{(1)}\tilde\delta^{(1)}) + c_4^\pi\partial_i\left(\frac{\partial_j\partial_k\tilde\delta^{(1)}}{\partial^2}\frac{\partial_j\partial_k\tilde\delta^{(1)}}{\partial^2}\right) + c_5^\pi\frac{\partial_i\partial_j\partial_k}{\partial^2}\left(\frac{\partial_j\partial_l\tilde\delta^{(1)}}{\partial^2}\frac{\partial_l\partial_k\tilde\delta^{(1)}}{\partial^2}\right)\Bigg),$$

and

$$\frac{{k_{\rm NL}}^2\mathcal{O}^{ij}_{\pi_h v}}{\bar\rho_h(aHf)^2} = D^2\delta_{ij}c_0^{\pi v} + D^3\left(c_1^{\pi v}\frac{\partial_i\partial_j\tilde\delta^{(1)}}{\partial^2} + c_3^{\pi v}\delta_{ij}\tilde\delta^{(1)}\right) + D^4\Bigg(c_1^{\pi v}\partial_k\frac{\partial_i\partial_j\tilde\delta^{(1)}}{\partial^2}\frac{\partial_k\tilde\delta^{(1)}}{\partial^2}$$
$$+ c_3^{\pi v}\delta_{ij}\partial_k\tilde\delta^{(1)}\frac{\partial_k\tilde\delta^{(1)}}{\partial^2} + c_2^{\pi v}\frac{\partial_i\partial_j\tilde\delta^{(2)}}{\partial^2} - c_2^{\pi v}\partial_k\frac{\partial_i\partial_j\tilde\delta^{(1)}}{\partial^2}\frac{\partial_k\tilde\delta^{(1)}}{\partial^2} + c_4^{\pi v}\delta_{ij}\tilde\delta^{(2)}$$
$$- c_4^{\pi v}\delta_{ij}\partial_k\tilde\delta^{(1)}\frac{\partial_k\tilde\delta^{(1)}}{\partial^2} + c_5^{\pi v}\tilde\delta^{(1)}\frac{\partial_i\partial_j\tilde\delta^{(1)}}{\partial^2} + c_6^{\pi v}\frac{\partial_i\partial_k\tilde\delta^{(1)}}{\partial^2}\frac{\partial_k\partial_j\tilde\delta^{(1)}}{\partial^2} + c_7^{\pi v}\delta_{ij}\tilde\delta^{(1)}\tilde\delta^{(1)}\Bigg). \quad (6.149)$$

We cannot write down any terms in $\mathcal{O}^{ijk}_{\pi_h v^2}$ or $\mathcal{O}^{ijkl}_{\pi_h v^3}$ that are Galilean scalars and contribute at the order that we work. In addition to the terms explicitly written above, we also need to include the terms in Eq. (6.139) that are inherited from the Galilean transformation properties. The ones that contribute to the order that we work are $v^i\mathcal{O}_{\rho_h}$, $v^i\mathcal{O}^j_{\pi_h} + v^j\mathcal{O}^i_{\pi_h}$, $(v^i\mathcal{O}^{jk}_{\pi_h v} + 2\text{ perms.})$, and $(v^iv^j\mathcal{O}^{kl}_{\pi_h v} + 5\text{ perms.})$. Also, notice that the last two terms just mentioned here are only present because we allow a constant piece in $\mathcal{O}^{ij}_{\pi_h v}$.

We also point out the presence of the new non-locally-contributing counterterm proportional to c_5^π, which is included with a free coefficient following the argument in Sec. 6.6.3 and is indeed needed to match the UV limit of $B^{r,h}_{411}$, for example. [14] A nice check of Eq. (6.146) is to consider the UV matching with SPT loops, and compare the matching of coefficients for the non-locally-contributing terms in $\mathcal{O}^i_{\pi_h}/\bar\rho_h$ for biased tracers and $\mathcal{O}^i_\pi/\bar\rho$ for dark matter. For biased tracers this comes from c_5^π, and for dark matter this comes from c_1, c_2, c_3, c_5, and c_6, as mentioned under Eq. (6.63). Specifically, decomposing the dark-matter terms in Eq. (6.54) into the biased tracer basis in Eq. (6.148), we find that $\mathcal{O}^i_{\pi,(2)}|_{\rm NLC}/\bar\rho = \mathcal{O}^i_{\pi_h,(2)}|_{\rm NLC}/\bar\rho_h$ implies $c_5^\pi = (2/99)(2c_1 - c_2 + c_3 - c_5 - c_6)$, which is indeed true for the UV matching that we found in Eqs. (B.102) and (B.37).

[14] Even though c_5^π is determined by the dark-matter value, this is still an unknown number for the sake of galaxy-clustering data analysis, which justifies the choice in Chs. 7 and 8 to treat it as a free parameter.

For the stochastic terms, we include the counterterms

$$\frac{{k_{\rm NL}}^2\mathcal{O}_{\rho_h}}{\bar{\rho}_h} = D^2\epsilon_1 + D^3\left(\partial_i\epsilon_1\frac{\partial_i\tilde{\delta}^{(1)}}{\partial^2} + \epsilon_3^{ij}\frac{\partial_i\partial_j\tilde{\delta}^{(1)}}{\partial^2} + \epsilon_4^{ijk}\frac{\partial_i\partial_j\partial_k\tilde{\delta}^{(1)}}{\partial^2} + \epsilon_5^{ijkl}\frac{\partial_i\partial_j\partial_k\partial_l\tilde{\delta}^{(1)}}{\partial^2}\right), \tag{6.150}$$

$$\frac{{k_{\rm NL}}^2\mathcal{O}^i_{\pi_h}}{\bar{\rho}_h aHf} = D^2\epsilon_6^i + D^3\left(\partial_j\epsilon_6^i\frac{\partial_j\tilde{\delta}^{(1)}}{\partial^2} + \epsilon_8^{ijk}\frac{\partial_j\partial_k\tilde{\delta}^{(1)}}{\partial^2} + \epsilon_9^{ijkl}\frac{\partial_j\partial_k\partial_l\tilde{\delta}^{(1)}}{\partial^2} + \frac{\partial_i\partial_j\partial_k}{\partial^2}\left(\epsilon_{13}^{jl}\frac{\partial_l\partial_k\tilde{\delta}^{(1)}}{\partial^2}\right)\right), \tag{6.151}$$

and

$$\frac{{k_{\rm NL}}^2\mathcal{O}^{ij}_{\pi_h v}}{\bar{\rho}_h(aHf)^2} = D^2\epsilon_{10}^{ij} + D^3\left(\partial_k\epsilon_{10}^{ij}\frac{\partial_k\tilde{\delta}^{(1)}}{\partial^2} + \epsilon_{12}^{ijkl}\frac{\partial_k\partial_l\tilde{\delta}^{(1)}}{\partial^2}\right). \tag{6.152}$$

In addition to the terms explicitly written above, we also need to include the terms in Eq. (6.139) that are inherited from the Galilean transformation properties. The ones that contribute to the order that we work are $v^i\mathcal{O}_{\rho_h}$, $v^i\mathcal{O}^j_{\pi_h} + v^j\mathcal{O}^i_{\pi_h}$, ($v^i\mathcal{O}^{jk}_{\pi_h v}$ + 2 perms.). The correlations of the stochastic fields $\epsilon_n^{ij\cdots}$ are computed analogously to those in Sec. 6.4.2, but expanded to the appropriate order in k to match the terms that we are renormalizing. Again, we point out the presence of the new non-locally-contributing counterterm containing ϵ_{13}^{jl} which has the form discussed in Sec. 6.6.3 and is indeed needed to match the UV of $B_{321}^{r,h,(I)}$. Note also that above we have included the flow terms so that we have the correct IR limit Eq. (6.91) for Galilean scalars. These were obtained in the same way as in Sec. 6.4.2, which is a generalization of [129] (with the clarification in App. B.1.5 for the stochastic terms) to different tensor structures. The above list of counterterms is the full set of independent terms with given tensor structures (at the order in fields and derivatives that we consider) that are Galilean scalars so that the theory satisfies the equivalence principle, and therefore it is the minimal complete set one can consider.

Explicitly, the above leads to the following forms of the kernels and contractions. Quantities and contributions to observables are defined in App. B.4.1. Starting with the response terms, we have

$$K_1^{r,h,ct}(\vec{k};\hat{z}) = \frac{k^2}{{k_{\rm NL}}^2}\left(-c_1^h + \left(c_1^\pi - \frac{1}{2}c_3^{\pi v}f\right)f(\hat{k}\cdot\hat{z})^2 - \frac{1}{2}c_1^{\pi v}f^2(\hat{k}\cdot\hat{z})^4\right). \tag{6.153}$$

We expand $K_2^{r,h,ct}$ in the following way

$$K_2^{r,h,ct}(\vec{k}_1,\vec{k}_2;\hat{z}) = \sum_{i=1}^{14} \alpha_i \, e_i^{K_2}(\vec{k}_1,\vec{k}_2;\hat{z}) \ , \tag{6.154}$$

with

$$\alpha_i = \{c_1^h, c_2^h, c_3^h, c_4^h, c_5^h, c_1^\pi, c_5^\pi, c_1^{\pi v}, c_2^{\pi v}, c_3^{\pi v}, c_4^{\pi v}, c_5^{\pi v}, c_6^{\pi v}, c_7^{\pi v}\} \ , \tag{6.155}$$

and the basis elements $e_i^{K_2}$ and UV matching are given in App. B.4.2, where one can see that the new non-locally-contributing counterterm enters through the term $c_5^\pi e_7^{K_2}$ in $K_2^{r,h,ct}$. We have found that the EFT parameters $\{c_2^\pi, c_3^\pi, c_4^\pi, c_0^{\pi v}\}$ are degenerate with other EFT parameters included above for the expressions for $K_1^{r,h,ct}$ and $K_2^{r,h,ct}$; this of course may not be true when including higher order kernels.

For the stochastic terms, we have (where $\bar{n}$ is the tracer number density)

$$P_{22}^{r,h,\epsilon}(k,\hat{k}\cdot\hat{z}) = \frac{1}{\bar{n}}\left(c_1^{\rm St} + c_2^{\rm St}\frac{k^2}{{k_{\rm NL}}^2} + c_3^{\rm St}\frac{k^2}{{k_{\rm NL}}^2} f(\hat{k}\cdot\hat{z})^2\right) \ , \tag{6.156}$$

and

$$B_{321}^{r,h,(I),\epsilon} = \bar{B}_{321}^{r,h,(I),\epsilon}(\vec{k}_1,\vec{k}_2,\vec{k}_3;\hat{z}) + \bar{B}_{321}^{r,h,(I),\epsilon}(\vec{k}_3,\vec{k}_1,\vec{k}_2;\hat{z}) + \bar{B}_{321}^{r,h,(I),\epsilon}(\vec{k}_2,\vec{k}_3,\vec{k}_1;\hat{z}) \ , \tag{6.157}$$

where we have defined

$$\begin{aligned} &\bar{B}_{321}^{r,h,(I),\epsilon}(\vec{k}_1,\vec{k}_2,\vec{k}_3;\hat{z}) = \\ &\quad = \langle \tilde{\delta}_{r,h}^{(1)}(\vec{k}_1,\hat{z})\tilde{\delta}_{r,h,\epsilon}^{(1)}(\vec{k}_2,\hat{z})\tilde{\delta}_{r,h,\epsilon}^{(2)}(\vec{k}_3,\hat{z})\rangle' + \langle \tilde{\delta}_{r,h}^{(1)}(\vec{k}_1,\hat{z})\tilde{\delta}_{r,h,\epsilon}^{(1)}(\vec{k}_3,\hat{z})\tilde{\delta}_{r,h,\epsilon}^{(2)}(\vec{k}_2,\hat{z})\rangle' \ . \end{aligned} \tag{6.158}$$

Then, we have

$$\bar{B}_{321}^{r,h,(I),\epsilon}(\vec{k}_1,\vec{k}_2,\vec{k}_3;\hat{z}) = \frac{b_1 + f(\hat{k}_1\cdot\hat{z})^2}{\bar{n}} P_{11}(k_1) \sum_{i=1}^{13} c_i^{\rm St} e_i^{\rm St}(\vec{k}_1,\vec{k}_2,\vec{k}_3;\hat{z}) \ , \tag{6.159}$$

with $e_3^{\rm St} = 0$; the basis elements $e_i^{\rm St}$ and UV matching is given in App. B.4.3. In particular, the new non-locally-contributing counterterm enters through $e_{13}^{\rm St}$. [15] Re-

[15] Note that Eq. (6.146) also in principle implies a relationship between the non-locally-contributing stochastic terms of dark matter (in Eq. (6.52)) and tracers (ϵ_{13}^{ij} in Eq. (6.151)). However, since the dark-matter non-linear term is contracted with other dark-matter stochastic terms and the tracer non-linear term is contracted with other tracer stochastic terms, the resulting EFT coefficients after contractions will in general be different. Non-trivial relationships may result at higher orders in perturbation theory, for example when the non-locally-contributing terms contract with themselves.

call that the renormalization of $B_{222}^{r,h}$ involves three-point functions of the stochastic fields, which can in general be independent from the two-point functions (but they can be related after assuming a Poisson distribution, which is a reasonable assumption). We find

$$B_{222}^{r,h,\epsilon} = \frac{1}{\bar{n}^2}\left(c_1^{(222)} + \frac{1}{{k_{\rm NL}}^2}\left(c_2^{(222)}(k_1^2+k_2^2+k_3^2) + c_5^{(222)}\hat{z}^i\hat{z}^j\left(k_1^i k_2^j + k_1^i k_3^j + k_2^i k_3^j\right)\right)\right), \tag{6.160}$$

which indeed is the most general function up to $\mathcal{O}(k^2)$, symmetric in $\{\vec{k}_1,\vec{k}_2,\vec{k}_3\}$, that can be made out of contractions of these vectors, when momentum conservation $\vec{k}_1+\vec{k}_2+\vec{k}_3=0$ is considered.

For convenience, we quote here the dependencies of the counterterm quantities on biases and EFT parameters

$$\begin{aligned}
&P_{13}^{r,h,ct}[b_1, c_1^h, c_1^\pi, c_1^{\pi v}, c_3^{\pi v}]\ , \quad P_{22}^{r,h,\epsilon}[c_1^{\rm St}, c_2^{\rm St}, c_3^{\rm St}]\ ,\\
&B_{321}^{r,h,(II),ct}[b_1, b_2, b_5, c_1^h, c_1^\pi, c_1^{\pi v}, c_3^{\pi v}]\ , \quad B_{321}^{r,h,(I),\epsilon}[b_1, c_1^{\rm St}, c_2^{\rm St}, \{c_i^{\rm St}\}_{i=4,\ldots,13}]\ ,\\
&B_{411}^{r,h,ct}[b_1, \{c_i^h\}_{i=1,\ldots,5}, c_1^\pi, c_5^\pi, \{c_j^{\pi v}\}_{j=1,\ldots,7}]\ , \quad B_{222}^{r,h,\epsilon}[c_1^{(222)}, c_2^{(222)}, c_5^{(222)}]\ .
\end{aligned} \tag{6.161}$$

Thus, overall, to the order that we work in this chapter, we have 11 independent bias parameters, 14 independent response counterterms, and 16 independent stochastic counterterms. For a conversion from the parameters used here to those used in `PyBird`, see App. B.4.4.

7

Constraints: The BOSS Bispectrum Analysis at One Loop from the EFTofLSS

7.1 Summary

We analyze the BOSS power spectrum monopole and quadrupole, and the bispectrum monopole and quadrupole data, using the predictions from the Effective Field Theory of Large-Scale Structure (EFTofLSS). Specifically, we use the one loop prediction for the power spectrum and the bispectrum monopole, and the tree level for the bispectrum quadrupole. After validating our pipeline against numerical simulations as well as checking for several internal consistencies, we apply it to the observational data. We find that analyzing the bispectrum monopole to higher wavenumbers thanks to the one-loop prediction, as well as the addition of the tree-level quadrupole, significantly reduces the error bars with respect to our original analysis of the power spectrum at one loop and bispectrum monopole at tree level. After fixing the spectral tilt to Planck preferred value and using a Big Bang Nucleosynthesis prior, we measure $\sigma_8 = 0.794 \pm 0.037$, $h = 0.692 \pm 0.011$, and $\Omega_m = 0.311 \pm 0.010$ to about 4.7%, 1.6%, and 3.2%, at 68% CL, respectively. This represents an error bar reduction with respect to the power spectrum-only analysis of about 30%, 18%, and 13% respectively. Remarkably, the results are compatible with the ones obtained with a power-spectrum-only analysis, showing the power of the EFTofLSS in simultaneously predicting several observables. We find no tension with Planck.

7.2 Introduction, Main Results and Conclusion

The SDSS-III Baryon Oscillation Spectroscopic Survey (BOSS) has mapped the clustering of galaxies in the nearby Universe in an unprecedented amount and with great accuracy [9]. Although BOSS' survey volume is modest with respect to upcoming experiments such as DESI [160] or Euclid [161], the BOSS data are remarkable as they have been revealing a wealth of cosmological information from the large-scale structure of the Universe.

In the last couple of years, the Effective Field Theory of Large-Scale Structure (EFTofLSS) prediction at one-loop order has been used to analyze the BOSS Full Shape (FS) of the galaxy Power Spectrum (PS) [7, 142, 143], and Correlation Function (CF) [162, 163]. The BOSS galaxy-clustering bispectrum monopole using the tree-level prediction was first analyzed in [7] (see [164] for a recent slight generalization). See also [165, 166, 167] for other techniques and analysis using linear theory with higher multipoles. All ΛCDM cosmological parameters have been measured from these data by only imposing a prior from Big Bang Nucleosynthesis (BBN), reaching a remarkable, and perhaps surprising, precision on some of these. For example, the present amount of matter, Ω_m, and the Hubble constant (see also [168, 169] for subsequent refinements) have error bars that are not far from the ones obtained from the Cosmic Microwave Background (CMB) [24]. As we will see in Ch. 10, for clustering and smooth quintessence models, limits on the dark energy equation of state w parameter of $\lesssim 5\%$ have been set using only late-time measurements (see also [169]). This is again quite close to the ones obtained with the CMB [24]. These measurements provide a new, CMB-independent, method for determining the Hubble constant [7], resulting in a measurement that is comparable, if not better, to the one based on the cosmic ladder [170, 171] and CMB. Therefore, this tool has been used to shed light on how some models that were proposed to alleviate the tension in the Hubble measurements (see e.g. [20]) between the CMB and cosmic ladder [172, 173] (see also [174, 175]) actually perform.

Very recently, in [176], the one-loop EFTofLSS prediction for the bispectrum was used to set the first and strong limits on primordial inflationary non-Gaussianities from Large-Scale Structure (LSS) (see also [177, 178] for a contemporary and a subsequent paper, where, once put together, the same shapes are constrained but stopping at the tree-level EFTofLSS prediction, and so obtaining much weaker constraints for the same data). We obtained limits on three of the so-called $f_{\rm NL}$ para-

meters, $f_{\rm NL}^{\rm equil.} = 217 \pm 297$, $f_{\rm NL}^{\rm orth.} = -64 \pm 74$, $f_{\rm NL}^{\rm loc.} = 49 \pm 36$, at 68% confidence level, which are predicted to be produced by some single-clock [179, 54] or multiple fields [180, 181, 182, 183, 56] inflationary models. Perhaps quite surprisingly, those constraints were already quite on par with the ones of the powerful CMB experiment WMAP [184], though largely inferior to the more recent CMB experiment Planck [60]. Significant limits from LSS on just $f_{\rm NL}^{\rm loc.}$ were obtained using the power spectrum only, first in [185], using the so-called non-local bias [186, 187, 188], but the analysis of [176] uses for the first time the bispectrum, obtaining much stronger constraints using the data from the same experiments.

In this chapter we upgrade our original analysis of the one-loop power spectrum monopole and quadrupole and tree-level bispectrum monopole [7], to include the full one-loop bispectrum monopole and the tree-level bispectrum quadrupole. We scan over all the ΛCDM parameters with BBN prior on the baryon abundance, $\Omega_b h^2$, with the exception of the tilt, n_s, that we fix to the Planck preferred value.

Our main results are summarized in Fig. 7.1, where we plot the posteriors on the cosmological parameters that are effectively scanned. This analysis improves the error bars on the ΛCDM parameters σ_8, h, and Ω_m with respect to the power spectrum-only analysis by about 30%, 18%, and 13% respectively, achieving a precision of about 4.7%, 1.6%, and 3.2% at 68% CL, respectively. [1] Notice also that the results improve significantly upon the ones obtained using instead the tree-level prediction for the bispectrum monopole: in particular, σ_8 is better determined by about 30%. Naively, a 30% improvement corresponds to doubling the data volume of the survey. As it can be seen in the same figure, the results are compatible with the ones obtained with a power-spectrum-only analysis. We find no tension with Planck: we measure σ_8, h, and Ω_m to values consistent at $0.3\sigma, 1.4\sigma, 0.5\sigma$, respectively, with the ones of Planck $\nu\Lambda$CDM [24].

The chapter is organized as follows. In Sec. 7.3 we describe the data products and the measurements we use. In Sec. 7.4 we describe the theory model including the observational aspects. In Sec. 7.5, we present the likelihood we use to describe the data. In Sec. 7.6, we provide some tests for our pipeline. Finally, in Sec. 7.7, we provide some additional details about the main results. Technical aspects and additional materials are relegated to the appendices.

[1] Here and in the rest of this work, we quote parameter constraints as the Bayesian 68% credible interval from the one-dimensional marginalized posterior.

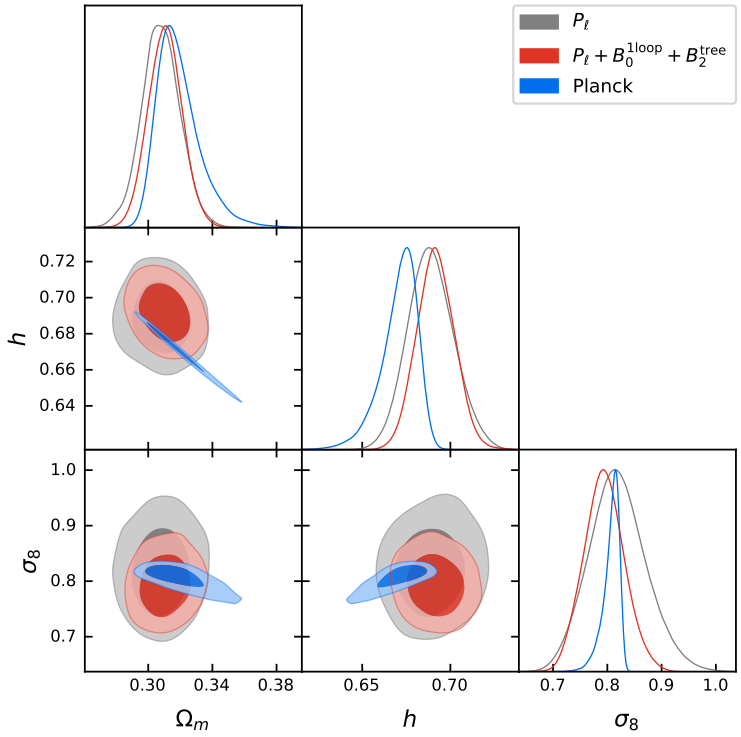

best-fit mean $\pm\,\sigma$	Ω_m	h	σ_8	ω_{cdm}	$\ln(10^{10}A_s)$	S_8
P_ℓ	0.2984 0.308 ± 0.012	0.6763 $0.689^{+0.012}_{-0.014}$	0.8305 $0.819^{+0.049}_{-0.055}$	0.1143 0.1232 ± 0.0075	3.123 3.02 ± 0.15	0.8283 $0.830^{+0.051}_{-0.060}$
$P_\ell + B_0^{\text{tree}}$	0.3101 0.309 ± 0.011	0.6907 0.691 ± 0.012	0.8063 0.804 ± 0.049	0.1248 0.1246 ± 0.0058	2.98 2.97 ± 0.13	0.8197 $0.816^{+0.050}_{-0.057}$
$P_\ell + B_0^{1\text{loop}}$	0.3210 0.314 ± 0.011	0.6956 0.693 ± 0.011	0.7882 $0.790^{+0.033}_{-0.037}$	0.1331 0.1278 ± 0.0061	2.82 2.90 ± 0.11	0.8153 $0.807^{+0.037}_{-0.043}$
$P_\ell + B_0^{1\text{loop}} + B_2^{\text{tree}}$	0.3082 0.311 ± 0.010	0.6928 0.692 ± 0.011	0.7856 0.794 ± 0.037	0.1258 0.1255 ± 0.0057	2.88 2.94 ± 0.11	0.7962 0.808 ± 0.041
Planck	$0.3191^{+0.0085}_{-0.016}$	$0.671^{+0.012}_{-0.0067}$	$0.807^{+0.018}_{-0.0079}$	0.1201 ± 0.0013	3.046 ± 0.015	0.832 ± 0.013

Figure 7.1: Triangle plots, best-fit values, and relative 68%-credible intervals of base cosmological parameters measured from the analysis of BOSS power spectrum multipoles P_ℓ, $\ell = 0, 2$, at one-loop, bispectrum monopole B_0 at tree or one-loop level, and bispectrum quadrupole B_2 at tree-level. Planck $\nu\Lambda$CDM results are shown for comparison.

7.3 Data

BOSS DR12 LRG Sample. The main data sample analyzed in this work is the SDSS-III BOSS DR12 luminous red galaxies (LRG) sample [9]. We use the BOSS catalogs DR12 (v5) combined CMASS-LOWZ [189]. [2] To each galaxy we assign the standard FKP weights for optimality together with the correction weights described in [189] for BOSS data and in [190] for the patchy mocks. The inverse covariances

[2]Publicly available at https://data.sdss.org/sas/dr12/boss/lss/

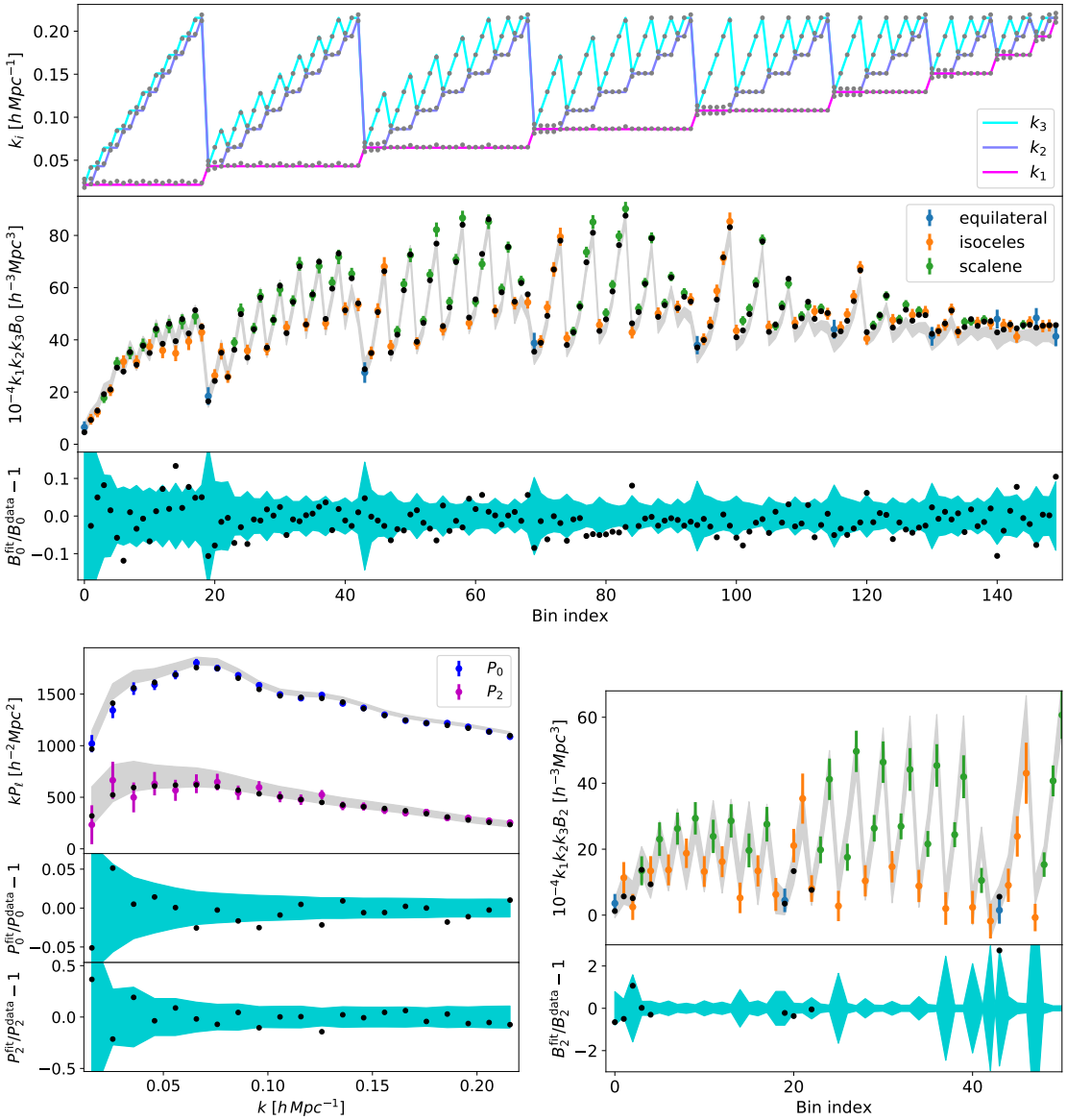

Figure 7.2: Measurements and best fits of bispectrum monopole B_0 (top), power spectrum multipoles P_ℓ (bottom left), and bispectrum quadrupole B_2 (bottom right) from BOSS (points and error bars) and 2048 Patchy (grey regions) CMASS NGC sky. The bispectrum is shown in bins ordered by their central values forming either an equilateral, isoceles, or scalene triangle, shown in blue, orange, or green, respectively. The bin triangle sides (top panel) are shown either by the bin central values (colored lines) or by their effective values (grey points). The best fit (black points) is shown only for the scales analyzed. The relative error bars (turquoise regions) are shown with the best fit residuals for comparison. While only CMASS NGC is shown for clarity, the best fit depicted here is obtained fitting the full combination $P_\ell + B_0 + B_2$ on all BOSS 4 skies.

are corrected by the Hartlap factor to account for the finite number of mocks used in their estimation [191]. In order to test our analysis pipeline, we will analyze the mean over the 2048 Patchy mocks of CMASS NGC (hereafter referred as 'Patchy'). We will also make use of the Nseries mocks, which are full N-body simulations populated with a Halo Occupation Distribution (HOD) model and selection function similar to the one of BOSS CMASS NGC [9]. [3] We will analyze the mean of the 84 Nseries realizations (hereafter referred as 'Nseries'). All celestial coordinates are converted to comoving distance assuming $\Omega_m^{\rm fid} = 0.310$.

BOSS P+B Full-Shape Measurements. In this work, we analyze the full shape of the power spectrum multipoles $\ell = 0, 2$, and of the bispectrum monopole and quadrupole (respectively abbreviated 'P_ℓ', 'B_0' and 'B_2'). Those measurements are shown in Fig. 7.2 (together with the best fit from our theory model that we discuss later). The estimator for the power spectrum is the standard 'FKP' estimator [192], generalised to redshift space in [193, 194, 195]. The bispectrum is estimated using the estimator outlined in [196] (see also [197, 198, 152, 199]). The measurements are obtained using the code `Rustico` [196]. [4] For the power spectrum, we find excellent agreement between the measurements from `Rustico` and `Nbodykit` [200]. [5] We use `Nbodykit` to measure the window functions as described in [201], with consistent normalization in the power spectrum as discussed in [202, 203, 204].

The configurations of the measurements are the following. We use a box of side length $L_{\rm box} = 3500\,(2300){\rm Mpc}\,h^{-1}$ for CMASS (LOWZ), with Piecewise Cubic Spline (PCS) particle assignment scheme and grid interlacing as described in [205]. The grid is consisting of 512^3 cells. The power spectrum is binned in $\Delta k \simeq 0.01h\,{\rm Mpc}^{-1}$. Instead, we bin the bispectrum in $\Delta n = 12\,(9)$ units of the fundamental frequency of the box k_f for CMASS (LOWZ), starting from the bin centered at $n_{\rm min} = 6 + \Delta n/2$, up to the one centered on $n_{\rm max} = 126\,(69) - \Delta n/2$, which correspond in frequencies to bins of size $\Delta k = 0.02154\,(0.02459)h\,{\rm Mpc}^{-1}$, with first and last bins centered on $k_{\rm min} = 0.0215\,(0.029)h\,{\rm Mpc}^{-1}$ and $k_{\rm max} = 0.215\,(0.176)h\,{\rm Mpc}^{-1}$, respectively. This choice of bin size is motivated to keep the Hartlap factor at a value safely close to 1 to limit the effect from the bias of the inverse covariance estimator. Given that we have 2048 patchy mocks at our disposal to estimate the covariance, and, in our analysis, we will analyze 42 (36) k-bins

[3] Made available at https://www.ub.edu/bispectrum/page11.html
[4] https://github.com/hectorgil/Rustico
[5] https://github.com/bccp/nbodykit

in P_ℓ and 150 (62) triangle bins in B_0, this makes for the Hartlap factor of about 0.91 (0.95) for CMASS (LOWZ). B_2, as analyzed at tree-level, only adds 9 bins per quadrupole (for both CMASS and LOWZ), which lead to the Hartlap factor of the same order of about 0.9. Importantly, we keep all bins whose centers form a closed triangle. Explicitly, we choose the following bins according to their centers ordered as:

$$\begin{aligned}(n_1, n_2, n_3)\,, \quad & n_1, n_2, n_3 = n_{\rm min}, n_{\rm min} + dn, \ldots, n_{\rm max}\,, \\ & \text{if } n_1 \le n_2 \le n_3 \text{ and } n_3 \le n_1 + n_2\,.\end{aligned} \tag{7.1}$$

It follows that there are several bins that contain fundamental triangles that are not closed. How to properly account for them is discussed in Sec. 7.4.5.

7.4 Theory Model

Our model for the power spectrum multipoles P_ℓ, $\ell = 0, 2$, the bispectrum monopole, B_0, and the bispectrum quadrupole, B_2, consists in the prediction of EFTofLSS at one loop for P_ℓ and B_0, and at tree-level for B_2. We also incorporate a number of observational effects in our modeling to make contact with the measurements. The loop integrals are evaluated using the techniques described in [206].

7.4.1 EFTofLSS at One Loop

Details for the one-loop power spectrum and bispectrum for halos in redshift space $P^{r,h}$ and $B^{r,h}$ can be found in Ch. 6, but we summarize the dependence on bias parameters and EFT parameters here for convenience. For the perturbation theory contributions, we have

$$\begin{aligned}&P^{r,h}_{11}[b_1]\,, \quad P^{r,h}_{13}[b_1, b_3, b_8]\,, \quad P^{r,h}_{22}[b_1, b_2, b_5]\,, \\ &B^{r,h}_{211}[b_1, b_2, b_5]\,, \quad B^{r,h,(II)}_{321}[b_1, b_2, b_3, b_5, b_8]\,, \quad B^{r,h}_{411}[b_1, \ldots, b_{11}]\,, \\ &B^{r,h}_{222}[b_1, b_2, b_5]\,, \quad B^{r,h,(I)}_{321}[b_1, b_2, b_3, b_5, b_6, b_8, b_{10}]\,,\end{aligned} \tag{7.2}$$

while for the counterterms, we have

$$\begin{aligned}&P^{r,h,ct}_{13}[b_1, c_{h,1}, c_{\pi,1}, c_{\pi v,1}, c_{\pi v,3}]\,, \quad P^{r,h,\epsilon}_{22}[c^{\rm St}_1, c^{\rm St}_2, c^{\rm St}_3]\,, \\ &B^{r,h,(II),ct}_{321}[b_1, b_2, b_5, c_{h,1}, c_{\pi,1}, c_{\pi v,1}, c_{\pi v,3}]\,, \quad B^{r,h,(I),\epsilon}_{321}[b_1, c^{\rm St}_1, c^{\rm St}_2, \{c^{\rm St}_i\}_{i=4,\ldots,13}]\,, \\ &B^{r,h,ct}_{411}[b_1, \{c_{h,i}\}_{i=1,\ldots,5}, c_{\pi,1}, c_{\pi,5}, \{c_{\pi v,j}\}_{j=1,\ldots,7}]\,, \quad B^{r,h,\epsilon}_{222}[c^{(222)}_1, c^{(222)}_2, c^{(222)}_5]\,.\end{aligned} \tag{7.3}$$

Notice that the diagrams $P_{13}^{r,h}$, $B_{321}^{r,h,(II)}$, and $B_{411}^{r,h}$ depend on less biases than the kernels in Eq. (6.134) would suggest. This is because, when considering the particular momentum-configuration of the kernels that enter the loop in Eqs. (6.120) and (6.123), they are degenerate with EFT parameters.

To make contact with our measurements described in Sec. 7.3, what we analyze in the data are various multipoles with respect to the line-of-sight $\hat{z}$. In particular, we analyze the power-spectrum and bispectrum monopole and quadrupoles. The power-spectrum multipoles are given by

$$P_\ell^{r,h}(k) = \frac{2\ell+1}{2}\int_{-1}^{1} \mathrm{d}\mu\, \mathcal{P}_\ell(\mu) P^{r,h}(k,\mu) \ , \tag{7.4}$$

where $\mathcal{P}_\ell$ are the Legendre polynomials, and $\mu = \hat{k}\cdot\hat{z}$. The bispectrum monopole is the average over the line-of-sight angles [207, 199, 208] [6]

$$B_0^{r,h}(k_1,k_2,k_3) = \frac{1}{4\pi}\int_{-1}^{1}\mathrm{d}\mu_1 \int_0^{2\pi} \mathrm{d}\phi\, B^{r,h}(k_1,k_2,k_3,\mu_1,\mu_2(\mu_1,\phi)) \ , \tag{7.5}$$

where $\mu_i = \hat{k}_i\cdot\hat{z}$, and explicitly, from the triangle conditions:

$$\mu_2(\mu_1,\phi) = \mu_1 \hat{k}_1\cdot\hat{k}_2 + \sqrt{1-\mu_1^2}\sqrt{1-(\hat{k}_1\cdot\hat{k}_2)^2}\,\sin\phi \ , \tag{7.6}$$

$$\mu_3(\mu_1,\phi) = -k_3^{-1}(k_1\mu_1 + k_2\mu_2(\mu_1,\phi)) \ . \tag{7.7}$$

The expectation values of the estimator used by `Rustico` for the quadrupoles are:

$$B_{(2,1)}^{r,h}(k_1,k_2,k_3) \equiv \frac{5}{4\pi}\int_{-1}^{1}\mathrm{d}\mu_1\int_0^{2\pi}\mathrm{d}\phi\, \mathcal{P}_2(\mu_1) B^{r,h}(k_1,k_2,k_3,\mu_1,\mu_2(\mu_1,\phi)) \ , \tag{7.8}$$

$$B_{(2,2)}^{r,h}(k_1,k_2,k_3) \equiv \frac{5}{4\pi}\int_{-1}^{1}\mathrm{d}\mu_1\int_0^{2\pi}\mathrm{d}\phi\, \mathcal{P}_2(\mu_2(\mu_1,\phi)) B^{r,h}(k_1,k_2,k_3,\mu_1,\mu_2(\mu_1,\phi)) \ ,$$

$$B_{(2,3)}^{r,h}(k_1,k_2,k_3) \equiv \frac{5}{4\pi}\int_{-1}^{1}\mathrm{d}\mu_1\int_0^{2\pi}\mathrm{d}\phi\, \mathcal{P}_2(\mu_3(\mu_1,\phi)) B^{r,h}(k_1,k_2,k_3,\mu_1,\mu_2(\mu_1,\phi)) \ .$$

We work directly in this basis of quadrupoles, that are linear combinations of the B_{2m} coefficients of the spherical-harmonics expansion defined in [207]. We note that if only considering the bispectrum monopole, $c_2^{(222)}$ and $c_5^{(222)}$ become degenerate, so we redefine $c_2^{(222)} \to c_2^{(222)} - c_5^{(222)}/6$ ([7]).

[6] We have corrected a factor of $1/(4\pi)$ in Eq. (14) of [208].

[7] When considering in addition the bispectrum quadrupole at one loop, this degeneracy breaks.

7.4.2 IR-Resummation

The IR-resummation is a crucial effect to include in our theory model, in order to correctly reproduce the BAO. For the power spectrum, we use the full resummation of [209] as implemented in Pybird [169]. For the bispectrum instead we rely on a wiggle-no wiggle approximation, following [210]. For the linear bispectrum, the formula we implement is:

$$B_{211}^{r,h} = 2K_1^{r,h}(\vec{k}_1;\hat{z})K_1^{r,h}(\vec{k}_2;\hat{z})K_2^{r,h}(\vec{k}_1,\vec{k}_2;\hat{z})P_{\rm LO}(k_1)P_{\rm LO}(k_2) + \text{ 2 perms.}\,, \tag{7.9}$$

where

$$P_{\rm LO}(k) = P_{\rm nw}(k) + (1+k^2\Sigma^2_{\rm tot})e^{-k^2\Sigma^2_{\rm tot}}P_{\rm w}(k)\,. \tag{7.10}$$

Here $P_{\rm w}(k) = P_{11}(k) - P_{\rm nw}(k)$, and $P_{\rm nw}(k)$ is the no-wiggle power spectrum, which we obtain using the sine-transform algorithm described in [211] and detailed in [212]. Then $\Sigma^2_{\rm tot}$ is defined by

$$\Sigma^2_{\rm tot} = -\frac{2}{15}f^2\,\delta\Sigma^2 + \left(1+\frac{1}{3}f(2+f)\right)\Sigma^2\,, \tag{7.11}$$

$$\Sigma^2 = \frac{4\pi}{3}\int_0^\Lambda \frac{{\rm d}q}{(2\pi)^3}P_{\rm nw}(q)\left[1 - j_0(qx_{\rm osc}) + 2j_2(qx_{\rm osc})\right]\,, \tag{7.12}$$

$$\delta\Sigma^2 = 4\pi\int_0^\Lambda \frac{{\rm d}q}{(2\pi)^3}P_{\rm nw}(q)j_2(qx_{\rm osc})\,, \tag{7.13}$$

where we choose $\Lambda = 1\,h\,{\rm Mpc}^{-1}$ and $x_{\rm osc} = 110\,{\rm Mpc}\,h^{-1}$, and j_l are the spherical Bessel functions. [8] For the loop, our choice is to only substitute the non-integrated $P_{11}(k)$ with

$$P_{\rm NLO}(k) = P_{\rm nw}(k) + e^{-k^2\Sigma^2_{\rm tot}}P_{\rm w}(k)\,, \tag{7.14}$$

while for linear power spectra whose argument are being integrated, we use P_{11}. We discuss the goodness of this approximation in Sec. 7.6. Another method of BAO damping for the tree-level bispectrum was given and tested on Patchy mocks in [167].

[8] We have checked that changing Λ to $0.12h\,{\rm Mpc}^{-1}$ leads to insignificant differences in the posteriors.

7.4.3 Window Function

The power spectrum and bispectrum need to be convolved with the window function of the survey. For the power spectrum, this is standard and does not present numerical challenges. However, for the bispectrum this becomes more challenging. Therefore, we resort to an approximation used in [213], which amounts to evaluating the linear bispectrum with the windowed power spectrum. In formula, we have:

$$B_{211}^{r,h} = 2K_1^{r,h}(\vec{k}_1;\hat{z})K_1^{r,h}(\vec{k}_2;\hat{z})K_2^{r,h}(\vec{k}_1,\vec{k}_2;\hat{z})[W*P_{11}](\vec{k}_1)[W*P_{11}](\vec{k}_2) + \text{ 2 perms.}\,, \tag{7.15}$$

where $[W*P_{11}](\vec{k}) = \int \frac{\mathrm{d}^3k'}{(2\pi)^3} W(\vec{k}-\vec{k}')P_{11}(\vec{k}')$. Rather than projecting Eq. (7.15) into multipoles, we project Eq. (7.15) as if there was no window function, and for $[W*P_{11}](\vec{k})$ we use the following: for the monopole, we use $W \to W_{00}$ and, for the quadrupole we use $W \to W_{22}$, where W_{00} and W_{22} are defined in [7]. Because the window is a small effect, we do not apply it to the loop bispectrum. We discuss the goodness of this approximation in Sec. 7.6.

7.4.4 Alcock-Paczynski Effect

To estimate the galaxy spectra from data, a reference cosmology is assumed to transform the measured redshifts and celestial coordinates into three-dimensional cartesian coordinates. The difference between the reference cosmology and the true cosmology produces a geometrical distortion known as the Alcock-Paczynski (AP) effect [214]. We introduce the transverse and parallel distortion parameters:

$$q_\perp = \frac{D_A(z)H_0}{D_A^{\rm ref}(z)H_0^{\rm ref}}\,, \qquad q_\parallel = \frac{H^{\rm ref}(z)/H_0^{\rm ref}}{H(z)/H_0}\,, \tag{7.16}$$

where D_A is the angular diameter distance, and the factors of H_0 are there since our wavenumbers are in units $h\,\mathrm{Mpc}^{-1}$. In terms of these, the true wavenumber and angle with the line of sight are related to the ones in the reference cosmology by:

$$\begin{aligned} k &= \frac{k^{\rm ref}}{q_\perp}\left[1+(\mu^{\rm ref})^2\left(\frac{1}{F^2}-1\right)\right]^{1/2}\,, \\ \mu &= \frac{\mu^{\rm ref}}{F}\left[1+(\mu^{\rm ref})^2\left(\frac{1}{F^2}-1\right)\right]^{-1/2}\,, \end{aligned} \tag{7.17}$$

where $F = q_\parallel/q_\perp$. To match the measured power spectrum multipoles, we do the following integral:

$$P_\ell(k^{\rm ref}) = \frac{2\ell+1}{2q_\parallel q_\perp^2}\int_{-1}^{1} {\rm d}\mu^{\rm ref}\mathcal{L}_\ell(\mu^{\rm ref})P(k(k^{\rm ref},\mu^{\rm ref}),\mu(\mu^{\rm ref}))\,. \tag{7.18}$$

The formula for the bispectrum is:

$$B_{(\ell,i)}(k_1^{\rm ref},k_2^{\rm ref},k_3^{\rm ref}) = \frac{2\ell+1}{2q_\parallel^2 q_\perp^4}\int_{-1}^{1}{\rm d}\mu_1^{\rm ref}\int_0^{2\pi}\frac{{\rm d}\phi^{\rm ref}}{2\pi}B(k_1,k_2,k_3,\mu_1,\mu_2,\mu_3)\mathcal{P}_\ell(\mu_i)\,. \tag{7.19}$$

For the bispectrum, we only apply the Alcock-Paczynski effect on the tree-level part, as it is a small effect: we find that, within BOSS error bars (on Ω_m), it is an effect of at most $\sim 1\sigma$, and accordingly, the change in χ^2 is at most 1 if neglecting it completely. Given the size of the loop terms and counterterms, it is thus safe to neglect it there. We find that we can achieve sufficient numerical accuracy using a nested trapezoidal rule with only 13 points in μ and 4 points in ϕ, after using symmetries to restrict the integration domain to $\mu_1 \in [0,1]$, and $\phi \in [-\pi/2,\pi/2]$.

7.4.5 Binning

For the power spectrum, data are an average over spherical shells in momentum space. The theoretical prediction needs therefore to be averaged over the fundamental modes of the chosen grid. Since our bins have many fundamental modes, in practice we do an integral of the power spectrum over a bin, which is numerically very simple. The effect of binning is anyway small for the power spectrum, with respect to the error bars of our data and simulations.

For the bispectrum, we have an average over fundamental (closed) triangles in a bin of width Δk around a central triangle with sides k_1, k_2, k_3. Especially for our chosen bins with $\Delta k \simeq 0.02$, it is important to take into account the binning effects when comparing the theory to the data. The average should be done as a sum over fundamental triangles:

$$B^{r,h}_{(\ell,i),{\rm bin}}(k_1,k_2,k_3) = \frac{2\ell+1}{N_T}\sum_{\vec{q}_1\in k_1}\sum_{\vec{q}_2\in k_2}\sum_{\vec{q}_2\in k_2}\delta_K(\vec{q}_1+\vec{q}_2+\vec{q}_3)B^{r,h}(\vec{q}_1,\vec{q}_2,\vec{q}_3)\mathcal{P}_\ell(\mu_i)\,, \tag{7.20}$$

and we note that, here and elsewhere, $B^{r,h}(\vec{q}_1,\vec{q}_2,\vec{q}_3)$ is the full redshift-space bispectrum, i.e. we have suppressed the dependence on $\hat{z}$ for notational convenience.

Here N_T is the number of fundamental triangles in the bin, δ_K is the Kronecker delta function, and the notation $\vec{q}_i \in k_i$ means a sum over the fundamental modes $\vec{q}_i$ for which $k_i - \frac{\Delta k}{2} \leq |\vec{q}_i| < k_i + \frac{\Delta k}{2}$. Calculating such a sum is numerically very challenging. However, since in each bin there are many fundamental triangles, we expect that an integral approximation should work well. The only caveat is that one needs to integrate only over the closed triangles. In particular, this is very important for bins such that $k_3 + \Delta k/2 > k_1 + k_2 - \Delta k$ (remember that our ordering is $k_1 \leq k_2 \leq k_3$), for which there are configurations of modes that do not form a closed triangle in the bin.

Therefore, we implement the following formula:

$$B^{r,h}_{(\ell,i),\mathrm{bin}}(k_1,k_2,k_3) = \tag{7.21}$$
$$= \frac{2\ell+1}{V_T}\left(\prod_{i=1}^{3}\int_{V_i}\frac{\mathrm{d}^3q_i}{(2\pi)^3}\right)(2\pi)^3\delta_D^{(3)}(\vec{q}_1+\vec{q}_2+\vec{q}_3)B^{r,h}(\vec{q}_1,\vec{q}_2,\vec{q}_3)\mathcal{P}_\ell(\mu_i)\,,$$

where

$$V_T \equiv \left(\prod_{i=1}^{3}\int_{V_i}\frac{\mathrm{d}^3q_i}{(2\pi)^3}\right)(2\pi)^3\delta_D^{(3)}(\vec{q}_1+\vec{q}_2+\vec{q}_3)\,, \tag{7.22}$$

and we used the notation

$$\int_{V_i}\frac{\mathrm{d}^3q_i}{(2\pi)^3} = \int_{k_i}\frac{\mathrm{d}q_i}{2\pi^2}q_i^2\int\frac{\mathrm{d}^2\hat{q}_i}{4\pi}\,, \quad \text{where} \quad \int_{k_i} \equiv \int_{k_i-\frac{\Delta k}{2}}^{k_i+\frac{\Delta k}{2}}\mathrm{d}q_i\,. \tag{7.23}$$

As shown in App. C.1, we can perform the angular integrals and find

$$B^{r,h}_{(\ell,i),\mathrm{bin}}(k_1,k_2,k_3) = \frac{1}{V_T}\int_{k_1}\mathrm{d}q_1\int_{k_2}\mathrm{d}q_2\int_{k_3}\mathrm{d}q_3\,q_1q_2q_3\,\frac{\beta\left(\Delta_q\right)}{8\pi^4}B^{r,h}_{(\ell,i)}(q_1,q_2,q_3)\,, \tag{7.24}$$

$$V_T = \int_{k_1}\mathrm{d}q_1\int_{k_2}\mathrm{d}q_2\int_{k_3}\mathrm{d}q_3\,q_1q_2q_3\,\frac{\beta\left(\Delta_q\right)}{8\pi^4}\,, \tag{7.25}$$

where $\beta(\Delta_q) = 1/2$ if q_1, q_2, q_3 form a folded triangle, $\beta(\Delta_q) = 1$ for all other (closed) triangles, and $\beta(\Delta_q) = 0$ otherwise.

We apply only the binning in this way to the tree-level part. For efficient numerical evaluation of the integrals in Eq. (7.24), we implement the bispectrum binning as follow. For a given bin centered in (k_1, k_2, k_3), we enforce that (q_1, q_2, q_3) forms a triangle by redefining the integration boundaries: $q_1 \in [k_1 - \Delta k/2, k_1 + \Delta k/2]$, $q_2 \in [k_2 - \Delta k/2, k_2 + \Delta k/2]$, and $q_3 \in [|k_1 - k_2|, k_1 + k_2]$. Whenever q_3 can not satisfy this triangle inequality, we drop this configuration. As such, we can

drop the $\beta(\Delta_q)$ function inside the integral. We perform a change of variable $q_3 \to \cos(\theta_{12}) \equiv (q_3^2 - q_1^2 - q_2^2)/(2q_1q_2)$, such that the integral measure becomes $q_1q_2q_3\,\mathrm{d}q_1\mathrm{d}q_2\mathrm{d}q_3 \to q_1^2q_2^2\,\mathrm{d}q_1\mathrm{d}q_2\mathrm{d}\cos(\theta_{12})$, We then discretize the integration domain in 6 evenly-spaced points in q_1, 6 in q_2, and 4 in $\cos(\theta_{12})$. On each point of this grid, we evaluate the 14 pieces of the tree-level part of the bispectrum. The binning integrals are then performed with a nested trapezoidal rule over the grid. Given that the AP integrals, Eq. (7.19), need to be performed for each of those evaluations, we limit the number of evaluations by first looking for (and storing) the common triangles of the discretized domains over all the bins we need to evaluate. For our 150 bins in CMASS, this reduces the total number of evaluations by about a factor 1.5, from $6 \cdot 6 \cdot 4 \cdot 150 = 21600$ to 13782. After compilation of the integrand expressions going in the AP integrals, we are able to evaluate the binned bispectrum in our Python code with an overall runtime of ~ 1 second on 1 CPU. The numerical precision of such evaluation has been extensively tested, in particular against Monte-Carlo integrations, and is found to be under control for the data and simulations error bars we analyze in this work.

The loop pieces and counterterms, that are small with respect to the linear term, are instead evaluated on effective wavenumbers. [9] They are defined, as described in [215], by the following averages:

$$k_{\mathrm{eff},1} = \frac{1}{V_T}\int_{k_1}\frac{\mathrm{d}q_1}{2\pi}\int_{k_2}\frac{\mathrm{d}q_2}{2\pi}\int_{k_3}\frac{\mathrm{d}q_3}{2\pi}\, q_1q_2q_3\,\beta\left(\Delta_q\right)\min(q_1,q_2,q_3)\,, \tag{7.26}$$

$$k_{\mathrm{eff},2} = \frac{1}{V_T}\int_{k_1}\frac{\mathrm{d}q_1}{2\pi}\int_{k_2}\frac{\mathrm{d}q_2}{2\pi}\int_{k_3}\frac{\mathrm{d}q_3}{2\pi}\, q_1q_2q_3\,\beta\left(\Delta_q\right)\mathrm{med}(q_1,q_2,q_3)\,, \tag{7.27}$$

$$k_{\mathrm{eff},3} = \frac{1}{V_T}\int_{k_1}\frac{\mathrm{d}q_1}{2\pi}\int_{k_2}\frac{\mathrm{d}q_2}{2\pi}\int_{k_3}\frac{\mathrm{d}q_3}{2\pi}\, q_1q_2q_3\,\beta\left(\Delta_q\right)\max(q_1,q_2,q_3)\,. \tag{7.28}$$

As expected from the size of those terms and the size of the binning effect ($\sim 1\sigma$), we have checked that properly binning the loop instead of evaluating them on these effective wavenumbers lead to negligible shift in the $\min\chi^2$ and in the posteriors for the analyses presented in this work.

[9] We checked that binning the loop did not lead to appreciable different posteriors.

7.5 Likelihood

To analyze the data, we start from a Gaussian likelihood, which is multiplied by the prior to arrive at the Bayesian posterior $\mathcal{P}$ over cosmological and bias parameters:

$$-2\ln\mathcal{P} = (T_i - D_i)C_{ij}^{-1}(T_j - D_j) - 2\ln\mathcal{P}_{\rm pr}\,, \tag{7.29}$$

where T_i is the full vector of theory predictions in bin i, containing power spectrum multipoles and bispectra, D_i the corresponding data measurement in bin i, C_{ij} is the full covariance between bins i and j, and $\mathcal{P}_{\rm pr}$ is a generic prior on the parameters.

Our theory model depends on cosmological and EFT parameters. It is the case that many EFT parameters appear linearly in the theory model. Denoting them by g_α, we can write

$$T_i = g_\alpha T^\alpha_{G,i} + T_{NG,i}\ , \tag{7.30}$$

where $T^\alpha_{G,i}$ and $T_{NG,i}$ depend non-linearly (that is, at least quadratically) on the other cosmological parameters and three biases for each sky cut. Since we are interested in the marginalized posteriors over cosmological parameters, it is very convenient to do the analytical Gaussian integration over the g_α. We will also choose a Gaussian prior on them, with covariance $\sigma_{\alpha\beta}$ and mean $\hat{g}_\alpha$. [10] Collecting the powers of g_α, we can write the posterior in the following form:

$$-2\ln\mathcal{P} = g_\alpha F_{2,\alpha\beta} g_\beta - 2g_\alpha F_{1,\alpha} + F_0\,, \tag{7.31}$$

where the F's are defined as:

$$F_{2,\alpha\beta} = T^\alpha_{G,i}C^{-1}_{ij}T^\beta_{G,j} + \sigma^{-1}_{\alpha\beta}\,, \tag{7.32}$$

$$F_{1,\alpha} = -T^\alpha_{G,i}C^{-1}_{ij}(T_{NG,j} - D_j) + \sigma^{-1}_{\alpha\beta}\hat{g}_\beta\,, \tag{7.33}$$

$$F_0 = (T_{NG,i} - D_i)C^{-1}_{ij}(T_{NG,j} - D_j) + \hat{g}_\alpha\sigma^{-1}_{\alpha\beta}\hat{g}_\beta - 2\ln\Pi\,, \tag{7.34}$$

where Π is a generic prior on the cosmological and bias parameters non analytically marginalized. In other words, we assume that $\mathcal{P}_{\rm pr}$ is a sum of a Gaussian prior over the g_α and a remaining prior on the other parameters. After integrating the g_α, we have the marginalized posterior:

$$-2\ln\mathcal{P}_{\rm marg} = -F_{1,\alpha}F^{-1}_{2,\alpha\beta}F_{1,\beta} + F_0 + \ln\det\left(\frac{F_2}{2\pi}\right)\,. \tag{7.35}$$

[10] We only use $\hat{g}_\alpha \neq 0$ in one of the checks in Sec. 7.6.

Prior. In our analysis, we vary the cosmological parameters ω_{cdm}, h, and $\ln(10^{10}A_s)$ with a flat uninformative prior, while we use a Gaussian prior on ω_b of mean $\omega_{b,\rm BBN} = 0.02233$ and standard deviation $\sigma_{\rm BBN} = 0.00036$, motivated from Big-Bang Nucleosynthesis (BBN) experiments [216]. We instead fix n_s to the truth of the simulations or to the Planck preferred value when analyzing the data [24]. When analyzing the BOSS data, we also fix the neutrino to minimal mass following Planck prescription. [11]

The EFT parameters should instead be restricted to be $\mathcal{O}(1)$ numbers, for consistency of the perturbative expansion. The EFTofLSS is an expansion in the size of fluctuations and derivatives. Both of these are suppressed by a nonlinear scale $k_{\rm NL} \simeq k_{\rm M} \simeq 0.7h\,{\rm Mpc}^{-1}$, where $k_{\rm NL}$ is the nonlinear scale for the matter field, and $k_{\rm M}$ is the typical wavenumber associated to galaxy size. However, it was recognized in [144, 217] that terms involving expectation values of velocity fields, coming from the transformation to redshift space, define a new scale, which we denote by $k_{\rm NL,R} \simeq k_{\rm NL}/\sqrt{8}$. We therefore write down each operator in the EFT expansion with either a $k_{\rm M}$ or a $k_{\rm NL,R}$ suppression, depending on its origin. We then use a Gaussian prior of width 2 centered on 0 on all the EFT parameters that we analytically marginalize, with the following exception: on $c_{h,1}, c_{\pi,1}, c_{\pi v,1}$, and $c_2^{\rm St}$, that already appear in the power spectrum (see their definitions in Ch. 6), we put instead a Gaussian prior of width 4 centered on 0, such that the prior is the same as the ones used in our previous series of analyses with the power spectrum only (see e.g. [7, 143, 162]). For the quadratic biases, we define the linear combinations $c_2 = (b_2+b_5)/\sqrt{2}$, $c_4 = (b_2-b_5)/\sqrt{2}$, and we assign on them a Gaussian prior of width 2 centered on 0. Finally, for b_1, which is positive definite, we use a lognormal prior of mean 0.8 (since $e^{0.8} = 2.23$), and variance 0.8, such that $[0, 3.4]$ is the 68% bound for this prior on b_1. For definiteness, in our prior, we take $k_{\rm NL} = k_{\rm M} = 0.7h\,{\rm Mpc}^{-1}$ and $\bar{n} = 4 \cdot 10^{-4}({\rm Mpc}/h)^3$.

When analyzing more than one sky, we can use the information that the bias and EFT parameters should be the same at the same redshift, and their time evolution is expected to be comparable to the growth factor to some small power. This allows us to estimate the variation of b_1 between CMASS or LOWZ effective redshifts, to be about 20%. Therefore, in our multisky analyses the biases are correlated, which, as explained in the following section, helps to mitigate prior volume effects. In practice, let us consider the 4-sky analysis and the b_1 parameters, which will be a

[11] As we describe later in Sec. 7.6, we add a linear prior on Ω_m, h and b_1 in order to mitigate phase-space projection effects.

vector $(b_1^{(1)}, b_1^{(2)}, b_1^{(3)}, b_1^{(4)})$, with one $b_1^{(i)}$ for each sky. The prior on it is a multivariate lognormal with correlation matrix:

$$\begin{pmatrix} 1 & \rho_{12} & \rho_{13} & \rho_{12}\rho_{13} \\ \rho_{12} & 1 & \rho_{12}\rho_{13} & \rho_{13} \\ \rho_{13} & \rho_{12}\rho_{13} & 1 & \rho_{12} \\ \rho_{12}\rho_{13} & \rho_{13} & \rho_{12} & 1 \end{pmatrix}, \tag{7.36}$$

where $\rho_{ij} = 1 - \epsilon_{ij}^2/2$, and we choose $\epsilon_{12} = 0.1$, $\epsilon_{13} = 0.2$. This formula is motivated by the fact that two variables distributed according to a bivariate normal with correlation ρ, the standard deviation of the difference is $\epsilon = \sqrt{2(1-\rho)}$. Our choices of ϵ_{ij} then reflect that we expect the values of b_1 to be different only by about 10% between NGC and SGC, given slightly different selection function, and only by about 20% between CMASS and LOWZ, given the redshift evolution of b_1. We use the same correlation matrix for the Gaussian priors on all the quadruplets c_2, c_4 and the g_α parameters.

Posterior Sampling. Our analyses are performed using the Metropolis-Hastings sampler as implemented in `MontePython 3` [218], with the theory model evaluated using `CLASS` [27] and `PyBird`. We declare our MCMC converged when the Gelman-Rubin criterion [219] is ≤ 0.02. The plots and summary statistics are calculated with the `GetDist` [220] package.

7.6 Pipeline Validation

For our analyses, we use the following scale cut: $k_{\rm min} = 0.01h\,{\rm Mpc}^{-1}$ for all observables, $k_{\rm max} = 0.23h\,{\rm Mpc}^{-1}$ for P_ℓ and B_0, and $k_{\rm max} = 0.08h\,{\rm Mpc}^{-1}$ for B_2, on CMASS. For LOWZ instead, we use $k_{\rm max} = 0.20h\,{\rm Mpc}^{-1}$ for P_ℓ and B_0 , following [7]. We keep $k_{\rm max} = 0.08h\,{\rm Mpc}^{-1}$ for B_2 on LOWZ. [12] In this section, we perform multiple checks to validate our method at this scale cut.

[12]For comparison purpose, we sometimes fit B_0 using the tree-level prediction instead. When doing so, B_0 is denoted $B_0^{\rm tree}$ (to distinguish from $B_0^{\rm 1loop}$) and is fitted up to $k_{\rm max} = 0.08h\,{\rm Mpc}^{-1}$ for both CMASS and LOWZ.

7.6.1 Measuring and Fixing Phase-Space Effects

Our likelihood has several EFT parameters on top of the cosmological parameters. Some of these appear in the likelihood in a Gaussian way, and we analytically marginalize over them. Performing such a Gaussian integral corresponds to putting these parameters to their best fit values, given all the other parameters and observational data. At this point, we are left with a likelihood which has a non-Gaussian dependence on the EFT and the cosmological parameters.

Now, there is an interesting phenomenon that we would like to describe. Let us analyze data that are generated with our theory model: the EFTofLSS plus observational effects as described in Sec. 7.4. We refer to these as 'synthetic' data. We generate these synthetic data by choosing the best fit EFT parameters that we find by fitting the average of 2048 Patchy simulations, on the Patchy cosmology, so that the resulting EFT and cosmological parameters are at realistic values. In this case, the best fit has $\chi^2 = 0$ once we put flat priors on the EFT parameters, and we should clearly recover the correct cosmological parameters. However, as it can be seen from Fig. 7.3, in green, the sampled posteriors show biases in all 1D posteriors of the cosmological parameters, and in particular in σ_8 and Ω_m. What is going on?

The first hypothesis is that there could be an error in our pipeline. This hypothesis can be discarded by noticing that if we analyze the data with a covariance that is about 100 times smaller, we recover the truth with exquisite precision (see the blue curve in Fig. 7.3). So, we exclude this hypothesis.

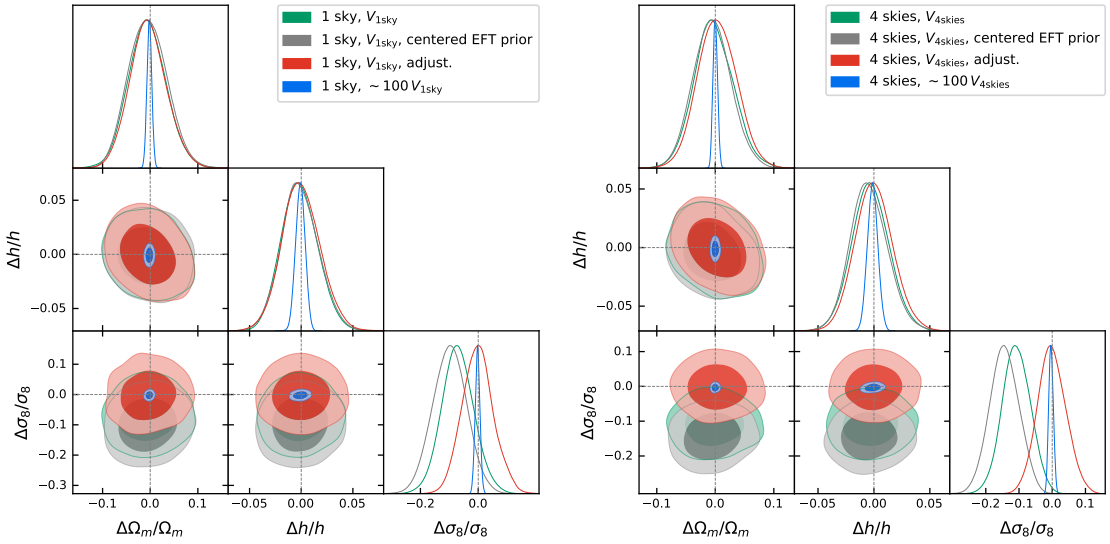

$\sigma_{\rm proj}/\sigma_{\rm stat}$	Ω_m	h	σ_8	ω_{cdm}	$\ln(10^{10}A_s)$	S_8
1 sky, $\sim 100\,V_{1\rm sky}$	-0.1	-0.14	-0.21	-0.2	-0.07	-0.23
1 sky, $V_{1\rm sky}$, adjust.	0.13	0.06	0.04	0.15	-0.04	0.08
4 skies, $V_{4\rm skies}$, adjust.	0.1	0.	-0.05	0.07	-0.06	-0.01

Figure 7.3: Triangle plots of base cosmological parameters obtained fitting synthetic data analyzed using a covariance with BOSS volume $V_{\rm BOSS}$ or rescaled to a large volume $\sim 100V_{\rm BOSS}$, with prior on the EFT parameters centered on their truth, or with phase-space projection adjustment. Here the synthetic data are corresponding exactly to our model $P_\ell + B_0 + B_2$ on the best fit of patchy. '1 sky' or '4 skies' correspond to CMASS NGC or all BOSS skycuts, respectively. The grey lines in the triangle plots represent the truth. We also show the relative deviations $\sigma_{\rm proj}/\sigma_{\rm stat}$ on the base cosmological parameters from the truth from those various analyses. In summary, the addition of a phase-space correction prior to our likelihood allows us to recover unbiased mean in the 1D posteriors of the cosmological parameters of interest.

$\sigma_{\rm proj}/\sigma^{\rm data}_{\rm stat}$		Ω_m	h	σ_8	ω_{cdm}	$\ln(10^{10}A_s)$	S_8
Nseries	P_ℓ	-0.02	0.05	0.08	0.02	0.05	0.07
	$P_\ell + B_0$	-0.06	-0.03	-0.04	-0.08	0.03	-0.06
	$P_\ell + B_0 + B_2$	-0.12	-0.	-0.04	-0.11	0.04	-0.08
1 sky	P_ℓ	-0.15	0.07	-0.11	-0.06	-0.08	-0.15
	$P_\ell + B_0$	0.07	0.06	0.09	0.11	0.02	0.1
	$P_\ell + B_0 + B_2$	0.13	0.06	0.04	0.15	-0.04	0.08
4 skies	P_ℓ	-0.01	0.05	-0.03	0.02	-0.04	-0.03
	$P_\ell + B_0$	0.05	-0.	0.01	0.03	0.01	0.03
	$P_\ell + B_0 + B_2$	0.1	0.	-0.05	0.07	-0.06	-0.01

Table 7.1: Residual deviations $\sigma_{\rm proj}$ after phase-space projection adjustment measured on synthetic data generated and fitted with our model $P_\ell + B_0 + B_2$ with truth given by the best fits of Nseries, Patchy 1 sky, or Patchy 4 skies, relative to BOSS error bars $\sigma^{\rm data}_{\rm stat}$.

Another reason for the offset of the green curve in Fig. 7.3 could be the prior

on the EFT parameters. In fact, while on the synthetic data the EFT parameters have some definite values (which are well within the priors), our Gaussian priors are centered at zero, and so the true value of the EFT parameters are slightly disfavored by the priors. We check if this can be the reason to the offset seen in the posteriors of the cosmological parameters by sampling instead with priors centered around the synthetic truth. We find that the resulting posteriors are close to previous results (grey vs. green in Fig. 7.3), suggesting that the central value of the prior of the bias parameters does not play a substantial role. This means that even if the truth is the maximum likelihood point, the posteriors will not recover it.

Having excluded that the bias in the posteriors on synthetic data is due to an error in our pipeline or due to our priors, we conclude that it must be due to phase-space projection effects. In fact, if the posteriors of the EFT parameters are effectively non-Gaussian (*i.e.* if the error bars are sufficiently large that the Taylor expansion at second order around the maximum of the posterior is not accurate enough to describe the actual posterior), then, upon marginalization, one can get projection effects on the remaining parameters, which, in this case, are the cosmological ones, even if the maximum likelihood point is the truth. Given the large number of EFT parameters, it is not so surprising that this might be the case. We call this effect 'phase space effect,' but it is also known as 'prior volume effect' or 'projection effect.'

We decide to fix this issue with the following procedure. As a measurement of the phase-space effect, for all analyses in this work, we take the shift in the 1D posteriors from the truth obtained fitting synthetic data with the same modeling and covariance. We add a prior of the following form to the log-likelihood of $P_\ell + B_0(+B_2)$:

$$\begin{aligned} \ln \mathcal{P}_{\rm pr}^{\text{ph. sp. 1sky}} &= -18\left(\frac{b_1}{2}\right) + 8\left(\frac{\Omega_m}{0.31}\right) + 14\left(\frac{h}{0.68}\right) \ , \\ \ln \mathcal{P}_{\rm pr}^{\text{ph. sp. 4sky}} &= -48\left(\frac{b_1}{2}\right) + 32\left(\frac{\Omega_m}{0.31}\right) + 48\left(\frac{h}{0.68}\right) \ , \end{aligned} \tag{7.37}$$

respectively for 1 sky and 4 skies. [13] As such, upon marginalization, we recover

[13] When analyzing the power spectrum multipoles P_ℓ alone, we put the following prior instead:

$$\begin{aligned} \ln \mathcal{P}_{\rm pr}^{\text{ph. sp. 1sky}} &= 2\left(\frac{b_1}{2}\right) - 2\left(\frac{\Omega_m}{0.31}\right) \ , \\ \ln \mathcal{P}_{\rm pr}^{\text{ph. sp. 4sky}} &= -4\left(\frac{b_1}{2}\right) + 10\left(\frac{\Omega_m}{0.31}\right) + 14\left(\frac{h}{0.68}\right) \ . \end{aligned} \tag{7.38}$$

$\Delta_{\rm sys}/\sigma_{\rm stat}$	Ω_m	h	σ_8	ω_{cdm}	$\ln(10^{10}A_s)$	S_8
$P_\ell + B_0$: base - w/ NNLO	-0.03	-0.09	-0.03	-0.1	0.05	-0.04
$P_\ell + B_0$: base - w/o B_0 window	0.11	-0.05	0.01	0.05	-0.01	0.05
$P_\ell + B_0 + B_2$: base - w/o B_0, B_2 window	0.51	0.09	0.02	0.51	-0.25	0.19

Table 7.2: Relative shifts $\Delta_{\rm sys}/\sigma_{\rm stat}$ on base cosmological parameters measured from various modeling choices compared to our baseline: inclusion of the NNLO or removal of the window function in the bispectrum.

unbiased 1D posteriors from the fit to the synthetic data (see the red curve in Fig. 7.3 and also the associated table). More in detail, in Tab. 7.1, we show the residual deviation from phase-space projection on the base cosmological parameters measured from synthetic data. We see that for all data volume (either the one of CMASS NGC or of all BOSS 4 skies) and cosmologies tested here (either the one of Nseries or the one of Patchy), we find that the residual deviation are negligibly small ($\lesssim 0.15$ or the error bars obtained with BOSS-volume covariance). Since the synthetic data are close to the Patchy ones (and so to the data), and since we expect the phase-space projection effects to be a slowly-varying function of the cosmological and EFT parameters, we add the same phase-space-correcting prior to the likelihood of the BOSS data.

7.6.2 Scale Cut from NNLO

A simulation-independent way to evaluate the theoretical error as a function of $k_{\rm max}$ is to analyze the data by adding to the theory model a part of the next order terms: for our one-loop model, this part consists in the next-to-next-to-leading-order (NNLO) terms. Such a procedure was successfully applied to estimate the scale cut for the CF [162]. Here we use the same technique. We add the following two-loop counterterms to the EFTofLSS prediction at one-loop for the power spectrum:

$$P_{\rm NNLO}(k,\mu) = \frac{1}{4}c_{r,4}b_1^2\mu^4\frac{k^4}{k^4_{\rm NL,R}}P_{11}(k) + \frac{1}{4}c_{r,6}b_1\mu^6\frac{k^4}{k^4_{\rm NL,R}}P_{11}(k)\,, \tag{7.39}$$

and for the bispectrum:

$$B_{\rm NNLO}(k_1,k_2,k_3,\mu,\phi) = 2c_{\rm NNLO,1}K_2^{r,h}(\vec{k}_1,\vec{k}_2;\hat{z})K_1^{r,h}(\vec{k}_2;\hat{z})f\mu_1^2\frac{k_1^4}{k_{\rm NL,R}^4}P_{11}(k_1)P_{11}(k_2)$$
$$+ c_{\rm NNLO,2}K_1^{r,h}(\vec{k}_1;\hat{z})K_1^{r,h}(\vec{k}_2;\hat{z})P_{11}(k_1)P_{11}(k_2)f\mu_3 k_3\frac{(k_1^2+k_2^2)}{4k_1^2k_2^2k_{\rm NL,R}^4}\times \tag{7.40}$$
$$\times\Big[-2\vec{k}_1\cdot\vec{k}_2(k_1^3\mu_1+k_2^3\mu_2)+2f\mu_1\mu_2\mu_3k_1k_2k_3(k_1^2+k_2^2)\Big]+\text{perm.}\,,$$

where $k_{\rm NL,R} = k_{\rm NL}/\sqrt{8}$, as discussed in Sec. 7.5. The prefactors $c_{r,4}, c_{r,6}, c_{\rm NNLO,1}$, and $c_{\rm NNLO,2}$ are given a Gaussian prior centered on zero and of width 2. We then analyze the data as a function of $k_{\rm max}$, and determine the maximum wavenumber by taking the largest $k_{\rm max}$ where the shift in all 1D posteriors of the cosmological parameters with respect to the analysis without these terms is equal to $1/3\cdot\sigma$. This would mean that our results would have become sensitive to these terms that we do not fully compute, and so we need to analyze the data only up to this threshold. For simplicity, rather than determining the $k_{\rm max}$ in this way, we check the effect of these NNLO terms close to the $k_{\rm max}$ that we find in simulations, and check that the effect of the NNLO terms is indeed not too large. The results are presented in Tab. 7.2. We see that the effect is negligibly small, confirming what we find in simulations next, *i.e.* that our scale cut is appropriate.

7.6.3 Tests of Additional Modeling Effects

Our implementation of the IR-resummation and of the window function is approximate, without a control parameter. We therefore check the accuracy of the two implementations in the following way.

For the window function, the correctness of our approximation has been checked in [221] for the monopole. In fact, as shown in the second line of Tab. 7.2, the difference between the bispectrum computed with our approximation, and the one where we apply no window is within 1/4 of the error bars obtained on all cosmological parameters from the fit to BOSS data. For the quadrupole, the third line of Tab. 7.2 shows that the difference with applying no window is about 0.5σ on the posterior of Ω_m (while negligible for the other cosmological parameters). While this might seem too large an effect to tolerate, one should keep in mind the following. Roughly speaking, the correct window function should consist of applying 3/2 factors of W to the bispectrum (*i.e.* one for each field). Applying no window therefore is a radical negligence of all these factors, much worse than the approximation we do (which

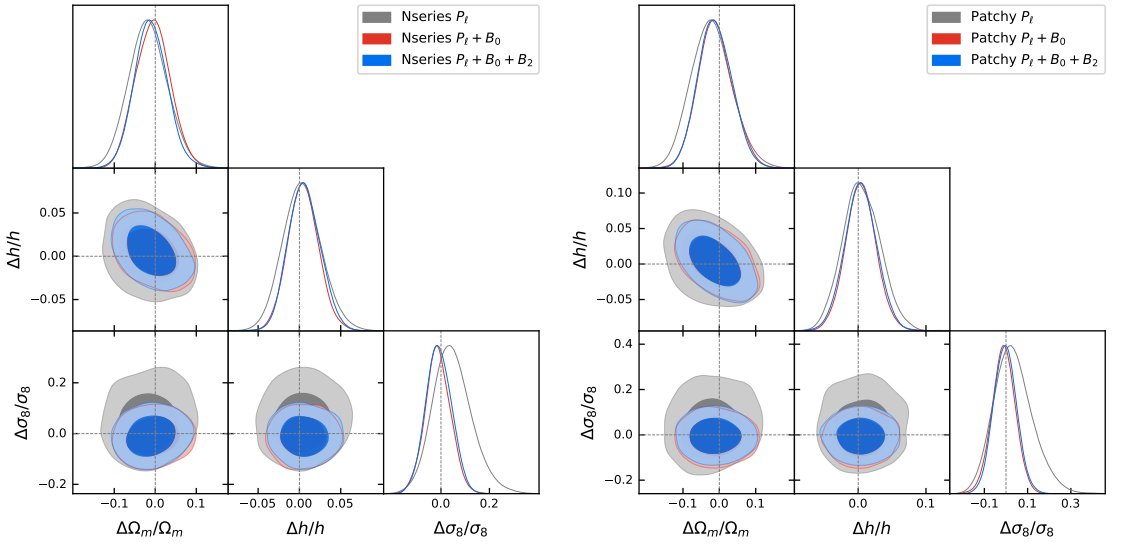

	$\Delta X/X$	Ω_m	h	σ_8	ω_{cdm}	$\ln(10^{10}A_s)$	S_8
Nseries	P_ℓ	-0.017 ± 0.048	$0.003^{+0.022}_{-0.024}$	$0.047^{+0.070}_{-0.086}$	$-0.013^{+0.063}_{-0.071}$	0.035 ± 0.055	$0.038^{+0.074}_{-0.092}$
	$P_\ell + B_0$	-0.005 ± 0.042	0.005 ± 0.019	-0.012 ± 0.052	$0.004^{+0.052}_{-0.058}$	-0.010 ± 0.040	-0.015 ± 0.058
	$P_\ell + B_0 + B_2$	-0.010 ± 0.041	$0.006^{+0.018}_{-0.021}$	-0.009 ± 0.053	0.001 ± 0.053	-0.007 ± 0.041	-0.014 ± 0.059
Patchy	P_ℓ	$-0.021^{+0.052}_{-0.059}$	0.005 ± 0.028	$0.034^{+0.076}_{-0.098}$	-0.014 ± 0.078	$0.026^{+0.056}_{-0.066}$	$0.022^{+0.083}_{-0.10}$
	$P_\ell + B_0$	$-0.011^{+0.044}_{-0.051}$	0.004 ± 0.023	-0.011 ± 0.054	$-0.004^{+0.052}_{-0.062}$	-0.006 ± 0.044	-0.017 ± 0.058
	$P_\ell + B_0 + B_2$	-0.012 ± 0.046	0.004 ± 0.024	-0.004 ± 0.053	$-0.006^{+0.052}_{-0.059}$	-0.001 ± 0.043	-0.011 ± 0.058

Figure 7.4: Triangle plots and relative 68%-credible intervals of base cosmological parameters measured from the Nseries and Patchy simulations analyzed using a covariance with CMASS NGC volume. The grey lines in the triangle plots represent the simulation truth.

applies two factors of W). We therefore believe that a more reliable estimate of the error associated to our implementation of the window function for the quadrupole is obtained by dividing the effect in Tab. 7.2 by a factor of 4. Even if our estimate were to be wrong by a factor 2, this would make the effect safely negligible. It would be interesting to compare our approach to an analysis using another estimator based on tri-polar spherical harmonics (described in [165] and tested on Patchy mocks in [167]) for which the window functions can be estimated on an equal footing, making its application more straightforward.

Let us now discuss the goodness of our approximate implementation of the IR-resummation of the bispectrum. It should be emphasized that the wiggle/no-wiggle procedure is affected by several uncontrolled approximations (*i.e.* not controlled by a small parameter, but numerically accidentally small) [140]. On top of those, our formulas neglect the angle dependence of the IR-resummation, and, perhaps even more quantitatively importantly, do not damp the oscillations in the power spectra

$\sigma_{\rm sys}^{\rm sim}/\sigma_{\rm stat}^{\rm data}$	Ω_m	h	σ_8	ω_{cdm}	$\ln(10^{10}A_s)$	S_8
Nseries $P_\ell + B_0$	0.02	0.17	0.15	-0.03	0.17	0.17
Nseries $P_\ell + B_0 + B_2$	0.16	0.25	0.08	-0.09	0.08	0.16
Patchy $P_\ell + B_0$	0.27	0.21	0.23	0.05	0.14	0.33
Patchy $P_\ell + B_0 + B_2$	0.31	0.2	0.07	0.09	0	0.2

Table 7.3: Report of systematic errors on base cosmological parameters measured from the Nseries and Patchy simulations. The systematic error, reported relative to the BOSS error bars $\sigma_{\rm stat}^{\rm data}$, is defined as $\sigma_{\rm sys}^{\rm sim} \equiv \max(|\text{mean} - \text{truth}| - \sigma_{\rm stat}^{\rm sim}/\sqrt{N_{\rm sim}}, 0)$. Here $\sigma_{\rm stat}^{\rm sim}/\sqrt{N_{\rm sim}}$ represents the uncertainty from the simulation cosmic variance, which corresponds to about 0.15 or 0.03 in $\sigma_{\rm stat}^{\rm data}$ for $N_{\rm sim} = 84$ Nseries or $N_{\rm sim} = 2048$ Patchy realizations, respectively.

whose momenta are integrated in the loop integrals, as for example proposed in [210]. We checked that applying the damping for those power spectra leads to a negligible ($\lesssim 0.25$) change in the χ^2 when keeping all the parameters of the model fixed. We therefore conclude that neglecting the IR-resummation on the 'wiggly' parts from inside the loop integrals is accurate enough for BOSS data. We leave to future work more careful inspection of the remaining approximations in our IR-resummation scheme.

7.6.4 Tests against Simulations

We now test the accuracy of the model by comparing against N-body simulations described in Sec. 7.3. This does not only test the effect of the theoretical error due to the next order terms not included in our baseline model or to the approximate IR-resummation, but also of the other observational effects that we model imperfectly, such as the window function. In Fig. 7.4, we show the posteriors from the analysis of the average of 84 Nseries boxes, analyzed with the covariance of one box, such that we also account for the phase space effect. Since the actual cosmic variance associated to this average of 84 boxes is about 1/9 of the posteriors in Fig. 7.4, we measure for each cosmological parameter the theoretical error as the distance of the mean of the posterior to the truth of the simulation minus 1/9 of the standard deviation (we take zero if this number is negative). This allows us to detect theoretical errors larger than 1/9 of a standard deviation of the posterior in Fig. 7.4, which corresponds to about 0.15 of the of the error bars obtained on the BOSS data. Our results show that the theoretical error that we can detect is safely below 1/3 of the error bars obtained on BOSS, as summarized in Tab. 7.3.

In Fig. 7.4, we also present the analogous analysis on the average of 2048 Patchy mocks. In this case, the detectable theoretical error is almost unaffected by cosmic

	$N_{\rm bin}$ // dof	$\min\chi^2$	$\min\chi^2$/dof	p-value
CMASS NGC	$42+150+9=201$	159.5	0.79	0.99
CMASS SGC	$42+150+9=201$	188.7	0.94	0.72
LOWZ NGC	$36+62+9=107$	98.3	0.92	0.71
LOWZ SGC	$36+62+9=107$	106.4	0.99	0.50
Parameter Prior	$3+41(1+0.1+0.2+0.1\cdot 0.2)\simeq 57$	8.9	-	-
Total	$616-57=559$	561.9	1.01	0.46

Table 7.4: Goodness of fit given by the maximal log-likelihood value $\log\mathcal{L}\equiv-\min\chi^2/2$ obtained fitting BOSS 4 skies $P_\ell+B_0+B_2$, and associated p-value. For each skycut, we detail the number of bins $N_{\rm bin}=N_{\rm bin}^{P_\ell}+N_{\rm bin}^{B_0}+N_{\rm bin}^{B_2}$, while in 'Parameter Prior' we give instead the degrees of freedom (dof). The dof are taken as the sum of 3 varied cosmological parameters (that are not prior dominated) plus an effective number of correlated EFT parameters. The p-value are calculated assuming there is no correlation within the data.

variance. Thus, assuming no systematic error in the Patchy simulations, the minimal detectable theoretical error is practically zero. Also in this case, the theoretical error is safely below 1/3 the error bars obtained on BOSS, as summarized in Tab. 7.3.

We conclude that our analysis pipeline is free from significant systematics for BOSS volume at the scale cuts chosen at the beginning of this section, and we now move on to the analysis of the observational data.

7.7 Results

When analyzing the BOSS data, we find that there is no additional gain by adding all the three independent quadrupoles after one has been included. We therefore present results including only $B^{r,h}_{(2,3)}$.

In Fig. 7.2, we show the best fit residuals and in Tab. 7.4 the best-fit χ^2 and associated p-value. The p-value is very good and we do not find any concerning systematic behavior in the residuals. In Fig. 7.1, we provide the best-fit parameters, which safely lie within our 68%-credible intervals.

The posteriors associated to the analysis of the BOSS data are presented in Figs. 7.1 and 7.5. They are discussed in the Introduction. In App. C.2 we provide the posteriors for the other non-marginalized parameters as well their confidence interval. One can see that the bispectrum improves their measurement by order 100%.

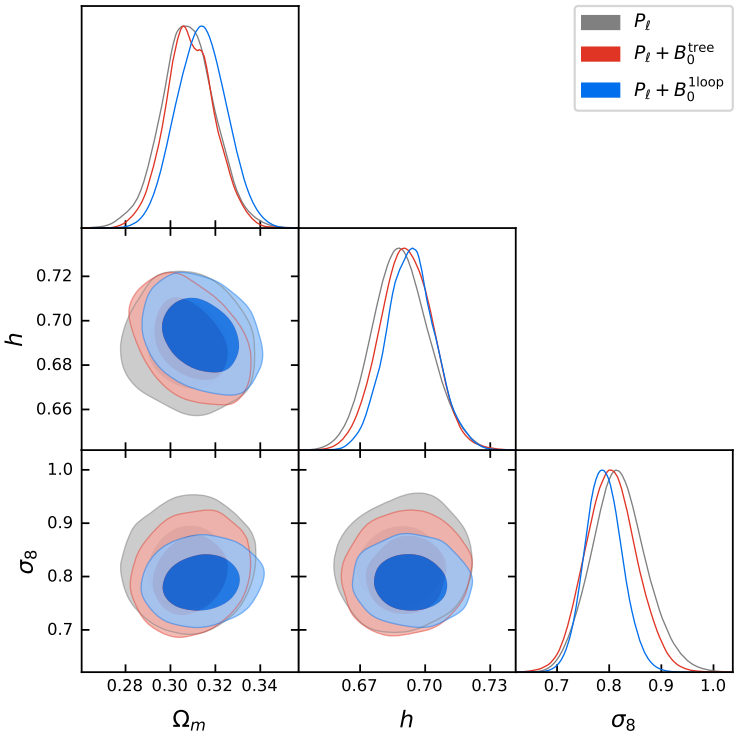

Figure 7.5: Triangle plots of base cosmological parameters measured from the analysis of BOSS power spectrum multipoles P_ℓ, $\ell = 0, 2$, at one-loop, and bispectrum monopole B_0 at tree or one-loop level.

8

Forecasts: Peeking into the Next Decade in LSS Cosmology with its EFT

8.1 Summary

After the successful full-shape analyses of BOSS data using the Effective Field Theory of Large-Scale Structure, we investigate what upcoming galaxy surveys might achieve. We introduce a “perturbativity prior" that ensures that loop terms are as large as theoretically expected, which is effective in the case of a large number of EFT parameters. After validating our technique by comparison with already-performed analyses of BOSS data, we provide Fisher forecasts using the one-loop prediction for power spectrum and bispectrum for two benchmark surveys: DESI and MegaMapper. We find overall great improvements on the cosmological parameters. In particular, we find that MegaMapper (DESI) should obtain at least a 12σ (2σ) evidence for non-vanishing neutrino masses, bound the curvature Ω_k to 0.0012 (0.012), and primordial inflationary non-Gaussianities as follows: $f_{NL}^{\text{loc.}}$ to ± 0.26 (3.3), $f_{\text{NL}}^{\text{eq.}}$ to ± 16 (92), $f_{\text{NL}}^{\text{orth.}}$ to ± 4.2 (27). Such measurements would provide much insight on the theory of Inflation. We investigate the limiting factor of shot noise and ignorance of the EFT parameters.

8.2 Introduction

In the last few years, Large-Scale Structure (LSS) survey data have started to be analyzed using the so-called Effective Field Theory of Large-Scale Structure (EFTofLSS) [30, 28]. The approach in which the data are analyzed in the context of this theory is rather simple: all data below a certain maximum wavenumber are used in the Bayesian inference. This technique goes under the name of "full shape analysis". Such an application to data has allowed a measurement of all cosmological parameters of the ΛCDM model using just a prior from Big Bang Nucleosynthesis [7, 142, 143]. The precision and accuracy achieved through this measurement were unexpectedly high, offering a new independent method for determining the Hubble constant with a percent-level precision [7], and for measuring Ω_m with a precision comparable to Planck [24], among other remarkable achievements. It should be stressed that the development of the EFTofLSS was a rather long journey in which the theory was developed in the various stages that are necessary to compare it to observations (dark matter, galaxies, redshift space distortions, IR-resummation, fast-evaluation techniques, MonteCarlo sampling, etc.), and along the way comparison with numerical simulations was essential to check that the theory was on the right track. Because of this, we find it fair, and also useful for the interested reader, to provide a footnote with a list of the references that were essential for the development of the EFTofLSS prior to its application to data, when it finally became clear that the approach was useful.

So far, the data analysis has mainly focused on the data from BOSS DR12 [9]. While there are certainly more ways in which these data can be analyzed, with many much-improved LSS surveys coming online and being designed, it is natural to ask what kind of measurement the application of the so-far developed EFTofLSS to these data will allow. In this chapter, we do this by Fisher forecasting the information content of two upcoming surveys, that we take as benchmarks, DESI [222], and MegaMapper [223], including some forecasts for further analyses on BOSS. Our intention is that the results for these two upcoming and planned surveys will give an idea of the capabilities of other further surveys, either already planned or to be planned. We primarily focus on the cosmological parameters of the flat ΛCDM model, while also considering neutrino masses, curvature, and primordial non-Gaussianities (for a forecast about CDM-isocurvature modes for Euclid and MegaMapper, using just the one-loop power spectrum and tree level bispectrum, see [224]). These are in fact parameters whose detection would allow us to extend

or ameliorate the standard model of cosmology and of particle physics.

For neutrinos, we know from neutrino oscillations that they are massive (see for example [225]), but we do not know the absolute value of their masses. For inflation, curvature should naturally be very small, to the order of the primordial perturbations $\sim 3 \cdot 10^{-5}$, though evidence of negative curvature could be extremely interesting, pointing towards the fact that our universe might come out of a bubble nucleation event (see for example [226] and references therein). A large positive curvature would essentially rule out eternal inflation, while a large negative curvature would rule out slow-roll eternal inflation [227]. Finally, non-Gaussianities could reveal the interaction structure of Inflation, which is actually the most insightful aspect to understand the particle physics origin of this theory. Concerning the shape of the non-Gaussianities we will explore, we will analyze the so-called $f_{NL}^{\rm loc.}$ (see e.g. [183]), $f_{\rm NL}^{\rm eq.}$ [179] and $f_{\rm NL}^{\rm orth.}$ [54] shapes, which parametrise a large class of non-Gaussianities that can be produced in single field inflation [47, 54], and, for $f_{NL}^{\rm loc.}$, also in multifield inflation (see e.g. [180, 181, 182, 56]) (see also recently [228] for a forecast on MegaMapper on these parameters using just the tree-level bispectrum). It should be stressed that there exist other shapes of non-Gaussianities that are well motivated (see e.g. [229]), and we leave their exploration to future work.

Let us summarize some important technical aspects of our analysis:

- We use the prediction of the EFTofLSS at one loop order for the power spectrum and the bispectrum. We provide the Fisher forecasts by utilizing all the multipoles of the line-of-sight angle.

- The model that we implement is the same as in the analyses of the BOSS data as in [3]. In particular, this includes the integration of the one-loop bispectrum integrals as developed in [206]. The modeling of primordial non-Gaussianities is done as in [176].

- We check the accuracy of our predictions against comparison with the posterior obtained by analyzing the BOSS data with the full-likelihood of [3]. We conclude that, approximately, our predictions for the error bars should be roughly accurate to about 30% or 40%, once the maximum wavenumber of the analysis has been fixed. This error is primarily influenced by our assumption of a diagonal covariance.

On top of the overall volume of the survey, we identify two limiting factors that affect the precision of the upcoming measurements. One is the discreteness of the

galaxy field, which induces a shot noise term in the data, and the second is the fact that dozens of EFT parameters, including biases, need to be fitted to the observations (these EFT parameters encode the effect at long distances from uncontrolled short distance physics, which includes the relation between galaxy overdensities and matter fields). We explore these issues in the following way:

1. **Shot noise:** In addition to our main analysis, we provide Fisher forecasts with shot noise set to zero, effectively assuming an infinitely dense distribution of galaxies.

2. **EFT parameters:** We investigate the impact of limited knowledge regarding the EFT parameters by conducting Fisher forecasts in the following three ways:

   (a) We set the width of the prior on the EFT parameters to zero, which is equivalent to fixing them. This represents the ultimate reach in terms of constraining power.

   (b) **Galaxy Formation Prior:** We set the width of the prior on the EFT parameters to 0.3 (rather than about 2 or 4 as in the normal analyses). This is meant to represent a perhaps realistic prior on the EFT parameters as informed by astrophysical galaxy formation studies.

   (c) **Perturbativity Prior:** Finally, we introduce a new, theoretically-justified prior on the EFT parameters that we call “perturbativity prior", which is based on the following reasoning. In the EFTofLSS, it is possible to estimate the correct size of a loop term given the lower order terms by simple scaling formulas. It is self-consistent to impose that the loop terms in the analysis obey this estimate. If the number of parameters to fit to observations is small, this criterium is automatically satisfied once the EFT parameters have been assigned a prior of $\mathcal{O}(1)$, which is the standard way in which priors are set (see for e.g. [3]). However, when the number of parameters becomes large, say $n \gg 1$, if each parameter is $\mathcal{O}(1)$, the size of the loop can be a factor of $\mathcal{O}\left(\sqrt{n}\right)$ too large, due to some random accumulation effect. It is easy to convince oneself that the data, which are most effective at the highest wavenumbers where the loop is sizable, might not provide sufficient constraining power to prevent such random accumulation effects from happening. In fact, due to cancellations among the various components of a loop term, it is possible that the loop is small at those high wavenumbers where both data and loop

are strong, while the loop could still be too large at intermediate and low wavenumbers. Indeed, at these intermediate and low wavenumbers, the data, being weaker, do not constrain the loop term, having this one become quite smaller in the meantime. We therefore set a Gaussian prior on the overall loop term, by favoring the configurations that satisfy the overall size and scaling as a function of wavenumber of the loop term. While this prior has not yet been tested on simulations or data, it is solidly theoretically justified, and we report results incorporating it.

We find the following results for DESI and MegaMapper for the various cosmological parameters:

- Ω_k: Planck 2018 constrains this parameter to 0.0065 [24]. For DESI, we forecast a constraint of about 0.051. MegaMapper instead will reduce this bound to 0.0012, representing an improvement of over 5 times compared to Planck, and just about 1.5 orders of magnitude away from the ultimate limit where it makes sense to measure this parameter, which is the amplitude of the primordial curvature fluctuation. We notice however that this bound depends quite strongly on the maximum wavenumber of the analysis.

- $\sum_i m_{\nu_i}$: Planck 2018 constrains this parameter to be <0.27 eV [24]. However, the most interesting side of the error for this parameter is the lower one, as it is associated to a detection of non vanishing masses. We find that DESI will constraint this parameter to about -0.07 eV from above the reference value (which is what is relevant for detection) with only the power spectrum (P) and -0.05 eV with the addition of the bispectrum, a significant improvement with respect to Planck. Since our bound depends on the central value of neutrino masses, a more invariant way to cast this bound is that we expect on DESI there will be a guaranteed 2σ-evidence for non vanishing neutrino masses. MegaMapper instead will reduce this bound to 0.008 eV, which should guarantee a $\gtrsim 12\sigma$ detection. After the measurement of the cosmological constant Λ, this would be the second parameter of the standard model of particle physics that is measured from cosmological observations.

- $f_{\rm NL}$: Planck 2018 constraints $f_{NL}^{\rm loc.}$ to ± 5, $f_{\rm NL}^{\rm eq.}$ to ± 47, $f_{\rm NL}^{\rm orth.}$ to ± 24 [60]. We find that DESI will constraint $f_{NL}^{\rm loc.}$ to ± 3.3, $f_{\rm NL}^{\rm eq.}$ to ± 92 (or ± 114 without the perturbativity prior), $f_{\rm NL}^{\rm orth.}$ to ± 27, which are quite comparable to the limits obtained by Planck. MagaMapper will further reduce these bounds as

$f_{NL}^{\rm loc.}$ to ± 0.26, $f_{\rm NL}^{\rm eq.}$ to ± 16 (or ± 18 without the perturbativity prior), $f_{\rm NL}^{\rm orth.}$ to ± 4. These are very significant improvements with respect to Planck, that range from factors of almost three for $f_{\rm NL}^{\rm eq.}$, six for $f_{\rm NL}^{\rm orth.}$, to about a factor of 20 for $f_{NL}^{\rm loc.}$. Such a level of improvement brings with it a clear chance of a discovery of primordial non-Gaussianities, opening the door to a deeper understanding at the particle physics level of the inflationary theory. Additionally, the allowed values for non-Gaussianities would begin to be close to that $\mathcal{O}(1)$ which represents the vague but significant threshold beyond which inflation is of the slow-roll kind.

We also study the limiting effect of shot noise and biases. We find that setting the shot noise to zero for DESI would reduce the error bars of practically all parameters by roughly a factor of two. For MegaMapper, the reduction would be of a factor of about three for the $f_{\rm NL}$'s, and about an order of magnitude for the other cosmological parameters.

Regarding the EFT parameters, assuming perfect prior knowledge of the biases in DESI would lead to varied reductions in the error bars, typically by a factor of two. For $f_{\rm NL}^{\rm eq.}$, the reduction would be around a factor of five. When considering our galaxy-formation benchmark prior of 0.3 instead of fixed parameters, the improvement is significantly diminished to approximately 30% for $f_{\rm NL}^{\rm eq.}$ and $f_{\rm NL}^{\rm orth.}$, with marginal impact on the other parameters. We find a similar behavior for MegaMapper. It appears that the perturbativity prior only captures a fraction of the potential improvement achievable through exact knowledge of the biases. It would be interesting to see if higher n-point functions or higher-order computations can improve on this.

Overall, this Fisher analysis tells us that even by just using the EFTofLSS at the current level of development, the next decade in LSS surveys could lead to great improvements in our knowledge of cosmological parameters. This includes parameters that have not yet been measured, such as neutrino masses, as well as those connected to inflation, such as primordial non-Gaussianities and the curvature of the universe. Improvements in the design of surveys to reduce shot noise, or advancements in the measurement of EFT parameters have the potential to further strengthen these already promising results.

Public Codes: The code to compute the Fisher forecasts is publicly available on GitHub [1].

8.3 Technical Aspects of the Fisher Matrix

Fisher analyses have become a key tool for forecasting in cosmology. Pioneered in [231], there have been numerous applications over the past years (for example [232, 233, 234]). We here briefly lay out which methods we will use for our forecasts and what contributes to our estimates.

At the heart of Fisher forecasts lies the Cramér-Rao lower bound. It states that the covariance of unbiased estimators for a set of parameters θ is bounded below by the inverse of the Fisher information matrix F_{ij}, defined as the expected value of the Hessian of the log-likelihood

$$F_{ij} = -\left\langle \frac{\partial^2 \log L}{\partial\theta_i \partial\theta_j} \right\rangle. \tag{8.1}$$

Under the assumption that the likelihood is Gaussian with mean X and covariance C, we can approximately write the Fisher matrix as [231]

$$F_{ij} = \frac{\partial X^T}{\partial\theta_i} C^{-1} \frac{\partial X}{\partial\theta_j}. \tag{8.2}$$

In order to calculate the Fisher matrix, we need to assume reference parameters $\theta^{\rm ref}$, on which we evaluate the derivatives. In particular, the reliability of the Fisher forecast depends on this reference cosmology being fairly accurate. An intuitive way to see the reference cosmology dependence and also an alternative derivation for Eq. (8.2) is to start directly with a Gaussian likelihood for an observable X depending on parameters θ, that has a true mean $\tilde{X}$, such that the log-likelihood is given by

$$-2\log L = (X(\theta) - \tilde{X})^T C^{-1} (X(\theta) - \tilde{X}) + p_1, \tag{8.3}$$

where p_1 is a θ-independent constant. We can then assume a reference value $\theta^{\rm ref}$, and Taylor expand around the reference value to first order, $X(\theta) \simeq X(\theta^{\rm ref}) + \sum_i \frac{\partial X}{\partial\theta_i}(\theta_i - \theta_i^{\rm ref})$. If $X(\theta^{\rm ref})$ is accurate we can identify that the $\tilde{X}$ term in Eq. (8.3) cancels with

[1] `https://github.com/YDonath/EFTofLSSFisher`

$X(\theta^{\rm ref})$ ([2]). What remains is the first order term, which we can substitute back into Eq. (8.3), to get

$$-2\log L = (\theta - \theta^{\rm ref})^T F(\theta - \theta^{\rm ref}) + p_1, \tag{8.4}$$

where we get the same formula for the Fisher matrix, F, as in Eq. (8.2). In Eq. (8.4) we can now clearly see that the Fisher matrix is the inverse covariance for the likelihood of the parameter vector θ. As can be seen from the derivation above, the Fisher formalism is sensitive to an accurate reference cosmology in order for $\tilde{X}$ to cancel with $X(\theta^{\rm ref})$ and also for the Taylor expansion to be an accurate approximation. Given that we now have precise measurements of all cosmological and EFT parameters from Ch. 7, we have good reason to believe we are making realistic predictions around a realistic reference cosmology. In fact, we will show in Sec. 8.4 that we can reproduce results from previous surveys to great precision. We also checked that slight deviations from this reference cosmology do not greatly alter our results.

Note that Eq. (8.2) is in principle simply an inverse-covariance weighted sum over all available information. Both the mean and the covariance can be modelled using perturbation theory. We will discuss this in Secs. 8.3.1 and 8.3.2. Then in Sec. 8.3.3 we will discuss further ingredients that go into calculating the Fisher matrix, such as fixing the reference bias parameters at different redshifts. We here always refer to the correlators of galaxies in redshift space. Therefore, unless explicitly mentioned, we drop the ^{h,r} index with respect to the notation in Ch. 6, and by $P, B, \delta, ...$ we always indicate the quantities for biased tracers in redshift space.

8.3.1 Power Spectrum and Bispectrum

For both the power spectrum and bispectrum there are well-established thin-shell averaged estimators that predict the mean and covariance for Eq. (8.2). We use the estimators that bin in the momenta, but not in the line of sight [3], since we have enough analytical control to integrate over the full line of sight information.

Furthermore, for both correlators, we use leading-order contributions in the covariance, in particular neglecting power spectrum-bispectrum cross-covariance. We will discuss the impact of this approximation in Sec. 8.4.2. This assumption in particular implies that we can write the combined power spectrum and bispectrum

[2] Note that the Taylor expansion to first order is sufficient exactly because of this cancelation.
[3] Binning in line of sight angles is also possible, see for example [233].

Fisher matrix, F^{P+B}, as the sum of the individual Fisher matrices

$$F^{P+B} = F^P + F^B, \tag{8.5}$$

where F^P and F^B are the power spectrum and bispectrum Fisher matrices respectively. Next, we will discuss these individual contributions.

Power Spectrum For the power spectrum, the estimator is given by [231, 192]

$$\hat{P}(k;\hat{z}) = \frac{1}{V_S V_P(k)} \int_{\Delta B_k} d^3q \delta(q;\hat{z})\delta(-q;\hat{z}), \tag{8.6}$$

where we used the notation $\Delta B_k = B(0, k + \frac{\Delta k}{2})\backslash B(0, k - \frac{\Delta k}{2})$ and $B(a, r)$ is the ball of radius r around the point a. V_S is the survey volume and $V_P(k) = 4\pi k^2 \Delta k$ is a normalization factor given by just the integral on the right-hand side of Eq. (8.6) without the prefactors and with the galaxy density contrast $\delta \to 1$, i.e. $V_P(k) = \int_{\Delta B_k} d^3q$.

The expected value of the estimator is simply the power spectrum itself and we will evaluate it up to the one-loop order. That is

$$P = P_{\text{Tree}} + P_{1L}. \tag{8.7}$$

Here the tree and loop contributions include their respective stochastic and response terms. We use the exact same model as in Chs. 6 and 7. Then, for the covariance, we get [4]

$$\begin{aligned} C_{PP}(k,k') &= \langle \hat{P}(k)\hat{P}(k')\rangle - \langle \hat{P}(k)\rangle\langle \hat{P}(k')\rangle \qquad (8.8)\\ &= \frac{1}{V_S^2 V_P^2(k)} \int_{\Delta B_k \times \Delta B'_k} d^3q_1 d^3q_2 \Big[\langle \delta(q_1;\hat{z})\delta(-q_1;\hat{z})\delta(q_2;\hat{z})\delta(-q_2;\hat{z})\rangle \\ &\qquad -\langle \delta(q_1;\hat{z})\delta(-q_1;\hat{z})\rangle\langle \delta(q_2;\hat{z})\delta(-q_2;\hat{z})\rangle\Big] \\ &= \frac{2}{V_S^2 V_P^2(k)} \int_{\Delta B_k \times \Delta B'_k} d^3q_1 d^3q_2 \langle \delta(q_1;\hat{z})\delta(q_2;\hat{z})\rangle\langle \delta(-q_1;\hat{z})\delta(-q_2;\hat{z})\rangle \\ &= \delta_{k,k'} \frac{4\pi^2}{V_S k^2 \Delta k} P_{\text{Tree}}(k;\hat{z})^2. \end{aligned}$$

[4] As mentioned in Sec. 3.4, any estimator is ultimately limited by the finite number of statistically independent realisations we have in the survey. For the power spectrum, this is exactly what we calculate here, i.e. we are estimating the power spectrum given N_k observations, where $N_k = V_S k^2 \Delta k/(2\pi)^2$.

Note that, schematically, we used $\langle\delta\delta\delta\delta\rangle = \langle\delta\delta\delta\delta\rangle_c + 3\langle\delta\delta\rangle\langle\delta\delta\rangle$, where, by the subindex $_c$, we mean the connected correlator. The connected four-point function is the trispectrum, which we neglect here. Of the three disconnected parts one cancels with the $\langle\hat{P}(k)\rangle\langle\hat{P}(k')\rangle$ term in the first line and the other two terms are the same, giving the factor of two in the third line. As mentioned, off-diagonal contributions to the above covariance are of the order of the trispectrum, and therefore similar in size to the one-loop power spectrum multiplied by a linear power spectrum. To be consistent in the perturbative order, given that we neglect the off-diagonal contributions, we also neglect loop contributions to the diagonal of the covariance. We will see in Sec. 8.4 that this leads to a roughly 10% effect. Finally, by substituting the mean and covariance into Eq. (8.2) we get the power spectrum Fisher matrix

$$F_{ij}^P = \sum_k \frac{k^2 V_S}{4\pi^2 \Delta k} \int_{-1}^{1} \frac{d\mu}{2} \frac{\partial P(k;\hat{z})}{\partial\theta_i} \frac{\partial P(k;\hat{z})}{\partial\theta_j} \frac{1}{\left(P_{\rm Tree}(k;\hat{z})\right)^2}, \tag{8.9}$$

with $\mu = \hat{k}\cdot\hat{z}$ the line of sight angle.

Bispectrum For the bispectrum, we use the estimator [197, 235]

$$\begin{aligned}\hat{B}(k_1,k_2,k_3;\hat{z}) = & \\ = \frac{1}{V_S V_B(k_1,k_2,k_3)} & \int\limits_{\Delta B_{k_{123}}} d^3q_1 d^3q_2 d^3q_3 \delta_D(q_1+q_2+q_3)\delta(q_1;\hat{z})\delta(q_2;\hat{z})\delta(q_3;\hat{z}),\end{aligned} \tag{8.10}$$

where we defined $\Delta B_{k_{123}} = \Delta B_{k_1}\times\Delta B_{k_2}\times\Delta B_{k_3}$. Similarly to the power spectrum discussion, the volume V_B is defined by just the above integral with $\delta\to 1$, without prefactors and is given by

$$\begin{aligned} V_B(k_1,k_2,k_3) &= \int\limits_{\Delta B_{k_{123}}} d^3q_1 d^3q_2 d^3q_3 \delta_D(q_1+q_2+q_3) \\ &= 8\pi^2 k_1 k_2 k_3 \Delta k_1 \Delta k_2 \Delta k_3 \beta(k_1,k_2,k_3), \end{aligned} \tag{8.11}$$

where, without loss of generality, we assume $k_3 \geq k_2 \geq k_1$ and $\beta(k_1,k_2,k_3) = 1$ unless $k_3 = k_1 + k_2$, in which case it is $\frac{1}{2}$. Again the mean of this estimator is simply the bispectrum itself, which we calculate up to the one-loop order in Ch. 6:

$$B = B_{\rm Tree} + B_{1L}. \tag{8.12}$$

Again the tree and loop contributions include their respective stochastic and response terms. To leading order, the bispectrum-bispectrum covariance is given by [5]

$$C_{BB}(k_1,k_2,k_3,k_1',k_2',k_3') = \frac{(2\pi)^6}{V_S V_B(k_1,k_2,k_3)} s_B \prod_{i=1}^{3}\left(\delta_{k_i,k_i'} P(k_i;\hat{z})\right), \quad (8.13)$$

where s_B is a symmetry factor that is equal to 6 for equilateral triangles, 2 for isosceles triangles and 1 otherwise. Again, we do not consider off-diagonal contributions, which would be the connected six-point function, as well as bispectra squared and products of trispectra and power spectra. While these contributions are suppressed relative to the diagonal, they may be sizable in some cases and we therefore check this approximation with respect to covariances measured in mocks in Sec. 8.4. Finally, we bin equally in all k_i, so that if we plug Eqs. (8.12) and (8.13) in to Eq. (8.2), we get the bispectrum Fisher matrix at fixed redshift (see Sec. 4.2 of [232] or Sec. 4.1.3 of [157] for more details):

$$F_{ij}^B = \frac{V_S}{(2\pi)^5}\sum_{(k_1,k_2,k_3)}\frac{1}{s_B}\int_{-1}^{1}\int_{0}^{2\pi} d\mu_1 d\phi \frac{\partial B}{\partial\theta^i}\frac{\partial B}{\partial\theta^j}\prod_{i=1}^{3}\left(\frac{k_i\Delta k}{P_{\rm Tree}(k_i;\hat{z})}\right)\begin{cases}\frac{1}{2}, \text{if } k_3 = k_1+k_2\\ 1, \text{else,}\end{cases} \quad (8.14)$$

where $\mu_i(\mu_1,\phi) = \hat{k}_i\cdot\hat{z}$ are the projected momenta, and we omitted writing the arguments of B to avoid clutter. We use the same parametrization of the μ_i as in Eqs. (7.6) - (7.7).

8.3.2 Combining Redshifts

In the previous section, we derived formulas for Fisher matrices for the power spectrum and bispectrum at a single redshift. However, for surveys that cover a range of redshifts, we need to combine the information from different redshift bins to compute the overall Fisher matrix. We will now lay out how we combine these redshifts.

Assuming that all EFT-parameters at different redshifts are uncorrelated [6], the

[5] The derivation of the bispectrum covariance follows analogously to Eq. (8.8): we expand the six-point function into a sum of products of connected correlators, and neglect terms that are higher order. For more details, see for example [236].

[6] Note that in Ch. 7 the fact that the EFT-parameters at different redshifts are in principle correlated has been used. But given the large range of redshifts and the mild correction from correlations, we neglect this here. For BOSS, where the redshift binning is finer than for DESI and MegaMapper, and thus the correlation is stronger, this is a 15-20% effect. Therefore we assume

full Fisher matrix for a survey with a set of redshift bins can be expressed as the sum of the power spectrum Fisher matrix and the bispectrum Fisher matrix over the redshift bins

$$F_{\rm survey} = \sum_z \big(F^P(z) + F^B(z)\big). \tag{8.15}$$

In all forecasts we consider, we split the survey into two sets of redshift bins, let us call them bin_1 and bin_2. Let us write $F_{\rm survey} = F_{\rm survey,1} + F_{\rm survey,2}$ and the sum in Eq. (8.15) for each of these two Fisher matrices simply runs over the redshifts in that particular set of bins (for BOSS this is, for example, LOWZ and CMASS, i.e. $\text{bin}_1 = \{z \in \text{Tab. D.2}\,|z \leq 0.45\}$ and $\text{bin}_2 = \{z \in \text{Tab. D.2}\,|z > 0.45\}$). A common approach is then to define effective redshifts $z_{\rm eff}$, background number density $n_{b,\rm eff}$, etc., and simply compute the $F_{\text{survey},i}$ with these values. This is a good approximation for the derivatives of the observables, given that the time dependence is largely dominated by the growth factors that have comparably weak time dependence. However, we find that this is not a very accurate estimate for the covariance [7]. To emphasize the different redshift-dependent contributions that enter the covariance, let us write the covariance from the previous sections in their full form:

$$C_{PP}(k,k';z) = \delta_{k,k'}\frac{4\pi^2}{V_S(z)k^2\Delta k}\left((b_1(z)+f(z)\mu^2)^2P_{11}(k) + \frac{c_1^{St}}{n_b(z)}\right)^2 \tag{8.16}$$

$$C_{BB}(k_i,k_i';z) = \frac{32\pi^4 s_B\prod_{i=1}^3\left(\delta_{k_i,k_i'}\right)}{V_S(z)k_1k_2k_3\Delta k^3\beta(k_1,k_2,k_3)}\prod_{i=1}^3\left((b_1(z)+f(z)\mu_i^2)^2P_{11}(k_i)+\frac{c_1^{St}}{n_b(z)}\right),$$

where P_{11} is the linear dark matter power spectrum, c_1^{St} is the tree-level stochastic term and we abbreviated the triangle dependence on the left-hand side $k_i = \{k_1, k_2, k_3\}$. Defining effective numbers as an approximation is not appropriate for the covariance since it is very sensitive to accurate estimates of the survey volume V_S, number density n_b, and linear bias b_1. Their numerical values are typically given by survey specifications, and vary greatly with redshift. Specifically, n_b greatly varies with redshift as it depends on the survey target selection and measurements. In contrast, the growth rate f and the linear power spectrum P_{11} have a comparably

for future surveys the impact will be negligible.

[7] Apart from the fact that $n_{b,\rm eff}$ simply gives a very bad estimate for a realistic covariance (i.e. reproducing the measured covariance), notice also that the power spectrum and bispectrum covariances scale with different powers of n_b, and their measured effective numbers would not be the same.

mild redshift dependence. However, in our analysis, we will nevertheless consider their redshift dependence for completeness.

To summarize, we have weak time dependence in the derivatives and strong redshift dependence in the covariance. Therefore, for $X \in \{P, B\}$ and $i \in \{1, 2\}$ we use the following approximation for the Fisher matrix of the two redshift bins: [8]

$$\begin{aligned}(F^X_{\text{survey},r})_{ij} &= \sum_{z\in \text{bin}_r} \frac{\partial X^T(z)}{\partial\theta_i} C^{-1}_{XX}(z) \frac{\partial X(z)}{\partial\theta_j} \\ &\simeq \frac{\partial X^T(z_{\text{eff},r})}{\partial\theta_i} \left(\sum_{z\in \text{bin}_r} C^{-1}_{XX}(z) \right) \frac{\partial X(z_{\text{eff},r})}{\partial\theta_j},\end{aligned} \tag{8.17}$$

where $z_{\text{eff},r}$ is the effective redshift for bin_r. The vector contractions in Eq. (8.17), represent the covariance weighted sum over the available information in the correlator X. For the modes, this leads to the sums over k in Eqs. (8.9) and (8.14). We also sum over all redshift space information, which in the continuum limit turns into an integral over the redshift space angles in Eqs. (8.9) and (8.14). The final full Fisher matrix that we use is $F_{\text{survey}} = F^P_{\text{survey},1} + F^B_{\text{survey},1} + F^P_{\text{survey},2} + F^B_{\text{survey},2}$.

8.3.3 Survey Specifications at Different Redshifts

Now that we established how to combine the information from different redshifts, let us discuss what reference parameters we choose for each of these redshifts. Predictions from the EFTofLSS rely on a number of redshift and survey-dependent parameters. While these factors have been measured to great precision at low redshifts for the BOSS survey, we need to discuss how we extrapolate these results to different redshifts and surveys.

EFT Parameters Let us first look at the approximate evolution of all EFT parameters entering the galaxy power spectrum and bispectrum. In particular, we analyze the time dependence of the physical (as opposed to the bare) parameters. There are at least two distinct origins of nuisance parameters in the EFTofLSS. On the one hand, we expand some functions (such as the stress tensor or the galaxy overdensity) in terms of all fields they can depend on, multiplied by parameters. Schematically

[8] Note that we can test the validity of $\sum_{z\in \text{bin}_r} C^{-1}_{XX}(z)$ as an approximation for the covariance on its own, given that we have measurements for the covariances of BOSS. We in part do this in Sec. 8.4.2 and Fig. 8.2, where we find very good agreement.

at linear order, with redshift space distortions implied, this is (see Ch. 6)

$$\delta(x,t) = b_1(t)\delta_{\rm dm}(x,t) + ... - c_1^h(t)\frac{k^2}{k_{\rm NL}^2}\delta_{\rm dm}(x,t) + ... \,, \tag{8.18}$$

where $\delta_{\rm dm}$ is the dark matter overdensity (note that δ without indices denotes the overdensity of galaxies in redshift space). We will refer to these parameters as biases (this includes response terms, but not stochastic fields). The BOSS best-fit for the biases, $\vec{b}_{\rm BOSS}$, has been determined in Ch. 7. The explicit numerical values are in App. D.1. When fixing the reference cosmology for surveys at higher redshifts, we rescale the biases according to the estimated linear bias given in the survey specifications [222, 237]. Specifically for any new survey we set the reference value for the vector of biases $\vec{b} = \{b_1, b_2, ..., c_1^h, c_2^h, ...\}$ according to

$$\vec{b}^{\rm ref} = \frac{b_1^{\rm ref}}{b_{1,\rm BOSS}}\vec{b}_{\rm BOSS}. \tag{8.19}$$

Note that the $b_1^{\rm ref}$ in the tables of Sec. 8.5, App. D.1 and [222, 237], account for different redshifts and different galaxy species. For the surveys we consider in this chapter, we give the numerical values for $b_1^{\rm ref}$ in Tabs. 8.1, 8.2 and 8.3.

Contrary to biases, there are parameters coming from correlators of stochastic fields. For example, we have

$$\langle\delta(k,t)\delta(k',t)\rangle' \supset \langle\epsilon_A(k,t)\epsilon_B(k',t)\rangle' = \frac{1}{n_b}\left(c_1^{St} + c_2^{St}\frac{k^2}{k_{\rm NL}^2} + ...\right). \tag{8.20}$$

We will call these terms stochastic. Importantly, since they are Poisson distributed, they are constant in time. Therefore, given that we have a vector of measured values for the stochastic terms from BOSS, we could in principle use these reference values for all redshifts. However, we here make a slight correction relative to the analysis done in Ch. 7. There, leading order stochastic terms, for example c_1^{St}, were varied freely, whereas they should be fixed to one, by definition of n_b ([9]). Therefore, for surveys other than BOSS, we fix the leading order stochastic parameters for the power spectrum and bispectrum, i.e. $c_1^{St,\rm ref} = c_1^{(222),\rm ref} = 1$, and we also do not take derivatives with respect to these parameters [10]. For all other terms in the vector of

[9] It is possible to have slight deviations from this condition [238], which we will study in future work.

[10] For BOSS, we will let the leading order stochastic terms vary freely to validate our pipeline against previous data analyses in Sec. 8.4, i.e. there we take derivatives with respect to these parameters. Instead, when predicting further results in Sec. 8.5, we will keep them fixed for BOSS

stochastic terms $\vec{\epsilon} = \{c_2^{St}, c_3^{St}, ...\}$ we use

$$\vec{\epsilon}^{\,\mathrm{ref}} = \frac{1}{c_{1,\mathrm{BOSS}}^{St}} \vec{\epsilon}_{\mathrm{BOSS}}, \tag{8.21}$$

where $\vec{\epsilon}_{\mathrm{BOSS}}$ is the vector of stochastic parameters measured for BOSS [11]. Explicit numerical values are given in App. D.1 and for details on the specific parameters see Ch. 6.

As a final remark, we note that we have tested the sensitivity of our results in Sec. 8.5 to small shifts in the reference values of EFT parameters and found that they do not significantly affect our findings. The parameters that have the greatest impact on our results are those used in the modeling of the covariance, namely b_1 and c_1^{St}. To ensure accurate predictions for future surveys, where the best-fit is yet unknown, we take b_1^{ref} directly from survey specifications and we set the reference value of c_1^{St} to one (with the exception of BOSS, as mentioned earlier).

Perturbative Reach The perturbative reach of the EFTofLSS, parametrised by k_{max}, can be determined in simulations by setting a threshold for the theory systematic error. This was the approach used for example, in [7] and Ch. 7. For the BOSS CMASS sample this is $k_{\mathrm{max}} = 0.22h\,\mathrm{Mpc}^{-1}$ at one-loop order and $k_{\mathrm{max}} = 0.1h\,\mathrm{Mpc}^{-1}$ at tree level. In the following, we will lay out how we estimate the k_{max} for a different survey at a different redshift, motivated by the method used in [7]. There, roughly, it was imposed that the signal-to-noise of the leading theoretical error should not be sizable in the k-bin containing the k_{max} (see footnote 23 in [7]). This is a good approximation, assuming that the signal-to-noise of the theoretical error only has a sizeable contribution in the highest k-bin. Here, however, we want to limit the full signal-to-noise of the theoretical error over all k-bins. The motivation for this is two-fold. First, this approach is binning independent, which is important to be consistent between surveys that have different bin sizes. Second even though the signal-to-noise of the leading theoretical error is well approximated by only considering contributions at large k since it grows very steeply with k, it leads to a slight overestimate of the k_{max} ([12]) since one does not consider the theoretical error at $k < k_{\mathrm{max}} - \frac{\Delta k}{2}$. We, therefore, consider the theoretical error contribution at all scales. Furthermore, as in Ch. 7, we will use the same k_{max} for the power spectrum

forecasts as well.

[11] In all forecasts for BOSS, we use $\vec{\epsilon}_{\mathrm{BOSS}}$ as reference values.

[12] We note that on small redshift differences for example between CMASS and LOWZ, the two approaches produce the same results. Therefore, the estimates in [7] are accurate.

and the bispectrum, since we expect the k-reach to be the same. To summarize, this means we impose that the signal-to-noise of the theoretical error is the same in all surveys, which then defines the $k_{\rm max}$ through

$$\sum_{k=k_{\rm min}}^{k_{\rm max,1}} \left(\frac{\sigma_{\rm theory,1}(k,z_1,...)}{\sigma_{\rm data,1}(k,z_1,...)}\right)^2 = \sum_{k=k_{\rm min}}^{k_{\rm max,2}} \left(\frac{\sigma_{\rm theory,2}(k,z_2,...)}{\sigma_{\rm data,2}(k,z_2,...)}\right)^2 , \tag{8.22}$$

where the sum runs over the k-bins of the respective survey, the dots represent further dependences, such as the EFT-parameter best-fit, and $\sigma_{\rm data/theory,i}$ are the respective theoretical and data errors that we will discuss next. The leading theoretical error is the next higher loop contribution, and we estimate the data error by perturbatively modeling the covariance. Let us focus on the theoretical error first. To good approximation [145] the L-th order loop scaling is given by

$$\sigma_{L-{\rm Loop}}(k,z) = P_{11}(k,z)\left(\frac{k}{k_{\rm NL}(z)}\right)^{(3+n(k,z))L} , \tag{8.23}$$

where $n(k,z)$ is the slope of the linear power spectrum around k. For the one-loop analysis, the theoretical error is, therefore, $\sigma_{\rm theory,i}(k,z_i,...) = \sigma_{2-{\rm Loop}}(k,z_i)$. Note that in Eq. (8.22), any constant factor will drop out, so we only care about the scaling. Furthermore given that from the BOSS analysis we have $k_{\rm NL}^{\rm BOSS} = 0.7h\,{\rm Mpc}^{-1}$, we can get $k_{\rm NL}$ at different redshifts by solving

$$\int_0^{k_{\rm NL}(z)} dq\; q^2 P_{11}(q,z) = \int_0^{0.7h\,{\rm Mpc}^{-1}} dq\; q^2 P_{11}(q,z=0.57). \tag{8.24}$$

To estimate the data error we use the square root of the covariance estimate from Eq. (8.16), including the summation over redshifts, mentioned in Eq. (8.17). We average over the redshiftspace dependence, and do not consider shot noise [13], that

[13] Setting shot noise contributions in the covariance to zero gives more conservative values for $k_{\rm max}$. However, in surveys with large shot noise (i.e. we underestimate $k_{\rm max}$ more), contributions from higher k are negligible exactly because of this large shot noise.

is

$$\begin{aligned}\sigma_{\mathrm{data},i}(k) &= \left(\sum_{z\in\mathrm{bin}_i}\int_{-1}^{1}\frac{d\mu}{2}C^{-1}_{PP,n_b\to\infty}(z,\mu)\right)^{-1/2} \\ &= \frac{2\pi}{\sqrt{k^2\Delta k}}\left(\sum_{z\in\mathrm{bin}_i}\frac{V_S(z)}{P_{11}(k,z)^2}\int_{-1}^{1}\frac{d\mu}{2}\frac{1}{\left(b_1(z)+f(z)\mu^2\right)^4}\right)^{-1/2} \\ &=: \frac{\tilde{\sigma}_{\mathrm{data},i}(k)}{\sqrt{\Delta k}}.\end{aligned} \tag{8.25}$$

In practice, the sum over $z \in \mathrm{bin}_i$ runs over the bins mentioned in Eq. (8.17). Furthermore, we defined $\tilde{\sigma}_{\mathrm{data,bin}_i}(k)$, since we will take the limit $\Delta k \to dk$, such that Eq. (8.22) turns into an integral with integration measure equal to dk. Then, for each survey bin with effective redshift z_{eff}, to estimate the L-th loop order k^L_{max} , we solve

$$\begin{aligned}&\int^{k^L_{\mathrm{max}}} dk\frac{P_{11}(k,z_{\mathrm{eff}})^2}{\tilde{\sigma}^2_{\mathrm{data},i}(k)}\left(\frac{k}{k_{\mathrm{NL}}(z_{\mathrm{eff}})}\right)^{(3+n(k,z_{\mathrm{eff}}))2(L+1)} \\ &= \int^{k^L_{\mathrm{max,\ CMASS}}} dk\frac{P_{11}(k,z=0.57)^2}{\tilde{\sigma}^2_{\mathrm{data,\ CMASS}}(k)}\left(\frac{k}{0.7h\,\mathrm{Mpc}^{-1}}\right)^{(3+n(k,z=0.57))2(L+1)}.\end{aligned} \tag{8.26}$$

8.3.4 Further Ingredients from Data Analyses

In principle, we now have all the ingredients to compute Fisher forecasts for a given survey. However, there are a number of aspects related to the data and the data-analysis that we want to consider here, in order to best predict future results. For one, there are priors that we put on cosmological parameters and EFT parameters. For completeness we also briefly discuss the Alcock-Paczynski(AP) effect.

Priors We impose priors on the EFT parameters that are very similar to those used in Ch. 7. Given that we are assuming a Gaussian likelihood in the Fisher analysis, imposing a Gaussian prior amounts to adding the inverse variance of the prior to the diagonal of the Fisher matrix. The key difference between the priors we have in the Fisher analysis and those in the MCMC is that all of our priors are centered around the best-fit value rather than around zero. However, we have verified that this difference has a negligible impact on the error bars. For the special case of the linear bias b_1, we use a log-normal prior of variance 0.8 to ensure its

positivity [14] For all other EFT parameters, we put a Gaussian prior of width 2, except for response and stochastic terms that are joint between the power spectrum and bispectrum, for which we use a Gaussian prior of width 4. These variance choices are analogous to the ones in Ch. 7.

We anticipate or hope that, in the coming years, our understanding of galaxy formation will advance to a level that will allow for stronger priors on the EFT parameters. In parts of Secs. 8.5 and 8.6.2 we, therefore, separately use a "galaxy-formation prior", where we put a Gaussian prior of width 0.3 on all EFT parameters, except for b_1 where we put again a log-normal prior, also with width 0.3. This value of the prior is a benchmark value we deemed reasonably close to what can be potentially achieved.

For the cosmological parameters, we use a Gaussian Big-Bang Nucleosynthesis (BBN) prior on the baryon abundance ω_b centered around the best-fit value and, with a width of $\sigma_{\rm BBN} = 0.00036$. Also, we analyze $\log m_\nu^{\rm tot.} := \log(\sum_i m_{\nu_i}/\text{eV})$ rather than $\sum_i m_{\nu_i}$ which implicitly ensures unbounded positivity, with support $(0, \infty)$, on the neutrino masses, since the logarithm ensures positivity [15]. In the results Sec. 8.5 we transform the predicted error on $\log m_\nu^{\rm tot.}$ back to a 68% interval on $\sum_i m_{\nu_i}$ ([16]). We do not assume any previous knowledge about the other cosmological parameters. Overall, our choice of priors is almost equivalent to those used in the data analyses [143] and Ch. 7.

[14] Even though the Fisher formalism only allows for Gaussians, we can put log-normal priors, by analyzing $\log(b_1)$ rather than b_1, since the derivative with respect to $\log(b_1)$ can easily be computed. Then imposing a log-normal prior is just a Gaussian on the "log of the parameter".

[15] In [143], a flat prior with, for example, width $[0.06\text{eV}, 0.9\text{eV}]$ was used, which would slightly ameliorate the results presented here.

[16] Note that the Fisher forecast predicts $\sum_i m_{\nu_i} \sim \text{Lognormal}\left((\log m_\nu^{\rm tot.})^{\rm ref}, \sigma\,(\log m_\nu^{\rm tot.})^2\right)$, thus the upper and lower bounds of the 68% confidence interval can be easily computed from the lognormal distribution. However, while the confidence interval bounds for the Gaussian posterior of $\log m_\nu^{\rm tot.}$ are independent of the reference neutrino mass (to the extent that the Fisher forecast is), the confidence interval for $\sum_i m_{\nu_i}$ derived from the Gaussian of $\log m_\nu^{\rm tot.}$, is in fact reference value dependent. To see this, note that the p-quantile for a Gaussian is of the form $(\log m_\nu^{\rm tot.})^{\rm ref} + \sigma\,(\log m_\nu^{\rm tot.})\,\sqrt{2}\ \text{erf}^{-1}(2p-1)$ whereas for the lognormal it is of the form $\sum_i m_{\nu_i}^{\rm ref} \times \exp\left[\sigma\,(\log m_\nu^{\rm tot.})\,\sqrt{2}\ \text{erf}^{-1}(2p-1)\right]$. Therefore, if we write confidence interval bounds in the Gaussian case, of the form $\left((\log m_\nu^{\rm tot.})^{\rm ref}\right)^{\sigma_+}_{\sigma_-}$, the error would be $\sigma_\pm = \sigma\,(\log m_\nu^{\rm tot.})\,\sqrt{2}\ \text{erf}^{-1}(2p_\pm - 1)$, so the $\sigma_\pm$ are reference value independent (as long as $\sigma\,(\log m_\nu^{\rm tot.})$ is). In the lognormal case, i.e. errors of the form $\left(\sum_i m_{\nu_i}^{\rm ref}\right)^{\sigma_+}_{\sigma_-}$, we instead have $\sigma_\pm = \sum_i m_{\nu_i}^{\rm ref} \times \left(\exp\left[\sigma\,(\log m_\nu^{\rm tot.})\,\sqrt{2}\ \text{erf}^{-1}(2p_\pm - 1)\right] - 1\right)$. We emphasize, therefore, that the upper and lower bounds of the confidence interval for the lognormal distribution scale linearly with the reference value. Therefore, when in Sec. 8.5, we present confidence intervals $[a, b]$ for $\sum_i m_{\nu_i}^{\rm ref} = 0.1$ eV, the confidence interval for $\sum_i m_{\nu_i}^{\rm ref} = 0.2$ eV would be $[2a, 2b]$.

Alcock-Paczynski Effect Galaxy spectra are measured on celestial coordinates. In order to transform to cartesian coordinates, a reference cosmology needs to be assumed, that might not correspond to the true cosmology. This discrepancy between the reference cosmology and the true cosmology introduces a geometric distortion known as the Alcock-Paczynski (AP) effect [214]. In order to account for this effect one has to evaluate the theory model on transformed wave numbers, given by

$$k = \frac{k^{\rm ref}}{q_\perp}\left[1+(\mu^{\rm ref})^2\left(\frac{1}{F^2}-1\right)\right]^{1/2}, \mu = \frac{\mu^{\rm ref}}{F}\left[1+(\mu^{\rm ref})^2\left(\frac{1}{F^2}-1\right)\right]^{-1/2}, \quad (8.27)$$

where

$$q_\perp = \frac{D_A(z)h}{D_A^{\rm ref}(z)h^{\rm ref}}, \qquad q_\parallel = \frac{H^{\rm ref}(z)/h^{\rm ref}}{H(z)/h}, \quad F = q_\parallel/q_\perp, \quad (8.28)$$

and D_A being the angular diameter distance.

Importantly, this transformation is invertible, and therefore, information preserving. Therefore, the AP effect does not lead to any addition or loss of information, when analyzing all (i.e. the full set of multipoles) information available from a given galaxy statistic at a given order. With the exception of a small part of Sec. 8.5.1, in Sec. 8.5 we will always analyze the full set of multipoles, where the AP effect is, therefore, irrelevant, and therefore we do not include it. The only forecasts where we do not analyze the full set of multipoles are in the beginning of Sec. 8.5.1, and in Sec. 8.4. The relevance of the AP effect on the Fisher forecasts is thus limited to these specific analyses and we, therefore, implement only approximate formulae. The general structure of the correlators we analyze are sums of products of rational functions in k and μ, multiplying linear power spectra and loop integrals. For both cases, we use that $\left(\frac{1}{F^2}-1\right)$ is very close to zero and we can Taylor expand it. For the rational functions, we use

$$k^n \simeq \left(\frac{k^{\rm ref}}{q_\perp}\right)^n\left(1+\frac{n}{2}(\mu^{\rm ref})^2\left(\frac{1}{F^2}-1\right)\right), \quad (8.29)$$
$$\mu^n \simeq \left(\frac{\mu^{\rm ref}}{F}\right)^n\left(1-\frac{n}{2}(\mu^{\rm ref})^2\left(\frac{1}{F^2}-1\right)\right).$$

Instead, when evaluating loop integrals or linear powers spectra, we average the k above over redshift space angles, and we, therefore, evaluate on

$$k_{\rm avg} = \frac{k^{\rm ref}}{q_\perp}\left(1+\frac{1}{6}\left(\frac{1}{F^2}-1\right)\right). \quad (8.30)$$

As we will see in Sec. 8.4, this approximation is enough to recover large parts of the AP effect.

8.4 Pipeline Validation against BOSS Data Analysis

Ultimately, the constraints derived from the Fisher formalism are an approximation to a more complicated MCMC analysis. For one, an MCMC will in general produce non-Gaussian posteriors (see Fig. 3 in [176] for an example). In addition, there are several modeling effects that are considered in the data analyses that we do not account for in our Fisher analysis. In this section, we quantify how much these unaccounted-for effects contribute to the constraints, and thereby estimate the level of precision we can have confidence in when performing Fisher forecasts.

We split this section into two parts. In Sec. 8.4.1, we focus on observational effects. To isolate the impact of observational effects on the posterior, we fix the covariance entering the Fisher matrix to the one obtained from the data analysis (i.e. the measured covariance extracted from mocks as in Ch. 7). The remaining difference is what we call observational effects, which we do not account for [17]. Then in Sec. 8.4.2 we validate the modeling of the covariance described in Sec. 8.3. In particular, we study the extent to which the off-diagonal entries in the covariance impact the Fisher forecast. Throughout this section, we consider the power spectrum multipoles P_ℓ for $\ell = 0, 2$ and the bispectrum monopole B_0 at 1-loop. We also focus mainly on constraints of base cosmological parameters (h, $\ln(10^{10}A_s)$ and Ω_m). We expect this to be sufficient to quantify the accuracy of the Fisher forecasts presented in Sec. 8.5. As mentioned in Sec. 8.3.3, we here vary the leading order stochastic parameters freely, since we compare to an MCMC that does not fix them either. This is in contrast to what we will do in Sec. 8.5.

However, let us discuss here also the validation of our results for primordial non-Gaussianity. While what we discuss in the next sections is also applicable to non-Gaussianity, we highlight here additional validations specific to non-Gaussianity. For example, while we use the best-fit of the data analysis from Ch. 7 as our reference cosmology (see App. D.1 for details), for $f_{\rm NL}$ we use $f_{\rm NL}^{\rm ref} = 0$ ([18]). The

[17] We call them observational effects because the error comes from neglecting window functions and only using an approximate version of the AP effect.

[18] We validated that non-zero background values for $f_{\rm NL}$, such as the ones allowed by the BOSS data analysis [176] or Planck [60], yield very similar constraints.

observational effects that we discuss in Sec. 8.4.1 affect non-Gaussianity constraints minimally. Furthermore, since almost all of the information about non-Gaussianity (with the exception of $f_{\rm NL}^{\rm loc.}$) lies in the bispectrum, the exclusion of the power spectrum bispectrum cross-correlation in the covariance is not as sizeable as for other parameters. In conclusion, we are able to estimate that our forecast for $f_{\rm NL}$ is accurate to roughly $10-25\%$, as we study in more detail in Sec. 8.4.2.

8.4.1 Fisher Prediction against full MCMC

Even when using the same covariance, the same perturbative model, and the same reference cosmology, there are still several effects that lead to a difference between data analysis constraints and Fisher constraints. The most important observational effects are the Alcock-Paczynski(AP) effect and the smoothing effect of the window function convolution. To evaluate the significance of these effects, we perform a Fisher forecast, using the same model, best-fit, priors, covariance, bins, etc. as in Chs. 6 and 7. The sole difference is that in one case we get the posteriors through the Fisher prediction (and only considering an approximate AP effect, and not considering window functions), and in the other through an MCMC that takes these effects into account [19]. This in particular means, we avoid most of the discussion from Sec. 8.3, since we are not estimating the covariance here and also do not change any of the bias parameters nor the $k_{\rm max}$. We highlight, that the AP effect will eventually not affect the results of the forecasts, since we consider all multipoles and the transformation in Eq. (8.27) is information preserving. We consider it here only because the analysis we use as reference point have been done on a limited number of multipoles. The results of the MCMC against the Fisher are shown in Fig. 8.1.

We observe that the largest discrepancy in the σ, at 27%, is found for Ω_m. However, for the other cosmological parameters, the difference is only around 15%. We expect a similar level of error, at approximately 15%, for the other parameters that we analyze in the following sections and attribute the higher discrepancy on Ω_m to not fully modelling the AP effect, which most notably depends on Ω_m. However, as argued above this effect will not be relevant for us in later sections. We note that if we remove the AP effect and window functions from the BOSS data analysis, the difference to the forecast is less than 5% [20].

[19] As a reference point, we take the same chain of the analysis in Ch. 7 (Fig. 7.1, $P_\ell + B_0^{1loop}$).

[20] Therefore, the non-Gaussian nature of the MCMC-posteriors and the Taylor expansion around the best-fit that the Fisher relies on have minimal impact on the results.

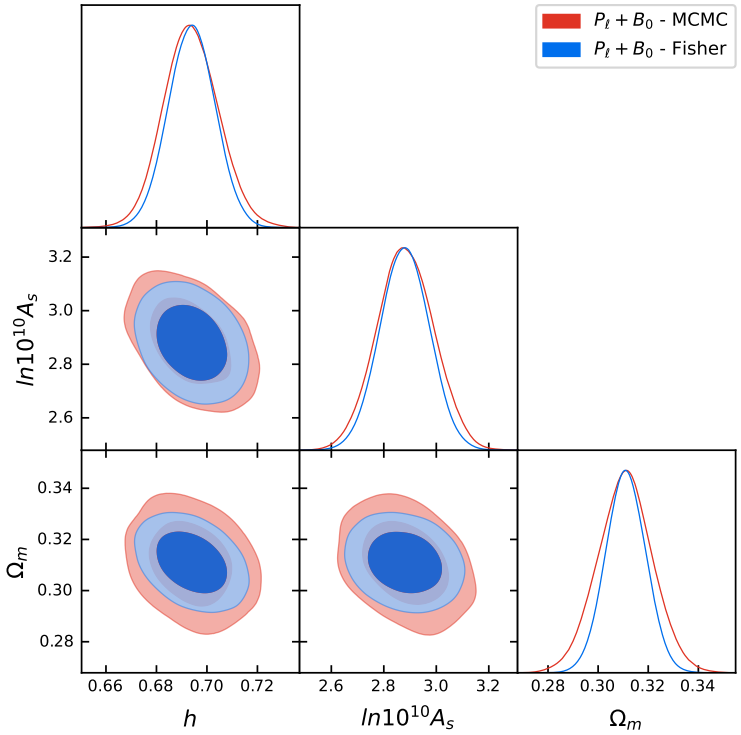

$\sigma(\cdot)$	h	$\ln(10^{10}A_s)$	Ω_m
$P_\ell + B_0$ - MCMC	0.011	0.11	0.011
$P_\ell + B_0$ - Fisher	0.0093	0.094	0.008

Figure 8.1: Triangle plots and errors comparing a Fisher forecast (blue) against the data analysis from Ch. 7 (Fig. 7.1, $P_\ell + B_0^{1loop}$) (red) for base ΛCDM parameters. For the Fisher forecast the full measured covariance is used including all cross-correlations. We here analyze $\ell = 0, 2$ power spectrum multipoles and the bispectrum monopole, both at one loop order. We implement the approximate AP effect as discussed in Sec. 8.3.4.

8.4.2 Fisher Prediction with Diagonal Covariance

For upcoming surveys, the fully measured covariance from mocks is not readily available. Although it is possible to compute these covariances with high accuracy using perturbation theory, the modeling of off-diagonal contributions can be very complex. Therefore, as described in Sec. 8.3, we do not consider any off-diagonal contributions here [21]. Explicitly this means we neglect cross-correlations between the power spectrum and bispectrum and also we neglect cross-correlations between

[21] However, whenever we analyze multipoles, we do consider multipole cross-correlations, which in multipole space appear as off-diagonal entries. In particular, we consider the P_0-P_2 cross-correlation.

k-bins (for the power spectrum and bispectrum respectively) [22].

By considering the diagonal elements of the measured covariance (actively putting the off-diagonal elements to zero), we can study two effects. First, we can better understand the contribution of off-diagonal elements to the covariance, without yet relying on perturbation theory. Secondly, we can investigate the precision of the analytical diagonal covariance as described in Sec. 8.3 by comparing them to the diagonals of the measured covariance.

The most significant effect of using a diagonal covariance is an overestimation of the bispectrum impact relative to the power spectrum. We find that the off-diagonal elements in the power spectrum covariance have a negligible effect. However, for the bispectrum, the impact is larger. This is expected, as neglecting the power spectrum-bispectrum cross-correlation is equivalent to a scenario where the bispectrum is providing purely independent, new, information from the power spectrum. At least on large enough scales, this is inaccurate as discussed in [236]. In that sense, neglecting the cross-covariance is a double counting of large-scale information. Keeping this in mind, we still want to emphasize that the relative impact of the bispectrum grows rapidly with higher $k_{\rm max}$.

In Fig. 8.2, we show the impact of these two isolated effects. First, by reducing the full covariance to just the diagonals, we obtain about $25\% - 30\%$ tighter constraints. Second, if we compare the measured diagonal covariance to the modelled one, the agreement is remarkably good with only a few percent difference [23]. In fact, this could be accounted for by loop order contributions that we did not consider in our analytic modeling of the diagonal covariance which is roughly of the same order.

By comparing the MCMC data analysis in Fig. 8.1 to the Fisher forecast using the analytical diagonal covariance shown in Fig. 8.2, we estimate our confidence in the Fisher results to be about 40%.

Finally, we perform the same comparison for non-Gaussianity constraints. The MCMC data analysis yields $\big(\sigma(f_{\rm NL}^{\rm loc.}), \sigma(f_{\rm NL}^{\rm eq.}), \sigma(f_{\rm NL}^{\rm orth.})\big) =$ (35, 298, 75), while the Fisher forecast with analytical diagonal covariance gives $\big(\sigma(f_{\rm NL}^{\rm loc.}), \sigma(f_{\rm NL}^{\rm eq.}), \sigma(f_{\rm NL}^{\rm orth.})\big) =$ (28, 275, 95). Thus for non-Gaussianity, we have a much closer agreement at around $10 - 25\%$.

[22] We also neglect any sky correlations since it is a comparably small effect.

[23] This strong agreement is present only when summing the different redshifts as described in Eq. (8.17) and footnote [8]. In contrast, the agreement is not as good if we summarize the survey information to an effective redshift bin.

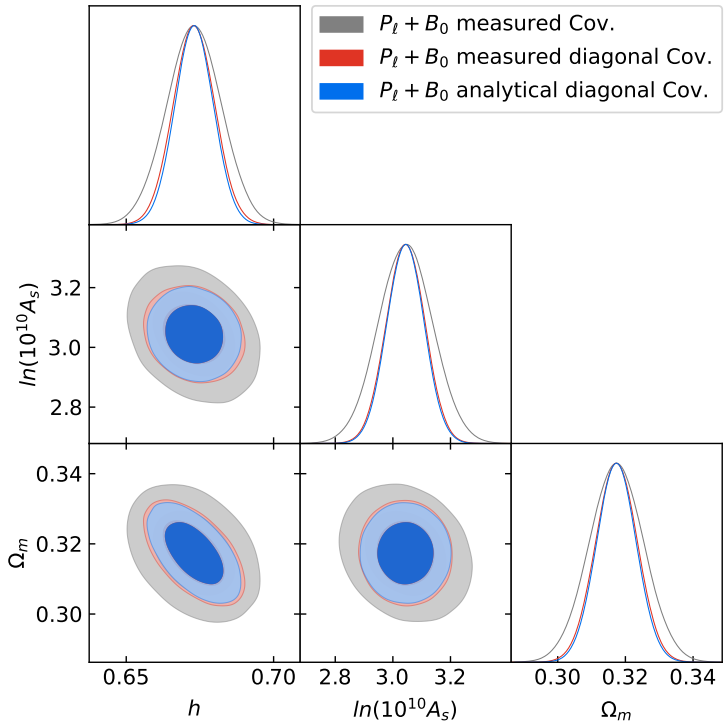

$\sigma(\cdot)$	h	$\ln(10^{10}A_s)$	Ω_m
$P_\ell + B_0$ measured Cov.	0.0093	0.094	0.008
$P_\ell + B_0$ measured diagonal Cov.	0.0070	0.066	0.0061
$P_\ell + B_0$ analytical diagonal Cov.	0.0065	0.064	0.0059

Figure 8.2: Triangle plots comparing different Fisher forecasts for base ΛCDM parameters using the $\ell = 0, 2$ power spectrum multipoles and the bispectrum monopole, all at one loop order. The plots differ only in their covariances, where we compare the measured covariance (grey) including all cross-covariances, the diagonal of the measured covariance (red), and the analytical prediction for the diagonal covariance (blue). We implement the approximate AP effect as discussed in Sec. 8.3.4.

8.5 Results

Having validated the Fisher methodology with BOSS data analysis results in Sec. 8.4, we now use it to predict the constraining power of DESI and MegaMapper, as well as to provide some additional results for BOSS. As discussed in the previous section, due to observational effects and covariance modeling, we expect the accuracy of cosmological parameter constraints to be roughly 40%, and the non-Gaussianity parameters to be accurate to $10-25\%$.

While BOSS has now been extensively analyzed, there are still some unexplored questions, which we aim to address here. The full set of cosmological parameters we study in various combinations is $\{h, \ln(10^{10}A_s), \Omega_m, n_s, \Omega_k, \log m_\nu^{\rm tot.}, f_{\rm NL}^{\rm loc.}, f_{\rm NL}^{\rm eq.}, f_{\rm NL}^{\rm orth.}\}$, where we defined $\log m_\nu^{\rm tot.} := \log(\sum_i m_{\nu_i}/{\rm eV})$. We refer to any subset of the first six parameters in this list (i.e. the list without the non-Gaussianity parameters) as "base" parameters. Throughout this section, we use the power spectrum and bispectrum of galaxies in redshift space at 1-loop order. For future surveys like DESI and MegaMapper, we use the full set of multipoles [24], and for BOSS we use either the full set of multipoles or the monopole and quadrupole for the power spectrum and the monopole for the bispectrum [25]. Furthermore, following the discussion in Sec. 8.3.3, we fix the leading stochastic terms to one, throughout this section. Therefore, the results we will find for BOSS in this section are slightly tighter than what we presented in Sec. 8.4. When quoting results for primordial non-Gaussianity, we fix the cosmological parameters, as we will discuss more later this has almost always a negligible effect on our results. Finally, we note that we use fixed relationships from [176, 239] between the non-Gaussianity bias parameters $b_i^{f_{\rm NL}}$ and galaxy bias parameters b_i, which we checked to be a negligible approximation with respect to putting an order one prior centered on $b_i^{f_{\rm NL,ref}}$ on $b_i^{f_{\rm NL}}$ and then let it vary freely [26].

[24] As we will see for the BOSS survey, using the full set of multipoles is roughly equivalent to just using the monopole and quadrupole for both the power spectrum and bispectrum.

[25] When analyzing a finite number of multipoles, we implement the approximate AP effect as discussed in Sec. 8.3.4. However, when we use the complete set of multipoles, in particular for DESI and MegaMapper, the AP effect is irrelevant

[26] Note that for $f_{\rm NL}^{\rm ref} = 0$, which is what we use here, in the context of the Fisher forecast, this is not even an approximation, but exact. However, even for non-zero reference values, the change in the error-bar due to this approximation can be quite well understood. If we were only to analyse the power spectrum, we would only constrain the joint parameter $b_1^{f_{\rm NL}} f_{\rm NL}$ rather than the individual parameters. With the inclusion of the bispectrum this degeneracy is broken due to the presence of $b_2^{f_{\rm NL}} f_{\rm NL}$, $b_1 f_{\rm NL}$, and $f_{\rm NL}$ on its own. The only relevant parameter in the context of this discussion is $f_{NL}^{\rm loc.}$, since for $f_{\rm NL}^{\rm eq.}$ and $f_{\rm NL}^{\rm orth.}$ almost all information lies in the bispectrum, and we also verified explicitly that the approximation is negligible. In contrast a large part of the constraint on $f_{NL}^{\rm loc.}$ comes from the power spectrum, where however, we can easily understand

8.5.1 BOSS

Base cosmological results with the one-loop power spectrum for BOSS have been presented in [7, 142, 143], neutrinos have also been analyzed in [143] and dark energy models in Ch. 10. The combination of the power spectrum and bispectrum has led to the measurement of h, $\ln(10^{10}A_s)$ and Ω_m in Ch. 7, with the non-Gaussian parameter $f_{\rm NL}$ being reported in [176] and at tree level in [177, 178]. In this section, we present forecasts for the power spectrum and bispectrum with the inclusion of the sum of neutrino masses $\sum_i m_{\nu_i}$, spectral tilt n_s and spatial curvature Ω_k. We also investigate the impact of shot noise and of the EFT parameters and explore the information contained in higher multipoles. The exact numerical values of the EFT parameters, survey specification and reference cosmology that we use here and in Sec. 8.6 are given in App. D.1. Following the binning scheme used in [9], we divide the sample into two redshift bins. We use the same values of $k_{\rm NL}$ and b_1 for both bins since the redshift difference of the bins is very small. The effective numbers we use are summarized in Tab. 8.1.

This section is divided into two parts, based on the type of covariance used. In the first part, we present results using the full measured covariance obtained in Ch. 7, which includes all cross-correlations. This implies that we expect our results to be accurate to about 15% (and 27% for Ω_m) as described in Sec. 8.4.1. In the second part, we investigate the impacts of shot noise and higher multipoles using a modelled covariance, as described in Sec. 8.4.2. This allows us to have better

the shift in error bar. Simple error propagation tells us that the error we obtain from the power spectrum with fixed $b_1^{f_{\rm NL}}$ or with the order one prior on $b_1^{f_{\rm NL}}$ are related to each other by

$$\sigma\left(f_{\rm NL}^{\rm loc.,full}\right) \simeq \sqrt{\sigma\left(f_{\rm NL}^{\rm loc.,approx.}\right)^2 + \sigma\left(b_1^{f_{\rm NL}}\right)^2 \frac{\left(f_{\rm NL}^{\rm loc.,ref}\right)^2}{\left(b_1^{f_{\rm NL},\rm ref}\right)^2}}, \tag{8.31}$$

where we note that $\sigma\left(b_1^{f_{\rm NL}}\right)$ is dominated by the prior width. Therefore these changes in the error bar are relevant, if $f_{\rm NL}^{\rm loc.,approx.}$ and $b_1^{f_{\rm NL}}$ have similar signal to noise $\frac{\sigma\left(f_{\rm NL}^{\rm loc.,approx.}\right)}{f_{\rm NL}^{\rm loc.,ref}} \simeq \frac{\sigma(b_1^{f_{\rm NL}})}{b_1^{f_{\rm NL},\rm ref}}$. For instance with quite large $f_{\rm NL}^{\rm loc.,ref}$ both sides of this ratio can roughly be equal to one, as was found in [176]. To be precise, using Planck constraints $f_{NL}^{\rm loc.} = -0.9 \pm 5.1$ and a prior $\sigma\left(b_1^{f_{\rm NL}}\right) = 2$, we find the full change in error bar for $f_{NL}^{\rm loc.}$ with inclusion of both power spectrum and bispectrum at $f_{\rm NL}^{\rm loc.,ref} = -0.9$ to be 0.01%, 5%, 15% for BOSS, DESI and MegaMapper respectively, and even at the Planck 1-σ level $f_{\rm NL}^{\rm loc.,ref} = -6$, we find changes of 0.5%, 47%, 54%. Given in particular that what is important is a detection of non-vanishing $f_{NL}^{\rm loc.}$, and within order one the actual value of $f_{NL}^{\rm loc.}$ is much less important, we conclude that our forecasts are robust even when the $b_i^{f_{\rm NL}}$ are free EFT parameters.

BOSS:	$z_{\rm eff}$	$n_{b,\rm eff}[(h\,\mathrm{Mpc}^{-1})^3]$	$b_1^{\rm ref}$	$(k_{\rm max}^{\rm Tree},\, k_{\rm max}^{1L},\, k_{\rm NL})$ $[h\,\mathrm{Mpc}^{-1}]$	$N_{\rm bins}^{1L}$	$N_\Delta^{\rm Tree}$	N_Δ^{1L}
Bin 1	0.32	2.9×10^{-3}	1.9	(0.09, 0.20, 0.7)	18	9	62
Bin 2	0.57	2.5×10^{-3}	1.9	(0.10, 0.22, 0.7)	21	17	150

Table 8.1: BOSS effective survey specifications, calculated according to the formulas in Sec. 8.3 and Tab. D.2 in App. D.1. $n_{b,\rm eff}$ is the background galaxy number density entering the derivatives (not the covariance), $N_{\rm bins}$ is the number of k-bins we consider for the power spectrum and N_Δ is the number of triangles we consider for the bispectrum.

analytical control, for example in order to analyze the shot noise influence on the results.

Additional Results: n_s, $\sum_i m_{\nu_i}$ and Ω_k We present the BOSS forecasts using the power spectrum monopole and quadrupole, as well as the bispectrum monopole, both at one loop order, for parameters that have previously only been analyzed with only the power spectrum (and in some cases with the tree-level bispectrum [7]). The results are summarized in Fig. 8.3.

Impact of Shot Noise, Biases and Multipoles For BOSS, we checked that adding the trispectrum at tree level and the 2-loop power spectrum [27] do not improve on the measurements. This is mostly attributable to the large shot noise of the survey. However, given the power of the Fisher formalism, we can investigate the effects of certain limits and configurations on parameter constraints. Of course, we here look at limiting cases, that are unrealistic in reality, but they show where information is lost. In particular, we are interested in the impact of EFT parameters and of the survey shot noise. Throughout this section, we will be using the analytical covariance, which gives us the most control but comes with the caveats mentioned in Sec. 8.4. We investigate several effects on both base cosmological parameters including n_s, and $f_{\rm NL}$. Just as in [176], unless mentioned otherwise, we fix the cosmological parameters when quoting errors on $f_{\rm NL}$. We checked that while $f_{\rm NL}^{\rm loc.}$ has a roughly 35% error bar reduction due to fixed cosmological parameters, $f_{\rm NL}^{\rm eq.}$ and $f_{\rm NL}^{\rm orth.}$ are very independent of the other cosmological parameters and their results would only change by roughly $5-10\%$ if we would not fix the cosmological

[27] While currently, we do not have the 2-loop power spectrum for galaxies in redshift space, we can simply run a Fisher analysis on the one loop correlators, with the 2-loop $k_{\rm max}$ reach. This then gives an upper bound estimate for the extra constraining power of the 2-loop correlators. The results on BOSS do not improve even with this optimal estimate, and therefore we believe, a 2-loop analysis will not improve the results on BOSS.

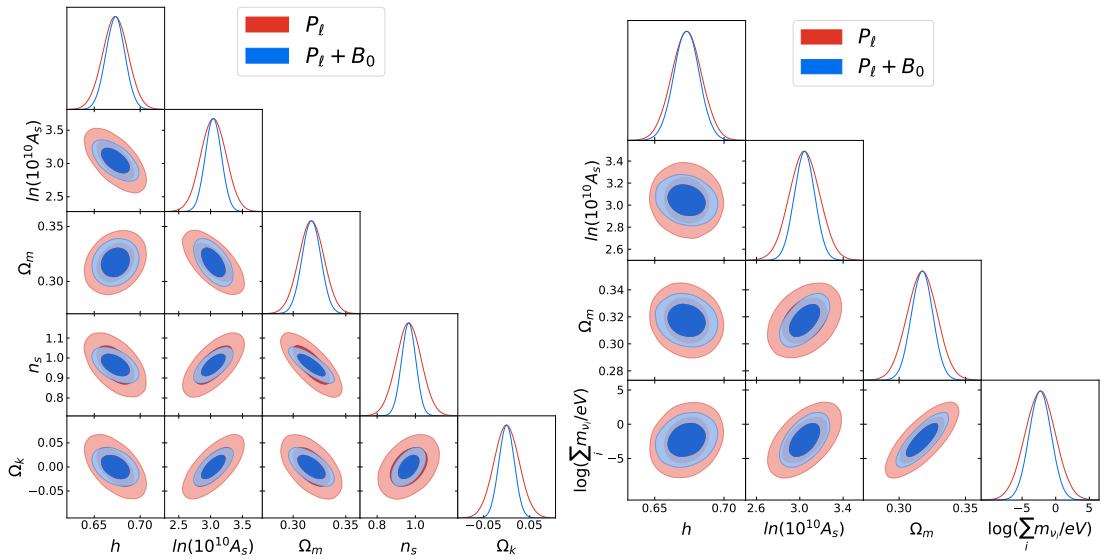

$\sigma(\cdot)$	h	$\ln(10^{10}A_s)$	Ω_m	n_s	Ω_k
P_ℓ	0.014	0.2	0.012	0.066	0.027
P_ℓ+B_0	0.01	0.13	0.009	0.037	0.017

$\sigma(\cdot)$	h	$\ln(10^{10}A_s)$	Ω_m	$\log m_\nu^{\rm tot.}$ (σ^+_-)
P_ℓ	0.011	0.14	0.011	2.3 $(^{+0.84}_{-0.089})$
P_ℓ+B_0	0.0092	0.095	0.008	1.6 $(^{+0.41}_{-0.080})$

$\sigma(\cdot)$	$f_{\rm NL}^{\rm loc.}$	$f_{\rm NL}^{\rm eq.}$	$f_{\rm NL}^{\rm orth.}$
P_ℓ+B_0	25	266	94

Figure 8.3: Triangle plots and errors from Fisher forecasts for BOSS including the spectral tilt and spatial curvature (left), massive neutrinos (right), and primordial non-Gaussianity (bottom). The power spectrum monopole and quadrupole, and the bispectrum monopole were used both at one loop order. In the table we also report the upper and lower bounds of the 68% confidence interval for the sum of massive neutrinos, i.e. $\mathbb{P}\left[\left(\sum_i m_{\nu_i} - \sum_i m_{\nu_i}^{\rm ref}\right) \in (\sigma^-, \sigma^+)\right] = 0.68$. The covariance used here is the full, measured covariance with all cross-correlations. We implemented the approximate AP effect as discussed in Sec. 8.3.4.

parameters.

First, we check the impact of using higher multipoles at one loop as opposed to using only the power spectrum monopole and quadrupole and the bispectrum monopole. While there is some improvement with the inclusion of additional multipoles for the bispectrum, we checked that almost all of this improvement comes from the bispectrum quadrupoles. Still, this improvement is very small, and so we do not present the posteriors. The numerical values can be found in the table of Fig. 8.4. We can conclude that using the monopole and quadrupole for both the power spectrum and bispectrum, one can extract almost the full redshift space information. As was shown in Ch. 7, we can already analyze data with the monopole and quadrupole for the power spectrum and bispectrum. Therefore, unless indicated otherwise we analyze using all multipoles.

Next in Fig. 8.4, we show additional constraints in the continuous field limit $n_b \to \infty$, i.e. having no shot noise. We roughly halve the error bars for both the base cosmological parameters and $f_{\rm NL}$. This should serve as motivation to include as many objects into our data sets even if they are faint or somewhat unresolved. This will also become important in Sec. 8.5.3.

Lastly, the EFTofLSS, like any EFT, will need a larger number of parameters when going to higher perturbative orders. This is in principle not a problem as long as they are independent enough from the parameters of interest. It is interesting to investigate how better knowledge of these parameters would impact the results. We put the "galaxy-formation prior" mentioned in Sec. 8.3.4, where we put stronger priors on all EFT parameters motivated by hopefully-realistic future knowledge on galaxy formation. We also take the limit in which these parameters are fixed, in other words representing the scenario in which all "nuisance" parameters are known and measured exactly with no error. This, in a sense, is the theoretical upper bound for the EFTofLSS at a given order. It is interesting to note from the results presented in the table in Fig. 8.4 that the biases have varying impacts on different cosmological parameters. Specifically, the biases overwhelmingly affect the primordial parameters, A_s, n_s and $f_{\rm NL}$. As we will see in Sec. 8.6, $f_{\rm NL}$-constraints are more sensitive to the EFT parameters than A_s and n_s. This is not so surprising, considering that the functional form of EFT counterterms resemble the functional form induced by primordial non-Gaussianities.

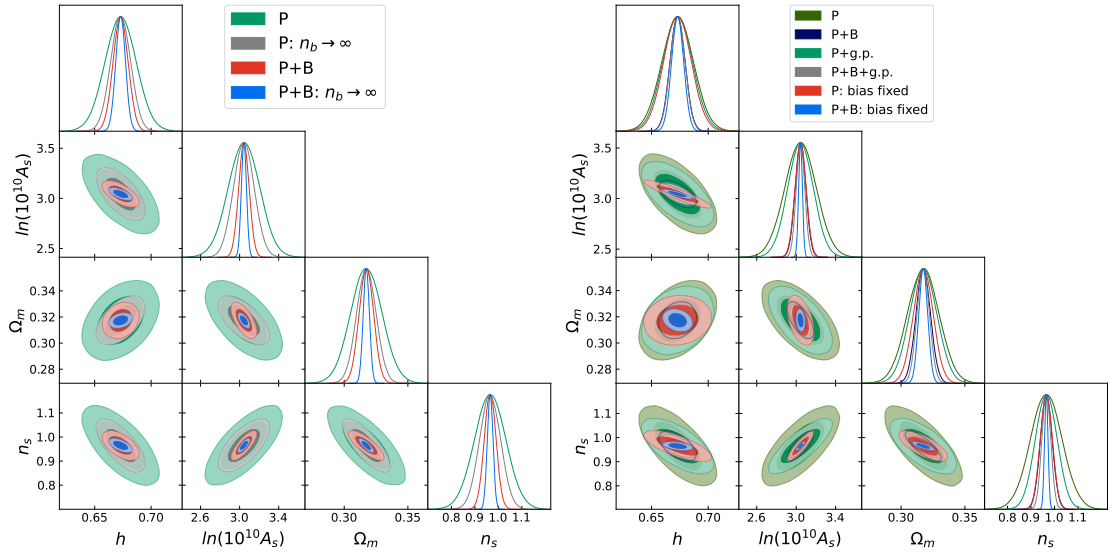

$\sigma(\cdot)$	h	$\ln(10^{10}A_s)$	Ω_m	n_s	$f_{\rm NL}^{\rm loc.}$	$f_{\rm NL}^{\rm eq.}$	$f_{\rm NL}^{\rm orth.}$
P_ℓ	0.014	0.16	0.012	0.067	-	-	-
P	0.014	0.16	0.012	0.067	-	-	-
$P + g.p.$:	0.013	0.13	0.011	0.047	-	-	-
P : bias fixed	0.012	0.06	0.008	0.026	-	-	-
$P : n_b \to \infty$	0.009	0.11	0.008	0.045	-	-	-
P_ℓ+B_0	0.0067	0.092	0.0060	0.029	25	266	94
P+B	0.0067	0.055	0.0057	0.025	23	253	67
$P + B + g.p.$:	0.0065	0.043	0.0049	0.019	19	187	51
$P + B$: bias fixed	0.0054	0.019	0.0035	0.007	4.8	45	26
$P + B : n_b \to \infty$	0.0043	0.026	0.0024	0.012	11	147	41

Figure 8.4: Triangle plots and errors from several different Fisher forecasts for BOSS using the analytical covariance. We compare base results to results obtained without shot noise (left) and with biases fixed or with a "galaxy-formation prior" (g.p.) (right). In the table, we also show the impact of including higher multipoles on the power spectrum and bispectrum and also see the impact on $f_{\rm NL}$. For the constraints on $f_{\rm NL}$, we fix the other cosmological parameters.

8.5.2 DESI

We now turn to predict the performance of upcoming surveys, starting with the imminent DESI survey. We base our results on the Emission Line Galaxies (ELGs) sample, which is the largest of the DESI surveys [222]. We note that while we are able to derive the value for the linear bias through specifications given in [222], we do not have values for the other EFT parameters. We therefore shift all biases according to the method described in Sec. 8.3.3, i.e. we shift them all according to the change in the linear bias with respect to the BOSS best-fit. The final numerical values we use for the DESI forecast are given in Tab. 8.2. For all the future surveys we use $k_{\rm min} = 0.001h\,{\rm Mpc}^{-1}$ for the power spectrum and $k_{\rm min} = 0.02h\,{\rm Mpc}^{-1}$ for the bispectrum. We bin with $\Delta k = 0.005h\,{\rm Mpc}^{-1}$ for the power spectrum and $\Delta k = 0.02h\,{\rm Mpc}^{-1}$ for the bispectrum. For binning consistency, we have checked that using a smaller binning does not affect our results. To reduce binning effects, ideally one would always average the observables over a k-bin. However, given the numerical complexity of doing such a procedure for every bin, especially for the bispectrum, we instead evaluate on a effective number $k_{\rm eff}$ to approximate this averaging. This is analogous to the method used in Ch. 7, with the difference that we also evaluate on $k_{\rm eff}$ the tree level contribution, rather than averaging it. The effect is minimal. Throughout this section, we use the analytical covariance from Eqs. (8.16) and (8.17) with all the ingredients discussed in Sec. 8.3.3. We remind that the validity of the covariance was discussed in Sec. 8.4.

DESI:	$z_{\rm eff}$	$n_{b,\rm eff}[(h\,{\rm Mpc}^{-1})^3]$	$b_1^{\rm ref}$	$(k_{\rm max}^{\rm Tree},\, k_{\rm max}^{1L},\, k_{\rm NL})$ $[h\,{\rm Mpc}^{-1}]$	$N_{\rm bins}^{1L}$	$N_\Delta^{\rm Tree}$	N_Δ^{1L}
Bin 1	0.84	8.0×10^{-4}	1.3	(0.08, 0.18, 0.9)	37	17	115
Bin 2	1.23	3.2×10^{-4}	1.5	(0.09, 0.23, 1.3)	45	17	191

Table 8.2: DESI effective survey specifications, calculated according to the formulas in Sec. 8.3 and Tab. D.3 in App. D.1. $n_{b,\rm eff}$ is the background galaxy number density entering the derivatives (not the covariance), $N_{\rm bins}$ is the number of k-bins we consider for the power spectrum and N_Δ is the number of triangles we consider for the bispectrum.

Results We present results, including the spectral tilt, spatial curvature, neutrino masses, and non-Gaussianity in Fig. 8.5, using all multipoles. The results for $f_{\rm NL}$ were obtained with fixed cosmological parameters. Analyzing $f_{\rm NL}$ in combination with cosmological parameters changes the $f_{\rm NL}$ constraints by less than 8%. For neutrino masses, with the caveats discussed in footnote [16], it seems likely that DESI

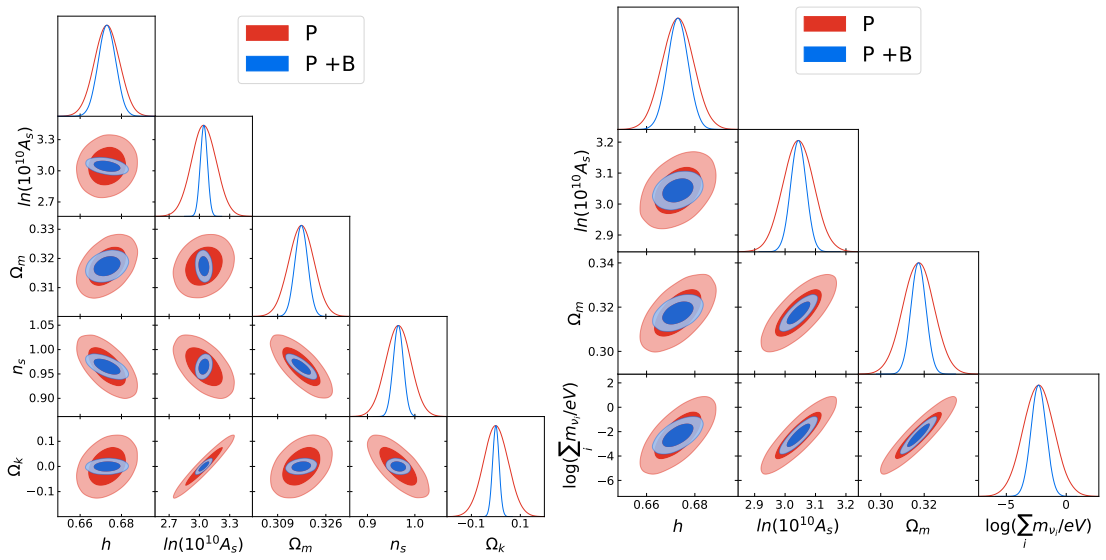

$\sigma(\cdot)$	h	$\ln(10^{10}A_s)$	Ω_m	n_s	Ω_k
P	0.0061	0.12	0.0045	0.027	0.051
P+B	0.0042	0.035	0.0023	0.011	0.013

$\sigma(\cdot)$	h	$\ln(10^{10}A_s)$	Ω_m	$\log m_\nu^{\rm tot.}(\sigma^+_-)$
P	0.0065	0.051	0.0072	1.3 $(^{+0.26}_{-0.072})$
P+B	0.0042	0.025	0.0034	0.63 $(^{+0.087}_{-0.047})$

$\sigma(\cdot)$	$f_{\rm NL}^{\rm loc.}$	$f_{\rm NL}^{\rm eq.}$	$f_{\rm NL}^{\rm orth.}$
P+B	3.5	114	30

Figure 8.5: Triangle plots and errors from Fisher forecasts for DESI including the spectral tilt and spatial curvature (left) and massive neutrinos (right) and Non-Gaussianity (bottom). In the table we also report the upper and lower bounds of the 68% confidence interval for the sum of massive neutrinos, i.e. $\mathbb{P}\left[\left(\sum_i m_{\nu_i} - \sum_i m_{\nu_i}^{\rm ref}\right) \in (\sigma^-, \sigma^+)\right] = 0.68$. We use all power spectrum and bispectrum multipoles at one loop order for the above results and use the analytical covariance without cross-correlations.

is already able to detect massive neutrinos at the 2σ level.

Impact of Shot Noise and Biases Similar to Sec. 8.5.1, it is interesting to investigate constraints with the "galaxy-formation prior" (g.p.) putting stronger priors on EFT parameters, and look at the theoretical limits of fixed biases and zero shot noise for DESI. As shown in Fig. 8.6, the g.p. mostly affects $f_{\rm NL}^{\rm eq.}$ and $f_{\rm NL}^{\rm orth.}$. However, in both the zero shot noise [28] and fixed bias limits, we observe improvements of roughly a factor of 2-3 in $\ln(10^{10}A_s), \Omega_m$ and n_s, while h improves less significantly in either of these limits. These results are consistent with those

[28] We note that due to still large shot noise, the 2-loop analysis for DESI does not much improve the results, which we verified with the same method as mentioned in footnote [27].

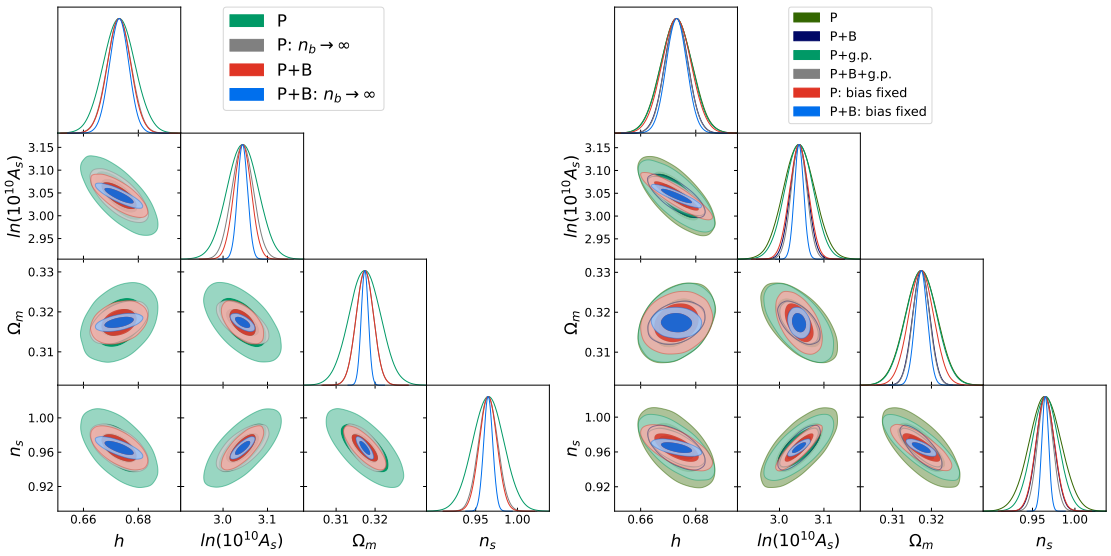

$\sigma(\cdot)$	h	$\ln(10^{10}A_s)$	Ω_m	n_s	$f_{\rm NL}^{\rm loc.}$	$f_{\rm NL}^{\rm eq.}$	$f_{\rm NL}^{\rm orth.}$
P	0.0057	0.036	0.0041	0.019	-	-	-
$P + g.p.:$	0.0056	0.032	0.0040	0.016	-	-	-
P : bias fixed	0.0053	0.021	0.0032	0.011	-	-	-
$P : n_b \to \infty$	0.0044	0.024	0.0022	0.011	-	-	-
P+B	0.0042	0.020	0.0022	0.010	3.5	114	30
$P + B + g.p.:$	0.0042	0.018	0.0022	0.009	3.4	83	23
$P + B$: bias fixed	0.0037	0.010	0.0016	0.004	2.0	21	11
$P + B : n_b \to \infty$	0.0035	0.011	0.0009	0.005	1.7	67	17

Figure 8.6: Triangle plots and errors from several different Fisher forecasts for DESI. We compare base results to results obtained without shot noise (left) and with biases fixed or with a "galaxy-formation prior" (g.p.) (right). In the table, we also show the impact of including higher multipoles on the power spectrum and bispectrum and also see the impact on $f_{\rm NL}$. For the constraints on $f_{\rm NL}$, we fix the other cosmological parameters.

obtained for BOSS in Sec. 8.5.1 since, as we noted, the biases have larger degeneracies with $\ln(10^{10}A_s)$, n_s, and non-Gaussianities. We find that the effect of shot noise accounts for approximately 50% of the constraints on $f_{\rm NL}$. Interestingly, fixing the bias parameters has a striking effect on non-Gaussianities, particularly for $f_{\rm NL}^{\rm eq.}$, for which we would obtain a six-fold reduction in the error bars. In combination with the results from the g.p., this strongly motivates the need for tighter priors and therefore better measurements of biases when performing the analysis of DESI in the near future. In order to further improve on this aspect, we present in Sec. 8.6 the $f_{\rm NL}$ constraints forecasted with the EFT-motivated perturbativity prior.

8.5.3 MegaMapper

For MegaMapper, we base our Fisher forecasts on the two scenarios mentioned in [223] (there called "idealized" and "fiducial"), which we call the optimistic (MMo) and pessimistic (MMp) scenarios. These two scenarios are in turn based on the specifications presented in Tab. 1 (MMo) and Tab. 2 (MMp) of [237]. It is important to note that these specifications are preliminary and may differ from the final specifications. We caution that our results are based on these preliminary specifications and may need to be revised as more information becomes available. We find that the constraints predicted by the two scenarios differ by $30-40\%$. Given the similarity of the results in these two situations, we present here the results in the optimistic scenario, leaving the pessimistic scenario in App. D.2.1. Thus, the numerical values that we will use in this section were derived from Tab. 1 of [237] and methods from Sec. 8.3. They are given in Tab. 8.3.

MMo:	$z_{\rm eff}$	$n_{b,\rm eff}[(h\,\mathrm{Mpc}^{-1})^3]$	$b_1^{\rm ref}$	$(k_{\rm max}^{\rm Tree},\, k_{\rm max}^{1L},\, k_{\rm NL})$ $[h\,\mathrm{Mpc}^{-1}]$	$N_{\rm bins}^{1L}$	$N_\Delta^{\rm Tree}$	N_Δ^{1L}
Bin 1	2.4	1.8×10^{-3}	3.1	(0.14, 0.36, 3.2)	73	62	696
Bin 2	4.3	1.1×10^{-4}	6.3	(0.28, 0.76, 10.1)	153	294	5491

Table 8.3: MegaMapper effective survey specifications, calculated according to the formulas in Sec. 8.3 and Tab. D.4 in App. D.1. $n_{b,\rm eff}$ is the background galaxy number density entering the derivatives (not the covariance), $N_{\rm bins}$ is the number of k-bins we consider for the power spectrum at 1-loop and N_Δ is the number of triangles we consider for the bispectrum at 1-loop.

As in the DESI forecast, we shift the rest of the biases parameters according to the method described in Sec. 8.3.3. Furthermore, we again use $k_{\rm min} = 0.001h\,\mathrm{Mpc}^{-1}$ for the power spectrum and $k_{\rm min} = 0.02h\,\mathrm{Mpc}^{-1}$ for the bispectrum, as well as $\Delta k = 0.005h\,\mathrm{Mpc}^{-1}$ for the power spectrum and $\Delta k = 0.02h\,\mathrm{Mpc}^{-1}$ for the bispectrum. Again, to reduce binning effects, we evaluate on $k_{\rm eff}$. The results for $f_{\rm NL}$ were again obtained with fixed cosmological parameters. Analyzing $f_{\rm NL}$ in combination with cosmological parameters changes the $f_{\rm NL}$ constraints by less than 3%. Finally, just like for the DESI forecasts, we use the analytical covariance from Eqs. (8.16) and (8.17), following the discussion in Sec. 8.3.3 and its precision discussed in Sec. 8.4.

Results We present base results for MegaMapper in a similar format to the previous sections in Fig. 8.7. We see that the bispectrum contains significant constraining power. As mentioned in Sec. 8.4.2, we expect that the constraints presented here

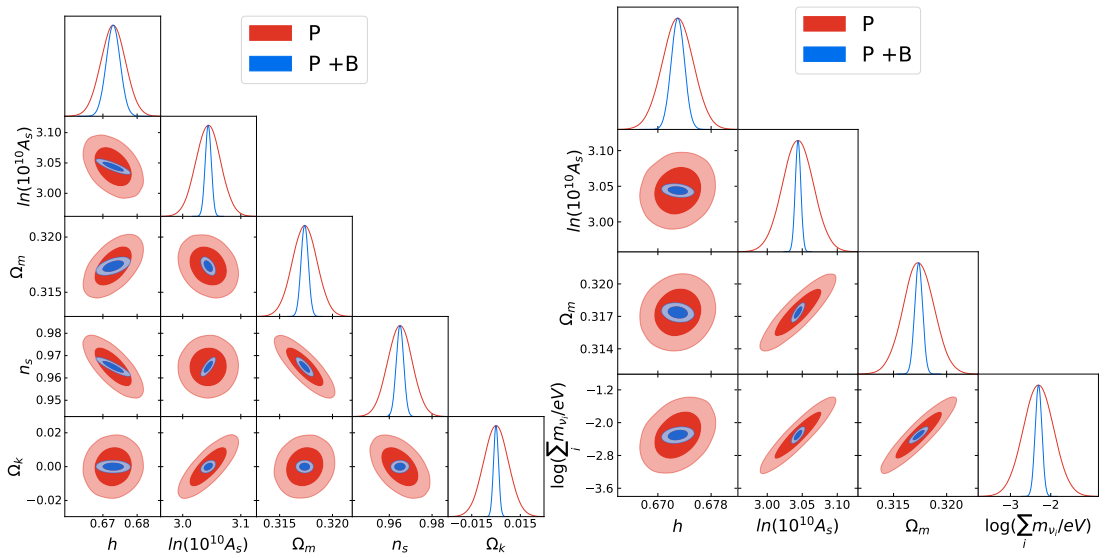

$\sigma(\cdot)$	h	$\ln(10^{10}A_s)$	Ω_m	n_s	Ω_k
P	0.0036	0.021	0.0012	0.006	0.0076
$P+B$	0.0021	0.0052	0.0003	0.002	0.0015

$\sigma(\cdot)$	h	$\ln(10^{10}A_s)$	Ω_m	$\log m_\nu^{\rm tot.}(\sigma^+_{\sigma^-})$
P	0.0023	0.022	0.0015	$0.38\ (^{+0.046}_{-0.031})$
$P+B$	0.0010	0.0039	0.0004	$0.083\ (^{+0.009}_{-0.008})$

$\sigma(\cdot)$	$f_{\rm NL}^{\rm loc.}$	$f_{\rm NL}^{\rm eq.}$	$f_{\rm NL}^{\rm orth.}$
$P+B$	0.27	17.7	4.6

Figure 8.7: Triangle plots and errors from Fisher forecasts for MegaMapper including the spectral tilt and spatial curvature (left) and massive neutrinos (right) and non-Gaussianity (bottom). In the table we also report the upper and lower bounds of the 68% confidence interval for the sum of massive neutrinos, i.e. $\mathbb{P}\left[\left(\sum_i m_{\nu_i} - \sum_i m_{\nu_i}^{\rm ref}\right) \in (\sigma^-, \sigma^+)\right] = 0.68$. We use all power spectrum and bispectrum multipoles for the above results and use the analytical covariance without cross-correlations.

will be an overestimate as we are neglecting cross-correlations. Nevertheless, the impact of the bispectrum at higher $k_{\rm max}$ becomes relatively more important, and therefore continues to be a very important tool for future data analyses.

In particular, shown in in Fig. 8.7, the inclusion of the bispectrum allows for very tight constraints on neutrino masses. Even with the caveats discussed in footnote [16], neutrino mass detection with MegaMapper seems very likely.

Impact of Shot Noise and Biases Given the long timeline until results will be available for MegaMapper, and target selection is yet to happen, we will discuss some aspects that might improve results as was discussed for DESI in Sec. 8.5.2. In particular, while the perturbative reach is far greater at higher redshifts, as can

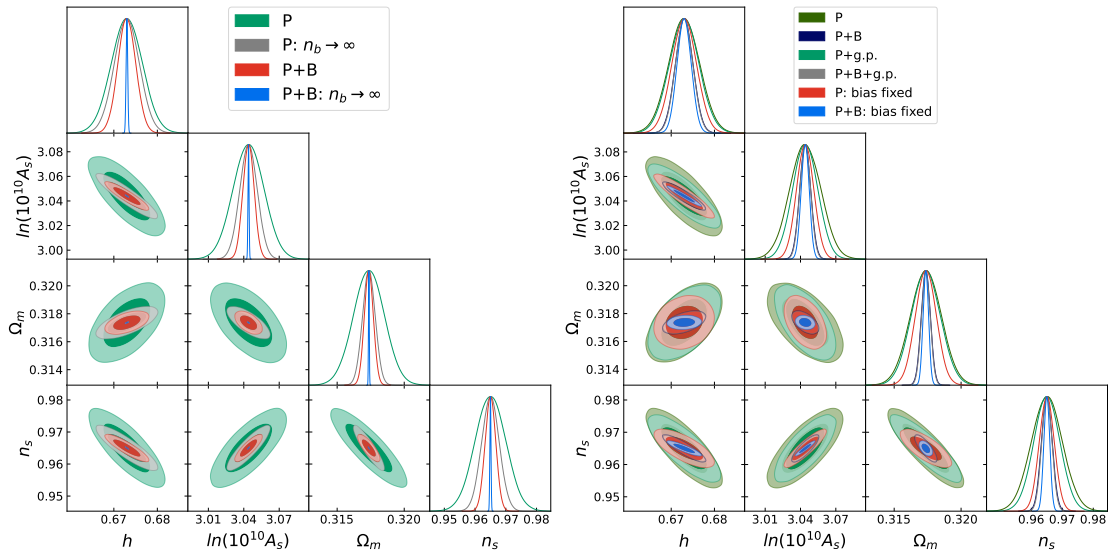

$\sigma(\cdot)$	h	$\ln(10^{10}A_s)$	Ω_m	n_s	$f_{\rm NL}^{\rm loc.}$	$f_{\rm NL}^{\rm eq.}$	$f_{\rm NL}^{\rm orth.}$
P	0.0036	0.013	0.0012	0.005	-	-	-
$P + g.p.$:	0.0034	0.011	0.0011	0.0043	-	-	-
P : bias fixed	0.0029	0.0074	0.00079	0.0024	-	-	-
$P : n_b \to \infty$	0.0029	0.0074	0.00047	0.0029	-	-	-
P+B	0.0021	0.0047	0.00034	0.0017	0.27	18	4.6
$P + B + g.p.$:	0.0020	0.0045	0.00033	0.016	0.26	13	3.6
$P + B$: bias fixed	0.0016	0.0034	0.00021	0.0010	0.17	3.6	1.7
$P + B : n_b \to \infty$	0.00019	0.00045	0.000029	0.00018	0.11	5.4	1.5

Figure 8.8: Triangle plots and errors from several different Fisher forecasts for MegaMapper. We compare base results to results obtained without shot noise (left) and with biases fixed or with a "galaxy-formation prior" (g.p.) (right). In the table, we also show the impact of including higher multipoles on the power spectrum and bispectrum and also see the impact on $f_{\rm NL}$. For the constraints on $f_{\rm NL}$, we fix the other cosmological parameters.

be seen from Tab. 8.8, the shot noise, especially for the higher redshift bin, is extremely large [29]. We, therefore, present the limiting case of zero shot noise to better understand the possible gain achievable by reducing the currently estimated shot noise. Equally motivated by the long timeline of MegaMapper, we present results with stronger bias priors, anticipating the better understanding of galaxy formation until the data release. Along with the zero shot noise and "galaxy-formation prior" results, we also present the impact of fixing biases in Fig. 8.8.

We see that stronger bias priors mostly have an effect on $f_{\rm NL}^{\rm eq.}$ and $f_{\rm NL}^{\rm orth.}$. Going further and fixing the biases we would again, roughly, reduce the error bar by a factor 2, with again the exception of $f_{\rm NL}^{\rm eq.}$ where the dependence is much stronger.

[29] This also means that the 2-loop analysis for MegaMapper just marginally improves on this results at $< 20\%$ error bar reduction, which we verified with the same method as mentioned in footnote [27].

This again motivates the perturbativity prior we discuss in Sec. 8.6. This is very similar to the case of BOSS and DESI shown in Secs. 8.5.1 and 8.5.2. Thus, the relative gain of putting the "galaxy-formation prior" or fixing the biases is very similar among the three surveys we consider.

However, shot noise affects the three surveys very differently. In particular, for MegaMapper, shot noise is quite significant for some cosmological parameters. Especially for the base parameters, we can see from the table in Fig. 8.8, that reduction of shot noise for MegaMapper can lead to a ∼10-fold error bar reduction. Instead for non-Gaussianity parameters, while shot noise still seems to be in an important factor, it is comparably less significant. In particular, the effect of setting shot noise to zero is similar to fixing the biases when analyzing $f_{\rm NL}$.

8.6 Further Constraining $f_{\rm NL}$ with a Perturbativity Prior

As we saw in Sec. 8.5, in particular Figs. 8.4, 8.6 and 8.8, fixing the biases leads to stronger constraints on the primordial parameters $\ln(10^{10}A_s)$ and n_s and to vast improvements on some $f_{\rm NL}$ parameters. We will see in this section that some non-Gaussianity parameters are greatly affected by EFT parameter constraints. In particular, small improvements on the constraints on the bias parameters can lead to significant improvements on $f_{\rm NL}^{\rm eq.}$ and $f_{\rm NL}^{\rm orth.}$. We are thus motivated to place stronger (and physically justifiable) priors on the nuisance parameters in order to further constrain single-field inflation.

As mentioned in Sec. 8.3.3, we put independent priors on the EFT parameters, restricting their individual size. This is motivated by the fact that the EFTofLSS predicts these parameters to be of order one. However, given that the MCMC explores the full parameter space in a random walk, the final loop contribution can be $\sqrt{n}$ larger than the truth, where n is the number of EFT parameters. We aim to address the issue that such parameter configurations are unphysical yet can still fit the data well. This happens because, at intermediate and low k's, where each term is not too small, even a too-large loop is comparably small with respect to the data error that scales like $k^{-3/2}$. Therefore, only at large k where the data error is sufficiently small, would parameter configurations exhibiting $\sqrt{n}$ enhancements to the loop be ruled out. However, there exist parameter configurations exhibiting $\sqrt{n}$ larger contributions at lower k's that cancel out at large k, making the loop appear

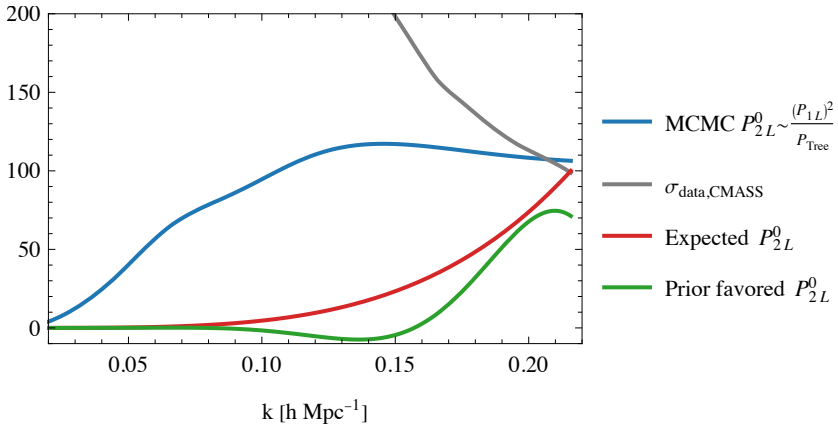

Figure 8.9: Plot showing various two-loop monopole power spectra, P^0_{2L} against the CMASS data error, $\sigma_{\rm data,CMASS}$ (grey). As an example of a typical MCMC, the BOSS CMASS P^0_{2L} was estimated using the relation $P_{2L} \sim \frac{P^2_{1L}}{P^{\rm Tree}}$, and is shown in blue. The expected P^0_{2L} size is shown in red and an example of a P^0_{2L} that would be favoured by the perturbativity prior is shown in green.

to have the correct size at those scales. Therefore, a loop contribution that is too large at low k can still fit the data well, but would go unnoticed, even though it would clearly be unphysical. Through scaling relations, this then translates to an overestimate of the expected higher loop contribution. This argument is shown for the estimated 2-loop contribution in Fig. 8.9.

We, therefore, propose an additional prior, which we call “perturbativity prior", on the size of the loop contributions, aimed at being effective in the intermediate and low k regions where the $\sqrt{n}$ enhancements are not sufficiently restricted by the data analysis. To formulate this “perturbativity prior”, we use the fact that, as we sample the different bias configurations, the two-loop contribution can have a maximal size, and therefore a maximal signal-to-noise. This maximal signal-to-noise was what defined the $k_{\rm max}$ in Eq. (8.22). In this section, we show that by using appropriate scaling relations between the two-loop and one-loop contributions, we can translate this threshold for the two-loop contribution into a prior on the size of the one-loop contribution.

8.6.1 Contribution to the Fisher Matrix

We impose a perturbativity prior for the power spectrum and bispectrum respectively, and the procedure is the same in both cases. We therefore keep the derivation generic, for the loop of some observable, X_{1L}, where $X \in \{P, B\}$. In a

later step, we will derive an estimate for the correct size of the loop, denoted by X_{1L}^C. As mentioned in the previous section, this estimate will come from a threshold for the signal-to-noise of two-loop contributions, through which we can infer properties about the correct one-loop contributions. The quantity we want to constrain is X_{1L}, whereas X_{1L}^C we assume to be estimated before the data analysis. We then impose that on average, X_{1L} is close to X_{1L}^C, therefore, we impose a Gaussian prior

$$\frac{1}{N_X}\sum_{k_i}\int_{-1}^{1}\int_{0}^{2\pi}\frac{d\mu_i}{2}\frac{d\phi}{2\pi}\frac{X_{1L}(k_i;\hat{z})}{X_{1L}^C(k_i;\hat{z})}\sim\mathcal{N}(1,1), \tag{8.32}$$

where $k_i \in \{k,(k_1,k_2,k_3)\}$, $\mu_i \in \{\mu,\mu_1\}$ and $N_X \in \{N_{\rm bins},N_\Delta\}$ for the power spectrum and bispectrum respectively. We here implement the real space part of the perturbativity prior [30]. For the remainder of this section, we, therefore, always refer to real space quantities, indicated by dropping the $\hat{z}$ argument. The real space prior we then impose is given by

$$\frac{1}{N_X}\sum_{k_i}\frac{X_{1L}(k_i)}{X_{1L}^C(k_i)}\sim\mathcal{N}(1,1). \tag{8.33}$$

One way to write the prior above is to impose the same, independent, prior for each bin. That is, we impose

$$X_{1L}(k_i)\sim\mathcal{N}\left(X_{1L}^C(k_i),N_X\left(X_{1L}^C(k_i)\right)^2\right), \tag{8.34}$$

which implies Eq. (8.33).

In order to use this prior for the Fisher matrix, we assume once again that our reference cosmology is accurate and we assume $X_{1L}^{\rm ref}\simeq X_{1L}^C$ ([31]). Then, for fixed k_i,

[30] We note that the real space perturbativity prior is on its own only restricting the size of the real space correlators. However, given that the size of the full redshift space observables is highly dependent on the real space EFT-parameter values, there is little room left for the full redshift space contribution to be large, if the real space contribution is restricted enough. We therefore expect that the full redshift space prior is highly correlated with the real space one, and, therefore, only do the real space version here. Adding the redshift space part is straightforward.

[31] Given that the best-fit we currently have was not obtained with the use of the perturbativity prior, this approximation is not guaranteed to be justified. However, as we will see in Fig. 8.10, the perturbativity prior only mildly affects the errors of EFT parameters. Therefore, we assume that the best-fit values are also only slightly modified, still making the reference values we use here, a good approximation. This issue will disappear once a data analysis with this additional prior is performed.

similarly to Eq. (8.3), we can Taylor expand to get [32]

$$\begin{aligned} -2\log \text{Prior} &= \frac{1}{N_X \left(X_{1L}^C\right)^2}\left(X_{1L}(\theta) - X_{1L}^C\right)^2 + r_1 \\ &\simeq (\theta - \theta^{\text{ref}})^T F^{X,\text{pert.}} (\theta - \theta^{\text{ref}}) + r_1, \end{aligned} \tag{8.35}$$

where $F_{ij}^{X,\text{pert.}} = \frac{1}{N_X\left(X_{1L}^C\right)^2}\frac{\partial X_{1L}}{\partial\theta_i}\frac{\partial X_{1L}}{\partial\theta_j}$ and r_1 is a parameter-independent constant. Therefore, summing over all bins, the perturbativity prior that we finally implement in the Fisher forecast is given by

$$\begin{aligned} F_{ij}^{\text{pert.}} &= \frac{1}{N_{\text{bins}}}\sum_k \frac{1}{P_{1L}^C(k)^2}\frac{\partial P_{1L}(k)}{\partial\theta_i}\frac{\partial P_{1L}(k)}{\partial\theta_j} \\ &\quad + \frac{1}{N_\Delta}\sum_{k_1,k_2,k_3}\frac{1}{B_{1L}^C(k_1,k_2,k_3)^2}\frac{\partial B_{1L}(k_1,k_2,k_3)}{\partial\theta_i}\frac{\partial B_{1L}(k_1,k_2,k_3)}{\partial\theta_j}. \end{aligned} \tag{8.36}$$

In order to be able to implement this prior, we need to derive the estimates for P_{1L}^C and B_{1L}^C. We derive the threshold for the size of the 1-loop contributions from limiting the 2-loop signal-to-noise ratio. This is similar to how we determined the k_{max} in Sec. 8.3.3. There, we demanded that the signal-to-noise of the 2-loop contribution for any new survey does not exceed its signal-to-noise of BOSS CMASS, where we know it is negligible. In particular, the maximal signal-to-noise that has previously been chosen in the data analysis to determine the k_{max} was $\frac{1}{9}$, which is also what we use here. Explicitly,

$$\begin{aligned} \int_0^{k_{\text{max}}}\left(\frac{P_{2L}(k)}{\tilde{\sigma}_{P,\text{data}}(k)}\right)^2 dk &\simeq \frac{1}{9}, \\ \int_{\nu_B}\left(\frac{B_{2L}(k_1,k_2,k_3)}{\tilde{\sigma}_{B,\text{data}}(k_1,k_2,k_3)}\right)^2 dk_1 dk_2 dk_3 &\simeq \frac{1}{9}, \end{aligned} \tag{8.37}$$

where $\tilde{\sigma}_{X,\text{data}}$ here is defined as in Eq. (8.25), using that in the continuum limit we get $\Delta k \to dk$, and ν_B is the set of all triangles with maximal wavenumber smaller than or equal to k_{max}. We then get the estimates for the correct one-loop contributions, through the approximate size relations between two-loop and one-loop, $P_{2L} \sim \frac{{P_{1L}^C}^2}{P_{\text{Tree}}^{NS}}$ and $B_{2L} \sim \frac{B_{1L}^C P_{1L}^C}{P_{\text{Tree}}^{NS}}$ ([33]). Finally, in order to perform the integrals in Eq. (8.37), we

[32] We would not need to do this Taylor expansion in an actual data analysis.

[33] Note that here the numerators have the usual stochastic contributions, but P_{Tree}^{NS} in the denominators has no shot noise.

assume scaling functions $S^X(k_i)$, defined by $\frac{S^X(k_i)}{S^X(k_{\rm max})} = \frac{X^C_{1L}(k_i)}{X^C_{1L}(k_{\rm max})}$ ([34]), that should approximate the k dependencies of $X^C_{1L}(k_i)$. Plugging in the size relations and scaling approximation into Eq. (8.37), we can solve for the $X^C_{1L}(k_i)$ to get

$$P^C_{1L}(k) = S^P(k)\left(9\int_0^{k_{\rm max}}\left(\frac{S^P(k')^2}{P^{NS}_{\rm Tree}(k')\tilde{\sigma}_{P,\rm data}(k')}\right)^2 dk'\right)^{-1/4}, \tag{8.38}$$

$$B^C_{1L} = S^B(k_1,k_2,k_3)\left(9\int_{\nu_B}\left(\frac{S^B(k_1',k_2',k_3')}{\tilde{\sigma}_{B,\rm data}(k_1',k_2',k_3')}\frac{1}{3}\left(\frac{P^C_{1L}(k_1')}{P^{NS}_{\rm Tree}(k_1')}+2p.\right)\right)^2 dk_1'dk_2'dk_3'\right)^{-1/2},$$

where we dropped the k-dependence for B^C_{1L} to avoid clutter and in the bottom line we symmetrize the $\frac{P^C_{1L}}{P^{NS}_{\rm Tree}}$. Note that P^C_{1L} and B^C_{1L} do not depend on the overall size of the scaling estimates S^X, as we are normalizing it at $k_{\rm max}$.

There are well established estimates for the behaviour of the power spectrum loop [145] and bispectrum loop [240] in a scaling universe. For biased tracers we adapt this to

$$\begin{aligned} S^P_{\rm int}(k) &= P_{\rm Tree}(k)\left(\frac{k}{k_{\rm NL}}\right)^{3+n(k)}, \\ S^B_{\rm int}(k_1,k_2,k_3) &= B_{\rm Tree}(k_1,k_2,k_3)\left(\left(\frac{k_1}{k_{\rm NL}}\right)^{3+n(k_1)}+2p.\right), \end{aligned} \tag{8.39}$$

which is very similar to the one used in Eq. (8.23), but with $P_{\rm Tree}$ and $B_{\rm Tree}$ being the (real space) biased tracers tree-level power spectrum and bispectrum. In order to have both the right IR and UV behaviour of the loop contributions we also include a loop counter term to the estimate. For the scaling of the counterterms, we use

$$\begin{aligned} S^P_c(k) &= -2b_1\beta P_{11}(k)\left(\frac{k}{k_{\rm NL}}\right)^2, \\ S^B_c(k_1,k_2,k_3) &= -2b_1^2\beta\left(P_{11}(k_1)P_{11}(k_2)\left(\frac{k_3}{k_{\rm NL}}\right)^2+2p.\right), \end{aligned} \tag{8.40}$$

where we use the reference value $\beta_{\rm BOSS} = 1$ and rescale with Eq. (8.19) for other surveys [35]. Finally, given that S^P and S^B should be upper bounds on the scaling of the loops, we want to avoid cancelations and ensure positivity. Therefore, the final

[34] One could have normalized this scaling factor to make it unitless, *i.e.* $S^X(k_i) \to \frac{S^X(k_i)}{S^X(k_{\rm max})}$ without changing anything in the final formulas.

[35] The representative counter terms here correspond to the terms multiplied by c_1^h and c_3^h in Ch. 6.

scalings we implement are

$$\begin{aligned} S^P(k) &= \max(|S^P_{\rm int}(k)|, |S^P_c(k)|), \\ S^B(k_1,k_2,k_3) &= \max(|S^B_{\rm int}(k_1,k_2,k_3)|, |S^B_c(k_1,k_2,k_3)|). \end{aligned} \tag{8.41}$$

8.6.2 Results

While the perturbativity prior further constrains both cosmological parameters and bias parameters, the largest effect comes from further constraining particular bias parameters. We present this improvement in Fig. 8.10. Indeed, there we can see that small improvements on particular EFT parameters [36] lead to vast improvements on $f^{\rm eq.}_{\rm NL}$. In the tables of Fig. 8.10 we also show the effect on the other types of non-Gaussianity we analyze. Each analysis was performed with fixed cosmological parameters and each type of non-Gaussianity was analyzed separately. For completeness, and to stress the importance of the bispectrum loop, we also compare it with bispectrum tree-level constraints. The survey specifications used for the tree-level analysis are also in Tabs. 8.1, 8.2, and 8.3. In the following, we will present results for each survey based on the plots in Fig. 8.10.

Finally, as we also discussed in Sec. 8.5, base cosmological parameters are less affected by constraints on bias parameters. However, we find that the inclusion of the perturbativity prior can have a relevant effect on them, which we discuss in App. D.2.2. In particular, we find that DESI will constrain curvature to 0.012 and MegaMapper to 0.0012.

BOSS As shown in the table of Fig. 8.10, the one-loop bispectrum already significantly improves the constraints on non-Gaussianities by $\sim 30-50\%$ with respect to the tree-level analysis. Additionally including the perturbativity prior to the one-loop bispectrum yields a further $\sim 24\%$ reduction in σ for $f^{\rm loc.}_{\rm NL}$, and $\sim 10\%$ reduction in σ for $f^{\rm eq.}_{\rm NL}$ and $f^{\rm orth.}_{\rm NL}$. The "galaxy-formation prior" would further reduce the error by $\sim 20-30\%$ for $f^{\rm eq.}_{\rm NL}$ and $f^{\rm orth.}_{\rm NL}$, and 14% for $f^{\rm loc.}_{\rm NL}$. The addition of the loop breaks the degeneracy between c_2 and c_4 ([37]), greatly improving constraints on both parameters, which translates to stronger constraints on $f^{\rm eq.}_{\rm NL}$. Furthermore, the inclusion of the perturbativity prior further breaks this degeneracy and improves upon the

[36] We remind the reader that c_2 and c_4 are the linear combinations of the second-order biases that enter the tree-level bispectrum, alongside the linear bias b_1. Explicitly they are $c_2 = (b_2+b_5)/\sqrt{2}$, $c_4 = (b_2-b_5)/\sqrt{2}$. For more details see Eq. (6.132) and Ch. 7.

[37] The breaking of this degeneracy due to the loop bispectrum is already present in Ch. 7.

constraints on b_1, which leads to additional improvements on the $f_{\rm NL}$ parameters.

DESI As it was seen in BOSS, the inclusion of the loop bispectrum and perturbativity prior breaks the degeneracy between c_2 and c_4 and tightens the constraints on EFT parameters for DESI as well. However, the resulting effect on $f_{\rm NL}$ parameters is different. Unlike BOSS, the inclusion of the one-loop bispectrum and perturbativity prior to DESI does not uniformly tighten all $f_{\rm NL}$ errors. For one, most of the information to constrain $f_{\rm NL}^{\rm loc.}$ is contained in the power spectrum and the tree-level bispectrum. In contrast, the one-loop bispectrum does improve the constraint of $f_{\rm NL}^{\rm eq.}$ and $f_{\rm NL}^{\rm orth.}$ by 19% and 58% respectively. The perturbativity prior reduces these errors further by 20% and 11% and the future galaxy formation prior by another 16% and 19%.

MegaMapper MegaMapper results are more similar to DESI than BOSS. $f_{\rm NL}^{\rm loc.}$ is mostly constrained through the power spectrum and does not improve much with the addition of the bispectrum loop or the perturbativity prior. Additionally, as was seen for DESI, the inclusion of the bispectrum loop leads to a more significant improvement in the constraint on $f_{\rm NL}^{\rm orth.}$ compared to $f_{\rm NL}^{\rm eq.}$, with 47% and 24% improvements respectively. To place these results into context, note that the tree level results we obtain are in agreement with those obtained in [228] [38]. Note, however, the tree-level $k_{\rm max}$ we estimate here is a bit lower, thus we predict slightly less optimistic constraints for the tree-level bispectrum, which makes the addition of the loop more important. The loop again breaks the degeneracy between c_2 and c_4, and the perturbativity prior enhances the constraints on c_2 in particular, thereby improving the constraints on $f_{\rm NL}^{\rm eq.}$ and $f_{\rm NL}^{\rm orth.}$ by 9% and the "galaxy-formation prior" further reduces the errors by 21% and 18% respectively.

[38] The results we present here would correspond to their MegaMapper - B results, with fixed cosmological parameters and free bias parameters. The disagreement with our results is $< 10\%$.

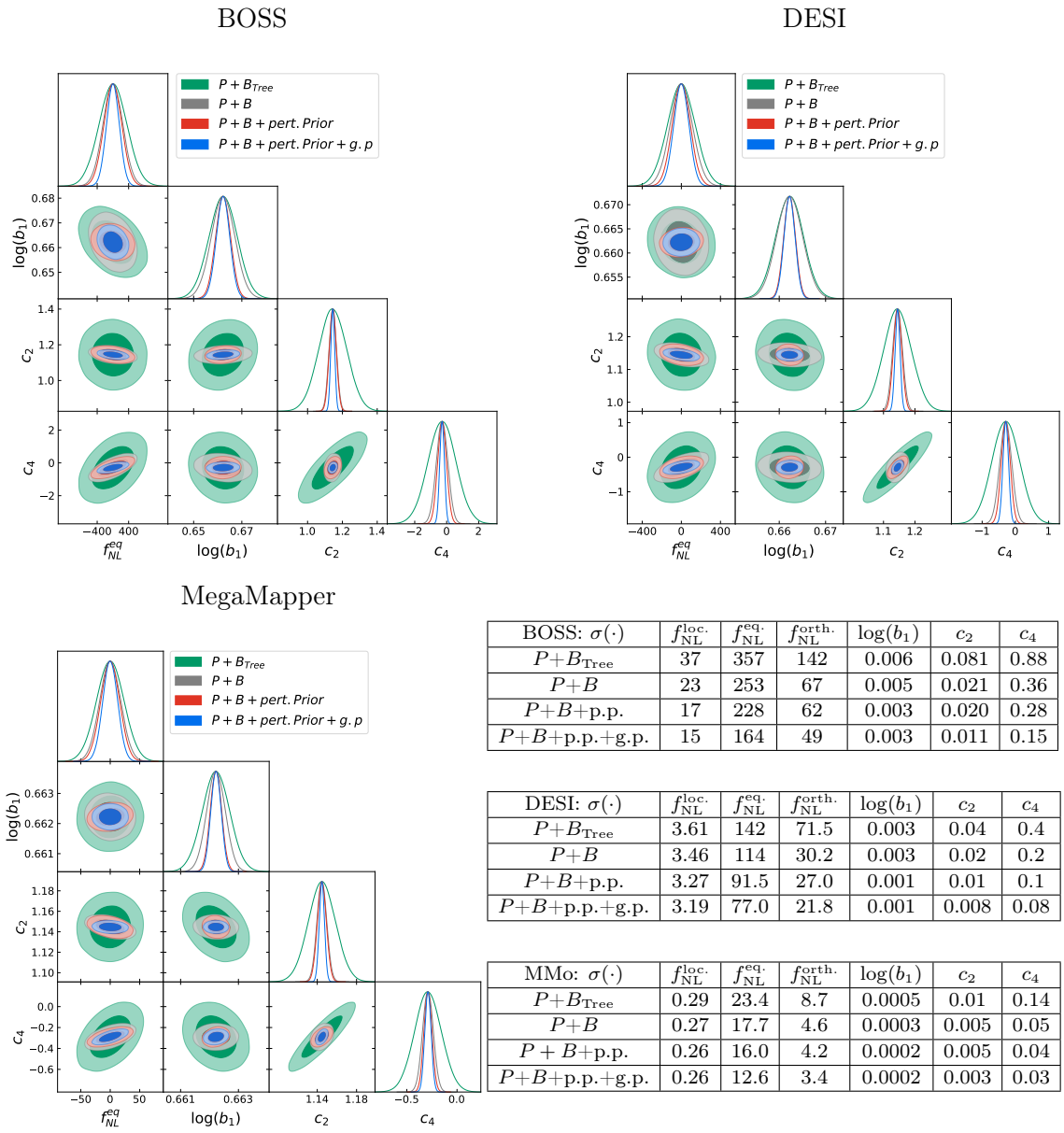

BOSS: $\sigma(\cdot)$	$f_{\rm NL}^{\rm loc.}$	$f_{\rm NL}^{\rm eq.}$	$f_{\rm NL}^{\rm orth.}$	$\log(b_1)$	c_2	c_4
P+$B_{\rm Tree}$	37	357	142	0.006	0.081	0.88
P+B	23	253	67	0.005	0.021	0.36
P+B+p.p.	17	228	62	0.003	0.020	0.28
P+B+p.p.+g.p.	15	164	49	0.003	0.011	0.15

DESI: $\sigma(\cdot)$	$f_{\rm NL}^{\rm loc.}$	$f_{\rm NL}^{\rm eq.}$	$f_{\rm NL}^{\rm orth.}$	$\log(b_1)$	c_2	c_4
P+$B_{\rm Tree}$	3.61	142	71.5	0.003	0.04	0.4
P+B	3.46	114	30.2	0.003	0.02	0.2
P+B+p.p.	3.27	91.5	27.0	0.001	0.01	0.1
P+B+p.p.+g.p.	3.19	77.0	21.8	0.001	0.008	0.08

MMo: $\sigma(\cdot)$	$f_{\rm NL}^{\rm loc.}$	$f_{\rm NL}^{\rm eq.}$	$f_{\rm NL}^{\rm orth.}$	$\log(b_1)$	c_2	c_4
P+$B_{\rm Tree}$	0.29	23.4	8.7	0.0005	0.01	0.14
P+B	0.27	17.7	4.6	0.0003	0.005	0.05
P + B+p.p.	0.26	16.0	4.2	0.0002	0.005	0.04
P+B+p.p.+g.p.	0.26	12.6	3.4	0.0002	0.003	0.03

Figure 8.10: Triangle plots and errors from Fisher forecasts for BOSS (top left), DESI (top right), and MegaMapper (bottom left), for the equilateral type of non-Gaussianity, and leading bias parameters. We also show errors on other non-Gaussianity parameters in the tables. Each analysis was done with cosmological parameters fixed and each non-Gaussianity parameter was analyzed separately. We always include the power spectrum at one loop order with the addition of either the tree-level bispectrum the loop bispectrum or the loop bispectrum with a perturbativity prior (p.p.) also in combination with the "galaxy-formation prior" (g.p.). We use all power spectrum and bispectrum multipoles in each case and use the analytical covariance without cross-correlations.

Part IV

The Late Universe

Dark Energy and the Formation Time of Galaxies

9

Direct Signatures of the Formation Time of Galaxies

9.1 Summary

We show that it is possible to directly measure the formation time of galaxies using large-scale structure. In particular, we show that the large-scale distribution of galaxies is sensitive to whether galaxies form over a narrow period of time before their observed times, or are formed over a time scale on the order of the age of the Universe. Along the way, we derive simple recursion relations for the perturbative terms of the most general bias expansion for the galaxy density, thus fully extending the famous dark-matter recursion relations to generic tracers.

9.2 Introduction and Conclusions

The establishment of the standard cosmological model, from the hot big bang at early times to the cosmological constant and cold dark-matter dominated late-time accelerated expansion, is one of the great triumphs of modern science. It gives a depiction of a dynamical Universe that has evolved over billions of years from a dense cosmic soup to a sparse sprinkling of stars, galaxies, and dark-matter halos. This familiar picture was not always obvious, however.

For example, there was much debate in the second half of the twentieth century about the so-called 1948 steady-state model of the Universe [11]. This model proposed that properties of the Universe, including number and types of galaxies, did not change over time. Empirical evidence, of course, eventually contradicted these ideas. One such set of evidence was the observation that properties of galaxies, including color and estimated ages, changed with their measured redshifts (see for example [12, 13]), suggesting that the galaxies themselves evolved over time. This confusion, though, is understandable. Indeed, we cannot watch objects in the Universe evolve for very long; we can only see static snapshots at various times in the past, making it quite challenging to *directly* probe cosmic time scales.

A concept that is related to, but distinct from, the time scale of cosmic evolution is what we call a cosmic *response time*, i.e. the temporal extent to which the past influences galaxies at a given time. [1] This in turn is related to the *formation time* of galaxies, which is at least as long as the response time.

In this work, we provide, as far as we can tell, the first directly cosmologically observable signals that are sensitive to the formation time of galaxies (or galaxy clusters and other gravitationally-bound objects in general). By studying the response time of galaxies, we show that the static pictures that we take of the Universe (in galaxy surveys, for example) can contain unique signatures that are only possible if galaxies have been forming over time periods on the order of the age of the Universe. Even if we have an incredibly large amount of evidence that this must be the case, the possibility of a direct cosmological observation is, to us, quite an extraordinary prospect. [2]

[1] Mathematically, this is the time scale of support of the Green's function describing the response.

[2] We stress that in this work, we are not concerned with ages or generic evolution of structures (for which there is abundant astrophysical evidence, some of which we mentioned above), but with the response time of structures. Previous studies in this direction include numerical simulations and the so-called assembly bias [241, 242], although it can be challenging to directly relate the latter to galaxy formation time [243].

Furthermore, since our reasoning is based on the Effective Field Theory of large-scale structure (EFT of LSS, [30, 28]), which is the unique theory of gravity, cold dark matter, baryons, and tracers on large scales, our conclusions do not depend on specific modeling choices about stars or galaxies. Given the recent success of using the EFT of LSS to analyze galaxy clustering data as in [7, 142, 143, 176] and Ch. 7, we now have the intriguing opportunity to explore the Universe in this exciting new way.

It has been known for some time (see e.g. [244, 245]) that on large scales, the galaxy distribution can be expressed as a Taylor expansion in the fluctuations of the underlying dark-matter distribution, an approach that goes by the general name of the *bias expansion* (for a modern review, see [157]). This makes intuitive sense, since galaxies tend to form in regions of space where the dark-matter density, and hence the gravitational potential, is highest. In [136] it was argued that this dependence should be on second spatial derivatives of the gravitational potential and gradients of the dark-matter velocity, and a straightforward extension allows for a dependence on spatial derivatives of these quantities. But is galaxy clustering only affected by the nearby dark-matter distribution at the time that we measure it (*local in time*), or does the configuration of the dark matter at earlier times, of order a Hubble time earlier, have an impact (*non-local in time*)? Said another way, given two identical localized dark-matter configurations at a given time, will the same galaxies always form, or do we need to know the whole history of that configuration?

This question was conceptually answered in [129], which pointed out that the most general dependence, based on the symmetries relevant to dark-matter and baryon dynamics and galaxy formation on large scales, which are the equivalence principle and diffeomorphism invariance (the non-relativistic limit of which is called Galilean invariance), is on second spatial derivatives of the gravitational potential, gradients of the matter velocity (and the relative velocity directly), and their spatial gradients, integrated over all past times. This makes the EFT of LSS generally local in space, but non-local in time. [3]

However, until now, the most advanced perturbative calculations, as done in Ch. 6, have shown that the non-local-in-time bias expansion up to fourth order is mathematically equivalent to the local-in-time expansion. As we show in this work, though, this is no longer true at fifth order, and thus it is possible to see distinctly non-local-in-time effects in the galaxy-clustering signal. Measuring the size of these effects would then give us a direct indication of the formation time scale of galaxies.

[3] See also [147, 246] for discussions of non-local-in-time effects in dark-matter clustering.

As a side observation, this time scale would also give a *direct* (versus indirect) lower bound on the age of the Universe.

Notes We work in the Newtonian approximation where $\Phi(\vec{x},t)$ is the gravitational potential, $a(t)$ is the scale factor of the Universe, the Hubble parameter is defined by $H(t) \equiv \dot{a}(t)/a(t)$, and the overdot '˙' stands for a derivative with respect to t. The dark-matter fluid is described by the overdensity $\delta(\vec{x},t)$ and fluid velocity $\vec{v}(\vec{x},t)$. The growth factor $D(t)$ is defined as the growing mode solution to the linear equation of motion for δ, i.e. satisfies $\ddot{D} + 2H\dot{D} - 3\Omega_{\rm m}H^2D/2 = 0$, where $\Omega_{\rm m}(t)$ is the time-dependent matter fraction.

The building blocks of Galilean scalars are the dimensionless tensors

$$r_{ij} \equiv \frac{2\partial_i\partial_j\Phi}{3\Omega_{\rm m}a^2H^2} \ , \quad \text{and} \quad p_{ij} \equiv -\frac{D}{a\dot{D}}\partial_i v^j \ . \tag{9.1}$$

For brevity, we will always denote the traces $\delta^{ij}r_{ij} = \delta$ (which is true because of the Poisson equation) and $\delta^{ij}p_{ij} \equiv \theta$ (which is our definition of θ). Then, for other contractions, we write the matrix products as simple multiplication, i.e. $r^2 = r_{ij}r_{ji}$, $r^2p = r_{ij}r_{jk}p_{ki}$, $rprp = r_{ij}p_{jk}r_{kl}p_{li}$, and so on (repeated indices are always summed over). We work in the so-called Einstein-de Sitter approximation, where the time dependence of perturbations is given by

$$\delta^{(n)}(\vec{x},t) = \left(\frac{D(t)}{D(t')}\right)^n \delta^{(n)}(\vec{x},t') \ , \quad \theta^{(n)}(\vec{x},t) = \left(\frac{D(t)}{D(t')}\right)^n \theta^{(n)}(\vec{x},t') \ . \tag{9.2}$$

In this work, we focus on the lowest-derivative bias terms that are sufficient to establish our claims, and leave a discussion of higher-derivative bias (and counterterms) for future work. Finally, we focus on the real space (as opposed to redshift space) prediction, which in any case is the leading signal if one restricts observations to directions near the line of sight. We leave extending our results to redshift space to future work. A more detailed explanation of the notation used here, is in Ch. 6.

9.3 Complete Bias Expansion and Recursion

We start by constructing the most general bias expansion for the galaxy overdensity $\delta_g(\vec{x},t) \equiv (n(\vec{x},t) - \bar{n}(t))/\bar{n}(t)$, where $n(\vec{x},t)$ is the galaxy number-density field and $\bar{n}(t)$ is the average number density of galaxies, that is consistent with the

equivalence principle, diffeomorphism invariance, and is non-local in time. [4] Up to N-th order in perturbations, we have

$$\delta_g(\vec{x},t)\big|_N = \sum_{n=1}^{N} \delta_g^{(n)}(\vec{x},t) \ , \tag{9.3}$$

where the expression at n-th order is given by the non-local-in-time integral over the sum of all possible local-in-time functions $\mathcal{O}_m$ up to order n [129]

$$\delta_g^{(n)}(\vec{x},t) = \sum_{\mathcal{O}_m} \int^t dt' H(t') c_{\mathcal{O}_m}(t,t') [\mathcal{O}_m(\vec{x}_{\rm fl}(\vec{x},t,t'),t')]^{(n)} \ , \tag{9.4}$$

evaluated along the fluid element

$$\vec{x}_{\rm fl}(\vec{x},t,t') = \vec{x} + \int_t^{t'} \frac{dt''}{a(t'')} \vec{v}\left(\vec{x}_{\rm fl}(\vec{x},t,t''),t''\right) \ , \tag{9.5}$$

and we use the square brackets and superscript notation $[\cdot]^{(n)}$ to mean that we perturbatively expand the expression inside of the brackets and take the n-th order piece. [5] Neglecting baryons, as they are a small effect [128, 31], in Eq. (9.4), since δ_g is a Galilean scalar, the equivalence principle implies that the set of functions $\{\mathcal{O}_m\}$ is given by all possible rotationally invariant contractions of the dark-matter fields r_{ij} and p_{ij}, and integrating the $\mathcal{O}_m$ along the fluid element is the most general way to write a non-local-in-time expression for δ_g. All of the complicated details of galaxy-formation physics is then encoded in the functions $c_{\mathcal{O}_m}$, which are a priori unknown (from the EFT point of view) time-dependent kernels, which physically can be thought of as the response of the galaxy overdensity to a given field at a given time. The local-in-time expansion is given by setting $c_{\mathcal{O}_m}(t,t') = c_{\mathcal{O}_m}(t)\delta_D(t-t')/H(t)$. Notice that we do not include any time derivatives of r_{ij} or p_{ij} in the set $\{\mathcal{O}_m\}$ because these operators are not present in the strictly local-in-time limit (i.e. they would be suppressed with respect to other terms by $H/\omega_{\rm short} \ll 1$ where $1/\omega_{\rm short}$ is the time-scale of the relevant local-in-time physics) [129]. Thus, our expansion covers all Hubble-scale non-local-in-time effects. From now on, in the list of functions $\{\mathcal{O}_m\}$, we identify the subscript m on $\mathcal{O}_m$ to denote that the function

[4] From an EFT perspective the galaxy overdensity δ_g and the halo overdensity δ_h from Ch. 6 can be viewed as interchangable.

[5] There was an interesting discussion [247] as to whether intrinsic alignments (see [248] for an EFT description) of galaxies are most affected by the gravitational field at late or early times [249, 250, 251]. Our non-local-in-time bias expansion Eq. (9.4) takes both possibilities into account.

starts at order m, i.e. $m = 3$ for $\delta^2\theta, \delta^3, r^2 p, \ldots$.

In this way, the bias expansion at order n is reduced to an algorithmic procedure. To create the list of seed functions $\{\mathcal{O}_m\}$, we list all contractions up to n factors of r_{ij} and p_{ij}. We then iteratively Taylor expand $\mathcal{O}_m(\vec{x}_{\rm fl}(\vec{x}, t, t'), t')$ around $\vec{x}$ using the recursive definition Eq. (9.5), and take the n-th order piece. After performing this expansion, we end up with an expression that can be cast into similar notation as Eq. (6.127)

$$[\mathcal{O}_m(\vec{x}_{\rm fl}(\vec{x}, t, t'), t')]^{(n)} = \sum_{\alpha=1}^{n-m+1} \left(\frac{D(t')}{D(t)}\right)^{\alpha+m-1} \mathbb{C}^{(n)}_{\mathcal{O}_m,\alpha}(\vec{x}, t) \ . \tag{9.6}$$

The resulting bias functions $\mathbb{C}^{(n)}_{\mathcal{O}_m,\alpha}$, which we say are in the fluid expansion of the seed function $\mathcal{O}_m$, are *defined* by the expansion in Eq. (9.6), whose form is guaranteed by assuming the scaling time dependence of the dark-matter fields Eq. (9.2), as well as the implied relation

$$\mathbb{C}^{(n)}_{\mathcal{O}_m,\alpha}(\vec{x}, t) = \left(\frac{D(t)}{D(t')}\right)^{n} \mathbb{C}^{(n)}_{\mathcal{O}_m,\alpha}(\vec{x}, t') \ . \tag{9.7}$$

Plugging Eq. (9.6) into Eq. (9.4), and defining the expansion coefficients

$$c_{\mathcal{O}_m,\alpha}(t) \equiv \int^t dt' H(t') c_{\mathcal{O}_m}(t, t') \left(\frac{D(t')}{D(t)}\right)^{\alpha+m-1} \ , \tag{9.8}$$

we finally have the most general expansion of the overdensity at order n in terms of fields at the same time

$$\delta^{(n)}_g(\vec{x}, t) = \sum_{\mathcal{O}_m} \sum_{\alpha=1}^{n-m+1} c_{\mathcal{O}_m,\alpha}(t)\, \mathbb{C}^{(n)}_{\mathcal{O}_m,\alpha}(\vec{x}, t) \ . \tag{9.9}$$

There is in fact a much simpler way to obtain the bias functions $\mathbb{C}^{(n)}_{\mathcal{O}_m,\alpha}$, using recursion relations, which is an additional key technical result of this work. While the procedure described above is conceptually straightforward, it can be practically quite cumbersome. The recursion relations come in two parts. The first is the *equal-time completeness relation*

$$\mathcal{O}^{(n)}_m(\vec{x}, t) = \sum_{\alpha=1}^{n-m+1} \mathbb{C}^{(n)}_{\mathcal{O}_m,\alpha}(\vec{x}, t) \ , \tag{9.10}$$

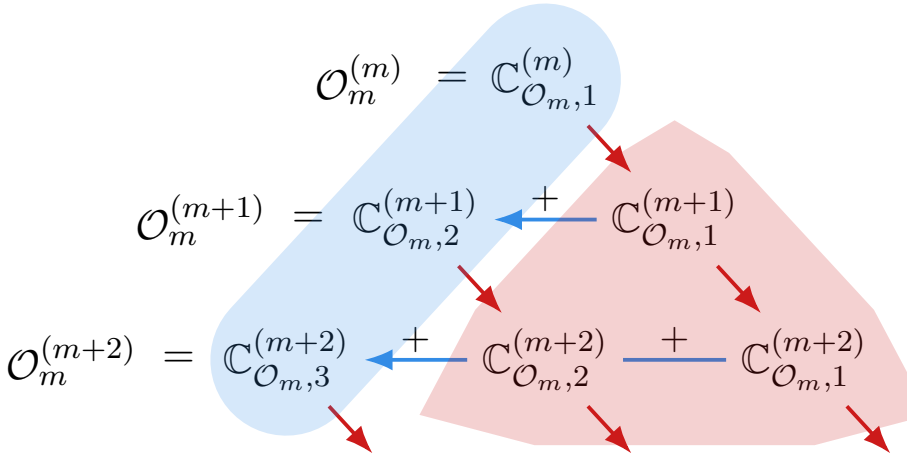

Figure 9.1: Diagrammatic representation of one way of using the recursion relations Eqs. (9.10) and (9.11) to determine the full set of bias functions $\mathbb{C}^{(n)}_{\mathcal{O}_m,\alpha}$ in the fluid expansion of a seed function $\mathcal{O}_m$. The red arrows indicate the use of the fluid recursion Eq. (9.11), while the blue arrows indicate the use of the completeness relation Eq. (9.10). Thus, the terms in the red shading ($\alpha < n - m + 1$) are determined by the fluid recursion Eq. (9.11) and the terms in the blue shading ($\alpha = n - m + 1$) are determined by the completeness relation Eq. (9.10).

which is trivially obtained by setting $t = t'$ in Eq. (9.6), and where $\mathcal{O}_m^{(n)}$ is the standard expansion of $\mathcal{O}_m$ at n-th order in perturbations. The second, which captures the consequences of expanding $\vec{x}_{\rm fl}$ in Eq. (9.6), is the *fluid recursion*

$$\mathbb{C}^{(n)}_{\mathcal{O}_m,\alpha}(\vec{x},t) = \frac{1}{n-\alpha-m+1}\sum_{\ell=m+\alpha-1}^{n-1}\partial_i\mathbb{C}^{(\ell)}_{\mathcal{O}_m,\alpha}(\vec{x},t)\frac{\partial_i}{\partial^2}\theta^{(n-\ell)}(\vec{x},t)\ , \tag{9.11}$$

which is valid for $n - \alpha - m + 1 > 0$. We explicitly derive Eq. (9.11) at the end of this section. This recursion is reminiscent of the famous dark-matter recursion relations [150], and provides, for the first time, a full generalization to generic biased tracers. We give a diagrammatic representation of this recursion relation in Fig. 9.1.

It is worth stressing that, unlike other treatments of biased tracers (such as [252, 253] and subsequent works), we do *not* assume an instantaneous formation time of galaxies, nor do we assume a continuity equation for galaxies. Indeed, Eq. (9.11) is a consequence of Galilean invariance (i.e. expanding $\vec{x}_{\rm fl}$), not of the conservation of galaxies.

Since we have formally done the integral over t' in Eq. (9.8), one might wonder where in Eq. (9.9) the non-local-in-time effect has gone. Comparing Eq. (9.9) to the

local-in-time expression

$$\delta^{(n)}_{g,\rm loc}(\vec{x},t) = \sum_{\mathcal{O}_m} c_{\mathcal{O}_m}(t)\,\mathcal{O}^{(n)}_m(\vec{x},t)\ , \tag{9.12}$$

we see that the difference is in the basis functions of the expansion (which as we will discuss below control the possible functional forms of the clustering signals), since Eq. (9.9) is equivalent to Eq. (9.12) under the restriction that, for all α, $c_{\mathcal{O}_m,\alpha}(t) = c_{\mathcal{O}_m}(t)$.

Proof of Fluid Recursion To derive Eq. (9.11), we will want to take d/dt of Eq. (9.6), which means that we will need to know $\partial_t \vec{x}_{\rm fl}(\vec{x},t,t')$. To find that, we notice that by definition the fluid element satisfies the composition rule

$$\vec{x}_{\rm fl}\left(\vec{x}_{\rm fl}(\vec{x},t_{\rm in},t),t,t'\right) = \vec{x}_{\rm fl}(\vec{x},t_{\rm in},t')\ . \tag{9.13}$$

Since the right-hand side is independent of t, this implies

$$\frac{d}{dt}\vec{x}_{\rm fl}\left(\vec{x}_{\rm fl}(\vec{x},t_{\rm in},t),t,t'\right) = 0\ . \tag{9.14}$$

Using the chain rule, and

$$\frac{d}{dt}\vec{x}_{\rm fl}(\vec{x},t_{\rm in},t) = \frac{1}{a(t)}\vec{v}(\vec{x}_{\rm fl}(\vec{x},t_{\rm in},t),t)\ , \tag{9.15}$$

which follows immediately from the definition of $\vec{x}_{\rm fl}$ Eq. (9.5), this implies

$$\Big[\frac{\partial}{\partial t}\vec{x}_{\rm fl}(\vec{y},t,t') + \frac{v^i(\vec{y},t)}{a(t)}\frac{\partial}{\partial y^i}\vec{x}_{\rm fl}(\vec{y},t,t')\Big]\Big|_{\vec{y}=\vec{x}_{\rm fl}(\vec{x},t_{\rm in},t)} = 0\ . \tag{9.16}$$

Since the initial $t_{\rm in}$ is arbitrary, we can take $t_{\rm in} = t$, which gives

$$\left(\frac{\partial}{\partial t} + \frac{v^i(\vec{x},t)}{a(t)}\frac{\partial}{\partial x^i}\right)\vec{x}_{\rm fl}(\vec{x},t,t') = 0\ . \tag{9.17}$$

This equation simply says that the convective derivative of the fluid element is zero, which makes intuitive sense since the convective derivative is defined to be along the fluid flow. Now we take d/dt of both sides of Eq. (9.6). The right-hand side is

simple, and we have (defining $D_m^\alpha(t',t) \equiv (D(t')/D(t))^{\alpha+m-1}$ to reduce clutter)

$$\frac{D(t)}{\dot{D}(t)}\frac{d}{dt}\sum_{\alpha=1}^{n-m+1} D_m^\alpha(t',t)\mathbb{C}^{(n)}_{\mathcal{O}_m,\alpha}(\vec{x},t) = \sum_{\alpha=1}^{n-m+1} D_m^\alpha(t',t)(n-\alpha-m+1)\mathbb{C}^{(n)}_{\mathcal{O}_m,\alpha}(\vec{x},t)\ , \tag{9.18}$$

where we have used Eq. (9.7) for the time dependence of $\mathbb{C}^{(n)}_{\mathcal{O}_m,\alpha}$. On the left-hand side, we have

$$\begin{aligned}
\frac{d}{dt}[\mathcal{O}_m(\vec{x}_{\rm fl}(\vec{x},t,t'),t')]^{(n)} &= \left[\frac{d}{dt}\mathcal{O}_m(\vec{x}_{\rm fl}(\vec{x},t,t'),t')\right]^{(n)} \\
&= \left[\frac{\partial}{\partial t}x^i_{\rm fl}(\vec{x},t,t')\frac{\partial}{\partial y^i}\mathcal{O}_m(\vec{y},t')\Big|_{\vec{y}=\vec{x}_{\rm fl}(\vec{x},t,t')}\right]^{(n)} \\
&= \left[-\frac{v^j(\vec{x},t)}{a(t)}\frac{\partial}{\partial x^j}x^i_{\rm fl}(\vec{x},t,t')\frac{\partial}{\partial y^i}\mathcal{O}_m(\vec{y},t')\Big|_{\vec{y}=\vec{x}_{\rm fl}(\vec{x},t,t')}\right]^{(n)} \\
&= \left[-\frac{v^j(\vec{x},t)}{a(t)}\frac{\partial}{\partial x^i}\mathcal{O}_m(\vec{x}_{\rm fl}(\vec{x},t,t'),t')\right]^{(n)} \\
&= \frac{\dot{D}(t)}{D(t)}\left[\frac{\partial_i}{\partial^2}\theta(\vec{x},t)\frac{\partial}{\partial x^i}\mathcal{O}_m(\vec{x}_{\rm fl}(\vec{x},t,t'),t')\right]^{(n)} \\
&= \frac{\dot{D}(t)}{D(t)}\sum_{\ell=m}^{n-1}\frac{\partial_i}{\partial^2}\theta^{(n-\ell)}(\vec{x},t)\frac{\partial}{\partial x^i}\left[\mathcal{O}_m(\vec{x}_{\rm fl}(\vec{x},t,t'),t')\right]^{(\ell)}\ ,
\end{aligned} \tag{9.19}$$

where we have used Eq. (9.17) to go from the second to third line, the chain rule to go from the third to fourth line, and the definition of θ from Eq. (9.1) in the fifth line. Now, we use Eq. (9.6) to replace $[\mathcal{O}_m(\vec{x}_{\rm fl}(\vec{x},t,t'),t')]^{(\ell)}$ to get

$$\begin{aligned}
\frac{D(t)}{\dot{D}(t)}\frac{d}{dt}[\mathcal{O}_m(\vec{x}_{\rm fl}(\vec{x},t,t'),t')]^{(n)} &= \sum_{\ell=m}^{n-1}\sum_{\alpha=1}^{\ell-m+1} D_m^\alpha(t',t)\frac{\partial_i}{\partial^2}\theta^{(n-\ell)}(\vec{x},t)\partial_i\mathbb{C}^{(\ell)}_{\mathcal{O}_m,\alpha}(\vec{x},t) \\
&= \sum_{\alpha=1}^{n-m} D_m^\alpha(t',t)\sum_{\ell=m+\alpha-1}^{n-1}\frac{\partial_i}{\partial^2}\theta^{(n-\ell)}(\vec{x},t)\partial_i\mathbb{C}^{(\ell)}_{\mathcal{O}_m,\alpha}(\vec{x},t)
\end{aligned} \tag{9.20}$$

where we have simply changed the order of the sums between the second and third lines. Equating the coefficients of each power of $D(t')$ in Eqs. (9.18) and (9.20) then gives our recursion relation Eq. (9.11).

9.4 Non-Local-in-Time Bias in LSS

We can now return to the main question posed by this work: *is it possible to directly measure the effects of non-locality in time on galaxy clustering?* In our perturbative description, this is equivalent to the following mathematical question: *does the basis for the non-local-in-time expansion Eq. (9.9) span a larger space than the basis for the local-in-time expansion Eq. (9.12)?* The answer, as we will show below, is yes.

As shown in Ch. 6, the non-local-in-time and local-in-time expansions *are* indeed equivalent up to fourth order in perturbations. [6] However, from the findings of this work, this seems to simply be a consequence of expanding to low orders in perturbation theory where there are too few independent spatially local and Galilean invariant functional forms available, since non-locality-in-time is generically expected in the bias expansion [129].

So, to discover a non-local-in-time effect, we look to fifth order. In particular, we will now find the non-local-in-time basis for the expansion in Eq. (9.9). To find the fifth-order functions $\mathbb{C}^{(n)}_{\mathcal{O}_m,\alpha}$, we form the set $\{\mathcal{O}_m\}$ by finding all rotationally invariant contractions of r_{ij} and p_{ij} up to fifth order. Writing the first few terms, we have $\{\mathcal{O}_m\} = \{\delta, \theta, \delta^2, \delta\theta, \theta^2, r^2, rp, p^2, \dots\}$, and overall there are 63 contractions with up to five factors. [7] We then find the functions $\mathbb{C}^{(n)}_{\mathcal{O}_m,\alpha}$ for $n \leq 5$ either by expanding $\vec{x}_{\rm fl}$ as in Eq. (9.6), or, equivalently, using the recursion relations Eqs. (9.10) and (9.11). After this, there are 151 bias functions for $n = 5$. However, as described in App. E.1, not all of these functions are independent. In particular, we find a set of 122 degeneracy equations for $n = 5$, which means that there are 29 independent functions that form the basis of the non-local-in-time expansion Eq. (9.9). [8] We provide all of the Fourier-space kernels relevant for the fifth-order expansion, and confirm all degeneracy equations, in an associated auxiliary file.

Next, we consider the basis of bias functions for the local-in-time expression Eq. (9.12). At fifth order, this expansion starts with 63 terms, however, as before, not all of them are linearly independent. We find 37 independent degeneracy equations,

[6] Focusing on up to fourth order, [130, 157] discussed how it is possible to map non-local-in-time terms into very special non-local-in-space terms. The bases discussed there are degenerate with a local-in-time and local-in-space one from Ch. 6, though.

[7] Here and in the rest of this work, since we work up to fifth order, we have already taken into account degeneracies that come from the fact that $r^{(1)}_{ij} = p^{(1)}_{ij}$ in terms that start at fifth order. If we do not do this, there are 130 contractions with up to five factors.

[8] Using the Lagrangian basis expansion, [254, 255] derived the number of independent fifth-order biases as 29, which is in agreement with our findings.

and hence 26 independent functions for the local-in-time bias expansion at fifth order. Indeed, this is three less than the non-local-in-time expansion, and hence *the galaxy-clustering signal at fifth order is sensitive to whether or not galaxies form on time scales of order Hubble.*

We are now in a position to explicitly give the fifth-order basis derived for this work. To be more concrete, we can write the fifth-order galaxy expansion in a basis with 26 elements that are local in time, and three that are non-local in time. In this *starting-from-time-locality (STL) basis*, we explicitly write

$$\delta_g^{(5)}(\vec{x},t) = \sum_{j=1}^{29} \tilde{b}_j(t)\mathbb{L}_j^{(5)}(\vec{x},t) \ . \tag{9.21}$$

We choose the basis such that the elements with $j = 1,\ldots,26$ are a basis of the local expansion Eq. (9.12). Explicitly, we take $\mathbb{L}_j^{(5)} = \mathcal{O}_m^{(5)}$ with the corresponding $\mathcal{O}_m$ given by

$$\begin{aligned}\{&\delta, \theta, \delta\theta, \theta^2, r^2, rp, p^2, \theta^3, r^2p, rp^2, p^3, r^2\theta, rp\theta, p^2\theta, rp^3,\\ &rprp, rp^2\delta, r^3\delta^2, \delta^5, r^3\theta, rp^2\theta, rp\delta\theta, r^2\theta^2, rp\theta^2, \delta\theta^3, \theta^4\} \ ,\end{aligned} \tag{9.22}$$

for $j = 1,\ldots,26$. Thus, the non-locality in time is contained in the final three basis elements, which we take to be

$$\mathbb{L}_{27}^{(5)} = \mathbb{C}_{\delta,5}^{(5)} \ , \quad \mathbb{L}_{28}^{(5)} = \mathbb{C}_{r^2,4}^{(5)} \ , \quad \mathbb{L}_{29}^{(5)} = \mathbb{C}_{p^3,3}^{(5)} \ . \tag{9.23}$$

Non-zero $\tilde{b}_{27}$, $\tilde{b}_{28}$, and $\tilde{b}_{29}$ can only come from non-local-in-time physics, so we call them non-local-in-time bias parameters. [9] We connect this basis to the so-called basis of descendants and show how fourth- and lower-order biases automatically consistently appear in Eq. (9.21) in App. E.2.

To see more quantitatively how the non-local-in-time bias parameters measure the time scale of galaxy formation, consider the expression Eq. (9.8) for the bias parameters. Assuming that the kernel $c_{\mathcal{O}_m}(t,t')$ has support over a time scale of order $1/\omega$ and expanding around the local-in-time limit, we have

$$c_{\mathcal{O}_m,\alpha}(t) \approx c_{\mathcal{O}_m}(t)\left(1 + g_{\mathcal{O}_m,\alpha}(t)\frac{H}{\omega} + \ldots\right) \ , \tag{9.24}$$

[9] Here we reference the size of the physical bias parameters, which are generally made up of a combination of bare and counterterm contributions.

where the ... represents terms higher order in H/ω, and $g_{\mathcal{O}_m,\alpha}(t) \sim \mathcal{O}(1)$. Since the non-local-in-time bias parameters $\tilde{b}_{27}$, $\tilde{b}_{28}$ and $\tilde{b}_{29}$ all vanish in the local-in-time limit, they are proportional to (at least) H/ω. The size of the deviation from the first term, which is the local-in-time piece, is controlled by H/ω: if there is a sizable deviation from the local-in-time limit, then $\omega \sim H$, and thus the time scale of the kernel $c_{\mathcal{O}_m}(t,t')$ is of the order $1/H$. [10] In our case, this happens if $\tilde{b}_{27}$, $\tilde{b}_{28}$, or $\tilde{b}_{29}$ are order unity. This in turn would mean that the formation of the observed population of galaxies has been affected by the state of the Universe up to a Hubble time ago, and thus that it has formed on a time scale on the order of the age of the Universe.

It can be illuminating to momentarily consider a system that is truly local in time. In this case, as we have discussed above, the bias parameters are expected to scale like $H/\omega_{\rm short} \ll 1$. However, in the EFT, higher-order loops will generically contribute to the lower-order bias parameters. Importantly, for a system that is truly local in time, those loops are expected to shift the bias parameters also by an amount that scales like $H/\omega_{\rm short}$. Given, though, that the cold dark-matter fluid is itself non-local in time [147, 246], we expect that higher-order dark-matter loops will generically contribute $\sim \mathcal{O}(1)$ to the galaxy bias parameters. We remind the reader that by galaxies in this work, we mean gravitationally-bound structures that form around the non-linear scale at a given Hubble time.

9.5 Observable Signatures

Until now, we have focused on the perturbative galaxy overdensity field itself. In large-scale structure analyses, we typically compare to data using correlation functions (or n-point functions if they contain n fields) of the overdensity fields of various tracers. Thus, one way to measure the non-local-in-time effect that we have discovered in this work is in correlation functions. Since we found that this effect arises at fifth order in perturbations, the lowest order observables sensitive to it are the two-loop two-point function through

$$\langle \delta^{(5)}_{g_1}(\vec{x}_1)\delta^{(1)}_{g_2}(\vec{x}_2)\rangle \ , \tag{9.25}$$

[10] Of course, the measurement of a smaller deviation from the local-in-time limit means that the formation time scale could be correspondingly smaller. It could also mean that the theory is fine tuned in the sense that higher-order loop contributions accidentally largely cancel the lower-order biases. On the other hand, it could also be that for a quasi-local-in-time theory, the coefficients of some non-local-in-time operators are accidentally large, which we refer to as being anomalous. These accidents become more and more unlikely as one measures more parameters.

the two-loop three-point function through

$$\langle \delta^{(5)}_{g_1}(\vec{x}_1)\delta^{(2)}_{g_2}(\vec{x}_2)\delta^{(1)}_{g_3}(\vec{x}_3)\rangle \ , \tag{9.26}$$

the one-loop four-point function through

$$\langle \delta^{(5)}_{g_1}(\vec{x}_1)\delta^{(1)}_{g_2}(\vec{x}_2)\delta^{(1)}_{g_3}(\vec{x}_3)\delta^{(1)}_{g_4}(\vec{x}_4)\rangle \ , \tag{9.27}$$

the one-loop five-point function through

$$\langle \delta^{(5)}_{g_1}(\vec{x}_1)\delta^{(2)}_{g_2}(\vec{x}_2)\delta^{(1)}_{g_3}(\vec{x}_3)\delta^{(1)}_{g_4}(\vec{x}_4)\delta^{(1)}_{g_5}(\vec{x}_5)\rangle \ , \tag{9.28}$$

and the tree-level six-point function through

$$\langle \delta^{(5)}_{g_1}(\vec{x}_1)\delta^{(1)}_{g_2}(\vec{x}_2)\delta^{(1)}_{g_3}(\vec{x}_3)\delta^{(1)}_{g_4}(\vec{x}_4)\delta^{(1)}_{g_5}(\vec{x}_5)\delta^{(1)}_{g_6}(\vec{x}_6)\rangle \ , \tag{9.29}$$

where we have used the subscript g_i to denote possibly different tracer samples (each of which can have a different set of bias parameters), and we have taken all fields to be at the same time t and dropped that argument to remove clutter.

As two explicit examples, consider the contributions to the two-loop two-point function Eq. (9.25) and the tree-level six-point function Eq. (9.28) for $g_i = g$ for $i = 1, \ldots, 6$. Using the STL basis Eq. (9.21), we have the explicit non-local-in-time contributions

$$\begin{aligned} &\sum_{j=27}^{29} \tilde{b}_j \langle \mathbb{L}^{(5)}_j(\vec{x}_1)\delta^{(1)}_g(\vec{x}_2)\rangle \ , \\ &\sum_{j=27}^{29} \tilde{b}_j \langle \mathbb{L}^{(5)}_j(\vec{x}_1)\delta^{(1)}_g(\vec{x}_2)\delta^{(1)}_g(\vec{x}_3)\delta^{(1)}_g(\vec{x}_4)\delta^{(1)}_g(\vec{x}_5)\delta^{(1)}_g(\vec{x}_6)\rangle \ , \end{aligned} \tag{9.30}$$

to the two-point and six-point functions respectively. As we have seen, these would not be present in the galaxy correlation functions if galaxies formed in a local-in-time way. This makes them concrete, direct, observable signatures of the formation time of galaxies.

10

Limits on Clustering and Smooth Quintessence from the EFTofLSS

10.1 Summary

We apply the Effective Field Theory of Large-Scale Structure (EFTofLSS) to analyze cosmological models with clustering quintessence, which allows us to consistently describe the parameter region in which the quintessence equation of state $w < -1$. First, we extend the description of biased tracers in redshift space to the presence of clustering quintessence, and compute the one-loop power spectrum. We solve the EFTofLSS equations using the exact time dependence, which is relevant to obtain unbiased constraints. Then, fitting the full shape of BOSS pre-reconstructed power spectrum measurements, the BOSS post-reconstruction BAO measurements, BAO measurements from 6DF/MGS and eBOSS, the Supernovae from Pantheon, and a prior from BBN, we bound the clustering quintessence equation of state parameter $w = -1.011^{+0.053}_{-0.048}$ at 68% C.L.. Further combining with Planck, we obtain $w = -1.028^{+0.037}_{-0.030}$ at 68% C.L.. We also obtain constraints on smooth quintessence, in the physical regime $w \geq -1$: combining all datasets, we get $-1 \leq w < -0.979$ at 68% C.L.. These results strongly support a cosmological constant.

10.2 Introduction and Summary

Introduction The analysis of the Full Shape (FS) of the BOSS galaxy power spectrum with the Effective Field Theory of Large-scale Structure (EFTofLSS) at one loop has provided us with a measurement of all parameters in ΛCDM with just a Big Bang Nucleosynthesis (BBN) prior [7, 142, 143] (see also [256] for other prior choices and [7] for a joint analysis with the BOSS bispectrum using the tree-level prediction). The combination with BOSS reconstructed measurements and baryon acoustic oscillations (BAO) from eBOSS, as well as with supernovae redshift-distance or cosmic microwave background (CMB) measurements, has further allowed us to bound the total neutrino mass, and put limits on the effective number of relativistic species, on smooth dark energy, or on curvature [7, 143, 257, 168, 169, 258]. In particular, the FS analysis can help constrain models invented to address the Hubble tension as it provides measurements independent on the CMB or local distance ladders [172, 173, 174, 175].

In this chapter, we analyze the BOSS FS power spectrum using the EFTofLSS at one loop in the context of clustering quintessence [51, 48, 259] and smooth quintessence. In clustering quintessence, dark energy is made of a scalar field (the quintessence field) whose fluctuations have effectively zero speed of sound, c_s, and therefore 'cluster', as they can fall into gravitational potentials. It is a particularly appealing model since the dark energy equation of state parameter w can cross the so-called phantom divide, $w = -1$ and consistently describe the regime $w < -1$. This is allowed thanks to the presence of higher-derivative operators in the Lagrangian that stabilize gradient instabilities, but this can only happen if $c_s^2 \to 0$ such that they remain not parametrically suppressed. Clustering quintessence has been considered within the context of structure formation in [260, 261, 262, 263] and in the EFTofLSS in [264] (see also [265, 266, 267] for embeddings of other dark energy theories in the EFTofLSS). In this work, we extend the description to biased tracers in redshift space with exact-time dependence in order to apply it to data from galaxy surveys. We remark that we find it quantitatively important to solve the EFTofLSS equations with the exact time dependence, rather than with the approximate, so-called 'EdS', approximation. As for smooth quintessence, which has already been analyzed in light of the BOSS FS and LSS data in [169], we will perform here the analysis by imposing a physical flat prior $-1 \leq w$ on the smooth quintessence equation of state parameter. By wCDM, we refer to a Universe that includes a smooth dark energy component, i.e. a scalar quintessence field with $c_s^2 \to 1$, whose perturb-

ations can be neglected since the sound horizon is of the size of the cosmological horizon. In this picture, $w < -1$ is an unphysical region where the vacuum is unstable, therefore we should analyze wCDM excluding this region (see discussions in e.g. [268, 51]).

This chapter is organized as follows. We compute the power spectrum at one loop in redshift space for biased tracers with exact time dependence for the clustering quintessence model in Sec. 10.3. Further details concerning this derivation are given in the appendices. In Sec. 10.4, we apply our framework to LSS data, and in App. F.4 we show the full posteriors including nuisance parameters. Our results are summarized at the end of this Introduction.

Data Sets We analyze the FS of BOSS DR12 pre-reconstructed power spectrum measurements [196], baryon acoustic oscillations (BAO) of BOSS DR12 post-reconstructed power spectrum measurements [269], 6DF [270] and SDSS DR7 MGS [271], as well as high redshift Lyman-α forest auto-correlation and cross-correlation with quasars from eBOSS DR14 measurements [272, 273]. We also consider combinations with Supernovae (SN) measurements from the Pantheon sample [274] and with Planck2018 TT,TE,EE+lowE+lensing [275].

Methodology We analyze the BOSS FS using the galaxy power spectrum in redshift space at one loop in the EFTofLSS [133] following the methodology described in [7, 143]. The description of the likelihood, including the covariances and priors used, can be found in [7]. The theory of biased tracers in redshift space with exact time dependence in clustering quintessence cosmology at one loop is derived in Sec. 10.3 (see also [276] which has already derived the same expressions, but just in real space, with a different approach), and the scale cut up to which the FS is analyzed is discussed in Sec. 10.4.1. The power spectrum is IR-resummed [137, 139, 140, 169], and includes corrections to observational systematics: the Alcock-Paczynski effect [214], window functions [201], and fiber collisions [277].

We sample over the following cosmological parameters: the abundance of baryons ω_b, the abundance of cold dark matter $\omega_{\rm cdm}$, the Hubble constant H_0, the amplitude of the primordial fluctuations $\ln(10^{10}A_s)$, the tilt of the primordial power spectrum n_s, and the quintessence equation of state parameter w. We impose no prior on the cosmological parameters but a BBN prior on ω_b: a Gaussian prior centered on 0.02235 with $\sigma_{\rm BBN} = 0.0005$, obtained by adding up the theory and statistical errors of [278]. We use the Planck prescription of one single massive neutrino with mass

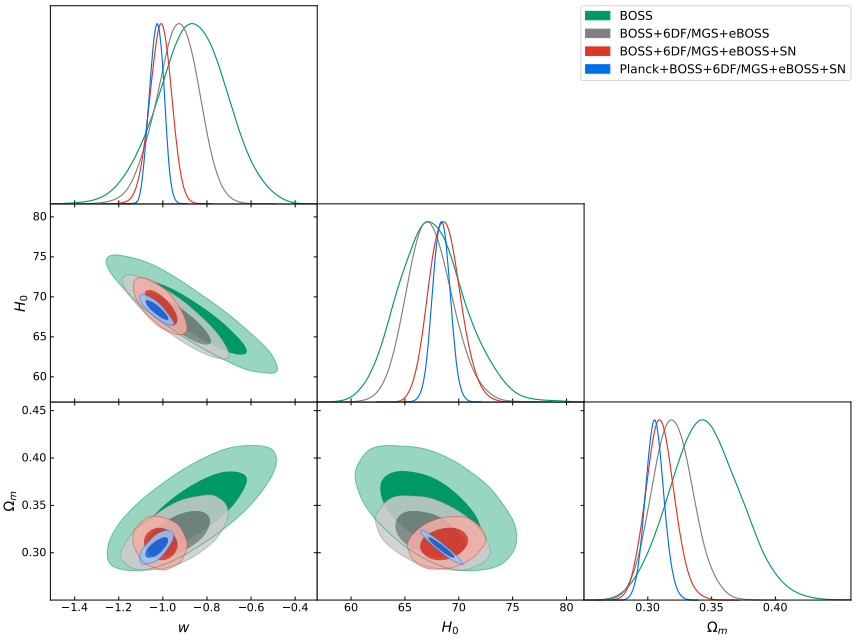

Figure 10.1: 1D and 2D posteriors of w, H_0 and Ω_m in clustering quintessence from various analyses performed in this work. When not analyzed in combination with Planck, we use a BBN prior.

0.06 eV as done in [275]. Allowing the EFT parameters to vary only within physical ranges, we impose priors on them as in [169].

The BAO measurements from the post-reconstructed BOSS power spectrum are correlated with BOSS pre-reconstructed (FS) measurements. The joint analysis is described in [169] (see also [168]). When adding BAO from 6DF/MGS or eBOSS, SN from Pantheon, or Planck data, we simply add the log-likelihoods as these measurements are uncorrelated among each other. We neglect the small cross-correlation between LSS data with Planck weak lensing and the integrated Sachs-Wolfe (ISW) effect.

Main Results Our main results are best represented by Fig. 10.1. Fitting BOSS FS + BOSS reconstructed BAO with a BBN prior on clustering quintessence, we are able to measure all cosmological parameters. In particular, we determine the quintessence equation of state parameter w, the present matter fraction Ω_m, and the Hubble constant H_0, to $18\%, 8.2\%$, and 4.6% precision, respectively, at 68% confidence level (C.L.), finding $w = -0.867^{+0.17}_{-0.15}$, $\Omega_m = 0.3456^{+0.03}_{-0.027}$, and $H_0 = 67.58^{+2.7}_{-3.5}$. We also determine $\ln(10^{10}A_s) = 2.64^{+0.16}_{-0.17}$ and $n_s = 0.8884^{+0.072}_{-0.059}$ at 68% C.L.. Upon addition of the BAO measurements from 6DF/MGS and eBOSS, and

SN measurements from Pantheon, we get $w = -1.011^{+0.053}_{-0.048}$, $\Omega_m = 0.3099^{+0.012}_{-0.011}$, and $H_0 = 68.72^{+1.4}_{-1.6}$, which amounts to error bar reductions of $68\%, 60\%$, and 52%, respectively. We also find $\ln(10^{10}A_s) = 2.806^{+0.15}_{-0.16}$ and $n_s = 0.9335^{+0.054}_{-0.05}$ at 68% C.L.. Adding Planck data (Tab. 10.3), we finally constrain w, Ω_m, and H_0 to $3.3\%, 2.4\%$, and 1.2% precision, respectively, obtaining $w = -1.028^{+0.037}_{-0.030}$, $\Omega_m = 0.3055^{+0.0074}_{-0.0073}$, and $H_0 = 68.38^{+0.78}_{-0.84}$, and also obtain $\ln(10^{10}A_s) = 3.046^{+0.014}_{-0.014}$ and $n_s = 0.9665^{+0.0042}_{-0.0036}$ at 68% C.L..

All analyses performed here show that our Universe is consistent with ΛCDM. First, clustering quintessence in the limit $w = -1$ reduces to ΛCDM, and we find that w is consistent with -1 at $\lesssim 68\%$ C.L. Second, the values obtained for the other cosmological parameters in clustering quintessence are consistent within 68% C.L. with the ΛCDM ones obtained by fitting BOSS FS with the EFTofLSS [7, 142, 143], in combination with other probes [257, 168, 169], or fitting Planck alone [275] [1].

A similar observation applies when fitting wCDM with a flat prior on the dark energy equation of state parameter of $w \geq -1$ (Tab. 10.4). Fitting BOSS data with a BBN prior, we find in this case $\Omega_m = 0.337^{+0.017}_{-0.022}$ and $H_0 = 68.6 \pm 1.8$, and we bound $-1 \leq w < -0.91$ at 68% C.L. ($-1 \leq w < -0.81$ at 95% C.L.). We also get $\ln(10^{10}A_s) = 2.77 \pm 0.19$ and $n_s = 0.885^{+0.069}_{-0.058}$ at 68% C.L.. Adding BAO measurements, Pantheon SN and Planck data we obtain the very stringent constraint $-1 \leq w < -0.979$ at 68% C.L. ($-1 \leq w < -0.956$ at 95% C.L.). Thus, allowing wCDM only within the physical region gives tight posteriors that are also consistent with the ones obtained on ΛCDM fitting BOSS or Planck. This is illustrated in Fig. 10.2.

We end this summary of the main results with a note of warning. It should be emphasized that in performing this analysis, as well as the preceding ones using the EFTofLSS by our group [7, 143, 169, 172], we have assumed that the observational data are not affected by any unknown systematic error, such as, for example, line of sight selection effects or undetected foregrounds. In other words, we have simply analyzed the publicly available data for what they were declared to be: the power spectrum of the galaxy density in redshift space. Given the additional cosmological information that the theoretical modeling of the EFTofLSS allows us to exploit in BOSS data, it might be worthwhile to investigate if potential undetected systematic errors might affect our results. We leave an investigation of these issues to future work.

[1] With an exception on $\ln(10^{10}A_s)$ which is consistent at $\sim 2\sigma$ with Planck.

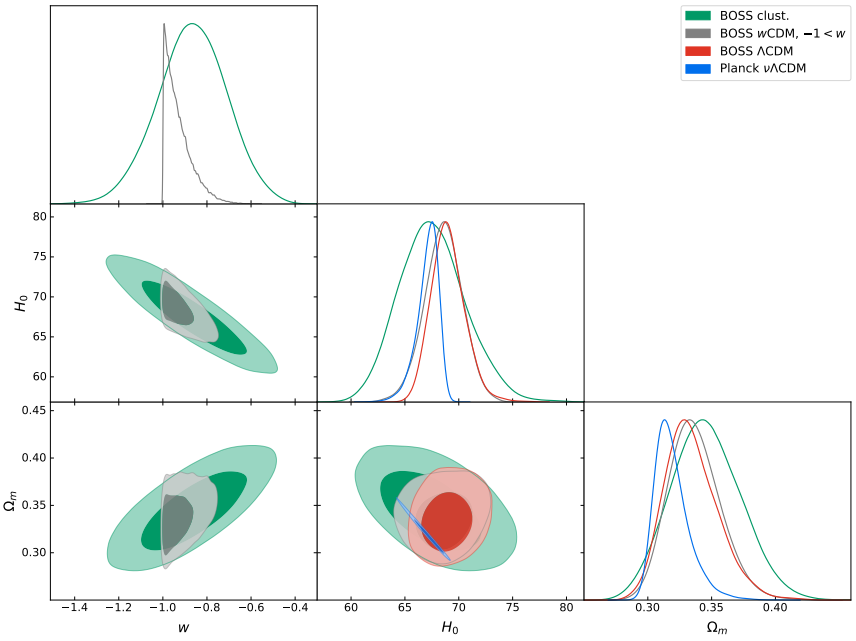

Figure 10.2: 1D and 2D posteriors of w, H_0 and Ω_m obtained by fitting clustering quintessence, wCDM or ΛCDM to BOSS with a BBN prior. For wCDM, i.e. smooth quintessence, we restrict to the physical region $w \geq -1$. For comparison, we show the contours of Planck obtained in ΛCDM in the presence of massive neutrinos. The neutrinos introduce additional degeneracies in the $\Omega_m - H_0$ plane in the CMB analysis. On the contrary, fixing the neutrinos when analyzing BOSS does not significantly change the constraints on the shown cosmological parameters, see e.g. Table 2 in [143]. This plot illustrates the consistency of the datasets as well as the consistency of the present analyses with a cosmological constant.

Public Code The redshift-space one-loop galaxy power spectra in the EFTofLSS are evaluated using PyBird: Python code for Biased tracers in ReDshift space [169] [2]. The exact time dependence and the clustering quintessence modifications are publicly available in PyBird. The linear power spectra are evaluated with the CLASS Boltzmann code [279] [3]. The posteriors are sampled using the MontePython cosmological parameter inference code [218, 280] [4]. The triangle plots are obtained using the GetDist package [220].

[2] https://github.com/pierrexyz/pybird
[3] http://class-code.net
[4] https://github.com/brinckmann/montepython_public

10.3 Biased Tracers with Exact Time Dependence in Clustering Quintessence

In this section, we extend the study of biased tracers in redshift space with exact time dependence, first studied in [135, 276], to clustering quintessence.

10.3.1 Review of the EFTofLSS with Clustering Quintessence

We start by reviewing the underlying equations of motion for dark matter and the dark energy component. For a more detailed discussion, we refer the reader to [264]. In the EFT of dark energy, previously studied in [51, 47, 48, 49], the dark energy degree of freedom is assumed to be the Goldstone boson arising from the spontaneous breaking of time diffeomorphisms. To write the most general theory, we work in unitary gauge where the scalar degree of freedom appears in the metric. The gravitational action will contain operators that break time diffeomorphisms, while remaining invariant under time-dependent spatial diffeomorphisms. Up to second order in perturbations, and at leading order in the derivatives, the action reads

$$S_G = \int d^4x \sqrt{-g}\Big[\frac{M_{\rm Pl}^2}{2}R - \Lambda(t) - c(t)g^{00}_{\rm u} + \frac{M_2^4(t)}{2}(\delta g^{00}_{\rm u})^2 - \frac{\bar{m}_1^3}{2}\delta g^{00}_{\rm u}\delta K_{\rm u} \\ -\frac{\hat{m}_1^2}{2}\delta K_{\rm u}^2 - \frac{\hat{m}_2^2}{2}\delta K_{{\rm u},ij}\delta K_{\rm u}^{ij}\Big], \tag{10.1}$$

where we use the 'u' subscript, to emphasize that the metric in the action above is in unitary gauge. Here $g^{00}_{\rm u} = -1 + \delta g^{00}_{\rm u}$ is the 00 component of the (inverse) metric, and $\Lambda(t)$, $c(t)$, $M_2(t)$, $\bar{m}_1(t)$, $\hat{m}_1(t)$, $\hat{m}_2(t)$ are coefficients which depend on the background evolution. Then δK_{ij} is the perturbation of the extrinsic curvature tensor, and δK is its trace. For simplicity, in the following we work with $\bar{m}_1 = 0$, but it can be checked [51, 48] that this operator describes a clustering quintessence at cosmological scales. The operators proportional to $\hat{m}_i$ are negligible on large scales as they scale as $\sim k^4$, but are necessary to guarantee the stability of perturbations, as discussed below. To S_G, we add the action for matter S_M, which we take to be fully diffeomorphism invariant. This guarantees that, once we explicitly reintroduce the Goldstone mode π, there will be no direct couplings of π to matter.

The background equations we obtain from $S_G + S_M$ are the familiar Friedmann

equations:

$$3H^2M_{\rm Pl}^2 = \bar{\rho}_m + \bar{\rho}_D \,, \tag{10.2}$$

$$-2\dot{H}M_{\rm Pl}^2 = \bar{\rho}_m + \bar{\rho}_D + \bar{p}_D \,, \tag{10.3}$$

where we set the cold dark matter pressure $p_m = 0$, and define the background dark energy density, $\bar{\rho}_D$, and pressure, p_D, by

$$c(t) = \frac{1}{2}\left(\bar{\rho}_D + \bar{p}_D\right), \tag{10.4}$$

$$\Lambda(t) = \frac{1}{2}\left(\bar{\rho}_D - \bar{p}_D\right) \ . \tag{10.5}$$

From the Friedmann equations we obtain the background solutions for the dark matter and dark energy densities:

$$\bar{\rho}_m = \bar{\rho}_{m,0}a^{-3}, \qquad \bar{\rho}_D = \bar{\rho}_{D,0}a^{-3(1+w)} \ , \tag{10.6}$$

where the sub index $_0$ stands for the present day value, and we use the equation of state parameter for dark energy $w = \bar{p}_D/\bar{\rho}_D$. In the following, we will often use the present day fractional densities $\Omega_{x,0} = \frac{\bar{\rho}_{x,0}}{\bar{\rho}_{D,0}+\bar{\rho}_{m,0}}$, with $x \in \{m, D\}$.

Starting from the action in unitary gauge, it is useful to explicitly reintroduce the Goldstone mode doing the Stueckelberg trick. We perform the time diffeomorphism $x^0 \to x^0+\xi^0(\vec{x},t)$ and $x^i \to x^i$, and then substitute $\xi^0(x) \to -\pi(x)$. The replacement rules for the coefficients and the metric are (for details see for example [264])

$$c(t) \to c(t+\pi) = c(t) + \dot{c}(t)\pi + \frac{1}{2}\ddot{c}(t)\pi^2 + \dots \,, \tag{10.7}$$

$$g_{\rm u}^{00} \to g^{00} + 2g^{0\mu}\partial_\mu\pi + g^{\mu\nu}\partial_\mu\pi\partial_\nu\pi \,. \tag{10.8}$$

Gravitational perturbations will be described by the spatially flat perturbed FLRW metric in Newtonian gauge:

$$ds^2 = -(1+2\Phi)dt^2 + a(t)^2(1-2\Psi)d\vec{x}^2 \,, \tag{10.9}$$

where Φ and Ψ are the gravitational potentials, and we ignore tensor fluctuations.

We then obtain the action for the Goldstone boson π up to second order:

$$\int d^4x\sqrt{-g}\Big[\bar{p}_D+\dot{\bar{p}}_D\pi+\frac{1}{2}\ddot{\bar{p}}_D\pi^2-\frac{1}{2}(\bar{\rho}_D+\bar{p}_D)\left(2\Phi-2\dot{\pi}+4\Phi\dot{\pi}-\dot{\pi}^2+a^{-2}(\partial\pi)^2\right)$$
$$-(\dot{\bar{\rho}}_D+\dot{\bar{p}}_D)(\Phi-\dot{\pi})\pi+2M_2^4(t)(\Phi-\dot{\pi})^2\Big]\,. \tag{10.10}$$

At short distances, one can focus on the action of the Goldstone boson. We can see that the kinetic part is given by

$$S_{\rm kin.}=\int d^4x\sqrt{-g}\left[\frac{1}{2}\left(\bar{\rho}_D+\bar{p}_D+4M_2^4(t)\right)\dot{\pi}^2-\frac{1}{2}\left(\bar{\rho}_D+\bar{p}_D\right)a^{-2}\partial^2\pi\right]\,, \tag{10.11}$$

and thus the speed of sound is

$$c_s^2=\frac{\bar{\rho}_D+\bar{p}_D}{\bar{\rho}_D+\bar{p}_D+4M_2^4(t)}\,. \tag{10.12}$$

The theory must be free of ghosts, which implies that the denominator has to be positive. Therefore the speed of sound needs to have the same sign as $1+w$. In particular, $w<-1$ implies $c_s^2<0$, which would produce gradient instabilities. One can circumvent this instability by including the higher derivative terms proportional to $\hat{m}_{1,2}$, which scale as k^4 and give a stable dispersion relation at small scales [51, 48]. In order for the higher derivative terms not to be highly suppressed (which would make them irrelevant on cosmological scales), we need the speed of sound to be bound by $|c_s^2|<10^{-30}$, which means it is practically zero. These considerations hold also when a careful analysis including the mixing with gravity is performed. Similar considerations are obtained by including the higher derivative operator proportional to $\bar{m}_1$ [51, 48]. In conclusion, it *is* possible to have viable theories with $w<-1$, but they need to have $c_s^2\to 0$, which are called clustering dark energy or clustering quintessence. We notice furthermore that in order to have a stable theory, we need to have $w\gtrsim -2$ if we use the operators in $\hat{m}_{1,2}$, or ≥ -1.17 if we use the operator in $\bar{m}_1$ [51, 48] [5].

The name "clustering quintessence" stems from the fact that the dark energy can cluster with the dark matter, and they jointly contribute to the gravitational potential. Hence the adiabatic mode (i.e. the perturbations of the total energy density, which source the gravitational potential) depends on both the dark matter

[5] These lower limits will play essentially no role in our analysis, as the data constrain w to be far from this boundary.

and dark energy perturbations. As a result, dark energy perturbations leave an imprint on biased tracers such as galaxies, which are the main interest in this work. Therefore, next we wish to give a quick overview of how we derive the equations of motion for the adiabatic mode in the presence of clustering quintessence.

Before analyzing the equations for π, it is useful to write down the EFT equations for dark matter, which couples to dark energy through gravity [264]:

$$\dot{\delta}_m + \frac{1}{a}\partial_i((1+\delta_m)v_m^i) = 0\,, \tag{10.13}$$

$$\partial_i \dot{v}_m^i + H\partial_i v_m^i + \frac{1}{a}\partial_i(v_m^j \partial_j v_m^i) + \frac{1}{a}\partial^2\Phi = -\frac{1}{a}\partial_i\left(\frac{1}{\bar{\rho}_m}\partial_j \tau^{ij}\right)\,, \tag{10.14}$$

where δ_m and v_m are the dark matter overdensity and velocity, $\dot{} = d/dt$ and τ^{ij} is the effective stress tensor.

Let us start analyzing the linear equations, and we will study the non-linear equations subsequently. The linear equation for π [264, 48, 259], which we get from Eq. (10.10), reads:

$$\frac{1}{a^3}\frac{1}{M_2^4}\frac{d}{dt}\left[a^3 M_2^4(\dot{\pi}-\Phi)\right] = \frac{c_s^2}{1-c_s^2}\frac{\partial^2\pi}{a^2}\,. \tag{10.15}$$

This shows that, in the limit $c_s \to 0$, the RHS can be neglected. We can, therefore, write $\dot{\pi} - \Phi \propto (a^3 M_2^4)^{-1}$, which is a decaying mode, assuming the speed of sound to be approximately constant. In particular, we have $\partial_i\dot{\pi} - \partial_i\Phi = 0$, and, using the linear-level Euler equation Eq. (10.14), we get that $\frac{d}{dt}\left[a v_m^i + \partial^i\pi\right] = 0$. This means that on the growing adiabatic mode we have

$$\partial^i\pi = -a v_m^i\,, \tag{10.16}$$

which implies that the two species are comoving. This will eventually allow us to write a closed set of differential equations for the adiabatic mode, defined by $\delta_A = 2M_{pl}^2 a^{-2}\partial^2\Psi/\bar{\rho}_m$. The Poisson equation is [48, 259, 49]

$$a^{-2}\partial^2\Psi = \frac{\bar{\rho}_m}{2M_{pl}^2}\left(\delta_m + \frac{4M_2^4}{\bar{\rho}_m}(\dot{\pi}-\Phi)\right)\,. \tag{10.17}$$

Using the definition of the adiabatic mode, we find

$$\delta_A = \delta_m + \frac{4a^3M_2^4}{\bar{\rho}_{m,0}}(\dot{\pi}-\Phi) = \delta_m + \frac{(1+w)}{c_s^2}\frac{\bar{\rho}_{D,0}}{\bar{\rho}_{m,0}}a^{-3w}(\dot{\pi}-\Phi)\,. \tag{10.18}$$

We can now take the derivative of the above equation and plug in the equation of motion for π, Eq. (10.15), the solution for $\bar{\rho}_D$, Eq. (10.6), and substitute the dark matter velocity for the spatial derivatives of π, Eq. (10.16). We then get

$$\begin{aligned} \dot{\delta}_A &= \dot{\delta}_m - \frac{1}{a}(1+w)\frac{\bar{\rho}_{D,0}}{\bar{\rho}_{m,0}}a^{-3w}\theta_m \,. \qquad (10.19) \\ &= -\frac{1}{a}C(a)\theta_m, \end{aligned}$$

where we have introduced the dark matter velocity divergence $\theta_m = \partial_i v^i_m$ and we have defined

$$C(a) = 1 + (1+w)\frac{\Omega_{D,0}}{\Omega_{m,0}}a^{-3w}\,. \qquad (10.20)$$

We now move on to the full non-linear equations of motion for the adiabatic mode, which is somewhat more technical. We will just mention the main results and refer to [264] (see also [281]) for more details. First, we can easily see that the two species remain comoving at the non-linear level. Using the equations of motion, one can show that $\delta g^{00}_u \propto c_s^2$ also at non-linear level. Taking a spatial derivative, $\partial_i \delta g^{00}_u = 0$ in the limit $c_s^2 \to 0$, yields

$$0 = \partial_i\left(\dot{\pi} - \Phi - \frac{1}{2}a^{-2}(\partial\pi)^2\right) \qquad (10.21)$$

$$= \frac{d}{dt}\left(a v^i_m + \partial_i\pi\right) + v^j_m\partial_j v^i_m - a^{-2}\partial_j\pi\partial_j\partial_i\pi \,. \qquad (10.22)$$

This is satisfied by simply using Eq. (10.16), thus the two species are comoving also at non-linear level. The full non-relativistic equation of motion for the dark energy field π is given by

$$-\frac{2}{a^3}\partial_t\left(a^3 M_2^4\,\delta g^{00}_{\rm u}\right) = M_2^4\frac{c_s^2}{1-c_s^2}\frac{\partial^2\pi}{a^2} - 2a^{-2}\partial^2\pi M_2^4\delta g^{00}_{\rm u}\,, \qquad (10.23)$$

where we used that $\partial_i\delta g^{00}_u = 0$. The full Poisson equation introduces non-linearities in the definition of the adiabatic mode, which reads

$$\delta_A = \delta_m - \frac{(1+w)}{2c_s^2}\frac{\bar{\rho}_{D,0}}{\bar{\rho}_{m,0}}a^{-3w}\delta g^{00}_u\,. \qquad (10.24)$$

Now we can take a time derivative and obtain a non-linear continuity equation for the adiabatic mode. The only difference is that we have to include the non-linear terms for $\dot{\delta}_m$ and we have an additional term in the equations of motion for π on

the right-hand side of Eq. (10.23). We then get

$$\begin{aligned}\dot{\delta}_A &= -\frac{1}{a}C(a)\theta_m - \frac{1}{a}\partial_i(\delta_m v_m^i) - \partial^2\pi\frac{2aM_2^4}{\bar{\rho}_{m,0}}\delta g_u^{00} \\ &= -\frac{1}{a}C(a)\theta_m - \frac{1}{a}\partial_i(\delta_m v_m^i) + \frac{1}{a}\theta_m(\delta_m - \delta_A) \\ &= -\frac{1}{a}C(a)\theta_m - \frac{1}{a}\partial_i(\delta_A v_m^i),\end{aligned} \tag{10.25}$$

where in the second line we use Eq. (10.24), and in the last line we use $\partial_i\delta_m = \partial_i\delta_A$.

Since the two species are comoving, $\theta_A = \theta_m$ and the Euler equation for the adiabatic mode is simply obtained by using the definition of the adiabatic mode in terms of the gravitational potential in Eq. (10.14). We finally get the governing equations for the clustering quintessence - dark matter system (without counterterms):

$$\dot{\delta}_A + \frac{1}{a}C(a)\theta_m = -\frac{1}{a}\partial_i\left(\delta_A v_m^i\right) \tag{10.26}$$

$$\dot{\theta}_m + H\theta_m + \frac{3}{2}\frac{\Omega_{m,0}H_0^2}{a^2}\delta_A = -\frac{1}{a}\partial_i\left(v_m^j\partial_j v_m^i\right)\,, \tag{10.27}$$

where $\bar{\rho}_m/(2M_{\rm Pl}^2) = 3\Omega_{m,0}\mathcal{H}_0^2 a_0/(2a^3)$. As explained in [264], since clustering quintessence is comoving with dark matter, there is no isocurvature mode, and the counterterms are the same as for standard dark matter. To solve the equations above perturbatively we transform into Fourier space, where they read (still neglecting the counterterms):

$$a\delta'_{\vec{k}} - f_+\theta_{\vec{k}} = \frac{(2\pi)^3 f_+}{C(a)}\int\frac{d^3q_1}{(2\pi)^3}\frac{d^3q_2}{(2\pi)^3}\delta_D(\vec{k}-\vec{q}_1-\vec{q}_2)\alpha(\vec{q}_1,\vec{q}_2)\theta_{\vec{q}_1}\delta_{\vec{q}_2}, \tag{10.28}$$

$$\begin{aligned}a\theta'_{\vec{k}} - f_+\theta_{\vec{k}} - \frac{f_-}{f_+}(\theta_{\vec{k}} - \delta_{\vec{k}}) = \\ = \frac{(2\pi)^3 f_+}{C(a)}\int\frac{d^3q_1}{(2\pi)^3}\frac{d^3q_2}{(2\pi)^3}\delta_D(\vec{k}-\vec{q}_1-\vec{q}_2)\beta(\vec{q}_1,\vec{q}_2)\theta_{\vec{q}_1}\theta_{\vec{q}_2}\,,\end{aligned} \tag{10.29}$$

and we drop the indices m and A from now on since we will only talk about the adiabatic mode. We define $\delta = \delta_A$ and $\theta = -\frac{C}{f_+ aH}\partial_i v^i$ for the rescaled velocity divergence such that $\delta^{(1)} = \theta^{(1)}$. Furthermore, we use the scale factor as time variable such that $' = d/da$ and defined the growth rates $f_\pm = \frac{d\ln D_\pm}{d\ln a}$ in terms of the growth factors, further discussed in App. F.1. [6]. We will not use the commonly applied Einstein-

[6] We here explicitly keep track of the growing and decaying growth factors and growth rates $D_\pm$ and $f_\pm$ as opposed to Eqs. (6.23) and (6.26) in Ch. 6 as they are key to getting the greens functions. In Ch. 6 we simply dropped the $_+$-subscript.

de Sitter (EdS) approximation, where one approximates the time dependence of a perturbation by powers of the growth factor, for instance $\delta^{(n)}_{\vec{k}}(a) \overset{\text{EdS}}{\propto} D^n(a)\delta^{(n)}_{\vec{k}}(a_i)$, for some intital time a_i. Instead, we will use the exact time dependence solution discussed below. As we will see later, the EdS approximation significantly biases the determination of the cosmological parameters in the presence of clustering quintessence.

Eqs. (10.28) - (10.30) are slightly different from the dark matter equations in the presence of smooth dark energy with $c_s^2 = 1$, i.e. wCDM. In fact, in the limit $(1+w) \to 0$, with $\Omega_{D,0}$ =const, we recover, at large distances where we can neglect the higher derivative terms, the equations of motion for the matter overdensity in ΛCDM. This difference in the equations of motion between the two models results in a modified definition of the time functions that appear in the exact time solutions for δ and θ. Exact solutions for the adiabatic mode δ in the presence of clustering quintessence have been previously studied in [264, 260, 281]. The time-dependent integral kernel solutions in Fourier space are given by [264]

$$
\begin{aligned}
K^{(1)}_{\lambda}(\vec{q}_1, a) &= 1\,, && (10.30)\\
K^{(2)}_{\lambda}(\vec{q}_1, \vec{q}_2, a) &= \alpha_s(\vec{q}_1, \vec{q}_2)\mathcal{G}^{\lambda}_1(a) + \beta(\vec{q}_1, \vec{q}_2)\mathcal{G}^{\lambda}_2(a)\,, && (10.31)\\
K^{(3)}_{\lambda}(\vec{q}_1, \vec{q}_2, \vec{q}_3, a) &= \alpha^{\sigma}(\vec{q}_1, \vec{q}_2, \vec{q}_3)\mathcal{U}^{\lambda}_{\sigma}(a) + && (10.32)\\
&\quad + \beta^{\sigma}(\vec{q}_1, \vec{q}_2, \vec{q}_3)\mathcal{V}^{\lambda}_{\sigma 2}(a) + \gamma^{\sigma}(\vec{q}_1, \vec{q}_2, \vec{q}_3)\mathcal{V}^{\lambda}_{\sigma 1}(a)\,,
\end{aligned}
$$

where repeated $\sigma \in \{1, 2\}$ are summed over and $\lambda \in \{\delta, \theta\}$. The explicit time functions are defined in App. F.1, and the momentum functions in App. F.2. The kernels in Eqs. (10.30) - (10.32), and in the following sections are defined by

$$
\begin{aligned}
X^{(n)}(\vec{k}, a) = \int \frac{d^3q_1}{(2\pi)^3} \ldots \frac{d^3q_n}{(2\pi)^3} (2\pi)^3 \delta_D(\vec{k} - \vec{q}_1 - \ldots - \vec{q}_n) \times && (10.33)\\
\times\, K^{(n)}_X(\vec{q}_1, \ldots, \vec{q}_n, a)\; \delta^{(1)}_{\vec{q}_1}(a) \ldots \delta^{(1)}_{\vec{q}_n}(a)\,,
\end{aligned}
$$

where X may for instance stand for δ or θ. In the next section, we will see how the solution with exact time dependence for clustering quintessence leaves an imprint in the bias expansion of biased tracers such as galaxies.

10.3.2 Perturbative Expansions of δ_h and θ_h

To find the bias expansion for the galaxy overdensity δ_h following the exact time dependence solution of the adiabatic mode, we can follow a procedure similar to

[135]. Recently, in [276], the same result has also been derived using a different approach. Here equations will change with respect to [135], as a consequence of the modified equations of motion for δ_A, relative to the equations for the dark matter solutions in wCDM. As has been previously studied in [129], the bias expansion for δ_h is given by

$$\begin{aligned}\delta_h(\vec{x},a) \simeq \int^a \frac{da'}{a'}\ \Big[& c_\delta(a,a')\ :\delta(\vec{x}_{\rm fl},a'): \\ & +c_{\delta^2}(a,a')\ :\delta(\vec{x}_{\rm fl},a')^2: +c_{s^2}(a,a')\ :s^2(\vec{x}_{\rm fl},a'): \\ & +c_{\delta^3}(a,a')\ :\delta(\vec{x}_{\rm fl},a')^3: +c_{\delta s^2}(a,a')\ :\delta(\vec{x}_{\rm fl},a')s^2(\vec{x}_{\rm fl},a'): \\ & +c_\psi(a,a')\ :\psi(\vec{x}_{\rm fl},a'): +c_{st}(a,a')\ :st(\vec{x}_{\rm fl},a'): +c_{s^3}(a,a')\ :s^3(\vec{x}_{\rm fl},a'): \\ & +c_\epsilon(a,a')\,\epsilon(\vec{x}_{\rm fl},a') + c_{\partial^2\delta}(a,a')\ \frac{\partial^2_{x_{\rm fl}}}{{k_{\rm M}}^2}\delta(\vec{x}_{\rm fl},a') + \dots\ \Big]\ ,\end{aligned} \tag{10.34}$$

where we include all possible operators [7] allowed by the equivalence principle, including stochastic contributions and higher derivative terms [8]. Their definitions are found in App. F.2. As for the dark matter equations, since clustering quintessence is comoving with dark matter, there is no isocurvature mode, and the bias expansion depends on the same fields as for the dark-matter-only universe [264]. The time-kernels, such as $c_\delta(a,a')$, that account for the time non-locality, can be formally integrated over a' after the perturbative solutions are substituted in. All operators (which are explicitly given in App. F.2) are evaluated along the fluid line-element:

$$\vec{x}_{\rm fl}(\vec{x},a,a') = \vec{x} - \int_{a'}^a \frac{da''}{a''^2 H(a'')}\vec{v}(a'',\vec{x}_{\rm fl}(\vec{x},a,a'')). \tag{10.35}$$

This results in Taylor expansions in the fields around $\vec{x}$ given by

$$\begin{aligned}\delta(\vec{x}_{\rm fl}(a,a'),a') = \delta(\vec{x},a') & - \partial_i\delta(x,a')\int_{a'}^a \frac{da''}{a''^2H(a'')}\ v^i(\vec{x},a'') \\ & +\frac{1}{2}\partial_i\partial_j\delta(x,a')\int_{a'}^a \frac{da''}{a''^2H(a'')}\ v^i(\vec{x},a'')\int_{a'}^a \frac{da'''}{a'''^2H(a''')}\ v^j(\vec{x},a''') \\ & +\partial_i\delta(x,a')\int_{a'}^a \frac{da''}{a''^2H(a'')}\ \partial_j v^i(\vec{x},a'')\int_{a''}^a \frac{da'''}{a'''^2H(a''')}\ v^j(\vec{x},a''') + \dots\ .\end{aligned} \tag{10.36}$$

[7] The notation $:\mathcal{O}:$ means that the operator $\mathcal{O}$ is subtracted of its vacuum expectation value, i.e. $:\mathcal{O}:=\mathcal{O}-\langle\mathcal{O}\rangle$. We do this explicitly in Ch. 6 as well under Eq. (6.112).

[8] The notation of the operators here is different to Ch. 6, and the difference is for historical reasons. However, if one were to use the EdS approximation here, the space spanned by the operators is the same as in Eq. (B.78), i.e. Ch. 6, to third order. As one can see from the definitions in Eqs. (B.76) and (F.29), we have for example $s_{ij} = r_{ij} - \frac{1}{3}\delta_{ij}\delta$.

It turns out that even in the presence of clustering quintessence, once we perturbatively expand the overdensity and velocity, the time integrals in Eq. (B.79) can be done analytically and the solutions are given in terms of the time functions and kernels that appear in Eqs. (10.30) - (10.32). This is explicitly derived in App. F.3. Then, as mentioned before, after perturbatively expanding the fields, the time integrals in Eq. (10.34) are formally done, and result in the definition of coefficients such as

$$c_{\delta,1}(a) = \int^a \frac{da'}{a'} c_\delta(a,a') \frac{D_+(a')}{D_+(a)}, \qquad c_{\delta^2,1}(a) = \int^a \frac{da'}{a'} c_{\delta^2}(a,a') \frac{D_+(a')^2}{D_+(a)^2}, \quad \dots \,. \tag{10.37}$$

For a complete list see App. F.2. After this procedure, the resulting halo overdensity can then be written as a sum of functions of time multiplied by functions of momentum. As was shown in [135], some of the momentum functions are degenerate and can all be expressed in terms of the basis $\{\mathbb{I}, \alpha, \beta, \alpha_1, \alpha_2, \beta_1, \beta_2, \gamma_1, \gamma_2\}$, which are the kernels that appear in Eqs. (10.30) - (10.32). This is true in wCDM as well as the clustering quintessence case, because the momentum functions are the same in both cases, and only the time functions change. We can therefore write

$$\begin{aligned}
K^{(1)}_{\delta_h}(\vec{q}_1, a) &= c_{\delta,1}(a)\,, \\
K^{(2)}_{\delta_h}(\vec{q}_1, \vec{q}_2, a) &= c_{\mathbb{I},(2)}(a) + c_{\alpha,(2)}(a)\alpha(\vec{q}_1,\vec{q}_2) + c_{\beta,(2)}(a)\beta(\vec{q}_1,\vec{q}_2)\,, \\
K^{(3)}_{\delta_h}(\vec{q}_1, \vec{q}_2, \vec{q}_3, a) &= c_{\alpha_\sigma,(3)}(a)\alpha^\sigma(\vec{q}_1,\vec{q}_2,\vec{q}_3) + c_{\beta_\sigma,(3)}(a)\beta^\sigma(\vec{q}_1,\vec{q}_2,\vec{q}_3) \\
&\quad + c_{\gamma_\sigma,(3)}(a)\gamma^\sigma(\vec{q}_1,\vec{q}_2,\vec{q}_3) + c_{\alpha,(3)}(a)\alpha(\vec{q}_1,\vec{q}_2) \\
&\quad + c_{\beta,(3)}(a)\beta(\vec{q}_1,\vec{q}_2) + c_{\mathbb{I},(3)}(a)\,,
\end{aligned} \tag{10.38}$$

where in the last expression a sum is implied over $\sigma \in \{1,2\}$. The main reason that the time coefficients c_i change, relative to wCDM, is because the integrals from the flow terms that stem from the Taylor expansion of Eq. (B.79) now have an additional dependence on $C(a)$ (for a comparison see App. F.3). The coefficients in Eq. (10.38) are explicitly defined in App. F.2. For more details on the derivation of the halo overdensity kernels, see [135].

From here we can proceed in a very similar fashion to [135]. We reduce the number of coefficients by looking for degeneracies in the time coefficients. Luckily all the identities from [135] still hold in a slightly more general form. The main difference here is that we define the calculable function $\mathcal{G} = \mathcal{G}^\delta_1 + \mathcal{G}^\delta_2$, with $\mathcal{G}^\delta_i$ defined

in App. F.1, which for wCDM is $\mathcal{G} \overset{w\text{CDM}}{=} 1$. The identities then read

$$\begin{aligned}
&c_{\alpha,(2)} + c_{\beta,(2)} = \mathcal{G}\, c_{\delta,1}\,, \\
&c_{\alpha,(3)} + c_{\beta,(3)} = 2\,\mathcal{G}\, c_{\mathbb{I},(2)}\,, \\
&c_{\beta_2,(3)} + \mathcal{G}\, c_{\alpha,(2)} - c_{\alpha_1,(3)} = \frac{\mathcal{G}^2}{2} c_{\delta,1}\,, \\
&c_{\alpha_1,(3)} + c_{\alpha_2,(3)} = c_{\gamma_1,(3)} + c_{\gamma_2,(3)}\,, \\
&c_{\beta_1,(3)} + c_{\beta_2,(3)} + c_{\gamma_1,(3)} + c_{\gamma_2,(3)} = \frac{\mathcal{G}^2}{2} c_{\delta,1}\,, \\
&c_{\gamma_1,(3)} + c_{\beta_1,(3)} = \left(\frac{3}{14} + Y(a)\right) c_{\delta,1}\,,
\end{aligned} \tag{10.39}$$

where in the limit $\mathcal{G} \overset{w\text{CDM}}{=} 1$ we recover the identities from [135]. $Y(a)$ is defined by

$$Y(a) = -\frac{3}{14} + \mathcal{V}^{\delta}_{11}(a) + \mathcal{V}^{\delta}_{12}(a). \tag{10.40}$$

However, it is useful to define

$$\tilde{Y}(a) = -\frac{3}{14}\mathcal{G}(a)^2 + \mathcal{V}^{\delta}_{11}(a) + \mathcal{V}^{\delta}_{12}(a), \tag{10.41}$$

so that, taking limits, we have $\tilde{Y}(a) \overset{w\text{CDM}}{=} Y(a) \overset{\text{EdS}}{=} 0$. We can then write the final halo overdensity (see also [276]):

$$\begin{aligned}
\delta_h(\vec{k},a) \;=\;& c_{\delta,1}(a)\left(\mathbb{C}^{(1)}_{\delta}(\vec{k},a) + \mathcal{G}(a)\mathbb{C}^{(2)}_{\delta}(\vec{k},a) + \mathcal{G}(a)^2\mathbb{C}^{(3)}_{\delta}(\vec{k},a) + \tilde{Y}(a)\mathbb{C}^{(3)}_{Y}(\vec{k},a)\right) \\
+\;& c_{\alpha,(2)}(a)\left(\mathbb{C}^{(2)}_{\alpha}(\vec{k},a) + \mathcal{G}(a)\mathbb{C}^{(3)}_{\alpha_1}(\vec{k},a)\right) \\
+\;& c_{\mathbb{I},(2)}(a)\left(\mathbb{C}^{(2)}_{\mathbb{I}}(\vec{k},a) + 2\,\mathcal{G}(a)\mathbb{C}^{(3)}_{\beta}(\vec{k},a)\right) \\
+\;& c_{\beta_1,(3)}(a)\,\mathbb{C}^{(3)}_{\beta_1}(\vec{k},a) + c_{\gamma_2,(3)}(a)\,\mathbb{C}^{(3)}_{\gamma_2}(\vec{k},a) \\
+\;& c_{\alpha,(3)}(a)\,\mathbb{C}^{(3)}_{\alpha}(\vec{k},a) + c_{\mathbb{I},(3)}(a)\mathbb{C}^{(3)}_{\mathbb{I}}(\vec{k},a)\,,
\end{aligned} \tag{10.42}$$

where we can see that no new $\mathbb{C}_i$ operators have to be included compared to the exact wCDM case or EdS approximated case. The $\mathbb{C}_i$ are defined in the same way as in [135] and are explicitly given in App. F.2. Similarly to what happens when we use the exact time dependence for smooth dark energy and ΛCDM, we see that there are additional calculable time dependencies in the final bias expansion for the galaxy overdensity. However, there are no new bias coefficients. We can take two interesting limits to see how the above expansion generalizes previous models.

In the $\mathcal{G} \to 1$ limit, we obtain the galaxy overdensity in wCDM with exact time dependence. Furthermore, in the limit where we use the EdS approximation, the time functions in Eqs. (10.30) - (10.32) become independent of a and with a value so that $\mathcal{G} \to 1$ and $\tilde{Y} \to 0$ [9]. Eq. (10.42) can then simply be linearly transformed into the BoD basis from [131], therefore the space spanned by the kernels in Eq. (10.42) is the same as the one spanned by the BoD basis from [131] (for a transformation see [135]). For illustration, we plot in Fig. 10.3 the values of $\tilde{Y}$ and $\mathcal{G}$ as functions of the redshift $z = 1/(1+a)$ and w.[10]

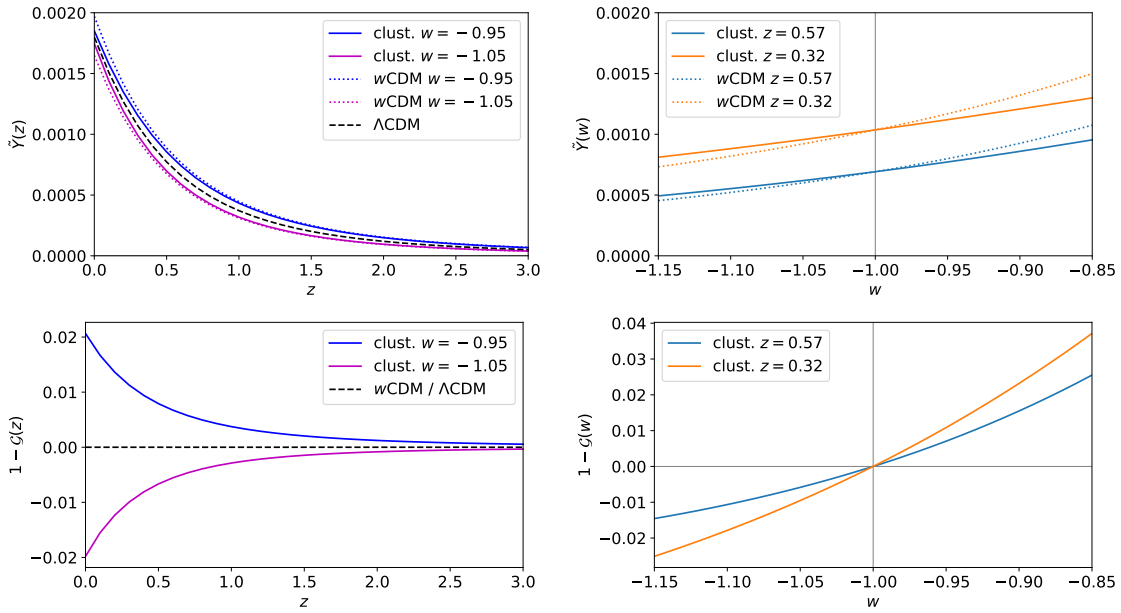

Figure 10.3: $\tilde{Y}$ and $\mathcal{G}$ as a function of redshift z and quintessence equation of state parameter w. We show ΛCDM and wCDM cases for comparison. Notice that, as we argued earlier, for $w < -1$ we need $c_s^2 \to 0$ and thus for $c_s^2 = 1$, i.e. wCDM, $w < -1$ is not allowed in the EFT of dark energy. We, nevertheless, plot it here for illustration.

In a last step, we write the expansion for θ_h, which appears in the redshift space expansion. For the velocity divergence, there is no bias [133], up to higher derivative terms. We can thus model the velocity divergence as a species of biased

[9] Note that in the presence of clustering quintessence the EdS approximation does not only rely on $\Omega_m/f_+^2 \approx 1$ but also on $C(a) \approx 1$ which is needed to cancel the time dependence in the continuity Eq. (10.28). Therefore, from Eq. (F.26) one can see that in the EdS approximation one takes the limit $\mathcal{G} \to 1$.

[10] As discussed in [260], the function $1 - \mathcal{G}(z)$, as shown in Fig. 10.3 describes the relative time evolution of the linear dark energy perturbation in clustering quintessence (in [260] the notation $\epsilon = 1 - \mathcal{G}$ is used). Specifically, $1 - \mathcal{G}(a) = \delta\rho_D^{(1)}(k,a)/\delta\rho_A^{(1)}(k,a)$, where $\delta\rho_D = \bar{\rho}_D \frac{1+w}{c_s^2}(\dot{\pi} - \Phi)$ as in [264]. Since the k dependence of both perturbations is the same [48], $1 - \mathcal{G}$ quantifies the relative size of the linear dark energy perturbations and hence of the dark energy linear power spectrum.

tracer. Specifically, we obtain the velocity divergence by plugging in the following choice of functions into Eq. (10.42):

$$\begin{aligned} c^{\theta}_{\delta,1}(a) &= 1 \\ c^{\theta}_{\mathbb{I},(2)}(a) &= c^{\theta}_{\mathbb{I},(3)}(a) = c^{\theta}_{\alpha,(3)}(a) = 0 \\ c^{\theta}_{\alpha,(2)}(a) &= \mathcal{G}^{\theta}_{1}(a) \\ c^{\theta}_{\beta_1,(3)}(a) &= \mathcal{V}^{\theta}_{12}(a) \\ c^{\theta}_{\gamma_2,(3)}(a) &= \mathcal{V}^{\theta}_{21}(a). \end{aligned} \tag{10.43}$$

The counterterms will take the exact same form as for wCDM [264, 135]. We will now transform into redshift space and compute the power spectrum.

10.3.3 Galaxy Power Spectrum in Redshift Space

As the next step, we wish to compute the full galaxy power spectrum in redshift space, which we will later use to fit the data. As shown in [135], the EdS approximation has no influence on the transformation into redshift space [11]. This means we can proceed in the same way as described in [133]. The galaxy overdensity kernels in redshift space in terms of the real space quantities δ_h and θ_h are given by (without counterterms)

$$\begin{aligned} K^{(1)}_{\delta_{h,r}}(\vec{q}_1,a) &= K^{(1)}_{\delta_h}(\vec{q}_1,a) + f_+\,\mu_1^2 K^{(1)}_{\theta_h}(\vec{q}_1,a) = b_1 + f_+\,\mu_1^2, \\ K^{(2)}_{\delta_{h,r}}(\vec{q}_1,\vec{q}_2,\mu,a) &= K^{(2)}_{\delta_h}(\vec{q}_1,\vec{q}_2,a) + f_+\,\mu_{12}^2 K^{(2)}_{\theta_h}(\vec{q}_1,\vec{q}_2,a) \\ &\quad + \frac{1}{2} f_+\,\mu\,q\left[\frac{\mu_2}{q_2} K^{(1)}_{\theta_h}(\vec{q}_2,a) K^{(1)}_{\delta_{h,r}}(\vec{q}_1,a) + \text{perm.}\right], \\ K^{(3)}_{\delta_{h,r}}(\vec{q}_1,\vec{q}_2,\vec{q}_3,\mu,a) &= K^{(3)}_{\delta_h}(\vec{q}_1,\vec{q}_2,\vec{q}_3,a) + f_+\,\mu_{123}^2 K^{(3)}_{\theta_h}(\vec{q}_1,\vec{q}_2,\vec{q}_3,a) \\ &\quad + \frac{1}{3} f_+\,\mu\,q\left[\frac{\mu_3}{q_3} K^{(1)}_{\theta_h}(\vec{q}_3,a) K^{(2)}_{\delta_{h,r}}(\vec{q}_1,\vec{q}_2,\mu_{123},a)\right. \\ &\quad \left. + \frac{\mu_{23}}{q_{23}} K^{(2)}_{\theta_h}(\vec{q}_2,\vec{q}_3,a) K^{(1)}_{\delta_{h,r}}(\vec{q}_1,a) + \text{cyc.}\right], \end{aligned} \tag{10.44}$$

where $\delta_{h,r}$ is the halo overdensity in redshift space. Using $\hat{z}$ as the line of sight unit vector, we have defined $\mu = \vec{q}\cdot\hat{z}/q$, with $\vec{q} = \vec{q}_1 + \cdots + \vec{q}_n$, and $\mu_{i_1\ldots i_n} = \vec{q}_{i_1\ldots i_n}\cdot\hat{z}/q_{i_1\ldots i_n}$, $\vec{q}_{i_1\ldots i_m} = \vec{q}_{i_1} + \cdots + \vec{q}_{i_m}$. As we mentioned previously, the counterterms and stochastic terms that come from real and redshift space (see [133, 135] for a discussion) do not

[11] Of course since the halo overdensity in redshift space depends on δ_h and θ_h, the exact time dependence has an impact, just not on the transformation itself.

change in the presence of clustering quintessence. Therefore, the final expression for the galaxy power spectrum in redshift space, including the counterterms, reads

$$\begin{aligned} P_g(k,\mu,a) &= K^{(1)}_{\delta_{h,r}}(\mu,a)^2 P_{11}(k,a) \\ &+ 2\int \frac{d^3q}{(2\pi)^3}\, K^{(2)}_{\delta_{h,r}}(\vec{q},\vec{k}-\vec{q},\mu,a)^2 P_{11}(|\vec{k}-\vec{q}|,a)P_{11}(q,a) \\ &+ 6K^{(1)}_{\delta_{h,r}}(\mu,a)P_{11}(k,a)\int \frac{d^3q}{(2\pi)^3}\, K^{(3)}_{\delta_{h,r}}(\vec{q},-\vec{q},\vec{k},\mu,a)P_{11}(q,a) \\ &+ 2K^{(1)}_{\delta_{h,r}}(\mu,a)P_{11}(k,a)\left(c_{\rm ct}\frac{k^2}{k_{\rm M}^2} + c_{r,1}\mu^2\frac{k^2}{k_{\rm M}^2} + c_{r,2}\mu^4\frac{k^2}{k_{\rm M}^2}\right) \\ &+ \frac{1}{\bar{n}}\left(c_{\epsilon,0} + c_{\epsilon,1}\frac{k^2}{k_{\rm M}^2} + c_{\epsilon,2}f_+\mu^2\frac{k^2}{k_{\rm M}^2}\right), \end{aligned} \tag{10.45}$$

where $P_{11}(k,a)$ is the time-dependent linear power spectrum for the adiabatic mode, $k_{\rm M} \lesssim k_{\rm NL}$ is the comoving wavenumber which controls the bias derivative expansion, and $\bar{n}$ is the background galaxy number density [12]. In the first line, we have the linear power spectrum in redshift space. In the second and third line, we have the P_{13} and P_{22} contributions of the loop and in the fourth and fifth line we have the counterterms and stochastic terms, respectively.

Finally, the power spectrum is IR-resummed following [137, 139, 140, 169]. Since quintessence is comoving with dark matter, the equations for the IR-resummation only change by a shift $P_{11}(k,a) \to \mathcal{G}(a)^2 P_{11}(k,a)$ [13]. We then apply corrections to take into account the Alcock-Pacszynski effect [214], window functions [201], and fiber collisions [277].

In Fig. 10.4, we show the difference between the one-loop galaxy power spectrum multipoles $\ell = 0, 2$ evaluated in different cosmologies: ΛCDM, wCDM and clustering quintessence, for $w = -0.95$ and $w = -1.05$. We also show the difference between the evaluation with and without the EdS approximation for clustering quintessence. It is apparent that the difference between wCDM and clustering quintessence is important with respect to the BOSS error bars. The difference between

[12] These are the same response and stochastic terms as in Ch. 6 in Eqs. (6.153) and (6.156), just with a renaming of coefficients for simplicity.

[13] The additional factors of $\mathcal{G}$ come from the integral over the velocity, when expressing the displacement field in terms of the overdensity

$$s^{(1)j}(a) = \int^a \frac{da'}{a'^2 H(a')} v^{(1)j}(a'). \tag{10.46}$$

This integral, which is explicitly computed for the flow terms in Eq. (F.46), results in $s^{(1)j}(a) = -\mathcal{G}(a)\frac{\partial^j}{\partial^2}\delta^{(1)}$.

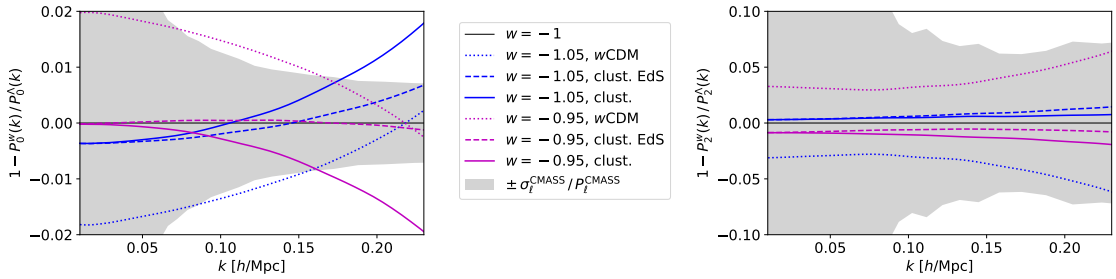

Figure 10.4: One-loop galaxy power spectrum multipole ratio of wCDM or clustering quintessence, with $w = -0.95$ and $w = -1.05$, to ΛCDM, at $z = 0.57$. We show for clustering quintessence the evaluation with and without the EdS approximation. The evaluation in ΛCDM and wCDM are with exact time dependence. The EFT parameters are the same for all evaluations, with values as the best fit of BOSS on ΛCDM. The BOSS CMASS error bars are depicted for comparison. Notice that, as we argued earlier, for $w < -1$ we need $c_s^2 \to 0$ and thus for $c_s^2 = 1$, i.e. wCDM, $w < -1$ is not allowed in the EFT of dark energy. We, nevertheless, plot it here for illustration.

the evaluation with and without the EdS approximation for clustering quintessence is clearly important, especially in the monopole. Given how large the differences in the power spectrum are, we expect to see differences at the level of the posteriors of the cosmological and EFT parameters[14].

10.4 LSS Data Analysis

In this section, after calibrating the scale cut of the theory against simulations, we present the results from fitting clustering and smooth quintessence to the BOSS FS, and its combinations with BAO, SN and CMB measurements.

Likelihood and Priors The theory prediction is given by the galaxy power spectrum in redshift space at one-loop order in the EFTofLSS, Eq. (10.45). Its evaluation is performed using `PyBird` [169], and we sample from a Gaussian likelihood. The kernels $K^{(1)}_{\delta_{h,r}}$, $K^{(2)}_{\delta_{h,r}}$, $K^{(3)}_{\delta_{h,r}}$ depend on 4 biases: b_1, b_2, b_3, b_4. In our analysis, we use the monopole and quadrupole of the galaxy power spectrum. We vary the cosmological parameters ω_{cdm}, h, $\ln(10^{10} A_s)$, n_s, w, on which we impose no priors, and ω_b with

[14] We note that the $w = -0.95$ clustering quintessence curve seems to exactly agree the $w = -1$ monopole as $k \to 0$. This is, however, an artefact of the particular best fit. Indeed, while for the real space power spectrum, the ratio would be dictated by the growth factors, for the monopole, the growth rate f_+, and the linear bias b_1 from the best fit contribute as well, leading to more complex relationships more dependent on the best fit.

a Gaussian prior motivated from Big Bang Nucleosynthesis (BBN) with standard deviation $\sigma_{\omega_b,\mathrm{BBN}} = 0.00036$ [216]. For the simulations, we will center the prior on the truth, while on BOSS data, we will use $\omega_{b,\mathrm{BBN}} = 0.02233$ [216]. When analyzing BOSS data [9] (alone and in combination with other datasets) we fix the neutrinos to minimal mass, 0.06 eV, as done in the Planck analysis [24]. As for the EFT parameters, we define the linear combinations $c_2 = (b_2 + b_4)/\sqrt{2}$, $c_4 = (b_2 - b_4)/\sqrt{2}$, and we set $c_4 = 0$ since b_2, b_4 are almost completely anticorrelated. Then, we define the two combinations $c_{\epsilon,\mathrm{mono}} = c_{\epsilon,1} + f c_{\epsilon,2}/3$, $c_{\epsilon,\mathrm{quad}} = 2f c_{\epsilon,2}/3$. We put a Gaussian prior of mean 0 and standard deviation 2, $\mathcal{N}(0,2)$, on b_3, c_{ct}, $c_{\epsilon,0}$, $c_{\epsilon,\mathrm{mono}}$, $c_{\epsilon,\mathrm{quad}}$, and a Gaussian prior of mean 0 and standard deviation 8, $\mathcal{N}(0,8)$, on the redshift-space counterterm $c_{r,1}$. We fix $c_{r,2} = 0$ since it is exactly degenerate with $c_{r,1}$ when only analyzing the monopole and quadrupole. As explained in [7, 169], we analytically marginalize over b_3, c_{ct}, $c_{\epsilon,0}$, $c_{\epsilon,\mathrm{mono}}$, $c_{\epsilon,\mathrm{quad}}$, $c_{r,1}$ as they appear linearly in the power spectrum and therefore quadratically in the likelihood. Finally, the linear bias b_1 has a flat prior $[0,4]$, and c_2 has a flat prior $[-4,4]$, which play no role.

10.4.1 Tests against Simulations

To assess the theory-systematic error of the FS analysis, we fit the power spectrum multipoles measured from large-volume N-body simulations on clustering quintessence with a BBN prior. We consider two independent realizations of the BOSS 'lettered' challenge simulations, which are boxes of side length $2.5\,\mathrm{Gpc}/h$, described in e.g. [7]. The first realization is made of four boxes, labelled A, B, F, and G, populated by four different Halo Occupation Distribution (HOD) models, of which we analyze the snapshot at $z = 0.56$. The second realization, labelled D, is populated by another HOD model, of which we analyze the snapshot at $z = 0.5$. Using one box, we can measure for each cosmological parameter the theory-systematic error as the distance in the 1D posterior of the 1σ region to the truth of the simulation. Therefore, the theory-systematic error is zero if the truth lies within the 1σ region. For A, B, F, and G, which are correlated, we average the posteriors for the cosmological parameters, that we label ABFG. Moreover, we can combine ABFG with D, as they are independent realizations, allowing us to measure the theory error using a volume about 14 times the one of BOSS data. To do so, we combine for each cosmological parameter the 1D posterior of the shift of the mean with respect to the truth, as the product of two Gaussian distributions. The distance of the 1σ region to zero in each resulting 1D posterior gives a measure of the theory-systematic error for the

combination ABFG+D. For each cosmological parameter, the error bar obtained on ABFG+D represents the smallest theory-systematic error which we can measure, which is between $0.3 \cdot \sigma_{\rm data}$ and $0.5 \cdot \sigma_{\rm data}$, where $\sigma_{\rm data}$ is the error bar obtained by fitting BOSS data.

	ω_{cdm} $\sigma_{\rm stat}\|\sigma_{\rm sys}$	h $\sigma_{\rm stat}\|\sigma_{\rm sys}$	$\ln(10^{10}A_s)$ $\sigma_{\rm stat}\|\sigma_{\rm sys}$	n_s $\sigma_{\rm stat}\|\sigma_{\rm sys}$	w $\sigma_{\rm stat}\|\sigma_{\rm sys}$	Ω_m $\sigma_{\rm stat}\|\sigma_{\rm sys}$
ABFG	0.007|0.000	0.027|0.000	0.11|0.04	0.044|0.000	0.139|0.000	0.021|0.000
D	0.006|0.000	0.018|0.000	0.11|0.04	0.039|0.000	0.093|0.000	0.014|0.000
ABFG+D	0.005|0.000	0.015|0.000	0.08|0.07	0.029|0.000	0.077|0.000	0.012|0.000

Table 10.1: 68%-confidence intervals $\sigma_{\rm stat}$ and theory-systematic errors $\sigma_{\rm sys}$ obtained fitting clustering quintessence to the lettered challenge simulations with a BBN prior.

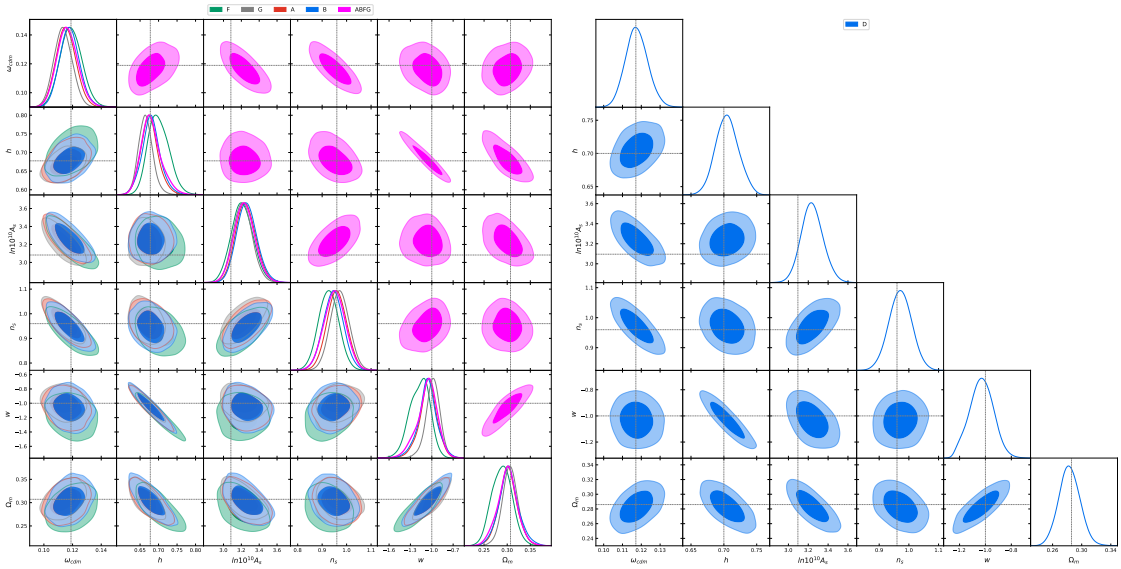

Figure 10.5: Triangle plots obtained by fitting clustering quintessence to the lettered challenge simulations with a BBN prior. The dashed lines represent the truth of the simulations.

In Fig. 10.5 and Tab. 10.1, we show the results obtained by fitting the lettered challenge simulations at scale cut $k_{\rm max} = 0.23h\,{\rm Mpc}^{-1}$. We find for all cosmological parameters zero theory-systematic error, with the exception of $\ln(10^{10}A_s)$, where we find a marginal theory-systematic error of 0.07, which is $\sim 0.4 \cdot \sigma_{\rm data}$ [15]. These results show that we can confidently fit the data up to $k_{\rm max} = 0.23h\,{\rm Mpc}^{-1}$ on our

[15] Given the number of cosmological parameters, we find the likelihood of such a large value of one cosmological parameter to be sufficiently high, so that we do not include this in the systematic error budget.

	BOSS		BOSS+6DF/MGS+eBOSS		BOSS+6DF/MGS+eBOSS+SN	
	best-fit	mean$\pm\sigma$	best-fit	mean$\pm\sigma$	best-fit	mean$\pm\sigma$
ω_{cdm}	0.1271	$0.1346^{+0.011}_{-0.016}$	0.1188	$0.122^{+0.0083}_{-0.0099}$	0.1196	$0.1234^{+0.008}_{-0.01}$
H_0	66.75	$67.58^{+2.7}_{-3.5}$	66.99	$67.35^{+2}_{-2.3}$	67.97	$68.72^{+1.4}_{-1.6}$
$\ln(10^{10}A_s)$	2.733	$2.64^{+0.16}_{-0.17}$	2.837	$2.79^{+0.14}_{-0.16}$	2.848	$2.806^{+0.15}_{-0.16}$
n_s	0.9103	$0.8884^{+0.072}_{-0.059}$	0.9406	$0.9416^{+0.053}_{-0.051}$	0.972	$0.9335^{+0.054}_{-0.05}$
w	-0.878	$-0.8666^{+0.17}_{-0.15}$	-0.9212	$-0.9358^{+0.11}_{-0.092}$	-0.9928	$-1.011^{+0.053}_{-0.048}$
Ω_m	0.337	$0.3456^{+0.03}_{-0.027}$	0.3166	$0.3197^{+0.017}_{-0.015}$	0.3083	$0.3099^{+0.012}_{-0.011}$
σ_8	0.684	$0.6675^{+0.061}_{-0.067}$	0.7043	$0.7034^{+0.047}_{-0.057}$	0.7371	$0.7285^{+0.043}_{-0.049}$

Table 10.2: Results obtained by fitting clustering quintessence to BOSS in combination with other late-time probes with a BBN prior.

high redshift ($z_{\rm eff} = 0.57$) sample CMASS. For LOWZ sample at $z_{\rm eff} = 0.32$, we rescale the scale cut as in [7] and fit up to $k_{\rm max} = 0.2h\,{\rm Mpc}^{-1}$.

10.4.2 LSS Constraints

In Fig. 10.6 and Tab. 10.2, we show the results obtained by fitting BOSS FS+BAO, and in combination with BAO measurements from 6DF/MGS and eBOSS, and with Pantheon SN, on clustering quintessence with a BBN prior. We see that all cosmological parameters can be measured (we do not quote ω_b since it is dominated by the BBN prior we impose). For all analyses performed, w is consistent with -1 at $\lesssim 1\sigma$.

Physical Considerations We now discuss why all cosmological parameters can be measured by analyzing the FS using the EFTofLSS, and how the addition of the SN measurements helps to obtain better constraints. Let us start with the contribution from the BAO information. The two angles corresponding to the BAO components perpendicular and parallel to the line of sight are given by:

$$\theta_{\rm LSS,\perp} \simeq \frac{r_d(z_{\rm CMB})}{D_A(z_{\rm LSS})} \qquad \theta_{\rm LSS,\parallel} \simeq \frac{r_d(z_{\rm CMB})}{cz_{\rm LSS}/H(z_{\rm LSS})}\,. \tag{10.47}$$

Here $r_d(z_{\rm CMB})$ is the sound horizon at the end of the baryon-drag epoch $z_{\rm CMB}$, and $D_A(z_{\rm LSS})$ and $H(z_{\rm LSS})$ are the angular diameter distance and the Hubble parameter at the effective redshift of the survey $z_{\rm LSS}$. As discussed in e.g. [7, 169], these angles carry information about h, Ω_m and w. The dependence on parameters is the same

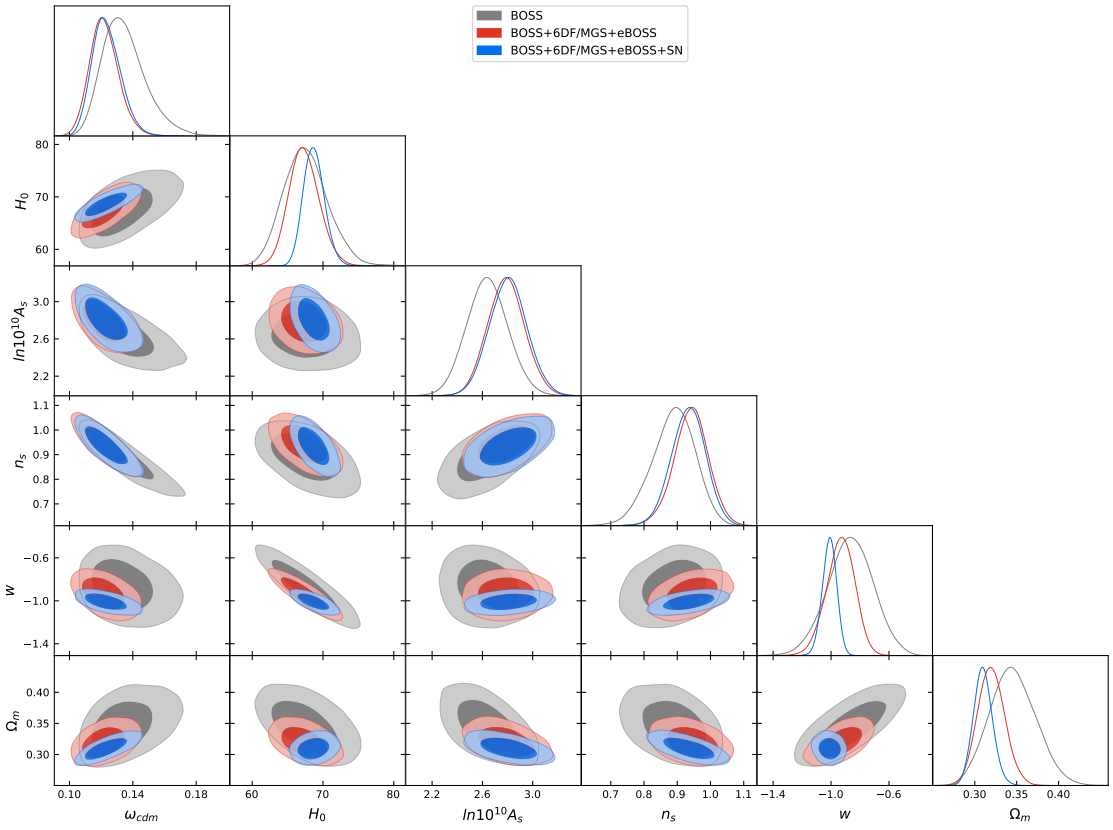

Figure 10.6: Triangle plots obtained by fitting clustering quintessence to BOSS in combination with other late-time probes with a BBN prior.

as in wCDM, as the angles only depend on the background geometry [169]:

$$\begin{aligned}
&\theta_{\mathrm{LSS},\parallel}(z_{\mathrm{Ly}\alpha}) \sim \Omega_m^{0.17} h^{0.42} |w|^{-0.11}, \quad \theta_{\mathrm{LSS},\perp}(z_{\mathrm{Ly}\alpha}) \sim \Omega_m^{0.01} h^{0.48} |w|^{-0.19} \,, \\
&\theta_{\mathrm{LSS},\parallel}(z_{\mathrm{CMASS}}) \sim \Omega_m^{-0.02} h^{0.49} |w|^{-0.25}, \quad \theta_{\mathrm{LSS},\perp}(z_{\mathrm{CMASS}}) \sim \Omega_m^{-0.12} h^{0.53} |w|^{-0.17} \,, \\
&\theta_{\mathrm{LSS},\parallel}(z_{\mathrm{LOWZ}}) \sim \Omega_m^{-0.10} h^{0.52} |w|^{-0.21}, \quad \theta_{\mathrm{LSS},\perp}(z_{\mathrm{LOWZ}}) \sim \Omega_m^{-0.16} h^{0.54} |w|^{-0.12} \,, \\
&\theta_{\mathrm{LSS,V}}(z_{\mathrm{6dF}}) \sim \Omega_m^{-0.19} h^{0.55} |w|^{-0.07}, \quad \theta_{\mathrm{LSS,V}}(z_{\mathrm{MGS}}) \sim \Omega_m^{-0.18} h^{0.55} |w|^{-0.09} \,. \qquad (10.48)
\end{aligned}$$

where $z_{\mathrm{Ly}\alpha} = 2.35$, $z_{\mathrm{CMASS}} = 0.57$, $z_{\mathrm{LOWZ}} = 0.32$ and $z_{\mathrm{6dF/MGS}} = 0.106$. $\theta_{\mathrm{LSS,V}}$ is a combination of $\theta_{\mathrm{LSS},\perp}$ and $\theta_{\mathrm{LSS},\parallel}$ (see e.g. [169]). The dependences on the cosmological parameters above and in the rest of this section are obtained expanding around a fiducial cosmology ($\Omega_m = 0.3$, $h = 0.7$, $w = -1$). Furthermore, the relative amplitude of the BAO wiggles with respect to the smooth part instead gives a measurement of $\sim \Omega_m h^2$ (though the amplitude is not part of the standard BAO analysis). Clearly, at least in principle, this information allows for a determination of w, Ω_m and h. Notice however that the measurements for w and Ω_m are strongly de-

generate when using solely the BAO information from CMASS and LOWZ, and the breaking of the degeneracy by measuring both $\theta_{\rm LSS,\perp}$ and $\theta_{\rm LSS,\parallel}$ is mild, insufficient to get strong constraints [169]. Of course, the situation is greatly ameliorated by the addition of the information from 6dF/MGS and eBOSS, but it is also ameliorated by the inclusion of the FS analysis.

In fact, the FS contains information not only through the BAO signal, but also by its shape and amplitude [7]. The shape depends on the equality scale, and therefore on $\Omega_m h^2$. The amplitude and the anisotropy of the FS can be roughly summarized by the fact that the monopole and quadrupole mainly depend on the combinations $b_1(z)^2 D_+(z)^2 A_s^{(k_{\rm max})}$ and $b_1(z) f_+(z) D_+(z)^2 A_s^{(k_{\rm max})}$. Here $A_s^{(k_{\rm max})}$ is the amplitude of the linearly evolved power spectrum at the maximum wavenumber of our analysis, $A_s^{(k_{\rm max})} \sim (k/k_0)^{n_s-1} (k_{\rm eq}/k_{\rm max})^2 A_s$, with $k_{\rm eq}$ being the wavenumber that re-enters the horizon at equality and k_0 the pivot scale. D_+ and f_+ are respectively the growth factor and growth rate of the growing adiabatic mode. $k_{\rm max}$ is the maximum wavenumber of our analysis, which is where the signal to noise is dominated. Given that there are two redshifts in BOSS, this clearly offers a way to measure both A_s and n_s, together with $b_1(z_{\rm CMASS})$ and $b_1(z_{\rm LOWZ})$. In this way, all cosmological parameters are, at least in principle, measured. However, we should keep in mind that the FS offers an independent measurement for each wavenumber, therefore, by combining the information from several k's, further information on w and Ω_m is obtained. In fact, just by looking at the dependence at linear level of the monopole and quadrupole at $z_{\rm CMASS}$ and $z_{\rm LOWZ}$, one can see that on top of b_1 and A_s, one can measure the combination $\left.\frac{f(z_{\rm CMASS})D(z_{\rm CMASS})}{f(z_{\rm LOWZ})D(z_{\rm LOWZ})}\right|_{\rm clust.}$, which, around the fiducial cosmology, goes as $\sim \Omega_m^{-0.12}|w|^{0.44}$. This can be seen by using the fitting functions for D_+ and f_+ as a function of Ω_m and w given in [260], which read:

$$\begin{aligned}\frac{D_+(a)}{a} &= \frac{5}{2}\Omega_m(a) \times \\ &\times \left[\Omega_m(a)^{4/7} + \frac{3}{2}\Omega_m(a) + \left(\frac{1}{70} - \frac{1+w}{4}\right)\Omega_D(a)\left(1 + \frac{\Omega_m(a)}{2}\right)\right]^{-1}, \\ f_+(a) &= C(a)\left[\Omega_m(a)^{4/7} + \left(\frac{1}{70} - \frac{1+w}{4}\right)\Omega_D(a)\left(1 + \frac{\Omega_m(a)}{2}\right)\right],\end{aligned} \tag{10.49}$$

where $C(a) = 1 + (1+w)\Omega_D(a)/\Omega_m(a)$. This is to be contrasted with the same ratio for the case of a smooth dark energy component, namely wCDM, around the same cosmology: $\left.\frac{f(z_{\rm CMASS})D(z_{\rm CMASS})}{f(z_{\rm LOWZ})D(z_{\rm LOWZ})}\right|_{w\rm CDM} \sim \Omega_m^{-0.12}|w|^{0.006}$. We can see that the change in the dependence on w going from LOWZ to CMASS is stronger in the case of

clustering quintessence compared to wCDM, physically originating from the fact that clustering quintessence contributes to the clustering. The mild degeneracy present for wCDM between Ω_m and w is thus less pronounced in clustering quintessence when jointly fitting LOWZ and CMASS. Furthermore, these measurements give different correlations between Ω_m and w with respect to the ones in $\theta_{\rm LSS}$, thus further breaking the degeneracies. This can be seen in Fig. 10.7, where we compare the posteriors obtained fitting BOSS FS+BAO on clustering quintessence and wCDM. To summarize, Ω_m, h, w, A_s, n_s and b_1 can be measured from the BAO angles in combination with the broadband signal.

By looking at the same Fig. 10.7, one can also see that in wCDM there is a large degeneracy in lowering w and lowering A_s. This can be explained by the fact that, in wCDM with $w < -1$ (which, we remind, is physically inconsistent at the quantum level but can still be analyzed as a model), matter domination lasts longer, so that structures grow more and therefore the power spectrum is left unchanged by lowering A_s. In clustering quintessence, this degeneracy is broken by the fact that the adiabatic mode receives a contribution from clustering quintessence proportional to $1 + w$. This can be see from solving the linear equations, which, at early times, give (see e.g. [264], Eq. (4.15)):

$$\delta_A(a_{\rm early}) = \left(1 + \frac{(1+w)}{1-3w}\frac{\Omega_{D,0}}{\Omega_{m,0}}\left(\frac{a_{\rm early}}{a_0}\right)^{-3w}\right)\delta_m(a_{\rm early}) \ , \tag{10.50}$$

with a_0 the present epoch and $a_{\rm early}$ a time early on during matter domination. This effect acts in a direction contrary to the extra growth that one gets from the extension of the epoch of matter domination for $1 + w < 0$, in practice bounding the degeneracy between w and A_s.

Note that this discussion gives only rough estimates of the parameter dependence of the FS. In practice, there is no separation between the broadband and the other sources of information within the FS analysis as all the signal is analyzed up to the chosen scale cut. In particular, the loop provides additional information. For example, the growth function enters as D_+^4 in the loop, providing yet another parametric dependence on w. In Fig. 10.7, we also show the posteriors obtained on clustering quintessence with the EdS approximation [16]. The difference with the posteriors obtained with exact time dependence is clearly visible: most notably, about $0.2\,\sigma$ for H_0 and Ω_m, and $0.3\,\sigma$ for w. At the level of the power spectrum in Fig. 10.4,

[16] In App. F.4 we show the full posterior including the nuisance parameters

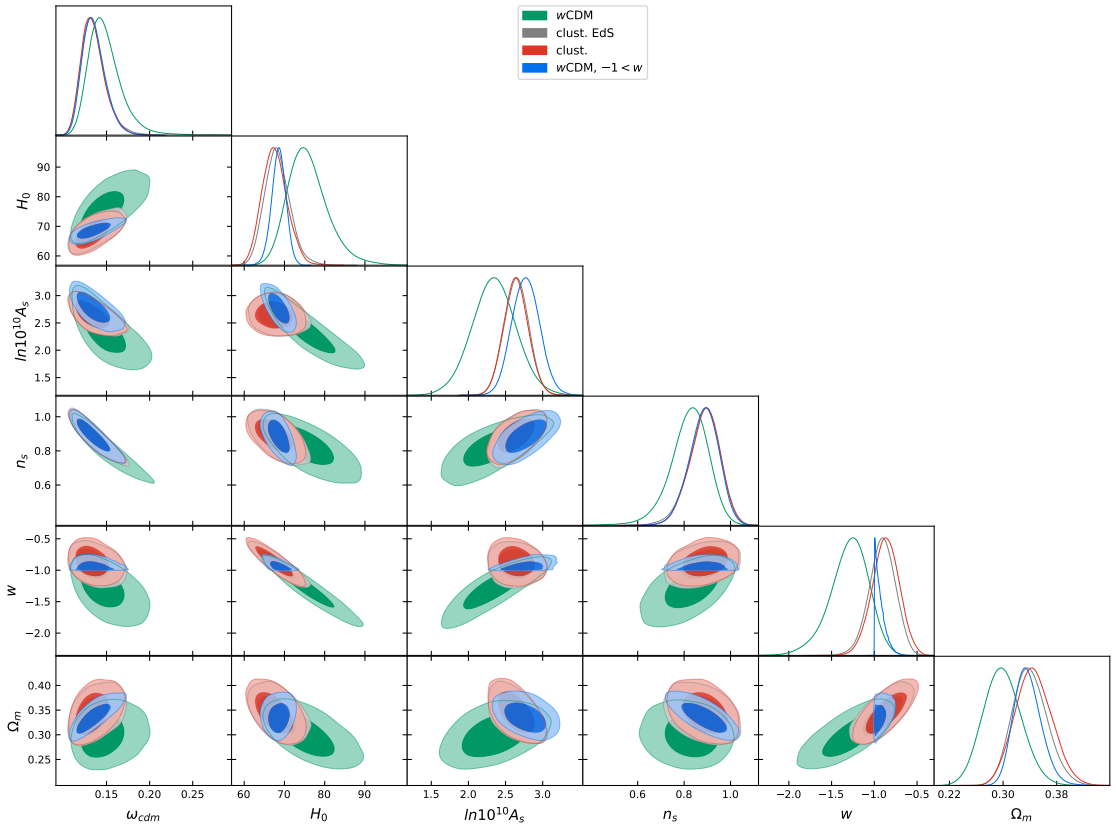

Figure 10.7: Triangle plots obtained by fitting clustering quintessence to BOSS with a BBN prior, with or without the EdS approximation. For comparison, we show wCDM fit to BOSS with a BBN prior, with and without physical prior $w \geq 1$.

the difference is somewhat larger in terms of error bars, but we should remember that in that figure the EFT parameters are fixed. In particular, the large deviation that can be seen in the monopole of Fig. 10.4 can be partially absorbed below the error bars with a small offset in the shot noise $c_{\epsilon,0}/\bar{n}$ of ~ 0.1. The difference we see between the EdS evaluation and the exact-time one can be traced to the time functions, as for example $\mathcal{G}^2$, in some loop terms when evaluated with exact time dependence: $\mathcal{G}(z_{\rm LOWZ})^2 \sim |w|^{0.42}$ and $\mathcal{G}(z_{\rm CMASS})^2 \sim |w|^{0.27}$. Because of this, the EdS approximation leads to noticeable shifts in the posteriors for clustering quintessence. The shifts are of the same order as the theory-systematic error we find in Sec. 7.6.4, so it may look like we can neglect them. However, we would then introduce an additional systematic error on the parameters. Contrary to the uncertainty from next orders in perturbation theory, the exact time dependence can be easily computed, with the same computational cost and without adding new nuisance parameters. Therefore, we prefer to use the exact time dependence.

Finally, the distance-redshift relation of SN data from Pantheon brings evidently more constraints. Approximately, the line degeneracy of the luminosity distance $D_L = (1+z)^2 D_A$ is $D_L(z = 0.25) = \Omega_m^{-0.05}|w|^{0.1}$, which further helps break the degeneracy between Ω_m and w when fitting jointly with the FS and BAO.

10.4.3 CMB+LSS Constraints

In Fig. 10.8 and Tab. 10.3, we show the results obtained fitting clustering quintessence with Planck data in combination with BOSS FS+BAO, BAO measurements from 6DF/MGS and eBOSS and with Pantheon SN.

Planck +	BOSS		BOSS+6DF/MGS+eBOSS		BOSS+6DF/MGS+eBOSS+SN	
	best-fit	mean$\pm\sigma$	best-fit	mean$\pm\sigma$	best-fit	mean$\pm\sigma$
$100\ \omega_b$	2.247	2.236 ± 0.050	2.275	2.233 ± 0.050	2.247	2.246 ± 0.013
ω_{cdm}	0.141	$0.135^{+0.010}_{-0.015}$	0.1211	$0.1198^{+0.0071}_{-0.0080}$	0.11849	0.11896 ± 0.00094
H_0	70.25	68.6 ± 1.8	68.45	68.0 ± 1.2	67.98	$67.37^{+0.57}_{-0.45}$
$\ln(10^{10} A_s)$	2.703	2.77 ± 0.19	2.84	2.88 ± 0.16	3.045	$3.050^{+0.013}_{-0.015}$
n_s	0.8754	$0.885^{+0.069}_{-0.058}$	0.95	0.953 ± 0.047	0.97	0.9681 ± 0.0037
w	-0.9955	$< -0.808(2\sigma)$	-1.000	$< -0.927(2\sigma)$	-0.998	$< -0.956(2\sigma)$
Ω_m	0.3325	$0.337^{+0.017}_{-0.022}$	0.3084	0.309 ± 0.011	0.3065	$0.3131^{+0.0056}_{-0.0066}$
σ_8	0.7345	0.728 ± 0.047	0.733	$0.740^{+0.044}_{-0.050}$	0.8065	0.8054 ± 0.0072

Table 10.3: Results obtained by fitting clustering quintessence to Planck and BOSS in combination with other late-time probes.

As expected and apparent from the posteriors, we can see that Planck gives precise measurements on ω_b, ω_{cdm}, $\ln(10^{10} A_s)$ and n_s, while constraints on H_0 or Ω_m are obtained by the combination with late-time probes, that break the degeneracy in the $H_0 - \Omega_m$ plane present in the CMB. As discussed in the previous subsection, w is mainly measured thanks to low-redshift measurements. However, the constraints on w are better when adding Planck since the precise measurements of the other cosmological parameters by Planck helps to further break the degeneracies.

10.4.4 wCDM with $w \geq -1$

From an Effective Field Theory point of view, there is no known theory, at least to us, that can realize $w < -1$ with $c_s^2 \to 1$. As discussed in previous sections, such theory has a negative kinetic term. For a theory with no Lorentz-violating UV cutoff, the scalar perturbations are unstable, and the vacuum decays into gravitons at an infinite rate [268]. Therefore, $w < -1$ would either need some other, physical, motivation or one can posit that w is not allowed to be smaller than -1 in wCDM.

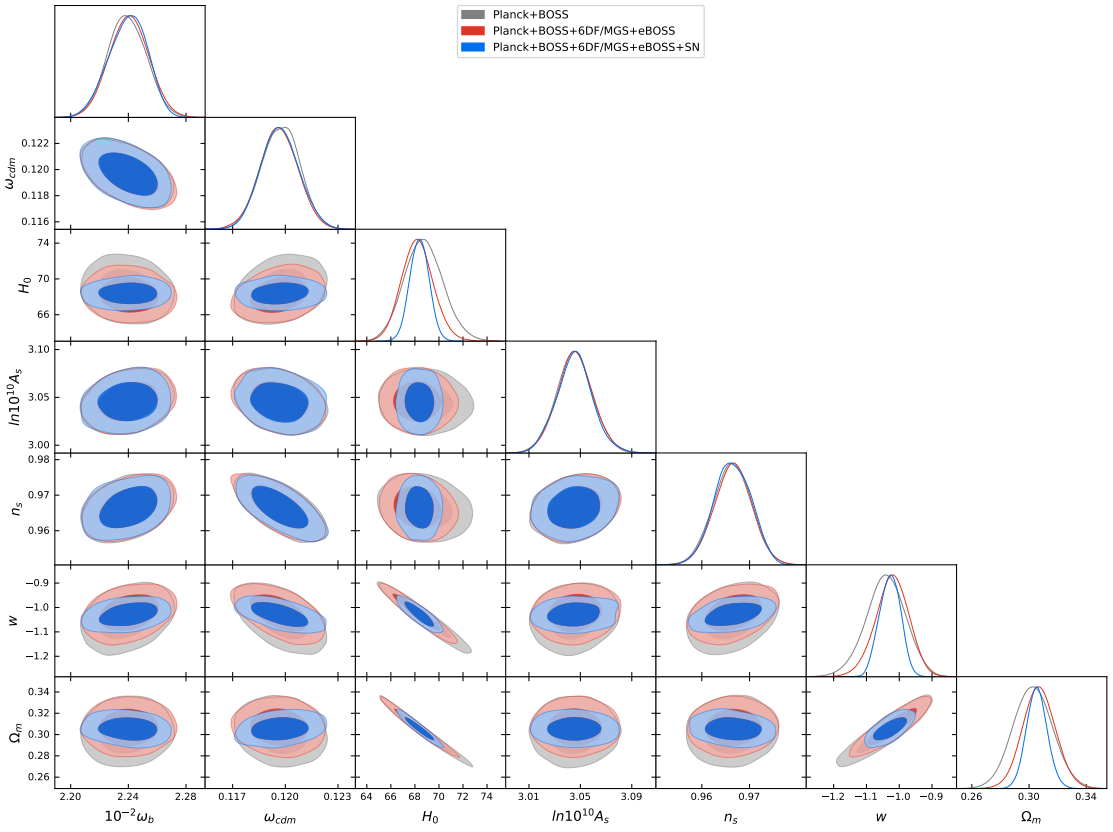

Figure 10.8: Triangle plots obtained by fitting clustering quintessence to Planck and BOSS in combination with other late-time probes.

By doing so, we get the results in Fig. 10.7 obtained by fitting BOSS data on wCDM with a BBN prior and a flat prior $w \geq -1$. We see that the results differ substantially from the ones obtained without a prior on w. In particular, the degeneracy line $w - H_0$, open when allowing w to vary below -1, can not be exploited to lift H_0 to higher values than the one found in ΛCDM analyzing CMB or LSS data.

In Fig. 10.9 and Tab. 10.4, we show the results obtained fitting BOSS, and in combination with BAO measurements from 6DF/MGS and eBOSS, with Pantheon SN, and with Planck data, on wCDM with a BBN prior and a prior $w \geq -1$. BOSS data alone gives a mild constraint $-1 \leq w < -0.91$ at 68% C.L. ($-1 \leq w < -0.81$ at 95% C.L.). Adding BAO information and Pantheon SN, the constraints on H_0 and especially Ω_m improve, giving the much stronger constraint $-1 \leq w < -0.96$ at 68% C.L. ($-1 \leq w < -0.93$ at 95% C.L.). Finally, Planck improves this to $-1 \leq w < -0.979$ at 68% C.L. ($-1 \leq w < -0.956$ at 95% C.L.), which means our Universe is consistent with a cosmological constant at 4% precision.

	BOSS		BOSS+6DF/MGS+eBOSS+SN		Planck+BOSS+6DF/MGS+eBOSS+SN	
	best-fit	mean$\pm\sigma$	best-fit	mean$\pm\sigma$	best-fit	mean$\pm\sigma$
$100\ \omega_b$	2.247	2.236 ± 0.050	2.172	2.233 ± 0.050	2.243	2.246 ± 0.013
ω_{cdm}	0.141	$0.135^{+0.010}_{-0.015}$	0.106	$0.1198^{+0.0071}_{-0.0080}$	0.18965	0.11896 ± 0.00094
H_0	70.25	68.6 ± 1.8	65.0	68.0 ± 1.2	67.32	$67.37^{+0.57}_{-0.45}$
$\ln(10^{10} A_s)$	2.703	2.77 ± 0.19	3.15	2.88 ± 0.16	3.044	$3.050^{+0.013}_{-0.015}$
n_s	0.8754	$0.885^{+0.069}_{-0.058}$	1.026	0.953 ± 0.047	0.9728	0.9681 ± 0.0037
w	-0.9955	$< -0.808 (2\sigma)$	-0.936	$< -0.927 (2\sigma)$	-0.976	$< -0.956 (2\sigma)$
Ω_m	0.3325	$0.337^{+0.017}_{-0.022}$	0.304	0.309 ± 0.011	0.3123	$0.3131^{+0.0056}_{-0.0066}$
σ_8	0.7345	0.728 ± 0.047	0.799	$0.740^{+0.044}_{-0.050}$	0.8004	0.8054 ± 0.0072

Table 10.4: Results obtained by fitting smooth quintessence to BOSS in combination with other late-time probes, and to Planck, with a prior $w \geq -1$. When not fitting with Planck, we use a BBN prior. For w, we quote the 95% confidence bound instead of the 68% confidence interval.

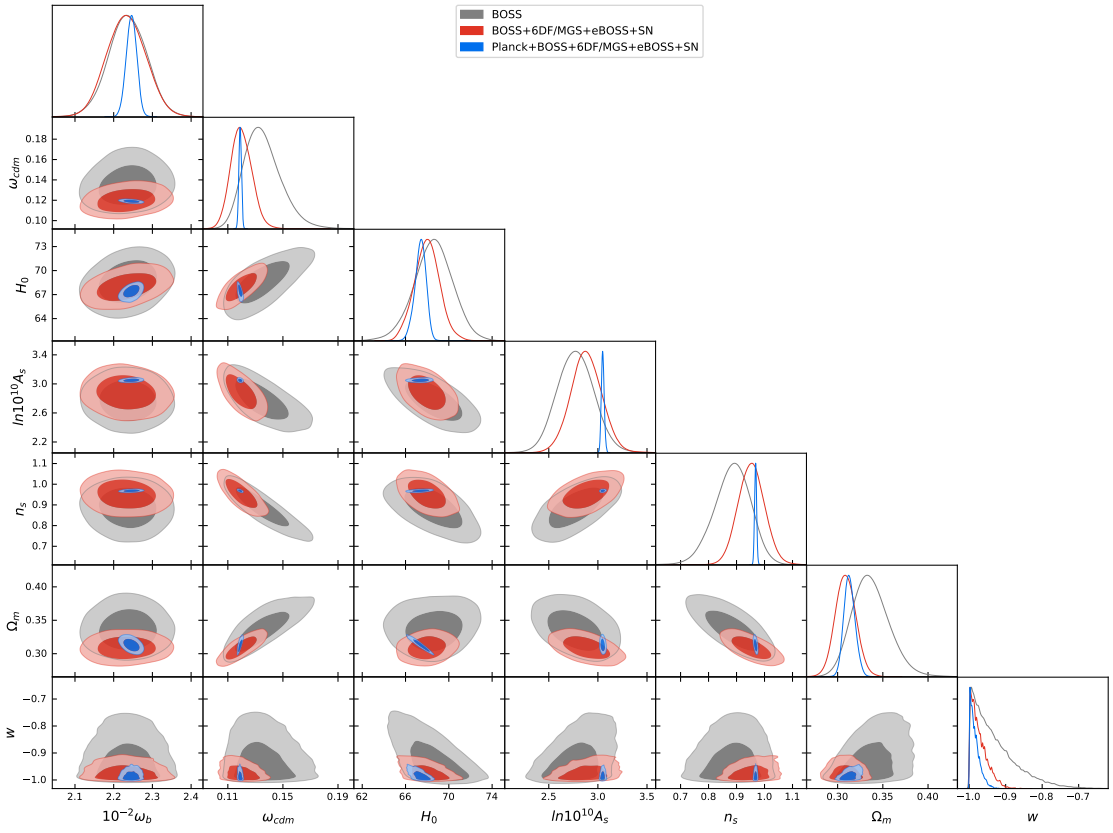

Figure 10.9: Triangle plots obtained by fitting smooth quintessence to BOSS in combination with other late-time probes, and to Planck, with a prior $w \geq -1$. When not fitting with Planck, we use a BBN prior.

Appendices

A

Appendix: The In-Out Formalism for In-In Correlators

A.1 In-In Equals In-Out: the Exchange Diagram for General Masses

After having established that for conformally coupled and massless scalars the in-in and in-out formalisms give the same result for an exchange diagram, we here establish this result for general masses. The derivation for the rr, rl and lr cases, hold for general masses, since they only rely on the equivalence for the contact diagram case, as shown in Sec. 5.3.3. Therefore, the only remaining part is the ll case, which we discuss in the following. We start with the definitions of the in-in and in-out correlators for the exchange from Sec. 5.3.3, where we set couplings $\lambda_1\lambda_2 = -1$ for simplicity. We have

$$\begin{aligned} B^{ll}_{\text{in-in}} = &\int_{-\infty(1+i\epsilon)}^{0}\int_{-\infty(1+i\epsilon)}^{0}\frac{d\eta}{\eta^4}\frac{d\eta'}{\eta'^4}\times \\ &\times F_1F_2\left[G^*_F(\eta,\eta';s)\prod_{a=1}^{n}G_l(\eta,\eta_a;k_a)\prod_{b=n+1}^{n+m}G_l(\eta',\eta_b;k_b)\right], \\ B^{ll}_{\text{in-out}} = &\int_{0}^{\infty(1-i\epsilon)}\int_{0}^{\infty(1-i\epsilon)}\frac{d\eta}{\eta^4}\frac{d\eta'}{\eta'^4}\times \\ &\times F_1F_2\left[G_F(\eta,\eta';s)\prod_{a=1}^{n}G_F(\eta,\eta_a;k_a)\prod_{b=n+1}^{n+m}G_F(\eta',\eta_b;k_b)\right]. \end{aligned} \tag{A.1}$$

Let us first do some simplification on $B^{ll}_{\text{in-in}}$. Note that from the contact diagram case, we know $\int_{-\infty(1+i\epsilon)}^{+\infty(1-i\epsilon)}\frac{d\eta'}{\eta'^4}F_1\left[\prod_a G_l(\eta',\eta_a,k_a)\right]\to 0$. Therefore, for any intermedi-

ary η we have

$$\int_{-\infty(1+i\epsilon)}^{\eta} \frac{d\eta'}{\eta'^4} F_1 \left[\prod_a G_l(\eta', \eta_a, k_a) \right] = - \int_{\eta}^{+\infty(1-i\epsilon)} \frac{d\eta'}{\eta'^4} F_1 \left[\prod_a G_l(\eta', \eta_a, k_a) \right] . \quad \text{(A.2)}$$

Let us expand the Feynman propagator in $B^{ll}_{\text{in-in}}$, and then apply the identity above. We then have

$$\begin{aligned}
B^{ll}_{\text{in-in}} \quad &= \int_{-\infty(1+i\epsilon)}^{0} \frac{d\eta}{\eta^4} \int_{-\infty(1+i\epsilon)}^{\eta} \frac{d\eta'}{\eta'^4} \times \qquad \text{(A.3)} \\
&\qquad \times F_1 F_2 \left[G_l(\eta', \eta; s) \prod_{a=1}^{n} G_l(\eta, \eta_a; k_a) \prod_{b=n+1}^{n+m} G_l(\eta', \eta_b; k_b) \right] , \\
&\quad + \int_{-\infty(1+i\epsilon)}^{0} \frac{d\eta'}{\eta'^4} \int_{-\infty(1+i\epsilon)}^{\eta'} \frac{d\eta}{\eta^4} \times \\
&\qquad \times F_1 F_2 \left[G_l(\eta, \eta'; s) \prod_{a=1}^{n} G_l(\eta, \eta_a; k_a) \prod_{b=n+1}^{n+m} G_l(\eta', \eta_b; k_b) \right] , \\
&= - \int_{-\infty(1+i\epsilon)}^{0} \frac{d\eta}{\eta^4} \int_{\eta}^{\infty(1-i\epsilon)} \frac{d\eta'}{\eta'^4} \times \\
&\qquad \times F_1 F_2 \left[G_l(\eta', \eta; s) \prod_{a=1}^{n} G_l(\eta, \eta_a; k_a) \prod_{b=n+1}^{n+m} G_l(\eta', \eta_b; k_b) \right] , \\
&\quad - \int_{-\infty(1+i\epsilon)}^{0} \frac{d\eta'}{\eta'^4} \int_{\eta'}^{\infty(1-i\epsilon)} \frac{d\eta}{\eta^4} \times \\
&\qquad \times F_1 F_2 \left[G_l(\eta, \eta'; s) \prod_{a=1}^{n} G_l(\eta, \eta_a; k_a) \prod_{b=n+1}^{n+m} G_l(\eta', \eta_b; k_b) \right] .
\end{aligned}$$

Now we can also expand $B^{ll}_{\text{in-out}}$ and subtract $B^{ll}_{\text{in-in}}$ from it, to see that they combine

in a similar way as in the contact diagram case

$$B^{ll}_{\text{in-out}} - B^{ll}_{\text{in-in}} = \int_{-\infty(1+i\epsilon)}^{\infty(1-i\epsilon)} \frac{d\eta}{\eta^4} \int_{\eta}^{\infty(1-i\epsilon)} \frac{d\eta'}{\eta'^4} \times \tag{A.4}$$
$$\times F_1 F_2 \left[G_l(\eta,\eta';s) \prod_{a=1}^{n} G_l(\eta,\eta_a;k_a) \prod_{b=n+1}^{n+m} G_l(\eta',\eta_b;k_b) \right] ,$$
$$+ \int_{-\infty(1+i\epsilon)}^{\infty(1-i\epsilon)} \frac{d\eta'}{\eta'^4} \int_{\eta'}^{\infty(1-i\epsilon)} \frac{d\eta}{\eta^4} \times$$
$$\times F_1 F_2 \left[G_l(\eta,\eta';s) \prod_{a=1}^{n} G_l(\eta,\eta_a;k_a) \prod_{b=n+1}^{n+m} G_l(\eta',\eta_b;k_b) \right] .$$

In the following, we will show that these terms vanish separately, and the derivation is the same for both terms. For concreteness, we focus on the second term. Furthermore, let us for now restrict F_1 and F_2 only to contain spatial derivatives. This simply leads to an overall factor, which we can drop. Furthermore, since we assume the integral is IR-finite, we simply need to show that the class of integrals

$$\Delta B := \int_{-\infty(1+i\epsilon)}^{\infty(1-i\epsilon)} d\eta' \int_{\eta'}^{\infty(1-i\epsilon)} d\eta\, \eta^{p_1} \eta'^{p_2} f_s(\eta) f_s(\eta')^* \prod_{a=1}^{n} f_{k_a}(\eta) \prod_{b=n+1}^{n+m} f_{k_b}(\eta'), \tag{A.5}$$

with $p_1, p_2 \geq 0$, vanishes, where we dropped the overall factor of the external mode functions.

Let us first focus on the inner integral over η. We note that η' always has a small negative imaginary part, and therefore this integral is always in the lower half complex plane where $f_k(\eta)$ is analytic, and convergent at infinity. This means we can draw a contour along the $\eta' = const$ axis, up to $-i\infty$, and close the contour at infinity, to get a different representation of this integral. We show the contour in Fig. A.1. The contribution at infinity is zero, given the exponential convergence of $H^{(1)}_\nu$ in the lower half complex plane, and the inner integral can be written as

$$\int_{\eta'-i\infty}^{\eta'} d\eta \eta^{p_1} f_s(\eta) \prod_{a=1}^{n} f_{k_a}(\eta) = i \int_0^{\infty} d\eta (\eta' - i\eta)^{p_1} f_s(\eta' - i\eta) \prod_{a=1}^{n} f_{k_a}(\eta' - i\eta) ,$$

where we substituted $\eta \to \eta' - i\eta$.

Now let us get back to the main integral, where we can now change the order of integration. Furthermore, expanding out the factor $(\eta' - i\eta)^{p_1}$, the integral again

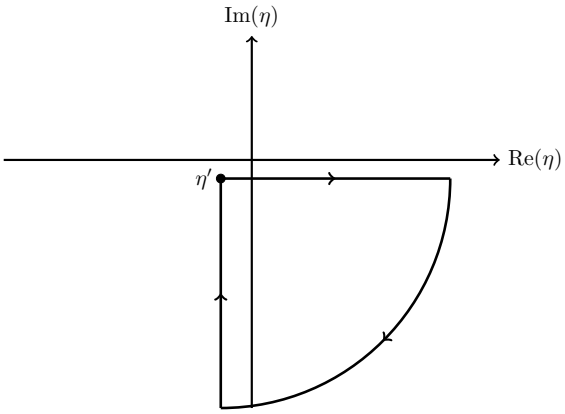

Figure A.1: Choice of contour in the η plane

falls into the classes of integrals

$$\Delta B = -i \int_0^\infty d\eta \int_{-\infty(1+i\epsilon)}^{\infty(1-i\epsilon)} d\eta' \eta^{p_3} \eta'^{p_4} f_s(\eta' - i\eta) f_s(\eta')^* \prod_{a=1}^{n} f_{k_a}(\eta' - i\eta) \prod_{b=n+1}^{n+m} f_{k_b}(\eta') \,. \tag{A.6}$$

for some $p_3, p_4 \geq 0$. Now note that since $\eta > 0$ and since η' has a small negative imaginary part, the mode functions are always evaluated in the lower half complex plane. Therefore, the integrand in η' is analytical over the whole region of integration. We, therefore, simply need to show that on the arc at negative infinity in the lower half complex plane, the integral vanishes.

Let us label $\sum_{a=1}^{n+m} k_a = k_T$, then in the limit $\eta' \to -i\infty$ we have

$$\eta^{p_3} \eta'^{p_4} f_s(\eta' - i\eta) f_s(\eta')^* \prod_{a=1}^{n} f_{k_a}(\eta' - i\eta) \prod_{b=n+1}^{n+m} f_{k_b}(\eta') \to \eta'^{p_3+1} \eta^{p_4+1} e^{-ik_T\eta'} e^{-(k_T+s)\eta}, \tag{A.7}$$

where we see that the integral over η' goes to zero, and that the integral over η is finite. Therefore we conclude that the integral Eq. (A.6) vanishes. Finally, we note a couple of generalisations. The derivation for the term that comes from the Feynman propagator with $\eta \leftrightarrow \eta'$, is the same, simply with the consistent exchange $\eta \leftrightarrow \eta'$. Furthermore, in the presence of temporal derivatives, the derivation follows analogously, since time derivatives of the Hankel functions is a sum of Hankel functions with shifted mass. Therefore, since the formulas above only depend on the asymptotic behaviour and the analyticity of the mode functions, the resulting

integrals fall under the same class of integrals as in Eq. (A.5), which vanishes.

A.2 Diagrammatic Cutting Rules for Three Vertices

In this appendix, we give details for the derivation of propagator identities for three-vertex diagrams. We do not show how to use hermitian analyticity to turn these relations into cutting rules for correlators with flipped energies. While our rules generalize to any number of external legs and loops, we focus on diagrams at tree level where all the external lines attached to a single vertex have been combined into a single one (this can always be done in Minkowksi and for conformally coupled scalars in de Sitter).

For three vertices we get multiple propagator identities, depending on the choice of operators. For the cases we study here, we always take two of the three external vertices to form *together* one of the operators in the largest time equation. Then we consider a double exchange tree-level diagram with the following contractions: where $n_1+n_2+n_3 = n$. Then we also consider a one-loop diagram with three vertices

$$\begin{array}{ccccccc} \mathcal{O}_1 = \phi(t_0)^{n_1} & & & \mathcal{O}_2 = \phi(t_0)^{n_2} & & & \mathcal{O}_3 = \phi(t_0)^{n_3} \\ \updownarrow & & & \updownarrow & & & \updownarrow \\ \mathcal{O}_4 = H^{(1)}_{\rm int}(t) & \leftrightarrow & & \mathcal{O}_5 = H^{(2)}_{\rm int}(t') & \leftrightarrow & & \mathcal{O}_6 = H^{(3)}_{\rm int}(t'') \end{array}$$

and the same contractions of operators as above with the addition of a contraction connecting $\mathcal{O}_4$ and $\mathcal{O}_6$ to make a loop. The presence of a loop will make a difference in the end result. Let us now proceed to derive the cutting rules simultaneously for both cases.

As mentioned above, we get several different rules, depending on our choice of operators. We start by combining the left two vertices and take $\mathcal{O}_1 = \phi(t_0)^{n_1+n_2}$ and the rest remains as is. To not have to go over the same parity argument as in

the one and two vertex case again, we directly only write half the terms. We have

$$\begin{aligned} 0 \;\sim\; & \langle T[\phi(t_0)^n H^{(1)}_{\rm int}(t) H^{(2)}_{\rm int}(t') H^{(3)}_{\rm int}(t'')]\rangle \\ - \; & \langle \phi(t_0)^{n_1+n_2} T[\phi(t_0)^{n_3} H^{(1)}_{\rm int}(t) H^{(2)}_{\rm int}(t') H^{(3)}_{\rm int}(t'')]\rangle \\ + \; & \langle \bar{T}[\phi(t_0)^{n_1+n_2} H^{(1)}_{\rm int}(t)] T[\phi(t_0)^{n_3} H^{(2)}_{\rm int}(t') H^{(3)}_{\rm int}(t'')]\rangle \\ + \; & \langle \bar{T}[\phi(t_0)^{n_1+n_2} H^{(1)}_{\rm int}(t) H^{(2)}_{\rm int}(t') H^{(3)}_{\rm int}(t'')] \phi(t_0)^{n_3}\rangle \\ - \; & \langle \bar{T}[\phi(t_0)^{n_1+n_2} H^{(1)}_{\rm int}(t) H^{(2)}_{\rm int}(t')] T[\phi(t_0)^{n_3} H^{(3)}_{\rm int}(t'')]\rangle \\ + \; & \langle \bar{T}[\phi(t_0)^{n_1+n_2} H^{(2)}_{\rm int}(t')] T[\phi(t_0)^{n_3} H^{(1)}_{\rm int}(t) H^{(3)}_{\rm int}(t'')], \rangle \end{aligned} \tag{A.8}$$

Again the ~ 0 indicates that the identity is valid only after integrating over the time insertion of the Hamiltonian interactions. Note that for the double exchange the last term is zero, because $H^{(1)}_{\rm int}$ does not have a time ordering relative to t_0. Finally Eq. (A.8) results in the following rules in terms of diagrams

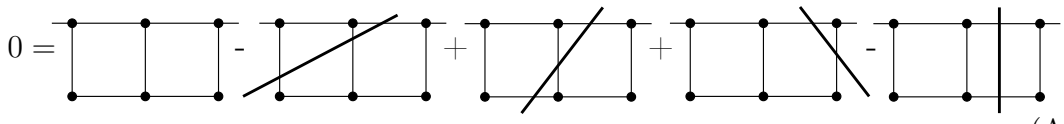

(A.9)

and for the box-Loop

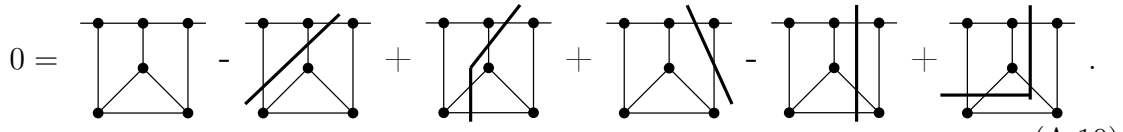

(A.10)

On a diagrammatic level, if we change $n_1 \leftrightarrow n_3$ we simply get the same cutting rules, just mirrored along the middle axis. There are separate double-cutting rules if we consider the change $n_2 \leftrightarrow n_3$, which can be derived as well, but we omit writing them here explicitly.

A.3 Relating Cut Diagrams to Diagrams with Flipped Energies

In this appendix, we derive the relation of a cut diagram to a correlator with shifted kinematics. These are Eqs. (5.132), (5.133) and (5.134). We largely focus on conformally coupled and massless fields in de Sitter and in the end we comment on

general masses in flat space. Notice that the derivations are largely the same. To streamline our notation we set the coupling constant λ and H to one since they can be easily reinstated.

Conformally Coupled and Massless Scalars in dS The key ingredient to this derivation is that the mode functions enjoy the nice property

$$f_k(\eta) = f_k(-\eta)^*, \tag{A.11}$$

which in particular also translates to all time derivatives

$$a(\eta)^n \partial_\eta^n f_k(\eta) = (a(-\eta)^n \partial_{-\eta}^n f_k(-\eta))^*. \tag{A.12}$$

Because time derivatives enjoy the same property as the mode function, henceforth we focus on interactions without time derivatives. As in the main text, we assume that all interactions are IR-finite. Using Eq. (A.11) we find that the propagators obey

$$G^+(-\eta, -\eta', k) = G^+(\eta, \eta', k)^*, \quad \text{and} \quad G_F(-\eta, -\eta', k) = G_F(\eta, \eta', k). \tag{A.13}$$

Finally, we note that our cutting rules are valid to leading order in $\eta_0 \to 0$, where η_0 is the time when operators are inserted. The order in η_0 in which we are interested is even for diagrams that are even under spatial parity, and odd for odd diagrams.

Let us start with deriving the result in Eq. (5.132). We consider a general scale invariant Hamiltonian interaction of the form [1]

$$H_{\rm int} = \int_{\mathbf{x}} \frac{1}{(n+2L)!} F(\partial_i) \eta^{n_d} \phi^{n+2L}, \tag{A.14}$$

where n_d is the number of spatial derivatives. In the following, we shorten the notation for $F(\partial_i)$, simply to F, since in Fourier space it is just a multiplicative factor. Now let us write out the cut diagram from Eq. (5.132), where we leave the integrals over the loop momenta implicit:

$$\int_{-\infty}^{\infty} \frac{d\eta}{\eta^4} F \eta^{n_d} \left(\prod_{i=1}^{m} G^+(\eta_0, \eta, k_i) \right) \left(\prod_{i=m+1}^{n} G_F(\eta_0, \eta, k_i) \right) \left(\prod_{i=1}^{L} G_F(\eta, \eta, y_i) \right). \tag{A.15}$$

[1] In order for the interaction Hamiltonian to be IR-finite, we eventually need additional factors of η^{2n}, coming from time derivatives. Crucially, however, this factor is invariant under $\eta \to -\eta$.

Next, we transform $\eta \to -\eta$. For brevity of notation, we will not write out the loop propagators because, being invariant under time reversal, they are just spectators in the derivation. We have

$$\begin{aligned}
&\int_{-\infty}^{\infty} \frac{d\eta}{\eta^4} F \eta^{n_d} (-1)^{n_d} \left(\prod_{i=1}^{m} G^+(\eta_0, -\eta, k_i) \right) \left(\prod_{i=m+1}^{n} G_F(\eta_0, -\eta, k_i) \right) \qquad \text{(A.16)} \\
&= \int_{-\infty}^{\infty} \frac{d\eta}{\eta^4} F \eta^{n_d} (-1)^{n_d} \left(\prod_{i=1}^{m} G^+(-\eta_0, \eta, k_i)^* \right) \left(\prod_{i=m+1}^{n} G_F(-\eta_0, \eta, k_i) \right) \\
&= \int_{-\infty}^{\infty} \frac{d\eta}{\eta^4} F \eta^{n_d} \left(\prod_{i=1}^{m} G^+(\eta_0, \eta, k_i)^* \right) \left(\prod_{i=m+1}^{n} G_F(\eta_0, \eta, k_i) \right),
\end{aligned}$$

where from the first to the second line we used the propagator identities under time reversal, and from the second to the last line we used that at the order in η_0 we are interested in, the correlator is even (odd) in η_0 exactly when we have an even (odd) number of spatial derivatives. We have therefore shown that to leading order we can use G^+ or $(G^+)^*$ for the cut legs interchangeably. If we now average these two contributions, we can write the cut diagram as

$$\begin{aligned}
&\frac{1}{2} \int_{-\infty}^{\infty} \frac{d\eta}{\eta^4} F \eta^{n_d} \left(\prod_{i=1}^{m} G^+(\eta_0, \eta, k_i) + \prod_{i=1}^{m} G^+(\eta_0, \eta, k_i)^* \right) \prod_{i=m+1}^{n} G_F(\eta_0, \eta, k_i) \qquad \text{(A.17)} \\
&= \frac{1}{2} \int_{-\infty}^{\infty} \frac{d\eta}{\eta^4} F \eta^{n_d} \left(\prod_{i=1}^{m} G_F(\eta_0, \eta, k_i) + \prod_{i=1}^{m} G_F(\eta_0, \eta, k_i)^* \right) \prod_{i=m+1}^{n} G_F(\eta_0, \eta, k_i) \\
&= \frac{1}{2} \int_{-\infty}^{\infty} \frac{d\eta}{\eta^4} F \eta^{n_d} \Bigg(\prod_{i=1}^{m} G_F(\eta_0, \eta, k_i) + \\
&\qquad\qquad + (-1)^m \prod_{i=1}^{m} G_F(\eta_0, \eta, -k_i) \Bigg) \prod_{i=m+1}^{n} G_F(\eta_0, \eta, k_i) \\
&= \frac{1}{2} \left[B_n^c(\{k_i\}_{i=1}^n) + (-1)^m B_n^c(\{-k_i\}_{i=1}^m, \{k_i\}_{i=m+1}^n) \right],
\end{aligned}$$

where from the first to the second line we used the propagator identity that $G^+ + (G^+)^* = G_F + G_F^*$, which generalises to products, and from the third to the fourth line we used the Hermitian analyticity property. This concludes the derivation for the contact diagram case Eq. (5.126). Next, we can do a very similar derivation for the exchange diagram.

Again, we do not explicitly write out any temporal derivatives, since any time

derivative will not alter the time-reversal properties of the mode functions. We therefore consider the two Hamiltonian interactions

$$H_{\rm int} = \int_{\mathbf{x}} \frac{1}{(m+L+1)!} F_1(\partial_i)\eta^{n_{d_1}}\phi^{m+L+1} + \frac{1}{(n-m+L+1)!} F_2(\partial_i)\eta^{n_{d_2}}\phi^{n-m+L+1}. \tag{A.18}$$

The spatial derivatives again only act as an external factor and we can omit writing them out explicitly. Next, we want to write the cut exchange diagram in Eq. (5.127) in terms of propagators. Similarly to the contact case, we leave the loop integrals implicit, the cut diagram reads

$$\int_{-\infty}^{\infty} \frac{d\eta}{\eta^4}\frac{d\eta'}{\eta'^4} F_1F_2\eta^{n_{d_1}}\eta'^{n_{d_2}} \prod_{i=1}^{m} G^+(\eta_0,\eta,k_i) \prod_{i=m+1}^{n} G_F(\eta_0,\eta',k_i) \prod_{i=1}^{L+1} G_F(\eta,\eta',y_i).$$

Now let us flip both η and η' and directly apply the propagator identities,

$$\begin{aligned}\int_{-\infty}^{\infty} \frac{d\eta}{\eta^4}\frac{d\eta'}{\eta'^4} F_1F_2(-1)^{n_{d_1}+n_{d_2}}\eta^{n_{d_1}}\eta'^{n_{d_2}} \prod_{i=1}^{m} G^+(-\eta_0,\eta,k_i)^* \times \\ \times \prod_{i=m+1}^{n} G_F(-\eta_0,\eta',k_i) \prod_{i=1}^{L+1} G_F(\eta,\eta',y_i) \\ = \int_{-\infty}^{\infty} \frac{d\eta}{\eta^4}\frac{d\eta'}{\eta'^4} F_1F_2\eta^{n_{d_1}}\eta'^{n_{d_2}} \prod_{i=1}^{m} G^+(\eta_0,\eta,k_i)^* \prod_{i=m+1}^{n} G_F(\eta_0,\eta',k_i) \prod_{i=1}^{L+1} G_F(\eta,\eta',y_i),\end{aligned} \tag{A.19}$$

where again we used that the exchange diagram at leading order in η_0 is even (odd) if the total number of derivatives is even (odd). Therefore using the same procedure of averaging the G^+ and $(G^+)^*$ terms, using propagator identities and Hermitian

analyticity we get

$$
\begin{aligned}
&= \int_{-\infty}^{\infty} \frac{d\eta}{\eta^4}\frac{d\eta'}{\eta'^4} F_1 F_2 \eta^{n_{d_1}} \eta'^{n_{d_2}} \left(\prod_{i=1}^{m} G^+(\eta_0,\eta,k_i) + \prod_{i=1}^{m} G^+(\eta_0,\eta,k_i)^* \right) \times \qquad \text{(A.20)} \\
&\qquad\qquad \times \prod_{i=m+1}^{n} G_F(\eta_0,\eta',k_i) \prod_{i=1}^{L+1} G_F(\eta,\eta',y_i) \\
&= \int_{-\infty}^{\infty} \frac{d\eta}{\eta^4}\frac{d\eta'}{\eta'^4} F_1 F_2 \eta^{n_{d_1}} \eta'^{n_{d_2}} \left(\prod_{i=1}^{m} G_F(\eta_0,\eta,k_i) + \prod_{i=1}^{m} G_F(\eta_0,\eta,k_i)^* \right) \times \\
&\qquad\qquad \times \prod_{i=m+1}^{n} G_F(\eta_0,\eta',k_i) \prod_{i=1}^{L+1} G_F(\eta,\eta',y_i) \\
&= \int_{-\infty}^{\infty} \frac{d\eta}{\eta^4}\frac{d\eta'}{\eta'^4} F_1 F_2 \eta^{n_{d_1}} \eta'^{n_{d_2}} \left(\prod_{i=1}^{m} G_F(\eta_0,\eta,k_i) + (-1)^m \prod_{i=1}^{m} G_F(\eta_0,\eta,-k_i) \right) \times \\
&\qquad\qquad \times \prod_{i=m+1}^{n} G_F(\eta_0,\eta',k_i) \prod_{i=1}^{L+1} G_F(\eta,\eta',y_i) \\
&= \frac{1}{2}\left[B_n^{ex}(\{k_i\}_{i=1}^n) + (-1)^m B_n^{ex}(\{-k_i\}_{i=1}^m, \{k_i\}_{i=m+1}^n) \right],
\end{aligned}
$$

where these last steps work in the same way as for the contact diagram.

Finally let us come to the last remaining identity, namely the internal cut, Eq. (5.134). We again consider the interactions in Eq. (A.18). We note here that even if we have an interaction that involved different fields, the only propagator identity we will need is that for the mode functions f^i and f^j associated with the fields σ_i and σ_j we can write

$$
G^+_{i,j}(\eta,\eta',y) = \frac{f^i_y(\eta) f_y(\eta_0)^* f_y(\eta_0) f^j_y(\eta')^*}{f_y(\eta_0)^* f_y(\eta_0)} = \frac{G^+_i(\eta_0,\eta,y)^* G^+_j(\eta_0,\eta',y)}{P(y,\eta_0)}, \qquad \text{(A.21)}
$$

where $P(y,\eta_0)$ is the power spectrum of ϕ, and

$$
G^+_{i,j}(\eta,\eta',y) = \langle \sigma_i(\eta)\sigma_j(\eta') \rangle , \qquad G^+_i(\eta,\eta',y) = \langle \sigma_i(\eta)\phi(\eta') \rangle . \qquad \text{(A.22)}
$$

Let us return to the case where $\sigma_i = \phi$, since the derivation is the same. The diagram with L cut loops reads

$$
\int_{-\infty}^{\infty} \frac{d\eta}{\eta^4}\frac{d\eta'}{\eta'^4} F_1 F_2 \eta^{n_{d_1}} \eta'^{n_{d_2}} \prod_{i=1}^{m} G_F(\eta_0,\eta,k_i)^* \prod_{i=m+1}^{n} G_F(\eta_0,\eta',k_i) \prod_{i=1}^{L+1} G^+(\eta,\eta',y_i). \qquad \text{(A.23)}
$$

Now using Eq. (A.21) and putting it back into the cut diagram, we see that the integral over η and η' are now independent. Omitting an overall factor of $\left[\prod_i^{L+1} P(y_i)\right]$ we get

$$\begin{aligned}
&\int_{-\infty}^{\infty} \frac{d\eta}{\eta^4} F_1 \eta^{n_{d_1}} \prod_{i=1}^{m} G_F(\eta_0, \eta, k_i)^* \prod_{i=1}^{L+1} G^+(\eta_0, \eta, y)^* \times \qquad \text{(A.24)}\\
&\quad \times \int_{-\infty}^{\infty} \frac{d\eta'}{\eta'^4} F_2 \eta'^{n_{d_2}} \prod_{i=m+1}^{n} G_F(\eta_0, \eta', k_i) \prod_{i=1}^{L+1} G^+(\eta_0, \eta', y)\\
&\quad = (-1)^{m+L+1} \int_{-\infty}^{\infty} \frac{d\eta}{\eta^4} F_1 \eta^{n_{d_1}} \prod_{i=1}^{m} G_F(\eta_0, \eta, -k_i) \prod_{i=1}^{L+1} G^+(\eta_0, \eta, -y_i) \times\\
&\qquad \times \int_{-\infty}^{\infty} \frac{d\eta'}{\eta'^4} F_2 \eta'^{n_{d_2}} \prod_{i=m+1}^{n} G_F(\eta_0, \eta', k_i) \prod_{i=1}^{L+1} G^+(\eta_0, \eta', y_i)\\
&= -\frac{1}{2}\left[B^c_{m+L+1}(\{k_i\}_{i=1}^m, \{y_i\}_{i=1}^{L+1}) + (-1)^{L+1} B^c_{m+L+1}(\{k_i\}_{i=1}^m, \{-y_i\}_{i=1}^{L+1})\right] \times\\
&\times \frac{1}{2}\left[B^c_{n-m+L+1}(\{k_i\}_{i=m+1}^{n+m}, \{y_i\}_{i=1}^{L+1}) + (-1)^{L+1} B^c_{n-m+L+1}(\{k_i\}_{i=m+1}^n, \{-y_i\}_{i=1}^{L+1})\right],
\end{aligned}$$

where we have used Eq. (5.136) to flip signs in the contact diagram. Finally, if we define

$$\begin{aligned}
&B^{\rm c,cut}_{n,L}(\{E_i\}_{i=1}^n, \{y_i\}_{i=1}^L) = \qquad \text{(A.25)}\\
&\quad = \frac{1}{2}\left[B^{\rm c}_{n+L}(\{E_i\}_{i=1}^n, \{y_i\}_{i=1}^L) + (-1)^L B^{\rm c}_{n+L}(\{E_i\}_{i=1}^n, \{-y_i\}_{i=1}^L))\right],
\end{aligned}$$

and reintroduce the power spectrum factors, we can write Eq. (5.134) as

$$-\frac{B^{\rm c,cut}_{m,L+1}(\{E_i\}_{i=1}^m, \{y_i\}_{i=1}^{L+1}) B^{\rm c,cut}_{n-m,L+1}(\{E_i\}_{i=m+1}^n, \{y_i\}_{i=1}^{L+1})}{\prod_{i=1}^{L+1} P(y_i)}, \qquad \text{(A.26)}$$

Here $B^{\rm c,cut}_{m,L+1}$ refers of to one interaction Hamiltonian and $B^{\rm c,cut}_{n-m,L+1}$ to the other.

Minkowski The proof for the same relations in flat space is roughly the same. We notice that the mode functions for any mass in flat space enjoy the same identity as in the dS case, namely

$$f_E(t) = \frac{e^{-iEt}}{\sqrt{2E}} \quad \Rightarrow \quad f_E(t) = f_E(-t)^* \,. \qquad \text{(A.27)}$$

This means, that if we do not consider temporal derivatives the proofs from above follow through immediately after we set $t_0 = 0$ without loss of generality.

Finally, when considering time derivatives in Minkowski, the rules derived above also hold. While derivatives of the mode functions do not satisfy Eq. (A.27) any longer, pairs of derivatives do. Since in flat space, diagrams with an odd number of time derivatives vanish, the results are true for any Hamiltonian.

B

Appendix: The One-Loop Bispectrum - Theory

B.1 Details for Dark Matter

B.1.1 EdS Green's Function

In this section we give some details about the growing-mode EdS Green's function for the overdensity. The equation of motion for δ can be written as

$$a^2\delta''(\vec{k},a) + \left(2 + \frac{a\mathcal{H}'}{\mathcal{H}}\right) a\delta'(\vec{k},a) - \frac{3}{2}\Omega_{\rm m}(a)\delta(\vec{k},a) = S_\delta(\vec{k},a) \ , \tag{B.1}$$

where $S_\delta(\vec{k},a)$ is the non-linear source term. For the n-th order perturbation, we take $\delta^{(n)}(\vec{k},a) = D(a)^n\tilde{\delta}^{(n)}(\vec{k})$, where $D(a)$ is the linear growth factor, which solves Eq. (6.23). Plugging this $\delta^{(n)}(\vec{k},a)$ into Eq. (B.1) and using Eq. (6.23) to replace $D''(a)$, we obtain

$$\frac{1}{2}(n-1)D(a)^n\left(3\Omega_{\rm m}(a) + 2n\frac{a^2D'(a)^2}{D(a)^2}\right)\tilde{\delta}^{(n)}(\vec{k}) = S_\delta^{(n)}(\vec{k},a) \ . \tag{B.2}$$

Now we use that in SPT we have two different time dependences for the source terms, which we write as $\tilde{S}^{(n)}_{\delta,1}(\vec{k})$ and $\tilde{S}^{(n)}_{\delta,2}(\vec{k})$, giving

$$S_\delta^{(n)}(\vec{k},a) = D(a)^n\left(\Omega_{\rm m}(a)\tilde{S}^{(n)}_{\delta,1}(\vec{k}) + \left(\frac{aD'(a)}{D(a)}\right)^2\tilde{S}^{(n)}_{\delta,2}(\vec{k})\right) \ , \tag{B.3}$$

which can be seen from Eq. (6.20). We see that all terms in Eqs. (B.2) and (B.3) have the same time dependence, proportional to $D^n\Omega_{\rm m}$, if we assume the standard

EdS condition Eq. (6.28), after which we obtain

$$\tilde{\delta}^{(n)}(\vec{k}) = \frac{2}{(n-1)(3+2n)} \left(S^{(n)}_{\delta,1}(\vec{k}) + S^{(n)}_{\delta,2}(\vec{k}) \right) \ . \tag{B.4}$$

The numerical factor $2/(n-1)(3+2n)$ comes from the EdS approximation of the Green's function.

We can see how this relates to the actual Green's function of the linear equations in the EdS universe, where $\Omega_{\rm m} = 1$ and $a\mathcal{H}'/\mathcal{H} = -1/2$. In that case, the linear equation of motion is

$$a^2\delta'' + \frac{3}{2}a\delta' - \frac{3}{2}\delta = 0 \ , \tag{B.5}$$

which has two solutions, $\delta(a) = a$ and $\delta(a) = a^{-3/2}$. These can be combined to form the Green's function $G(a, a_1)$ satisfying the boundary conditions $G(a_1, a_1) = 0$ and $\partial_a G(a, a_1)|_{a=a_1} = a_1^{-2}$

$$G(a, a_1) = \frac{2}{5\, a_1} \left(\frac{a}{a_1} - \frac{a^{-3/2}}{a_1^{-3/2}} \right) \theta_H(a - a_1) \ , \tag{B.6}$$

where θ_H is the Heaviside step function. The connection with Eq. (B.4) is that applying the above to a source term $\propto a^n$, we have

$$\int_0^a da_1 G(a, a_1)\, a_1^n = \frac{2\, a^n}{(n-1)(3+2n)} \ , \tag{B.7}$$

which gives exactly the same factor that we found.

B.1.2 Counterterm Expressions in Real Space

The response terms are proportional only to powers of the linear field, and specifically we can write

$$\tilde{\delta}^{(1)}_{ct}(\vec{k}) = F_1^{ct}(\vec{k})\tilde{\delta}^{(1)}_{\vec{k}} \ , \quad \text{and} \quad \tilde{\delta}^{(2)}_{ct}(\vec{k}) = \int^{\vec{k}}_{\vec{q}_1,\vec{q}_2} F_2^{ct}(\vec{q}_1, \vec{q}_2)\tilde{\delta}^{(1)}_{\vec{q}_1}\tilde{\delta}^{(1)}_{\vec{q}_2} \ , \tag{B.8}$$

where definitions of the tilde fields are given in Eq. (6.43). We group all of the terms that are only proportional to the stochastic fields in $\delta^{(1)}_\epsilon(\vec{k}, a)$ and terms that contain one stochastic field and one long-wavelength field (semi-stochastic) in $\delta^{(2)}_\epsilon(\vec{k}, a)$.

The response counterterms enter in

$$\begin{aligned}
&P_{13}^{ct}(k) \equiv 2F_1^{ct}(\vec{k})P_{11}(k) \ , \\
&B_{411}^{ct}(k_1,k_2,k_3) \equiv 2P_{11}(k_1)P_{11}(k_2)F_2^{ct}(-\vec{k}_1,-\vec{k}_2) + \text{ 2 perms.} \ , \\
&B_{321}^{(II),ct}(k_1,k_2,k_3) \equiv 2P_{11}(k_1)P_{11}(k_2)F_1^{ct}(\vec{k}_1)F_2(-\vec{k}_1,-\vec{k}_2) + \text{ 5 perms.} \ ,
\end{aligned} \tag{B.9}$$

so that the combinations

$$\begin{aligned}
&P_{13}(k) + P_{13}^{ct}(k) \ , \\
&B_{411}(k_1,k_2,k_3) + B_{411}^{ct}(k_1,k_2,k_3) \ , \\
&B_{321}^{(II)}(k_1,k_2,k_3) + B_{321}^{(II),ct}(k_1,k_2,k_3) \ ,
\end{aligned} \tag{B.10}$$

are renormalized. Furthermore, for the stochastic fields, we define

$$\begin{aligned}
&\langle\tilde{\delta}_\epsilon^{(1)}(\vec{k})\tilde{\delta}_\epsilon^{(1)}(\vec{k}')\rangle \equiv (2\pi)^3\delta_D(\vec{k}+\vec{k}')P_{22}^\epsilon(k) \ , \\
&\langle\tilde{\delta}_\epsilon^{(1)}(\vec{k}_1)\tilde{\delta}_\epsilon^{(1)}(\vec{k}_2)\tilde{\delta}_\epsilon^{(1)}(\vec{k}_3)\rangle \equiv (2\pi)^3\delta_D(\vec{k}_1+\vec{k}_2+\vec{k}_3)B_{222}^\epsilon(k_1,k_2,k_3) \ , \\
&\langle\tilde{\delta}^{(1)}(\vec{k}_1)\tilde{\delta}_\epsilon^{(1)}(\vec{k}_2)\tilde{\delta}_\epsilon^{(2)}(\vec{k}_3)\rangle + 5 \text{ perms.} \equiv (2\pi)^3\delta_D(\vec{k}_1+\vec{k}_2+\vec{k}_3)B_{321}^{(I),\epsilon}(k_1,k_2,k_3) \ ,
\end{aligned} \tag{B.11}$$

so that the combinations

$$\begin{aligned}
&P_{22}(k) + P_{22}^\epsilon(k) \ , \\
&B_{222}(k_1,k_2,k_3) + B_{222}^\epsilon(k_1,k_2,k_3) \ , \\
&B_{321}^{(I)}(k_1,k_2,k_3) + B_{321}^{(I),\epsilon}(k_1,k_2,k_3) \ ,
\end{aligned} \tag{B.12}$$

are renormalized.

B.1.3 Response Terms

Here we show some details for the results given in Sec. 6.4.1 for the response terms. First we write the response stress tensor τ_{ct}^{ij} as a sum of first- and second-order terms

$$\tau_{ct}^{ij}(a) = \Omega_{\rm m}(a)\left(\hat{\tau}_{ct,(1)}^{ij}(a) + \hat{\tau}_{ct,(2)}^{ij}(a)\right) \ , \tag{B.13}$$

where, in order to cancel the UV terms coming from the SPT loop expansion, the time dependence must be

$$\hat{\tau}^{ij}_{ct,(1)}(a) = \frac{a^2 H(a)^2 \bar{\rho}(a) D(a)^3}{{k_{\rm NL}}^2} \tilde{\tau}^{ij}_{ct,(1)} \ , \quad \text{and} \quad \hat{\tau}^{ij}_{ct,(2)}(a) = \frac{a^2 H(a)^2 \bar{\rho}(a) D(a)^4}{{k_{\rm NL}}^2} \tilde{\tau}^{ij}_{ct,(2)} \ , \tag{B.14}$$

where $\tilde{\tau}^{ij}_{ct,(1)}$ and $\tilde{\tau}^{ij}_{ct,(2)}$ are time independent (the factor of $\Omega_{\rm m}(a)$ can be seen from App. B.1.1). We suppress spatial dependence of all fields in this section to remove clutter.

Being careful to keep track of the time dependence $D(a)^n$ and the EdS Green's functions (which are simply numerical factors coming from the linear equations and the time dependence $D(a)^n$, see App. B.1.1), we have

$$\begin{aligned} \delta^{(1)}_{ct}(a) &= \frac{1}{9a^2H^2\bar{\rho}} \partial_i \partial_j \hat{\tau}^{ij}_{ct,(1)}(a) \ , \quad \pi^{(1)}_{S,ct}(a) = \frac{-f}{3aH} \partial_i \partial_j \hat{\tau}^{ij}_{ct,(1)}(a) \ , \\ \pi^i_{V,ct,(1)}(a) &= \frac{-2f}{7aH} \epsilon^{ijk} \partial_j \partial_l \hat{\tau}^{kl}_{ct,(1)}(a) \ , \quad \text{and} \quad \pi^i_{ct,(1)}(a) = -\frac{f}{3aH} \frac{\partial_i \partial_j \partial_k}{\partial^2} \hat{\tau}^{jk}_{ct,(1)}(a) \end{aligned} \tag{B.15}$$

where, as in Sec. 6.4.1, we assume that $\partial_i \partial_j \partial_k \tilde{\tau}^{jk}_{ct,(1)} = \partial^2 \partial_j \tilde{\tau}^{ij}_{ct,(1)}$. Note that in the above, and in all instances, we solve for π_S and π^i_V directly through the equations of motion Eq. (6.19), and then we form π^i using the definition Eq. (6.18). [1]

The second-order expressions are

$$\begin{aligned} \delta^{(2)}_{ct}(a) &= \frac{2}{33a^2H^2\bar{\rho}} \partial_i \partial_j \hat{\tau}^{ij}_{ct,(2)}(a) + \frac{2}{33a^2H^2\bar{\rho}f} \partial_i \partial_j \Bigg[4M_{\rm Pl}^2 a^{-2} \Bigg(\partial_i \Phi^{(1)}(a) \partial_j \Phi^{(1)}_{ct}(a) \\ &\qquad - \frac{1}{2} \delta_{ij} \left(\partial_k \Phi^{(1)}(a) \partial_k \Phi^{(1)}_{ct}(a) \right) \Bigg) + \frac{2}{\bar{\rho}} \pi^i_{(1)}(a) \pi^j_{ct,(1)}(a) \Bigg] \ , \\ \pi^{(2)}_{S,ct}(a) &= -4a\bar{\rho}Hf\delta^{(2)}_{ct}(a) \ , \\ \pi^i_{V,ct,(2)}(a) &= \frac{-2}{9aHf} \epsilon^{ijk} \partial_j \partial_l \Bigg[2M_{\rm Pl}^2 a^{-2} \left(\partial_k \Phi^{(1)}(a) \partial_l \Phi^{(1)}_{ct}(a) + \partial_k \Phi^{(1)}_{ct}(a) \partial_l \Phi^{(1)}(a) \right) \\ &\qquad + \frac{1}{\bar{\rho}} \left(\pi^k_{(1)}(a) \pi^l_{ct,(1)}(a) + \pi^k_{ct,(1)}(a) \pi^l_{(1)}(a) \right) + \tau^{kl}_{ct,(2)}(a) \Bigg] \ , \end{aligned} \tag{B.17}$$

[1] A useful manipulation to remember is that for any vector V^i satisfying $V^i = \epsilon^{ijk} \partial_j \partial_l A_{kl}$, we have

$$\epsilon^{ijk} \frac{\partial_j}{\partial^2} V^k = \frac{\partial_i \partial_j \partial_k}{\partial^2} A_{jk} - \partial_j A_{ij} \ . \tag{B.16}$$

and some extra terms that we need to plug in to the above are

$$\partial_i \Phi^{(1)}(a) = \frac{3}{2}\Omega_{\rm m} a^2 H^2 \frac{\partial_i}{\partial^2}\delta^{(1)}(a) \ , \quad \pi^i_{(1)}(a) = -aH\bar{\rho} f \frac{\partial_i}{\partial^2}\delta^{(1)}(a), \tag{B.18}$$
$$\partial_i \Phi^{(1)}_{ct}(a) = \frac{\Omega_{\rm m}}{6\bar{\rho}} \frac{\partial_i \partial_j \partial_k}{\partial^2} \hat{\tau}^{jk}_{ct,(1)}(a) \ .$$

We then factorize the time dependence by defining $\tilde{\pi}^{(1)}_{S,ct}$, $\tilde{\pi}^{(2)}_{S,ct}$, $\tilde{\pi}^i_{V,ct,(1)}$, and $\tilde{\pi}^i_{V,ct,(2)}$ in the same way as $\tilde{\pi}^i_{ct,(1)}$ and $\tilde{\pi}^i_{ct,(2)}$ in Eq. (6.45), which leads to the linear solutions

$$\tilde{\pi}^{(1)}_{S,ct} = \frac{1}{3{k_{\rm NL}}^2}\partial_i \partial_j \tilde{\tau}^{ij}_{ct,(1)} \ , \quad \text{and} \quad \tilde{\pi}^i_{V,ct,(1)} = 0 \ , \tag{B.19}$$

along with $\tilde{\delta}^{(1)}_{ct}$ and $\tilde{\pi}^i_{ct,(1)}$ given in Eq. (6.47). The second order expressions are $\tilde{\pi}^{(2)}_{S,ct} = 4\tilde{\delta}^{(2)}_{ct}$ and

$$\tilde{\pi}^i_{V,ct,(2)} = \frac{1}{9{k_{\rm NL}}^2}\epsilon^{ijk}\partial_j\partial_l \left[\frac{\partial_k \tilde{\delta}^{(1)}}{\partial^2}\frac{\partial_l\partial_m\partial_n}{\partial^2}\tilde{\tau}^{mn}_{ct,(1)} + \frac{\partial_l \tilde{\delta}^{(1)}}{\partial^2}\frac{\partial_k\partial_m\partial_n}{\partial^2}\tilde{\tau}^{mn}_{ct,(1)} + 2\tilde{\tau}^{kl}_{ct,(2)} \right] \ , \tag{B.20}$$

with $\tilde{\delta}^{(2)}_{ct}$ and $\tilde{\pi}^i_{ct,(2)}$ given in Eqs. (6.48) and (6.49) respectively.

B.1.4 Stochastic Terms

Here we show some details for the results given in Sec. 6.4.1 for the stochastic terms. First we write the stochastic stress tensor τ^{ij}_ϵ as a sum of first- and second-order terms

$$\tau^{ij}_\epsilon(a) = \Omega_{\rm m}(a)\left(\hat{\tau}^{ij}_{\epsilon,(1)}(a) + \hat{\tau}^{ij}_{\epsilon,(2)}(a)\right) \ , \tag{B.21}$$

where, in order to cancel the UV terms coming from the SPT loop expansion the time dependence must be

$$\hat{\tau}^{ij}_{\epsilon,(1)}(a) = \frac{a^2 H(a)^2 \bar{\rho}(a) D(a)^2}{{k_{\rm NL}}^2}\tilde{\tau}^{ij}_{\epsilon,(1)} \ , \quad \text{and} \quad \hat{\tau}^{ij}_{\epsilon,(2)}(a) = \frac{a^2 H(a)^2 \bar{\rho}(a) D(a)^3}{{k_{\rm NL}}^2}\tilde{\tau}^{ij}_{\epsilon,(2)} \ , \tag{B.22}$$

where $\tilde{\tau}^{ij}_{\epsilon,(1)}$ and $\tilde{\tau}^{ij}_{\epsilon,(2)}$ are time independent. We suppress spatial dependence of all fields in this section to remove clutter.

Being careful to keep track of the time dependence $D(a)^n$ and the EdS Green's functions (which are simply numerical factors coming from the linear equations and

the time dependence $D(a)^n$, see App. B.1.1), we have

$$\begin{aligned}
\delta^{(1)}_{\epsilon}(a) &= \frac{2}{7a^2H^2\bar{\rho}}\partial_i\partial_j\hat{\tau}^{ij}_{\epsilon,(1)}(a)\ , \quad \pi^{(1)}_{S,\epsilon}(a) = \frac{-4f}{7aH}\partial_i\partial_j\hat{\tau}^{ij}_{\epsilon,(1)}(a)\ , \\
\pi^{i(1)}_{V,\epsilon}(a) &= \frac{-2f}{5aH}\epsilon^{ijk}\partial_j\partial_l\hat{\tau}^{kl}_{\epsilon,(1)}(a)\ , \\
\pi^{i}_{\epsilon,(1)}(a) &= -\frac{f}{aH}\left[\frac{4}{7}\frac{\partial_i\partial_j\partial_k}{\partial^2}\hat{\tau}^{jk}_{\epsilon,(1)}(a) - \frac{2}{5}\left(\frac{\partial_i\partial_j\partial_k}{\partial^2}\hat{\tau}^{jk}_{\epsilon,(1)}(a) - \partial_j\hat{\tau}^{ij}_{\epsilon,(1)}(a)\right)\right]\ .
\end{aligned} \tag{B.23}$$

The second-order expressions are

$$\begin{aligned}
\delta^{(2)}_{\epsilon}(a) &= \frac{1}{9a^2H^2\bar{\rho}}\partial_i\partial_j\hat{\tau}^{ij}_{\epsilon,(2)}(a) + \frac{1}{9a^2H^2\bar{\rho}f}\partial_i\partial_j\Bigg[4M_{\rm Pl}^2a^{-2}\Bigg(\partial_i\Phi^{(1)}(a)\partial_j\Phi^{(1)}_{\epsilon}(a) \\
&\qquad -\frac{1}{2}\delta_{ij}\left(\partial_k\Phi^{(1)}(a)\partial_k\Phi^{(1)}_{\epsilon}(a)\right)\Bigg) + \frac{2}{\bar{\rho}}\pi^{i}_{(1)}(a)\pi^{j}_{\epsilon,(1)}(a)\Bigg]\ , \\
\pi^{(2)}_{S,\epsilon}(a) &= -3a\bar{\rho}Hf\delta^{(2)}_{\epsilon}(a)\ , \\
\pi^{i}_{V,\epsilon,(2)}(a) &= \frac{-2}{7aHf}\epsilon^{ijk}\partial_j\partial_l\Bigg[2M_{\rm Pl}^2a^{-2}\left(\partial_k\Phi^{(1)}(a)\partial_l\Phi^{(1)}_{\epsilon}(a) + \partial_k\Phi^{(1)}_{\epsilon}(a)\partial_l\Phi^{(1)}(a)\right) \\
&\qquad +\frac{1}{\bar{\rho}}\left(\pi^{k}_{(1)}(a)\pi^{l}_{\epsilon,(1)}(a) + \pi^{k}_{\epsilon,(1)}(a)\pi^{l}_{(1)}(a)\right) + \tau^{kl}_{\epsilon,(2)}(a)\Bigg]\ .
\end{aligned} \tag{B.24}$$

Some extra terms that we need to plug in to the above are given in Eq. (B.18) and

$$\partial_i\Phi^{(1)}_{\epsilon}(a) = \frac{3\Omega_{\rm m}}{7\bar{\rho}}\frac{\partial_i\partial_j\partial_k}{\partial^2}\hat{\tau}^{jk}_{\epsilon,(1)}(a)\ . \tag{B.25}$$

We then factorize the time dependence by defining $\tilde{\pi}^{(1)}_{S,\epsilon}$, $\tilde{\pi}^{(2)}_{S,\epsilon}$, $\tilde{\pi}^{i}_{V,\epsilon,(1)}$, and $\tilde{\pi}^{i}_{V,\epsilon,(2)}$ in the same way as $\tilde{\pi}^{i}_{\epsilon,(1)}$ and $\tilde{\pi}^{i}_{\epsilon,(2)}$ in Eq. (6.45), which leads to the linear solutions

$$\tilde{\pi}^{(1)}_{S,\epsilon} = \frac{4}{7{k_{\rm NL}}^2}\partial_i\partial_j\tilde{\tau}^{ij}_{(1)}\ , \quad \text{and} \quad \tilde{\pi}^{i}_{V,\epsilon,(1)} = \frac{2}{5{k_{\rm NL}}^2}\epsilon^{ijk}\partial_j\partial_l\tilde{\tau}^{kl}_{\epsilon,(1)}\ , \tag{B.26}$$

along with $\tilde{\delta}^{(1)}_{\epsilon}$ and $\tilde{\pi}^{i}_{\epsilon,(1)}$ given in Eq. (6.50). The second order are $\tilde{\pi}^{(2)}_{S,\epsilon} = 3\tilde{\delta}^{(2)}_{\epsilon}$ and

$$\begin{aligned}\tilde{\pi}^{i}_{V,\epsilon,(2)} = \frac{2}{7{k_{\rm NL}}^2}\epsilon^{ijk}\partial_j\partial_l\left[\frac{\partial_k\tilde{\delta}^{(1)}}{\partial^2}\frac{\partial_l\partial_m\partial_n}{\partial^2}\tilde{\tau}^{mn}_{\epsilon,(1)} + \frac{\partial_l\tilde{\delta}^{(1)}}{\partial^2}\frac{\partial_k\partial_m\partial_n}{\partial^2}\tilde{\tau}^{mn}_{\epsilon,(1)} + \tilde{\tau}^{kl}_{\epsilon,(2)}\right] \\ -\frac{4}{35{k_{\rm NL}}^2}\epsilon^{ijk}\partial_j\partial_l\Bigg[\frac{\partial_k\tilde{\delta}^{(1)}}{\partial^2}\left(\frac{\partial_l\partial_m\partial_n}{\partial^2}\tilde{\tau}^{mn}_{\epsilon,(1)} - \partial_m\tilde{\tau}^{lm}_{\epsilon,(1)}\right) \\ +\frac{\partial_l\tilde{\delta}^{(1)}}{\partial^2}\left(\frac{\partial_k\partial_m\partial_n}{\partial^2}\tilde{\tau}^{mn}_{\epsilon,(1)} - \partial_m\tilde{\tau}^{km}_{\epsilon,(1)}\right)\Bigg]\,,\end{aligned} \tag{B.27}$$

with $\tilde{\delta}^{(2)}_{\epsilon}$ and $\tilde{\pi}^{i}_{\epsilon,(2)}$ given in Eqs. (6.51) and (6.52) respectively.

B.1.5 Stochastic Flow Terms

Here we derive the expression given in Eq. (6.55) for the stochastic counterterms. The only subtlety is in the way that the flow term enters, and here we sharpen and clarify the expressions in [129, 131]. Let us start with two stochastic fields $e^{ij}_1(\vec{x},a)$ and $e^{ijkl}_3(\vec{x},a)$ and write the general non-local in time expression

$$\begin{aligned}\tau^{ij}_{\epsilon}(\vec{x},a) = \int^a \frac{da'}{a'}\Bigg(&\kappa_1(a,a')e^{ij}_1(\vec{x}_{\rm fl}(\vec{x},a,a'),a') \\ &+\kappa_3(a,a')e^{ijkl}_3(\vec{x}_{\rm fl}(\vec{x},a,a'),a')\frac{\partial_k\partial_l\delta(\vec{x}_{\rm fl}(\vec{x},a,a'),a')}{\partial^2}\Bigg)\,,\end{aligned} \tag{B.28}$$

for some non-local kernels κ_1 and κ_3. Next, we expand this expression up to second order to get

$$\begin{aligned}\tau^{ij}_{\epsilon}(\vec{x},a) \approx \int^a \frac{da'}{a'}\Bigg(&\kappa_1(a,a')\left[e^{ij}_{1,(1)}(\vec{x},a') + \frac{\partial_k\delta^{(1)}(\vec{x},a)}{\partial^2}\partial_k e^{ij}_{1,(1)}(\vec{x},a')\left(1-\frac{D(a')}{D(a)}\right)\right] \\ &+\kappa_1(a,a')e^{ij}_{1,(2)}(\vec{x},a') + \kappa_3(a,a')e^{ijkl}_{3,(1)}(\vec{x},a')\frac{\partial_k\partial_l\delta^{(1)}(\vec{x},a')}{\partial^2}\Bigg)\,.\end{aligned} \tag{B.29}$$

This expression for $\tau^{ij}_{\epsilon}(\vec{x},a)$ is a Galilean scalar as long as both $e^{ij}_1(\vec{x},a)$ and $e^{ijkl}_3(\vec{x},a)$ are Galilean scalars, which at the order that we work, means

$$e^{ij}_{1,(2)}(\vec{x},a') = \partial_k e^{ij}_{1,(1)}(\vec{x},a')\frac{\partial_k\delta^{(1)}(\vec{x},a')}{\partial^2} + e^{ijkl}_{2,(1)}(\vec{x},a')\frac{\partial_k\partial_l\delta^{(1)}(\vec{x},a')}{\partial^2}\,, \tag{B.30}$$

for some new field $e^{ijkl}_{2,(1)}$. The first term above is fixed by the assumption that e^{ij}_1 is a Galilean scalar, while the second term is the most general second-order term that can be included. We assume that $e^{ij}_{1,(1)}$ contains all of the purely stochastic terms, so we do not include any of those in the second-order expression. Plugging Eq. (B.30) into Eq. (B.29), we get

$$\tau^{ij}_\epsilon(\vec{x},a) \approx \int^a \frac{da'}{a'}\left(\kappa_1(a,a')\left[e^{ij}_{1,(1)}(\vec{x},a') + \frac{\partial_k\delta^{(1)}(\vec{x},a)}{\partial^2}\partial_k e^{ij}_{1,(1)}(\vec{x},a')\right]\right. \tag{B.31}$$
$$\left. + \left[\kappa_1(a,a')e^{ijkl}_{2,(1)}(\vec{x},a') + \kappa_3(a,a')e^{ijkl}_{3,(1)}(\vec{x},a')\right]\frac{\partial_k\partial_l\delta^{(1)}(\vec{x},a')}{\partial^2}\right) ,$$

where there is now crucially only one flow term, with $\partial_k\delta^{(1)}/\partial^2$ evaluated at the external time a. [2] We finally get the form Eq. (6.55) by setting

$$\epsilon^{ij}_1(\vec{x}) = \frac{{k_{\rm NL}}^2}{\Omega_{\rm m}(a)\mathcal{H}(a)^2\bar{\rho}(a)D(a)^2}\int^a \frac{da'}{a'}\kappa_1(a,a')e^{ij}_{1,(1)}(\vec{x},a') , \tag{B.32}$$

$$\epsilon^{ijkl}_3(\vec{x}) = \frac{{k_{\rm NL}}^2}{\Omega_{\rm m}(a)\mathcal{H}(a)^2\bar{\rho}(a)D(a)^2}\int^a \frac{da'}{a'}\frac{D(a')}{D(a)}\left[\kappa_1(a,a')e^{ijkl}_{2,(1)}(\vec{x},a')\right. \tag{B.33}$$
$$\left. + \kappa_3(a,a')e^{ijkl}_{3,(1)}(\vec{x},a')\right] ,$$

where above, to match Eq. (6.55), we have assumed EdS time dependence. So we see how the final ϵ^{ijkl}_3 is made up of contributions from the originally included e^{ijkl}_3 and the second order piece $e^{ijkl}_{2,(1)}$, both integrated over past times. Since they are both unknown non-linear stochastic fields, we combine them into the single field ϵ^{ijkl}_3. As always, these integrals can be formally done to define the final coefficients used in Sec. 6.4.2.

B.1.6 UV Matching in Real Space

The UV limits of the loops that are renormalized by response terms are

$$P_{13}(k) \to -\frac{61}{630\pi^2}k^2P_{11}(k)\int dq\, P_{11}(q) , \tag{B.34}$$

[2] As a piece of intuition, one could take the quadratic bias δ^2 and inspect the resulting flow terms. One sees that there is only one free coefficient for the flow terms. The second flow term that would naively come from integration over time has a fixed coefficient that cancels the IR limit of the third order expression of δ^2. This matches what we find here because one can think of a stochastic term as arising from the limit of $\delta(\vec{x})^2$ where each $\delta(\vec{x})$ is taken to be as short wavelength as possible.

$$B_{411}(k_1,k_2,k_3) \to -\frac{P_{11}(k_1)P_{11}(k_2)}{1358280\,\pi^2 k_1^2 k_2^2}\Bigg[12409k_3^6+20085k_3^4(k_1^2+k_2^2) \\ +k_3^2(-44518k_1^4+76684k_1^2k_2^2-44518k_2^4) \\ +12024(k_1^2-k_2^2)^2(k_1^2+k_2^2)\Bigg]\int dq\,P_{11}(q)+\ 2\text{ perms.}\,, \tag{B.35}$$

and

$$B_{321}^{(II)}(k_1,k_2,k_3) \to P_{11}(k_2)F_2(\vec{k}_1,\vec{k}_2)\left(\frac{-61k_1^2P_{11}(k_1)}{630\pi^2}\int dq\,P_{11}(q)\right)+\ 5\text{ perms.}\,. \tag{B.36}$$

An explicit solution for the EFT coefficients that absorbs the UV contributions above is

$$\begin{aligned} c_3 &= -\frac{61{k_{\rm NL}}^2}{140\pi^2}\int dqP_{11}(q)\,, \quad c_4 = -\frac{12409{k_{\rm NL}}^2}{11760\pi^2}\int dq\,P_{11}(q)\,, \\ c_5 &= -\frac{6997{k_{\rm NL}}^2}{6860\pi^2}\int dq\,P_{11}(q)\,, \quad c_7 = \frac{63149{k_{\rm NL}}^2}{82320\pi^2}\int dq\,P_{11}(q)\,, \end{aligned} \tag{B.37}$$

with all of the other coefficients zero (they are degenerate for these observables).

The UV limits of the loops that are renormalized by stochastic terms are

$$P_{22}(k) \to \frac{9}{196\pi^2}k^4\int dq\frac{P_{11}(q)^2}{q^2}\,, \tag{B.38}$$

$$B_{321}^{(I)}(k_1,k_2,k_3) \to \frac{P_{11}(k_1)}{35280\pi^2k_1^2}\Bigg[1060k_1^6-2337k_1^4(k_2^2+k_3^2)-217(k_2^2-k_3^2)^2(k_2^2+k_3^2) \\ +2k_1^2(747k_2^4+512k_2^2k_3^2+747k_3^4)\Bigg]\int dq\frac{P_{11}(q)^2}{q^2}+\ 2\text{ cyclic perms.}\,. \tag{B.39}$$

and

$$B_{222}(k_1,k_2,k_3) \to -\frac{15}{2401\pi^2}\Bigg[k_1^6-k_1^4(k_2^2+k_3^2)+(k_2^2-k_3^2)^2(k_2^2+k_3^2) \\ -k_1^2\left(k_2^4-\frac{k_2^2k_3^2}{30}+k_3^4\right)\Bigg]\int dq\frac{P_{11}(q)^3}{q^4}\,. \tag{B.40}$$

If we write the final forms of the stochastic counterterms as

$$P^{\epsilon}_{22}(k) = \frac{c^{\rm St}_{\rm DM,1}}{\bar{n}_{\rm DM}}\frac{k^4}{{k_{\rm NL}}^4} \ , \tag{B.41}$$

$$\begin{aligned} B^{(I),\epsilon}_{321}(k_1,k_2,k_3) = \frac{P_{11}(k_1)}{\bar{n}_{\rm DM}\,{k_{\rm NL}}^4}\Bigg[& \\ & c^{\rm St}_{\rm DM,1}\frac{-7k_1^6 - 14(k_2^2-k_3^2)^2(k_2^2+k_3^2) + k_1^2(21k_2^4 - 2k_2^2k_3^2 + 21k_3^4)}{72k_1^2} \\ & + c^{\rm St}_{\rm DM,2}(k_1-k_2-k_3)(k_1-k_2+k_3)(k_1+k_2-k_3)(k_1+k_2+k_3) + c^{\rm St}_{\rm DM,3}k_2^2k_3^2 \\ & + c^{\rm St}_{\rm DM,4}\frac{-2k_1^2(k_2^2-k_3^2)^2 + (k_1^4 + (k_2^2-k_3^2)^2)(k_2^2+k_3^2)}{k_1^2} + c^{\rm St}_{\rm DM,5}(k_1^2-k_2^2-k_3^2)^2 \\ & - c^{\rm St}_{\rm DM,6}\frac{(-k_1^2+k_2^2+k_3^2)(k_1^2-k_2^2+k_3^2)(k_1^2+k_2^2-k_3^2)}{k_1^2}\Bigg] + \ 2 \text{ cyclic perms.} \ , \end{aligned} \tag{B.42}$$

and

$$\begin{aligned} & B^{\epsilon}_{222}(k_1,k_2,k_3) = \\ & \quad = \frac{1}{\bar{n}^2_{\rm DM}\,{k_{\rm NL}}^6}\left(c^{(222)}_{\rm DM,1}k_1^2k_2^2k_3^2 + c^{(222)}_{\rm DM,2}(k_1^6+k_2^6+k_3^6 - (k_1^4k_2^2 + k_1^2k_2^4 + \ 2 \text{ perms.}))\right) \end{aligned} \tag{B.43}$$

then an explicit solution to the UV matching is

$$\begin{aligned} & c^{\rm St}_{\rm DM,1} = -\frac{9\,\bar{n}_{\rm DM}\,{k_{\rm NL}}^4}{196\pi^2}\int dq\frac{P_{11}(q)^2}{q^2} \ , \quad c^{\rm St}_{\rm DM,4} = \frac{683\,\bar{n}_{\rm DM}\,{k_{\rm NL}}^4}{70560\pi^2}\int dq\frac{P_{11}(q)^2}{q^2} \ , \\ & c^{\rm St}_{\rm DM,5} = -\frac{389\,\bar{n}_{\rm DM}\,{k_{\rm NL}}^4}{17640\pi^2}\int dq\frac{P_{11}(q)^2}{q^2} \ , \quad c^{\rm St}_{\rm DM,6} = -\frac{293\,\bar{n}_{\rm DM}\,{k_{\rm NL}}^4}{23520\pi^2}\int dq\frac{P_{11}(q)^2}{q^2} \ , \end{aligned} \tag{B.44}$$

and

$$c^{(222)}_{\rm DM,1} = \frac{\bar{n}^2_{\rm DM}{k_{\rm NL}}^6}{4802\pi^2}\int dq\frac{P_{11}(q)^3}{q^4} \ , \quad c^{(222)}_{\rm DM,2} = \frac{15\,\bar{n}^2_{\rm DM}{k_{\rm NL}}^6}{2401\pi^2}\int dq\frac{P_{11}(q)^3}{q^4} \ , \tag{B.45}$$

with other coefficients zero (they are degenerate for these observables).

B.1.7 Counterterm Expressions in Redshift Space

The response terms are proportional only to powers of the linear field, and specifically we can write

$$\tilde{\delta}^{(1)}_{r,ct}(\vec{k},\hat{z}) = F_1^{r,ct}(\vec{k};\hat{z})\tilde{\delta}^{(1)}_{\vec{k}} \ , \quad \text{and} \quad \tilde{\delta}^{(2)}_{r,ct}(\vec{k},\hat{z}) = \int^{\vec{k}}_{\vec{q}_1,\vec{q}_2} F_2^{r,ct}(\vec{q}_1,\vec{q}_2;\hat{z})\tilde{\delta}^{(1)}_{\vec{q}_1}\tilde{\delta}^{(1)}_{\vec{q}_2} \ . \quad \text{(B.46)}$$

where definitions of the tilde fields are given in Eq. (6.88). We group all of the terms that are only proportional to the stochastic fields in $\delta^{(1)}_{r,\epsilon}(\vec{k},\hat{z},a)$ and terms that contain one stochastic field and one long-wavelength field (semi-stochastic) in $\delta^{(2)}_{r,\epsilon}(\vec{k},\hat{z},a)$. The response counterterms enter in

$$\begin{aligned} P^{r,ct}_{13}(k,\hat{k}\cdot\hat{z}) &\equiv 2F_1^r(\vec{k};\hat{z})F_1^{r,ct}(-\vec{k};\hat{z})P_{11}(k) \ , \quad \text{(B.47)} \\ B^{r,ct}_{411} &\equiv 2P_{11}(k_1)P_{11}(k_2)F_1^r(\vec{k}_1;\hat{z})F_1^r(\vec{k}_2;\hat{z})F_2^{r,ct}(-\vec{k}_1,-\vec{k}_2;\hat{z}) + \text{ 2 perms.} \ , \\ B^{r,(II),ct}_{321} &\equiv 2P_{11}(k_1)P_{11}(k_2)F_1^{r,ct}(\vec{k}_1;\hat{z})F_1^r(\vec{k}_2;\hat{z})F_2^r(-\vec{k}_1,-\vec{k}_2;\hat{z}) + \text{ 5 perms.} \ , \end{aligned}$$

(we have suppressed the argument $(k_1,k_2,k_3,\hat{k}_1\cdot\hat{z},\hat{k}_2\cdot\hat{z})$ of the bispectra terms to remove clutter) so that the combinations

$$\begin{aligned} &P^r_{13}(k,\hat{k}\cdot\hat{z}) + P^{r,ct}_{13}(k,\hat{k}\cdot\hat{z}) \ , \\ &B^r_{411}(k_1,k_2,k_3,\hat{k}_1\cdot\hat{z},\hat{k}_2\cdot\hat{z}) + B^{r,ct}_{411}(k_1,k_2,k_3,\hat{k}_1\cdot\hat{z},\hat{k}_2\cdot\hat{z}) \ , \quad \text{(B.48)} \\ &B^{r,(II)}_{321}(k_1,k_2,k_3,\hat{k}_1\cdot\hat{z},\hat{k}_2\cdot\hat{z}) + B^{r,(II),ct}_{321}(k_1,k_2,k_3,\hat{k}_1\cdot\hat{z},\hat{k}_2\cdot\hat{z}) \ , \end{aligned}$$

are renormalized. Furthermore, for the stochastic fields, we define

$$\begin{aligned} &\langle\tilde{\delta}^{(1)}_{r,\epsilon}(\vec{k},\hat{z})\tilde{\delta}^{(1)}_{r,\epsilon}(\vec{k}',\hat{z})\rangle \equiv (2\pi)^3\delta_D(\vec{k}+\vec{k}')P^{r,\epsilon}_{22}(k,\hat{k}\cdot\hat{z}) \ , \quad \text{(B.49)} \\ &\langle\tilde{\delta}^{(1)}_{r,\epsilon}(\vec{k}_1,\hat{z})\tilde{\delta}^{(1)}_{r,\epsilon}(\vec{k}_2,\hat{z})\tilde{\delta}^{(1)}_{r,\epsilon}(\vec{k}_3,\hat{z})\rangle \equiv (2\pi)^3\delta_D(\vec{k}_1+\vec{k}_2+\vec{k}_3)B^{r,\epsilon}_{222}(k_1,k_2,k_3,\hat{k}_1\cdot\hat{z},\hat{k}_2\cdot\hat{z}), \\ &\langle\tilde{\delta}^{(1)}_{r}(\vec{k}_1,\hat{z})\tilde{\delta}^{(1)}_{r,\epsilon}(\vec{k}_2,\hat{z})\tilde{\delta}^{(2)}_{r,\epsilon}(\vec{k}_3,\hat{z})\rangle + 5 \text{ perms.} \equiv \\ &\qquad\qquad \equiv (2\pi)^3\delta_D(\vec{k}_1+\vec{k}_2+\vec{k}_3)B^{r,(I),\epsilon}_{321}(k_1,k_2,k_3,\hat{k}_1\cdot\hat{z},\hat{k}_2\cdot\hat{z}), \end{aligned}$$

so that the combinations

$$\begin{aligned} &P^r_{22}(k,\hat{k}\cdot\hat{z}) + P^{r,\epsilon}_{22}(k,\hat{k}\cdot\hat{z}) \ , \\ &B^r_{222}(k_1,k_2,k_3,\hat{k}_1\cdot\hat{z},\hat{k}_2\cdot\hat{z}) + B^{r,\epsilon}_{222}(k_1,k_2,k_3,\hat{k}_1\cdot\hat{z},\hat{k}_2\cdot\hat{z}) \ , \quad \text{(B.50)} \\ &B^{r,(I)}_{321}(k_1,k_2,k_3,\hat{k}_1\cdot\hat{z},\hat{k}_2\cdot\hat{z}) + B^{r,(I),\epsilon}_{321}(k_1,k_2,k_3,\hat{k}_1\cdot\hat{z},\hat{k}_2\cdot\hat{z}) \ , \end{aligned}$$

are renormalized.

The basis elements $e_i^{F_2}$ used to define $F_2^{r,ct}$ in Eq. (6.101) are related to the functions that we use for biased tracers in App. B.4.2 by

$$\begin{aligned}
e_1^{F_2} &= \frac{1}{9}e_1^{K_2} + \frac{8}{99}e_2^{K_2} - \frac{19}{693}e_3^{K_2} - \frac{16}{693}e_4^{K_2} - \frac{1}{33}e_5^{K_2} \\
&\quad + \frac{2}{99}e_7^{K_2} + \frac{2}{3f}e_{10}^{K_2} + \frac{7}{99f}e_{11}^{K_2} - \frac{2}{3}e_{12}^{K_2} + \frac{8}{99f}e_{14}^{K_2} \ , \\
e_2^{F_2} &= \frac{10}{231}e_3^{K_2} + \frac{4}{231}e_4^{K_2} + \frac{16}{33f}e_{11}^{K_2} \ , \\
e_3^{F_2} &= \frac{1}{33}e_2^{K_2} + \frac{2}{231}e_3^{K_2} - \frac{2}{231}e_4^{K_2} + \frac{1}{33}e_5^{K_2} + \frac{2}{9}e_6^{K_2} \\
&\quad - \frac{2}{99}e_7^{K_2} + \frac{4}{9f}e_{10}^{K_2} - \frac{7}{99f}e_{11}^{K_2} - \frac{4}{9}e_{12}^{K_2} + \frac{29}{99f}e_{14}^{K_2} \ , \\
e_4^{F_2} &= \frac{2}{33}e_3^{K_2} + \frac{16}{33f}e_{14}^{K_2} \ , \\
e_n^{F_2} &= e_{n+3}^{K_2} \quad \text{for} \quad n = 5, \ldots, 11 \ .
\end{aligned} \tag{B.51}$$

As discussed in more detail in Sec. 6.5.4, we note that the new non-locally-contributing counterterm comes from the function $e_7^{K_2}$, and so enters the expression for $e_1^{F_2}$ and $e_3^{F_2}$ above. This means that in the basis that we have chosen, c_3 and c_5 contribute the non-locally-contributing counterterm.

Next, we give the UV matching. The values for the dark-matter parameters c_3, c_4, c_5, and c_7 are given in Eq. (B.37), and the rest are

$$\begin{aligned}
c_{\mathrm{DM},1}^{\pi v} &= -\frac{(46+35f){k_{\mathrm{NL}}}^2}{210\pi^2}\int dq P_{11}(q) \ , \quad c_{\mathrm{DM},2}^{\pi v} = -\frac{(11+15f){k_{\mathrm{NL}}}^2}{150\pi^2}\int dq\, P_{11}(q) \ , \\
c_{\mathrm{DM},3}^{\pi v} &= -\frac{83{k_{\mathrm{NL}}}^2}{210\pi^2}\int dq\, P_{11}(q) \ , \quad c_{\mathrm{DM},4}^{\pi v} = -\frac{172{k_{\mathrm{NL}}}^2}{735\pi^2}\int dq\, P_{11}(q) \ , \\
c_{\mathrm{DM},5}^{\pi v} &= -\frac{2683{k_{\mathrm{NL}}}^2}{5145\pi^2}\int dq\, P_{11}(q) \ , \quad c_{\mathrm{DM},6}^{\pi v} = -\frac{(4626+1715f){k_{\mathrm{NL}}}^2}{25725\pi^2}\int dq\, P_{11}(q) \ , \\
c_{\mathrm{DM},7}^{\pi v} &= -\frac{269{k_{\mathrm{NL}}}^2}{686\pi^2}\int dq\, P_{11}(q) \ .
\end{aligned} \tag{B.52}$$

B.2 Bispectrum Loop Integrals in Redshift Space

In this appendix, we give some information on how to evaluate the one-loop bispectrum integrals in redshift space in Eq. (6.123). The most straightforward way to evaluate the one-loop bispectrum integrals is by choosing a coordinate system and integrating numerically. Because of rotation invariance, a generic bispectrum

one-loop term B is given by

$$B(k_1, k_2, k_3, \mu_1, \mu_2) = \int_{\vec{q}} \mathcal{K}(k_1, k_2, k_3, \mu_1, \mu_2, q, \hat{k}_1 \cdot \hat{q}, \hat{k}_2 \cdot \hat{q}, \hat{q} \cdot \hat{z}) \ , \tag{B.53}$$

where we have used momentum conservation $\vec{k}_3 = -\vec{k}_1 - \vec{k}_2$, and as always $\mu_i \equiv \hat{k}_i \cdot \hat{z}$. One choice of coordinate system is

$$\begin{aligned} \vec{k}_1 &= k_1 \, (0, 0, 1) \ , \\ \vec{k}_2 &= k_2 \left(0, \sqrt{1-y^2}, y\right) \ , \\ \vec{q} &= q \left(\cos(\beta)\sqrt{1-x^2}, \sin(\beta)\sqrt{1-x^2}, x\right) \ , \\ \hat{z} &= \left(\cos(\phi)\sqrt{1-\mu_1^2}, \sin(\phi)\sqrt{1-\mu_1^2}, \mu_1\right) \ , \end{aligned} \tag{B.54}$$

where $y \equiv (k_3^2 - k_1^2 - k_2^2)/(2k_1k_2)$, $x \in [-1, 1]$, $\mu_1 \in [-1, 1]$, $\phi \in [0, 2\pi)$, and $\beta \in [0, 2\pi)$. In this coordinate system the measure is simply

$$\int_{\vec{q}} = \int \frac{dq \, q^2}{(2\pi)^3} \int_{-1}^{1} dx \int_0^{2\pi} d\beta \ . \tag{B.55}$$

Next we move to a tensor reduction method that is better suited for analytic integration. For this, we write a generic bispectrum one-loop term B as

$$B(k_1, k_2, k_3, \mu_1, \mu_2) = \sum_a f_a(k_1, k_2, k_3, \mu_1, \mu_2) \int_{\vec{q}} \mathcal{K}_a(q, |\vec{k}_1 + \vec{q}|, |\vec{k}_2 - \vec{q}|; \hat{q} \cdot \hat{z}) \ , \tag{B.56}$$

where the functions f_a do not depend on the loop momentum $\vec{q}$ and the kernels $\mathcal{K}_a$ depend on the scalar combinations q, $|\vec{k}_1 + \vec{q}|$, $|\vec{k}_2 - \vec{q}|$ because of momentum conservation, and on the projection along $\hat{z}$ of the integrated momentum, $\hat{q} \cdot \hat{z}$. For reasons that we will comment on later, we choose to parameterize $\hat{k}_1 \cdot \hat{q}$ and $\hat{k}_2 \cdot \hat{q}$ by $|\vec{k}_1 + \vec{q}|$ and $|\vec{k}_2 - \vec{q}|$ respectively. The specific form in Eq. (B.56) is possible because the dependence on μ_1 and μ_2 is polynomial, and we choose to include any k_i dependence that does not come through $|\vec{k}_1 + \vec{q}|$ or $|\vec{k}_2 - \vec{q}|$ in the functions f_a to reduce the number of terms in the sum. Note that both f_a and $\mathcal{K}_a$ can depend on the linear power spectrum P_{11}. If there were no dependence on $\hat{q} \cdot \hat{z}$, the integrals over $\mathcal{K}_a$ could be done using analytic techniques, see for example [282, 206]. Luckily, the dependence on $\hat{q} \cdot \hat{z}$ is very simple: the $\mathcal{K}_a$ are polynomials in $\hat{q} \cdot \hat{z}$ (which simply comes from the redshift space expression Eq. (6.113)), of order up to six for B_{222},

up to four for B_{321}^{I}, and up to two for B_{321}^{II} and B_{411}. Thus, each $\mathcal{K}_a$ can be written as

$$\mathcal{K}_a(q, |\vec{k}_1 + \vec{q}|, |\vec{k}_2 - \vec{q}|; \hat{q} \cdot \hat{z}) = \sum_n \mathcal{T}_{a,(n)}(q, |\vec{k}_1 + \vec{q}|, |\vec{k}_2 - \vec{q}|)(\hat{q} \cdot \hat{z})^n \ , \tag{B.57}$$

where the sum over n is over a finite number of terms as stated above.

We would now like to write Eq. (B.57) in such a way that allows us to express the integral over $\vec{q}$ as a sum over integrals of functions of $(q, |\vec{k}_1 + \vec{q}|, |\vec{k}_2 - \vec{q}|)$, which is a form conducive to analytic integration. To do that, we first define

$$I_{a,(n)}^{i_1 \ldots i_n}(\vec{k}_1, \vec{k}_2) = \int_{\vec{q}} \mathcal{T}_{a,(n)}(q, |\vec{k}_1 + \vec{q}|, |\vec{k}_2 - \vec{q}|)\, \hat{q}^{i_1} \cdots \hat{q}^{i_n} \ , \tag{B.58}$$

and from Eq. (B.57), we are interested in computing $\hat{z}^{i_1} \ldots \hat{z}^{i_n} I_{a,(n)}^{i_1 \ldots i_n}(\vec{k}_1, \vec{k}_2)$. Now, because of rotation invariance, the function $I_{a,(n)}^{i_1 \ldots i_n}(\vec{k}_1, \vec{k}_2)$ can be generally written as

$$I_{a,(n)}^{i_1 \ldots i_n}(\vec{k}_1, \vec{k}_2) = \sum_{\alpha=1}^{N_n} c_{a,(n),\alpha}(k_1, k_2, \hat{k}_1 \cdot \hat{k}_2) T_{a,(n),\alpha}^{i_1 \ldots i_n}(\hat{k}_1, \hat{k}_2, \delta_{ij}) \ , \tag{B.59}$$

where the functions $c_{a,(n),\alpha}$ depend on scalar products of $\vec{k}_1$ and $\vec{k}_2$, and the functions $T_{a,(n),\alpha}^{i_1 \ldots i_n}$ are all of the N_n symmetric tensors with indices $i_1 \ldots i_n$ made up of products of $\hat{k}_1$, $\hat{k}_2$, and δ_{ij}. To see how this has helped us, we go back to the expression that we are interested in, which now becomes

$$\hat{z}^{i_1} \ldots \hat{z}^{i_n} I_{a,(n)}^{i_1 \ldots i_n}(\vec{k}_1, \vec{k}_2) = \sum_{\alpha} c_{a,(n),\alpha}(k_1, k_2, \hat{k}_1 \cdot \hat{k}_2) t_{a,(n),\alpha}(\mu_1, \mu_2) \ , \tag{B.60}$$

where we have defined $t_{a,(n),\alpha}(\mu_1, \mu_2) \equiv \hat{z}^{i_1} \ldots \hat{z}^{i_n} T_{a,(n),\alpha}^{i_1 \ldots i_n}(\hat{k}_1, \hat{k}_2, \delta_{ij})$. This is now exactly the form that we wanted: all of the loop integrals are contained in the $c_{a,(n),\alpha}$ functions, which is over functions of $(q, |\vec{k}_1 + \vec{q}|, |\vec{k}_2 - \vec{q}|)$, and all of the $\hat{z}$ dependence has been transferred to the external momenta in the $t_{a,(n),\alpha}$ functions.

Let us now determine the $c_{a,(n),\alpha}$ functions explicitly. To do that, we contract Eq. (B.59) with the N_n symmetric tensors $T_{a,(n),\beta}^{i_1 \ldots i_n}$, giving

$$\begin{aligned} &\int_{\vec{q}} \mathcal{T}_{a,(n)}(q, |\vec{k}_1 + \vec{q}|, |\vec{k}_2 - \vec{q}|)\, T_{a,(n),\beta}^{i_1 \ldots i_n}(\hat{k}_1, \hat{k}_2, \delta_{ij}) \hat{q}^{i_1} \cdots \hat{q}^{i_n} \\ &\qquad = \sum_{\alpha=1}^{N_n} c_{a,(n),\alpha}(k_1, k_2, \hat{k}_1 \cdot \hat{k}_2) T_{a,(n),\alpha}^{i_1 \ldots i_n}(\hat{k}_1, \hat{k}_2, \delta_{ij}) T_{a,(n),\beta}^{i_1 \ldots i_n}(\hat{k}_1, \hat{k}_2, \delta_{ij}) \ , \end{aligned} \tag{B.61}$$

which is a system of N_n equations that can be used to solve for the N_n functions $c_{a,(n),\alpha}$; on the left-hand side, using

$$\hat{q}\cdot\hat{k}_1 = \frac{1}{2qk_1}\left(|\vec{k}_1+\vec{q}|^2 - k_1^2 - q^2\right), \text{ and } \hat{q}\cdot\hat{k}_2 = \frac{1}{2qk_2}\left(k_2^2 + q^2 - |\vec{k}_2-\vec{q}|^2\right) , \quad \text{(B.62)}$$

we have our desired form of loop integrals over $\vec{q}$ of functions of $(q, |\vec{k}_1+\vec{q}|, |\vec{k}_2-\vec{q}|)$, while on the right-hand side, we have the $c_{a,(n),\alpha}$ functions multiplied by scalar products between $\hat{k}_1$ and $\hat{k}_2$. In particular, defining the matrix

$$M^{\alpha\beta}_{a,(n)}(\hat{k}_1\cdot\hat{k}_2) \equiv T^{i_1\ldots i_n}_{a,(n),\alpha}(\hat{k}_1,\hat{k}_2,\delta_{ij})T^{i_1\ldots i_n}_{a,(n),\beta}(\hat{k}_1,\hat{k}_2,\delta_{ij}) , \quad \text{(B.63)}$$

we have

$$c_{a,(n),\alpha}(k_1,k_2,\hat{k}_1\cdot\hat{k}_2) = \quad \text{(B.64)}$$
$$\sum_{\beta=1}^{N_n}[M^{-1}_{a,(n)}]^{\alpha\beta}(\hat{k}_1\cdot\hat{k}_2)\int_{\vec{q}}\mathcal{T}_{a,(n)}(q,|\vec{k}_1+\vec{q}|,|\vec{k}_2-\vec{q}|)\,T^{i_1\ldots i_n}_{a,(n),\beta}(\hat{k}_1,\hat{k}_2,\delta_{ij})\hat{q}^{i_1}\cdots\hat{q}^{i_n} .$$

Thus, this solution for the $c_{a,(n),\alpha}$ functions, plugged into Eq. (B.60), gives our final result.

The above manipulations can also be presented in a slightly different way. Again, we are interested in computing the right-hand side of Eq. (B.58) contracted with $\hat{z}^{i_1}\cdots\hat{z}^{i_n}$, which, using Eqs. (B.58) and (B.59), is given by

$$\int_{\vec{q}}\mathcal{T}_{a,(n)}(q,|\vec{k}_1+\vec{q}|,|\vec{k}_2-\vec{q}|)\,(\hat{q}\cdot\hat{z})^n = \sum_\alpha c_{a,(n),\alpha}(k_1,k_2,\hat{k}_1\cdot\hat{k}_2)t_{a,(n),\alpha}(\mu_1,\mu_2) . \quad \text{(B.65)}$$

Now, given the solution Eq. (B.64) for the $c_{a,(n),\alpha}$ functions, we can rewrite this as

$$\int_{\vec{q}}\mathcal{T}_{a,(n)}(q,|\vec{k}_1+\vec{q}|,|\vec{k}_2-\vec{q}|)\,(\hat{q}\cdot\hat{z})^n = \int_{\vec{q}}\mathcal{T}_{a,(n)}(q,|\vec{k}_1+\vec{q}|,|\vec{k}_2-\vec{q}|)\times \quad \text{(B.66)}$$
$$\times\sum_{\alpha=1}^{N_n}\sum_{\beta=1}^{N_n}[M^{-1}_{a,(n)}]^{\alpha\beta}(\hat{k}_1\cdot\hat{k}_2)\,T^{i_1\ldots i_n}_{a,(n),\beta}(\hat{k}_1,\hat{k}_2,\delta_{ij})\hat{q}^{i_1}\cdots\hat{q}^{i_n}t_{a,(n),\alpha}(\mu_1,\mu_2) ,$$

which implies that, under the integrals that we are interested in, we can simply replace

$$(\hat{q}\cdot\hat{z})^n \to \sum_{\alpha=1}^{N_n}\sum_{\beta=1}^{N_n}[M^{-1}_{a,(n)}]^{\alpha\beta}(\hat{k}_1\cdot\hat{k}_2)\,T^{i_1\ldots i_n}_{a,(n),\beta}(\hat{k}_1,\hat{k}_2,\delta_{ij})\hat{q}^{i_1}\cdots\hat{q}^{i_n}t_{a,(n),\alpha}(\mu_1,\mu_2) , \quad \text{(B.67)}$$

which again, using Eq. (B.62), is in the form that we want.

At this point, a number of comments are in order. First, the above form of the loop integrals is well suited for situations where integrals over functions of $(q, |\vec{k}_1 + \vec{q}|, |\vec{k}_2 - \vec{q}|)$ can be done analytically, see for example [282, 206]. If this is not the case, one can simply use an explicit coordinate system to perform the integrals, as described above. Second, it turns out that for the bispectrum, it can be quite slow to invert the matrix $M^{\alpha\beta}_{a,(n)}$ for values of n greater than four (which is relevant in particular for the B_{222} diagram).

Thus, in practice, it is sometimes easier to use the following more straightforward way to arrive at the above result, again with an eye towards analytic integration. We start with the form of the loop in Eq. (B.56), and using the above definitions, we recall that we need to evaluate terms of the form

$$\int_{\vec{q}} \mathcal{T}_{a,(n)}(q, |\vec{k}_1 + \vec{q}|, |\vec{k}_2 - \vec{q}|) \, (\hat{q} \cdot \hat{z})^n \ , \tag{B.68}$$

so we would like to find a replacement for $(\hat{q} \cdot \hat{z})^n$ in terms of q, $|\vec{k}_1 + \vec{q}|$, and $|\vec{k}_2 - \vec{q}|$. For this, we can simply use the coordinate system Eq. (B.54). Without loss of generality we can take the first component of $\hat{z}$ to be positive, and use $\mu_2 = \hat{k}_2 \cdot \hat{z}$ to get

$$\hat{z} = \left(\sqrt{\frac{-\mu_1^2 - \mu_2^2 - y^2 + 2\mu_1\mu_2 y + 1}{1 - y^2}}, \frac{\mu_2 - \mu_1 y}{\sqrt{1 - y^2}}, \mu_1 \right) \ . \tag{B.69}$$

To see why the sign of the first component of $\hat{z}$ does not matter, consider Eq. (B.68) and send $\hat{z}_1 \to -\hat{z}_1$, where the subscript $_1$ denotes the first component. This can be compensated by sending $\hat{q}_1 \to -\hat{q}_1$, and since none of q, $|\vec{k}_1 + \vec{q}|$, or $|\vec{k}_2 - \vec{q}|$ depend on $\hat{q}_1$ for the parameterization Eq. (B.54), the integral is invariant. Dotting this with $\hat{q}$ from Eq. (B.54), we get

$$\begin{aligned} \hat{q} \cdot \hat{z} = \cos(\beta)\sqrt{1 - x^2}\sqrt{\frac{-\mu_1^2 - \mu_2^2 - y^2 + 2\mu_1\mu_2 y + 1}{1 - y^2}} \\ + \frac{\sin(\beta)\sqrt{1 - x^2}\,(\mu_2 - \mu_1 y)}{\sqrt{1 - y^2}} + \mu_1 x \ . \end{aligned} \tag{B.70}$$

Now, we raise this to the n-th power, and plug it into Eq. (B.68). The resulting expression can be simplified by noting the following. First, $|\vec{k}_1 + \vec{q}|$ does not depend on β, and $|\vec{k}_2 - \vec{q}|$ only depends on $\sin(\beta)$. Thus, in terms of β dependence, the

integral in Eq. (B.68) is equal to a sum over terms of the form

$$\int_0^{2\pi} d\beta f(\sin(\beta))\cos(\beta)^m \tag{B.71}$$

for some functions f and integer powers m. This integral is clearly zero when m is odd, since in that case $\cos(\beta)^m$ is an odd function around $\beta = \pi/2$ and $\sin(\beta)$ is an even function around $\beta = \pi/2$, and both are periodic with periods 2π. Thus, we see that when we expand out $(\hat{q}\cdot\hat{z})^n$, we can immediately set to zero any terms with an odd power of $\cos(\beta)$, and any time that we encounter an even power of $\cos(\beta)$ we can replace it with $\cos(\beta)^2 = 1 - \sin(\beta)^2$, so our result only depends on $\sin(\beta)$.

It now remains to express x and $\sin(\beta)$ in terms of the desired $(q, |\vec{k}_1+\vec{q}|, |\vec{k}_2-\vec{q}|)$. This is straightforward using Eq. (B.54), and we find

$$x = \frac{-k_1^2 + |\vec{k}_1+\vec{q}|^2 - q^2}{2k_1 q} \ , \tag{B.72}$$

and

$$\sin(\beta) = \frac{-2k_2\, q\, x\, y + k_2^2 - |\vec{k}_2-\vec{q}|^2 + q^2}{2k_2 q\sqrt{1-x^2}\sqrt{1-y^2}} \ . \tag{B.73}$$

Taking into account that only even powers of $\cos(\beta)$ contribute, and defining

$$\nu \equiv \sqrt{1-x^2}\sin(\beta) \ , \tag{B.74}$$

this means that we can replace $(\hat{q}\cdot\hat{z})^n$ in Eq. (B.68) with (using the multinomial theorem)

$$\begin{aligned}(\hat{q}\cdot\hat{z})^n \to \sum_{i+j+2k=n} \frac{n!\,(\mu_1 x)^{\,i}}{i!j!(2k)!}\left[\nu\,(\mu_2-\mu_1 y)\right]^j \left(1-y^2\right)^{-\frac{1}{2}(j+2k)} \\ \times\left[\left(1-x^2-\nu^2\right)\left(-\mu_1^2-\mu_2^2-y^2+2\mu_1\mu_2 y+1\right)\right]^k\end{aligned} \tag{B.75}$$

which, using Eqs. (B.72) and (B.73), again puts the loop integral in Eq. (B.68) in the desired form (notice that since Eq. (B.75) depends on $\sin(\beta)$ only through ν, the possible non-analytic dependence $\sqrt{1-x^2}$ cancels and does not appear in the final answer). One can check that the right-hand sides of the expressions in Eqs. (B.67) and (B.75) are equal.

B.3 Details for Biased Tracers to Fourth Order

In this appendix, we give the explicit calculation to obtain Eq. (6.130). We do this in three steps. First, we expand the bias expansion in terms of all operators allowed by the equivalence principle. This gives the list of operators that we schematically wrote in Eq. (6.126). Next we do the explicit Taylor expansion of the operators evaluated at $\vec{x}_{\rm fl}$ around $\vec{x}$, and define the explicit $\mathbb{C}^{(n)}_{\mathcal{O},i}$ that are in Eq. (6.127). In a last step we put them together, and remove degeneracies, to obtain Eq. (6.130). In this whole appendix, we focus on the fourth order calculation and refer to [129, 131, 132] for the calculation up to third order. The dark-matter kernels, in real space and redshift space, can be obtained from the expressions in this appendix by setting $b_1 = b_2 = b_3 = b_4 = 1$ and $b_5, \ldots, b_{15} = 0$.

B.3.1 Bias Expansion

As mentioned in Sec. 6.6.2, the tracer overdensity can only depend on second derivatives of the gravitational potential, and first derivatives of the velocity field (and higher spatial derivatives of these). To look at all possible operators, we define the building blocks

$$r_{ij} = \frac{2}{3\Omega_{\rm m}\mathcal{H}^2}\partial_i\partial_j\Phi \ , \quad \text{and} \quad p_{ij} = -\frac{1}{faH}\partial_i v^j \ , \tag{B.76}$$

so that $\delta^{ij}r_{ij} = \delta$ and $\delta^{ij}p_{ij} = \theta$, with $\theta \equiv -\partial_i v^i/(faH)$. [3] For notational convenience, we further define

$$\begin{aligned} &r^2 = r_{ij}r_{ij} \ , \qquad rp = r_{ij}p_{ij} \ , \qquad p^2 = p_{ij}p_{ij} \ , \qquad r^3 = r_{ij}r_{jl}r_{li} \ , \\ &r^2p = r_{ij}r_{jl}p_{li} \ , \qquad rp^2 = r_{ij}p_{jl}p_{il} \ , \qquad p^3 = p_{ij}p_{jl}p_{il} \ , \qquad r^4 = r_{ij}r_{jl}r_{lk}r_{ki} \ . \end{aligned} \tag{B.77}$$

We can now write down the full expansion for the tracer overdensity up to fourth order, which we only schematically gave in Eq. (6.126). To determine the operators,

[3] Notice that p_{ij} is symmetric for a velocity with vanishing vorticity. For the biases that we discuss in this section, this is true.

we write down all contractions of r_{ij} and p_{ij} up to fourth order, and obtain

$$\begin{aligned}\delta_h(\vec{x},t) = \int^t dt' H(t') \big[& c_\delta(t,t')\delta(\vec{x}_{\rm fl},t') + c_\theta(t,t')\theta(\vec{x}_{\rm fl},t') \\ & + c_{\delta^2}(t,t')\delta^2(\vec{x}_{\rm fl},t') + c_{\delta\theta}(t,t')\delta\theta(\vec{x}_{\rm fl},t') + c_{\theta^2}(t,t')\theta^2(\vec{x}_{\rm fl},t') \\ & + c_{r^2}(t,t')r^2(\vec{x}_{\rm fl},t') + c_{rp}(t,t')rp(\vec{x}_{\rm fl},t') + c_{p^2}(t,t')p^2(\vec{x}_{\rm fl},t') \\ & + c_{\delta^3}(t,t')\delta^3(\vec{x}_{\rm fl},t') + c_{\delta^2\theta}(t,t')\delta^2\theta(\vec{x}_{\rm fl},t') + c_{\delta\theta^2}(t,t')\delta\theta^2(\vec{x}_{\rm fl},t') + c_{\theta^3}(t,t')\theta^3(\vec{x}_{\rm fl},t') \\ & + c_{r^3}(t,t')r^3(\vec{x}_{\rm fl},t') + c_{r^2p}(t,t')r^2p(\vec{x}_{\rm fl},t') + c_{rp^2}(t,t')rp^2(\vec{x}_{\rm fl},t') + c_{p^3}(t,t')p^3(\vec{x}_{\rm fl},t') \\ & + c_{r^2\delta}(t,t')r^2\delta(\vec{x}_{\rm fl},t') + c_{rp\delta}(t,t')rp\delta(\vec{x}_{\rm fl},t') + c_{p^2\delta}(t,t')p^2\delta(\vec{x}_{\rm fl},t') \\ & + c_{r^2\theta}(t,t')r^2\theta(\vec{x}_{\rm fl},t') + c_{rp\theta}(t,t')rp\theta(\vec{x}_{\rm fl},t') + c_{p^2\theta}(t,t')p^2\theta(\vec{x}_{\rm fl},t') \\ & + c_{\delta^4}(t,t')\delta^4(\vec{x}_{\rm fl},t') + c_{\delta r^3}(t,t')\delta r^3(\vec{x}_{\rm fl},t') + c_{\delta^2 r^2}(t,t')\delta^2 r^2(\vec{x}_{\rm fl},t') \\ & + c_{(r^2)^2}(t,t')\left(r^2\right)^2(\vec{x}_{\rm fl},t') + c_{r^4}(t,t')r^4(\vec{x}_{\rm fl},t')\big]\big|_{\vec{x}_{\rm fl}=\vec{x}_{\rm fl}(\vec{x},t,t')} \,. \end{aligned} \tag{B.78}$$

Since we only go up to fourth order in perturbations, terms that explicitly start at fourth order above are evaluated on the linear fields, and for those terms we have used $\theta^{(1)} = \delta^{(1)}$.

B.3.2 Expansion in Fluid Element

The operators in Eq. (B.78) are all evaluated at $\vec{x}_{\rm fl}$, where $\vec{x}_{\rm fl}$ is given implicitly in Eq. (10.35). In this section, we Taylor expand all the fields evaluated at $\vec{x}_{\rm fl}$ around $\vec{x}$. Going up to products of four fields, for a generic operator $\mathcal{O}$ we have

(following [129])

$$\begin{aligned}\mathcal{O}(\vec{x}_{\text{fl}}(\vec{x},t,t'),t') \approx \mathcal{O}(\vec{x},t') &+ \partial_i\mathcal{O}(\vec{x},t')\int_t^{t'}\frac{dt_1}{a(t_1)}\,v^i(\vec{x},t_1) \\ &+\frac{1}{2}\partial_i\partial_j\mathcal{O}(\vec{x},t')\int_t^{t'}\frac{dt_1}{a(t_1)}\,v^i(\vec{x},t_1)\int_t^{t'}\frac{dt_2}{a(t_2)}\,v^j(\vec{x},t_2) \\ &+\partial_i\mathcal{O}(\vec{x},t')\int_t^{t'}\frac{dt_1}{a(t_1)}\,\partial_j v^i(\vec{x},t_1)\int_t^{t_1}\frac{dt_2}{a(t_2)}\,v^j(\vec{x},t_2) \\ &+\frac{1}{6}\partial_i\partial_j\partial_k\mathcal{O}(\vec{x},t')\int_t^{t'}\frac{dt_1}{a(t_1)}\,v^i(\vec{x},t_1)\int_t^{t'}\frac{dt_2}{a(t_2)}\,v^j(\vec{x},t_2)\int_t^{t'}\frac{dt_3}{a(t_3)}\,v^k(\vec{x},t_3) \\ &+\frac{1}{2}\partial_i\mathcal{O}(\vec{x},t')\int_t^{t'}\frac{dt_1}{a(t_1)}\,\partial_j\partial_k v^i(\vec{x},t_1)\int_t^{t_1}\frac{dt_2}{a(t_2)}\,v^j(\vec{x},t_2)\int_t^{t_1}\frac{dt_3}{a(t_3)}\,v^k(\vec{x},t_3) \\ &+\partial_i\mathcal{O}(\vec{x},t')\int_t^{t'}\frac{dt_1}{a(t_1)}\,\partial_j v^i(\vec{x},t_1)\int_t^{t_1}\frac{dt_2}{a(t_2)}\,\partial_k v^j(\vec{x},t_2)\int_t^{t_2}\frac{dt_3}{a(t_3)}\,v^k(\vec{x},t_3) \\ &+\partial_i\partial_j\mathcal{O}(\vec{x},t')\int_t^{t'}\frac{dt_1}{a(t_1)}\,v^i(\vec{x},t_1)\int_t^{t'}\frac{dt_2}{a(t_2)}\,\partial_k v^j(\vec{x},t_2)\int_t^{t_2}\frac{dt_3}{a(t_3)}\,v^k(\vec{x},t_3)\ .\end{aligned} \tag{B.79}$$

We now perturbatively expand and rewrite the velocity in terms of the divergence only

$$v^i_{(n)}(\vec{x},t') = -\frac{a(t')\dot{D}(t')}{D(t')}\frac{D(t')^n}{D(t)^n}\frac{\partial_i}{\partial^2}\theta^{(n)}(\vec{x},t)\ . \tag{B.80}$$

With the EdS approximation as done above (and potentially also without it [135]), it is always possible to solve the time integrals in Eq. (B.79) analytically, since all integrals can be reduced to

$$\int_t^{t'} dt_1\,\frac{\dot{D}(t_1)D(t_1)^{n-1}}{D(t)^n} = \frac{1}{n}\left[\frac{D(t')^n}{D(t)^n}-1\right]\ . \tag{B.81}$$

This then gives the expression for a Taylor expanded operator at fourth order in perturbations

$$
\begin{aligned}
\mathcal{O}^{(4)}(\vec{x}_{\rm fl}(\vec{x},t,t'),t') &= \mathcal{O}^{(4)}\frac{D(t')^4}{D(t)^4} + \partial_i\mathcal{O}^{(1)}\frac{\partial_i\theta^{(3)}}{\partial^2}\left[\frac{1}{3}\frac{D(t')}{D(t)} - \frac{1}{3}\frac{D(t')^4}{D(t)^4}\right] \\
&+\partial_i\mathcal{O}^{(2)}\frac{\partial_i\theta^{(2)}}{\partial^2}\left[\frac{1}{2}\frac{D(t')^2}{D(t)^2} - \frac{1}{2}\frac{D(t')^4}{D(t)^4}\right] + \partial_i\mathcal{O}^{(3)}\frac{\partial_i\theta^{(1)}}{\partial^2}\left[\frac{D(t')^3}{D(t)^3} - \frac{D(t')^4}{D(t)^4}\right] \\
&+\partial_i\partial_j\mathcal{O}^{(1)}\frac{\partial_i\theta^{(1)}}{\partial^2}\frac{\partial_j\theta^{(2)}}{\partial^2}\left[\frac{1}{2}\frac{D(t')}{D(t)} - \frac{1}{2}\frac{D(t')^2}{D(t)^2} - \frac{1}{2}\frac{D(t')^3}{D(t)^3} + \frac{1}{2}\frac{D(t')^4}{D(t)^4}\right] \\
&+\partial_i\partial_j\mathcal{O}^{(2)}\frac{\partial_i\theta^{(1)}}{\partial^2}\frac{\partial_j\theta^{(1)}}{\partial^2}\left[\frac{1}{2}\frac{D(t')^2}{D(t)^2} - \frac{D(t')^3}{D(t)^3} + \frac{1}{2}\frac{D(t')^4}{D(t)^4}\right] \\
&+\partial_i\mathcal{O}^{(1)}\frac{\partial_j\partial_i\theta^{(1)}}{\partial^2}\frac{\partial_j\theta^{(2)}}{\partial^2}\left[\frac{1}{3}\frac{D(t')}{D(t)} - \frac{1}{2}\frac{D(t')^2}{D(t)^2} + \frac{1}{6}\frac{D(t')^4}{D(t)^4}\right] \\
&+\partial_i\mathcal{O}^{(1)}\frac{\partial_i\partial_j\theta^{(2)}}{\partial^2}\frac{\partial_j\theta^{(1)}}{\partial^2}\left[\frac{1}{6}\frac{D(t')}{D(t)} - \frac{1}{2}\frac{D(t')^3}{D(t)^3} + \frac{1}{3}\frac{D(t')^4}{D(t)^4}\right] \\
&+\partial_i\mathcal{O}^{(2)}\frac{\partial_i\partial_j\theta^{(1)}}{\partial^2}\frac{\partial_j\theta^{(1)}}{\partial^2}\left[\frac{1}{2}\frac{D(t')^2}{D(t)^2} - \frac{D(t')^3}{D(t)^3} + \frac{1}{2}\frac{D(t')^4}{D(t)^4}\right] \\
&+\partial_i\partial_j\partial_k\mathcal{O}^{(1)}\frac{\partial_i\theta^{(1)}}{\partial^2}\frac{\partial_j\theta^{(1)}}{\partial^2}\frac{\partial_k\theta^{(1)}}{\partial^2}\left[\frac{1}{6}\frac{D(t')}{D(t)} - \frac{1}{2}\frac{D(t')^2}{D(t)^2} + \frac{1}{2}\frac{D(t')^3}{D(t)^3} - \frac{1}{6}\frac{D(t')^4}{D(t)^4}\right] \\
&+\partial_i\mathcal{O}^{(1)}\frac{\partial_i\partial_j\partial_k\theta^{(1)}}{\partial^2}\frac{\partial_j\theta^{(1)}}{\partial^2}\frac{\partial_k\theta^{(1)}}{\partial^2}\left[\frac{1}{6}\frac{D(t')}{D(t)} - \frac{1}{2}\frac{D(t')^2}{D(t)^2} + \frac{1}{2}\frac{D(t')^3}{D(t)^3} - \frac{1}{6}\frac{D(t')^4}{D(t)^4}\right] \\
&+\partial_i\mathcal{O}^{(1)}\frac{\partial_i\partial_j\theta^{(1)}}{\partial^2}\frac{\partial_j\partial_k\theta^{(1)}}{\partial^2}\frac{\partial_k\theta^{(1)}}{\partial^2}\left[\frac{1}{6}\frac{D(t')}{D(t)} - \frac{1}{2}\frac{D(t')^2}{D(t)^2} + \frac{1}{2}\frac{D(t')^3}{D(t)^3} - \frac{1}{6}\frac{D(t')^4}{D(t)^4}\right]\Big] \\
&+\partial_i\partial_j\mathcal{O}^{(1)}\frac{\partial_i\theta^{(1)}}{\partial^2}\frac{\partial_j\partial_k\theta^{(1)}}{\partial^2}\frac{\partial_k\theta^{(1)}}{\partial^2}\left[\frac{1}{2}\frac{D(t')}{D(t)} - \frac{3}{2}\frac{D(t')^2}{D(t)^2} + \frac{3}{2}\frac{D(t')^3}{D(t)^3} - \frac{1}{2}\frac{D(t')^4}{D(t)^4}\right] ,
\end{aligned}
\tag{B.82}
$$

where all fields $\mathcal{O}^{(n)}$ and $\theta^{(n)}$ are evaluated at $(\vec{x},t)$, and we refer the reader to [131, 132] for expressions up to third order.

From the above expansion, we can now define the $\mathbb{C}_{\mathcal{O},i}$ operators that appear in Eq. (6.127) and later in Eq. (6.130). Note that for an operator $\mathcal{O}_m$ that starts at order m, such as a product operator of m fields, $\mathcal{O}_m^{(n)} = 0$ for $n < m$. Finally, for an operator $\mathcal{O}_m$ starting at order m, we collect the terms that multiply the same power of $D(t')/D(t)$, which gives the n-th order terms in the expansion

$$
\mathcal{O}_m^{(n)}(\vec{x}_{\rm fl}(\vec{x},t,t'),t') = \sum_{\alpha=1}^{n-m+1}\left(\frac{D(t')}{D(t)}\right)^{\alpha+m-1}\mathbb{C}^{(n)}_{\mathcal{O}_m,\alpha}(\vec{x},t) \ , \tag{B.83}
$$

which allows us to read off the $\mathbb{C}_{\mathcal{O},i}$ from Eq. (B.82). Summing up all the orders

gives Eq. (6.127).

After also performing the time integrals and defining coefficients following Eq. (6.128), we obtain the Taylor expanded and time integrated version of Eq. (B.78) at fourth order,

$$\begin{aligned}\delta_h^{(4)}(\vec{x},t) = {} & c_{\delta,1}\mathbb{C}^{(4)}_{\delta,1}+c_{\delta,2}\mathbb{C}^{(4)}_{\delta,2}+c_{\delta,3}\mathbb{C}^{(4)}_{\delta,3}+c_{\delta,4}\mathbb{C}^{(4)}_{\delta,4}+c_{\theta,1}\mathbb{C}^{(4)}_{\theta,1}+c_{\theta,2}\mathbb{C}^{(4)}_{\theta,2}+c_{\theta,3}\mathbb{C}^{(4)}_{\theta,3} \\ & +c_{\theta,4}\mathbb{C}^{(4)}_{\theta,4}+c_{\delta^2,1}\mathbb{C}^{(4)}_{\delta^2,1}+c_{\delta^2,2}\mathbb{C}^{(4)}_{\delta^2,2}+c_{\delta^2,3}\mathbb{C}^{(4)}_{\delta^2,3}+c_{\delta\theta,1}\mathbb{C}^{(4)}_{\delta\theta,1}+c_{\delta\theta,2}\mathbb{C}^{(4)}_{\delta\theta,2} \\ & +c_{\delta\theta,3}\mathbb{C}^{(4)}_{\delta\theta,3}+c_{\theta^2,1}\mathbb{C}^{(4)}_{\theta^2,1}+c_{\theta^2,2}\mathbb{C}^{(4)}_{\theta^2,2}+c_{\theta^2,3}\mathbb{C}^{(4)}_{\theta^2,3}+c_{r^2,1}\mathbb{C}^{(4)}_{r^2,1}+c_{r^2,2}\mathbb{C}^{(4)}_{r^2,2} \\ & +c_{r^2,3}\mathbb{C}^{(4)}_{r^2,3}+c_{rp,1}\mathbb{C}^{(4)}_{rp,1}+c_{rp,2}\mathbb{C}^{(4)}_{rp,2}+c_{rp,3}\mathbb{C}^{(4)}_{rp,3}+c_{p^2,1}\mathbb{C}^{(4)}_{p^2,1}+c_{p^2,2}\mathbb{C}^{(4)}_{p^2,2} \\ & +c_{p^2,3}\mathbb{C}^{(4)}_{p^2,3}+c_{\delta^3,1}\mathbb{C}^{(4)}_{\delta^3,1}+c_{\delta^3,2}\mathbb{C}^{(4)}_{\delta^3,2}+c_{\theta^3,1}\mathbb{C}^{(4)}_{\theta^3,1}+c_{\theta^3,2}\mathbb{C}^{(4)}_{\theta^3,2}+c_{\delta^2\theta,1}\mathbb{C}^{(4)}_{\delta^2\theta,1} \\ & +c_{\delta^2\theta,2}\mathbb{C}^{(4)}_{\delta^2\theta,2}+c_{\delta\theta^2,1}\mathbb{C}^{(4)}_{\delta\theta^2,1}+c_{\delta\theta^2,2}\mathbb{C}^{(4)}_{\delta\theta^2,2}+c_{r^3,1}\mathbb{C}^{(4)}_{r^3,1}+c_{r^3,2}\mathbb{C}^{(4)}_{r^3,2}+c_{p^3,1}\mathbb{C}^{(4)}_{p^3,1} \\ & +c_{p^3,2}\mathbb{C}^{(4)}_{p^3,2}+c_{r^2p,1}\mathbb{C}^{(4)}_{r^2p,1}+c_{r^2p,2}\mathbb{C}^{(4)}_{r^2p,2}+c_{rp^2,1}\mathbb{C}^{(4)}_{rp^2,1}+c_{rp^2,2}\mathbb{C}^{(4)}_{rp^2,2}+c_{r^2\delta,1}\mathbb{C}^{(4)}_{r^2\delta,1} \\ & +c_{r^2\delta,2}\mathbb{C}^{(4)}_{r^2\delta,2}+c_{rp\delta,1}\mathbb{C}^{(4)}_{rp\delta,1}+c_{rp\delta,2}\mathbb{C}^{(4)}_{rp\delta,2}+c_{p^2\delta,1}\mathbb{C}^{(4)}_{p^2\delta,1}+c_{p^2\delta,2}\mathbb{C}^{(4)}_{p^2\delta,2}+c_{r^2\theta,1}\mathbb{C}^{(4)}_{r^2\theta,1} \\ & +c_{r^2\theta,2}\mathbb{C}^{(4)}_{r^2\theta,2}+c_{rp\theta,1}\mathbb{C}^{(4)}_{rp\theta,1}+c_{rp\theta,2}\mathbb{C}^{(4)}_{rp\theta,2}+c_{p^2\theta,1}\mathbb{C}^{(4)}_{p^2\theta,1}+c_{p^2\theta,2}\mathbb{C}^{(4)}_{p^2\theta,2} \\ & +c_{\delta^4,1}\mathbb{C}^{(4)}_{\delta^4,1}+c_{\delta r^3,1}\mathbb{C}^{(4)}_{\delta r^3,1}+c_{\delta^2 r^2,1}\mathbb{C}^{(4)}_{\delta^2 r^2,1}+c_{(r^2)^2,1}\mathbb{C}^{(4)}_{(r^2)^2,1}+c_{r^4,1}\mathbb{C}^{(4)}_{r^4,1}\ ,\end{aligned} \tag{B.84}$$

where all of the $c_{\mathcal{O},i}$ functions are evaluated at t, and all of the $\mathbb{C}^{(4)}_{\mathcal{O},i}$ functions are evaluated at $(\vec{x},t)$. As mentioned in the main text, the expansion above is not yet irreducible, for instance $\mathbb{C}^{(4)}_{r^2,1} = \frac{7}{2}\mathbb{C}^{(4)}_{\delta,2} - \frac{5}{2}\mathbb{C}^{(4)}_{\delta^2,1}$. Therefore by a redefinition of coefficients, we can reduce the number of coefficients needed. A full list of degeneracies is given in Eq. (B.86) in the next section.

B.3.3 Degeneracies and Local Basis

We find that at fourth order, the number of independent operators is fifteen, and we choose the basis

$$\{\mathbb{C}^{(4)}_{\delta,1},\mathbb{C}^{(4)}_{\delta,2},\mathbb{C}^{(4)}_{\delta,3},\mathbb{C}^{(4)}_{\delta,4},\mathbb{C}^{(4)}_{\delta^2,1},\mathbb{C}^{(4)}_{\delta^2,2},\mathbb{C}^{(4)}_{\delta^2,3},\mathbb{C}^{(4)}_{r^2,2},\mathbb{C}^{(4)}_{r^2,3},\mathbb{C}^{(4)}_{\delta^3,1},\mathbb{C}^{(4)}_{\delta^3,2},\mathbb{C}^{(4)}_{r^3,2},\mathbb{C}^{(4)}_{r^2\delta,2},\mathbb{C}^{(4)}_{\delta^4,1},\mathbb{C}^{(4)}_{\delta r^3,1}\}\ . \tag{B.85}$$

We give these fifteen functions explicitly in App. B.3.4. The other operators are given in terms of these by the following relationships

$$\begin{aligned}&\mathbb{C}^{(4)}_{r^2,1} = \tfrac{7}{2}\mathbb{C}^{(4)}_{\delta,2} - \tfrac{5}{2}\mathbb{C}^{(4)}_{\delta^2,1}\ , \quad \mathbb{C}^{(4)}_{r^3,1} = \tfrac{45}{4}\mathbb{C}^{(4)}_{\delta,3} - \tfrac{105}{16}\mathbb{C}^{(4)}_{\delta^2,2} - \tfrac{3}{4}\mathbb{C}^{(4)}_{r^2,2} + \tfrac{35}{8}\mathbb{C}^{(4)}_{\delta^3,1}\ , \\ &\mathbb{C}^{(4)}_{r^2\delta,1} = \tfrac{7}{4}\mathbb{C}^{(4)}_{\delta^2,2} - \tfrac{5}{2}\mathbb{C}^{(4)}_{\delta^3,1}\ , \quad \mathbb{C}^{(4)}_{r^2\delta^2} = \tfrac{7}{6}\mathbb{C}^{(4)}_{\delta^3,2} - \tfrac{5}{2}\mathbb{C}^{(4)}_{\delta^4,1}\ , \\ &\mathbb{C}^{(4)}_{(r^2)^2,1} = \tfrac{735}{32}\mathbb{C}^{(4)}_{\delta^2,3} - \tfrac{105}{4}\mathbb{C}^{(4)}_{\delta^3,2} - \tfrac{49}{16}\mathbb{C}^{(4)}_{r^2\delta,2} + \tfrac{2315}{96}\mathbb{C}^{(4)}_{\delta^4,1} - \tfrac{49}{12}\mathbb{C}^{(4)}_{\delta r^3,1}\ ,\end{aligned} \tag{B.86}$$

$$\mathbb{C}^{(4)}_{r^4,1} = \tfrac{735}{64}\mathbb{C}^{(4)}_{\delta^2,3} - \tfrac{343}{24}\mathbb{C}^{(4)}_{\delta^3,2} - \tfrac{49}{32}\mathbb{C}^{(4)}_{r^2\delta,2} + \tfrac{2827}{192}\mathbb{C}^{(4)}_{\delta^4,1} - \tfrac{17}{24}\mathbb{C}^{(4)}_{\delta r^3,1} \ ,$$
$$\mathbb{C}^{(4)}_{\theta,1} = \mathbb{C}^{(4)}_{\delta,1} \ , \quad \mathbb{C}^{(4)}_{\theta,2} = 2\mathbb{C}^{(4)}_{\delta,2} - \mathbb{C}^{(4)}_{\delta^2,1} \ , \quad \mathbb{C}^{(4)}_{\theta,3} = 3\mathbb{C}^{(4)}_{\delta,3} - \tfrac{3}{2}\mathbb{C}^{(4)}_{\delta^2,2} + \mathbb{C}^{(4)}_{\delta^3,1} \ ,$$
$$\mathbb{C}^{(4)}_{\theta,4} = 4\mathbb{C}^{(4)}_{\delta,4} - 2\mathbb{C}^{(4)}_{\delta^2,3} + \tfrac{4}{3}\mathbb{C}^{(4)}_{\delta^3,2} - \mathbb{C}^{(4)}_{\delta^4,1} \ , \quad \mathbb{C}^{(4)}_{\delta\theta,1} = \mathbb{C}^{(4)}_{\delta^2,1} \ ,$$
$$\mathbb{C}^{(4)}_{\delta\theta,2} = \tfrac{3}{2}\mathbb{C}^{(4)}_{\delta^2,2} - \mathbb{C}^{(4)}_{\delta^3,1} \ , \quad \mathbb{C}^{(4)}_{\delta\theta,3} = 2\mathbb{C}^{(4)}_{\delta^2,3} - \tfrac{4}{3}\mathbb{C}^{(4)}_{\delta^3,2} + \mathbb{C}^{(4)}_{\delta^4,1} \ , \quad \mathbb{C}^{(4)}_{\theta^2,1} = \mathbb{C}^{(4)}_{\delta^2,1} \ ,$$
$$\mathbb{C}^{(4)}_{\theta^2,2} = 2\mathbb{C}^{(4)}_{\delta^2,2} - 2\mathbb{C}^{(4)}_{\delta^3,1} \ , \quad \mathbb{C}^{(4)}_{\theta^2,3} = \tfrac{39}{8}\mathbb{C}^{(4)}_{\delta^2,3} - 5\mathbb{C}^{(4)}_{\delta^3,2} - \tfrac{1}{4}\mathbb{C}^{(4)}_{r^2\delta,2} + \tfrac{107}{24}\mathbb{C}^{(4)}_{\delta^4,1} - \tfrac{1}{3}\mathbb{C}^{(4)}_{\delta r^3,1} \ ,$$
$$\mathbb{C}^{(4)}_{rp,1} = \tfrac{7}{2}\mathbb{C}^{(4)}_{\delta,2} - \tfrac{5}{2}\mathbb{C}^{(4)}_{\delta^2,1} \ , \quad \mathbb{C}^{(4)}_{rp,2} = \tfrac{9}{2}\mathbb{C}^{(4)}_{\delta,3} - \tfrac{21}{8}\mathbb{C}^{(4)}_{\delta^2,2} + \tfrac{1}{2}\mathbb{C}^{(4)}_{r^2,2} + \tfrac{7}{4}\mathbb{C}^{(4)}_{\delta^3,1} \ ,$$
$$\mathbb{C}^{(4)}_{rp,3} = \tfrac{55}{2}\mathbb{C}^{(4)}_{\delta,4} - \tfrac{387}{16}\mathbb{C}^{(4)}_{\delta^2,3} + \tfrac{643}{30}\mathbb{C}^{(4)}_{\delta^3,2} - \tfrac{2}{5}\mathbb{C}^{(4)}_{r^3,2} + \tfrac{49}{40}\mathbb{C}^{(4)}_{r^2\delta,2} - \tfrac{4627}{240}\mathbb{C}^{(4)}_{\delta^4,1} + \tfrac{17}{30}\mathbb{C}^{(4)}_{\delta r^3,1} \ ,$$
$$\mathbb{C}^{(4)}_{p^2,1} = \tfrac{7}{2}\mathbb{C}^{(4)}_{\delta,2} - \tfrac{5}{2}\mathbb{C}^{(4)}_{\delta^2,1} \ , \quad \mathbb{C}^{(4)}_{p^2\theta,1} = \tfrac{7}{4}\mathbb{C}^{(4)}_{\delta^2,2} - \tfrac{5}{2}\mathbb{C}^{(4)}_{\delta^3,1} \ ,$$
$$\mathbb{C}^{(4)}_{p^2,2} = 9\mathbb{C}^{(4)}_{\delta,3} - \tfrac{21}{4}\mathbb{C}^{(4)}_{\delta^2,2} + \tfrac{7}{2}\mathbb{C}^{(4)}_{\delta^3,1}, \quad \mathbb{C}^{(4)}_{p^2,3} = \tfrac{33}{2}\mathbb{C}^{(4)}_{\delta,4} - 9\mathbb{C}^{(4)}_{\delta^2,3} + 6\mathbb{C}^{(4)}_{\delta^3,2} - \tfrac{9}{2}\mathbb{C}^{(4)}_{\delta^4,1} \ ,$$
$$\mathbb{C}^{(4)}_{\delta^2\theta,1} = \mathbb{C}^{(4)}_{\delta^3,1} \ , \quad \mathbb{C}^{(4)}_{\delta^2\theta,2} = \tfrac{4}{3}\mathbb{C}^{(4)}_{\delta^3,2} - \mathbb{C}^{(4)}_{\delta^4,1} \ , \quad \mathbb{C}^{(4)}_{\delta\theta^2,1} = \mathbb{C}^{(4)}_{\delta^3,1} \ ,$$
$$\mathbb{C}^{(4)}_{\delta\theta^2,2} = \tfrac{5}{3}\mathbb{C}^{(4)}_{\delta^3,2} - 2\mathbb{C}^{(4)}_{\delta^4,1} \ , \quad \mathbb{C}^{(4)}_{\theta^3,1} = \mathbb{C}^{(4)}_{\delta^3,1} \ , \quad \mathbb{C}^{(4)}_{\theta^3,2} = 2\mathbb{C}^{(4)}_{\delta^3,2} - 3\mathbb{C}^{(4)}_{\delta^4,1} \ ,$$
$$\mathbb{C}^{(4)}_{pr^2,1} = \tfrac{45}{4}\mathbb{C}^{(4)}_{\delta,3} - \tfrac{105}{16}\mathbb{C}^{(4)}_{\delta^2,2} - \tfrac{3}{4}\mathbb{C}^{(4)}_{r^2,2} + \tfrac{35}{8}\mathbb{C}^{(4)}_{\delta^3,1} \ ,$$
$$\mathbb{C}^{(4)}_{pr^2,2} = \tfrac{147}{32}\mathbb{C}^{(4)}_{\delta^2,3} - \tfrac{343}{60}\mathbb{C}^{(4)}_{\delta^3,2} + \tfrac{13}{15}\mathbb{C}^{(4)}_{r^3,2} - \tfrac{49}{80}\mathbb{C}^{(4)}_{r^2\delta,2} + \tfrac{2827}{480}\mathbb{C}^{(4)}_{\delta^4,1} - \tfrac{17}{60}\mathbb{C}^{(4)}_{\delta r^3,1} \ ,$$
$$\mathbb{C}^{(4)}_{rp^2,1} = \tfrac{45}{4}\mathbb{C}^{(4)}_{\delta,3} - \tfrac{105}{16}\mathbb{C}^{(4)}_{\delta^2,2} - \tfrac{3}{4}\mathbb{C}^{(4)}_{r^2,2} + \tfrac{35}{8}\mathbb{C}^{(4)}_{\delta^3,1} \ ,$$
$$\mathbb{C}^{(4)}_{rp^2,2} = \tfrac{147}{16}\mathbb{C}^{(4)}_{\delta^2,3} - \tfrac{343}{30}\mathbb{C}^{(4)}_{\delta^3,2} + \tfrac{11}{15}\mathbb{C}^{(4)}_{r^3,2} - \tfrac{49}{40}\mathbb{C}^{(4)}_{r^2\delta,2} + \tfrac{2827}{240}\mathbb{C}^{(4)}_{\delta^4,1} - \tfrac{17}{30}\mathbb{C}^{(4)}_{\delta r^3,1} \ ,$$
$$\mathbb{C}^{(4)}_{p^3,1} = \tfrac{45}{4}\mathbb{C}^{(4)}_{\delta,3} - \tfrac{105}{16}\mathbb{C}^{(4)}_{\delta^2,2} - \tfrac{3}{4}\mathbb{C}^{(4)}_{r^2,2} + \tfrac{35}{8}\mathbb{C}^{(4)}_{\delta^3,1} \ ,$$
$$\mathbb{C}^{(4)}_{p^3,2} = \tfrac{441}{32}\mathbb{C}^{(4)}_{\delta^2,3} - \tfrac{343}{20}\mathbb{C}^{(4)}_{\delta^3,2} + \tfrac{3}{5}\mathbb{C}^{(4)}_{r^3,2} - \tfrac{147}{80}\mathbb{C}^{(4)}_{r^2\delta,2} + \tfrac{2827}{160}\mathbb{C}^{(4)}_{\delta^4,1} - \tfrac{17}{20}\mathbb{C}^{(4)}_{\delta r^3,1} \ ,$$
$$\mathbb{C}^{(4)}_{p^2\delta,1} = \tfrac{7}{4}\mathbb{C}^{(4)}_{\delta^2,2} - \tfrac{5}{2}\mathbb{C}^{(4)}_{\delta^3,1} \ , \quad , \quad \mathbb{C}^{(4)}_{rp\delta,1} = \tfrac{7}{4}\mathbb{C}^{(4)}_{\delta^2,2} - \tfrac{5}{2}\mathbb{C}^{(4)}_{\delta^3,1} \ ,$$
$$\mathbb{C}^{(4)}_{r^2\theta,1} = \tfrac{7}{4}\mathbb{C}^{(4)}_{\delta^2,2} - \tfrac{5}{2}\mathbb{C}^{(4)}_{\delta^3,1} \ , \quad \mathbb{C}^{(4)}_{rp\theta,1} = \tfrac{7}{4}\mathbb{C}^{(4)}_{\delta^2,2} - \tfrac{5}{2}\mathbb{C}^{(4)}_{\delta^3,1} \ ,$$
$$\mathbb{C}^{(4)}_{rp\delta,2} = \tfrac{21}{16}\mathbb{C}^{(4)}_{\delta^2,3} - \tfrac{4}{3}\mathbb{C}^{(4)}_{\delta^3,2} + \tfrac{5}{8}\mathbb{C}^{(4)}_{r^2\delta,2} + \tfrac{49}{48}\mathbb{C}^{(4)}_{\delta^4,1} + \tfrac{1}{6}\mathbb{C}^{(4)}_{\delta r^3,1} \ ,$$
$$\mathbb{C}^{(4)}_{p^2\delta,2} = \tfrac{21}{8}\mathbb{C}^{(4)}_{\delta^2,3} - \tfrac{8}{3}\mathbb{C}^{(4)}_{\delta^3,2} + \tfrac{1}{4}\mathbb{C}^{(4)}_{r^2\delta,2} + \tfrac{49}{24}\mathbb{C}^{(4)}_{\delta^4,1} + \tfrac{1}{3}\mathbb{C}^{(4)}_{\delta r^3,1} \ ,$$
$$\mathbb{C}^{(4)}_{r^2\theta,2} = \tfrac{105}{16}\mathbb{C}^{(4)}_{\delta^2,3} - \tfrac{47}{6}\mathbb{C}^{(4)}_{\delta^3,2} + \tfrac{1}{8}\mathbb{C}^{(4)}_{r^2\delta,2} + \tfrac{365}{48}\mathbb{C}^{(4)}_{\delta^4,1} - \tfrac{7}{6}\mathbb{C}^{(4)}_{\delta r^3,1} \ ,$$
$$\mathbb{C}^{(4)}_{rp\theta,2} = \tfrac{63}{8}\mathbb{C}^{(4)}_{\delta^2,3} - \tfrac{55}{6}\mathbb{C}^{(4)}_{\delta^3,2} - \tfrac{1}{4}\mathbb{C}^{(4)}_{r^2\delta,2} + \tfrac{69}{8}\mathbb{C}^{(4)}_{\delta^4,1} - \mathbb{C}^{(4)}_{\delta r^3,1} \ ,$$
$$\mathbb{C}^{(4)}_{p^2\theta,2} = \tfrac{147}{16}\mathbb{C}^{(4)}_{\delta^2,3} - \tfrac{21}{2}\mathbb{C}^{(4)}_{\delta^3,2} - \tfrac{5}{8}\mathbb{C}^{(4)}_{r^2\delta,2} + \tfrac{463}{48}\mathbb{C}^{(4)}_{\delta^4,1} - \tfrac{5}{6}\mathbb{C}^{(4)}_{\delta r^3,1} \ .$$

The local-in-time limit is obtained by setting $c_{\mathcal{O}_m}(t,t') = c_{\mathcal{O}_m}(t)\delta_D(t-t')/H(t)$ in Eq. (6.128). Using that, along with Eq. (6.127) with $t = t'$, in Eq. (6.129), we have the local-in-time expansion

$$\delta^{(n)}_{h,\,\mathrm{loc}}(\vec{x},t) = \sum_{\mathcal{O}_m} c_{\mathcal{O}_m}(t)\mathcal{O}^{(n)}_m(\vec{x},t) \ , \tag{B.87}$$

where $\mathcal{O}^{(n)}_m(\vec{x},t)$ is the normal expression for the operator $\mathcal{O}_m$ at n-th order in

perturbations. For $n = 4$, we find that a basis for all of the $\mathcal{O}_m^{(4)}(\vec{x}, t)$ is $\vec{B}_{\rm loc} = \{\mathcal{O}_m^{(4)}\}$ where $\mathcal{O}_m$ is given by

$$\{p^2, r^2, r^2r^2, r^2p, r^3, r^4, rp, \delta, r^2\delta, r^3\delta, rp\delta, \delta^2, r^2\delta^2, \delta^3, \theta\} \ . \tag{B.88}$$

Then, calling $\vec{B}$ the basis given in Eq. (B.85), we find that

$$\vec{B}_{\rm loc} = M \cdot \vec{B} \ , \tag{B.89}$$

where the change of basis matrix M is given by

$$M = \begin{pmatrix}
0 & \frac{7}{2} & 9 & \frac{33}{2} & -\frac{5}{2} & -\frac{21}{4} & -9 & 0 & 0 & \frac{7}{2} & 6 & 0 & 0 & -\frac{9}{2} & 0 \\
0 & \frac{7}{2} & 0 & 0 & -\frac{5}{2} & 0 & 0 & 1 & 1 & 0 & 0 & 0 & 0 & 0 & 0 \\
0 & 0 & 0 & 0 & 0 & 0 & \frac{735}{32} & 0 & 0 & 0 & -\frac{105}{4} & 0 & -\frac{49}{16} & \frac{2315}{96} & -\frac{49}{12} \\
0 & 0 & \frac{45}{4} & 0 & 0 & -\frac{105}{16} & \frac{147}{32} & -\frac{3}{4} & 0 & \frac{35}{8} & -\frac{343}{60} & \frac{13}{15} & -\frac{49}{80} & \frac{2827}{480} & -\frac{17}{60} \\
0 & 0 & \frac{45}{4} & 0 & 0 & -\frac{105}{16} & 0 & -\frac{3}{4} & 0 & \frac{35}{8} & 0 & 1 & 0 & 0 & 0 \\
0 & 0 & 0 & 0 & 0 & 0 & \frac{735}{64} & 0 & 0 & 0 & -\frac{343}{24} & 0 & -\frac{49}{32} & \frac{2827}{192} & -\frac{17}{24} \\
0 & \frac{7}{2} & \frac{9}{2} & \frac{55}{2} & -\frac{5}{2} & -\frac{21}{8} & -\frac{387}{16} & \frac{1}{2} & 0 & \frac{7}{4} & \frac{643}{30} & -\frac{2}{5} & \frac{49}{40} & -\frac{4627}{240} & \frac{17}{30} \\
1 & 1 & 1 & 1 & 0 & 0 & 0 & 0 & 0 & 0 & 0 & 0 & 0 & 0 & 0 \\
0 & 0 & 0 & 0 & 0 & \frac{7}{4} & 0 & 0 & 0 & -\frac{5}{2} & 0 & 0 & 1 & 0 & 0 \\
0 & 0 & 0 & 0 & 0 & 0 & 0 & 0 & 0 & 0 & 0 & 0 & 0 & 0 & 1 \\
0 & 0 & 0 & 0 & 0 & \frac{7}{4} & \frac{21}{16} & 0 & 0 & -\frac{5}{2} & -\frac{4}{3} & 0 & \frac{5}{8} & \frac{49}{48} & \frac{1}{6} \\
0 & 0 & 0 & 0 & 1 & 1 & 1 & 0 & 0 & 0 & 0 & 0 & 0 & 0 & 0 \\
0 & 0 & 0 & 0 & 0 & 0 & 0 & 0 & 0 & 0 & \frac{7}{6} & 0 & 0 & -\frac{5}{2} & 0 \\
0 & 0 & 0 & 0 & 0 & 0 & 0 & 0 & 0 & 1 & 1 & 0 & 0 & 0 & 0 \\
1 & 2 & 3 & 4 & -1 & -\frac{3}{2} & -2 & 0 & 0 & 1 & \frac{4}{3} & 0 & 0 & -1 & 0
\end{pmatrix} . \tag{B.90}$$

Since $\det M \neq 0$, this means that M is invertible and thus the local-in-time basis is equivalent to the non-local-in-time basis.

B.3.4 Explicit Expressions for Fourth Order Kernels

We here give the final $\mathbb{C}_{\mathcal{O},i}$ used in Eq. (6.130) that are linearly independent, as Fourier space kernels. We use the notation

$$\mathbb{C}_{\mathcal{O},i}^{(n)}(\vec{k}, t) = D(t)^n \int_{\vec{q}_1,...,\vec{q}_n}^{\vec{k}} K_n^{\mathcal{O},i}(\vec{q}_1, ..., \vec{q}_n)\tilde{\delta}_{\vec{q}_1}^{(1)} \cdots \tilde{\delta}_{\vec{q}_n}^{(1)} \ . \tag{B.91}$$

Dropping the $(\vec{q}_1, \vec{q}_2, \vec{q}_3, \vec{q}_4)$ dependence on the left-hand sides to avoid clutter, we explicitly have

$$
\begin{aligned}
K_4^{\delta,1} =& \frac{(\vec{q}_1 \cdot (\vec{q}_3 + \vec{q}_4)\, \vec{q}_2 \cdot (\vec{q}_3 + \vec{q}_4) + \vec{q}_1 \cdot \vec{q}_2\, (3\vec{q}_1 + 2\vec{q}_2) \cdot (\vec{q}_3 + \vec{q}_4))\, G_2\,(\vec{q}_3, \vec{q}_4)}{6 q_2^2\, (\vec{q}_3 + \vec{q}_4)^{\,2}} \\
&+ \frac{\vec{q}_1 \cdot (\vec{q}_2 + \vec{q}_3 + \vec{q}_4)\, G_3\,(\vec{q}_2, \vec{q}_3, \vec{q}_4)}{3\,(\vec{q}_2 + \vec{q}_3 + \vec{q}_4)^{\,2}} \\
&+ \frac{\vec{q}_1 \cdot \vec{q}_2\, (\vec{q}_2 \cdot \vec{q}_3 \vec{q}_4 \cdot (\vec{q}_2 + \vec{q}_3) + \vec{q}_1 \cdot \vec{q}_3 \vec{q}_4 \cdot (\vec{q}_1 + 3\vec{q}_3))}{6 q_2^2 q_3^2 q_4^2}\,, \\
K_4^{\delta,2} =& \frac{(\vec{q}_1 + \vec{q}_2) \cdot (\vec{q}_3 + \vec{q}_4)\, (q_2^2 F_2\,(\vec{q}_1, \vec{q}_2) - \vec{q}_1 \cdot \vec{q}_2)\, G_2\,(\vec{q}_3, \vec{q}_4)}{2 q_2^2\, (\vec{q}_3 + \vec{q}_4)^{\,2}} \\
&+ \frac{\vec{q}_3 \cdot (\vec{q}_1 + \vec{q}_2)\, \vec{q}_4 \cdot (\vec{q}_1 + \vec{q}_2 + \vec{q}_3)\, F_2\,(\vec{q}_1, \vec{q}_2)}{2 q_3^2 q_4^2} \\
&- \frac{\vec{q}_1 \cdot \vec{q}_2\, (\vec{q}_2 \cdot \vec{q}_3 \vec{q}_4 \cdot (\vec{q}_2 + \vec{q}_3) + \vec{q}_1 \cdot \vec{q}_3 \vec{q}_4 \cdot (\vec{q}_1 + 3\vec{q}_3))}{2 q_2^2 q_3^2 q_4^2}\,, \\
K_4^{\delta,3} =& \frac{\vec{q}_4 \cdot (\vec{q}_1 + \vec{q}_2 + \vec{q}_3)\, F_3\,(\vec{q}_1, \vec{q}_2, \vec{q}_3)}{q_4^2} \\
&+ \frac{\vec{q}_1 \cdot \vec{q}_2\, (\vec{q}_2 \cdot \vec{q}_3 \vec{q}_4 \cdot (\vec{q}_2 + \vec{q}_3) + \vec{q}_1 \cdot \vec{q}_3 \vec{q}_4 \cdot (\vec{q}_1 + 3\vec{q}_3))}{2 q_2^2 q_3^2 q_4^2} \\
&- \frac{\vec{q}_4 \cdot (\vec{q}_1 + \vec{q}_2 + \vec{q}_3)\, \vec{q}_3 \cdot (\vec{q}_1 + \vec{q}_2)}{q_4^2} \left(\frac{F_2\,(\vec{q}_1, \vec{q}_2)}{q_3^2} + \frac{G_2\,(\vec{q}_1, \vec{q}_2)}{2\,(\vec{q}_1 + \vec{q}_2)^{\,2}} \right)\,, \\
\cdot K_4^{\delta,4} =& F_4\,(\vec{q}_1, \vec{q}_2, \vec{q}_3, \vec{q}_4) - \sum_{i=1}^{3} K_4^{\delta,i}\,(\vec{q}_1, \vec{q}_2, \vec{q}_3, \vec{q}_4)\,, \\
K_4^{\delta^2,1} =& \frac{\vec{q}_2 \cdot (\vec{q}_3 + \vec{q}_4)\, G_2\,(\vec{q}_3, \vec{q}_4)}{(\vec{q}_3 + \vec{q}_4)^{\,2}} + \frac{\vec{q}_1 \cdot \vec{q}_3 \vec{q}_2 \cdot \vec{q}_4 + \vec{q}_2 \cdot \vec{q}_3 \vec{q}_4 \cdot (\vec{q}_2 + \vec{q}_3)}{q_3^2 q_4^2}\,, \\
K_4^{\delta^2,2} =& \frac{2\vec{q}_4 \cdot (\vec{q}_1 + \vec{q}_2 + \vec{q}_3)\, F_2\,(\vec{q}_1, \vec{q}_2)}{q_4^2} - \frac{2\,(\vec{q}_1 \cdot \vec{q}_3 \vec{q}_2 \cdot \vec{q}_4 + \vec{q}_2 \cdot \vec{q}_3 \vec{q}_4 \cdot (\vec{q}_2 + \vec{q}_3))}{q_3^2 q_4^2}\,, \\
K_4^{\delta^2,3} =& 2F_3\,(\vec{q}_1, \vec{q}_2, \vec{q}_3) + F_2\,(\vec{q}_1, \vec{q}_2)\, F_2\,(\vec{q}_3, \vec{q}_4) - \sum_{i=1}^{2} K_4^{\delta^2,i}\,(\vec{q}_1, \vec{q}_2, \vec{q}_3, \vec{q}_4)\,, \\
K_4^{r^2,2} =& \frac{2\,(\vec{q}_3 \cdot (\vec{q}_1 + \vec{q}_2))^{\,2} \vec{q}_4 \cdot (\vec{q}_1 + \vec{q}_2 + \vec{q}_3)\, F_2\,(\vec{q}_1, \vec{q}_2)}{(\vec{q}_1 + \vec{q}_2)^{\,2} q_3^2 q_4^2} \\
&- \frac{2\,(\vec{q}_1 \cdot \vec{q}_2)^{\,2}\,(\vec{q}_1 \cdot \vec{q}_3 \vec{q}_2 \cdot \vec{q}_4 + \vec{q}_2 \cdot \vec{q}_3 \vec{q}_4 \cdot (\vec{q}_2 + \vec{q}_3))}{q_1^2 q_2^2 q_3^2 q_4^2}\,, \\
K_4^{r^2,3} =& \frac{((\vec{q}_1 + \vec{q}_2) \cdot (\vec{q}_3 + \vec{q}_4))^{\,2} F_2\,(\vec{q}_1, \vec{q}_2)\, F_2\,(\vec{q}_3, \vec{q}_4)}{(\vec{q}_1 + \vec{q}_2)^{\,2}\,(\vec{q}_3 + \vec{q}_4)^{\,2}} \\
&- \frac{2F_2\,(\vec{q}_1, \vec{q}_2)\,(\vec{q}_3 \cdot (\vec{q}_1 + \vec{q}_2))^{\,2} \vec{q}_4 \cdot (\vec{q}_1 + \vec{q}_2 + \vec{q}_3)}{(\vec{q}_1 + \vec{q}_2)^{\,2} q_3^2 q_4^2} \\
&+ \frac{2\,(\vec{q}_4 \cdot (\vec{q}_1 + \vec{q}_2 + \vec{q}_3))^{\,2} F_3\,(\vec{q}_1, \vec{q}_2, \vec{q}_3)}{(\vec{q}_1 + \vec{q}_2 + \vec{q}_3)^{\,2} q_4^2} - \frac{\vec{q}_3 \cdot (\vec{q}_1 + \vec{q}_2)\,(\vec{q}_3 \cdot \vec{q}_4)^{\,2} G_2\,(\vec{q}_1, \vec{q}_2)}{(\vec{q}_1 + \vec{q}_2)^{\,2} q_3^2 q_4^2}
\end{aligned}
\tag{B.92}
$$

$$
\begin{aligned}
&+\frac{\left(\vec{q}_1\cdot\vec{q}_3\vec{q}_2\cdot\vec{q}_4+\vec{q}_2\cdot\vec{q}_3\left(\vec{q}_2\cdot\vec{q}_4+\vec{q}_3\cdot\vec{q}_4\right)\right)\left(\vec{q}_1\cdot\vec{q}_2\right)^2}{q_1^2q_2^2q_3^2q_4^2}\,,\\
K_4^{\delta^3,1}=&\frac{3\vec{q}_4\cdot\vec{q}_3}{q_4^2}\,,\quad K_4^{\delta^3,2}=3F_2\left(\vec{q}_1,\vec{q}_2\right)-\frac{3\vec{q}_4\cdot\vec{q}_3}{q_4^2}\,,\\
K_4^{r^3,2}=&\frac{3\vec{q}_3\cdot\left(\vec{q}_1+\vec{q}_2\right)\vec{q}_3\cdot\vec{q}_4\vec{q}_4\cdot\left(\vec{q}_1+\vec{q}_2\right)F_2\left(\vec{q}_1,\vec{q}_2\right)}{\left(\vec{q}_1+\vec{q}_2\right)^2q_3^2q_4^2}-\frac{3\vec{q}_1\cdot\vec{q}_2\vec{q}_1\cdot\vec{q}_3\vec{q}_2\cdot\vec{q}_3\vec{q}_3\cdot\vec{q}_4}{q_1^2q_2^2q_3^2q_4^2}\,,\\
K_4^{r^2\delta,2}=&\frac{2\left(\vec{q}_3\cdot\left(\vec{q}_1+\vec{q}_2\right)\right)^2F_2\left(\vec{q}_1,\vec{q}_2\right)}{\left(\vec{q}_1+\vec{q}_2\right)^2q_3^2}\\
&+\frac{+q_4^2}{-}\frac{\vec{q}_3\cdot\vec{q}_4\left(2\left(\vec{q}_2\cdot\vec{q}_3\right)^2q_1^2+\left(\vec{q}_1\cdot\vec{q}_2\right)^2q_3^2\right)}{q_1^2q_2^2q_3^2q_4^2}\,,\\
K_4^{\delta^4,1}=&1\,,\quad K_4^{\delta r^3,1}=\frac{\vec{q}_1\cdot\vec{q}_2\vec{q}_2\cdot\vec{q}_3\vec{q}_3\cdot\vec{q}_1}{q_1^2q_2^2q_3^2},
\end{aligned}
$$

The above, combined with Eq. (6.130), defines the final biased tracer kernels K_n^h up to $n=4$. The conversion to redshift space to get $K_4^{r,h}(\vec{q}_1,\vec{q}_2,\vec{q}_3,\vec{q}_4;\hat{z})$ is then given by

$$
\begin{aligned}
K_4^{r,h}=&K_4^h(\vec{q}_1,\vec{q}_2,\vec{q}_3,\vec{q}_4)+f\mu^2G_4(\vec{q}_1,\vec{q}_2,\vec{q}_3,\vec{q}_4)\\
&+k\mu f\frac{(\vec{q}_1+\vec{q}_2+\vec{q}_3)\cdot\hat{z}}{(\vec{q}_1+\vec{q}_2+\vec{q}_3)^2}G_3(\vec{q}_1,\vec{q}_2,\vec{q}_3)K_1^h(\vec{q}_4)\\
&+k\mu f\frac{(\vec{q}_1+\vec{q}_2)\cdot\hat{z}}{(\vec{q}_1+\vec{q}_2)^2}G_2(\vec{q}_1,\vec{q}_2)K_2^h(\vec{q}_3,\vec{q}_4)+k\mu f\frac{\vec{q}_1\cdot\hat{z}}{q_1^2}K_3^h(\vec{q}_2,\vec{q}_3,\vec{q}_4)\\
&+k^2\mu^2f^2\frac{(\vec{q}_1+\vec{q}_2+\vec{q}_3)\cdot\hat{z}}{(\vec{q}_1+\vec{q}_2+\vec{q}_3)^2}\frac{\vec{q}_4\cdot\hat{z}}{q_4^2}G_3(\vec{q}_1,\vec{q}_2,\vec{q}_3)\\
&+k^2\mu^2f^2\frac{(\vec{q}_1+\vec{q}_2)\cdot\hat{z}}{(\vec{q}_1+\vec{q}_2)^2}\frac{\vec{q}_3\cdot\hat{z}}{q_3^2}G_2(\vec{q}_1,\vec{q}_2)K_1^h(\vec{q}_4)+\frac{1}{2}k^2\mu^2f^2\frac{\vec{q}_1\cdot\hat{z}}{q_1^2}\frac{\vec{q}_2\cdot\hat{z}}{q_2^2}K_2^h(\vec{q}_3,\vec{q}_4)\\
&+\frac{1}{2}k^2\mu^2f^2\frac{(\vec{q}_1+\vec{q}_2)\cdot\hat{z}}{(\vec{q}_1+\vec{q}_2)^2}\frac{(\vec{q}_3+\vec{q}_4)\cdot\hat{z}}{(\vec{q}_3+\vec{q}_4)^2}G_2(\vec{q}_1,\vec{q}_2)G_2(\vec{q}_3,\vec{q}_4)\\
&+\frac{1}{2}k^3\mu^3f^3\frac{(\vec{q}_1+\vec{q}_2)\cdot\hat{z}}{(\vec{q}_1+\vec{q}_2)^2}\frac{\vec{q}_3\cdot\hat{z}}{q_3^2}\frac{\vec{q}_4\cdot\hat{z}}{q_4^2}G_2(\vec{q}_1,\vec{q}_2)+\frac{1}{6}k^3\mu^3f^3\frac{\vec{q}_1\cdot\hat{z}}{q_1^2}\frac{\vec{q}_2\cdot\hat{z}}{q_2^2}\frac{\vec{q}_3\cdot\hat{z}}{q_3^2}K_1^h(\vec{q}_4)\\
&+\frac{1}{24}k^4\mu^4f^4\frac{\vec{q}_1\cdot\hat{z}}{q_1^2}\frac{\vec{q}_2\cdot\hat{z}}{q_2^2}\frac{\vec{q}_3\cdot\hat{z}}{q_3^2}\frac{\vec{q}_4\cdot\hat{z}}{q_4^2}\,,
\end{aligned}
\tag{B.93}
$$

where $\mu=\hat{k}\cdot\hat{z}$ and $\vec{k}\equiv\vec{q}_1+\vec{q}_2+\vec{q}_3+\vec{q}_4$, and see [133] for the analogous redshift space expression up to third order.

B.4 Details for Biased Tracers in Redshift Space Renormalization

B.4.1 Counterterm Expressions for Biased Tracers in Redshift Space

For the response counterterms, we define the kernels $K_1^{r,h,ct}$ and $K_2^{r,h,ct}$ from

$$\tilde{\delta}^{(1)}_{r,h,ct}(\vec{k},\hat{z}) = K_1^{r,h,ct}(\vec{k};\hat{z})\tilde{\delta}^{(1)}(\vec{k}) \ , \ \tilde{\delta}^{(2)}_{r,h,ct}(\vec{k},\hat{z}) = \int_{\vec{q}_1,\vec{q}_2}^{\vec{k}} K_2^{r,h,ct}(\vec{q}_1,\vec{q}_2;\hat{z})\tilde{\delta}^{(1)}(\vec{q}_1)\tilde{\delta}^{(1)}(\vec{q}_2) \ , \tag{B.94}$$

where the tilde fields are defined analogously to Eq. (6.88), just with $r \to r, h$. The response counterterms enter in

$$\begin{aligned}
&P_{13}^{r,h,ct}(k,\hat{k}\cdot\hat{z}) \equiv 2K_1^{r,h}(\vec{k};\hat{z})K_1^{r,h,ct}(-\vec{k};\hat{z})P_{11}(k) \ , \\
&B_{411}^{r,h,ct} \equiv 2P_{11}(k_1)P_{11}(k_2)K_1^{r,h}(\vec{k}_1;\hat{z})K_1^{r,h}(\vec{k}_2;\hat{z})K_2^{r,h,ct}(-\vec{k}_1,-\vec{k}_2;\hat{z}) + \ 2 \text{ perms.} \ , \\
&B_{321}^{r,h,(II),ct} \equiv 2P_{11}(k_1)P_{11}(k_2)K_1^{r,h,ct}(\vec{k}_1;\hat{z})K_1^{r,h}(\vec{k}_2;\hat{z})K_2^{r,h}(-\vec{k}_1,-\vec{k}_2;\hat{z}) + \ 5 \text{ perms.} \ ,
\end{aligned} \tag{B.95}$$

(we have suppressed the argument $(k_1,k_2,k_3,\hat{k}_1\cdot\hat{z},\hat{k}_2\cdot\hat{z})$ of the bispectra terms to remove clutter) so that the combinations

$$\begin{aligned}
&P_{13}^{r,h}(k,\hat{k}\cdot\hat{z}) + P_{13}^{r,h,ct}(k,\hat{k}\cdot\hat{z}) \ , \\
&B_{411}^{r,h}(k_1,k_2,k_3,\hat{k}_1\cdot\hat{z},\hat{k}_2\cdot\hat{z}) + B_{411}^{r,h,ct}(k_1,k_2,k_3,\hat{k}_1\cdot\hat{z},\hat{k}_2\cdot\hat{z}) \ , \\
&B_{321}^{r,h,(II)}(k_1,k_2,k_3,\hat{k}_1\cdot\hat{z},\hat{k}_2\cdot\hat{z}) + B_{321}^{r,h,(II),ct}(k_1,k_2,k_3,\hat{k}_1\cdot\hat{z},\hat{k}_2\cdot\hat{z}) \ ,
\end{aligned} \tag{B.96}$$

are renormalized.

For the stochastic terms, we write the first order solution as $\delta^{(1)}_{r,h,\epsilon}(\vec{k},\hat{z},a) = D(a)^2\tilde{\delta}^{(1)}_{r,h,\epsilon}(\vec{k},\hat{z})$ and the second order as

$$\tilde{\delta}^{(2)}_{r,h,\epsilon}(\vec{k},\hat{z}) = \int_{\vec{q}_1,\vec{q}_2}^{\vec{k}} \delta_2^{r,h,\epsilon}(\vec{q}_1,\vec{q}_2;\hat{z})\tilde{\delta}^{(1)}_{\vec{q}_2} \ , \tag{B.97}$$

The term that renormalizes $P_{22}^{r,h}$ is

$$P_{22}^{r,h,\epsilon}(k,\hat{k}\cdot\hat{z}) \equiv \langle\tilde{\delta}^{(1)}_{r,h,\epsilon}(\vec{k},\hat{z})\tilde{\delta}^{(1)}_{r,h,\epsilon}(\vec{k}',\hat{z})\rangle' \ , \tag{B.98}$$

the term that renormalizes $B_{222}^{r,h}$ is

$$B_{222}^{r,h,\epsilon}(k_1,k_2,k_3,\hat{k}_1\cdot\hat{z},\hat{k}_2\cdot\hat{z}) = \langle\tilde{\delta}_{r,h,\epsilon}^{(1)}(\vec{k}_1,\hat{z})\tilde{\delta}_{r,h,\epsilon}^{(1)}(\vec{k}_2,\hat{z})\tilde{\delta}_{r,h,\epsilon}^{(1)}(\vec{k}_3,\hat{z})\rangle' \ , \tag{B.99}$$

and the term that renormalizes $B_{321}^{r,h,(I)}$ is defined in Eqs. (6.157) and (6.158). In this way,

$$\begin{gathered} P_{22}^{r,h}(k,\hat{k}\cdot\hat{z}) + P_{22}^{r,h,\epsilon}(k,\hat{k}\cdot\hat{z}) \ , \\ B_{222}^{r,h}(k_1,k_2,k_3,\hat{k}_1\cdot\hat{z},\hat{k}_2\cdot\hat{z}) + B_{222}^{r,h,\epsilon}(k_1,k_2,k_3,\hat{k}_1\cdot\hat{z},\hat{k}_2\cdot\hat{z}) \ , \\ B_{321}^{r,h,(I)}(k_1,k_2,k_3,\hat{k}_1\cdot\hat{z},\hat{k}_2\cdot\hat{z}) + B_{321}^{r,h,(I),\epsilon}(k_1,k_2,k_3,\hat{k}_1\cdot\hat{z},\hat{k}_2\cdot\hat{z}) \ , \end{gathered} \tag{B.100}$$

are renormalized.

B.4.2 Response Terms

The functions that enter $K_2^{r,h,ct}$ in Eq. (6.154) are given by

$$\begin{aligned}
e_1^{K_2} &= -\frac{\vec{k}_1\cdot\vec{k}_2 k_2^2}{2{k_{\rm NL}}^2 k_1^2} + \frac{f\vec{k}_3\cdot\hat{z}\vec{k}_1\cdot\hat{z}k_2^2}{2{k_{\rm NL}}^2 k_1^2} + (1\leftrightarrow 2) \ , \\
e_2^{K_2} &= -\frac{k_3^2}{{k_{\rm NL}}^2}F_2(\vec{k}_1,\vec{k}_2) + \frac{\vec{k}_1\cdot\vec{k}_2}{2{k_{\rm NL}}^2}\left(\frac{k_1^2}{k_2^2}+\frac{k_2^2}{k_1^2}\right) \ , \\
e_3^{K_2} &= -\frac{k_3^2}{{k_{\rm NL}}^2} \ , \quad e_4^{K_2} = -\frac{(\vec{k}_1\cdot\vec{k}_2)^2 k_3^2}{{k_{\rm NL}}^2 k_1^2 k_2^2} \ , \quad e_5^{K_2} = -\frac{\vec{k}_1\cdot\vec{k}_2}{{k_{\rm NL}}^2} \ , \\
e_6^{K_2} &= -\frac{f\vec{k}_3\cdot\hat{z}\vec{k}_1\cdot\hat{z}\vec{k}_1\cdot\vec{k}_2}{2{k_{\rm NL}}^2 k_2^2} + \frac{f^2(\vec{k}_3\cdot\hat{z})^2\vec{k}_2\cdot\hat{z}\vec{k}_1\cdot\hat{z}}{2{k_{\rm NL}}^2 k_2^2} + (1\leftrightarrow 2) \ , \\
e_7^{K_2} &= \frac{f(\vec{k}_3\cdot\hat{z})^2\vec{k}_1\cdot\vec{k}_2\vec{k}_2\cdot\vec{k}_3\vec{k}_3\cdot\vec{k}_1}{{k_{\rm NL}}^2 k_1^2 k_2^2 k_3^2} \ , \\
e_8^{K_2} &= -\frac{f^2(\vec{k}_3\cdot\hat{z})^2\vec{k}_1\cdot\vec{k}_2(\vec{k}_1\cdot\hat{z})^2}{4{k_{\rm NL}}^2 k_1^2 k_2^2} + \frac{f^3(\vec{k}_3\cdot\hat{z})^3\vec{k}_1\cdot\hat{z}(\vec{k}_2\cdot\hat{z})^2}{4{k_{\rm NL}}^2 k_1^2 k_2^2} + (1\leftrightarrow 2) \ , \\
e_9^{K_2} &= -\frac{f^2(\vec{k}_3\cdot\hat{z})^2}{2{k_{\rm NL}}^2}\left(\frac{(\vec{k}_3\cdot\hat{z})^2}{k_3^2}F_2(\vec{k}_1,\vec{k}_2) - \frac{\vec{k}_1\cdot\vec{k}_2[(\vec{k}_1\cdot\hat{z})^2+(\vec{k}_2\cdot\hat{z})^2]}{2k_1^2k_2^2}\right) \ , \\
e_{10}^{K_2} &= -\frac{f^2(\vec{k}_3\cdot\hat{z})^2\vec{k}_1\cdot\vec{k}_2}{4{k_{\rm NL}}^2 k_2^2} + \frac{f^3(\vec{k}_3\cdot\hat{z})^3\vec{k}_2\cdot\hat{z}}{4{k_{\rm NL}}^2 k_2^2} + (1\leftrightarrow 2) \ , \\
e_{11}^{K_2} &= -\frac{f^2(\vec{k}_3\cdot\hat{z})^2}{2{k_{\rm NL}}^2}\left(F_2(\vec{k}_1,\vec{k}_2) - \frac{\vec{k}_1\cdot\vec{k}_2}{2}\left(\frac{1}{k_1^2}+\frac{1}{k_2^2}\right)\right) \ , \\
e_{12}^{K_2} &= -\frac{f^2(\vec{k}_3\cdot\hat{z})^2}{4{k_{\rm NL}}^2}\left(\frac{(\vec{k}_1\cdot\hat{z})^2}{k_1^2}+\frac{(\vec{k}_2\cdot\hat{z})^2}{k_2^2}\right) \ ,
\end{aligned} \tag{B.101}$$

$$e_{13}^{K_2} = -\frac{f^2(\vec{k}_3\cdot\hat{z})^2\vec{k}_1\cdot\hat{z}\vec{k}_2\cdot\hat{z}\vec{k}_1\cdot\vec{k}_2}{2{k_{\rm NL}}^2k_1^2k_2^2}\ , \quad e_{14}^{K_2} = -\frac{f^2(\vec{k}_3\cdot\hat{z})^2}{2{k_{\rm NL}}^2}\ ,$$

where we have defined $\vec{k}_3 \equiv -\vec{k}_1 - \vec{k}_2$. The new non-locally-contributing counterterm enters $K_2^{r,h,ct}$ through the term $e_7^{K_2}$.

The UV matching for the response terms is given by

$$\begin{aligned}
c_1^h &= \frac{\sigma^2k_{\rm NL}^2\left(3b_1 - 64\left(b_3+15b_8\right)\right)}{1260\pi^2}\ , \qquad\qquad (B.102)\\
c_2^h &= \frac{\sigma^2k_{\rm NL}^2}{679140\pi^2}\big(8\big(-792b_2 - 2926b_3 + 1522b_4 + 462\left(6b_7 - 95b_8\right)\\
&\qquad\qquad - 6215b_9 + 6930b_{11}\big) - 27335b_1\big)\ ,\\
c_3^h &= \frac{\sigma^2k_{\rm NL}^2}{4753980\pi^2}\Big(194348b_1 + 95205b_2 + 160160b_3 - 431040b_4 - 6529248b_9\\
&\qquad\qquad + 77\left(147b_5 - 5248b_7 + 31200b_8\right) - 2217600b_{11}\Big)\ ,\\
c_4^h &= \frac{\sigma^2k_{\rm NL}^2}{1584660\pi^2}\big(20559b_1 - 2\big(17677b_2 - 13552b_3 + 5664b_4 + 7392b_7\\
&\qquad\qquad - 203280b_8 + 55088b_9 + 18480b_{11}\big)\big)\ ,\\
c_5^h &= -\frac{2\sigma^2k_{\rm NL}^2}{169785\pi^2}\big(6083b_1 + 792b_2 + 1078b_3 - 6450b_4 - 7700b_7\\
&\qquad\qquad + 16170b_8 - 35673b_9 - 62370b_{11}\big)\ ,\\
c_1^\pi &= -\frac{\sigma^2k_{\rm NL}^2\left(4725b_1 + 32\left(36b_2 + 35\left(b_3+15b_8\right)\right)\right)}{30870\pi^2}\ ,\\
c_5^\pi &= \frac{668\,\sigma^2k_{\rm NL}^2}{56595\pi^2}\ ,\\
c_1^{\pi v} &= -\frac{\sigma^2k_{\rm NL}^2(35f+46)}{210\pi^2}\ , \quad c_2^{\pi v} = -\frac{\sigma^2k_{\rm NL}^2(15f+11)}{150\pi^2}\ ,\\
c_3^{\pi v} &= -\frac{\sigma^2k_{\rm NL}^2\left(147\left(35b_1+48\right)f + 9156b_1 + 2304b_2 + 2240b_3 + 33600b_8 + 9261\right)}{30870\pi^2 f}\ ,\\
c_4^{\pi v} &= \frac{\sigma^2k_{\rm NL}^2\left(-6b_2(245f+514) + 273b_1 + 448b_3 + 6720b_8 - 594f - 1785\right)}{8820\pi^2 f}\ ,\\
c_5^{\pi v} &= \frac{\sigma^2k_{\rm NL}^2\left(2394b_1 + 2304b_2 + 2240b_3 + 33600b_8 - 75\right)}{30870\pi^2}\ ,\\
c_6^{\pi v} &= -\frac{\sigma^2k_{\rm NL}^2(1715f+4626)}{25725\pi^2}\ ,\\
c_7^{\pi v} &= -\frac{\sigma^2k_{\rm NL}^2}{679140\pi^2 f}\big(924b_1(168f+97) + 3234b_5(35f-2) - 205920b_2\\
&\qquad\qquad + 19712b_3 + 295680b_8 + 111078f + 70809\big)\ ,
\end{aligned}$$

with all other coefficients set to zero (*i.e.* they are degenerate for the observables

that we consider). Above, $\sigma^2 = \int dq\, P_{11}(q)$. Notice that, as expected, the $c^{\pi v}_{\mathrm{DM},i}$ from Eq. (B.52) are related to the $c^{\pi v}_i$ above when the biases are evaluated on the dark-matter values $b_1 = b_2 = b_3 = b_4 = 1$ and $b_5, \ldots, b_{15} = 0$. Using the expression for $F_1^{r,ct}$ in Eq. (6.100), the expression for $K_1^{r,h,ct}$ in Eq. (6.153), the expression for $F_2^{r,ct}$ in Eq. (6.101), the expression for $K_2^{r,h,ct}$ in Eq. (6.154), and the basis relation Eq. (B.51), we find $c^{\pi v}_j\big|_{\text{DM bias}} = c^{\pi v}_{\mathrm{DM},j}$ for $j = 1, 2, 6$, and

$$\begin{aligned}
c^{\pi v}_3\big|_{\text{DM bias}} &= c^{\pi v}_{\mathrm{DM},3} + \frac{2}{3f}c_3 + \frac{4}{9f}c_5 \ , \\
c^{\pi v}_4\big|_{\text{DM bias}} &= c_{\mathrm{DM},4} + \frac{7}{99f}c_3 + \frac{16}{33f}c_4 - \frac{7}{99f}c_5 \ , \\
c^{\pi v}_5\big|_{\text{DM bias}} &= c^{\pi v}_{\mathrm{DM},5} - \frac{2}{3}c_3 - \frac{4}{9}c_5 \ , \\
c^{\pi v}_7\big|_{\text{DM bias}} &= c^{\pi v}_{\mathrm{DM},7} + \frac{8}{99f}c_3 + \frac{29}{99f}c_5 + \frac{16}{33f}c_7 \ ,
\end{aligned} \tag{B.103}$$

where $c|_{\text{DM bias}}$ means to evaluate c on the dark-matter values for the bias parameters, which one can indeed confirm is true for the UV matching that we found in Eqs. (B.37), (B.52), and (B.102).

B.4.3 Stochastic Terms

The functions that enter the stochastic counterterm $\bar{B}^{r,h,(I),\epsilon}_{321}$ in Eq. (6.159) are

$$\begin{aligned}
e^{\mathrm{St}}_1 &= f\mu_1^2 - 1 \ , \\
e^{\mathrm{St}}_2 &= -\frac{k_1^2\left(k_2^2\left(1-2f\mu_1^2\right)+k_3^2\right)+2f\left(k_3^2-k_2^2\right)k_1\mu_1 k_2\mu_2+\left(k_2^2-k_3^2\right)^2}{2k_1^2k_{\mathrm{NL}}^2} \ , \\
e^{\mathrm{St}}_3 &= 0 \ , \\
e^{\mathrm{St}}_4 &= -\frac{f^2k_1\mu_1}{4k_1^2k_{\mathrm{NL}}^2}\Big(k_1^3\mu_1\left(2f\mu_1^2-1\right)+4fk_1^2\mu_1^2k_2\mu_2 \\
&\qquad\qquad + k_1\mu_1\left(k_2^2\left(4f\mu_2^2-1\right)+k_3^2\right)+2\left(k_3^2-k_2^2\right)k_2\mu_2\Big) \ , \\
e^{\mathrm{St}}_5 &= \frac{f^2k_1\mu_1\left(4fk_1^2\mu_1^2k_2\mu_2+k_1\mu_1\left(k_2^2\left(4f\mu_2^2-1\right)+k_3^2\right)+k_1^3\mu_1+2\left(k_3^2-k_2^2\right)k_2\mu_2\right)}{4k_1^2k_{\mathrm{NL}}^2} \ , \\
e^{\mathrm{St}}_6 &= 2 \ , \quad e^{\mathrm{St}}_7 = -\frac{k_2^2+k_3^2}{k_{\mathrm{NL}}^2} \ , \quad e^{\mathrm{St}}_8 = -\frac{k_1^4+\left(k_2^2-k_3^2\right)^2}{2k_1^2k_{\mathrm{NL}}^2} \ , \\
e^{\mathrm{St}}_9 &= -\frac{k_1^2}{k_{\mathrm{NL}}^2} \ , \quad e^{\mathrm{St}}_{10} = -\frac{f\left(k_1\mu_1+2k_2\mu_2\right)\left(\left(k_1^2-k_2^2+k_3^2\right)k_1\mu_1+2k_1^2k_2\mu_2\right)}{4k_1^2k_{\mathrm{NL}}^2} \ ,
\end{aligned} \tag{B.104}$$

$$
\begin{aligned}
e_{11}^{\rm St} &= \frac{f k_1\mu_1\left(\left(k_1^2+k_2^2-k_3^2\right)k_1\mu_1+2\left(k_2^2-k_3^2\right)k_2\mu_2\right)}{2k_1^2k_{\rm NL}^2}\,,\\
e_{12}^{\rm St} &= -\frac{2f k_2\mu_2\left(k_1\mu_1+k_2\mu_2\right)}{k_{\rm NL}^2}\,,\\
e_{13}^{\rm St} &= \frac{f}{4k_1^2k_2^2k_3^2k_{\rm NL}^2}\Big(\left(k_1^2-k_2^2+k_3^2\right)^2k_1^2\mu_1^2k_2^2+2\left(k_1^2-k_2^2+k_3^2\right)^2k_1\mu_1k_2^3\mu_2\\
&\qquad+\left(\left(k_2^2+k_3^2\right)k_1^4-2\left(k_2^2-k_3^2\right)^2k_1^2+\left(k_2^2-k_3^2\right)^2\left(k_2^2+k_3^2\right)\right)k_2^2\mu_2^2\Big)\,.
\end{aligned}
$$

All of the above $e_i^{\rm St}$ are symmetric when swapping $\vec{k}_2$ and $\vec{k}_3$, as expected from Eq. (6.158). To see it, one must swap $k_2 \leftrightarrow k_3$ and $\mu_2 \leftrightarrow \mu_3$, and then replace $\mu_3 = -k_3^{-1}(k_1\mu_1 + k_2\mu_2)$.

Since, for the stochastic terms, we match terms of order k^0 and k^2, there are non-zero contributions coming from expanding factors of $P_{11}(|\vec{k}-\vec{q}|)$ for small k/q inside of the loops in Eq. (6.123). Thus, UV matching includes terms proportional to $P'_{11}(q)$ and $P''_{11}(q)$. We give the full expressions for all terms below, apart from $c_7^{\rm St}$ and $c_8^{\rm St}$, which are too long to display here; all full values are given in the accompanying Mathematica notebook of [2]. For the UV matching, we find

$$
\begin{aligned}
c_1^{\rm St} &= -\frac{\omega^2\bar{n}\left(-b_1+b_2+b_5\right)^2}{\pi^2}\,, \qquad\qquad (B.105)\\
c_2^{\rm St} &= \frac{\bar{n}k_{\rm NL}^2\left(b_1-b_2-b_5\right)\left[\left(14b_1-16b_2\right)\gamma^2-7(b_1-b_2-b_5)(2\gamma_1^2+\gamma_2^2)\right]}{42\pi^2}\,,\\
c_3^{\rm St} &= -\frac{\gamma^2\bar{n}k_{\rm NL}^2\left(b_1-b_2-b_5\right)\left(-7b_1+7f+9\right)}{21\pi^2}\,,\\
c_4^{\rm St} &= \frac{\gamma^2\bar{n}k_{\rm NL}^2\left(b_1(35f+54)-35\left(b_2+b_5\right)f-2\left(19b_2+8b_3+23b_5+8b_6+22b_8\right)\right)}{105\pi^2 f}\,,\\
c_5^{\rm St} &= 0\,,\\
c_6^{\rm St} &= -\frac{\omega^2\bar{n}\left(b_1-b_2-b_5\right)\left(13b_1+34b_2-47b_3+42b_5-110b_6-82b_8-63b_{10}\right)}{21\pi^2}\,,\\
c_7^{\rm St} &= -\frac{\gamma^2\bar{n}k_{\rm NL}^2}{1470\pi^2}\Big(301b_1^2+\left(656b_2-7\left(183b_3-124b_5+282b_6+638b_8+105b_{10}\right)\right)b_1\\
&\quad-982b_2^2+14b_5\left(47b_3-35b_5+44b_6+236b_8\right)\\
&\quad+2b_2\left(653b_3-784b_5+1052b_6+2228b_8+420b_{10}\right)\Big)+\mathcal{O}(P'_{11}(q),P''_{11}(q))\,,\\
c_8^{\rm St} &= \frac{\gamma^2\bar{n}k_{\rm NL}^2}{4410\pi^2}\Big(-21b_1^2+\left(1689b_2-7\left(122b_3-51b_5+168b_6+192b_8\right)\right)b_1-1188b_2^2\\
&\quad+2\left(\left(187b_3-546b_5+348b_6+12b_8\right)b_2+7b_5\left(13b_3+36b_6-36b_8\right)\right)\Big)\\
&\quad+\mathcal{O}(P'_{11}(q),P''_{11}(q))\,,
\end{aligned}
$$

$$
\begin{aligned}
c_9^{\rm St} &= -\frac{\gamma^2\bar{n}k_{\rm NL}^2\,(7b_1-6b_2-14b_5)\,(b_1-b_2-b_5)}{42\pi^2}\,,\\
c_{10}^{\rm St} &= \frac{\gamma^2\bar{n}k_{\rm NL}^2}{735\pi^2}\Big(7b_1^2(35f+22)+b_1\big(-7b_2(35f+79)-7b_5(35f+103)+399b_3\\
&\qquad +1134b_6+546b_8+735b_{10}+224f+256\big)\\
&\qquad +b_2(287f+417)-7\,(73b_3-57b_5+178b_6+122b_8+105b_{10})\,f\\
&\qquad -673b_3+553b_5-1618b_6-1142b_8-945b_{10}\Big)\,,\\
c_{11}^{\rm St} &= \frac{\gamma^2\bar{n}k_{\rm NL}^2}{1470\pi^2}\Big(7b_1^2(6-35f)\\
&\quad +b_1\Big(7b_2(35f+123)+49b_5(5f+13)-623b_3-1358b_6-1162b_8\\
&\qquad\qquad -735b_{10}-469f-634\Big)\\
&\quad +511b_3f-154b_5f-b_2\,(280b_5+42f+151)+1246b_6f\\
&\quad +854b_8f+105b_{10}(7f+9)-280b_2^2+785b_3-231b_5+1730b_6+1450b_8\Big)\,,\\
c_{12}^{\rm St} &= \frac{\gamma^2\bar{n}k_{\rm NL}^2\,(7b_1^2+(-109b_2+32b_3-93b_5+32b_6+88b_8)\,b_1+70\,(b_2+b_5)^{\,2})}{210\pi^2}\,,\\
c_{13}^{\rm St} &= \frac{\gamma^2\bar{n}k_{\rm NL}^2\,(-97b_1+b_2+96b_3+49b_5+96b_6+264b_8)}{1470\pi^2}\,,
\end{aligned}
$$

where $\gamma^2=\int dq\,P_{11}(q)^2$, $\gamma_1^2=\int dq\,qP_{11}(q)P'_{11}(q)$,
$\gamma_2^2=\int dq\,q^2P_{11}(q)P''_{11}(q)$, and $\omega^2=\int dq\,q^2\,P_{11}(q)^2$. UV matching for Eq. (6.160) is

$$
\begin{aligned}
c_1^{(222)} &= \frac{4(b_1-b_2-b_5)^3\bar{n}^2}{\pi^2}\int dq\,q^2P_{11}(q)^3\,, \qquad\qquad (B.106)\\
c_2^{(222)} &= \frac{2(b_1-b_2-b_5)^2\bar{n}^2{k_{\rm NL}}^2}{63\pi^2}\left(3(7b_1-8b_2)\vartheta^3-7(b_1-b_2-b_5)(4\vartheta_1^3+\vartheta_2^3+2\vartheta_3^3)\right)\,,\\
c_5^{(222)} &= \frac{4(b_1-b_2-b_5)^2(-9+7b_1-7f)f\bar{n}^2{k_{\rm NL}}^2\vartheta^3}{21\pi^2}\,.
\end{aligned}
$$

where $\vartheta^3=\int dq\,P_{11}(q)^3$, $\vartheta_1^3=\int dq\,qP_{11}(q)^2P'_{11}(q)$, $\vartheta_2^3=\int dq\,q^2P_{11}(q)P'_{11}(q)^2$, and $\vartheta_3^3=\int dq\,q^2P_{11}(q)^2P''_{11}(q)$.

B.4.4 Parameter Matching with `PyBird`

For reference, we give the conversion between the parameters used here and those used in `PyBird` (which we write in the `typewriter font`). For the counterterm

parameters, we have

$$\begin{aligned}
&\texttt{Bc1} = c_1^h \ , \texttt{Bc2} = c_1^\pi \ , \texttt{Bc3} = c_1^{\pi v} \ , \texttt{Bc4} = c_3^{\pi v} \ , \texttt{Bc5} = c_2^h \ , \texttt{Bc6} = c_3^h \ , \texttt{Bc7} = c_4^h \\
&\texttt{Bc8} = c_5^h \ , \texttt{Bc9} = c_5^\pi \ , \texttt{Bc10} = c_2^{\pi v} \ , \texttt{Bc11} = c_4^{\pi v} \ , \texttt{Bc12} = c_5^{\pi v} \ , \texttt{Bc13} = c_6^{\pi v} \ , \\
&\texttt{Bc14} = c_7^{\pi v} \ , \texttt{ce2} = (2/3) f c_3^{\rm St} \ , \texttt{Be1} = c_1^{\rm St} \ , \texttt{Be2} = c_2^{\rm St} \ , \texttt{Be3} = c_4^{\rm St} \ , \texttt{Be4} = c_5^{\rm St} \ , \\
&\texttt{Be5} = 2c_6^{\rm St} \ , \texttt{Be6} = 2c_9^{\rm St} \ , \texttt{Be7} = -c_7^{\rm St} - c_9^{\rm St} \ , \texttt{Be8} = -c_8^{\rm St} - 2c_9^{\rm St} \ , \texttt{Be9} = 2c_{12}^{\rm St} \\
&\texttt{Be10} = c_{11}^{\rm St} \ , \texttt{Be11} = c_{10}^{\rm St} \ , \texttt{Be12} = c_{13}^{\rm St} \ , \\
&\texttt{Bd1} = c_1^{(222)} \ , \texttt{Bd2} = c_2^{(222)} - c_5^{(222)}/6 \ , \quad \text{and} \quad \texttt{Bd3} = -c_5^{(222)} \ .
\end{aligned} \tag{B.107}$$

For the bias parameters, we have $\texttt{Bbi} = b_i$ for $i = 1, \ldots, 6, 8, \ldots, 11$, and $\texttt{Bb7} = b_7 + 15 b_{13}/2$. Other parameters in the `PyBird` code are derived from the ones above, and were used in the power-spectrum-only analysis. These are given by

$$\begin{aligned}
&\texttt{b1} = \texttt{Bb1} \ , \quad \texttt{b2} = \texttt{Bb2} \ , \ \texttt{b3} = \texttt{Bb3} + 15\,\texttt{Bb8} \ , \ \texttt{b4} = \texttt{Bb5} \ , \ \texttt{cct} = -\texttt{Bc1} \ , \\
&\texttt{cr1} = f\texttt{Bc2} - f^2\texttt{Bc4}/2 \ , \ \texttt{cr2} = -f^2\texttt{Bc3}/2 \ , \ \texttt{ce0} = \texttt{Be1} \ , \ \texttt{ce1} = \texttt{Be2} + \texttt{ce2}/2 \ , \\
&\texttt{c2} = (\texttt{b2} + \texttt{b4})/\sqrt{2} \ , \quad \text{and} \quad \texttt{c4} = (\texttt{b2} - \texttt{b4})/\sqrt{2} \ .
\end{aligned} \tag{B.108}$$

C

Appendix: The One-Loop Bispectrum - Constraints

C.1 Binning Formula Details

In this appendix, we want to show that the binning formula for the bispectrum

$$B^{r,h}_{(l,i),\mathrm{bin}}(k_1,k_2,k_3) = \\ = \frac{2l+1}{V_T}\left(\prod_i \int_{V_i} \frac{\mathrm{d}^3 q_i}{(2\pi)^3}\right)(2\pi)^3\delta_D^{(3)}(\vec{q}_1+\vec{q}_2+\vec{q}_3)\mathcal{P}_l(\mu_i)B^{r,h}(\vec{q}_1,\vec{q}_2,\vec{q}_3)\ , \tag{C.1}$$

is equivalent to

$$B^{r,h}_{(l,i),\mathrm{bin}}(k_1,k_2,k_3) = \frac{1}{V_T}\left(\prod_i \int_{k_i} \mathrm{d}q_i\, q_i\right)\frac{\beta\left(\Delta_q\right)}{8\pi^4}B^{r,h}_{(l,i)}(q_1,q_2,q_3)\ , \tag{C.2}$$

We do the calculation here for general l, which is relevant to us for $l = 0, 2$.

Given that the bispectrum is a polynomial in μ_1 and μ_2, and switching to a basis of Legendre polynomials, we can write

$$B^{r,h}(\vec{q}_1,\vec{q}_2,\vec{q}_3) = \sum_{n_1,n_2} B^{r,h}_{n_1,n_2}(q_1,q_2,q_3)\mathcal{P}_{n_1}(\mu_1)\mathcal{P}_{n_2}(\mu_2)\,. \tag{C.3}$$

We can focus on the case of $\mathcal{P}_l(\mu_1)$, since the other cases just correspond to a permutation of μ_i in Eq. (C.3). Let us then start by writing the delta function as an integral over plane waves:

$$B^{r,h}_{(l,1),\mathrm{bin}} = \frac{2l+1}{V_T}\left(\prod_i \int_{V_i} \frac{\mathrm{d}^3 q_i}{(2\pi)^3}\right)\int \mathrm{d}^3x\, e^{i\vec{x}\cdot(\vec{q}_1+\vec{q}_2+\vec{q}_3)}\mathcal{P}_l(\mu_1) \\ \times \sum_{n_1,n_2} B^{r,h}_{n_1,n_2}(q_1,q_2,q_3)\mathcal{P}_{n_1}(\mu_1)\mathcal{P}_{n_2}(\mu_2)\,. \tag{C.4}$$

The integral over $\mathrm{d}^2\hat{q}_3$, is just

$$\int \mathrm{d}^2\hat{q}_3\, e^{i\vec{q}_3\cdot\vec{x}} = 4\pi j_0(q_3 x)\,. \tag{C.5}$$

And the rest of the exponentials we expand the plane wave:

$$e^{i\vec{q}_1\cdot\vec{x}} = \sum_{l_1} i^{l_1}(2l_1+1) j_{l_1}(q_1 x)\mathcal{P}_{l_1}(\hat{q}_1\cdot\hat{x}). \tag{C.6}$$

Putting all of this into Eq. (C.4) we get:

$$\begin{aligned} B^{r,h}_{(l,1),\mathrm{bin}} = \frac{2l+1}{V_T}\sum_{n_1,n_2}\sum_{l_1,l_2}\left(\prod_{i=1}^{2} i^{l_i}(2l_i+1)\int_{V_i}\frac{\mathrm{d}^3 q_i}{(2\pi)^3}\right)\int_{k_3}\frac{\mathrm{d}q_3}{2\pi^2}q_3^2 B^{r,h}_{n_1,n_2}(q_1,q_2,q_3) \\ \times\int \mathrm{d}^3x j_0(q_3 x)\left(\prod_{i=1}^{2} j_{l_i}(q_i x)\mathcal{P}_{l_i}(\hat{q}_i\cdot\hat{x})\mathcal{P}_{n_i}(\hat{q}_i\cdot\hat{z})\right)\mathcal{P}_l(\hat{q}_1\cdot\hat{z})\,. \end{aligned} \tag{C.7}$$

Now we can do all the angular integrals, using the formula,

$$\int \mathrm{d}^2\hat{x}\mathcal{P}_{l_1}(\hat{q}_1\cdot\hat{x})\mathcal{P}_{l_2}(\hat{q}_2\cdot\hat{x}) = \delta_{l_1,l_2}\frac{4\pi}{2l_1+1}\mathcal{P}_{l_1}(\hat{q}_1\cdot\hat{q}_2)\ , \tag{C.8}$$

to evaluate

$$\begin{aligned} &\int \mathrm{d}^2\hat{x}\int \mathrm{d}^2\hat{q}_1\int \mathrm{d}^2\hat{q}_2\,\mathcal{P}_{l_1}(\hat{q}_1\cdot\hat{x})\mathcal{P}_{l_2}(\hat{q}_2\cdot\hat{x})\mathcal{P}_l(\hat{q}_1\cdot\hat{z})\mathcal{P}_{n_1}(\hat{q}_1\cdot\hat{z})\mathcal{P}_{n_2}(\hat{q}_2\cdot\hat{z}) \\ &= \delta_{l_1,l_2}\frac{4\pi}{2l_1+1}\int \mathrm{d}^2\hat{q}_1\int \mathrm{d}^2\hat{q}_2\,\mathcal{P}_{l_1}(\hat{q}_1\cdot\hat{q}_2)\mathcal{P}_l(\hat{q}_1\cdot\hat{z})\mathcal{P}_{n_1}(\hat{q}_1\cdot\hat{z})\mathcal{P}_{n_2}(\hat{q}_2\cdot\hat{z}) \\ &= \delta_{l_1,l_2}\,\delta_{l_1,n_2}\frac{(4\pi)^2}{(2l_1+1)^2}\int \mathrm{d}^2\hat{q}_1\,\mathcal{P}_{l_1}(\hat{q}_1\cdot\hat{z})\mathcal{P}_l(\hat{q}_1\cdot\hat{z})\mathcal{P}_{n_1}(\hat{q}_1\cdot\hat{z}) \\ &= \delta_{l_1,l_2}\,\delta_{l_1,n_2}\frac{(4\pi)^3}{(2l_1+1)^2}\begin{pmatrix} n_2 & l & n_1 \\ 0 & 0 & 0\end{pmatrix}^2\ , \end{aligned} \tag{C.9}$$

and additionally we used the integral of three Legendre polynomials in terms of the Wigner 3-j symbol in the last line. We are now only left with integrals over the

magnitudes:

$$B^{r,h}_{(l,1),\mathrm{bin}} = 4\pi\frac{(2l+1)}{V_T}\sum_{n_1,n_2}(-1)^{n_2}\left(\prod_{i=1}^{3}\int_{k_i}\frac{\mathrm{d}q_i}{2\pi^2}q_i^2\right) \times\int_0^\infty \mathrm{d}x x^2 j_{n_2}(q_1x)j_{n_2}(q_2x)j_0(q_3x)\begin{pmatrix} n_2 & l & n_1\\ 0 & 0 & 0\end{pmatrix}^2 B^{r,h}_{n_1,n_2}(q_1,q_2,q_3)\,. \tag{C.10}$$

Further using the following integral over three spherical Bessel functions:

$$\int_0^\infty \mathrm{d}x x^2 j_{n_2}(q_1x)j_{n_2}(q_2x)j_0(q_3x) = \frac{\pi}{4q_1q_2q_3}\beta(\hat{q}_1\cdot\hat{q}_2)\mathcal{P}_{n_2}\left(\frac{q_1^2+q_2^2-q_3^2}{2q_1q_2}\right)\,, \tag{C.11}$$

where $\beta(\Delta)=1$ for $-1<\Delta<1$, $\beta(\Delta)=1/2$ for $\Delta=\pm1$, and $\beta(\Delta)=0$ otherwise, and recognizing that the last Legendre is $\mathcal{P}_{n_2}(-\hat{q}_1\cdot\hat{q}_2)=(-1)^{n_2}\mathcal{P}_{n_2}(\hat{q}_1\cdot\hat{q}_2)$, we can put everything together and we get that Eq. (C.1) reduces to

$$B^{r,h}_{(l,1),\mathrm{bin}} = \frac{2l+1}{V_T}\sum_{n_1,n_2}\left(\prod_{i=1}^{3}\int_{k_i}\mathrm{d}q_i q_i\right)\times \times\frac{\beta(\hat{q}_1\cdot\hat{q}_2)}{8\pi^4}\mathcal{P}_{n_2}(\hat{q}_1\cdot\hat{q}_2)\begin{pmatrix} n_2 & l & n_1\\ 0 & 0 & 0\end{pmatrix}^2 B^{r,h}_{n_1,n_2}(q_1,q_2,q_3)\,. \tag{C.12}$$

To get our formula Eq. (C.2), it is now sufficient to show that the unbinned bispectrum satisfies

$$B^{r,h}_{(l,1)}(q_1,q_2,q_3) = (2l+1)\sum_{n_1,n_2}\mathcal{P}_{n_2}(\hat{q}_1\cdot\hat{q}_2)\begin{pmatrix} n_2 & l & n_1\\ 0 & 0 & 0\end{pmatrix}^2 B^{r,h}_{n_1,n_2}(q_1,q_2,q_3)\,. \tag{C.13}$$

So next, we write the left hand side of the above explicitly, and expand the redshift space bispectrum, plugging Eq. (C.3) into a generalization of Eqs. (7.5) and (7.8):

$$B^{r,h}_{(l,1)}(q_1,q_2,q_3) = (2l+1)\sum_{n_1,n_2}\int_{-1}^{1}\frac{\mathrm{d}\mu_1}{2}\int_0^{2\pi}\frac{\mathrm{d}\phi}{2\pi}\mathcal{P}_l(\mu_1)\mathcal{P}_{n_1}(\mu_1)\mathcal{P}_{n_2}(\mu_2)B^{r,h}_{n_1,n_2}(q_1,q_2,q_3). \tag{C.14}$$

This can be calculated in a coordinate system in which we fix $\hat{q}_1$, $\hat{q}_2$ and integrate over $\mathrm{d}^2\hat{z}$:

$$B^{r,h}_{(l,1)}(q_1,q_2,q_3) = (2l+1)\sum_{n_1,n_2}\int\frac{\mathrm{d}^2\hat{z}}{4\pi}\mathcal{P}_l(\hat{q}_1\cdot\hat{z})\mathcal{P}_{n_1}(\hat{q}_1\cdot\hat{z})\mathcal{P}_{n_2}(\hat{q}_2\cdot\hat{z})B^{r,h}_{n_1,n_2}(q_1,q_2,q_3)\,. \tag{C.15}$$

Next, we use that the product of two Legendre polynomials is

$$\mathcal{P}_l(\hat{q}_1\cdot\hat{z})\mathcal{P}_{n_1}(\hat{q}_1\cdot\hat{z}) = \sum_{L=|n_1-l|}^{n_1+l}(2L+1)\begin{pmatrix} n_1 & l & L \\ 0 & 0 & 0\end{pmatrix}^2 \mathcal{P}_L(\hat{q}_1\cdot\hat{z})\ , \tag{C.16}$$

and plug Eq. (C.16) into Eq. (C.15) to get

$$\begin{aligned} B^{r,h}_{(l,1)}(q_1,q_2,q_3) &= (2l+1)\sum_{n_1,n_2}\sum_{L=|n_1-l|}^{n_1+l}(2L+1)\begin{pmatrix} n_1 & l & L \\ 0 & 0 & 0\end{pmatrix}^2 \\ &\qquad\times\int\frac{\mathrm{d}^2\hat{z}}{4\pi}\mathcal{P}_L(\hat{q}_1\cdot\hat{z})\mathcal{P}_{n_2}(\hat{q}_2\cdot\hat{z})B^{r,h}_{n_1,n_2}(q_1,q_2,q_3) \\ &= (2l+1)\sum_{n_1,n_2}\begin{pmatrix} n_1 & l & L \\ 0 & 0 & 0\end{pmatrix}^2 \mathcal{P}_{n_2}(\hat{q}_1\cdot\hat{q}_2)B^{r,h}_{n_1,n_2}(q_1,q_2,q_3)\ , \end{aligned} \tag{C.17}$$

as desired.

For completeness we also calculate the volume

$$\begin{aligned} V_T &= \left(\prod_i\int_{V_i}\frac{\mathrm{d}^3q_i}{(2\pi)^3}\right)(2\pi)^3\delta_D^{(3)}(\vec{q}_1+\vec{q}_2+\vec{q}_3) \\ &= \left(\prod_i\int_{V_i}\frac{\mathrm{d}^3q_i}{(2\pi)^3}\right)\int\mathrm{d}^3x\, e^{i\vec{q}_1\cdot\vec{x}}e^{i\vec{q}_2\cdot\vec{x}}e^{i\vec{q}_3\cdot\vec{x}}\,. \end{aligned}$$

We then integrate over the plane waves using Eq. (C.5) and the three Bessel functions using Eq. (C.11) to get

$$V_T = \left(\prod_i\int_{k_i}\mathrm{d}q_i\,q_i\right)\frac{\beta(\hat{q}_1\cdot\hat{q}_2)}{8\pi^4}\ . \tag{C.18}$$

C.2 Additional Parameter Posteriors

In Fig. C.1, we show the full triangle plots obtained fitting BOSS 4 skies $P_\ell + B_0 + B_2$. In Tab. C.1, we show the 68%-credible intervals of b_1, c_2, and c_4 obtained on this same fit.

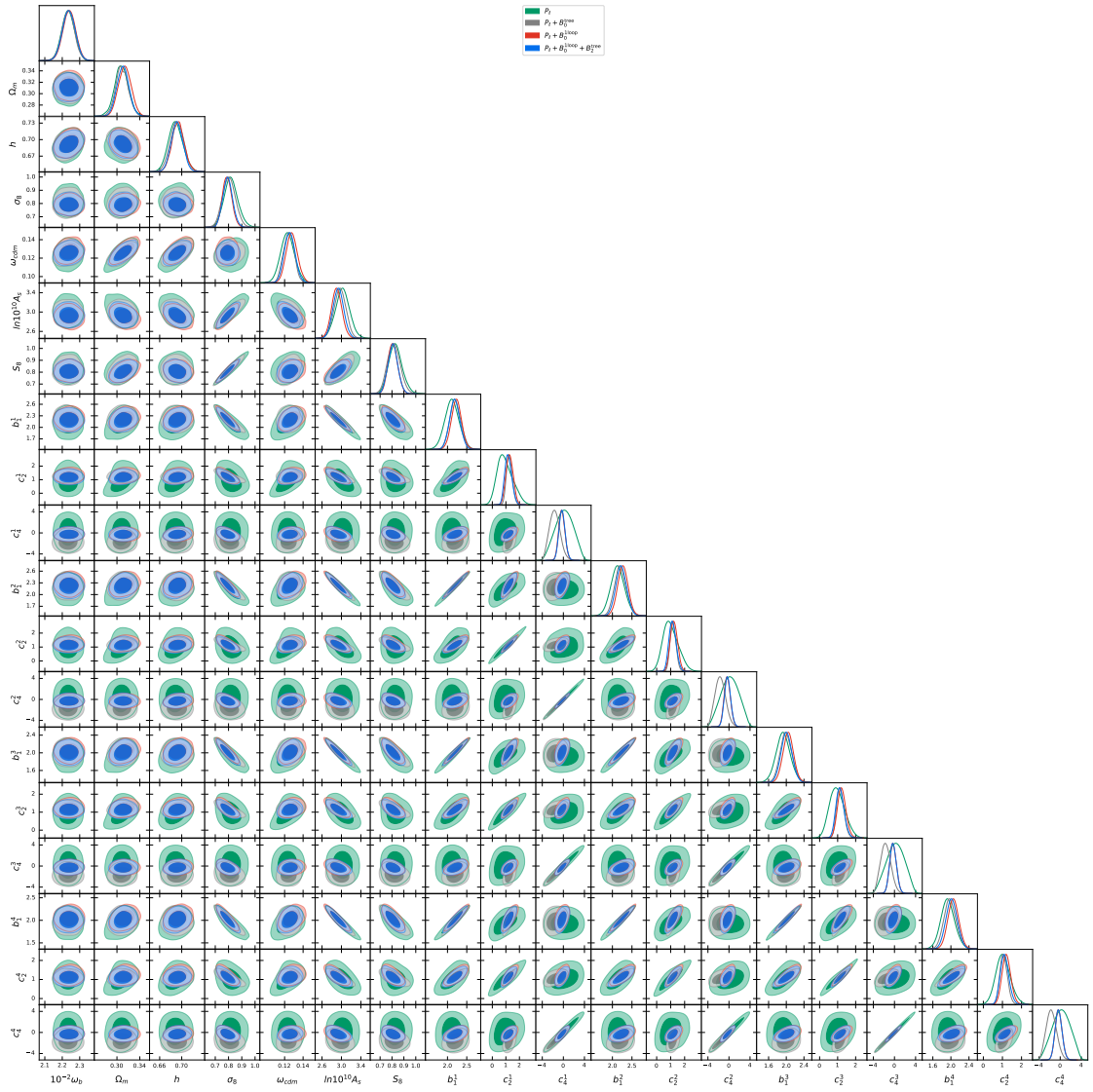

Figure C.1: Full triangle plots from the analysis of BOSS power spectrum multipoles P_ℓ at one loop, bispectrum monopole B_0 at tree level or one loop, and bispectrum quadrupole B_2 at tree level.

mean $\pm\sigma$		b_1	c_2	c_4
CMASS NGC	P_ℓ	2.12 ± 0.18	$0.95^{+0.45}_{-0.68}$	0.2 ± 1.7
	$P_\ell + B_0$	2.23 ± 0.13	1.27 ± 0.26	$-0.29^{+0.55}_{-0.61}$
	$P_\ell + B_0 + B_2$	2.19 ± 0.13	$1.18^{+0.22}_{-0.28}$	$-0.25^{+0.54}_{-0.60}$
CMASS SGC	P_ℓ	2.13 ± 0.18	$1.01^{+0.45}_{-0.62}$	0.2 ± 1.7
	$P_\ell + B_0$	2.27 ± 0.13	1.23 ± 0.26	$-0.32^{+0.56}_{-0.63}$
	$P_\ell + B_0 + B_2$	2.22 ± 0.14	$1.14^{+0.23}_{-0.27}$	-0.27 ± 0.60
LOWZ NGC	P_ℓ	1.93 ± 0.16	$0.98^{+0.37}_{-0.47}$	0.2 ± 1.7
	$P_\ell + B_0$	2.04 ± 0.12	$1.23^{+0.21}_{-0.24}$	-0.26 ± 0.64
	$P_\ell + B_0 + B_2$	2.00 ± 0.12	$1.14^{+0.20}_{-0.24}$	$-0.27^{+0.60}_{-0.67}$
LOWZ SGC	P_ℓ	1.93 ± 0.15	$1.04^{+0.34}_{-0.40}$	0.2 ± 1.7
	$P_\ell + B_0$	2.05 ± 0.12	$1.21^{+0.21}_{-0.24}$	-0.30 ± 0.65
	$P_\ell + B_0 + B_2$	2.02 ± 0.12	$1.12^{+0.20}_{-0.24}$	$-0.30^{+0.61}_{-0.68}$

Table C.1: 68%-credible intervals of b_1, c_2, and c_4 from the analysis of BOSS power spectrum multipoles P_ℓ at the one-loop, bispectrum monopole B_0 at the one-loop, and bispectrum quadrupole B_2 at tree-level.

D

Appendix: The One-Loop Bispectrum - Forecast

D.1 Survey Details and Best-Fits

Shown below are the exact parameter values that we use in the analyzes for each survey. Regarding cosmological parameters, for all surveys, we use the following best-fit as the reference cosmology [1] for the cosmological parameters (noted with a $^{\text{ref}}$).

$$h^{\text{ref}} = 0.673\,,\ \ln\left(10^{10}A_s\right)^{\text{ref}} = 3.044\,,\ \Omega_m^{\text{ref}} = 0.317\,,\ n_s^{\text{ref}} = 0.965\,, \tag{D.1}$$
$$\Omega_k^{\text{ref}} = 0\,,\ \omega_b^{\text{ref}} = 0.022\,,\ \sum_i m_{\nu_i}^{\text{ref}} = 0.1\,\text{eV}\,,\ f_{\text{NL}}^{\text{loc.,ref}} = f_{\text{NL}}^{\text{eq.,ref}} = f_{\text{NL}}^{\text{orth.,ref}} = 0\,.$$

Furthermore, in Tab. D.1 we give the EFT parameter best-fit that we use, coming from Ch. 7. Note, this is what we denote as $\vec{b}_{\text{BOSS}}$ (`b1` - `Bc14`) and $\vec{\epsilon}_{\text{BOSS}}$ (`Bd1` - `Be12`) in Sec. 8.3.3. Furthermore, we use the notation as in `PyBird` [169]. For a conversion to the notation of Ch. 7, see App. B.4.4. The best-fit values of the 41 EFT parameters are given in Tab. D.1.

Next, we show the survey specifications that were used in each survey. With the methods from Sec. 8.3, this builds the basis for the numerical values that we use in the forecasts.

BOSS For the BOSS survey, we use the survey specifications as presented in [9, 189, 283, 284]. We display them in the same way they enter our formulas in Tab. D.2.

[1] All cosmological parameters with the exception of f_{NL} and $\sum_i m_{\nu_i}$ are fixed to Planck preferred values [24].

Parameter	Value	Parameter	Value	Parameter	Value	Parameter	Value
b1	1.94	c2	1.14	b3	−0.37	c4	−0.29
b4	0.13	b6	−0.35	b7	0.22	b8	−0.30
b9	0.015	b10	0.043	b11	0.036	Bc1	5.46
Bc2	−1.54	Bc3	1.31	Bc4	−0.48	Bc5	0.11
Bc6	0.87	Bc7	−0.46	Bc8	0.44	Bc9	−0.42
Bc10	−0.65	Bc11	−0.088	Bc12	−0.37	Bc13	−0.16
Bc14	−0.20	Bd1	5.4	Bd2	−0.72	Bd3	−0.43
ce2	0.55	Be1	1.69	Be2	0.91	Be3	0.074
Be4	−0.14	Be5	6.07	Be6	−0.093	Be7	−0.97
Be8	0.26	Be9	0.26	Be10	−0.15	Be11	0.43
Be12	−0.43						

Table D.1: Best-fit EFT parameters.

z	N_g	$V[(\mathrm{Mpc}\,h^{-1})^3]$	$n_b[(h\,\mathrm{Mpc}^{-1})^3]$	b_1
0.05	7370	2.55×10^7	2.9×10^{-4}	1.48
0.15	47560	1.64×10^8	2.9×10^{-4}	1.56
0.25	120600	4.02×10^8	3.0×10^{-4}	1.65
0.35	214016	7.04×10^8	3.0×10^{-4}	1.73
0.45	287040	1.04×10^9	2.8×10^{-4}	1.83
0.55	445740	1.38×10^9	3.2×10^{-4}	1.92
0.65	206400	1.72×10^9	1.2×10^{-4}	2.02
0.75	20400	2.04×10^9	1.0×10^{-5}	2.12

Table D.2: Survey details for each redshift bin for BOSS. We show the number of mapped galaxies N_g, the volume of the redshift bin V as well as the number density n_b and the linear bias b_1.

DESI As mentioned in the main text, for DESI we focus on the largest sample which is the set of Emission Line Galaxies. The numerical values we use are calculated from table 2.3 in [222]. We present the specifications in Tab. D.3.

MegaMapper Finally, for MegaMapper, the specifications are still to be finalized given the early stage of the experiment compared to BOSS or DESI. We take the numerical values from [237, 223], where as mentioned in the main text there is an “idealized”, and a “fiducial” scenario. The specifications for the optimistic (or “idealized") scenario are in Tab. D.4. They are based on Tab. 1 of [237]. For the “fiducial" or what we call “pessimistic" scenario, we refer to table 2 in [237].

z	N_g	$V[(\mathrm{Mpc}\,h^{-1})^3]$	$n_b[(h\,\mathrm{Mpc}^{-1})^3]$	b_1
0.65	432600	2.63×10^9	1.64×10^{-4}	1.18
0.75	3.18×10^6	3.15×10^9	1.01×10^{-3}	1.23
0.85	2.70×10^6	3.65×10^9	7.38×10^{-4}	1.29
0.95	2.93×10^6	4.1×10^9	7.15×10^{-4}	1.35
1.05	2.02×10^6	4.52×10^9	4.46×10^{-4}	1.41
1.15	1.89×10^6	4.89×10^9	3.87×10^{-4}	1.47
1.25	1.87×10^6	5.22×10^9	3.59×10^{-4}	1.53
1.35	732200	5.5×10^9	1.33×10^{-4}	1.59
1.45	652400	5.75×10^9	1.13×10^{-4}	1.65
1.55	460600	5.97×10^9	7.71×10^{-5}	1.72
1.65	176400	6.15×10^9	2.87×10^{-5}	1.78

Table D.3: Survey details for each redshift bin for DESI. We show the number of mapped galaxies N_g, the volume of the redshift bin V as well as the number density n_b and the linear bias b_1.

z	N_g	$V[(\mathrm{Mpc}\,h^{-1})^3]$	$n_b[(h\,\mathrm{Mpc}^{-1})^3]$	b_1
2	6.75×10^7	2.70×10^{10}	2.5×10^{-3}	2.5
2.5	3.32×10^7	2.76×10^{10}	1.2×10^{-3}	3.3
3	1.63×10^7	2.72×10^{10}	6×10^{-4}	4.1
3.5	7.88×10^6	2.63×10^{10}	3×10^{-4}	4.9
4	3.76×10^6	2.51×10^{10}	1.5×10^{-4}	5.8
4.5	1.90×10^6	2.38×10^{10}	8×10^{-5}	6.6
5	901730	2.25×10^{10}	4×10^{-5}	7.4

Table D.4: Survey details for each redshift bin for MegaMapper (optimistic). We show the number of mapped galaxies N_g, the volume of the redshift bin V as well as the number density n_b and the linear bias b_1.

D.2 Further Analyses

Two further analyses, which to us do not carry the same significance as those presented in the main sections, are presented here for completeness. In App. D.2.1 we present results for the “pessimistic" scenario for MegaMapper as opposed to the “optimistic" scenario presented in Sec. 8.5.3. In App. D.2.2 we also present the impact of the perturbativity prior, as discussed in Sec. 8.6, on base cosmological parameters.

D.2.1 MegaMapper "Pessimistic" Results

The survey specifications for the "pessimistic" scenario given in Tab. D.5 are determined with the methods described in Sec. 8.3.

MMp:	$z_{\rm eff}$	$n_{b,\rm eff}[(h\,{\rm Mpc}^{-1})^3]$	b_1	$(k_{\rm max}^{\rm Tree},\, k_{\rm max}^{1L},\, k_{\rm NL})$ $[h\,{\rm Mpc}^{-1}]$	$N_{\rm bins}^{1L}$	$N_\Delta^{\rm Tree}$	N_Δ^{1L}
Bin 1	2.1	8.8×10^{-4}	2.7	(0.12, 0.31, 2.2)	62	43	428
Bin 2	4.3	8.4×10^{-5}	4.0	(0.21, 0.57, 8.2)	114	150	2331

Table D.5: MegaMapper "pessimistic" effective survey specifications, calculated according to the formulas in Sec. 8.3. $n_{b,\rm eff}$ is the background galaxy number density entering the derivatives (not the covariance), $N_{\rm bins}$ is the number of k-bins we consider for the power spectrum at 1-loop and N_Δ is the number of triangles we consider for the bispectrum at 1-loop.

To avoid redundancy with the discussion of the optimistic scenario, we here simply focus on base results for the pessimistic MegaMapper scenario. The discussion on fixing biases, shot noise and the inclusion of the perturbativity prior is comparable to the optimistic case. The only difference are the absolute values, while the relative gains are similar. We present results in Fig. D.1, where we present the same base parameters as in the main section. Comparing to the figure and tables in Fig. 8.7 for almost all parameters we see only a $30-40\%$ difference compared to the optimistic case. The non-Gaussianity scenarios all differ by roughly $40-45\%$, independent on whether we use the tree-level bispectrum, the loop, or the perturbativity prior.

D.2.2 Perturbativity Prior Effect on Base Cosmological Parameters

We discuss here the effect of the perturbativity prior, also in combination with the galaxy formation prior, on base cosmological parameters. Results for all surveys are shown in Fig. D.2. We see that the most notable effect is on $\ln(10^{10}A_s)$, n_s and Ω_k, and a smaller effect on the other parameters. Furthermore, we found almost no improvement on constraints for neutrino masses.

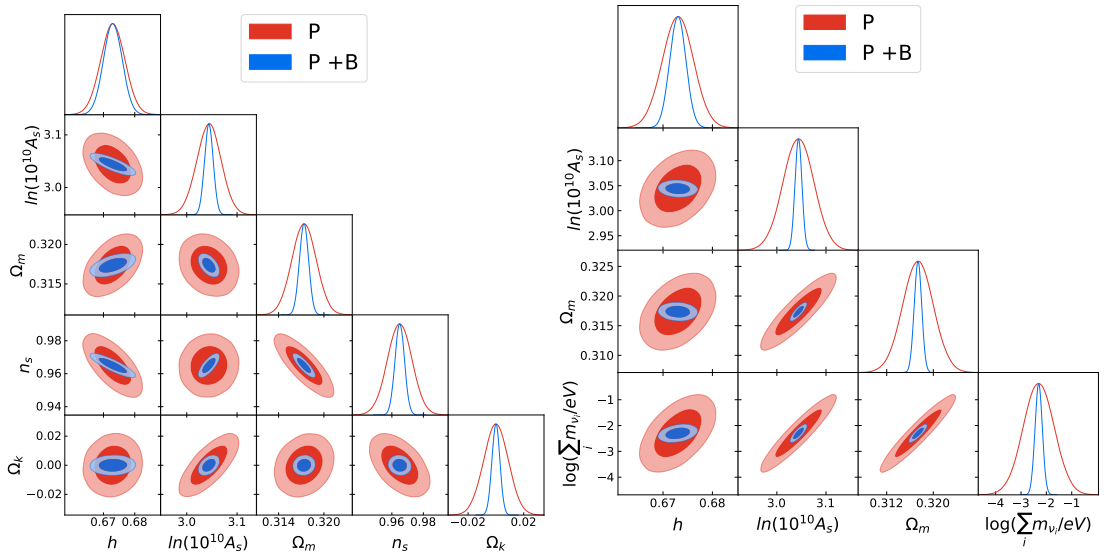

$\sigma(\cdot)$	h	$\ln(10^{10}A_s)$	Ω_m	n_s	Ω_k
P	0.0039	0.024	0.0016	0.0078	0.009
P+B	0.003	0.009	0.0006	0.0030	0.003

$\sigma(\cdot)$	h	$\ln(10^{10}A_s)$	Ω_m	$\log m_\nu^{\rm tot.}(\sigma^+_-)$
P	0.0032	0.031	0.0026	$0.61(^{+0.08}_{-0.05})$
P+B	0.0016	0.007	0.0007	$0.14\ (^{+0.015}_{-0.013})$

$\sigma(\cdot)$	$f_{\rm NL}^{\rm loc.}$	$f_{\rm NL}^{\rm eq.}$	$f_{\rm NL}^{\rm orth.}$
P+$B_{\rm Tree}$	0.45	40.8	18.1
P+B	0.44	32.9	8.5
P+B+p.p.	0.42	29.5	8.0
P+B+p.p.+g.p.	0.42	23.0	6.5

Figure D.1: Triangle plots and errors from Fisher forecasts for MegaMapper (pessimistic) including the spectral tilt and spatial curvature (left) and massive neutrinos (right) and Non-Gaussianity (bottom). We use all power spectrum and bispectrum multipoles for the above results, and use the analytical covariance without cross-correlations. In the table we also report the upper and lower bounds of the 68% confidence interval for the sum of massive neutrinos, i.e. $\mathbb{P}\left[\left(\sum_i m_{\nu_i} - \sum_i m_{\nu_i}^{\rm ref}\right) \in (\sigma^-, \sigma^+)\right] = 0.68$. For non-Gaussianity, we also present results with only the inclusion of the tree-level bispectrum and with the inclusion of a perturbativity prior (p.p) and the "galaxy-formation prior" (g.p.).

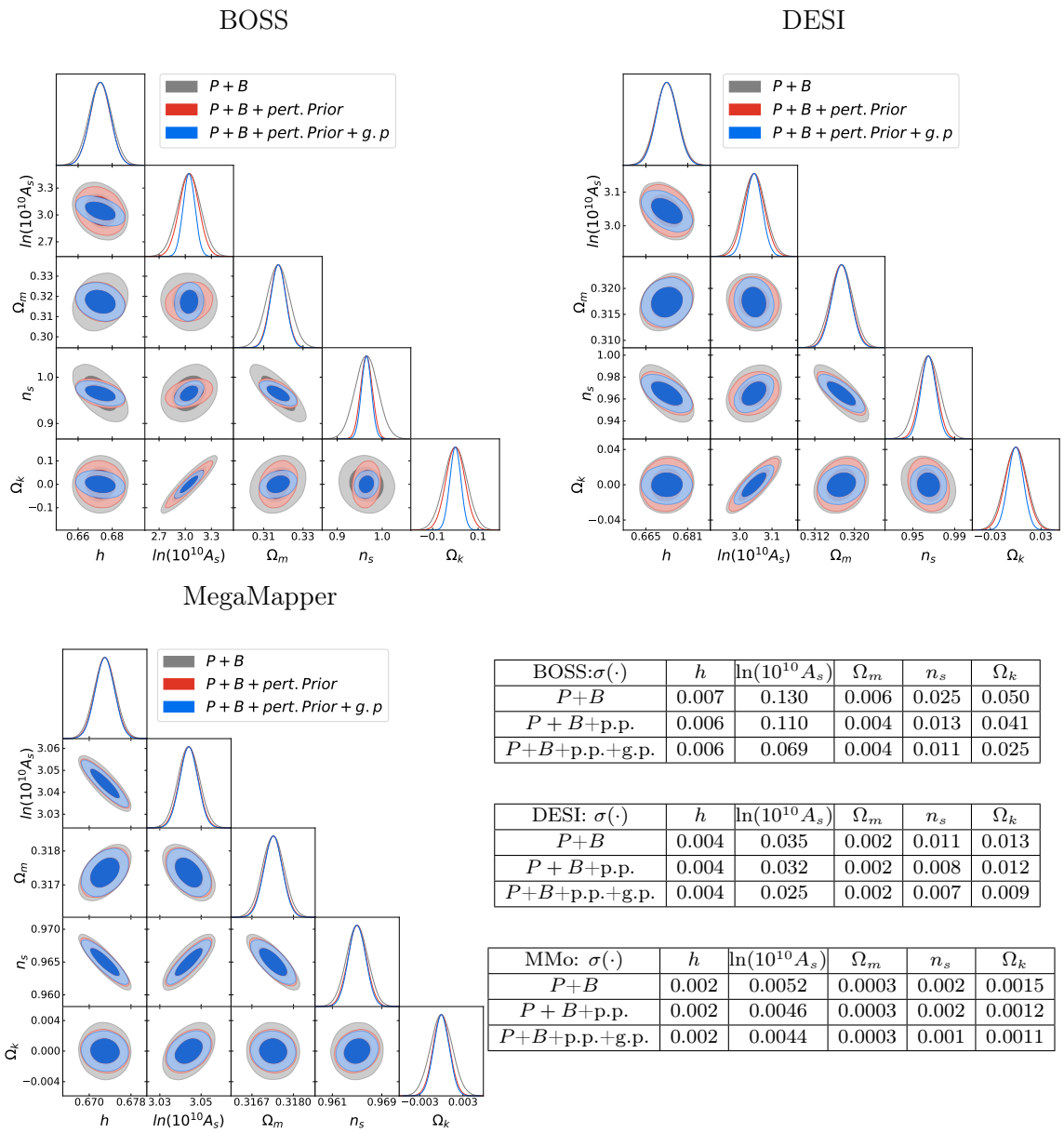

BOSS:$\sigma(\cdot)$	h	$\ln(10^{10}A_s)$	Ω_m	n_s	Ω_k
P+B	0.007	0.130	0.006	0.025	0.050
$P+B$+p.p.	0.006	0.110	0.004	0.013	0.041
P+B+p.p.+g.p.	0.006	0.069	0.004	0.011	0.025

DESI: $\sigma(\cdot)$	h	$\ln(10^{10}A_s)$	Ω_m	n_s	Ω_k
P+B	0.004	0.035	0.002	0.011	0.013
$P+B$+p.p.	0.004	0.032	0.002	0.008	0.012
P+B+p.p.+g.p.	0.004	0.025	0.002	0.007	0.009

MMo: $\sigma(\cdot)$	h	$\ln(10^{10}A_s)$	Ω_m	n_s	Ω_k
P+B	0.002	0.0052	0.0003	0.002	0.0015
$P+B$+p.p.	0.002	0.0046	0.0003	0.002	0.0012
P+B+p.p.+g.p.	0.002	0.0044	0.0003	0.001	0.0011

Figure D.2: Triangle plots and errors from Fisher forecasts for BOSS (top left), DESI (top right), and MegaMapper (bottom left), for base cosmological parameters including the spectral tilt and spatial curvature. We always include the power spectrum at one loop order with the addition of either the loop bispectrum or the loop bispectrum with a perturbativity prior (p.p.) or also in combination with the "galaxy-formation prior" (g.p.). We use all power spectrum and bispectrum multipoles in each case and use the analytical covariance without cross-correlations.

E

Appendix: Formation Time of Galaxies

E.1 Degeneracy Equations

As mentioned in the main text, not all of the bias functions $\mathbb{C}^{(n)}_{\mathcal{O}_m,\alpha}$ at a given n are linearly independent in the sense that

$$\sum_{\mathcal{O}_m}\sum_{\alpha=1}^{n-m+1} d^{(n)}_{i,\mathcal{O}_m,\alpha}\mathbb{C}^{(n)}_{\mathcal{O}_m,\alpha}(\vec{x},t) = 0 \ , \tag{E.1}$$

for some time-independent coefficients $d^{(n)}_{i,\mathcal{O}_m,\alpha}$ for $i = 1,\ldots,N^{(n)}_d$, where $N^{(n)}_d \equiv \text{rank}[d^{(n)}]$ is the number of independent degeneracy equations. In particular, we find $N^{(5)}_d = 122$, and in Ch. 6 we found $N^{(4)}_d = 73$. Additionally, letting $N^{(n)}_{\mathbb{C}}$ be the number of $\mathbb{C}^{(n)}_{\mathcal{O}_m,\alpha}$ functions that result after the procedure described in the main chapter, we find $N^{(5)}_{\mathbb{C}} = 151$ and in Ch. 6 we had $N^{(4)}_{\mathbb{C}} = 88$. [1] Finally, using $N^{(n)}_b \equiv N^{(n)}_{\mathbb{C}} - N^{(n)}_d$ to denote the number of basis elements at order n, this means that $N^{(5)}_b = 29$ and $N^{(4)}_b = 15$. [2] We confirm all of the fifth-order degeneracy equations in the associated ancillary file.

Thus, one can solve the degeneracy equations Eq. (E.1) in terms of $N^{(n)}_b$ basis elements, which we denote generically as $\mathbb{E}^{(n)}_j(\vec{x},t)$ for $j = 1,\ldots,N^{(n)}_b$. Since this is a basis, all of the original functions can be written in terms of it, so we have

$$\mathbb{C}^{(n)}_{\mathcal{O}_m,\alpha}(\vec{x},t) = \sum_{j=1}^{N^{(n)}_b} A^{(n)}_{\mathcal{O}_m,\alpha,j}\,\mathbb{E}^{(n)}_j(\vec{x},t) \ , \tag{E.2}$$

for some time-independent coefficients $A^{(n)}_{\mathcal{O}_m,\alpha,j}$. Plugging Eq. (E.2) into Eq. (9.9)

[1] Details can be found in Apps. B.3.2 and B.3.3.

[2] For completeness, we also have $N^{(3)}_b = 7$, $N^{(2)}_b = 3$, and $N^{(1)}_b = 1$ with this method [131].

then gives

$$\delta_g^{(n)}(\vec{x},t) = \sum_{j=1}^{N_b^{(n)}} e_j^{(n)}(t)\mathbb{E}_j^{(n)}(\vec{x},t) \ , \tag{E.3}$$

where $e_j^{(n)}(t) = \sum_{\mathcal{O}_m}\sum_{\alpha=1}^{n-m+1} c_{\mathcal{O}_m,\alpha}(t)A^{(n)}_{\mathcal{O}_m,\alpha,j}$. The coefficients $e_j(t)$ are called *bias parameters*, and we have now written the galaxy overdensity in terms of the minimal number of linearly independent functions.

E.2 Basis of Descendants

Another, perhaps more natural, choice of basis functions is the so-called basis of descendants [131], where if $\mathbb{C}^{(n)}_{\mathcal{O}_m,\alpha}$ is used at order n, then $\mathbb{C}^{(n+1)}_{\mathcal{O}_m,\alpha+1}$ is used at order $n+1$. We write the fifth-order expansion in the basis of descendants as

$$\delta_g^{(5)}(\vec{x},t) = \sum_{j=1}^{29} b_j(t)\mathbb{B}_j^{(5)}(\vec{x},t) \ . \tag{E.4}$$

As shown below, the first 15 terms in Eq. (E.4) are determined by the fourth-order terms. That is, for $j = 1,\ldots,15$, the b_j in Eq. (E.4) are the same as those in Eq. (6.130), and the basis functions are given by

$$\mathbb{B}_j^{(5)} = \mathbb{B}_j^{(4)}\Big|_{\mathbb{C}^{(4)}_{\mathcal{O}_m,\alpha}\to\mathbb{C}^{(5)}_{\mathcal{O}_m,\alpha}} \tag{E.5}$$

where the $\mathbb{B}_j^{(4)}$ are given explicitly in App. B.3.4. For the new elements derived here, i.e. $j = 16,\ldots,29$, we have $\mathbb{B}_j^{(5)} = \mathbb{C}^{(5)}_{\mathcal{O}_m,\alpha}$, where the indices $\mathcal{O}_m,\alpha$ take the following values for the given j

j :	16	17	18	19	20	21	22
$\mathcal{O}_m,\alpha$:	$\delta,5$	$\delta^2,4$	$r^2,4$	$\delta^3,3$	$r^3,3$	$r^2\delta,3$	$\delta^4,2$
j :	23	24	25	26	27	28	29
$\mathcal{O}_m,\alpha$:	$r^3\delta,2$	$r^4,2$	$\delta^5,1$	$r^5,1$	$r^4\delta,1$	$r^3\delta^2,1$	$p^3,3$

. (E.6)

We also note that fifth order is the first time that $\partial_i v^j$ has to be used as a seed function to form a basis, for example through $\mathbb{C}^{(5)}_{p^3,3}$ above. This is contrasted with the case at fourth order where $\partial_i\partial_j\Phi$ is enough.

Converting between the STL basis and the basis of descendants, we find the following expression for the non-local-in-time bias parameters and the basis-of-

descendants bias parameters

$$\begin{aligned}\tilde{b}_{27} &= b_1 - 4b_2 + 6b_3 - 4b_4 + 90b_8 - 76b_9 + b_{16} \ , \\ \tilde{b}_{28} &= b_{18} - b_9 \ , \\ \tilde{b}_{29} &= -\frac{4b_8}{3} + \frac{4b_9}{3} - \frac{10b_{11}}{3} + \frac{7b_{20}}{3} + b_{29} \ .\end{aligned} \tag{E.7}$$

E.3 Lower-Order Bias Parameters

Here we show how bias parameters at fourth order appear automatically as biases at fifth order. For notational convenience, in this Appendix we will use Γ as the combined index $\mathcal{O}_m, \alpha$, as in $\mathbb{C}^{(n)}_\Gamma \equiv \mathbb{C}^{(n)}_{\mathcal{O}_m,\alpha}$, and Γ_n as the set of the relevant $\mathcal{O}_m$ and α at order n, as defined in the sum in Eq. (9.9). We start with the fifth-order degeneracy equations. It turns out, as we explicitly check in the ancillary file, that the full set of degeneracy equations satisfied by $\mathbb{C}^{(5)}_\Gamma$, Eq. (E.1) with $n = 5$, can be put in the block form

$$0 = \sum_{\Gamma\in\Gamma_4} d^{(4)}_{i,\Gamma}\mathbb{C}^{(5)}_\Gamma(\vec{x},t) + \sum_{\Gamma\in\Gamma_5\setminus\Gamma_4} \tilde{d}^{(5)}_{i,\Gamma}\mathbb{C}^{(5)}_\Gamma(\vec{x},t) \ , \tag{E.8}$$

for $i = 1,\ldots,N^{(5)}_d$, with $d^{(4)}_{i,\Gamma} = 0$ for $i \in [N^{(4)}_d + 1, N^{(5)}_d]$ and $\tilde{d}^{(5)}_{i,\Gamma} = 0$ for $i \in [1, N^{(4)}_d]$. For $i = 1,\ldots,N^{(4)}_d$, the second term on the right-hand side of Eq. (E.8) vanishes, so the $\mathbb{C}^{(5)}_\Gamma$ with $\Gamma \in \Gamma_4$ satisfy the same equations as the fourth-order functions, Eq. (E.1) with $n = 4$. Therefore we can write them in an analogous way to the $n = 4$ case of Eq. (E.2), that is

$$\mathbb{C}^{(5)}_\Gamma(\vec{x},t) = \sum_{j=1}^{N^{(4)}_b} A^{(4)}_{\Gamma,j}\,\mathbb{E}^{(5)}_j(\vec{x},t) \ , \tag{E.9}$$

for $\Gamma \in \Gamma_4$, with

$$\mathbb{E}^{(5)}_j \equiv \mathbb{E}^{(4)}_j\Big|_{\mathbb{C}^{(4)}_\Gamma\to\mathbb{C}^{(5)}_\Gamma} \ , \tag{E.10}$$

for $j = 1,\ldots,N^{(4)}_b$. Said another way, since the $\mathbb{E}^{(4)}_j$ are just linear combinations of some $\mathbb{C}^{(4)}_\Gamma$, we define $\mathbb{E}^{(5)}_j$ for $j = 1,\ldots,N^{(4)}_b$ to be the same expressions as $\mathbb{E}^{(4)}_j$, but

with $\mathbb{C}_\Gamma^{(4)}$ replaced with $\mathbb{C}_\Gamma^{(5)}$, i.e.

$$\begin{aligned}\mathbb{E}_j^{(4)}(\vec{x},t) &= \sum_{\Gamma\in\Gamma_4} \beta_{j,\Gamma}^{(4)} \mathbb{C}_\Gamma^{(4)}(\vec{x},t) \ , \\ \mathbb{E}_j^{(5)}(\vec{x},t) &= \sum_{\Gamma\in\Gamma_4} \beta_{j,\Gamma}^{(4)} \mathbb{C}_\Gamma^{(5)}(\vec{x},t) \ ,\end{aligned} \tag{E.11}$$

for some coefficients $\beta_{j,\Gamma}^{(4)}$.

Now, the bias expansion at fifth order is

$$\delta_g^{(5)}(\vec{x},t) = \sum_{\Gamma\in\Gamma_5} c_\Gamma(t) \mathbb{C}_\Gamma^{(5)}(\vec{x},t) \ . \tag{E.12}$$

The sum above can be split into a sum over $\Gamma \in \Gamma_4$ and a sum over $\Gamma \in \Gamma_5 \setminus \Gamma_4$. For the sum over Γ_4, we have

$$\sum_{\Gamma\in\Gamma_4} c_\Gamma(t) \mathbb{C}_\Gamma^{(5)}(\vec{x},t) = \sum_{j=1}^{N_b^{(4)}} e_j^{(4)}(t) \mathbb{E}_j^{(5)}(\vec{x},t) \ , \tag{E.13}$$

where we have used Eq. (E.9) and the definition of $e_j^{(4)}(t)$ below Eq. (E.3). Thus, the degeneracy equations Eq. (E.8) ensure that it is exactly the fourth-order bias parameters $e_j^{(4)}(t)$ that appear in Eq. (E.13). Then, for the sum over $\Gamma \in \Gamma_5 \setminus \Gamma_4$ in Eq. (E.12), one can solve for the remaining $N_b^{(5)} - N_b^{(4)}$ basis elements using the rest of the degeneracy equations in Eq. (E.8), and this will introduce the additional bias parameters that were not present at fourth order. Since this is true for generic bias parameters $e_j^{(4)}(t)$, it is true in particular for the basis of descendants bias parameters $b_j^{(4)}(t)$ in Eq. (E.4).

F

Appendix: Quintessence

F.1 Green's Functions

At linear order, the time dependence is completely captured by the growth factor, defined as the solution of [128, 135]:

$$\frac{d^2}{d\ln a^2}\left(\frac{D}{H}\right)+\left(2+3\frac{d\ln H}{d\ln a}-\frac{d\ln C}{d\ln a}\right)\frac{d}{d\ln a}\left(\frac{D}{H}\right)=0\ , \tag{F.1}$$

The equation has two solutions, a growing mode

$$D_+(a)=\frac{5}{2}\int_0^a C(\tilde{a})\Omega_m(\tilde{a})\frac{H(a)}{H(\tilde{a})}d\tilde{a}, \tag{F.2}$$

and a decaying mode

$$D_-(a)=\frac{H(a)}{H_0\Omega_{m,0}^{1/2}}\ . \tag{F.3}$$

From these, we get the linear growth rates $f_\pm\equiv\frac{d\ln D_\pm}{d\ln a}$, given as

$$f_+(a)=\left(\frac{5}{2}\frac{a}{D_+(a)}-\frac{3}{2}\right)\Omega_m(a)C(a)\,, \tag{F.4}$$

and

$$f_-(a)=-\frac{3}{2}\Omega_m(a)C(a)\,, \tag{F.5}$$

where

$$\Omega_m(a)\equiv\Omega_{m,0}\frac{H_0^2}{H(a)^2}a^{-3}\ ,\qquad \Omega_D(a)\equiv\Omega_{D,0}\frac{H_0^2}{H(a)^2}a^{-3(1+w)} \tag{F.6}$$

are the fractional matter and dark energy densities in terms of their present-day values $\Omega_{m,0}$ and $\Omega_{d,0}$. To construct higher order solutions, it is useful to define

Green's functions, coming from Eqs. (10.28) and (10.30):

$$a\frac{dG_\sigma^\delta(a,\tilde{a})}{da} - f_+(a)G_\sigma^\theta(a,\tilde{a}) = \lambda_\sigma\delta(a-\tilde{a}), \tag{F.7}$$

$$a\frac{dG_\sigma^\theta(a,\tilde{a})}{da} - f_+(a)G_\sigma^\theta(a,\tilde{a}) - \frac{f_-(a)}{f_+(a)}\Big(G_\sigma^\theta(a,\tilde{a}) - G_\sigma^\delta(a,\tilde{a})\Big) = (1-\lambda_\sigma)\delta(a-\tilde{a}), \tag{F.8}$$

where $\sigma \in \{1,2\}$, $\lambda_1 = 1$ and $\lambda_2 = 0$. Explicitly they are given by

$$G_1^\delta(a,\tilde{a}) = \frac{1}{\tilde{a}W(\tilde{a})}\left(\frac{dD_-(\tilde{a})}{d\tilde{a}}D_+(a) - \frac{dD_+(\tilde{a})}{d\tilde{a}}D_-(a)\right)\Theta(a-\tilde{a}) \ , \tag{F.9}$$

$$G_2^\delta(a,\tilde{a}) = \frac{f_+(\tilde{a})/\tilde{a}^2}{W(\tilde{a})}\Big(D_+(\tilde{a})D_-(a) - D_-(\tilde{a})D_+(a)\Big)\Theta(a-\tilde{a}) \ , \tag{F.10}$$

$$G_1^\theta(a,\tilde{a}) = \frac{a/\tilde{a}}{f_+(a)W(\tilde{a})}\left(\frac{dD_-(\tilde{a})}{d\tilde{a}}\frac{dD_+(a)}{da} - \frac{dD_+(\tilde{a})}{d\tilde{a}}\frac{dD_-(a)}{da}\right)\Theta(a-\tilde{a}) \ , \tag{F.11}$$

$$G_2^\theta(a,\tilde{a}) = \frac{f_+(\tilde{a})a/\tilde{a}^2}{f_+(a)W(\tilde{a})}\left(D_+(\tilde{a})\frac{dD_-(a)}{da} - D_-(\tilde{a})\frac{dD_+(a)}{da}\right)\Theta(a-\tilde{a}) \ , \tag{F.12}$$

where $\Theta(a-\tilde{a})$ is the Heaviside step function, $W(\tilde{a})$ is the Wronskian of D_+ and D_-:

$$W(\tilde{a}) = \frac{dD_-(\tilde{a})}{d\tilde{a}}D_+(\tilde{a}) - \frac{dD_+(\tilde{a})}{d\tilde{a}}D_-(\tilde{a}) \ , \tag{F.13}$$

and we impose the boundary conditions

$$G_\sigma^\delta(a,\tilde{a}) = 0 \qquad \text{and} \qquad G_\sigma^\theta(a,\tilde{a}) = 0 \qquad \text{for} \qquad \tilde{a} > a \ , \tag{F.14}$$

$$G_\sigma^\delta(\tilde{a},\tilde{a}) = \frac{\lambda_\sigma}{\tilde{a}} \qquad \text{and} \qquad G_\sigma^\theta(\tilde{a},\tilde{a}) = \frac{(1-\lambda_\sigma)}{\tilde{a}}. \tag{F.15}$$

At second order, the resulting time-dependent functions are given by

$$\mathcal{G}_\sigma^\delta(a) = \int_0^1 G_\sigma^\delta(a,\tilde{a})\frac{f_+(\tilde{a})D_+^2(\tilde{a})}{C(\tilde{a})D_+^2(a)}d\tilde{a} \ , \tag{F.16}$$

$$\mathcal{G}_\sigma^\theta(a) = \int_0^1 G_\sigma^\theta(a,\tilde{a})\frac{f_+(\tilde{a})D_+^2(\tilde{a})}{C(\tilde{a})D_+^2(a)}d\tilde{a}, \tag{F.17}$$

for $\sigma = 1, 2$. At third order we have

$$\mathcal{U}^{\delta}_{\sigma}(a) = \int_0^1 G^{\delta}_1(a,\tilde{a}) \frac{f_+(\tilde{a}) D^3_+(\tilde{a})}{C(\tilde{a}) D^3_+(a)} \mathcal{G}^{\delta}_{\sigma}(\tilde{a}) d\tilde{a}, \tag{F.18}$$

$$\mathcal{U}^{\theta}_{\sigma}(a) = \int_0^1 G^{\theta}_1(a,\tilde{a}) \frac{f_+(\tilde{a}) D^3_+(\tilde{a})}{C(\tilde{a}) D^3_+(a)} \mathcal{G}^{\delta}_{\sigma}(\tilde{a}) d\tilde{a}, \tag{F.19}$$

$$\mathcal{V}^{\delta}_{\sigma\tilde{\sigma}}(a) = \int_0^1 G^{\delta}_{\tilde{\sigma}}(a,\tilde{a}) \frac{f_+(\tilde{a}) D^3_+(\tilde{a})}{C(\tilde{a}) D^3_+(a)} \mathcal{G}^{\theta}_{\sigma}(\tilde{a}) d\tilde{a}, \tag{F.20}$$

$$\mathcal{V}^{\theta}_{\sigma\tilde{\sigma}}(a) = \int_0^1 G^{\theta}_{\tilde{\sigma}}(a,\tilde{a}) \frac{f_+(\tilde{a}) D^3_+(\tilde{a})}{C(\tilde{a}) D^3_+(a)} \mathcal{G}^{\theta}_{\sigma}(\tilde{a}) d\tilde{a}. \tag{F.21}$$

The degeneracies pointed out in Eq. (B.86) result from the following identities:

$$\begin{aligned}
\mathcal{G}^{\delta}_1 + \mathcal{G}^{\delta}_2 = \mathcal{G}^{\theta}_1 + \mathcal{G}^{\theta}_2 &= \mathcal{G} \\
\mathcal{V}^{\delta}_{11} + \mathcal{V}^{\delta}_{21} &= \mathcal{U}^{\delta}_1 + \mathcal{U}^{\delta}_2 \\
\mathcal{V}^{\theta}_{11} + \mathcal{V}^{\theta}_{21} &= \mathcal{U}^{\theta}_1 + \mathcal{U}^{\theta}_2 \\
\mathcal{V}^{\delta}_{\sigma 1} + \mathcal{V}^{\delta}_{\sigma 2} &= \mathcal{V}^{\theta}_{\sigma 1} + \mathcal{V}^{\theta}_{\sigma 2} \\
\mathcal{V}^{\delta}_{11} + \mathcal{V}^{\delta}_{21} + \mathcal{V}^{\delta}_{12} + \mathcal{V}^{\delta}_{22} &= \frac{\mathcal{G}^2}{2} \\
\mathcal{V}^{\theta}_{11} + \mathcal{V}^{\theta}_{21} + \mathcal{V}^{\theta}_{12} + \mathcal{V}^{\theta}_{22} &= \frac{\mathcal{G}^2}{2} \\
\mathcal{U}^{\delta}_1 - \mathcal{V}^{\delta}_{22} &= \frac{\mathcal{G}}{2} \left(\mathcal{G}^{\delta}_1 - \mathcal{G}^{\delta}_2 \right) \\
\mathcal{U}^{\theta}_1 - \mathcal{V}^{\theta}_{22} &= \frac{\mathcal{G}}{2} \left(\mathcal{G}^{\theta}_1 - \mathcal{G}^{\theta}_2 \right)
\end{aligned} \tag{F.22}$$

where again $\sigma \in \{1, 2\}$. One can derive these relations using Eqs. (F.16) - (F.21) and the fact that

$$G^{\delta}_1(a,\tilde{a}) + G^{\delta}_2(a,\tilde{a}) = G^{\theta}_1(a,\tilde{a}) + G^{\theta}_2(a,\tilde{a}) = \frac{D_+(a)}{\tilde{a} D_+(\tilde{a})} \Theta(a - \tilde{a}) \tag{F.23}$$

$$G^{\delta}_1(a,\tilde{a}) - G^{\theta}_1(a,\tilde{a}) = \frac{W(a)}{\tilde{a} W(\tilde{a})} \frac{D'_+(\tilde{a})}{D'_+(a)} \Theta(a - \tilde{a}). \tag{F.24}$$

Furthermore, for the derivation of some of the flow terms in App. F.3 it is important to use the following relations:

$$\mathcal{V}^{\delta}_{\sigma 1}(a) + \mathcal{V}^{\delta}_{\sigma 2}(a) = \int_0^a \frac{D'_+(\tilde{a})D_+(\tilde{a})}{C(\tilde{a})D^2_+(a)} \mathcal{G}^{\theta}_{\sigma}(\tilde{a}) d\tilde{a}\,, \tag{F.25}$$

$$\mathcal{G} = \int_0^a \frac{D'_+(\tilde{a})}{C(\tilde{a})D_+(a)} d\tilde{a}\,, \tag{F.26}$$

$$\int_0^a \mathcal{G}(\tilde{a}) \frac{D'_+(\tilde{a})D_+(\tilde{a})}{C(\tilde{a})D_+(a)^2} d\tilde{a} = \frac{\mathcal{G}^2}{2}\,. \tag{F.27}$$

F.2 Bias Operators, Halo Kernels and Degeneracy of Halo Bias Parameters

In this section we quickly wish to outline how we get from equation Eq. (10.34) to Eq. (10.42). First, we define the operators that appear in Eq. (10.34). In the exact same way as in [135], we follow the approach used by [136], generalised to exact time dependence. Using

$$\eta(\vec{x}, t) = \theta(\vec{x}, t) - \delta(\vec{x}, t)\,, \tag{F.28}$$

we define

$$s_{ij}(\vec{x}, a) = \mathcal{D}_{ij}\delta(\vec{x}, a) \quad \text{and} \quad t_{ij}(\vec{x}, a) = \mathcal{D}_{ij}\eta(\vec{x}, a), \tag{F.29}$$

where $\mathcal{D}_{ij} = \frac{\partial_i\partial_j}{\partial^2} - \frac{1}{3}\delta_{ij}$. Then we get the contractions

$$\begin{aligned} &s^2(\vec{x}_{\rm fl}, a) = s_{ij}(\vec{x}_{\rm fl}, a)s^{ij}(\vec{x}_{\rm fl}, a)\,, \quad s^3(\vec{x}_{\rm fl}, a) = s_{ij}(\vec{x}_{\rm fl}, a)s^{il}(\vec{x}_{\rm fl}, a)s_l{}^j(\vec{x}_{\rm fl}, a)\,, \\ &st(\vec{x}_{\rm fl}, a) = s_{ij}(\vec{x}_{\rm fl}, a)t^{ij}(\vec{x}_{\rm fl}, a)\,. \end{aligned} \tag{F.30}$$

Furthermore, ψ is given by

$$\psi(\vec{x}, a) = \theta(\vec{x}, a) - \delta(\vec{x}, a) - \left(\mathcal{G}^{\delta}_1(a) - \mathcal{G}^{\theta}_1(a)\right)\left(s^2(\vec{x}, a) - \frac{2}{3}\delta^2(\vec{x}, a)\right), \tag{F.31}$$

so that it only starts at third order.

The ϵ stochastic operators, are uncorrelated with the density field. Their correlation functions will not depend on the initial power spectrum and contain all terms allowed by rotational invariance in a derivative expansion as in (6.56), that is $\langle\epsilon(\vec{k})\epsilon(\vec{k}')\rangle' = c_0 + c_1\frac{k^2}{k^2_{\rm M}} + \ldots$. The $\langle\ldots\rangle'$ notation means that the correlation is stripped of the momentum-conserving Dirac delta.

One can show that all operators in Eq. (10.34), including the flow terms, up to cubic order in the fluctuations, can be expressed as linear combinations of the following nine momentum kernels (see [135], we can call the 'exact-time' basis or the 'Greek' basis):

$$\mathbb{I} = 1 \tag{F.32}$$

$$\alpha(\vec{q}_1, \vec{q}_2) = 1 + \frac{\vec{q}_1 \cdot \vec{q}_2}{q_1^2} \tag{F.33}$$

$$\beta(\vec{q}_1, \vec{q}_2) = \frac{(\vec{q}_1 + \vec{q}_2)^2 \vec{q}_1 \cdot \vec{q}_2}{2q_1^2 q_2^2} \tag{F.34}$$

$$\alpha^1(\vec{q}_1, \vec{q}_2, \vec{q}_3) = \alpha(\vec{q}_3, \vec{q}_1 + \vec{q}_2)\alpha_s(\vec{q}_1, \vec{q}_2), \tag{F.35}$$

$$\alpha^2(\vec{q}_1, \vec{q}_2, \vec{q}_3) = \alpha(\vec{q}_3, \vec{q}_1 + \vec{q}_2)\beta(\vec{q}_1, \vec{q}_2), \tag{F.36}$$

$$\beta^1(\vec{q}_1, \vec{q}_2, \vec{q}_3) = 2\beta(\vec{q}_3, \vec{q}_1 + \vec{q}_2)\alpha_s(\vec{q}_1, \vec{q}_2), \tag{F.37}$$

$$\beta^2(\vec{q}_1, \vec{q}_2, \vec{q}_3) = 2\beta(\vec{q}_3, \vec{q}_1 + \vec{q}_2)\beta(\vec{q}_1, \vec{q}_2), \tag{F.38}$$

$$\gamma^1(\vec{q}_1, \vec{q}_2, \vec{q}_3) = \alpha(\vec{q}_1 + \vec{q}_2, \vec{q}_3)\alpha_s(\vec{q}_1, \vec{q}_2), \tag{F.39}$$

$$\gamma^2(\vec{q}_1, \vec{q}_2, \vec{q}_3) = \alpha(\vec{q}_1 + \vec{q}_2, \vec{q}_3)\beta(\vec{q}_1, \vec{q}_2). \tag{F.40}$$

The resulting redefinitions of parameters that appear in Eqs. (10.38) and (10.42)

are given by

$$
\begin{aligned}
c_{\alpha,(2)} &= \mathcal{G}\cdot c_{\delta,1} - c_{\delta_2,\mathcal{G}_2^\delta} - c_{s^2,1} \\
c_{\beta,(2)} &= c_{\delta_2,\mathcal{G}_2^\delta} + c_{s^2,1} \\
c_{\mathbb{I},(2)} &= -\mathcal{G}\cdot c_{\delta,1} + c_{\delta_2,\mathcal{G}_1^\delta} + c_{\delta_2,\mathcal{G}_2^\delta} + c_{\delta^2,1} + \tfrac{2}{3} c_{s^2,1} \\
c_{\alpha_1,(3)} &= \tfrac{1}{2}\mathcal{G}^2\cdot c_{\delta,1} - \mathcal{G}\cdot c_{\delta_2,\mathcal{G}_2^\delta} - \tfrac{1}{2}\left(c_{\delta,\mathcal{G}_1^\delta} - c_{\delta,\mathcal{G}_2^\delta}\right) + c_{\delta,\mathcal{U}_1^\delta} - \mathcal{G}\cdot c_{s^2,1} + c_{s^2,\mathcal{G}_2^\delta} \\
&\quad - \tfrac{1}{2}\left(c_{st,\mathcal{G}_1^\theta} - c_{st,\mathcal{G}_1^\delta}\right) + c_{\psi,\mathcal{U}_1^\theta} - c_{\psi,\mathcal{U}_1^\delta} + c_{\psi,\mathcal{G}_1^\delta} + \tfrac{1}{2} c_{s^3} \\
c_{\alpha_2,(3)} &= \mathcal{G}\cdot c_{\delta_2,\mathcal{G}_2^\delta} - c_{\delta,\mathcal{G}_2^\delta} + c_{\delta,\mathcal{U}_2^\delta} + \mathcal{G}\cdot c_{s^2,1} - c_{s^2,\mathcal{G}_1^\delta} - 2\, c_{s^2,\mathcal{G}_2^\delta} - \tfrac{1}{2}\left(c_{st,\mathcal{G}_2^\theta} - c_{st,\mathcal{G}_2^\delta}\right) \\
&\quad + c_{\psi,\mathcal{U}_2^\theta} - c_{\psi,\mathcal{U}_2^\delta} + c_{\psi,\mathcal{G}_2^\delta} - c_{s^3} \\
c_{\beta_1,(3)} &= c_{\delta,\mathcal{V}_{12}^\delta} + c_{s^2,\mathcal{G}_1^\delta} + \tfrac{1}{2}\left(c_{st,\mathcal{G}_1^\theta} - c_{st,\mathcal{G}_1^\delta}\right) + c_{\psi,\mathcal{V}_{12}^\theta} - c_{\psi,\mathcal{V}_{12}^\delta} - c_{\psi,\mathcal{G}_1^\delta} \\
c_{\beta_2,(3)} &= c_{\delta,\mathcal{V}_{22}^\delta} + c_{s^2,\mathcal{G}_2^\delta} + \tfrac{1}{2}\left(c_{st,\mathcal{G}_2^\theta} - c_{st,\mathcal{G}_2^\delta}\right) + c_{\psi,\mathcal{V}_{22}^\theta} - c_{\psi,\mathcal{V}_{22}^\delta} - c_{\psi,\mathcal{G}_2^\delta} + \tfrac{1}{2} c_{s^3} \\
c_{\gamma_1,(3)} &= \left(\mathcal{V}_{11}^\delta + \mathcal{V}_{12}^\delta\right) c_{\delta,1} - c_{\delta,\mathcal{V}_{12}^\delta} - c_{s^2,\mathcal{G}_1^\delta} - \tfrac{1}{2}\left(c_{st,\mathcal{G}_1^\theta} - c_{st,\mathcal{G}_1^\delta}\right) + c_{\psi,\mathcal{V}_{11}^\theta} - c_{\psi,\mathcal{V}_{11}^\delta} + c_{\psi,\mathcal{G}_1^\delta} \\
c_{\gamma_2,(3)} &= \left(\mathcal{V}_{21}^\delta + \mathcal{V}_{22}^\delta\right) c_{\delta,1} - c_{\delta,\mathcal{V}_{22}^\delta} - c_{s^2,\mathcal{G}_2^\delta} - \tfrac{1}{2}\left(c_{st,\mathcal{G}_2^\theta} - c_{st,\mathcal{G}_2^\delta}\right) + c_{\psi,\mathcal{V}_{21}^\theta} - c_{\psi,\mathcal{V}_{21}^\delta} + c_{\psi,\mathcal{G}_2^\delta} - \tfrac{1}{2} c_{s^3} \\
c_{\alpha,(3)} &= -\tfrac{3}{2}\mathcal{G}^2\cdot c_{\delta,1} - \left(\mathcal{V}_{11}^\delta + \mathcal{V}_{12}^\delta\right) c_{\delta,1} + c_{\delta,\mathcal{V}_{11}^\delta} + c_{\delta,\mathcal{V}_{12}^\delta} + \mathcal{G}\cdot\left(2\, c_{\delta_2,\mathcal{G}_1^\delta} + 3\, c_{\delta_2,\mathcal{G}_2^\delta}\right) - \tfrac{1}{2}\left(c_{\delta,\mathcal{G}_1^\delta} + 3\, c_{\delta,\mathcal{G}_2^\delta}\right) \\
&\quad + 2\,\mathcal{G}\cdot c_{\delta^2,1} - 2\, c_{\delta^2,\mathcal{G}_2^\delta} + \tfrac{7}{3}\mathcal{G}\cdot c_{s^2,1} - c_{s^2,\mathcal{G}_1^\delta} - \tfrac{7}{3} c_{s^2,\mathcal{G}_2^\delta} + \tfrac{2}{3}\left(c_{st,\mathcal{G}_1^\theta} - c_{st,\mathcal{G}_1^\delta}\right) - c_{\delta s^2} - \tfrac{1}{2} c_{s^3} \\
c_{\beta,(3)} &= -\left(\mathcal{V}_{21}^\delta + \mathcal{V}_{22}^\delta\right) c_{\delta,1} + c_{\delta,\mathcal{V}_{21}^\delta} + c_{\delta,\mathcal{V}_{22}^\delta} - \mathcal{G}\cdot c_{\delta_2,\mathcal{G}_2^\delta} + c_{\delta,\mathcal{G}_2^\delta} \\
&\quad + 2\, c_{\delta^2,\mathcal{G}_2^\delta} - \mathcal{G}\cdot c_{s^2,1} + c_{s^2,\mathcal{G}_1^\delta} + \tfrac{7}{3} c_{s^2,\mathcal{G}_2^\delta} + \tfrac{2}{3}\left(c_{st,\mathcal{G}_2^\theta} - c_{st,\mathcal{G}_2^\delta}\right) + c_{\delta s^2} + \tfrac{1}{2} c_{s^3} \\
c_{\mathbb{I},(3)} &= \mathcal{G}^2\cdot c_{\delta,1} - 2\,\mathcal{G}\left(c_{\delta_2,\mathcal{G}_1^\delta} + c_{\delta_2,\mathcal{G}_2^\delta}\right) + c_{\delta,\mathcal{G}_1^\delta} + c_{\delta,\mathcal{G}_2^\delta} - 2\,\mathcal{G}\cdot c_{\delta^2,1} + 2\left(c_{\delta^2,\mathcal{G}_1^\delta} + c_{\delta^2,\mathcal{G}_2^\delta}\right) \\
&\quad - \tfrac{4}{3}\mathcal{G}\cdot c_{s^2,1} + \tfrac{4}{3}\left(c_{s^2,\mathcal{G}_1^\delta} + c_{s^2,\mathcal{G}_2^\delta}\right) + \tfrac{2}{9} c_{s^3} + \tfrac{2}{3} c_{\delta s^2} + c_{\delta^3}
\end{aligned}
\tag{F.41}
$$

where the coefficients that appear here are the symbolic integrals over the time-dependent functions defined in App. F.1 that come from the expansion Eq. (10.34).

They read

$$
\begin{aligned}
c_{\delta,1}(a) &= \int^a \frac{da'}{a'} c_\delta(a,a') \frac{D_+(a')}{D_+(a)}, \qquad \text{(F.42)}\\
c_{\delta_2,\mathcal{G}^\delta_\sigma}(a) &= \int^a \frac{da'}{a'} c_\delta(a,a') \frac{D_+(a')^2}{D_+(a)^2} \mathcal{G}^\delta_\sigma(a'),\\
c_{s^2,1}(a) &= \int^a \frac{da'}{a'} c_{s^2}(a,a') \frac{D_+(a')^2}{D_+(a)^2},\\
c_{\delta^2,1}(a) &= \int^a \frac{da'}{a'} c_{\delta^2}(a,a') \frac{D_+(a')^2}{D_+(a)^2},\\
c_{s^3}(a) &= \int^a \frac{da'}{a'} c_{s^3}(a,a') \frac{D_+(a')^3}{D_+(a)^3},\\
c_{\delta^3}(a) &= \int^a \frac{da'}{a'} c_{\delta^3}(a,a') \frac{D_+(a')^3}{D_+(a)^3},\\
c_{\delta,\mathcal{U}^\delta_\sigma}(a) &= \int^a \frac{da'}{a'} c_\delta(a,a') \frac{D_+(a')^3}{D_+(a)^3} \mathcal{U}^\delta_\sigma(a'),\\
c_{\delta,\mathcal{G}^\delta_\sigma}(a) &= \int^a \frac{da'}{a'} c_\delta(a,a') \frac{D_+(a')^3}{D_+(a)^3} \mathcal{G}(a') \mathcal{G}^\delta_\sigma(a'),\\
c_{\delta,\mathcal{V}^\delta_{\sigma\tilde\sigma}}(a) &= \int^a \frac{da'}{a'} c_\delta(a,a') \frac{D_+(a')^3}{D_+(a)^3} \mathcal{V}^\delta_{\sigma\tilde\sigma}(a'),\\
c_{\delta s^2}(a) &= \int^a \frac{da'}{a'} c_{\delta s^2}(a,a') \frac{D_+(a')^3}{D_+(a)^3},\\
c_{\delta^2,\mathcal{G}^\delta_\sigma}(a) &= \int^a \frac{da'}{a'} c_{\delta^2}(a,a') \frac{D_+(a')^3}{D_+(a)^3} \mathcal{G}^\delta_\sigma(a'),\\
c_{s^2,\mathcal{G}^\delta_\sigma}(a) &= \int^a \frac{da'}{a'} c_{s^2}(a,a') \frac{D_+(a')^3}{D_+(a)^3} \mathcal{G}^\delta_\sigma(a'),\\
c_{st,\mathcal{G}^\delta_\sigma}(a) &= \int^a \frac{da'}{a'} c_{st}(a,a') \frac{D_+(a')^3}{D_+(a)^3} \mathcal{G}^\delta_\sigma(a'),\\
c_{st,\mathcal{G}^\theta_\sigma}(a) &= \int^a \frac{da'}{a'} c_{st}(a,a') \frac{D_+(a')^3}{D_+(a)^3} \mathcal{G}^\theta_\sigma(a'),\\
c_{\psi,\mathcal{U}^\delta_\sigma}(a) &= \int^a \frac{da'}{a'} c_\psi(a,a') \frac{D_+(a')^3}{D_+(a)^3} \mathcal{U}^\delta_\sigma(a'),\\
c_{\psi,\mathcal{V}^\delta_{\sigma\tilde\sigma}}(a) &= \int^a \frac{da'}{a'} c_\psi(a,a') \frac{D_+(a')^3}{D_+(a)^3} \mathcal{V}^\delta_{\sigma\tilde\sigma}(a'),\\
c_{\psi,\mathcal{U}^\theta_\sigma}(a) &= \int^a \frac{da'}{a'} c_\psi(a,a') \frac{D_+(a')^3}{D_+(a)^3} \mathcal{U}^\theta_\sigma(a'),\\
c_{\psi,\mathcal{V}^\theta_{\sigma\tilde\sigma}}(a) &= \int^a \frac{da'}{a'} c_\psi(a,a') \frac{D_+(a')^3}{D_+(a)^3} \mathcal{V}^\theta_{\sigma\tilde\sigma}(a'),\\
c_{\psi\mathcal{G}^\delta_\sigma}(a) &= \int^a \frac{da'}{a'} c_\psi(a,a') \frac{D_+(a')^3}{D_+(a)^3} \mathcal{G}^\delta_\sigma(a') \big(\mathcal{G}^\delta_1(a') - \mathcal{G}^\theta_1(a')\big).
\end{aligned}
$$

For completeness, we here explicitly write the $\mathbb{C}_i$ operators that appear in Eq. (10.42):

$$\begin{aligned}
{}^*\mathbb{C}^{(1)}_{\delta}(\vec{q}_1) &= 1 \qquad \text{(F.43)}\\
{}^*\mathbb{C}^{(2)}_{\delta}(\vec{q}_1,\vec{q}_2) &= \beta(\vec{q}_1,\vec{q}_2)\\
{}^*\mathbb{C}^{(2)}_{\alpha}(\vec{q}_1,\vec{q}_2) &= \alpha(\vec{q}_1,\vec{q}_2)-\beta(\vec{q}_1,\vec{q}_2)\\
{}^*\mathbb{C}^{(2)}_{\mathbb{I}}(\vec{q}_1,\vec{q}_2) &= 1\\
{}^*\mathbb{C}^{(3)}_{\delta}(\vec{q}_1,\vec{q}_2,\vec{q}_3) &= -\frac{3}{14}\alpha_1(\vec{q}_1,\vec{q}_2,\vec{q}_3)+\frac{3}{7}\alpha_2(\vec{q}_1,\vec{q}_2,\vec{q}_3)\\
&\quad +\frac{2}{7}\beta_2(\vec{q}_1,\vec{q}_2,\vec{q}_3)+\frac{3}{14}\gamma_1(\vec{q}_1,\vec{q}_2,\vec{q}_3)\\
{}^*\mathbb{C}^{(3)}_{\alpha_1}(\vec{q}_1,\vec{q}_2,\vec{q}_3) &= \alpha_1(\vec{q}_1,\vec{q}_2,\vec{q}_3)-\alpha_2(\vec{q}_1,\vec{q}_2,\vec{q}_3)\\
{}^*\mathbb{C}^{(3)}_{\beta_1}(\vec{q}_1,\vec{q}_2,\vec{q}_3) &= -\alpha_2(\vec{q}_1,\vec{q}_2,\vec{q}_3)+\beta_1(\vec{q}_1,\vec{q}_2,\vec{q}_3)-\gamma_1(\vec{q}_1,\vec{q}_2,\vec{q}_3)\\
{}^*\mathbb{C}^{(3)}_{\gamma_2}(\vec{q}_1,\vec{q}_2,\vec{q}_3) &= -\alpha_1(\vec{q}_1,\vec{q}_2,\vec{q}_3)+2\alpha_2(\vec{q}_1,\vec{q}_2,\vec{q}_3)\\
&\quad -\beta_2(\vec{q}_1,\vec{q}_2,\vec{q}_3)+\gamma_2(\vec{q}_1,\vec{q}_2,\vec{q}_3)\\
{}^*\mathbb{C}^{(3)}_{\alpha}(\vec{q}_1,\vec{q}_2,\vec{q}_3) &= \alpha(\vec{q}_1,\vec{q}_2)-\beta(\vec{q}_1,\vec{q}_2)\\
{}^*\mathbb{C}^{(3)}_{\beta}(\vec{q}_1,\vec{q}_2,\vec{q}_3) &= \beta(\vec{q}_1,\vec{q}_2)\\
{}^*\mathbb{C}^{(3)}_{\mathbb{I}}(\vec{q}_1,\vec{q}_2,\vec{q}_3) &= 1\\
{}^*\mathbb{C}^{(3)}_{Y}(\vec{q}_1,\vec{q}_2,\vec{q}_3) &= -\alpha_1(\vec{q}_1,\vec{q}_2,\vec{q}_3)+2\alpha_2(\vec{q}_1,\vec{q}_2,\vec{q}_3)\\
&\quad -\beta_2(\vec{q}_1,\vec{q}_2,\vec{q}_3)+\gamma_1(\vec{q}_1,\vec{q}_2,\vec{q}_3),
\end{aligned}$$

where the $\mathbb{C}_i$ are related to the ${}^*\mathbb{C}_i$ by

$$\mathbb{C}^{(n)}_i(\vec{k},a)=\int\frac{d^3q_1}{(2\pi)^3}...\frac{d^3q_n}{(2\pi)^3}(2\pi)^3\delta_D(\vec{k}-\vec{q}_1-...-\vec{q}_n)\,{}^*\mathbb{C}^{(n)}_i(\vec{q}_1,...,\vec{q}_n)\delta^{(1)}_{\vec{q}_1}(a)...\delta^{(1)}_{\vec{q}_n}(a). \tag{F.44}$$

F.3 Deriving Flow Terms

We here derive the flow terms coming from the Taylor expansion

$$\begin{aligned}
\delta(\vec{x}_{\rm fl}(a,a'),a') &= \delta(\vec{x},a')-\partial_i\delta(x,a')\int_{a'}^{a}\frac{da''}{a''^2H(a'')}\,v^i(\vec{x},a'') \qquad \text{(F.45)}\\
&+\frac{1}{2}\partial_i\partial_j\delta(x,a')\int_{a'}^{a}\frac{da''}{a''^2H(a'')}\,v^i(\vec{x},a'')\int_{a'}^{a}\frac{da'''}{a'''^2H(a''')}\,v^j(\vec{x},a''')\\
&+\partial_i\delta(x,a')\int_{a'}^{a}\frac{da''}{a''^2H(a'')}\,\partial_jv^i(\vec{x},a'')\int_{a''}^{a}\frac{da'''}{a'''^2H(a''')}\,v^j(\vec{x},a''')+\dots\,.
\end{aligned}$$

In the bias expansion from [129, 135] we integrate over time integral kernels such as $c_\delta(a,a')$, which we will be including in the following. We will often us the former definition $v^i = -a^2 H \frac{D'_+}{D_+ C}\frac{\partial_i}{\partial^2}\theta$, as well as the star notation from Eq. (F.44).

First, we expand the overdensity and velocity divergence perturbatively. Apart from $\delta^{(2)}$, the only second-order term is in the first line, which is given by

$$
\begin{aligned}
&-\int^a \frac{da'}{a'}\, c_\delta(a,a')\, \partial_i\delta^{(1)}(a') \int_{a'}^a \frac{da''}{a''^2 H(a'')} v^{(1)i}(a'') = \\
&= \int^a \frac{da'}{a'}\, c_\delta(a,a')\, \frac{D_+(a')}{D_+(a)}\partial_i\delta^{(1)}(a) \int_{a'}^a da''\, \frac{D'_+(a'')}{C(a'')D_+(a)}\frac{\partial^i}{\partial^2}\theta^{(1)}(a) \\
&= \int^a \frac{da'}{a'}\, c_\delta(a,a')\, \frac{D_+(a')}{D_+(a)}\partial_i\delta^{(1)}(a)\frac{\partial^i}{\partial^2}\theta^{(1)}(a) \left[\mathcal{G}(a) - \frac{D_+(a')}{D_+(a)}\mathcal{G}(a')\right] \\
&= \left[c_{\delta,1}(a)\mathcal{G}(a) - c_{\delta_2,\mathcal{G}_1^\delta}(a) - c_{\delta_2,\mathcal{G}_2^\delta}(a)\right] \partial_i\delta^{(1)}(a)\frac{\partial^i}{\partial^2}\theta^{(1)}(a) \\
&\overset{w\text{CDM}}{=} c_{\delta,12}(a)\partial_i\delta^{(1)}(a)\frac{\partial^i}{\partial^2}\theta^{(1)}(a)\ .
\end{aligned}
\tag{F.46}
$$

Next, we take this same term with δ at second order and v at first order. This gives

$$
\begin{aligned}
&-\int^a \frac{da'}{a'}\, c_\delta(a,a')\, \partial_i\delta^{(2)}(a') \int_{a'}^a \frac{da''}{a''^2 H(a'')}\, v^{(1)i}(a'') = \\
&= \int^a \frac{da'}{a'}\, c_\delta(a,a')\, \left[\mathcal{G}(a) - \frac{D_+(a')}{D_+(a)}\mathcal{G}(a')\right] \partial_i\delta^{(2)}(a')\frac{\partial^i}{\partial^2}\theta^{(1)}(a)\ .
\end{aligned}
\tag{F.47}
$$

In Fourier space this reads

$$
\begin{aligned}
&= \left[\mathcal{G}(a)c_{\delta_2,\mathcal{G}_1^\delta} - c_{\delta,\mathcal{G}_1^\delta}\right] \left(\alpha^1(\vec{q}_1,\vec{q}_2,\vec{q}_3) - \alpha(\vec{q}_1,\vec{q}_2)\right) \\
&\quad + \left[\mathcal{G}(a)c_{\delta_2,\mathcal{G}_2^\delta} - c_{\delta,\mathcal{G}_2^\delta}\right] \left(\alpha^2(\vec{q}_1,\vec{q}_2,\vec{q}_3) - \beta(\vec{q}_1,\vec{q}_2)\right) \\
&\overset{\text{EdS}}{=} \left[c_{\delta,2}(a) - c_{\delta,3}(a)\right] {}^*[\partial_i\delta^{(2)}\frac{\partial^i}{\partial^2}\theta^{(1)}]_{\vec{k}}(a),
\end{aligned}
\tag{F.48}
$$

Again, from the same term, we can take δ at linear and v at second order. We have

$$
\begin{aligned}
&-\int^a \frac{da'}{a'}\, c_\delta(a,a')\, \partial_i\delta^{(1)}(a') \int_{a'}^a \frac{da''}{a''^2 H(a'')}\, v^{(2)i}(a'') = \\
&= \int^a \frac{da'}{a'}\, c_\delta(a,a')\, \frac{D_+(a')}{D_+(a)}\partial_i\delta^{(1)}(a) \int_{a'}^a da''\, \frac{D'_+(a'')}{C(a'')D_+(a'')}\frac{\partial^i}{\partial^2}\theta^{(2)}(a'')\ .
\end{aligned}
\tag{F.49}
$$

In terms of Fourier space kernels this reads

$$
\begin{aligned}
&= \int^a \frac{da'}{a'} c_\delta(a,a') \frac{D_+(a')}{D_+(a)} \int_{a'}^a da'' \frac{D'_+(a'')D_+(a'')}{C(a'')D_+(a)^2} \mathcal{G}_1^\theta(a'') \left(\gamma^1(\vec{q}_1,\vec{q}_2,\vec{q}_3) - \alpha(\vec{q}_1,\vec{q}_2)\right) \\
&\quad + \int^a \frac{da'}{a'} c_\delta(a,a') \frac{D_+(a')}{D_+(a)} \int_{a'}^a da'' \frac{D'_+(a'')D_+(a'')}{C(a'')D_+(a)^2} \mathcal{G}_2^\theta(a'') \left(\gamma^2(\vec{q}_1,\vec{q}_2,\vec{q}_3) - \beta(\vec{q}_1,\vec{q}_2)\right) \\
&= \left[\left(\mathcal{V}_{11}^\delta(a) + \mathcal{V}_{12}^\delta(a)\right) c_{\delta,1} - c_{\delta,\mathcal{V}_{11}^\delta} - c_{\delta,\mathcal{V}_{12}^\delta}\right] \left(\gamma^1(\vec{q}_1,\vec{q}_2,\vec{q}_3) - \alpha(\vec{q}_1,\vec{q}_2)\right) \\
&\quad + \left[\left(\mathcal{V}_{21}^\delta(a) + \mathcal{V}_{22}^\delta(a)\right) c_{\delta,1} - c_{\delta,\mathcal{V}_{21}^\delta} - c_{\delta,\mathcal{V}_{22}^\delta}\right] \left(\gamma^2(\vec{q}_1,\vec{q}_2,\vec{q}_3) - \beta(\vec{q}_1,\vec{q}_2)\right) \qquad \text{(F.50)} \\
&\overset{\text{EdS}}{=} \frac{1}{2}\left[c_{\delta,1}(a) - c_{\delta,3}(a)\right] * [\partial_i \delta^{(1)}(a) \frac{\partial^i}{\partial^2} \theta^{(2)}(a)]_{\vec{k}},
\end{aligned}
$$

where the expression for clustering quintessence takes the same form as for wCDM, and we used Eq. (F.25).

In the second and third lines of Eq. (F.45) we can take all fields at linear order. We have

$$
\begin{aligned}
&\int^a \frac{da'}{a'} c_\delta(a,a') \frac{1}{2} \partial_i\partial_j \delta(x,a') \int_{a'}^a \frac{da''}{a''^2 H(a'')} v^{(1)i}(\vec{x},a'') \int_{a'}^a \frac{da'''}{a'''^2 H(a''')} v^{(1)j}(\vec{x},a''') \\
&\quad + \int^a \frac{da'}{a'} c_\delta(a,a') \partial_i \delta(x,a') \int_{a'}^a \frac{da''}{a''^2 H(a'')} \partial_j v^{(1)i}(\vec{x},a'') \int_{a''}^a \frac{da'''}{a'''^2 H(a''')} v^{(1)j}(\vec{x},a''') \\
&= \int^a \frac{da'}{a'} c_\delta(a,a') \frac{1}{2} \frac{D_+(a')}{D_+(a)} \partial_i\partial_j \delta^{(1)} \frac{\partial^i}{\partial^2}\theta^{(1)} \frac{\partial^j}{\partial^2}\theta^{(1)} \int_{a'}^a da'' \frac{D'_+(a'')}{C(a'')D_+(a)} \int_{a'}^a da''' \frac{D'_+(a''')}{C(a''')D_+(a)} \\
&\quad + \int^a \frac{da'}{a'} c_\delta(a,a') \frac{D_+(a')}{D_+(a)} \partial_i \delta^{(1)} \frac{\partial_j\partial^i}{\partial^2}\theta^{(1)} \frac{\partial^j}{\partial^2}\theta^{(1)} \int_{a'}^a da'' \frac{D'_+(a'')}{C(a'')D_+(a)} \int_{a''}^a da''' \frac{D'_+(a''')}{C(a''')D_+(a)} \\
&= \int^a \frac{da'}{a'} c_\delta(a,a') \frac{1}{2} \frac{D_+(a')}{D_+(a)} \left(\mathcal{G}(a) - \frac{D_+(a')}{D_+(a)} \mathcal{G}(a')\right)^2 \times \qquad \text{(F.51)} \\
&\qquad\qquad \times \left[\partial_i\partial_j \delta^{(1)} \frac{\partial^i}{\partial^2}\theta^{(1)} \frac{\partial^j}{\partial^2}\theta^{(1)} + \partial_i \delta^{(1)} \frac{\partial_j\partial^i}{\partial^2}\theta^{(1)} \frac{\partial^j}{\partial^2}\theta^{(1)}\right](a) \\
&= \left(\frac{\mathcal{G}(a)^2}{2} c_{\delta,1} - \mathcal{G}(a)(c_{\delta_2,\mathcal{G}_1^\delta} + c_{\delta_2,\mathcal{G}_2^\delta}) + \frac{1}{2}(c_{\delta,\mathcal{G}_1^\delta} + c_{\delta,\mathcal{G}_2^\delta})\right) \times \\
&\qquad\qquad \times \left[\partial_i\partial_j \delta^{(1)} \frac{\partial^i}{\partial^2}\theta^{(1)} \frac{\partial^j}{\partial^2}\theta^{(1)} + \partial_i \delta^{(1)} \frac{\partial_j\partial^i}{\partial^2}\theta^{(1)} \frac{\partial^j}{\partial^2}\theta^{(1)}\right](a) \\
&\overset{w\text{CDM}}{=} c_{\delta,123}(a) \left[\partial_i\partial_j \delta^{(1)} \frac{\partial^i}{\partial^2}\theta^{(1)} \frac{\partial^j}{\partial^2}\theta^{(1)} + \partial_i \delta^{(1)} \frac{\partial_j\partial^i}{\partial^2}\theta^{(1)} \frac{\partial^j}{\partial^2}\theta^{(1)}\right](a) \ .
\end{aligned}
$$

For completeness, the flow terms from δ^2 and s^2 read

$$
\begin{aligned}
&2\left(\mathcal{G}(a) c_{\delta^2,1} - c_{\delta^2,\mathcal{G}_1^\delta} - c_{\delta^2,\mathcal{G}_2^\delta}\right) [\delta^{(1)} \partial_i \delta^{(1)} \frac{\partial^i}{\partial^2}\theta^{(1)}]_{\vec{k}}(a) \qquad \text{(F.52)} \\
&\overset{w\text{CDM}}{=} 2 c_{\delta^2,12} [\delta^{(1)} \partial_i \delta^{(1)} \frac{\partial^i}{\partial^2}\theta^{(1)}]_{\vec{k}}(a) \ ,
\end{aligned}
$$

$$2\left(\mathcal{G}(a)c_{s^2,1} - c_{s^2,\mathcal{G}_1^\delta} - c_{s^2,\mathcal{G}_2^\delta}\right)[s^{(1)}_{lm}\partial_i(s^{lm})^{(1)}\frac{\partial^i}{\partial^2}\theta^{(1)}]_{\vec{k}}(a) \tag{F.53}$$
$$\overset{w\text{CDM}}{=} 2c_{s^2,12}[s^{(1)}_{lm}\partial_i(s^{lm})^{(1)}\frac{\partial^i}{\partial^2}\theta^{(1)}]_{\vec{k}}(a)\ .$$

F.4 Full Posteriors

In Fig. F.1, we show the full posteriors for all cosmological and the non-analytically marginalized bias parameters for the analysis of BOSS data alone of Fig. 10.7.

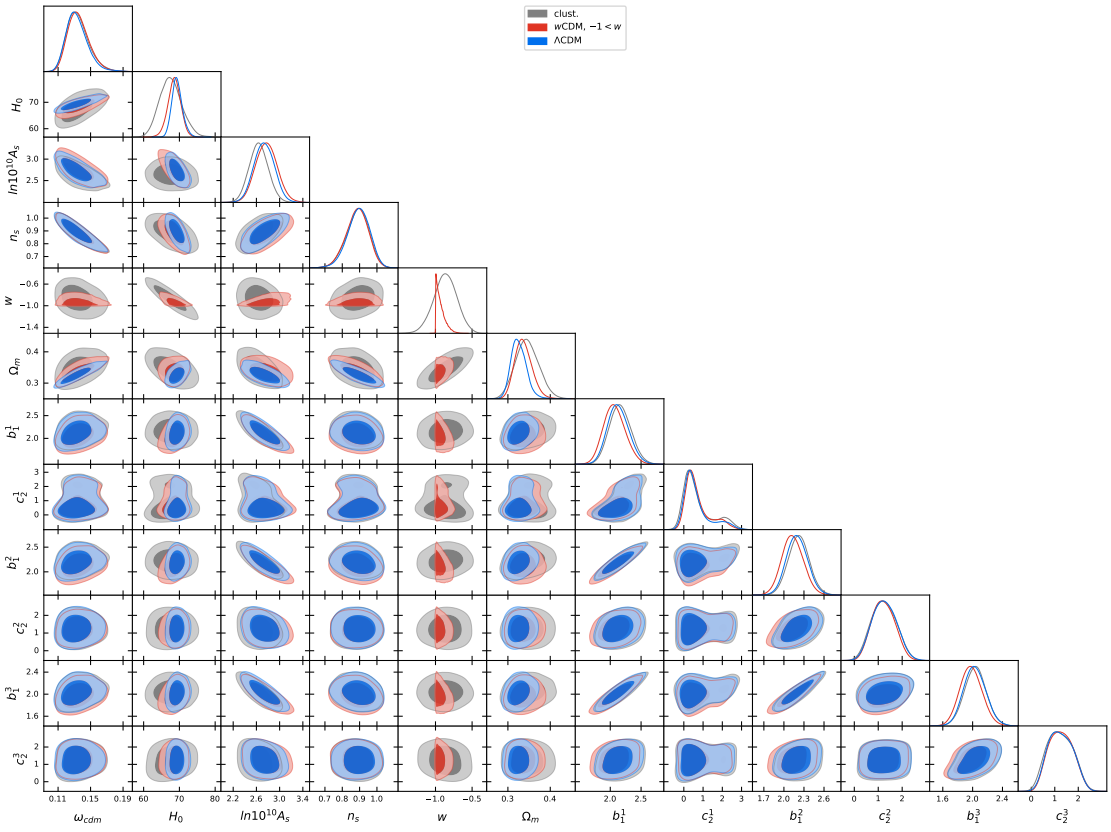

Figure F.1: Full posteriors for the fits of clustering quintessence, wCDM with physical prior $w \geq 1$, and ΛCDM, to BOSS with a BBN prior. We show the non-analytically marginalized biases b_1^i and c_2^i, where i denotes the skycuts: $i = 1$ is CMASS NGC, $i = 2$ is CMASS SGC, $i = 3$ is LOWZ NGC.

Bibliography

[1] Y. Donath and E. Pajer, *The in-out formalism for in-in correlators*, *JHEP* **07** (2024) 064 [2402.05999].

[2] G. D'Amico, Y. Donath, M. Lewandowski, L. Senatore and P. Zhang, *The one-loop bispectrum of galaxies in redshift space from the Effective Field Theory of Large-Scale Structure*, 2211.17130.

[3] G. D'Amico, Y. Donath, M. Lewandowski, L. Senatore and P. Zhang, *The BOSS bispectrum analysis at one loop from the Effective Field Theory of Large-Scale Structure*, 2206.08327.

[4] D. Braganca, Y. Donath, L. Senatore and H. Zheng, *Peeking into the next decade in Large-Scale Structure Cosmology with its Effective Field Theory*, 2307.04992.

[5] Y. Donath, M. Lewandowski and L. Senatore, *Direct signatures of the formation time of galaxies*, *Phys. Rev. D* **109** (2024) 123510 [2307.11409].

[6] G. D'Amico, Y. Donath, L. Senatore and P. Zhang, *Limits on Clustering and Smooth Quintessence from the EFTofLSS*, 2012.07554.

[7] G. D'Amico, J. Gleyzes, N. Kokron, D. Markovic, L. Senatore, P. Zhang et al., *The Cosmological Analysis of the SDSS/BOSS data from the Effective Field Theory of Large-Scale Structure*, *JCAP* **05** (2020) 005 [1909.05271].

[8] N. Arkani-Hamed and J. Maldacena, *Cosmological Collider Physics*, 1503.08043.

[9] BOSS collaboration, *The clustering of galaxies in the completed SDSS-III Baryon Oscillation Spectroscopic Survey: cosmological analysis of the DR12 galaxy sample*, *Mon. Not. Roy. Astron. Soc.* **470** (2017) 2617 [1607.03155].

[10] Planck collaboration, *Planck 2018 results. VII. Isotropy and Statistics of the CMB*, *Astron. Astrophys.* **641** (2020) A7 [1906.02552].

[11] H. Bondi and T. Gold, *The Steady-State Theory of the Expanding Universe*, *Mon. Not. Roy. Astron. Soc.* **108** (1948) 252.

[12] J. Stebbins and A.E. Whitford, *Six-Color Photometry of Stars. VI. The Colors of Extragalactic Nebulae*, *Astrophysical Journal* **108** (1948) 413.

[13] G. Gamow, *On the steady-state theory of the universe*, *Astronomical Journal* **59** (1954) 200.

[14] E.V. Linder, *Exploring the expansion history of the universe*, *Phys. Rev. Lett.* **90** (2003) 091301 [astro-ph/0208512].

[15] P.F. De Salas, S. Gariazzo, O. Mena, C.A. Ternes and M. Tórtola, *Neutrino Mass Ordering from Oscillations and Beyond: 2018 Status and Future Prospects*, *Front. Astron. Space Sci.* **5** (2018) 36 [1806.11051].

[16] R. de Belsunce and L. Senatore, *Tree-Level Bispectrum in the Effective Field Theory of Large-Scale Structure extended to Massive Neutrinos*, *JCAP* **02** (2019) 038 [1804.06849].

[17] D. Racco, P. Zhang and H. Zheng, *Neutrino masses from large-scale structures: Future sensitivity and theory dependence*, *Phys. Dark Univ.* **47** (2025) 101803 [2412.04959].

[18] Y.B. Zeldovich, *Cosmological Constant and Elementary Particles*, *JETP Lett.* **6** (1967) 316.

[19] Y.B. Zel'dovich, A. Krasinski and Y.B. Zeldovich, *The Cosmological constant and the theory of elementary particles*, *Sov. Phys. Usp.* **11** (1968) 381.

[20] L. Verde, T. Treu and A.G. Riess, *Tensions between the Early and the Late Universe*, *Nature Astron.* **3** (2019) 891 [1907.10625].

[21] E. Di Valentino, O. Mena, S. Pan, L. Visinelli, W. Yang, A. Melchiorri et al., *In the realm of the Hubble tension—a review of solutions*, *Class. Quant. Grav.* **38** (2021) 153001 [2103.01183].

[22] DESI collaboration, *DESI 2024 VII: Cosmological Constraints from the Full-Shape Modeling of Clustering Measurements*, 2411.12022.

[23] K. Lodha et al., *Extended Dark Energy analysis using DESI DR2 BAO measurements*, 2503.14743.

[24] Planck collaboration, *Planck 2018 results. VI. Cosmological parameters*, *Astron. Astrophys.* **641** (2020) A6 [1807.06209].

[25] PLANCK collaboration, *Planck 2018 results. X. Constraints on inflation*, *Astron. Astrophys.* **641** (2020) A10 [1807.06211].

[26] A. Lewis and A. Challinor, *CAMB: Code for Anisotropies in the Microwave Background*, .

[27] D. Blas, J. Lesgourgues and T. Tram, *The Cosmic Linear Anisotropy Solving System (CLASS) II: Approximation schemes*, *JCAP* **1107** (2011) 034 [1104.2933].

[28] J.J.M. Carrasco, M.P. Hertzberg and L. Senatore, *The Effective Field Theory of Cosmological Large Scale Structures*, *JHEP* **09** (2012) 082 [1206.2926].

[29] V. Springel et al., *Simulating the joint evolution of quasars, galaxies and their large-scale distribution*, *Nature* **435** (2005) 629 [astro-ph/0504097].

[30] D. Baumann, A. Nicolis, L. Senatore and M. Zaldarriaga, *Cosmological Non-Linearities as an Effective Fluid*, *JCAP* **1207** (2012) 051 [1004.2488].

[31] D.P. Bragança, M. Lewandowski, D. Sekera, L. Senatore and R. Sgier, *Baryonic effects in the Effective Field Theory of Large-Scale Structure and an analytic recipe for lensing in CMB-S4*, 2010.02929.

[32] SIMBIG collaboration, *Field-level simulation-based inference of galaxy clustering with convolutional neural networks*, *Phys. Rev. D* **109** (2024) 083536 [2310.15256].

[33] BEYOND-2PT collaboration, *A Parameter-Masked Mock Data Challenge for Beyond-Two-Point Galaxy Clustering Statistics*, 2405.02252.

[34] A. Amon and G. Efstathiou, *A non-linear solution to the S_8 tension?*, *Mon. Not. Roy. Astron. Soc.* **516** (2022) 5355 [2206.11794].

[35] A.H. Guth, *The Inflationary Universe: A Possible Solution to the Horizon and Flatness Problems*, *Phys. Rev. D* **23** (1981) 347.

[36] S. Kachru, R. Kallosh, A.D. Linde and S.P. Trivedi, *De Sitter vacua in string theory*, *Phys. Rev. D* **68** (2003) 046005 [hep-th/0301240].

[37] S. Weinberg, *Adiabatic modes in cosmology*, *Phys. Rev. D* **67** (2003) 123504 [astro-ph/0302326].

[38] V. Assassi, D. Baumann and D. Green, *Symmetries and Loops in Inflation*, *JHEP* **02** (2013) 151 [1210.7792].

[39] L. Senatore and M. Zaldarriaga, *The constancy of ζ in single-clock Inflation at all loops*, *JHEP* **09** (2013) 148 [1210.6048].

[40] N. Arkani-Hamed, D. Baumann, H. Lee and G.L. Pimentel, *The Cosmological Bootstrap: Inflationary Correlators from Symmetries and Singularities*, *JHEP* **04** (2020) 105 [1811.00024].

[41] J.S. Schwinger, *Brownian motion of a quantum oscillator*, *J. Math. Phys.* **2** (1961) 407.

[42] L.V. Keldysh, *Diagram technique for nonequilibrium processes*, *Zh. Eksp. Teor. Fiz.* **47** (1964) 1515.

[43] J.M. Maldacena, *Non-Gaussian features of primordial fluctuations in single field inflationary models*, *JHEP* **05** (2003) 013 [astro-ph/0210603].

[44] M. Gell-Mann and F. Low, *Bound states in quantum field theory*, *Phys. Rev.* **84** (1951) 350.

[45] C. Armendariz-Picon, T. Damour and V.F. Mukhanov, *k - inflation*, *Phys. Lett. B* **458** (1999) 209 [hep-th/9904075].

[46] M. Alishahiha, E. Silverstein and D. Tong, *DBI in the sky*, *Phys. Rev. D* **70** (2004) 123505 [hep-th/0404084].

[47] C. Cheung, P. Creminelli, A.L. Fitzpatrick, J. Kaplan and L. Senatore, *The Effective Field Theory of Inflation*, *JHEP* **03** (2008) 014 [0709.0293].

[48] P. Creminelli, G. D'Amico, J. Norena and F. Vernizzi, *The Effective Theory of Quintessence: the w<-1 Side Unveiled*, *JCAP* **0902** (2009) 018 [0811.0827].

[49] G. Gubitosi, F. Piazza and F. Vernizzi, *The Effective Field Theory of Dark Energy*, *JCAP* **1302** (2013) 032 [1210.0201].

[50] R.L. Arnowitt, S. Deser and C.W. Misner, *Dynamical Structure and Definition of Energy in General Relativity*, *Phys. Rev.* **116** (1959) 1322.

[51] P. Creminelli, M.A. Luty, A. Nicolis and L. Senatore, *Starting the Universe: Stable Violation of the Null Energy Condition and Non-standard Cosmologies*, *JHEP* **12** (2006) 080 [hep-th/0606090].

[52] C. Cheung, A.L. Fitzpatrick, J. Kaplan and L. Senatore, *On the consistency relation of the 3-point function in single field inflation*, *JCAP* **02** (2008) 021 [0709.0295].

[53] M. Liguori, E. Sefusatti, J.R. Fergusson and E.P.S. Shellard, *Primordial non-Gaussianity and Bispectrum Measurements in the Cosmic Microwave Background and Large-Scale Structure*, *Adv. Astron.* **2010** (2010) 980523 [1001.4707].

[54] L. Senatore, K.M. Smith and M. Zaldarriaga, *Non-Gaussianities in Single Field Inflation and their Optimal Limits from the WMAP 5-year Data*, *JCAP* **01** (2010) 028 [0905.3746].

[55] E. Komatsu and D.N. Spergel, *Acoustic signatures in the primary microwave background bispectrum*, *Phys. Rev. D* **63** (2001) 063002 [astro-ph/0005036].

[56] L. Senatore and M. Zaldarriaga, *The Effective Field Theory of Multifield Inflation*, *JHEP* **04** (2012) 024 [1009.2093].

[57] W. Sohn, D.-G. Wang, J.R. Fergusson and E.P.S. Shellard, *Searching for cosmological collider in the Planck CMB data*, *JCAP* **09** (2024) 016 [2404.07203].

[58] S.A. Salcedo, T. Colas and E. Pajer, *The open effective field theory of inflation*, *JHEP* **10** (2024) 248 [2404.15416].

[59] R. Flauger and E. Pajer, *Resonant Non-Gaussianity*, *JCAP* **01** (2011) 017 [1002.0833].

[60] Planck collaboration, *Planck 2018 results. IX. Constraints on primordial non-Gaussianity*, *Astron. Astrophys.* **641** (2020) A9 [1905.05697].

[61] T.S. Bunch and P.C.W. Davies, *Quantum Field Theory in de Sitter Space: Renormalization by Point Splitting*, *Proc. Roy. Soc. Lond. A* **360** (1978) 117.

[62] J.B. Hartle and S.W. Hawking, *Wave Function of the Universe*, *Phys. Rev. D* **28** (1983) 2960.

[63] S. Weinberg, *Quantum contributions to cosmological correlations*, *Phys. Rev. D* **72** (2005) 043514 [hep-th/0506236].

[64] X. Chen, Y. Wang and Z.-Z. Xianyu, *Schwinger-Keldysh Diagrammatics for Primordial Perturbations*, *JCAP* **12** (2017) 006 [1703.10166].

[65] R.P. Feynman and F. Vernon Jr, *The theory of a general quantum system interacting with a linear dissipative system*, *Annals of physics* **281** (2000) 547.

[66] H.-P. Breuer and F. Petruccione, *The theory of open quantum systems*, Oxford University Press, USA (2002).

[67] A. Kamenev, *Field theory of non-equilibrium systems*, Cambridge University Press (2023).

[68] D. Marolf, I.A. Morrison and M. Srednicki, *Perturbative S-matrix for massive scalar fields in global de Sitter space*, *Class. Quant. Grav.* **30** (2013) 155023 [1209.6039].

[69] S. Melville and G.L. Pimentel, *A de Sitter S-matrix for the masses*, 2309.07092.

[70] H. Goodhew, S. Jazayeri and E. Pajer, *The Cosmological Optical Theorem*, *JCAP* **04** (2021) 021 [2009.02898].

[71] S. Céspedes, A.-C. Davis and S. Melville, *On the time evolution of cosmological correlators*, *JHEP* **02** (2021) 012 [2009.07874].

[72] S. Melville and E. Pajer, *Cosmological Cutting Rules*, *JHEP* **05** (2021) 249 [2103.09832].

[73] H. Goodhew, S. Jazayeri, M.H. Gordon Lee and E. Pajer, *Cutting cosmological correlators*, *JCAP* **08** (2021) 003 [2104.06587].

[74] J. Bonifacio, E. Pajer and D.-G. Wang, *From amplitudes to contact cosmological correlators*, *JHEP* **10** (2021) 001 [2106.15468].

[75] G.L. Pimentel and D.-G. Wang, *Boostless Cosmological Collider Bootstrap*, 2205.00013.

[76] S. Jazayeri and S. Renaux-Petel, *Cosmological Bootstrap in Slow Motion*, 2205.10340.

[77] D. Baumann, D. Green, A. Joyce, E. Pajer, G.L. Pimentel, C. Sleight et al., *Snowmass White Paper: The Cosmological Bootstrap*, in *2022 Snowmass Summer Study*, 3, 2022 [2203.08121].

[78] S. Jazayeri, E. Pajer and D. Stefanyszyn, *From locality and unitarity to cosmological correlators*, *JHEP* **10** (2021) 065 [2103.08649].

[79] J. Bonifacio, H. Goodhew, A. Joyce, E. Pajer and D. Stefanyszyn, *The graviton four-point function in de Sitter space*, 2212.07370.

[80] G. Cabass, S. Jazayeri, E. Pajer and D. Stefanyszyn, *Parity violation in the scalar trispectrum: no-go theorems and yes-go examples*, 2210.02907.

[81] D. Baumann, W.-M. Chen, C. Duaso Pueyo, A. Joyce, H. Lee and G.L. Pimentel, *Linking the singularities of cosmological correlators*, *JHEP* **09** (2022) 010 [2106.05294].

[82] C. Duaso Pueyo and E. Pajer, *A Cosmological Bootstrap for Resonant Non-Gaussianity*, 2311.01395.

[83] M. Hogervorst, J.a. Penedones and K.S. Vaziri, *Towards the non-perturbative cosmological bootstrap*, 2107.13871.

[84] L. Di Pietro, V. Gorbenko and S. Komatsu, *Analyticity and unitarity for cosmological correlators*, *JHEP* **03** (2022) 023 [2108.01695].

[85] J. Bros, *Complexified de Sitter space: Analytic causal kernels and Kallen-Lehmann type representation*, *Nucl. Phys. B Proc. Suppl.* **18** (1991) 22.

[86] S. Hollands, *Massless interacting quantum fields in deSitter spacetime*, *Annales Henri Poincare* **13** (2012) 1039 [1105.1996].

[87] M. Loparco, J. Penedones, K. Salehi Vaziri and Z. Sun, *The Källén-Lehmann representation in de Sitter spacetime*, 2306.00090.

[88] H. Liu and P. Glorioso, *Lectures on non-equilibrium effective field theories and fluctuating hydrodynamics*, *PoS* **TASI2017** (2018) 008 [1805.09331].

[89] J. Cotler and A. Strominger, *The Universe as a Quantum Encoder*, 2201.11658.

[90] J. Cotler and K. Jensen, *Isometric Evolution in de Sitter Quantum Gravity*, *Phys. Rev. Lett.* **131** (2023) 211601 [2302.06603].

[91] N. Arkani-Hamed, P. Benincasa and A. Postnikov, *Cosmological Polytopes and the Wavefunction of the Universe*, 1709.02813.

[92] M. Gillioz, X. Lu and M.A. Luty, *Scale Anomalies, States, and Rates in Conformal Field Theory*, *JHEP* **04** (2017) 171 [1612.07800].

[93] D. Meltzer and A. Sivaramakrishnan, *CFT unitarity and the AdS Cutkosky rules*, *JHEP* **11** (2020) 073 [2008.11730].

[94] M.J.G. Veltman, *Diagrammatica: The Path to Feynman rules*, vol. 4, Cambridge University Press (5, 2012).

[95] N.P. Landsman and C.G. van Weert, *Real and Imaginary Time Field Theory at Finite Temperature and Density*, *Phys. Rept.* **145** (1987) 141.

[96] D. Marolf and I.A. Morrison, *The IR stability of de Sitter: Loop corrections to scalar propagators*, *Phys. Rev. D* **82** (2010) 105032 [1006.0035].

[97] R. Penrose, *Cycles of time: an extraordinary new view of the universe*, Random House (2010).

[98] M. Luscher and G. Mack, *Global Conformal Invariance in Quantum Field Theory*, *Commun. Math. Phys.* **41** (1975) 203.

[99] M. Gillioz, *Conformal field theory for particle physicists*, SpringerBriefs in Physics, Springer (2023), 10.1007/978-3-031-27086-4, [2207.09474].

[100] C. Sleight and M. Taronna, *From dS to AdS and back*, *JHEP* **12** (2021) 074 [2109.02725].

[101] S.R. Behbahani and D. Green, *Collective Symmetry Breaking and Resonant Non-Gaussianity*, *JCAP* **11** (2012) 056 [1207.2779].

[102] D. Green, M. Lewandowski, L. Senatore, E. Silverstein and M. Zaldarriaga, *Anomalous Dimensions and Non-Gaussianity*, *JHEP* **10** (2013) 171 [1301.2630].

[103] S. Chaykov, N. Agarwal, S. Bahrami and R. Holman, *Loop corrections in Minkowski spacetime away from equilibrium. Part II. Finite-time results*, *JHEP* **02** (2023) 094 [2206.11289].

[104] S. Chaykov, N. Agarwal, S. Bahrami and R. Holman, *Loop corrections in Minkowski spacetime away from equilibrium. Part I. Late-time resummations*, *JHEP* **02** (2023) 093 [2206.11288].

[105] C. McCulloch, E. Pajer and X. Tong, *A Cosmological Tachyon Collider: Enhancing the Long-Short Scale Coupling*, 2401.11009.

[106] I. Heemskerk, D. Marolf, J. Polchinski and J. Sully, *Bulk and Transhorizon Measurements in AdS/CFT*, *JHEP* **10** (2012) 165 [1201.3664].

[107] F.M. Haehl, R. Loganayagam, P. Narayan and M. Rangamani, *Classification of out-of-time-order correlators*, *SciPost Phys.* **6** (2019) 001 [1701.02820].

[108] H. Lee, D. Baumann and G.L. Pimentel, *Non-Gaussianity as a Particle Detector*, *JHEP* **12** (2016) 040 [1607.03735].

[109] A. Bzowski, P. McFadden and K. Skenderis, *Renormalisation of IR divergences and holography in de Sitter*, 2312.17316.

[110] H. Goodhew, *The Cosmological Implications of Unitarity*, Ph.D. thesis, Cambridge U., DAMTP, 2023. 10.17863/CAM.99550.

[111] S. Agüí Salcedo, M.H.G. Lee, S. Melville and E. Pajer, *The analytic wavefunction*, 2212.08009.

[112] S. Albayrak, P. Benincasa and C. Duaso Pueyo, *Perturbative Unitarity and the Wavefunction of the Universe*, 2305.19686.

[113] J. Chen and B. Feng, *Towards Systematic Evaluation of de Sitter Correlators via Generalized Integration-By-Parts Relations*, 2401.00129.

[114] R.E. Cutkosky, *Singularities and discontinuities of Feynman amplitudes*, *J. Math. Phys.* **1** (1960) 429.

[115] Z. Sun, *A note on the representations of* $SO(1, d+1)$, 2111.04591.

[116] J. Penedones, K. Salehi Vaziri and Z. Sun, *Hilbert space of Quantum Field Theory in de Sitter spacetime*, 2301.04146.

[117] A. Baidya, C. Jana, R. Loganayagam and A. Rudra, *Renormalization in open quantum field theory. Part I. Scalar field theory*, *JHEP* **11** (2017) 204 [1704.08335].

[118] L. Senatore and M. Zaldarriaga, *On Loops in Inflation*, *JHEP* **12** (2010) 008 [0912.2734].

[119] E. Pajer, *Building a Boostless Bootstrap for the Bispectrum*, *JCAP* **01** (2021) 023 [2010.12818].

[120] S. Agüí-Salcedo and S. Melville, *The Cosmological Tree Theorem*, 2308.00680.

[121] M.H.G. Lee, C. McCulloch and E. Pajer, *Leading loops in cosmological correlators*, *JHEP* **11** (2023) 038 [2305.11228].

[122] M.H.G. Lee, *From Amplitudes to Analytic Wavefunctions*, 2310.01525.

[123] D. Stefanyszyn, X. Tong and Y. Zhu, *Cosmological Correlators Through the Looking Glass: Reality, Parity, and Factorisation*, 2309.07769.

[124] N. Arkani-Hamed and P. Benincasa, *On the Emergence of Lorentz Invariance and Unitarity from the Scattering Facet of Cosmological Polytopes*, 1811.01125.

[125] P. Benincasa, *Cosmological Polytopes and the Wavefuncton of the Universe for Light States*, 1909.02517.

[126] D. Anselmi, *Algebraic cutting equations*, *Annals Phys.* **394** (2018) 294 [1612.07148].

[127] D. Anselmi, *Diagrammar of physical and fake particles and spectral optical theorem*, *JHEP* **11** (2021) 030 [2109.06889].

[128] M. Lewandowski, A. Perko and L. Senatore, *Analytic Prediction of Baryonic Effects from the EFT of Large Scale Structures*, *JCAP* **1505** (2015) 019 [1412.5049].

[129] L. Senatore, *Bias in the Effective Field Theory of Large Scale Structures*, *JCAP* **1511** (2015) 007 [1406.7843].

[130] M. Mirbabayi, F. Schmidt and M. Zaldarriaga, *Biased Tracers and Time Evolution*, *JCAP* **1507** (2015) 030 [1412.5169].

[131] R. Angulo, M. Fasiello, L. Senatore and Z. Vlah, *On the Statistics of Biased Tracers in the Effective Field Theory of Large Scale Structures*, *JCAP* **1509** (2015) 029 [1503.08826].

[132] T. Fujita, V. Mauerhofer, L. Senatore, Z. Vlah and R. Angulo, *Very Massive Tracers and Higher Derivative Biases*, *JCAP* **01** (2020) 009 [1609.00717].

[133] A. Perko, L. Senatore, E. Jennings and R.H. Wechsler, *Biased Tracers in Redshift Space in the EFT of Large-Scale Structure*, 1610.09321.

[134] E.O. Nadler, A. Perko and L. Senatore, *On the Bispectra of Very Massive Tracers in the Effective Field Theory of Large-Scale Structure*, *JCAP* **1802** (2018) 058 [1710.10308].

[135] Y. Donath and L. Senatore, *Biased Tracers in Redshift Space in the EFTofLSS with exact time dependence*, *JCAP* **10** (2020) 039 [2005.04805].

[136] P. McDonald and A. Roy, *Clustering of dark matter tracers: generalizing bias for the coming era of precision LSS*, *JCAP* **0908** (2009) 020 [0902.0991].

[137] L. Senatore and M. Zaldarriaga, *Redshift Space Distortions in the Effective Field Theory of Large Scale Structures*, 1409.1225.

[138] T. Baldauf, M. Mirbabayi, M. Simonovic and M. Zaldarriaga, *Equivalence Principle and the Baryon Acoustic Peak*, *Phys. Rev.* **D92** (2015) 043514 [1504.04366].

[139] L. Senatore and G. Trevisan, *On the IR-Resummation in the EFTofLSS*, *JCAP* **1805** (2018) 019 [1710.02178].

[140] M. Lewandowski and L. Senatore, *An analytic implementation of the IR-resummation for the BAO peak*, 1810.11855.

[141] D. Blas, M. Garny, M.M. Ivanov and S. Sibiryakov, *Time-Sliced Perturbation Theory II: Baryon Acoustic Oscillations and Infrared Resummation*, *JCAP* **1607** (2016) 028 [1605.02149].

[142] M.M. Ivanov, M. Simonović and M. Zaldarriaga, *Cosmological Parameters from the BOSS Galaxy Power Spectrum*, *JCAP* **05** (2020) 042 [1909.05277].

[143] T. Colas, G. D'amico, L. Senatore, P. Zhang and F. Beutler, *Efficient Cosmological Analysis of the SDSS/BOSS data from the Effective Field Theory of Large-Scale Structure*, *JCAP* **06** (2020) 001 [1909.07951].

[144] M. Lewandowski, L. Senatore, F. Prada, C. Zhao and C.-H. Chuang, *EFT of large scale structures in redshift space*, *Phys. Rev.* **D97** (2018) 063526 [1512.06831].

[145] J.J.M. Carrasco, S. Foreman, D. Green and L. Senatore, *The 2-loop matter power spectrum and the IR-safe integrand*, *JCAP* **1407** (2014) 056 [1304.4946].

[146] L. Mercolli and E. Pajer, *On the velocity in the Effective Field Theory of Large Scale Structures*, *JCAP* **1403** (2014) 006 [1307.3220].

[147] J.J.M. Carrasco, S. Foreman, D. Green and L. Senatore, *The Effective Field Theory of Large Scale Structures at Two Loops*, *JCAP* **1407** (2014) 057 [1310.0464].

[148] R. Takahashi, *Third Order Density Perturbation and One-loop Power Spectrum in a Dark Energy Dominated Universe*, *Prog. Theor. Phys.* **120** (2008) 549 [0806.1437].

[149] P. Zhang and Y. Cai, *BOSS full-shape analysis from the EFTofLSS with exact time dependence*, *JCAP* **01** (2022) 031 [2111.05739].

[150] M.H. Goroff, B. Grinstein, S.J. Rey and M.B. Wise, *Coupling of Modes of Cosmological Mass Density Fluctuations*, *Astrophys. J.* **311** (1986) 6.

[151] B. Jain and E. Bertschinger, *Second order power spectrum and nonlinear evolution at high redshift*, *Astrophys. J.* **431** (1994) 495 [astro-ph/9311070].

[152] T. Baldauf, L. Mercolli, M. Mirbabayi and E. Pajer, *The Bispectrum in the Effective Field Theory of Large Scale Structure*, *JCAP* **05** (2015) 007 [1406.4135].

[153] T. Matsubara, *Resumming Cosmological Perturbations via the Lagrangian Picture: One-loop Results in Real Space and in Redshift Space*, *Phys. Rev. D* **77** (2008) 063530 [0711.2521].

[154] B. Jain and E. Bertschinger, *Selfsimilar evolution of cosmological density fluctuations*, *Astrophys. J.* **456** (1996) 43 [astro-ph/9503025].

[155] P. Creminelli, J. Noreña, M. Simonović and F. Vernizzi, *Single-Field Consistency Relations of Large Scale Structure*, *JCAP* **12** (2013) 025 [1309.3557].

[156] M. Lewandowski, *Violation of the consistency relations for large-scale structure with dark energy*, *JCAP* **08** (2020) 044 [1912.12292].

[157] V. Desjacques, D. Jeong and F. Schmidt, *Large-Scale Galaxy Bias*, *Phys. Rept.* **733** (2018) 1 [1611.09787].

[158] A. Eggemeier, R. Scoccimarro and R.E. Smith, *Bias Loop Corrections to the Galaxy Bispectrum*, *Phys. Rev. D* **99** (2019) 123514 [1812.03208].

[159] P. McDonald, *Clustering of dark matter tracers: Renormalizing the bias parameters*, *Phys. Rev. D* **74** (2006) 103512 [astro-ph/0609413].

[160] M. Levi, C. Bebek, T. Beers, R. Blum, R. Cahn, D. Eisenstein et al., *The DESI Experiment, a whitepaper for Snowmass 2013*, *ArXiv e-prints* (2013) [1308.0847].

[161] Euclid Theory Working Group collaboration, *Cosmology and fundamental physics with the Euclid satellite*, *Living Rev. Rel.* **16** (2013) 6 [1206.1225].

[162] P. Zhang, G. D'Amico, L. Senatore, C. Zhao and Y. Cai, *BOSS Correlation Function analysis from the Effective Field Theory of Large-Scale Structure*, *JCAP* **02** (2022) 036 [2110.07539].

[163] S.-F. Chen, Z. Vlah and M. White, *A new analysis of galaxy 2-point functions in the BOSS survey, including full-shape information and post-reconstruction BAO*, *JCAP* **02** (2022) 008 [2110.05530].

[164] O.H.E. Philcox and M.M. Ivanov, *The BOSS DR12 Full-Shape Cosmology: ΛCDM Constraints from the Large-Scale Galaxy Power Spectrum and Bispectrum Monopole*, 2112.04515.

[165] N.S. Sugiyama, S. Saito, F. Beutler and H.-J. Seo, *A complete FFT-based de composition formalism for the redshift-space bispectrum*, *Mon. Not. Roy. Astron. Soc.* **484** (2019) 364 [1803.02132].

[166] N.S. Sugiyama, S. Saito, F. Beutler and H.-J. Seo, *Perturbation theory approach to predict the covariance matrices of the galaxy power spectrum and bispectrum in redshift space*, *Mon. Not. Roy. Astron. Soc.* **497** (2020) 1684 [1908.06234].

[167] N.S. Sugiyama, S. Saito, F. Beutler and H.-J. Seo, *Towards a self-consistent analysis of the anisotropic galaxy two- and three-point correlation functions on large scales: application to mock galaxy catalogues*, *Mon. Not. Roy. Astron. Soc.* **501** (2021) 2862 [2010.06179].

[168] O.H. Philcox, M.M. Ivanov, M. Simonović and M. Zaldarriaga, *Combining Full-Shape and BAO Analyses of Galaxy Power Spectra: A 1.6% CMB-independent constraint on H0*, *JCAP* **05** (2020) 032 [2002.04035].

[169] G. D'Amico, L. Senatore and P. Zhang, *Limits on wCDM from the EFTofLSS with the PyBird code*, *JCAP* **01** (2021) 006 [2003.07956].

[170] A.G. Riess, S. Casertano, W. Yuan, L.M. Macri and D. Scolnic, *Large Magellanic Cloud Cepheid Standards Provide a 1% Foundation for the Determination of the Hubble Constant and Stronger Evidence for Physics beyond ΛCDM*, *Astrophys. J.* **876** (2019) 85 [1903.07603].

[171] W.L. Freedman et al., *The Carnegie-Chicago Hubble Program. VIII. An Independent Determination of the Hubble Constant Based on the Tip of the Red Giant Branch*, 1907.05922.

[172] G. D'Amico, L. Senatore, P. Zhang and H. Zheng, *The Hubble Tension in Light of the Full-Shape Analysis of Large-Scale Structure Data*, *JCAP* **05** (2021) 072 [2006.12420].

[173] M.M. Ivanov, E. McDonough, J.C. Hill, M. Simonović, M.W. Toomey, S. Alexander et al., *Constraining Early Dark Energy with Large-Scale Structure*, *Phys. Rev. D* **102** (2020) 103502 [2006.11235].

[174] F. Niedermann and M.S. Sloth, *New Early Dark Energy is compatible with current LSS data*, *Phys. Rev. D* **103** (2021) 103537 [2009.00006].

[175] T.L. Smith, V. Poulin, J.L. Bernal, K.K. Boddy, M. Kamionkowski and R. Murgia, *Early dark energy is not excluded by current large-scale structure data*, *Phys. Rev. D* **103** (2021) 123542 [2009.10740].

[176] G. D'Amico, M. Lewandowski, L. Senatore and P. Zhang, *Limits on primordial non-Gaussianities from BOSS galaxy-clustering data*, 2201.11518.

[177] G. Cabass, M.M. Ivanov, O.H.E. Philcox, M. Simonović and M. Zaldarriaga, *Constraints on Single-Field Inflation from the BOSS Galaxy Survey*, *Phys. Rev. Lett.* **129** (2022) 021301 [2201.07238].

[178] G. Cabass, M.M. Ivanov, O.H.E. Philcox, M. Simonović and M. Zaldarriaga, *Constraints on multifield inflation from the BOSS galaxy survey*, *Phys. Rev. D* **106** (2022) 043506 [2204.01781].

[179] P. Creminelli, A. Nicolis, L. Senatore, M. Tegmark and M. Zaldarriaga, *Limits on non-gaussianities from wmap data*, *JCAP* **0605** (2006) 004 [astro-ph/0509029].

[180] F. Bernardeau and J.-P. Uzan, *NonGaussianity in multifield inflation*, *Phys. Rev. D* **66** (2002) 103506 [hep-ph/0207295].

[181] D.H. Lyth, C. Ungarelli and D. Wands, *The Primordial density perturbation in the curvaton scenario*, *Phys. Rev. D* **67** (2003) 023503 [astro-ph/0208055].

[182] M. Zaldarriaga, *Non-Gaussianities in models with a varying inflaton decay rate*, *Phys. Rev. D* **69** (2004) 043508 [astro-ph/0306006].

[183] D. Babich, P. Creminelli and M. Zaldarriaga, *The Shape of non-Gaussianities*, *JCAP* **08** (2004) 009 [astro-ph/0405356].

[184] WMAP collaboration, *Nine-Year Wilkinson Microwave Anisotropy Probe (WMAP) Observations: Final Maps and Results*, *Astrophys. J. Suppl.* **208** (2013) 20 [1212.5225].

[185] A. Slosar, C. Hirata, U. Seljak, S. Ho and N. Padmanabhan, *Constraints on local primordial non-Gaussianity from large scale structure*, *JCAP* **08** (2008) 031 [0805.3580].

[186] N. Dalal, O. Dore, D. Huterer and A. Shirokov, *The imprints of primordial non-gaussianities on large-scale structure: scale dependent bias and abundance of virialized objects*, *Phys. Rev. D* **77** (2008) 123514 [0710.4560].

[187] L. Verde and S. Matarrese, *Detectability of the effect of Inflationary non-Gaussianity on halo bias*, *Astrophys. J. Lett.* **706** (2009) L91 [0909.3224].

[188] F. Schmidt and M. Kamionkowski, *Halo Clustering with Non-Local Non-Gaussianity*, *Phys. Rev. D* **82** (2010) 103002 [1008.0638].

[189] B. Reid et al., *SDSS-III Baryon Oscillation Spectroscopic Survey Data Release 12: galaxy target selection and large scale structure catalogues*, *Mon. Not. Roy. Astron. Soc.* **455** (2016) 1553 [1509.06529].

[190] F.-S. Kitaura et al., *The clustering of galaxies in the SDSS-III Baryon Oscillation Spectroscopic Survey: mock galaxy catalogues for the BOSS Final Data Release*, *Mon. Not. Roy. Astron. Soc.* **456** (2016) 4156 [1509.06400].

[191] J. Hartlap, P. Simon and P. Schneider, *Why your model parameter confidences might be too optimistic: Unbiased estimation of the inverse covariance matrix*, *Astron. Astrophys.* **464** (2007) 399 [astro-ph/0608064].

[192] H.A. Feldman, N. Kaiser and J.A. Peacock, *Power spectrum analysis of three-dimensional redshift surveys*, *Astrophys. J.* **426** (1994) 23 [astro-ph/9304022].

[193] K. Yamamoto, *Optimal weighting scheme in redshift space power spectrum analysis and a prospect for measuring the cosmic equation of state*, *Astrophys. J.* **595** (2003) 577 [astro-ph/0208139].

[194] K. Yamamoto, M. Nakamichi, A. Kamino, B.A. Bassett and H. Nishioka, *A Measurement of the quadrupole power spectrum in the clustering of the 2dF QSO Survey*, *Publ. Astron. Soc. Jap.* **58** (2006) 93 [astro-ph/0505115].

[195] D. Bianchi, H. Gil-Marín, R. Ruggeri and W.J. Percival, *Measuring line-of-sight dependent Fourier-space clustering using FFTs*, *Mon. Not. Roy. Astron. Soc.* **453** (2015) L11 [1505.05341].

[196] H. Gil-Marín et al., *The clustering of galaxies in the SDSS-III Baryon Oscillation Spectroscopic Survey: RSD measurement from the LOS-dependent power spectrum of DR12 BOSS galaxies*, *Mon. Not. Roy. Astron. Soc.* **460** (2016) 4188 [1509.06386].

[197] R. Scoccimarro, S. Colombi, J.N. Fry, J.A. Frieman, E. Hivon and A. Melott, *Nonlinear evolution of the bispectrum of cosmological perturbations*, *Astrophys. J.* **496** (1998) 586 [astro-ph/9704075].

[198] E. Sefusatti, *Probing fundamental physics with large-scale structure: From Galaxy formation to inflation*, other thesis, 2005.

[199] R. Scoccimarro, *Fast Estimators for Redshift-Space Clustering*, *Phys. Rev. D* **92** (2015) 083532 [1506.02729].

[200] N. Hand, Y. Feng, F. Beutler, Y. Li, C. Modi, U. Seljak et al., *nbodykit: an open-source, massively parallel toolkit for large-scale structure*, *Astron. J.* **156** (2018) 160 [1712.05834].

[201] F. Beutler, E. Castorina and P. Zhang, *Interpreting measurements of the anisotropic galaxy power spectrum*, *JCAP* **03** (2019) 040 [1810.05051].

[202] A. de Mattia and V. Ruhlmann-Kleider, *Integral constraints in spectroscopic surveys*, *JCAP* **08** (2019) 036 [1904.08851].

[203] A. de Mattia et al., *The Completed SDSS-IV extended Baryon Oscillation Spectroscopic Survey: measurement of the BAO and growth rate of structure of the emission line galaxy sample from the anisotropic power spectrum between redshift 0.6 and 1.1*, *Mon. Not. Roy. Astron. Soc.* **501** (2021) 5616 [2007.09008].

[204] F. Beutler and P. McDonald, *Unified galaxy power spectrum measurements from 6dFGS, BOSS, and eBOSS*, *JCAP* **11** (2021) 031 [2106.06324].

[205] E. Sefusatti, M. Crocce, R. Scoccimarro and H. Couchman, *Accurate Estimators of Correlation Functions in Fourier Space*, *Mon. Not. Roy. Astron. Soc.* **460** (2016) 3624 [1512.07295].

[206] C. Anastasiou, D.P.L. Bragança, L. Senatore and H. Zheng, *Efficiently evaluating loop integrals in the EFTofLSS using QFT integrals with massive propagators*, 2212.07421.

[207] R. Scoccimarro, H.M.P. Couchman and J.A. Frieman, *The Bispectrum as a Signature of Gravitational Instability in Redshift-Space*, *Astrophys. J.* **517** (1999) 531 [astro-ph/9808305].

[208] H. Gil-Marín, W.J. Percival, L. Verde, J.R. Brownstein, C.-H. Chuang, F.-S. Kitaura et al., *The clustering of galaxies in the SDSS-III Baryon Oscillation Spectroscopic Survey: RSD measurement from the power spectrum and bispectrum of the DR12 BOSS galaxies*, *Mon. Not. Roy. Astron. Soc.* **465** (2017) 1757 [1606.00439].

[209] L. Senatore and M. Zaldarriaga, *The IR-resummed Effective Field Theory of Large Scale Structures*, *JCAP* **1502** (2015) 013 [1404.5954].

[210] M.M. Ivanov and S. Sibiryakov, *Infrared Resummation for Biased Tracers in Redshift Space*, *JCAP* **1807** (2018) 053 [1804.05080].

[211] J. Hamann, S. Hannestad, J. Lesgourgues, C. Rampf and Y.Y.Y. Wong, *Cosmological parameters from large scale structure - geometric versus shape information*, *JCAP* **2010** (2010) 022 [1003.3999].

[212] A. Chudaykin, M.M. Ivanov, O.H.E. Philcox and M. Simonović, *Nonlinear perturbation theory extension of the Boltzmann code CLASS*, *Phys. Rev. D* **102** (2020) 063533 [2004.10607].

[213] H. Gil-Marín, J. Noreña, L. Verde, W.J. Percival, C. Wagner, M. Manera et al., *The power spectrum and bispectrum of SDSS DR11 BOSS galaxies – I. Bias and gravity*, *Mon. Not. Roy. Astron. Soc.* **451** (2015) 539 [1407.5668].

[214] C. Alcock and B. Paczynski, *An evolution free test for non-zero cosmological constant*, *Nature* **281** (1979) 358.

[215] F. Rizzo, C. Moretti, K. Pardede, A. Eggemeier, A. Oddo, E. Sefusatti et al., *The Halo Bispectrum Multipoles in Redshift Space*, 2204.13628.

[216] V. Mossa et al., *The baryon density of the Universe from an improved rate of deuterium burning*, *Nature* **587** (2020) 210.

[217] G. D'Amico, L. Senatore, P. Zhang and T. Nishimichi, *Taming redshift-space distortion effects in the EFTofLSS and its application to data*, 2110.00016.

[218] T. Brinckmann and J. Lesgourgues, *MontePython 3: boosted MCMC sampler and other features*, 1804.07261.

[219] A. Gelman and D.B. Rubin, *Inference from Iterative Simulation Using Multiple Sequences*, *Statist. Sci.* **7** (1992) 457.

[220] A. Lewis, *GetDist: a Python package for analysing Monte Carlo samples*, 1910.13970.

[221] K. Pardede, F. Rizzo, M. Biagetti, E. Castorina, E. Sefusatti and P. Monaco, *Bispectrum-window convolution via Hankel transform*, 2203.04174.

[222] DESI collaboration, *The DESI Experiment Part I: Science,Targeting, and Survey Design*, 1611.00036.

[223] D.J. Schlegel et al., *The MegaMapper: A Stage-5 Spectroscopic Instrument Concept for the Study of Inflation and Dark Energy*, 2209.04322.

[224] D.J.H. Chung, M. Münchmeyer and S.C. Tadepalli, *Search for Isocurvature with Large-scale Structure: A Forecast for Euclid and MegaMapper using EFTofLSS*, 2306.09456.

[225] T. Kajita, *Nobel Lecture: Discovery of atmospheric neutrino oscillations*, *Rev. Mod. Phys.* **88** (2016) 030501.

[226] R. Bousso, D. Harlow and L. Senatore, *Inflation after False Vacuum Decay: observational Prospects after Planck*, *Phys. Rev. D* **91** (2015) 083527 [1309.4060].

[227] M. Kleban and M. Schillo, *Spatial Curvature Falsifies Eternal Inflation*, *JCAP* **06** (2012) 029 [1202.5037].

[228] G. Cabass, M.M. Ivanov, O.H.E. Philcox, M. Simonovic and M. Zaldarriaga, *Constraining single-field inflation with MegaMapper*, *Phys. Lett. B* **841** (2023) 137912 [2211.14899].

[229] R. Flauger, M. Mirbabayi, L. Senatore and E. Silverstein, *Productive Interactions: heavy particles and non-Gaussianity*, *JCAP* **10** (2017) 058 [1606.00513].

[230] G. D'Amico, Y. Donath, M. Lewandowski, L. Senatore and P. Zhang, *The boss bispectrum analysis at one loop from the effective field theory of large-scale structure*, 2022.

[231] M. Tegmark, *Measuring cosmological parameters with galaxy surveys*, *Phys. Rev. Lett.* **79** (1997) 3806 [astro-ph/9706198].

[232] N. Agarwal, V. Desjacques, D. Jeong and F. Schmidt, *Information content in the redshift-space galaxy power spectrum and bispectrum*, *JCAP* **03** (2021) 021 [2007.04340].

[233] V. Yankelevich and C. Porciani, *Cosmological information in the redshift-space bispectrum*, *Mon. Not. Roy. Astron. Soc.* **483** (2019) 2078 [1807.07076].

[234] D. Baumann, D. Green and B. Wallisch, *Searching for light relics with large-scale structure*, *JCAP* **08** (2018) 029 [1712.08067].

[235] K.C. Chan and L. Blot, *Assessment of the Information Content of the Power Spectrum and Bispectrum*, *Phys. Rev. D* **96** (2017) 023528 [1610.06585].

[236] E. Sefusatti, M. Crocce, S. Pueblas and R. Scoccimarro, *Cosmology and the Bispectrum*, *Phys. Rev. D* **74** (2006) 023522 [astro-ph/0604505].

[237] S. Ferraro et al., *Inflation and Dark Energy from Spectroscopy at $z > 2$*, *Bull. Am. Astron. Soc.* **51** (2019) 72 [1903.09208].

[238] N. Kokron, J. DeRose, S.-F. Chen, M. White and R.H. Wechsler, *Priors on red galaxy stochasticity from hybrid effective field theory*, *Mon. Not. Roy. Astron. Soc.* **514** (2022) 2198 [2112.00012].

[239] T. Baldauf, U. Seljak and L. Senatore, *Primordial non-Gaussianity in the Bispectrum of the Halo Density Field*, *JCAP* **04** (2011) 006 [1011.1513].

[240] T. Steele and T. Baldauf, *Precise Calibration of the One-Loop Trispectrum in the Effective Field Theory of Large Scale Structure*, *Phys. Rev. D* **103** (2021) 103518 [2101.10289].

[241] L. Gao, V. Springel and S.D.M. White, *The Age dependence of halo clustering*, *Mon. Not. Roy. Astron. Soc.* **363** (2005) L66 [astro-ph/0506510].

[242] D.J. Croton, L. Gao and S.D.M. White, *Halo assembly bias and its effects on galaxy clustering*, *Mon. Not. Roy. Astron. Soc.* **374** (2007) 1303 [astro-ph/0605636].

[243] Y.-Y. Mao, A.R. Zentner and R.H. Wechsler, *Beyond Assembly Bias: Exploring Secondary Halo Biases for Cluster-size Haloes*, *Mon. Not. Roy. Astron. Soc.* **474** (2018) 5143 [1705.03888].

[244] P. Coles, *Galaxy formation with a local bias*, *Mon. Not. Roy. Astron. Soc.* **262** (1993) 1065.

[245] J.N. Fry and E. Gaztanaga, *Biasing and hierarchical statistics in large scale structure*, *Astrophys. J.* **413** (1993) 447 [astro-ph/9302009].

[246] S.M. Carroll, S. Leichenauer and J. Pollack, *Consistent effective theory of long-wavelength cosmological perturbations*, *Phys. Rev.* **D90** (2014) 023518 [1310.2920].

[247] G. Camelio and M. Lombardi, *On the origin of intrinsic alignment in cosmic shear measurements: an analytic argument*, *Astron. Astrophys.* **575** (2015) A113 [1501.03014].

[248] Z. Vlah, N.E. Chisari and F. Schmidt, *An EFT description of galaxy intrinsic alignments*, *JCAP* **01** (2020) 025 [1910.08085].

[249] P. Catelan, M. Kamionkowski and R.D. Blandford, *Intrinsic and extrinsic galaxy alignment*, *Mon. Not. Roy. Astron. Soc.* **320** (2001) L7 [astro-ph/0005470].

[250] C.M. Hirata and U. Seljak, *Intrinsic alignment-lensing interference as a contaminant of cosmic shear*, *Phys. Rev. D* **70** (2004) 063526 [astro-ph/0406275].

[251] D.M. Schmitz, C.M. Hirata, J. Blazek and E. Krause, *Time evolution of intrinsic alignments of galaxies*, *JCAP* **07** (2018) 030 [1805.02649].

[252] J.N. Fry, *The Evolution of Bias*, *Astrophys. J. Lett.* **461** (1996) L65.

[253] M. Tegmark and P.J.E. Peebles, *The Time evolution of bias*, *Astrophys. J. Lett.* **500** (1998) L79 [astro-ph/9804067].

[254] F. Schmidt, *An n-th order Lagrangian Forward Model for Large-Scale Structure*, *JCAP* **04** (2021) 033 [2012.09837].

[255] F. Schmidt, *Sigma-Eight at the Percent Level: The EFT Likelihood in Real Space*, *JCAP* **04** (2021) 032 [2009.14176].

[256] O.H.E. Philcox, B.D. Sherwin, G.S. Farren and E.J. Baxter, *Determining the Hubble Constant without the Sound Horizon: Measurements from Galaxy Surveys*, *Phys. Rev. D* **103** (2021) 023538 [2008.08084].

[257] M.M. Ivanov, M. Simonović and M. Zaldarriaga, *Cosmological Parameters and Neutrino Masses from the Final Planck and Full-Shape BOSS Data*, *Phys. Rev. D* **101** (2020) 083504 [1912.08208].

[258] A. Chudaykin, K. Dolgikh and M.M. Ivanov, *Constraints on the curvature of the Universe and dynamical dark energy from the Full-shape and BAO data*, *Phys. Rev. D* **103** (2021) 023507 [2009.10106].

[259] P. Creminelli, G. D'Amico, J. Norena, L. Senatore and F. Vernizzi, *Spherical collapse in quintessence models with zero speed of sound*, *JCAP* **1003** (2010) 027 [0911.2701].

[260] E. Sefusatti and F. Vernizzi, *Cosmological structure formation with clustering quintessence*, *JCAP* **1103** (2011) 047 [1101.1026].

[261] G. D'Amico and E. Sefusatti, *The nonlinear power spectrum in clustering quintessence cosmologies*, *JCAP* **1111** (2011) 013 [1106.0314].

[262] S. Anselmi, G. Ballesteros and M. Pietroni, *Non-linear dark energy clustering*, *JCAP* **11** (2011) 014 [1106.0834].

[263] S. Anselmi, D. López Nacir and E. Sefusatti, *Nonlinear effects of dark energy clustering beyond the acoustic scales*, *JCAP* **07** (2014) 013 [1402.4269].

[264] M. Lewandowski, A. Maleknejad and L. Senatore, *An effective description of dark matter and dark energy in the mildly non-linear regime*, *JCAP* **1705** (2017) 038 [1611.07966].

[265] M. Lewandowski and L. Senatore, *IR-safe and UV-safe integrands in the EFTofLSS with exact time dependence*, *JCAP* **1708** (2017) 037 [1701.07012].

[266] G. Cusin, M. Lewandowski and F. Vernizzi, *Dark Energy and Modified Gravity in the Effective Field Theory of Large-Scale Structure*, *JCAP* **1804** (2018) 005 [1712.02783].

[267] B. Bose, K. Koyama, M. Lewandowski, F. Vernizzi and H.A. Winther, *Towards Precision Constraints on Gravity with the Effective Field Theory of Large-Scale Structure*, *JCAP* **1804** (2018) 063 [1802.01566].

[268] J.M. Cline, S. Jeon and G.D. Moore, *The Phantom menaced: Constraints on low-energy effective ghosts*, *Phys. Rev. D* **70** (2004) 043543 [hep-ph/0311312].

[269] H. Gil-Marín et al., *The clustering of galaxies in the SDSS-III Baryon Oscillation Spectroscopic Survey: BAO measurement from the LOS-dependent power spectrum of DR12 BOSS galaxies*, *Mon. Not. Roy. Astron. Soc.* **460** (2016) 4210 [1509.06373].

[270] F. Beutler, C. Blake, M. Colless, D.H. Jones, L. Staveley-Smith, L. Campbell et al., *The 6dF Galaxy Survey: Baryon Acoustic Oscillations and the Local Hubble Constant*, *Mon. Not. Roy. Astron. Soc.* **416** (2011) 3017 [1106.3366].

[271] A.J. Ross, L. Samushia, C. Howlett, W.J. Percival, A. Burden and M. Manera, *The clustering of the SDSS DR7 main Galaxy sample – I. A 4 per cent distance measure at $z = 0.15$*, *Mon. Not. Roy. Astron. Soc.* **449** (2015) 835 [1409.3242].

[272] V. de Sainte Agathe et al., *Baryon acoustic oscillations at $z = 2.34$ from the correlations of Lyα absorption in eBOSS DR14*, *Astron. Astrophys.* **629** (2019) A85 [1904.03400].

[273] M. Blomqvist et al., *Baryon acoustic oscillations from the cross-correlation of Lyα absorption and quasars in eBOSS DR14*, *Astron. Astrophys.* **629** (2019) A86 [1904.03430].

[274] D.M. Scolnic et al., *The Complete Light-curve Sample of Spectroscopically Confirmed SNe Ia from Pan-STARRS1 and Cosmological Constraints from the Combined Pantheon Sample*, *Astrophys. J.* **859** (2018) 101 [1710.00845].

[275] Planck collaboration, *Planck 2018 results. VI. Cosmological parameters*, 1807.06209.

[276] T. Fujita and Z. Vlah, *Perturbative description of biased tracers using consistency relations of LSS*, *JCAP* **10** (2020) 059 [2003.10114].

[277] C. Hahn, R. Scoccimarro, M.R. Blanton, J.L. Tinker and S.A. Rodriguez-Torres, *The effect of fibre collisions on the galaxy power spectrum multipoles*, *Mon. Not. Roy. Astron. Soc.* **467** (2017) 1940 [1609.01714].

[278] R.J. Cooke, M. Pettini and C.C. Steidel, *One Percent Determination of the Primordial Deuterium Abundance*, *Astrophys. J.* **855** (2018) 102 [1710.11129].

[279] D. Blas, J. Lesgourgues and T. Tram, *The cosmic linear anisotropy solving system (CLASS). part II: Approximation schemes*, *Journal of Cosmology and Astroparticle Physics* **2011** (2011) 034.

[280] B. Audren, J. Lesgourgues, K. Benabed and S. Prunet, *Conservative Constraints on Early Cosmology: an illustration of the Monte Python cosmological parameter inference code*, *JCAP* **1302** (2013) 001 [1210.7183].

[281] M. Fasiello and Z. Vlah, *Nonlinear fields in generalized cosmologies*, *Phys. Rev.* **D94** (2016) 063516 [1604.04612].

[282] M. Simonovic, T. Baldauf, M. Zaldarriaga, J.J. Carrasco and J.A. Kollmeier, *Cosmological perturbation theory using the FFTLog: formalism and connection to QFT loop integrals*, *JCAP* **1804** (2018) 030 [1708.08130].

[283] BOSS collaboration, *The clustering of galaxies in the completed SDSS-III Baryon Oscillation Spectroscopic Survey: Anisotropic galaxy clustering in Fourier-space*, *Mon. Not. Roy. Astron. Soc.* **466** (2017) 2242 [1607.03150].

[284] A. Font-Ribera, P. McDonald, N. Mostek, B.A. Reid, H.-J. Seo and A. Slosar, *DESI and other dark energy experiments in the era of neutrino mass measurements*, *JCAP* **05** (2014) 023 [1308.4164].